

JSR A

E-ISSN: 2687-6167

NUMBER 54

SEPTEMBER 2023

JOURNAL OF SCIENTIFIC REPORTS A



Kütahya Dumlupınar University Scientific Reports A
Fulya Çelebi Campus, Tınazlı Road, 10 km. 43270 Kütahya

Phone : (0274) 443 19 42

E-mail : journals@gmail.com
jsra.com

Dumlupınar University Press

gate of
science

Kütahya Dumlupınar University
Institute of Graduate Studies



Journal of Scientific
Reports-A

E-ISSN: 2687-6167

Number 54, September 2023

Owner

On Behalf of Kütahya Dumlupınar University
Prof. Dr. Süleyman KIZILTOPRAK (Rector),
On Behalf of Institute of Graduate Studies
Assoc. Prof. Dr. Eray ACAR (Director)

Editorial Board

Prof. Dr. Önder UYSAL
Prof. Dr. Fatih ŞEN
Prof. Dr. Cemal PARLAK
Prof. Dr. Oktay ŞAHBAZ
Assoc. Prof. Nevzat BEYAZIT
Assoc. Prof. Onur KARAMAN
Assoc. Prof. Cafer ÖZKUL
Assoc. Prof. Levent URTEKİN
Assoc. Prof. Durmuş ÖZDEMİR
Assist. Prof. Ümrhan ERÇETİN
Dr. Ceren KARAMAN

Kütahya Dumlupınar University/ Mining Engineering
Kütahya Dumlupınar University / Biochemistry
Ege University / Physics
Kütahya Dumlupınar University/ Mining Engineering
Ondokuz Mayıs University / Environmental Eng
Akdeniz University / Medical Services and Tech
Kütahya Dumlupınar University / Geological Eng.
Ahi Evran University / Mechanical Eng.
Kütahya Dumlupınar University / Computer Eng.
Kütahya Dumlupınar University / Mechanical Eng.
Akdeniz University / Electrical and Energy

Journal of Scientific Reports-A started its publication life in 2000 as name of Journal of Science and Technology of Dumlupınar University and is a national peer-reviewed journal published regularly twice a year in June and December. The language of the journal is English. Articles submitted to the journal are evaluated by at least two referees who are experts in the subject and selected by the editorial board. All articles submitted to the journal are evaluated by the double-blind method. Articles submitted to our journal for review should not be previously published, accepted for publication and in the process of being evaluated for publication in another journal. All responsibility for the articles published in the journal belongs to the author(s).

The journal aims to share scientific studies carried out in the fields of science and engineering at national and international level with scientists and the public. Original research articles, review articles and short notes in science and engineering disciplines are accepted for the journal. Original research articles are expected to contain theoretical and experimental results and should not be published in other journals. In the review articles, it is expected that scientific, technological and current developments on a specific subject are reflected by using an extensive bibliography and made a satisfying evaluation of these. Short notes should be brief writings prepared to announce the first findings of an original study.

Editorial Policy

The journal is open access and the article evaluation period is between 1-2 months.

Correspondence Address: Kütahya Dumlupınar Üniversitesi Evliya Çelebi Yerleşkesi Fen Bilimleri Enstitüsü
43270 KÜTAHYA

E-mail: joursra@gmail.com

Phone: 0 274 443 19 42

Webpage: gsjsra.com

Fax: 0 274 265 20 60

Section Editors

Civil Engineering Prof. Dr. M. Çağatay KARABÖRK	Kütahya Dumlupınar University
Mechanical Engineering Prof. Dr. Ramazan KÖSE	Kütahya Dumlupınar University
Electrical-Electronics Engineering Assist. Prof. Kadir VARDAR	Kütahya Dumlupınar University
Computer Engineering Assoc. Prof. Doğan AYDIN	Kütahya Dumlupınar University
Industrial Engineering Assist. Prof. Üyesi Kerem CİDDİ	Kütahya Dumlupınar University
Mining Engineering Assist. Prof. Uğur DEMİR	Kütahya Dumlupınar University
Geology Engineering Assist. Prof. Muzaffer ÖZBURAN	Kütahya Dumlupınar University
Metallurgical and Materials Engineering Prof. Dr. İskender IŞIK	Kütahya Dumlupınar University
Food Engineering Prof. Dr. Muhammet DÖNMEZ	Kütahya Dumlupınar University
Environmental Engineering Assoc. Prof. Dr. Nevzat BEYAZIT	Ondokuz Mayıs University
Mathematics Assist. Prof. Cansu KESKİN	Kütahya Dumlupınar University
Physics Assoc. Prof. Huriye Sanem AYDOĞU	Kütahya Dumlupınar University
Chemistry Assoc. Prof. Bülent ZEYBEK	Kütahya Dumlupınar University
Biology Assist. Prof. Nüket Akalın BİNGÖL	Kütahya Dumlupınar University
Biochemistry Assoc. Prof. Derya KOYUNCU ZEYBEK	Kütahya Dumlupınar University
Occupational Health and Safety Prof. Dr. Cem ŞENSÖĞÜT	Kütahya Dumlupınar University
Software Engineering Assist. Prof. Şerif Ali SADIK	Kütahya Dumlupınar University

Advisory Board

Prof. Dr. Sibel AKAR	Eskişehir Osmangazi University / Chemistry
Prof. Dr. Abdurrahman AKTÜMSEK	Selçuk University/ Bialogy
Prof. Dr. Mustafa ALTUNOK	Gazi University / Tree-Jobs Industrial Engineering
Prof. Dr. Uğur ARİFOĞLU	Sakarya University / Electirical and Electr. Engineering
Prof. Dr. Oktay ARSLAN	Balıkesir University / Chemistry
Prof. Dr. Şükrü ASLAN	Sivas Cumhuriyet University / Enviromental Engineering
Prof. Dr. Ülfet ATAV	Selçuk University / Pyhsics
Prof. Dr. Mustafa BAYRAKTAR	TOBB Ekonomi ve Teknoloji University / Mathamathics
Prof. Dr. Niyazi BİLİM	Konya Technical University / Mining Engineering
Prof. Dr. İsmail BOZTOSUN	Akdeniz University / Pyhsics
Prof. Dr. Erdal ÇELİK	Dokuz Eylül University / Metalurgical and Material Eng.
Prof. Dr. Hayri DAYIOĞLU	Kütahya Dumlupınar University / Bialogy
Prof. Dr. Muhammet DÖNMEZ	Kütahya Dumlupınar University / Food Engineering
Prof. Dr. Mehmet Ali EBEOĞLU	Kütahya Dumlupınar University / Elec.and Electr. Eng.
Prof. Dr. İsmail Göktay EDİZ	Kütahya Dumlupınar University / Mining Engineering
Prof. Dr. İsmail EKİNCİOĞLU	Kütahya Dumlupınar University / Mathematics
Prof. Dr. Kaan ERARSLAN	Kütahya Dumlupınar University / Mining Engineering
Prof. Dr. Zeynal Abiddin ERGÜLER	Kütahya Dumlupınar University / Geological Eng.
Prof. Dr. Seyhan FIRAT	Gazi University / Civil Engineering
Prof. Dr. Remzi GÖREN	Sakarya University / Metalurgical and Material Eng.
Prof. Dr. Rasim İPEK	Ege University / Mechanical Engineering
Prof. Dr. Refail KASIMBEYLİ	Eskişehir Technical University / Industrial Engineering
Prof. Dr. Hamdi Şükür KILIÇ	Selçuk University / Physics
Prof. Dr. Yaşar KİBİCİ	Bilecik Şeyh Edebali University / Geological Eng.
Prof. Dr. İsmail KOCAÇALIŞKAN	Yıldız Technical University / Molecular Bio. and Gen.
Prof. Dr. Mahmut KOÇAK	Eskişehir Osmangazi University / Math-Computer
Prof. Dr. Muhsin KONUK	Üsküdar University / Molecular Biology and Gen.
Prof. Dr. Mustafa KURU	Başkent University / Molecular Biology and Gen.
Prof. Dr. Ömer İrfan KÜFREVİOĞLU	Atatürk University / Biochemistry
Prof. Dr. Halim MUTLU	Ankara University / Geological Engineering
Prof. Dr. Ekrem SAVAŞ	İstanbul Ticaret University / Mathematics
Prof. Dr. Murat TANIŞLI	Eskişehir Technical University / Physics
Prof. Dr. Ali Rehber TÜRKER	Gazi University / Chemistry
Prof. Dr. Mustafa TÜRKMEN	Giresun University / Biology
Prof. Dr. Abdülmecit TÜRÜT	İstanbul Medeniyet University / Physics Engineering
Prof. Dr. Eşref ÜNLÜOĞLU	Eskişehir Osmangazi University / Civil Engineering
Prof. Dr. Nurettin YAYLI	Karadeniz Technical University / Pharmacy
Prof. Dr. Yusuf YAYLI	Ankara University / Mathematics
Prof. Dr. Elçin YUSUFOĞLU	Uşak University / Mathematics
Prof. Dr. Hüseyin Serdar YÜCESU	Gazi University / Automotive Engineering
Prof. Dr. Mehmet Tevfik ZEYREK	Middle East Technical University / Pyhsics

JOURNAL OF SCIENTIFIC REPORTS-A
E-ISSN: 2687-6167

CONTENTS

RESEARCH ARTICLES

- Evaluating the Robustness of Yolo Object Detection Algorithm in Terms of Detecting Objects in Noisy Environment* 1-25
Halit BAKIR*, Rezan BAKIR
- Detection of Exon and Intron Regions in Dna Sequences by the Proposed Hashing Function* 26-41
Fatma AKALIN*, Nejat YUMUŞAK
- Analysis and Clinical Evaluation of Muscle Dynamics in Adolescents with Sagittal Plane Deformity* 42-61
Kadir GÖK, Ela Naz GÖK*, KAdriye TOMBAK, Nehir SAMANCI KARAMAN, Ömer Halil ÇOLAK
- Altered Numbers of Lucas Number Squared* 62-75
Fikri KÖKEN*, Emre KANKAL
- Alamouti Space-Time Coding for Vehicular Communications in the Presence of Channel Estimation Errors* 76-93
Serdar Özgür ATA*
- Effects of Wind Speed and Mounting Type on Pv Module in Unbalanced Distribution Systems* 94-107
Salman Ahmed NUR*, Selçuk EMİROĞLU
- Detection and Characterization of Some Glaze Faults Encountered in Sanitarywares* 108-124
Eray ÇAŞIN, Nihal DERİN COŞKUN*, C. Eren IŞIK
- Experimental Thermal Performance Analysis of Nanofluid Assisted Slinky Ground Heat Exchanger in Space Cooling Application* 125-135
Abdullah KAPICIOĞLU*, Tahsin YÜKSEL
- Influence of Ti Microalloying on Zamak-5* 136-148
Melih KOÇYİĞİT, H. Erdem ÇAMURLU*
- Antibacterial, Antifungal, Antibiofilm, Antioxidant, and Anticancer Properties of Methanol Extracts of Some Acantholimon Boiss (Plumbaginaceae) Species* 149-163
Maside Temiz BOSTANCI, Ali Savaş BULBUL, Cihangir UYGUN, Muhammed

BEKMEZCİ, Ramazan BAYAT, Fatih ŞEN*	
<i>The Effect of Quercetin on Some Hematological Parameters Against Bisphenol-A Exposure in Streptozocin-Induced Rats</i>	164-175
Yılmaz KOÇAK*, Gökhan OTO, Seray ALPARSLAN	
<i>Numerical Modeling of Backward-Facing Step Flow via Computational Fluid Dynamics</i>	176-193
İlker GÖKTEPELİ*, Ulaş ATMACA	
<i>Evaluation of the Monitoring of Surface Deformations in Open-Pit Mines with Sentinel-1A Satellite Radar Data</i>	194-211
Bekir POYRAZ*, Yavuz GÜL, Fatih POYRAZ	
<i>Investigation of Mechanical Properties of Al 7075 Alloy Solidified under Vibration</i>	212-223
Mustafa GÜLMEZ, Ağah Ayğahoğlu*	
<i>Energy-Population Evaluation and Projection of Kütahya Province</i>	224-238
Oğuz Ozan YOLCAN*, Ramazan KÖSE	
<i>Valorization of Turkish Coffee Waste as a Biodiesel Feedstock</i>	239-250
Ayşe Hilal ULUKARDEŞLER*	
<i>Investigation of Recently Abused Drugs in Dried Blood Spots Using Fta Cards by Liquid Chromatography Tandem Mass Spectrometry: Validation and Application to Real Samples</i>	251-263
Yeter EROL ÖZTÜRK*	
<i>Antimicrobial Activity of Proton Salts of 3-(Sulfamoylphenylcarbamoyl)Acrylic Acid Derivatives with Aminopyridine Derivatives</i>	264-272
Halil İLKİMEN*, Cengiz YENİKAYA, Aysel GÜLBANDILAR	
<i>The First Light Curve Analysis of V1010 Cas Using Ground-Based and Tess Data</i>	273-284
Neslihan ALAN*	
<i>Enrichment of Sivas/Gemerek Lignite Coal by Oil Agglomeration Using Different Vegetable Oils</i>	285-295
Özlem KAYA*, Neriman TAŞDÖĞEN CEBE	
<i>Classification of Brain Tumors with Deep Learning Models</i>	296-306
Beyza Nur TÜZÜN*, Durmuş ÖZDEMİR	
<i>Effects of Cyanide on Some Enzyme Activities and Lipid Peroxidation in Some Tissues of Carp (Cyprinus carpio)</i>	307-321
Mustafa KAVASOĞLU*, Kazım UYSAL	

<i>Attainable Sets of Integral Constrained Seir Control System with Nonlinear Incidence</i>	322-337
Ali S. NAZLIPINAR*, Farideh MOHAMMADIMEHR	
<i>In Vitro Evaluation of Antioxidant and Cytotoxic Activities on Human Cervical Cancer Cells in Three Different Plant Extracts from Turkey</i>	338-352
Funda ULUSU*	
<i>Effect of Temperature on the Protein Profile of Macrovipera Lebetinus (Blunt-Nosed Viper) Venom: A Preliminary Study</i>	353-363
Naşit İĞCİ*	
<i>Characterization of Mortality Prediction: An Ensemble Learning Analysis Using the Mimic-Iii Dataset</i>	364-384
Anıl Burcu ÖZYURT SERİM*	



RESEARCH ARTICLE

**EVALUATING THE ROBUSTNESS OF YOLO OBJECT DETECTION ALGORITHM IN
TERMS OF DETECTING OBJECTS IN NOISY ENVIRONMENT**

Halit BAKIR^{1*}, Rezan BAKIR²

¹Sivas University of Science and Technology, Faculty of Engineering and Natural Sciences, Department of Computer Engineering , Sivas, Turkey, halit.bakir@sivas.edu.tr, ORCID: 0000-0003-3327-2822

²Sivas University of Science and Technology, Faculty of Engineering and Natural Sciences, Department of Computer Engineering , Sivas, Turkey, rezan.bakir@sivas.edu.tr, ORCID: 0000-0002-4373-2231

Receive Date: 27.02.2023

Accepted Date: 24.04.2023

ABSTRACT

Our daily lives are impacted by object detection in many ways, such as automobile driving, traffic control, medical fields, etc. Over the past few years, deep learning techniques have been widely used for object detection. Several powerful models have been developed over the past decade for this purpose. The YOLO architecture is one of the most important cutting-edge approaches to object detection. Researchers have used YOLO in their object detection tasks and obtained promising results. Since the YOLO algorithm can be used as an object detector in critical domains, it should provide a quite high accuracy both in noisy and noise-free environments. Consequently, in this study, we aim to carry out an experimental study to test the robustness of the YOLO v5 object detection algorithm when applied to noisy environments. To this end, four case studies have been conducted to evaluate this algorithm's ability to detect objects in noisy images. Specifically, four datasets have been created by injecting an original quality image dataset with different ratios of Gaussian noise. The YOLO v5 algorithm has been trained and tested using the original high-quality dataset. Then, the trained YOLO algorithm has been tested using the created noisy image datasets to monitor the changes in its performance in proportion to the injected Gaussian noise ratio. To our knowledge, this type of performance evaluation study did not conduct before in the literature. Furthermore, there are no such noisy image datasets have been shared before for conducting these types of studies. The obtained results showed that the YOLO algorithm failed to handle the noisy images efficiently besides degrading its performance in proportion to noise rates.

Keywords: *Deep learning, Image processing, YOLO, Object detection, Gaussian noise.*

1. INTRODUCTION

Technology has a life cycle just like humans. Every new technology is born, develops, and becomes a raw material for another technology. Deep learning and image processing have become the raw material of every technology today. The use of image processing and deep learning techniques has

gained importance in many fields such as medicine, the defense industry, astronomy, geology, etc. One area that has attained great progress in the last years is object detection. Object detection is a computer vision technique that generally utilizes machine learning or deep learning techniques for determining the location and scale of all object instances in images or videos. Nowadays, object detection has entered numerous fields, and its applications have varied, from identity detection and self-driving cars to security and medical uses. Object detection is considered a challenging problem due to various potential reasons such as the limited amount of annotated data, class imbalance, and so on.

Evaluating object detection algorithms in a noisy environment presents unique challenges and considerations. In a noisy environment, various sources of noise, such as sensor limitations, low lighting conditions, or environmental interferences, can significantly impact the performance of object detection algorithms. When evaluating these algorithms in such conditions, it becomes crucial to assess their robustness and reliability in accurately detecting and localizing objects amidst the noise. Evaluating object detection algorithms in a noisy environment typically involves analyzing their performance metrics, such as detection accuracy, localization precision, and false positive rates, while considering the specific noise characteristics and their potential effects on algorithm performance. Furthermore, researchers often employ specialized datasets or introduce synthetic noise to simulate realistic scenarios and assess the algorithms' ability to handle noise-induced challenges. The evaluation process helps in understanding the algorithm's performance limitations, guiding improvements, and facilitating the development of more noise-robust object detection systems.

This study focuses on evaluating the widely recognized YOLO object detection algorithm in various environments with different levels of noise. Specifically, our assessment involves examining the algorithm's performance in detecting objects within images that have been subjected to progressively increasing amounts of Gaussian noise.

1.1. Motivation and Contribution

Many successful deep learning architectures such as Yolo, VGG-19, ResNet, Inception, Xception, and MobileNet are used for detecting and recognizing objects in images. However, distortions may occur while acquiring images because of various sources. In other words, noises like electrical interference, poor lighting, and gaussian noise may lessen the quality of the image. In such situations, deep learning architectures that detect or classify objects rapidly and accurately in clear images may fail (i.e. in noisy images). On the other hand, as it's known, the information obtained in some critical fields such as the defense industry, radar systems, medicine, etc. should have zero or close to zero error rates. And since the images acquired in such domains do not always have a high quality due to the environmental conditions. Therefore, there is an urgent need for adaptive models that can be used in more than one domain and that can minimize the error rate when detecting objects in both noisy and noise-free images. With the advent of the YOLO algorithm, several applications have employed YOLO for object detection and recognition in various fields and the obtained results were encouraging, but in most cases, this algorithm has been trained and tested using high-quality images. This motivates us to conduct a specific study to evaluate YOLO robustness in detecting objects in noisy environments. A dataset consisting of 40 classes was used in this study to evaluate the object detection performance of the YOLO algorithm. YOLO was first evaluated using the original dataset's

high-quality images. Then four datasets have been created by injecting noise gradually into the original images. To the best of our knowledge, this type of dataset has not been publicly shared before in the literature. YOLO's detection performance is evaluated using the suggested and constructed datasets. The literature has not previously addressed this type of performance evaluation study to the best of our knowledge. Furthermore, doing such a study can help researchers realize the maximum rate of distortion at which the model can produce results whether it is good or bad results.

1.2. Research question

Verifying whether YOLO is good model for general object detection or not, and whether YOLO algorithm could be used as end-to-end model for conducting object detection task in critical systems.

The rest of the paper is organized as follows. Section 2 includes the related studies. Section 3 describes the used methodologies. Section 4 presents experimental results. Section 5 includes conclusion and future works.

2. RELATED WORKS

Due to the rapid technological change during the last years there has been a rapid and successful expansion of computer vision research. One area that has attained great advancement is object detection. Object detection is a fundamental task required by most computer vision systems. Researchers in the last years have made a great effort to make considerable progress in various directions in order to conduct a robust object detection algorithms and approaches. For example, some of the studies adopted machine learning methods [1] while others tried to develop new representations and models for specific computer vision problems or tried to develop efficient existing solutions [1–7]. As an instance, in [1] study, a new algorithm was proposed for visually salient object detection, then it was utilized to extract salient objects to be used for training the machine learning-based object detection part of the proposed system.

A lot of researchers recently have utilized deep learning algorithms in the domain of computer vision, especially in image classification and object detection. For example, Bakır et.al in their study[8], proposed CNN and ANN based approaches for diagnosing and detecting lung diseases. In another study [9], a ResNet deep learning architecture was employed to classify the malaria parasite effectively. Authors in [10] study proposed several deep learning architectures such as VGG-16, ResNet, and Inception v3 in order to extract features to be used in detecting cataract disease from retinal fundus images. On the other hand, in [11] study, an approach utilizing deep learning was introduced to detect objects by analyzing images captured by an unmanned aerial vehicle's (UAV) onboard camera during an autonomous flight trajectory. Subsequently, an algorithm was devised to autonomously guide the UAV to land in close proximity to the detected object.

The object detection algorithms are classified into two main categories: Single-stage models and multi-stage models. For example, in the two-stage models like R-CNN [12], the initial model is employed to identify object regions, while the subsequent model is utilized to classify the objects and further enhance the precision of their localization. As a result, learn the localization and classification stage separately makes this method relatively slow. SPP-Net [13] and Fast R-CNN [14] presented the

concept of region-wise feature extraction. Proposing to use spatial pyramid pooling (SPP), SPP-net can generate a fixed-length representation regardless of image size/scale [13]. On the other hand, Fast R-CNN utilizes various methods (such as using region of interest (RoI) pooling layer) to improve training and testing speed while boosting detection accuracy. Later, in Faster R-CNN [15] approach, a Region Proposal Network (RPN) was introduced to generate region proposals with minimal computational overhead. This was achieved by sharing convolutional features from the full image with the detection network.

In the single-stage approach, a fixed number of predictions is made on the grid which means the model can directly predict object bounding boxes for an image. The most famous single-stage models are You Only Look Once (YOLO) [16], YOLO v2 [17], YOLO v3 [18], YOLO v4 [19], and SSD: Single Shot MultiBox Detector [20]. Broadly speaking, research in the field of object detection can be categorized into two primary streams: conventional methods for object detection and detection methods based on deep learning techniques. Traditional object detection methods are built on handmade features and shallow trainable architecture, such as in [21–31]. However, these types of methods can easily fail to handle complex combinations of low-quality images beside being inaccurate, relatively slow with low performance on unfamiliar dataset [32]. With the rapid development in deep learning, more robust architectures have been introduced to address the problems present in traditional methods such as [31, 33–35].

There are few studies on object detection or classification in a noisy environment. As an example, Nayan, Al-Akhir, et al in their article [36] proposed a new low-cost technique for error-free object recognition in noisy images. In the study, a comprehensive experimental evaluation with conventional detectors retrained on noisy images is presented, taking advantage of the Single Shot MultiBox Detector SSD. In another study, Kushagra Yadav et al. [37] proposed a new method to reduce the effect of noise on the image object detection task. The proposed method consisted of two stages. In the first stage, Residual Dense Network (RDN) was used to reduce noise from the low-quality image, and in the second stage, the standard Single-Shot Multibox object detector was adopted to complete the object detection process. Furthermore, the proposed model is tested using Gaussian noise images. and the proposed approach is evaluated in the Pascal Visual Object Classes comparison. Moreover, Milyaev, S., and I. Laptev [38] proposed a new, low-cost method for image noise removal by considering object detection in noisy images. The proposed method is based on combining the standard Deformable Parts Model and Regions with Convolutional Neural Network object detectors. The proposed method is compared with other noise removal techniques as well as with standard detectors retrained on noisy images. In Elena Medvedeva's work [39], an improved method is proposed to detect moving objects in distorted images caused by white Gaussian noise. Including two stages, the proposed method represents the video sequence through a three-dimensional discrete Markov process. The first stage is the filtering of three-dimensional non-linear images, which allows objects' contours to be preserved. The second stage involves identifying objects of interest based on their boundaries and luminosity.

On the other hand, for detecting objects in noisy environments, J. F. Que et al. [40] proposed a Yolov3-based method. In particular, the YOLO v3 algorithm is used to create an LSS object detection system that can adapt to environmental noise. Multiple experiments were performed on both noisy and

noiseless datasets, and it is stated that the proposed method improves object detection accuracy in noisy environments. Geonsoo Lee et al. [41] proposed a Feature Enhancement Network (FEN) to deal with noise in small object detection. The authors presented a self-monitoring approach to training SEN without any labels. They also noted that the proposed approach can be seamlessly combined with a variety of off-the-shelf object detectors. Maheep Singh et al. [42] propose a new Distinctive Object Detection (SOD) technique in noisy environments using a convolutional neural network (CNN). Denoising the image is achieved using CNN, which uses coordinate descent to modulate the signal. Gaussian noise and white noise were tested in the study and the performance of the proposed V-SIN technique was evaluated on two publicly available image datasets with different evaluation metrics. Aditya Gautam and Mantosh Biswas [43] adopted Whale Optimization Algorithm (WOA) for edge detection in Gaussian noise images. According to them, experimental results showed that the proposed technique outperformed conventional edge detectors and the considered technique.

Furthermore, the YOLO is accepted as one of the most important and accurate object detection algorithms that has been used in a wide range of applications. For example, in [44] a YOLOv5 was utilized to detect the bacterial spot disease in the bell pepper plants from the symptoms seen on the leaves. As we can see from related works, the suggested performance evaluation study has not been previously addressed in the literature which encourages us to conduct such a study to provide insight into YOLOv5's performance in detecting objects in noisy environments. In [45], YOLO-SA which is a YOLO landslide detection model is proposed in order to improve the speed, accuracy, and parameters of landslide detection models. In [46], channel pruned YOLO v4 has been adopted for apple flower real-time detection. In [47], YOLO-Tomato, a YOLO based model has been proposed for handling the challenges of fruit detection. In [48], YOLO-face, a YOLO v3 based model has been proposed for improving the performance of face detection.

When we looked at the literature it can be concluded that the YOLO algorithm has accepted as an accurate algorithm which can be used in multiple domains such as agriculture and biomedical. The images that have been used in most of the literature works is high-quality images and the YOLO algorithm has been used as an end-to-end model without any pre-processing phase. So, this work aims at investigating the robustness of the YOLO algorithm in detecting objects in low-quality or noisy images. This type of investigation works is very important to shed the light on the acceptable amount of distortion or noise to save the performance of these types of models. To this end, we proposed to inject the Gaussian noise gradually into an image dataset and monitor the performance of this algorithm i.e. YOLO algorithm. The results showed that when the noise amount was 25% the performance of the YOLO algorithm did not be affected so much and it was still at an acceptable rate. On the other hand, the performance of YOLO started dropping significantly. The performance of YOLO became very bad when the amount of injected Gaussian noise reached 100%.

3. MATERIAL AND METHOD

In general, digital images became an important part of modern systems including airplanes, aircraft, autonomic systems, and medical systems. The images collected in such systems are not high quality in most cases. This is related to the fact that the quality of images degrades due to the existence of noise. Image noise is a random variation of brightness or color information. The noise can occur due to

different reasons such as electricity, heat, and sensor illumination levels. The noise in images can be manifest in different formats. we will briefly discuss the most important of it in the following section.

3.1. Types of Noise

Noise in images refers to unwanted random variations or distortions that affect the visual quality of a picture. It can appear as graininess, speckles, or artifacts, and is primarily caused by factors such as sensor limitations, low-light conditions, or compression algorithms. Noise can reduce the clarity, sharpness, and overall fidelity of an image, impacting its visual appeal and potentially hindering the interpretation of important details. To enhance image quality, various techniques like denoising algorithms and post-processing methods are employed to minimize or remove noise while preserving the essential information and maintaining a balance between noise reduction and image sharpness. There are several types of image noise: Gaussian Noise, Impulse Noise, Salt and Pepper Noise, Speckle Noise, and Poisson Noise.

3.1.1. Gaussian noise

Gaussian noise or Random noise (also called electronic noise) is statistical noise having values distributed in a normal Gaussian. The noise is created by adding a Gaussian function to the image. The type of noise is very similar to nature's noise types, thus this type of noise has been adopted in the present study to evaluate the robustness of the YOLO algorithm. The noise's values are Gaussian-distributed. In the case of a Gaussian random variable Z , the probability density function P can be expressed as in Eq. 1.

$$PG(z) = \frac{1}{\sigma\sqrt{2\pi}} e^{-\frac{(z-\mu)^2}{2\sigma^2}} \quad (1)$$

Where Z represents the grey level, μ the mean grey value and σ its standard deviation.

3.1.2. Impulse noise

Impulse noise is a type of random noise that affects digital images. It manifests as isolated pixels with significantly higher or lower intensity values compared to their neighboring pixels, resembling white and black specks. Impulse noise can occur due to various factors, such as transmission errors in digital communication, faults in image sensors, or data corruption during storage or processing. It can degrade image quality, introduce visual artifacts, and adversely impact subsequent image analysis tasks. Denoising techniques specifically designed to handle impulse noise are commonly employed to mitigate its effects and restore the clarity and integrity of the image. There are three main types of impulse noise. Salt Noise, Pepper Noise, Salt and Pepper Noise. Salt noise can be generated by adding random bright values to the image. Pepper noise can be generated by adding random dark values to the image. Bright values and dark values are produced by adding 255-pixel values and zero-pixel values, respectively.

3.1.3. Salt and pepper noise

This type of noise is a combination of salt and pepper noise. It can be injected into an image by adding both random bright and random dark values all over the image. The Salt & Pepper noise values can

range from 0 to 255. Pepper noise tends to have an intensity value close to 0, while salt noise tends to have an intensity value close to 255. See in Eq. 2.

$$\eta(x,y) = \begin{cases} 0, & \text{pepper noise} \\ 255, & \text{salt noise} \end{cases} \quad (2)$$

3.1.4. Poisson noise

Poisson noise, also known as photon noise or shot noise, is a type of statistical noise that commonly occurs in digital imaging systems, particularly in low-light conditions. It is caused by the inherent randomness associated with the detection of light particles (photons) by an image sensor. Poisson noise follows a Poisson distribution and is characterized by variations in the number of photons detected at each pixel, resulting in random fluctuations in pixel intensity. In images, Poisson noise appears as a granular pattern with slight intensity variations across the scene. It is more pronounced in darker regions where fewer photons are detected. Denoising techniques designed to handle Poisson noise typically involve statistical modeling and estimation to reduce the noise while preserving image details and avoiding excessive smoothing. These techniques are commonly used in applications such as astrophotography, medical imaging, and scientific imaging where low-light conditions are prevalent. A nonlinear response of image detectors and recorders causes this type of noise, known as quantum noise or shot noise. For a random variable $X \geq 0$ the Poisson noise can be dictated using in Eq. 3.

$$P_{Y|X}(y|x) = 1/y! (ax + y)e^{y-(ax+y)}, x \geq 0, y = 0,1, \dots \quad (3)$$

$\alpha > 0$: scaling factor, and $\lambda \geq 0$: the dark current parameter.

As a result, input random variable X is transformed into output random variable Y , which is indicated by Y as in in Eq. 4.

$$Y = P(aX + y) \quad (4)$$

3.1.5. Speckle noise

Speckle noise is a type of granular noise that commonly affects images acquired through coherent imaging systems such as ultrasound, synthetic aperture radar (SAR), and laser imaging. It arises from the interference patterns created by the constructive and destructive interference of coherent waves within the imaging system. Speckle noise appears as a grainy pattern with random variations in intensity, resulting in a speckled or textured appearance in images. It can obscure fine details, reduce contrast, and degrade the overall quality of the image. Denoising techniques for speckle noise often involve the use of filters, statistical models, or advanced algorithms specifically designed to reduce the noise while preserving important image structures and details. These techniques play a crucial role in enhancing the visual quality and interpretability of images acquired through coherent imaging systems. Speckle noise is a multiplicative noise that takes place in low-level luminance images such as Magnetic Resonance Image (MRI) images. This type of noise can be produced by multiplying random pixel values with different pixels of an image. Speckle noise can be modeled as in in Eq. 5.

$$g(m, n) = f(m, n)u(m, n) + \eta(m, n) \quad (5)$$

Where $g(m, n)$ point to a corrupted image matrix at the spatial position (m, n) ; $u(m, n)$ and $\eta(m, n)$ stand for the multiplicative and additive component of the noise, respectively; and f is the original image. Figure 1, illustrate an image injected with different types of noises.

Denoising techniques are utilized to reduce or eliminate noise from images, enhancing their visual quality and improving the accuracy of subsequent analysis. Various approaches are employed to tackle noise, such as spatial filtering, statistical methods, and machine learning algorithms. Spatial filtering methods, including median filtering and Gaussian filtering, work by replacing each pixel's value with a filtered value based on its neighboring pixels. Statistical methods, such as wavelet denoising or total variation denoising, exploit the statistical properties of noise to remove its presence while preserving image details. Machine learning-based techniques employ deep neural networks trained on large datasets to learn the noise patterns and perform denoising effectively. These techniques play a vital role in restoring image fidelity and enhancing the overall visual appeal of images in various domains, including photography, medical imaging, and computer vision. We intend to assess the efficacy of these denoising techniques in our forthcoming research endeavors, as their evaluation falls beyond the scope of the present paper.

3.2. Object Detection

Object detection is a fundamental task in computer vision that involves identifying and localizing objects of interest within an image or a video sequence. It plays a crucial role in various applications, such as autonomous driving, surveillance, and augmented reality. Object detection algorithms aim to automatically detect and classify objects in images, often using deep learning techniques. One popular approach is the region-based convolutional neural network (R-CNN) family of algorithms, which generate region proposals and then classify them using a convolutional neural network (CNN). Another widely used algorithm is the You Only Look Once (YOLO) model, which divides the input image into a grid and predicts bounding boxes and class probabilities directly from the grid cells. Other notable algorithms include Single Shot MultiBox Detector (SSD) and Faster R-CNN, which improve on speed and accuracy. These algorithms have significantly advanced the field of object detection, enabling robust and efficient detection of objects in various real-world scenarios. So, in this study, we will evaluate the performance of the well-known YOLOv5 in terms of detecting objects in noisy environments. Therefore, we will briefly talk about this algorithm in the next sub-section.

3.2.1. YOLOv5

Proposed by Redmond et. al YOLO (You Only Look Once) is one of the most common real-time object detection algorithms. The algorithm depends on dividing images into a grid system. Each cell in the grid is responsible for detecting objects within itself. The YOLO model solves object detection as a regression problem instead of a classification problem by directly predicting the image pixels as objects and its bounding box attributes [49]. Therefore, the YOLO algorithm uses bounding box regression to predict the center, height, width, and class of each object. Moreover, this algorithm uses the Intersection over union (IOU) concept to select the bounding boxes that fit the objects in the image as perfectly as possible, in this way the algorithm can prevent detecting the object more than one time.

After the invention of the YOLO algorithm, a multiple version of this algorithm has been proposed and developed such as YOLOv2 [17] and YOLOv3 [18], and YOLO v4 [19]. Each version of YOLO has been proposed for solving specific problem in the previous versions and improving the detection accuracy of the original YOLO algorithm. For example, in YOLO v2, it has been proposed to use batch normalization operation in the YOLO algorithm, which improves the performance of YOLO and solves the problem of detection of small objects. Also, in YOLO v3, it has been proposed to use the logic of residual neural networks (especially skip connections) in YOLO algorithm, which improved the performance of YOLO significantly compared with YOLO v2. In 2020, Glenn Jocher introduced YOLOv5 using the Pytorch framework. The algorithm is pre-trained on the MS COCO dataset. YOLOv5 is considered one of the authorized cutting-edge models with outstanding support and is convenient to use in production. All the versions of YOLO algorithm have been adopted in diverse applications mainly due to their faster inferences, high detection accuracy, and better generalization besides being open source.

Since YOLO is one of the state-of-the-art object detection algorithms used in a huge number of previously deep learning-based science studies, and since this algorithm has been introduced as one of the most advanced object detection algorithms that can be used in multiple domains and can achieve an outperforming performance, in this work we proposed to test the robustness of YOLO algorithms with low-quality images and see how its performance can be affected if the environment contains some type of noise.

3.3. Used and Created Datasets

Military Aircraft detection dataset has been utilized in this study. The dataset consists of images related to 43 different types of aircraft. Particularly, the dataset contains objects related to 43 different classes her object has been labelled with a bounding box in PASCAL VOC format. The original dataset contains 10658 different labelled images. The original dataset can be founded and downloaded from Kaggle repository [50]. In order to evaluate the robustness of the YOLO algorithm against Gaussian noise we propose to inject this noise gradually into the images in the original dataset and monitor how the performance of YOLO will be affected. The Gaussian noise has been added into the images using the formulas Eq.6 and Eq.7.

$$\text{noise} = \text{np.random.normal}(\text{loc} = 0, \text{scale} = 1, \text{size} = \text{image.shape}) \quad (6)$$

$$\text{noisyImage} = \text{image} + \text{noise} * \text{noiseRate} \quad (7)$$

In particular, in the first case study, we proposed creating a Gaussian noise matrix, multiplying it by 0.3 (noiseRate=0.3), and adding it to the original images' pixels. In the second case study, we proposed creating a Gaussian matrix, multiplying it by 0.5 (noiseRate=0.5), and adding it to the original images' pixels. In the third case study, we proposed creating a Gaussian matrix, multiplying it by 0.8 (noiseRate=0.8), and adding it to the original images' pixels. In the fourth case study, we proposed creating a Gaussian matrix, multiplying it by 1 (noiseRate=1), and adding it to the original images' pixels. Accordingly, in this way, we can control the proportion of noise that will be added to images, and we can create four different noisy image datasets from the original dataset namely 30%-Gaussian-Dataset, 50%-Gaussian-Dataset, 80%-Gaussian-Dataset, and 100%-Gaussian-Dataset. The

created datasets will be available on demand. To the best of our knowledge, this is the first time that these types of datasets are constructed and made available for future works. Algorithm 1, illustrates the Pseudocode of the Python script used for injecting the noise and creating the proposed noisy datasets. Figure 2 illustrate an example of image injected with different proportions of gaussian noise.



Figure 1. Example images injected with different types of noise.

a. Original image, **b.** Gaussian noisy image, **c.** Salt&paper noisy image, **d.** Speckle noisy image, **e.** Poisson noisy image.

3.4. Proposed Test Bed

In order to test the YOLO model in detecting noisy images we have to create a noisy image dataset with different noise rates. To this end, as explained in the previous section, we injected images with different Gaussian noise proportions. Then we applied YOLO to detect objects within created image datasets besides the original dataset to evaluate the overall performance. Figure 3 shows the block diagram of the conducted experiment. As can be seen in Figure 3 the test bed mainly consists of two phases. In the first phase, the original dataset was split into a training dataset utilized to train the YOLO model and a testing dataset used to evaluate the detection performance of the trained YOLO model. Thus, in the first phase, we trained and tested the YOLO v5 algorithm in order to evaluate its detection accuracy when the used image dataset contains high-quality images. Afterward, we saved the weights trained by the algorithm to be used to detect objects from the same images but after injecting some level of noise into them. Particularly, the second phase is composed of four different case studies as follows:

3.4.1. Case study 1

In this case study, we proposed to inject a very small amount of gaussian noise into the images. Particularly, we proposed to inject only 30% of gaussian noise into each image in the dataset. After that, we used the trained YOLO algorithm in order to investigate if YOLO algorithm can detect the object from the images with the same accuracy achieved on the original image dataset.

3.4.2. Case study 2

In this case study, we increased the amount of injected noise slightly to 50% and tested the performance of the trained YOLO algorithm in terms of detecting objects in these mild noise-contained images.

Algorithm 1. Algorithm used for constructing noisy image dataset.

```

Input: Image_dataset
Output: Noisy_image_dataset

For img in Image_dataset:
Image = read_Image_file(img)
Image = reScale_image_pizels(image)
#creating noise matrix with same shape of the original image
noise = np.random.normal(loc = 0, scale = 1, size = Image.shape)
noisy_image = np.clip((img + noise * noise_proportion),0,1)
Noisy_image_dataset ← image_saver(noisy_image)

```

Table 1. dataset description.

Number of classes	Number of objects	Number of images
43	17145	10658

3.4.3. Case study 3

In this case study, we increased the amount of noise to 80%, and again tried to detect the objects from the images using the trained YOLO algorithm.

3.4.4. Case study 4

In this case study, the injected amount of gaussian noise has been increased to 100%, and the trained YOLO algorithm has been applied to detect the objects from these fully obfuscated images.

In brief, in the second phase, we injected the original images with different gaussian noise rates to create four different datasets. Then we applied YOLO trained model to the created noisy image datasets.

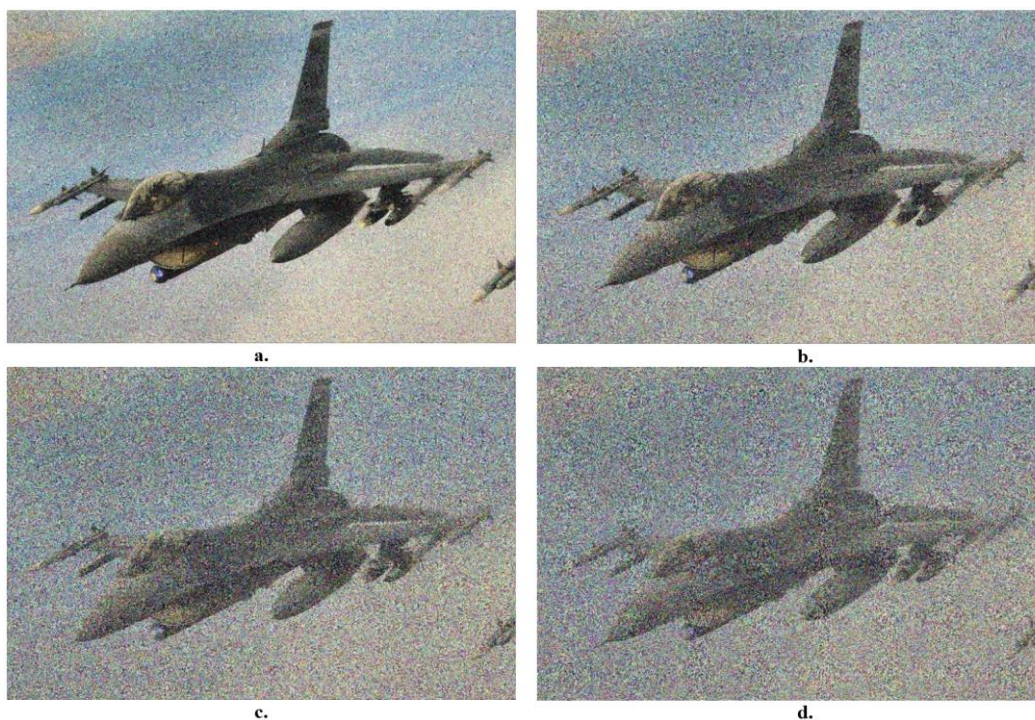


Figure 2. Example of an image injected with different proportions of noise.
a. Gaussian 30%, **b.** Gaussian 50%, **c.** Gaussian 80%, **d.** Gaussian 100%.

4. EXPERIMENTAL RESULTS

All the experimental studies have been conducted using Python programming language over Google-colab free GPU. Multiple python libraries and frameworks have been used during conducting this study such as Keras, Tensorflow, Open-CV, etc.

4.1. Evaluation Metrics

To evaluate the robustness of YOLOv5 in different noisy environments we utilized different standard evaluation metrics such as confusion matrix, Recall, Precision, F1-score, and mAP (mean Average Precision), but we only displayed F1-score and mAP in the results since it is enough to summarize the tradeoff of both Recall and Precision metrics and gives us a better idea of the overall accuracy of the model.

4.1.1. Confusion matrix

A confusion matrix is a table that defines how well a classification algorithm performs. Confusion matrixes consist of four components as can be seen in Figure 3.

4.1.2. True Positives (TP)

The model predicted a label correctly, which means the actual value matched the predicted value.

4.1.3. True Negatives (TN)

The model does not predict the label correctly; the actual value is negative while the predicted value is positive.

4.1.4. False Positives (FP)

The actual value is negative but the predicted value is positive.

4.1.5. False Negatives (FN)

The actual value is positive but the predicted value is negative.

4.1.6. Accuracy

This metric is calculated using Eq.8.

$$Acc = \frac{(TP + TN)}{(TP+TN+PF+FN)} \tag{8}$$

		Actual Class	
		1	0
Predicted Class	1	True Positive	False Positive
	0	False Negative	True Negative

Figure 3. confusion matrix.

4.1.7. Precision

This metric is calculated using Eq.9.

$$P = \frac{TP}{(TP+FP)} \tag{9}$$

4.1.8. Recall

This metric is calculated using Eq.10.

$$R = \frac{TP}{(TP+FN)} \tag{10}$$

4.1.9. F1-score

This metric is calculated using Eq.11.

$$F = 2 * \frac{(R*p)}{(R+p)} \quad (11)$$

4.1.10. mean Average Precision (mAP)

This metric is calculated using Eq.12.

$$mAP = \frac{1}{N} \sum_{i=1}^N AP_i \quad (12)$$

As it can clearly be seen from the results in Figure 4 the YOLO approved its efficiency for detecting objects from high-quality images relevant to the original dataset. Particularly, the average value of mAP reached 73.5% and the average value of F1 score values reached 69%, which denotes a great success in detecting objects in high quality images. After that, we tested the YOLO algorithms using the constructed four noisy image datasets. we saw that the YOLO algorithm obtained good results when tested in a noise-free environment. However, when adding noise to the images, the YOLO model showed a gradually decreasing in performance in a proportion to the amount of injected noise. For example, it can be noted from Figure 5 the big degrading in mAP score, where it decreased from 73.5% when applied to the original dataset to 48.6%, 35.6%,24.4 %, and 23.5 % when applied to detect the objects from the same images after injecting gaussian noise with 30%, 50%, 80%, and 100% proportions respectively. Moreover, Figure 6 illustrates the F1-score curve obtained when the trained YOLO algorithm has been applied for detecting objects from the created four noisy image datasets. We can note from the Figure that the average F1-score value degraded from 69% when the trained YOLO algorithm has been used for detecting objects from the original image dataset to 48%, 34%, 23%, and 21% obtained when the YOLO-trained algorithm adopted for detecting the objects from the same image but after injecting gaussian noise with 30%, 50%, 80%, and 100% proportions respectively. Moreover, Figure 7 illustrates some detection examples obtained by applying YOLO to the original dataset. We can see from the figure that the trained YOLO algorithm could detect all the objects in the image except one object, and almost all the detected labels were true.

Then when we have applied the YOLO algorithm on the 30% Gaussian-Dataset and 50% Gaussian-Dataset as can be seen in Figure 8, we can note from the figure that the number of undetected objects increased gradually based on the amount of the injected Gaussian noise, where the YOLO algorithm cannot detect 12 objects from the 30%-Gaussian images and 22 objects from 50%-Gaussian images. Also, we can note from the figure that almost all the labels of the detected objects have been defined wrongly by the YOLO algorithm.

By increasing the amount of noise injected into the original images the performance of YOLO continued to drop down as we can see from Figure 9, where the number of undetected objects reached 38 and 45 when the injected Gaussian noise proportion was 80% and 100% respectively.

5. CONCLUSION AND FUTURE WORKS

Object detection is a major task in most computer vision problems. It is typically working to identify and locate objects within an image. YOLO is one of the state-of-the-art algorithms highly used recently in various object detection tasks. The object detection forms the main task in different critical and real time systems such as aircraft goal tracking systems, radar systems, biomedical systems, and so on. And since the images collected in these systems cannot always be in the same quality as the images used for testing it, therefore, in this study, we made various experiments for testing the performance and the robustness of the YOLO detection algorithm in a noisy environment. To this end, we have trained and tested YOLO v5 algorithm using different noisy image datasets.

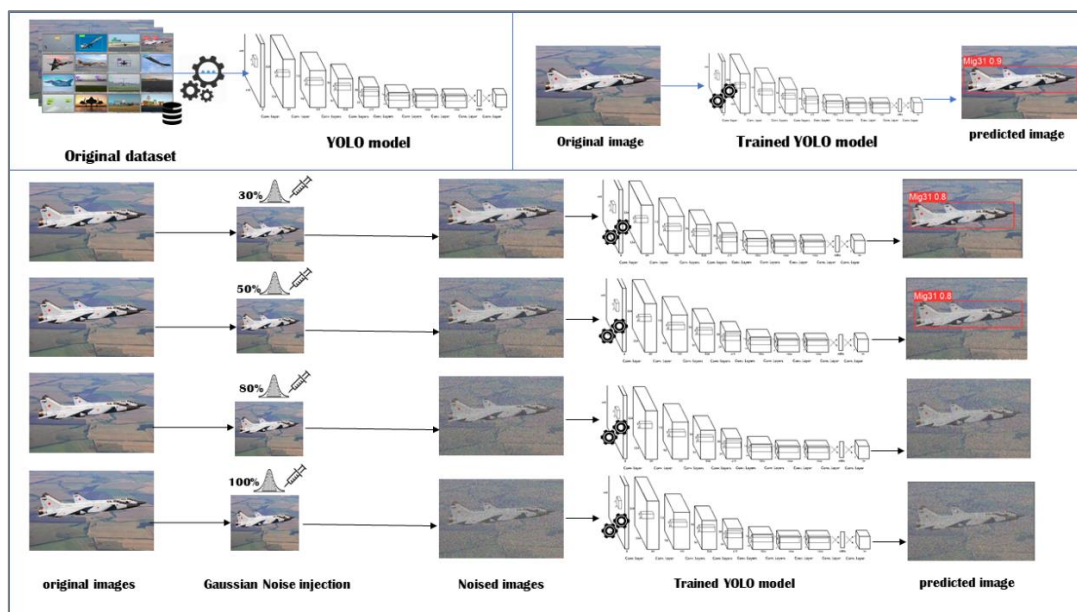


Figure 3. The block diagram of the conducted evaluation experiment.

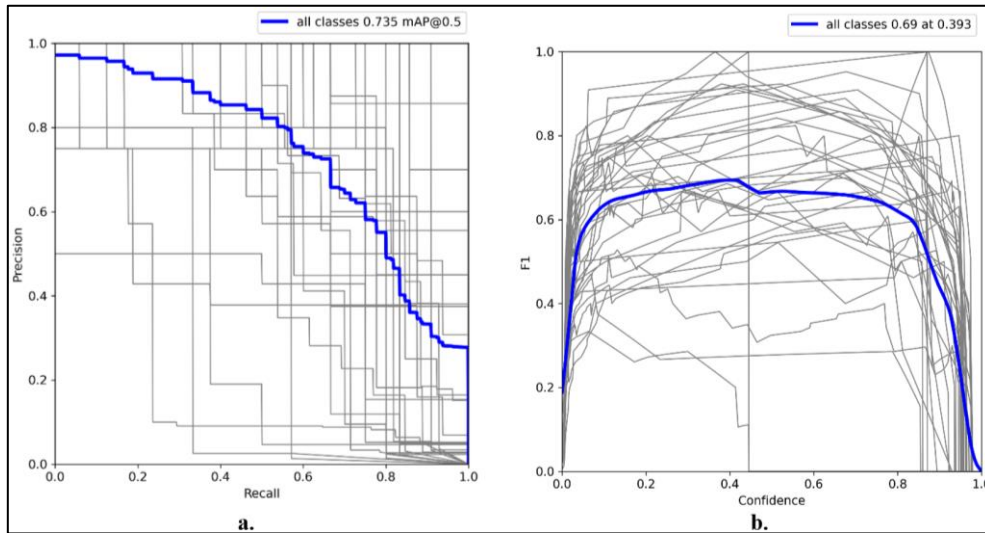


Figure 4. Test results on original dataset. (a. mAP, b. F1 Score).

Particularly, a test bed has been proposed to test the YOLO algorithm using four different noisy image datasets containing various proportions of gaussian noises. We proposed to inject 30% of gaussian noise into the original image dataset in order to create the first noisy image dataset. After that, we proposed injecting 50% of gaussian noise in order to create the second noisy image dataset. Then, we proposed injecting 75% of gaussian noise into the original image dataset in order to construct the third noisy image dataset, and finally, the fourth noisy image dataset has been constructed by injecting 100% of gaussian noise into the images in the original dataset.

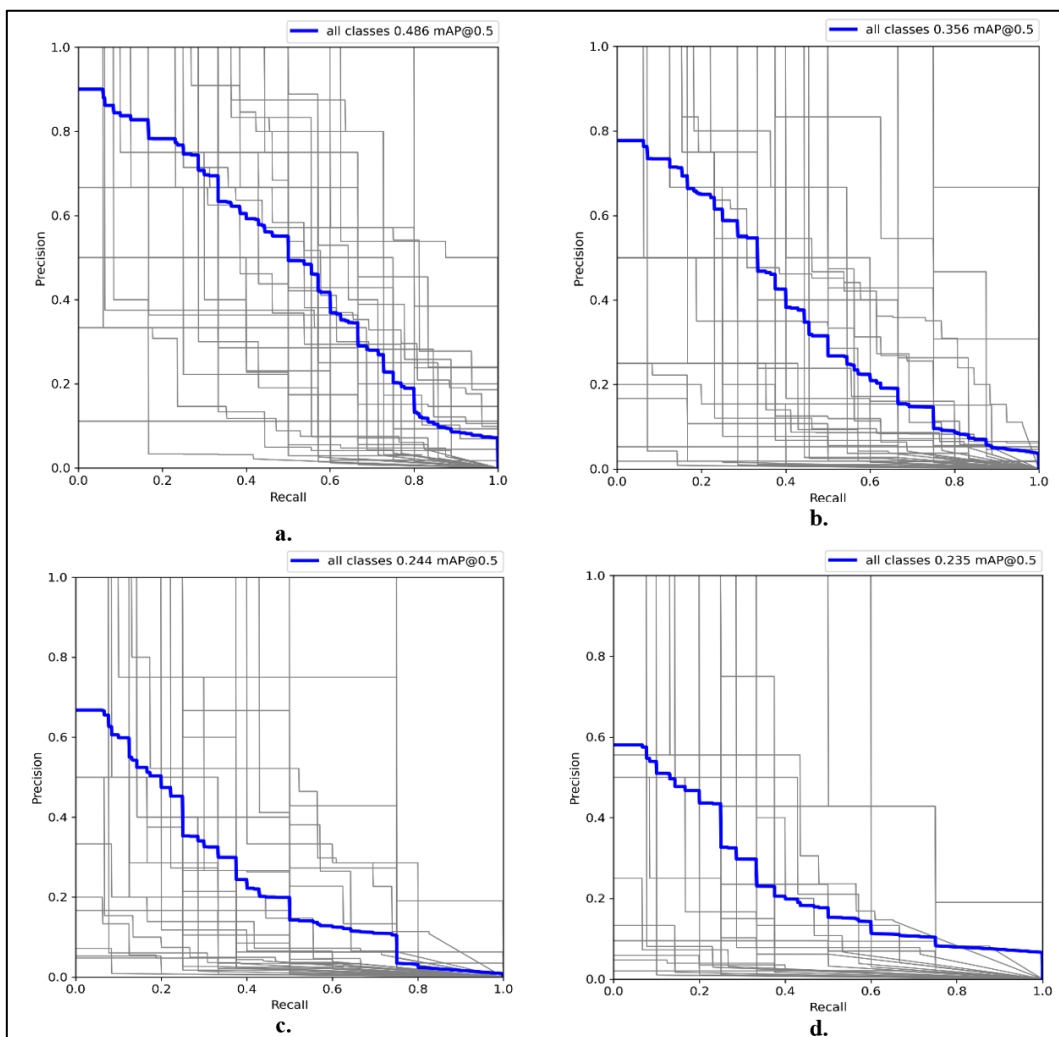


Figure 5. mAP results obtained by applying YOLO on noisy datasets.
a. 30% noise, **b.** 50% noise, **c.** 80% noise, **d.** 100% noise.

The obtained results using four proposed datasets showed that the YOLO model failed to handle noisy images efficiently, while the mAP score reached 73.5% when the trained YOLO v5 algorithm has been tested based on the original image dataset, this score dropped down to 48.6%, 35.6%, 24.4 %, and 23.5 % when applied to detect the objects from the same images after injecting gaussian noise with 30%, 50%, 80%, and 100% proportions respectively. Furthermore, the F1-score of the YOLO v5 algorithm was 69% when used for detected objects in the original image dataset compared with 48%, 34%, 23%, and 21% obtained when the YOLO-trained algorithm was adopted for detecting the

objects from the same image but after injecting gaussian noise with 30%, 50%, 80%, and 100% proportions respectively. Also, the results showed that the performance of the YOLO algorithm was still at an acceptable rate when the amount of injected noise was 30%. Also, the results showed that when the amount of injected noise reached 50% the performance of YOLO dropped significantly. The results were very bad when the amount of the injected noise reached 100%, where most of the objects could not be detected by YOLO, and the detected objects were detected incorrectly.

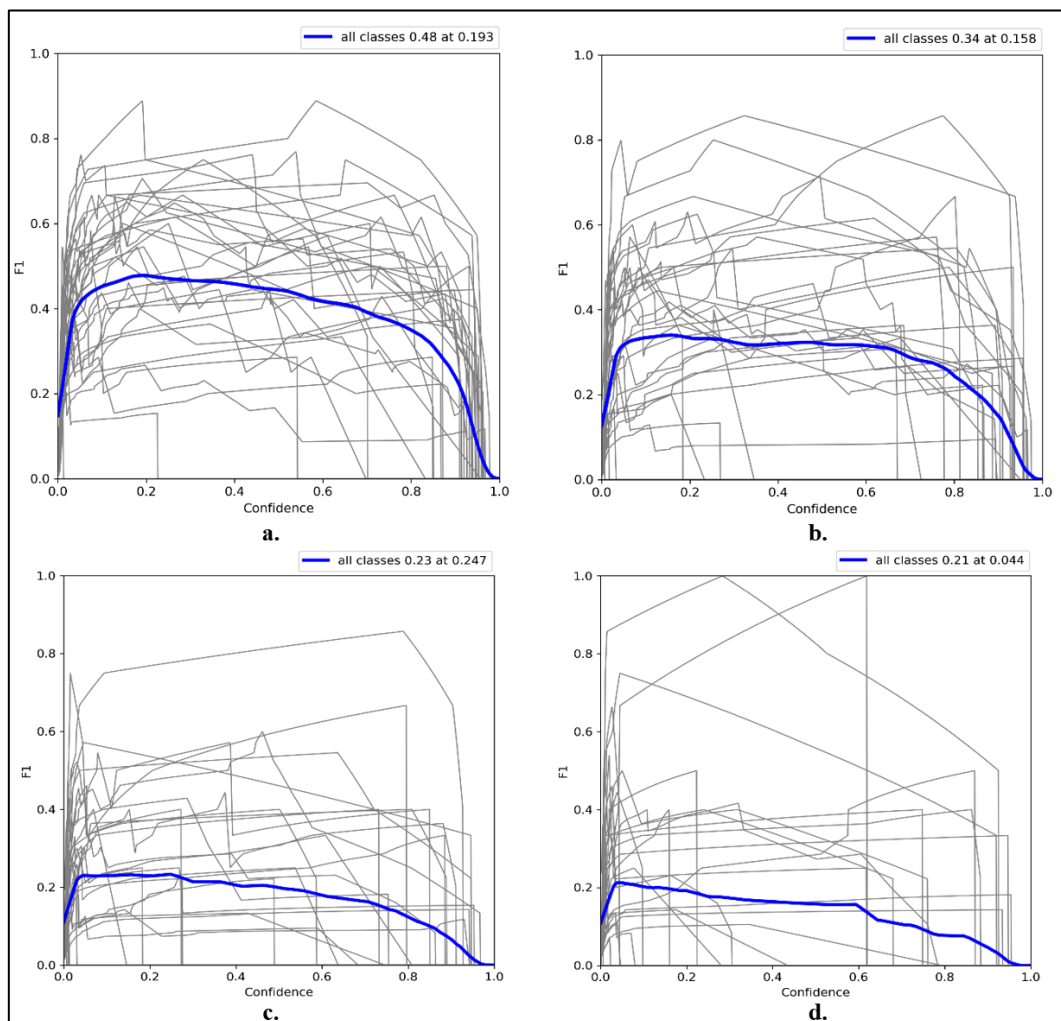


Figure 6. F1 score results obtained by applying YOLO on noisy datasets.
a. 30% noise, b. 50% noise, c. 80% noise, d. 100% noise.



Figure 7. Examples of the YOLO detection on the original images.



Figure 8. Examples of the YOLO detection on the 30%-Gaussian-Dataset and 50% Gaussian-Dataset.
a. 30% noise, b. 50% noise.



Figure 9. Examples of the YOLO detection on the 80% Gaussian-Dataset and 100% Gaussian-Dataset. **a.** 80% noise, **b.** 100% noise.

It can be concluded from this study that the well-known object detection algorithms can fail in detecting objects in real-life systems. Therefore, in order to make an efficient object detection in noisy environments there is an urgent need to add a co-model that can be utilized to denoising and processing images before handling them by these types of algorithms. In future works, we will try to propose and test some co-models that can be used alongside these types of algorithms in order to improve their performance such that they can detect objects both in noisy and noise-free environments. Several approaches can be utilized to improve the performance of the model such as fine-tuning auto-encoder models in order to obtain as clear version of the image as possible before handling it using the object detection architectures.

ACKNOWLEDGEMENT

This work has been supported by the Scientific Research Projects Coordination Unit of the Sivas University of Science and Technology. Project Number: 2023-GENL-Müh-0007.

CONFLICT OF INTEREST

The authors declare that they have no conflict of interest.

REFERENCES

- [1] Ramík, D.M., Sabourin, C., Moreno, R., and Madani, K. (2014). A machine learning based intelligent vision system for autonomous object detection and recognition. *Applied Intelligence*. 40, 358–375.
- [2] Nallasivam, M., and Senniappan, V. (2021). Moving human target detection and tracking in video frames. *Studies in informatics and control*. 30, 119–129.
- [3] Erhan, D., Szegedy, C., Toshev, A., and Anguelov, D. (2014). Scalable object detection using deep neural networks. In *Proceedings of the IEEE conference on computer vision and pattern recognition* (pp. 2147-2154).
- [4] Han, F., Liu, B., Zhu, J. and Zhang, B. (2019). Algorithm design for edge detection of high-speed moving target image under noisy environment. *Sensors*, 19(2), p.343.
- [5] Razakarivony, S., and Jurie, F. (2016). Vehicle detection in aerial imagery: A small target detection benchmark. *J Vis Commun Image Represent*. 34, 187–203.
- [6] Wang, Z., Du, L., Mao, J., Liu, B., and Yang, D. (2019). SAR target detection based on SSD with data augmentation and transfer learning. *IEEE Geoscience and Remote Sensing Letters*. 16, 150–154.
- [7] Xu, Q., Peng, J., Shen, J., Tang, H., and Pan, G. (2020). Deep CovDenseSNN: A hierarchical event-driven dynamic framework with spiking neurons in noisy environment. *Neural Networks*. 121, 512–519.
- [8] Bakır, H., Oktay, S., and Tabaru, E. (2023). Detection of pneumonia from x-ray images using deep learning techniques. *Journal of Scientific Reports-A*. 419–440.
- [9] Akgül, İ. and and Volkan, K.A.Y.A. (2022). Classification of cells infected with the malaria parasite with ResNet architectures. *Journal of Scientific Reports-A*, (048), pp.42-54.

- [10] Bakır, H. and Yılmaz, Ş. (2022). Using transfer learning technique as a feature extraction phase for diagnosis of cataract disease in the eye. *International Journal of Sivas University of Science and Technology*, 1(1), pp.17-33.
- [11] Tekin, S., Murat, G.O.K., Namdar, M. and Başgümüş, A. (2022). Autonomous guidance system for UAVs with image processing techniques. *Journal of Scientific Reports-A*, (051), pp.149-159.
- [12] Girshick, R., Donahue, J., Darrell, T. and Malik, J. (2014). Rich feature hierarchies for accurate object detection and semantic segmentation. In *Proceedings of the IEEE conference on computer vision and pattern recognition* (pp. 580-587).
- [13] He, K., Zhang, X., Ren, S. and Sun, J. (2015). Spatial pyramid pooling in deep convolutional networks for visual recognition. *IEEE transactions on pattern analysis and machine intelligence*, 37(9), pp.1904-1916.
- [14] Girshick, R. (2015). Fast r-cnn. In *Proceedings of the IEEE international conference on computer vision* (pp. 1440-1448).
- [15] Ren, S., He, K., Girshick, R. and Sun, J. (2015). Faster r-cnn: Towards real-time object detection with region proposal networks. *Advances in neural information processing systems*, 28.
- [16] Redmon, J., Divvala, S., Girshick, R. and Farhadi, A. (2016). You only look once: Unified, real-time object detection. In *Proceedings of the IEEE conference on computer vision and pattern recognition* (pp. 779-788).
- [17] Redmon, J. and Farhadi, A. (2017). YOLO9000: better, faster, stronger. In *Proceedings of the IEEE conference on computer vision and pattern recognition* (pp. 7263-7271).
- [18] Redmon, J. and Farhadi, A. (2018). Yolov3: An incremental improvement. *arXiv preprint arXiv:1804.02767*.
- [19] Bochkovskiy, A., Wang, C.Y. and Liao, H.Y.M. (2020). Yolov4: Optimal speed and accuracy of object detection. *arXiv preprint arXiv:2004.10934*.
- [20] Liu, W., Anguelov, D., Erhan, D., Szegedy, C., Reed, S., Fu, C.Y. and Berg, A.C. (2016). SSD: Single shot multibox detector. In *Computer Vision–ECCV 2016: 14th European Conference, Amsterdam, The Netherlands, October 11–14, 2016, Proceedings, Part I 14* (pp. 21-37). Springer International Publishing.
- [21] Felzenszwalb, P.F., Girshick, R.B., McAllester, D., and Ramanan, D. (2010). Object detection with discriminatively trained part-based models. *IEEE Trans Pattern Anal Mach Intell.* 32, 1627–1645.

- [22] Ferrari, V., Jurie, F. and Schmid, C. (2010). From images to shape models for object detection. *International journal of computer vision*, 87(3), pp.284-303.
- [23] Ren, X., and Ramanan, D. (2013). Histograms of sparse codes for object detection. In: *Proceedings of the IEEE Computer Society Conference on Computer Vision and Pattern Recognition*. pp. 3246–3253
- [24] Girshick, R., Felzenszwalb, P. and McAllester, D. (2011). Object detection with grammar models. *Advances in neural information processing systems*, 24.
- [25] Salakhutdinov, R., Torralba, A. and Tenenbaum, J. (2011). Learning to share visual appearance for multiclass object detection. In *CVPR 2011* (pp. 1481-1488). IEEE.
- [26] Alahi, A., Ortiz, R. and Vandergheynst, P. (2012). Freak: Fast retina keypoint. In *2012 IEEE conference on computer vision and pattern recognition* (pp. 510-517). Ieee.
- [27] Zhou, X., Yang, C. and Yu, W. (2012). Moving object detection by detecting contiguous outliers in the low-rank representation. *IEEE transactions on pattern analysis and machine intelligence*, 35(3), pp.597-610.
- [28] Zhu, L., Chen, Y., Yuille, A. and Freeman, W. (2010). Latent hierarchical structural learning for object detection. In *2010 IEEE computer society conference on computer vision and pattern recognition* (pp. 1062-1069). IEEE.
- [29] Felzenszwalb, P.F., Girshick, R.B., and McAllester, D. (2010). Cascade object detection with deformable part models. In: *Proceedings of the IEEE Computer Society Conference on Computer Vision and Pattern Recognition*. pp. 2241–2248
- [30] Jiang, H., Wang, J., Yuan, Z., Wu, Y., Zheng, N., and Li, S. (2013). Salient object detection: A discriminative regional feature integration approach. In: *Proceedings of the IEEE Computer Society Conference on Computer Vision and Pattern Recognition*. pp. 2083–2090
- [31] Kim, C., Lee, J., Han, T., and Kim, Y.M. (2018). A hybrid framework combining background subtraction and deep neural networks for rapid person detection. *J Big Data*. 5.
- [32] Zaidi, S.S.A., Ansari, M.S., Aslam, A., Kanwal, N., Asghar, M. and Lee, B. (2022). A survey of modern deep learning based object detection models. *Digital Signal Processing*, p.103514.
- [33] Nobis, F., Geisslinger, M., Weber, M., Betz, J., and Lienkamp, M. (2019). A deep learning-based radar and camera sensor fusion architecture for object detection; A Deep Learning-based Radar and Camera Sensor Fusion Architecture for Object Detection.
- [34] Elhoseny, M. (2020). Multi-object detection and tracking (modt) machine learning model for real-time video surveillance systems. *Circuits Syst Signal Process*. 39, 611–630.

- [35] Das, S., Pal, S. and Mitra, M. (2016). Real time heart rate detection from ppg signal in noisy environment. In 2016 International Conference on Intelligent Control Power and Instrumentation (ICICPI) (pp. 70-73). IEEE.
- [36] Nayan, A.-A., Saha, J., Mahmud, K.R., al Azad, A.K., and Kibria, M.G. (2020). Detection of objects from noisy images. In: 2020 2nd International Conference on Sustainable Technologies for Industry 4.0 (STI). pp. 1–6. IEEE
- [37] Yadav, K., Mohan, D., and Parihar, A.S. (2021). Image detection in noisy images. In: 2021 5th International Conference on Intelligent Computing and Control Systems (ICICCS). pp. 917–923
- [38] Milyaev, S. and Laptev, I. (2017). Towards reliable object detection in noisy images. *Pattern Recognition and Image Analysis*, 27, pp.713-722.
- [39] Medvedeva, E. (2019). Moving object detection in noisy images. In: 2019 8th Mediterranean Conference on Embedded Computing (MECO). pp. 1–4. IEEE
- [40] Que, J.F., Peng, H.F., and Xiong, J.Y. (2019). Low altitude, slow speed and small size object detection improvement in noise conditions based on mixed training. In: *Journal of Physics: Conference Series*. p. 012029. IOP Publishing
- [41] Lee, G., Hong, S., and Cho, D. (2021). Self-supervised feature enhancement networks for small object detection in noisy images. *IEEE Signal Process Lett.* 28, 1026–1030
- [42] Singh, M., Govil, M.C., and Pilli, E.S. (2018). V-SIN: visual saliency detection in noisy images using convolutional neural network. In: 2018 Conference on Information and Communication Technology (CICT). pp. 1–6. IEEE
- [43] Gautam, A., and Biswas, M. (2018). Whale optimization algorithm based edge detection for noisy image. In: 2018 Second International Conference on Intelligent Computing and Control Systems (ICICCS). pp. 1878–1883. IEEE
- [44] Mathew, M.P., and Mahesh, T.Y. (2022). Leaf-based disease detection in bell pepper plant using yolo v5. *Signal Image Video Process.* 1–7.
- [45] Cheng, L., Li, J., Duan, P., and Wang, M. (2021). A small attentional YOLO model for landslide detection from satellite remote sensing images. *Landslides*. 18, 2751–2765.
- [46] Wu, D., Lv, S., Jiang, M., and Song, H. (2020). Using channel pruning-based YOLO v4 deep learning algorithm for the real-time and accurate detection of apple flowers in natural environments. *Comput Electron Agric.* 178, 105742
- [47] Liu, G., Nouaze, J.C., Touko Mbouembe, P.L., and Kim, J.H. (2020). YOLO-tomato: A robust algorithm for tomato detection based on YOLOv3. *Sensors*. 20, 2145

- [48] Chen, W., Huang, H., Peng, S., Zhou, C., and Zhang, C. (2021). YOLO-face: a real-time face detector. *Vis Comput.* 37, 805–813
- [49] Zaidi, S.S.A., Ansari, M.S., Aslam, A., Kanwal, N., Asghar, M. and Lee, B. (2022). A survey of modern deep learning based object detection models. *Digital Signal Processing*, p.103514.
- [50] Nakamura, T. (2021). Military Aircraft Detection Dataset. Webpage: <https://www.kaggle.com/datasets/a2015003713/militaryaircraftdetectiondataset>



RESEARCH ARTICLE

**DETECTION OF EXON AND INTRON REGIONS IN DNA SEQUENCES BY THE
PROPOSED HASHING FUNCTION**

Fatma AKALIN^{1,*}, Nejat YUMUŞAK²

¹Sakarya University, Faculty of Computer and Information Sciences, Department of Information Systems Engineering, Sakarya, Turkey fatmaakalin@sakarya.edu.tr, ORCID: 0000-0001-6670-915X

²Sakarya University, Faculty of Computer and Information Sciences, Department of Information Systems Engineering, Sakarya, Turkey, nyumusak@sakarya.edu.tr, ORCID: 0000-0001-5005-8604

Receive Date: 11.04.2023

Accepted Date: 16.05.2023

ABSTRACT

Chromosomes, which are formed by the combination of DNA and special proteins, are structures that can show some changes with the effect of genetic or environmental factors. The DNA molecule in these structures carries vital information in elucidating critical information about life. DNA, which is formed by the combination of sugar, phosphate and organic bases, has exon and intron regions separation. Information about the processes in the life cycle of cells, the changes experienced by stem cells, the regulations in the growth and development stage, the development status of cancer, mutation occurrences and protein synthesis are stored in exon regions. Distinguishing exon regions that form 3% of a cell's DNA is challenging. However, detecting diseases on genetically based facts offers more precise outputs. For this reason, analyses were made on the BCR-ABL gene and BRCA-1 mutation carrier genes to analyse leukemia and breast cancer, which are genetically based diseases. First, these genes obtained from the NCBI gene bank were digitized by integer mapping technique. The digitized sequences were given as input to the hash function. This proposed hash function consists of the steps of finding the logarithmic equivalent of the total number of digitized organic bases, summing all logarithmic equivalents, rounding to the nearest integer, expressing it in binary and placing it in the hash table. These outputs, which define the exon and intron regions, were shown as clusters to find the new input region easily. The collision cluster is the binary representation of key values representing both exon and intron regions for the same region. The main goal is to have a small number of elements in this cluster. With the proposed hierarchy in this study, only one collision occurred for BCR-ABL and BRCA-1 genes. Accuracy rates of the proposed approach based on a mathematical basis and independent of nucleotide length were obtained 93.33%, and 96%, respectively.

Keywords: *DNA sequences, Exon and intron regions, Integer mapping technique, Hashing technique*

1. INTRODUCTION

The cell is the basic unit of life and has structural and functional properties. It provides the repair of injured tissues and regeneration of dead cells [1]. However, with the effect of genetic or environmental factors, some changes may occur in the genetic components of the cells [1,2]. These changes are expressed with chromosomes. Chromosomes are formed as a result of the fusion of DNA and special proteins [3]. The DNA molecule, which contains vital functionalities, is a structure formed by the combination of sugar, phosphate and organic bases [3,4]. This structure has a separation of exon and intron gene regions for eukaryotic cells [5]. Analysis of these regions is a source of information for elucidating critical information about life. Because, information about the processes in the life cycle of cells, the changes experienced by stem cells, the regulations in the growth and development stage, the development status of cancer, mutation occurrences and protein synthesis are stored in exon regions. In addition, the development status of cancer and mutation formation can also be evaluated by exon regions [3,6].

Cancer is a malignancy that requires early diagnosis for survival. The medical world uses different methods in the diagnosis of cancer. However, some of these methods produce unclear results. For example, manual assessments on imaging or pathological outputs depend on different parameters such as the person's knowledge, experience, mental intensity and physical fatigue [7,8]. However, the ratios in the blood elements can create a similar curve of change for different diseases [9]. Therefore, analyzing the disease using genetic data builds a successful decision process. However, due to the recent developments in genome technology, manual evaluations for the increasing amount of data [4,10] slow the analysis. On the other hand, since 3% of the DNA of a eukaryotic cell consists of exon regions [11], the investigations of these regions are complex. In addition, the detection process of exon and intron regions has been evaluated as a challenging problem in [4,11-13] studies.

In this study, leukemia malignancy, which is among the most common cancer types, was examined [4]. Leukemia is evaluated in two different ways according to the type of disease in the body. This distinction is characterized as acute and chronic. In acute leukemia, the spread of the disease in the body is rapid. In chronic leukemia, the spread of the disease in the body is slow [1,15]. Therefore, early diagnosis is necessary for the continuation of vitality, especially in acute leukemias. In this study, exon and intron regions in BCR-ABL genes presenting as an important indicator in the diagnosis of ALL and CML malignancies being the main types of leukemia, were analyzed [1,16]. Thus, a genetic-based evaluation was provided.

There is an active research area in the literature for the analysis of exon and intron gene regions from past to present. Until the 2000s, different statistical methods were used to evaluate these regions. In this direction, the detection of exons was provided in the [17] study, in which an estimation algorithm using a quadratic discriminant function for multivariate statistical pattern recognition was presented. Genetic evaluations were made with the information obtained in the [18] study, which provided a comprehensive analysis of various statistical features for human exon regions. In the [19] study, in which the program called GeneParser was developed, the fraction of exons was estimated by means of statistical results obtained from intron and exon regions. On the other hand, analytical and computational studies have been carried out for the interpretation of genomic data since the 2000s [2].

At the same time, the developed digital signal processing approach is preferred for data interpretation [2]. In this framework, the conversion process of the nucleotide sequence to the amino acid sequence was analyzed in the [20] study. Exon regions were distinguished from intron regions by means of entropic measures calculated from amino acid sequences. The [21] study proposed a method based on the Gabor wavelet transform. Thus, the detection of exon regions was provided. However, digital signal processing, which is a strong scientific field on large molecules formed by the polymerization of monomers, has been widely used since 2010 [2]. In this direction, digital signal processing was used in the [22] study in order to detect exon and intron regions and reveal anomalies in these regions. FIR and IIR filters were used to provide a successful estimation of exon regions. In order to detect exon regions in eukaryotic cells in the [23] study, a numerical mapping technique based on Walsh codes has been proposed. In the [24] study, the estimation of exon regions from eukaryotic DNA sequences was provided with the developed bidirectional LSTM and RNN-based deep learning models. In the [25] study, is introduced a convolutional neural network model for the classification of human exon and intron regions. In the [26] study, Frequency Chaos Game Representation and CNN structure were used together. Thus, human exon and intron regions were analyzed.

A study area is available to evaluate exon and intron regions. Especially the developments in the field of digital signal processing [3,4] have emerged as a preferred strong field for exploring the relationships, patterns and periodicity states in the data [10]. However, the [27] and [28] studies using the digital signal processing approach stated that digital signal processing approaches not only serve a successful decision process but also provide an inference based on DNA length. Therefore, it was planned to construct a structure independent of DNA length. In this study, a hierarchy based on the structural and mathematical basis was constructed in order to produce results independent of DNA length. First of all, DNA sequences, which have a symbolic structure in this hierarchy, were digitized according to the rules of the integer mapping technique. Secondly, the digitized sequences were given as input to the hash function. The logarithmic equivalents of the total number of each organic base in the sequences digitized within the scope of the hash function were obtained and rounded to the nearest integer. All integer values generated for exon and intron regions were expressed in binary system. In this study, in which open hashing is preferred, the values that define the exon and intron regions and are expressed in a binary system were placed in the hash table. Finally, it was compared with the results of analysis realized on the BRCA-1 gene [29] seen in breast cancer patients carried high-risk. Accuracy rates of this study for BCR-ABL gene and BRCA-1 gene were obtained as 93.33%, and 96%, respectively.

With this study, the analysis of exon regions that have vital functions related to life has been done. An alternative method for detecting these regions has been proposed compared to statistical methods, digital signal processing approaches, deep learning models, and analytical or computational studies. In this direction, the exon regions, constituting 3% of the eukaryotic cell DNA and having a complex analysis process, were evaluated with the proposed hashing function [4,11-13]. Thus, despite the increasing genome data and unclear manual evaluation methods, genetic-based inferences have been produced that are independent of DNA length, and have a simple hierarchy and a mathematical basis.

2. MATERIALS AND METHODS

This study aimed to distinguish exon regions containing vital life information from intron regions using the NCBI dataset supplied <https://www.ncbi.nlm.nih.gov/> site. In this direction, the BCR-ABL gene, characterized as an important indicator in the diagnosis of ALL and CML malignancies being the main types of leukemia was used. First, the BCR-ABL gene, which occurs from symbolic letters, was digitized by the integer mapping technique. Then the digitized DNA sequence was given to the hashing function. The values expressed in the binary system as function output were placed in the hash table. In this hierarchy where the open hashing approach is preferred, the outputs corresponding to the same hash value are kept in a list structure. Then, these key values, which define the exon and intron regions, were shown with clusters in order to easily find the region of the new input. At the same time, producing cases of the same output is examined for both exon and intron regions. The intensity of this situation, which is described as collision, was evaluated for the entire clusters. However, in order to generalize with the proposed hierarchy, the same methods were also performed for the BRCA-1 mutation carrier gene [29] seen in high-risk breast cancer patients. Finally, the analyzes performed for two separate DNA sequences were evaluated and comparisons were made. The flow chart of the proposed hierarchy was given in Figure 1.

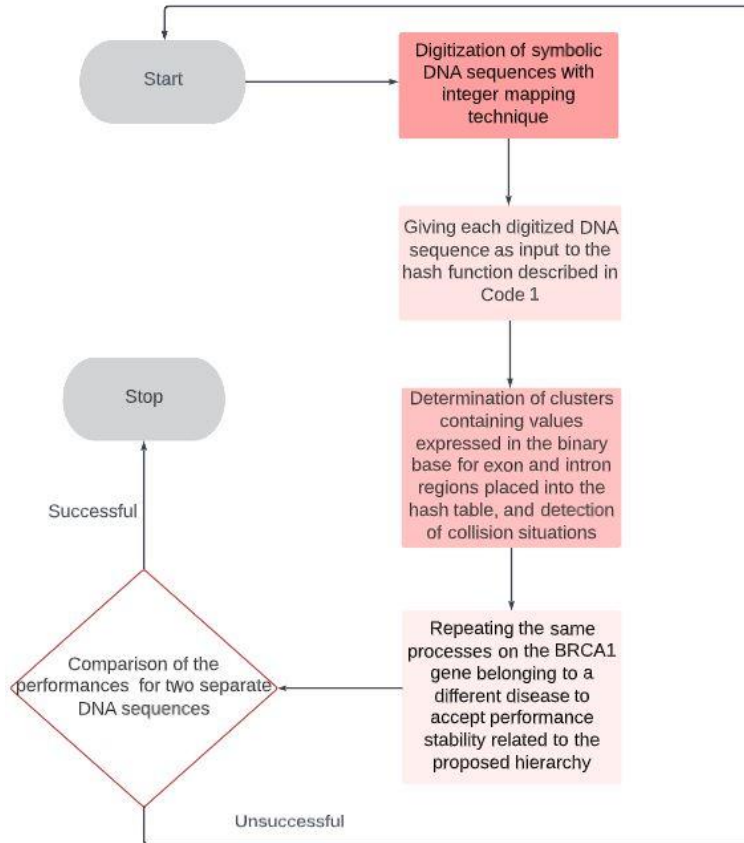


Figure 1. The flow diagram of the hierarchy proposed in this study.

2.1. Dataset

Leukemia, one of the most common types of cancer [14], affects the body's blood production mechanism [1]. Manual evaluations required for the diagnosis of this disease include different parameters. This complicates to produce a clear output. For this reason, the main aim of the study is to produce clearer results in diagnosing the disease using genetically based facts. In this direction, the molecular diagnosis was provided on 4 different BCR-ABL genes used as an indicator in the diagnosis of ALL and CML malignancies, which are the main types of leukemia disease. Nucleotide length information about the exon and intron regions of these genes is given in Table 1.

Table 1. Information about the BCR-ABL gene regions obtained from the NCBI dataset.

AM400881.1	Regions	Names Called of Regions
1-14	Exon Region	(1-Exon)
15-71	Intron Region	(2-Intron)
72-527	Intron Region	(3-Intron)
AM600680.1		
1-29	Exon Region	(4-Exon)
30-578	Intron Region	(5-Intron)
579-1114	Intron Region	(6-Intron)
1115-1180	Exon Region	(7-Exon)
AM886138.1		
1-31	Exon Region	(8-Exon)
32-280	Intron Region	(9-Intron)
281-790	Intron Region	(10-Intron)
791-853	Exon Region	(11-Exon)
EU447303.1		
1-70	Exon Region	(12-Exon)
71-145	Exon Region	(13-Exon)
274-448	Exon Region	(14-Exon)
449-488	Exon Region	(15-Exon)

In this study, the stability of the performance of the proposed framework was also investigated for a different gene type. In this direction, the same hierarchy was applied again for the BRCA-1 mutation carrier gene in breast cancer patients with high risk. The nucleotide length information of the exon and intron regions for the BRCA-1 gene is given in Table 2.

Table 2. Information about the BRCA-1 gene regions obtained from the NCBI dataset.

LC312442.1	Regions	Names Called of Regions
20-207	Intron Region	(1-Intron)
Y08757.1		
1-746	Intron Region	(2-Intron)
747-834	Exon Region	(3-Exon)
835-1482	Intron Region	(4-Intron)
LC312441.1		
1-203	Intron Region	(5-Intron)
NM_001407963.1		

1-94	Exon Region	(6-Exon)
95-183	Exon Region	(7-Exon)
184-323	Exon Region	(8-Exon)
324-429	Exon Region	(9-Exon)
430-475	Exon Region	(10-Exon)
476-552	Exon Region	(11-Exon)
553-3978	Exon Region	(12-Exon)
3979-4067	Exon Region	(13-Exon)
4068-4236	Exon Region	(14-Exon)
4237-4360	Exon Region	(15-Exon)
4361-4551	Exon Region	(16-Exon)
4552-4862	Exon Region	(17-Exon)
4863-4950	Exon Region	(18-Exon)
4951-5028	Exon Region	(19-Exon)
5029-5069	Exon Region	(20-Exon)
5070-5153	Exon Region	(21-Exon)
5154-5208	Exon Region	(22-Exon)
5209-5282	Exon Region	(23-Exon)
5283-5343	Exon Region	(24-Exon)
5344-6851	Exon Region	(25-Exon)

9 exons and 6 intron regions were selected for the BCR-ABL gene. In addition, 4 intron regions and 21 exon regions were created as unbalanced in the preferred BRCA-1 gene. In the last step, the performance of the inferences reached for the BRCA-1 gene was compared with the performance of the inferences reached for the BCR-ABL gene. The title "Names Called to Regions" in Table 1 and Table 2 has definitions related to each example. These definitions are used to illustrate the collision situations in Figure 2, Figure 3, and Figure 4.

2.2. Integer Mapping Technique

DNA is the part of the cell that has vital information for the maintenance of life functions and biological processes [4]. It has a symbolic structure. This complicates the analysis of DNA structure. Digitizing the sequences is a necessary step to provide successful inference. In this study, the integer mapping technique, which is one of the fixed mapping techniques, was chosen [6].

The integer mapping technique is a 1-dimensional mapping technique [28]. In order to digitize the DNA structure with this technique, firstly, the number of organic bases in the sequences is examined and then the assignment is done. The first rule for this mapping technique is that the total number of purine bases (A and G) is greater than the total number of pyrimidine bases (C and T). According to this rule, the 4 bases are assigned as T=0, C=1, A=2, and G=3 respectively. Another rule is that the total number of T organic base is greater than the total number of A organic base and the total number of G organic base is greater than the total number of C organic base. According to this rule, the 4 bases are assigned as A=0, C=1, T=2 and G=3 respectively [6]. In this study, it was also encountered

that the total number of T organic bases is larger than the total number of A organic bases and the total number of G organic bases is smaller than the total number of C organic bases. In such a case, A=0, T=2, C=3 and G=1 assignments were made for 4 bases, respectively. Thus, BCR-ABL genes and BRCA1 genes were digitized by integer mapping technique.

2.3. Hashing Technique

The process of creating a fixed-size output from inputs of different lengths with the help of the address function is called hashing. The outputs produced as a result of the hashing process are placed into a hash table. The data in the hash table, which consists of fixed-size outputs, is accessed with the key. Keys that produce an index are always unique and represent only one value. Each index defined with a key in the hash table is determined by the hash function. The hash function takes the data and places it in memory with the output it produces. This function should be simple to calculate, and produce results without any collision [30].

In this study, a hash function suitable for the structure of the DNA sequence was created. The pseudo code of this function is given below.

Code 1. The pseudo code of the proposed hash function

- 1-Start
- 2-Find the total number of organic bases A, T, G, and C for each digitized DNA sequence.
- 3-Find the logarithmic equivalents of the total number of each organic base in the sequences digitized.
- 4-Add these 4 separate logarithmic equivalents and round to the nearest integer.
- 5-Express in the binary system these values obtained in the fourth step.
- 6-Finish

After the key of each DNA sequence was calculated with the help of the hash function described in Code 1, it was placed in the hash table. By this hash function created suitable to DNA structure, values expressed in the binary system specific to exon and intron regions are obtained. Then the values reached for the exon and intron regions were shown in two separate clusters. The main purpose here is that succeed to avoid a collision situation. In this study, open hashing was preferred within the framework of hashing approach.

Open hashing is a method that provides a list structure solution for the case of hashing the elements calculated with the hash function to the same value. With this method, in the case being of different data corresponding to the same index, elements with the same properties are added to a list [30]. The hash tables of BCR-ABL genes expressed with 4 bits and BRCA-1 genes expressed with 5 bits are given in Figure 2 and Figure 3.

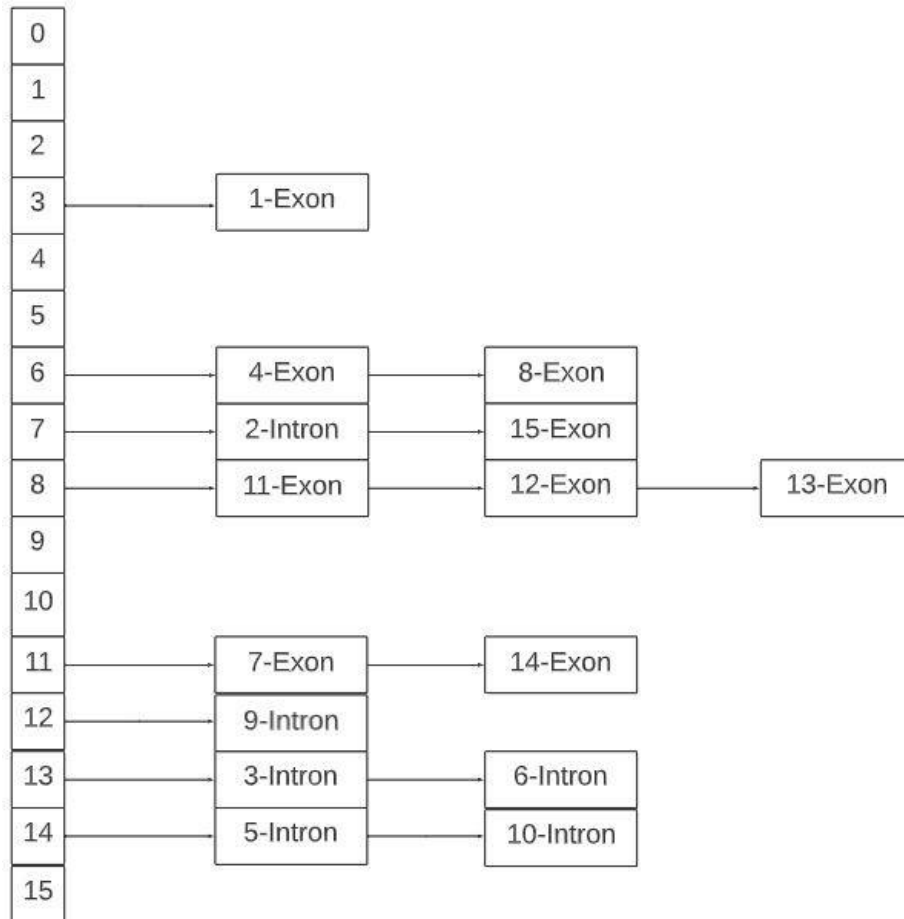


Figure 2. Hash table created for the BCR-ABL gene.

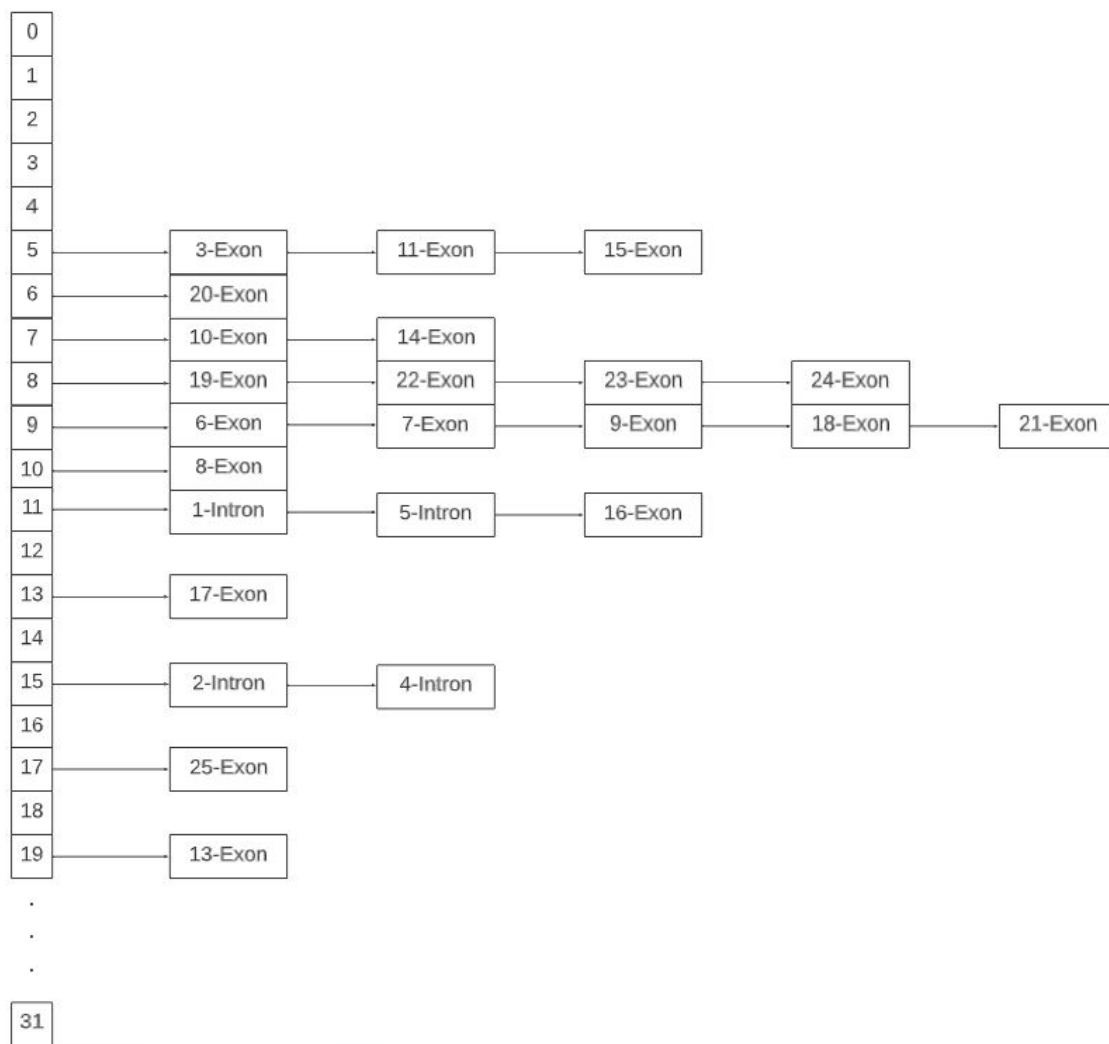


Figure 3. Hash table created for the BRCA-1 gene.

When the hash tables in Figure 2 and Figure 3 are examined, it is seen that there is only one collision for two different gene structures. In this direction, 14 correct detections were made for BCR-ABL genes containing 15 distinct gene regions. At the same time, 24 correct detections were made for BRCA1 genes containing 25 distinct gene regions. As a result of these detections, 93.33% and 96% success rates were produced, respectively. The clusters of numerical values in the binary system that define the exon and intron regions are given in Figure 4.

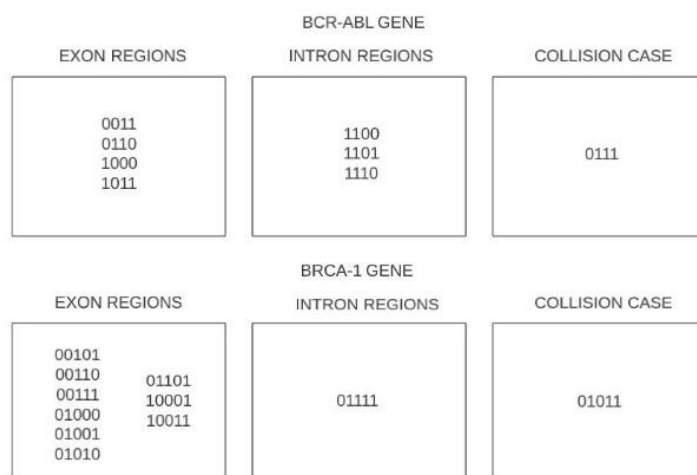


Figure 4. Clusters of numerical representations in the binary system that define exon and intron regions for BCR-ABL and BRCA-1 genes.

In this study, a successful result was produced at the end of the proposed region recognition process for the BCR-ABL gene. In order to examine the stability of this success in a different disease context, the BRCA-1 gene, which consists of an unbalanced number of exons and intron regions with more gene regions, was used and the success of the applied method was tested. At the end of the test process, 1 collision occurred. The proposed hierarchy for the BCR-ABL method was also successful on the dataset with different parameters. This shows the stability and generalizability of the proposed method.

3. RESULTS AND DISCUSSION

In this study, a hierarchy was proposed for the detection of exon and intron gene regions with different nucleotide lengths on the BCR-ABL gene that is an indicator in the detection of ALL and KML malignancies. Thus, the molecular diagnosis was provided on the BCR-ABL gene, which contains 9 exon regions and 6 intron regions. In this diagnostic process, firstly, DNA sequences with a symbolic structure were digitized by integer mapping technique. Then the digitized DNA sequences were given to the hash function. The outputs produced by the Hash function, which consists of 4 basic steps, are the values that define the exon and intron regions. It is expected that there will be any collisions in these values placed in the hash table.

In this study, the open hashing approach was used in the scope of hashing. By this approach, numerical representations defining the same region were placed in a list structure. In the hash table kept as a list structure, there was only 1 collision for the BCR-ABL gene and a success rate of 93.3% was achieved. Then, it was planned to test the performance stability so that the proposed hierarchy can be generalized. Therefore, an analysis was performed on the BRCA-1 mutation carrier gene seen in

high-risk breast cancer patients. In order to clarify the success and stability of the method, the number of selected gene regions was increased and an unbalanced dataset was created. However, the proposed hierarchy produced only 1 collision on a different gene and achieved a success rate of 96%. A successful detection process has been achieved with the stable outputs of this structure, which produces only one wrong prediction for both gene molecules with different parameters.

In addition, this work has two originalities. Its first originality is the generation of a hash function suitable for the structure of DNA. For example, the number of times a paper must be folded to create 4 separate squares is solved by $\log_2(4)$. Therefore, the organic base density in DNA sequences containing 4 different organic bases should be expressed in logarithm base 4. Thus, a mathematical basis suitable for the structure of DNA was created.

The second feature is to perform a study independent of nucleotide length. In this direction, it has been stated that inferences based on nucleotide length are produced in the [27] study, which uses the signal processing approach that has been prominent, especially since the 2000s. On the other hand, a study independent of nucleotide length was done in the [28] study, in which classification was provided with the structural and statistical features extracted from the sequences. The obtained results were more successful than the outputs produced using the signal-processing approach. On the other hand, a new mapping technique was proposed for digitizing DNA sequences in the [31] study. In this mapping technique, an independent study of nucleotide length was performed depending on the codon distributions. At the same time, it has been stated that more successful results were produced compared to other mapping techniques.

There are studies [3,5,11,13,22,23,32-34] in which statistical analyzes are made, inferences are produced within the scope of signal processing approach or artificial intelligence-based detections are performed. However, in this study, a new perspective was created using the field of data structures in the analysis of DNA molecules.

4. CONCLUSION

Cancer is a malignancy that occurs with the uncontrolled proliferation and spread of cells in a certain tissue or organ. The methods applied to the patient during the diagnosis of this malignancy produce unclear outcomes in some cases. At the same time, some important indicators used in the diagnosis of the disease form a similar curve of change within the scope of different diseases. For this reason, it is advantageous to diagnose the disease with inferences made on genetically based cases.

In this study, ALL and CML malignancies, which are the main types of leukemia, were analyzed with genetically based cases. In this direction, the BCR-ABL gene, which is an important indicator in the diagnosis of ALL and CML malignancies, was analyzed. In this analysis process, firstly, the BCR-ABL gene with symbolic structure was digitized by integer mapping technique. Then the digitized DNA sequences are given as input to the hash function. The proposed hash function is based on a mathematical basis created in suitable for the DNA structure. The outputs for this function are values that define the exon and intron regions. These values can be expressed with clusters in order to easily find the region of the new input. In this study, in which open hashing was used, 1 collision occurred

for the BCR-ABL gene. In addition, the current performance of the proposed hierarchy for the BCR-ABL gene for the gene structure affecting a different disease was also tested. For this, the BRCA-1 gene, which contains more gene regions and is created in an unbalanced way, was used. The proposed hierarchy created 1 collision in the BRCA-1 gene structure. This shows the stability of the proposed hierarchy.

In this study, a structure depended on a mathematical basis and independent of nucleotide length was created. In future studies, different bases, different mathematical calculations or different bit numbers can be used within the preferred data structure hierarchy for the detection of exon and intron regions. Thus, it is planned to reduce the possibility of a collision.

ACKNOWLEDGEMENT

The authors declare that they have no known competing financial interests or personal relationships that could have appeared to influence the work reported in this paper.

REFERENCES

- [1] Kocabıyık, V.B. (2011). ALL ve KML’li hastalarda BCR ve ABL genlerindeki mutasyonların incelenmesi. Yüksek Lisans Tezi, Selçuk Üniversitesi Sağlık Bilimleri Enstitüsü, Konya.
- [2] Khodaei, A., Feizi-Derakhshi, M.R., and Mozaffari-Tazehkand, B. (2020). A pattern recognition model to distinguish cancerous DNA sequences via signal processing methods. *Soft Computing*, 24(21), 16315–16334.
- [3] Das B., and Türkoğlu, I. (2016). Classification of DNA sequences using numerical mapping techniques and Fourier transformation. *Journal of the Faculty of Engineering and Architecture of Gazi University*, 31(4), 921–932, 2016.
- [4] Barman, S., Saha, S., Mandal, A., and Roy M. (2012). Prediction of protein coding regions of a DNA sequence through spectral analysis. 2012 International Conference on Informatics, Electronics and Vision, ICIEV 2012.
- [5] Hota, M. K., and Srivastava, V. K. (2010). Performance analysis of different DNA to numerical mapping techniques for identification of protein coding regions using tapered window based short-time discrete Fourier transform. ICPCES 2010 - International Conference on Power, Control and Embedded Systems 2010, 0–3.
- [6] Daş, B. (2018). DNA dizilimlerinden hastalık tanılanması için işaret işleme temelli yeni yaklaşımların geliştirilmesi. Doktora Tezi, Fırat Üniversitesi Fen Bilimleri Enstitüsü, Elazığ, 83s.
- [7] Al-jaboriy, S.S., Sjarif, N.N.A., Chuprat, S., and Abdulllah, W.M. (2019). Acute lymphoblastic leukemia segmentation using local pixel information. *Pattern Recognition Letters*, 125, 85–90.

- [8] Scotti F. (2005). Automatic morphological analysis for acute leukemia identification in peripheral blood microscope images. CIMSA 2005-IEEE International Conference on Computational Intelligence for Measurement Systems and Applications, 20–22.
- [9] Kutlu, H., Avcı, E., and Özyurt, F. (2020). White blood cells detection and classification based on regional convolutional neural networks. *Medical Hypotheses*, 135.
- [10] Chakraborty, S., and Gupta, V. (2016). DWT based cancer identification using EIIP. Proceedings - 2016 2nd International Conference on Computational Intelligence and Communication Technology, CICT 2016, 718–723.
- [11] Das, L., Das J.K., and Nanda, S. (2020). Detection of exon location in eukaryotic DNA using a fuzzy adaptive Gabor wavelet transform. *Genomics*, 112, 4406–4416.
- [12] Das, L., Nanda, S., and Das, J.K. (2019). An integrated approach for identification of exon locations using recursive gauss newton tuned adaptive kaiser window. *Genomics*, 111, 284–296.
- [13] Gupta, R., Mittal, A., Singh, K., Bajpai, P., and Prakash, S. (2007). A time series approach for identification of exons and introns. 10th International Conference on Information Technology (ICIT 2007), 91–93.
- [14] Hsu, C.H., Chen, X., Lin, W., Jiang, C., Zhang, Y., Hao, Z., and Chung, Y.C. (2021). Effective multiple cancer disease diagnosis frameworks for improved healthcare using machine learning. *Measurement*, 175.
- [15] Aydın, G. (2017). Quercetin'in KML kök hücreleri üzerine sitotoksik etkilerinin moleküler düzeyde incelenmesi. Erciyes Üniversitesi, Sağlık Bilimleri Enstitüsü, Yüksek Lisans Tezi, Kayseri.
- [16] Arslan, S. (2014). KML ve ALL Tanılı Hastalarda BCR/ABL füzyon geni mutasyonlarının taranması. Eskişehir Osmangazi Üniversitesi Sağlık Bilimleri Enstitüsü, Yüksek Lisans Tezi, 76s.
- [17] Audic S., and Claverie, J. M. (1998). Self-identification of protein-coding regions in microbial genomes. *Proceedings of the National Academy of Sciences of the United States of America*, 95(17), 10026–10031.
- [18] Zhang, M.Q. (1998). Statistical features of human exons and their flanking regions. *Human Molecular Genetics*, 7(5), 919–932, 1998.
- [19] Snyder, E.E., and Stormo, G.D. (1995). Identification of protein coding regions in genomic DNA. *Journal of Molecular Biology*, 248(1), 1–18.

- [20] Mereuta, S., and Munteanu, V. (2007). A new information theoretic approach to exon - intron classification. ISSCS 2007 - International Symposium on Signals, Circuits and Systems, Proceedings 2007, 2, 497–500.
- [21] Mena-Chalco, J., Carrer, H., Zana, Y., and Cesar, R. M. (2008). Identification of protein coding regions using the modified gabor-wavelet transform. IEEE/ACM Transactions on Computational Biology and Bioinformatics, 5(2), 198–206.
- [22] Kar, S., and Ganguly, M. (2022). Study of effectiveness of FIR and IIR filters in exon identification: a comparative approach. Materials Today: Proceedings, 58, 437–444.
- [23] M, R. K., and Vaegae, N. K. (2020). Walsh code based numerical mapping method for the identification of protein coding regions in eukaryotes. Biomedical Signal Processing and Control, 58.
- [24] Singh, N., Nath, R., and Singh, D.B. (2022). Splice-site identification for exon prediction using bidirectional LSTM-RNN approach. Biochemistry and Biophysics Reports, 30.
- [25] Ben Nasr, F., and Oueslati, A.E. (2021). CNN for human exons and introns classification. 18th International Multi-Conference on Systems. Signals & Devices SSD'21 2021, 249–254.
- [26] Ben Nasrand, F., Oueslati, A.E. (2022). A new automatic method for human coding and non-coding zones characterization and classification based on FCGR coding and CNN classifier. International Conference on Advanced Technologies for Signal and Image Processing, ATSIP, 8–9.
- [27] Akalın, F., and Yumuşak, N. (2022). Classification of exon and intron regions obtained using digital signal processing techniques on the DNA genome sequencing with EfficientNetB7 architecture. Journal of the Faculty of Engineering and Architecture of Gazi University, 37(3), 1355–1371.
- [28] Akalın, F., and Yumuşak, N. (2023). Classification of ALL and CML malignancies being among the main types of leukaemia with graph neural networks and fuzzy logic algorithm. Journal of the Faculty of Engineering and Architecture of Gazi University, 38(2), 707–719, 2023.
- [29] Yetim, E. (2018). Meme manyetik rezonans görüntülemeye BI-RADS kategori 3 lezyonlar; takip sonuçları. Akdeniz Üniversitesi Tıp Fakültesi Radyoloji Anabilim Dalı, Uzmanlık Tezi.
- [30] Yumuşak, N., and Adak, M.F. (2016). C/C++ ile veri yapıları.
- [31] Das, B., and Turkoglu, I. (2018). A novel numerical mapping method based on entropy for digitizing DNA sequences. Neural Computing and Applications, 29(8), 207–215.

- [32] Marhon, S. A., and Kremer, S. C. (2011). Protein coding region prediction based on the adaptive representation method. Canadian Conference on Electrical and Computer Engineering, 000415–000418.
- [33] Li, J., Zhang, L., Li, H., Ping, Y., Xu, Q., Wang, R., Tan, R., Zhen, W., Liu, B., and Wang, Y. (2019). Integrated entropy-based approach for analyzing exons and introns in DNA sequences. BMC Bioinformatics, 20.
- [34] Hota, M. K., and Srivastava, V. K. (2012). Identification of protein coding regions using antinotch filters. Digital Signal Processing: A Review Journal, 22(6), 869–877.



RESEARCH ARTICLE

**ANALYSIS AND CLINICAL EVALUATION OF MUSCLE DYNAMICS IN ADOLESCENTS
WITH SAGITTAL PLANE DEFORMITY**

Kadir GÖK¹, Ela Naz GÖK^{2*}, Kadriye TOMBAK³, Nehir SAMANCI KARAMAN⁴,
Ömer Halil ÇOLAK⁵

¹Akdeniz University, Faculty of Engineering, Department of Electrical and Electronics Engineering, Antalya,
kadirgok@akdeniz.edu.tr, ORCID: 0000-0003-3386-1512

²Akdeniz University, Faculty of Engineering, Department of Electrical and Electronics Engineering, Antalya,
elanazdoger@gmail.com, ORCID: 0009-0000-5626-4652

³Akdeniz University, Health Services Vocational School, Department of Physical Therapy and Rehabilitation, Antalya,
kadriyetombak@akdeniz.edu.tr, ORCID: 0000-0002-9574-7443

⁴Akdeniz University, Faculty of Medicine, Department of Internal Medicine, Department of Physical Medicine and
Rehabilitation, Antalya, nehirsamanci@akdeniz.edu.tr, ORCID: 0000-0002-0110-1650

⁵Akdeniz University, Faculty of Engineering, Department of Electrical and Electronics Engineering, Antalya,
omercol@akdeniz.edu.tr, ORCID: 0000-0003-0293-3931

Receive Date: 12.05.2023

Accepted Date: 08.06.2023

ABSTRACT

Sagittal plane deformity can be defined as a deviation from the normal curvature of the spine in the sagittal plane. This deformity can distort the natural shape of the spine and cause posture problems. In recent years, effects such as reduced activity in daily life, increased time spent in front of computers and mobile phones, and inactivity during the recent pandemic have also led to a significant increase in sagittal plane deformity. In this study, 16 healthy adolescents and 16 adolescents with sagittal plane deformity participated. Surface EMG (sEMG) recordings were obtained from thoracic kyphosis subjects and lumbar lordosis subjects, commonly seen in patients with sagittal plane deformity (SPD), and from healthy subjects. After filtering the raw sEMG data, wavelet packet transform analysis was performed. The energy values of the wavelet packets corresponding to the low and high frequency components have been calculated. These energy values were statistically analysed using the Mann-Whitney U test to determine muscle differences between SPD subjects and healthy subjects. This statistical analysis identified the channels with significant differences between SPD subjects and healthy subjects. Channels with a statistical significance level of $p < 0.05$ were included. When the muscle activation of these channels was compared, higher activity was found in SPD subjects, while in some movements activation was found in different channels in SPD subjects and healthy subjects. SPD subjects showed more muscle activity than healthy subjects and spent more energy to increase the quality of movements and to perform them with the correct muscle dynamics. It has been observed that SPD subjects develop compensations from different muscle regions in order to perform movements correctly due to postural changes. In healthy subjects, it was observed that movements

were completed in accordance with the kinematics of the movement and that maximum movement quality was observed with less energy.

Keywords: *surface electromyography, wavelet packet transform, lumbar lordosis, thoracic kyphosis, adolescence, bioelectric signals*

1. INTRODUCTION

There are natural anatomical curvatures in the spine that occur congenitally and with the transition to bipedal posture [1]. These natural curvatures are located at different angles and directions in the sagittal plane. Outward curvature of the spine in the thoracic region is called kyphosis, while inward curvature in the cervical and lumbar regions is called lordosis. For some reasons, abnormalities of kyphosis and lordosis (increased or decreased curvature) can occur. This can lead to a variety of postural problems, physical pain, breathing difficulties, reduced quality of life and sometimes medical intervention. In a study, the normal range for radiological measurement of thoracic kyphosis was reported as 20° to 50° degrees using radiographic images from 121 healthy children in a standard position [2]. In another study, lumbar lordotic angle (LSA) and lumbosacral angle (LSA) values were calculated from radiographs of 140 subjects of different ages. Normal LLA values were found between 20.9° and 68° degrees, and normal LSA values were found between 15° and 51° degrees [3]. It has been reported that when the thoracic kyphosis angle exceeds the normal value, musculoskeletal complaints such as postural affections, shoulder and cervical pain can affect all age groups [4], [5]. In the measurement of thoracic kyphosis, it has been stated that the evaluation of the muscular system as well as the skeletal system is an important aspect [6]. Most cases of adolescent idiopathic scoliosis (AIS) with coronal plane abnormalities are also associated with sagittal plane problems [7], [8]. In another study, it was mentioned that the correct assessment of sagittal alignment in AIS cases cannot be neglected due to the effect of both plane movements on each other. This study also reported that angular progression in AIS cases may be influenced by sagittal balance [9], [10]. Although it is difficult to restore the normal value of the kyphosis angle in subjects with only sagittal plane problems, it has been mentioned that the sagittal plane disorder, kyphosis, should be corrected [11].

There are studies that show that the functional and medical importance of lumbar lordosis has been recognised. [12], [13]. The natural curvature of the lumbar lordosis plays an important role in maintaining sagittal balance. The need to evaluate the effect of increasing changes in lumbar lordosis curvature on muscle dynamics and mechanics has been mentioned [14]. In one study, an 8-week exercise programme was designed for female students aged 19-22 years with lumbar lordosis. This study, designed to identify, train, prevent and improve unhealthy habits in corrective exercise and daily life, found no increase in lower extremity flexor muscle flexibility, a significant decrease in the lordosis curve, and an increase in abdominal muscle strength and endurance [15]. In the literature, it has been observed that the comprehensive muscle dynamics of thoracic kyphosis and lumbar lordosis have not been evaluated much and the follow-up and treatment of the cases is mostly focused on strengthening the muscle strength. In this process, it was observed that radiological methods were used as the gold standard. However, this gold standard cannot be used practically in clinics and is not preferred due to the negative secondary effects of radiation [16].

Surface EMG (sEMG) allows the assessment of muscle functional status by measuring bioelectrical signals from muscles using a non-invasive electrode placed on the muscle. sEMG signals are used in a variety of applications including assessment of muscle and nerve health, rehabilitation, biomechanics, sports performance, prosthetic control and ergonomics [17], [18], [19], [20], [21], [22]. Methods for extracting features from sEMG signals are generally divided into time domain features and frequency domain features. Commonly used time domain analyses include root mean square [23], variance [24], mean absolute value [25], zero crossing [26] and waveform length. In frequency domain analysis, after obtaining the frequency spectrum, the magnitude of the signal is evaluated using parameters such as power spectral density, mean frequency and median frequency [27]. The sEMG signal is an unstable, i.e. non-stationary, bioelectrical signal with different frequency components at different times [28]. Therefore, analysis of the sEMG signal in the time-frequency domain allows detailed examination of time- and frequency-dependent changes. Among the time-frequency analysis methods, Fast Fourier Transform [29] and Short-Time Fourier Transform [30] require the signal to be stable in order to effectively analyse the signal. However, the Wavelet transform [31], by multiplying the signal by more than one wavelet function, allows the decomposition of the components of the signal in different frequency bands. Wavelet packet transform is a widely used technique in many fields such as signal processing and data analysis. It is a method used to analyse the signal in frequency space. Wavelet Packet Transform has a significant impact on the processing of electromyography (EMG) signals. It is used to analyse the frequency content of the EMG signal and to determine the time-variance characteristics of the signal [32]. In this way, the frequency content of the EMG signal is better understood and the study of changes in muscle activity becomes more sensitive.

In this study, sEMG recordings were made to determine the multi-channel functional muscle dynamics of healthy subjects' spines and sagittal plane deformity (SPD) subjects in adolescence. The hypothesis of the study is that as the natural curvature of the spine increases in the sagittal plane, muscle dynamics will also change due to anatomical changes in the associated muscles. At the same time, although radiological measurement techniques are used in diagnosis and follow-up, studies on comprehensive electrophysiological signal-based assessment of muscle function are currently limited. In this context, adolescents with thoracic kyphosis and lumbar lordosis, which are common patient profiles of SPD subjects, were included in the study. A total of 32 subjects were recorded at a sampling frequency of 2000 Hz during 15 movements with electrodes placed in 18 muscle regions for 4 repetitions. Stable recordings of the subjects were completed using the prepared video and voice command interface. Raw sEMG data were filtered and analysed using wavelet packet transform analysis. Statistical analyses were performed on the analysis data.

2. MATERIALS AND METHODS

2.1. Ethics

This study contains human research data. Therefore, the ethics committee approval to confirm the ethical appropriateness of the study was determined as Akdeniz University Clinical Research Ethics Committee Approval number 70904504/271. All data used in our study were collected with the prior informed consent of the participants. Participants and their legal parents were fully informed about the aims of the study and their consent to participate as participants was obtained.

2.2. Subjects Information

In the study, sEMG recordings were obtained from 16 healthy participants in adolescence and 16 SPD subjects in adolescence. Since the data of healthy subjects were compared with those of SPD subjects, it was ensured that the age, weight, height and spinal curvature levels of the subjects were homogenous. For the healthy subjects group, 8 male and 8 female adolescents were enrolled. Thoracal kyphosis and lumbar lordosis were diagnosed by a specialist physician in 8 and 8 adolescents with SPD, respectively.

In our study, SPD subjects with major pathology of thoracal kyphosis or major pathology of lumbar lordosis were included in the study. When the demographic characteristics of the groups were compared, there was no statistically significant difference between the groups ($p>0.05$). The results of this evaluation, statistically analysed using the Mann-Whitney U test, are presented in Table 1. This result shows that the groups are similar in terms of the distribution of demographic and physical characteristics.

Table 1. Descriptive characteristics of the groups (Man Whitney U test, n; Sample Size, X; Mean, SD; Standard Deviation; p; p Value).

	Healthy Subjects (n=16)		SPD Subjects (n=16)		p
	X	SD	X	SD	
Age (years)	13.81	1.60	14.75	2.62	0.323
Height (cm)	1.63	0.10	1.62	0.11	0.752
Body mass (kg)	54.56	8.62	51.38	13.30	0.224

2.3. Inclusion and Exclusion Criteria in Research

The inclusion criteria for SPD subjects were that they had been diagnosed by a specialist as having a sagittal plane spinal deformity, had no congenital problems, and had been accepted into the appropriate physiotherapy and rehabilitation programme. SPD subjects with major pathology of thoracal kyphosis or major pathology of lumbar lordosis were selected. Inclusion criteria for healthy subjects were the absence of spinal deformity and the absence of any disease that would interfere with the study. Adolescents were included in the study. Exclusion criteria were that patients with other primary or secondary diagnoses or diseases such as neuromuscular, congenital or syndromic (connective tissue disorders) were not included in the study. Patients who could not participate 100% or who refused to participate during the study were not included in the analysis phase.

2.4. Surface Electromyography (sEMG) Recording

sEMG recordings were obtained using PowerLab 35/8 and PowerLab 35/16 units from ADInstruments. Bipolar 9 mm diameter electrodes were placed on the muscles to receive EMG data. sEMG data were recorded simultaneously from 18 muscle sites at a sampling frequency of 2000 Hz during movement. The locations of these channels are shown in which muscle region on the model in Figure 1.

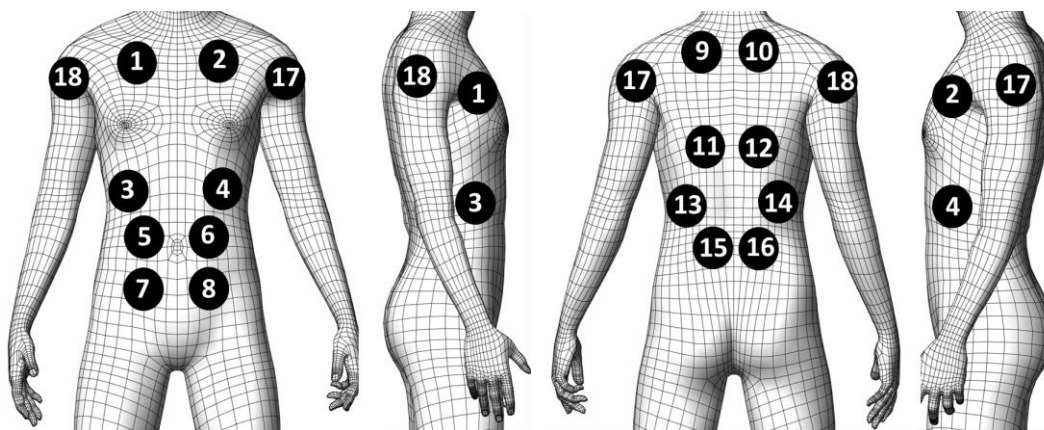


Figure 1. sEMG Recording Channels.

Channels 1,2,3,4,5,6,7,8 were used on the front of the body and channels 10,11,12,13,14,15,16 were used on the back of the body. Channel 17 was used on the left shoulder and channel 18 on the right shoulder. When viewed from the front of the body, odd numbered channels were placed on the left side of the body and even numbered channels were placed on the right side of the body. When viewed from the rear of the body, the odd numbered channels are attached to the left side of the body and the even numbered channels are attached to the right side of the body. Channels 1 and 2 are attached to the pectoralis major muscle (pectoral muscle region), channels 3 and 4 to the oblique muscle (lateral abdominal muscle region), channels 5, 6, 7 and 8 to the rectus abdominis muscle (abdominal muscle region), channels 9, 10, 11 and 12 to the trapezius muscle (upper back muscle region), channels 13,14,15 and 16 to the latissimus dorsi muscle (waist muscle region) and channels 17 and 18 to the deltoid muscle.

The movements performed in the recordings were selected accordingly, as it was planned that the movements performed in the recordings would provide data for the biomechanical model to be built in the future. A total of 15 movements were performed, including right shoulder flexion, left shoulder flexion, right shoulder extension, left shoulder extension, right shoulder abduction, left shoulder abduction, right shoulder adduction, left shoulder adduction, right shoulder horizontal, left shoulder horizontal, trunk flexion, right trunk flexion, left trunk flexion, scapula protraction, scapula retraction. Each movement was performed for 4 repetitions.

In order to make the movements of the recorded subjects as same as possible, an interface application was developed. In this interface, projected on the screen, the recorded subject was enabled to follow the muscle-rest commands. In this interface, the person performing the movement was visually and audibly monitored by the loudspeaker. Duration of the movement sequence: Starting with 4 seconds in the free state to prepare the movement, 4 repetitions were made in the form of 3 seconds in the free state for 3 seconds to be in the state of performing the movement for 3 seconds.

2.5. Surface Electromyography (sEMG) Analysis

In our study, EMG signals obtained from subjects were analysed by developing algorithms in Matlab using signal processing methods. A 50 Hz notch filter and a 5 degree Butterworth 10-500 Hz bandpass filter were applied to remove the mains hum of the electromyography responses and to work in the significant frequency domain. From the filtered data of each channel, 4 repetitions at the moment of contraction were selected to be processed separately. As the start of the recording was synchronised with the movement notification interface, this selection was made with the time of the start of the recording, the contraction and relaxation times of the movement. The data was then analysed using Wavelet Packet Transform (WPT). The method of analysis is shown in Figure 2.

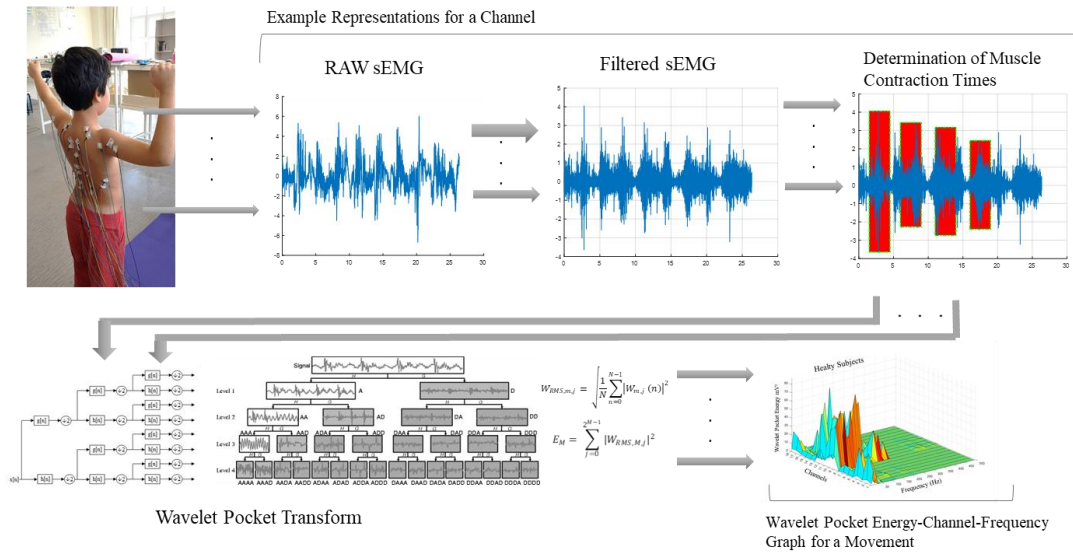


Figure 2. sEMG Data Analysis Scheme.

The wavelet transform method is a mathematical method used to analyse the signal at different scales and times [33]. It is based on the principles of wavelet analysis and helps to decompose the time and frequency components of data [34]. Daubechies level-7 was used for scaling. Daubechies wavelet filters are computationally efficient and effective, capable of capturing low and high frequency components in a consistent manner, supporting symmetrical and compact manner [35]. In the wavelet transform, high-pass filters are related to wavelet functions, while low-pass filters are related to scaling functions [32]. The following equations define the expansion equation for the scaling function $\phi(t)$ and the wavelet equation for the wavelet function $\psi(t)$ using the filter coefficients:

$$\phi(t) = \sqrt{2} \sum_{k=0}^N g(k)\phi(2t - k) \tag{1}$$

$$\psi(t) = \sqrt{2} \sum_{k=0}^N h(k)\phi(2t - k) \tag{2}$$

$$h(k) = (-1)^k g(N - k) \quad (3)$$

$g(k)$ in Eq. 1 are the low pass filter coefficients and $h(k)$ in Eq. 2 are the high pass filter coefficients. The relationship between the low pass filter coefficients and the high pass filter coefficients is shown in Eq. 3 [32]. Here N is the total number of filter coefficients. For WPT, the low pass filter $W_{2j+1}(t)$ and the high pass filter $W_{2j}(t)$ can be defined as follows [33,34].

$$W_{2j+1}(t) = \sqrt{2} \sum_{k=0}^{2^j-1} g(k) W_j(2t - k) \quad (4)$$

$$W_{2j}(t) = \sqrt{2} \sum_{k=0}^{2^j-1} h(k) W_j(2t - k) \quad (5)$$

For the WPT, we denote the scaling function by $W_0(t)$, the wavelet function by $W_1(t)$ and the node index j at each level. Low-pass filters are defined as $W_{2j+1}(t)$ and high-pass filters as $W_{2j}(t)$, while the wavelet function $W_j(t)$, a generalisation of the coupling between packets with three indices, can be calculated by Eq. 6 [35].

$$W_{m,j,n}(t) = 2^{-m/2} W_j(2^{-m}t - n) \quad (6)$$

The level index $j, j \in N$, the time shift parameter n and the scaling parameter m are defined as $(m, n) \in Z^2$. For each node, the root mean square (rms) value in the wavelet packet transform is calculated as in Eq. (7) [36].

$$W_{RMS,m,j} = \sqrt{\frac{1}{N} \sum_{n=0}^{N-1} |W_{m,j}(n)|^2} \quad (7)$$

$W_{m,j,n}(t)$ is the square root of the sum of squares of $W_{m,j}(n)$ divided by the length of $W_{m,j}(n)$ calculated by the reconstruction. After calculating the RMS value for each node in the WPT, the total wavelet packet energy (WPE) is found. It is obtained by taking the sum of the absolute squares of all RMS values from the initial node index to node $2^M - 1$ [36].

$$E_M = \sum_{j=0}^{2^M-1} |W_{RMS,M,j}|^2 \quad (8)$$

$W_{RMS,M,j}$ is the RMS value of each of the last level nodes at M levels of the WPT, and E_M is the total signal energy obtained as a result of the M level transformation. In order to identify the muscles that contract during the movements and to determine whether they produce significant values, the energy components obtained were summed for each channel and analysed statistically.

The sample size of the study was analysed using G*Power software (Universitat Kiel, Germany). As a result of the sample size analysis, it was determined that a minimum of 16 subjects should be included

in each group. In the study, it was aimed to reach an effect size of 0.92 and a power level of 0.80 [37]. The Mann-Whitney U test was used to determine the differences in characteristics between healthy and SPD subjects. The level of statistical significance was accepted as $p < 0.05$. Below this value, statistically significant differences were found between healthy subjects and SPD subjects in terms of the channels activated by movement. In the conclusion section, the results of the statistical analyses of the movements with significant differences between healthy subjects and SPD subjects are presented.

3. RESULTS

Upon completion of the recording stages, signal processing techniques were applied. Raw sEMG data were filtered. Wavelet packet energy (WPE) values of muscle activations were obtained from these filtered sEMG data using the WPT method. The WPE value of a muscle was compared between healthy subjects and SPD subjects. For muscles with high WPE values during movement, we have information about the number and amount of contracted muscle fibres. In addition to this, it is expected that the muscle with high activity will cause more energy requirement and energy consumption [38]. WPE values were calculated at 64 nodes. Three-dimensional graphs were generated using the WPE values, frequency and channel axis information corresponding to each node in the low and high frequency ranges. For statistical analysis, the WPE values of the channels at 64 nodes were summed and statistical values were extracted.

Table 2. Statistical analysis of trunk flexion movement results with significant differences between healthy subjects and SPD subjects. (Mann-Whitney U test, n; Sample Size, X; Mean, SD; Standard Deviation; p; p Value).

Movement	Channels	Healthy Subjects (n=16)		Sagittal Plane Deformity Subjects (n=16)		p
		X	SD	X	SD	
Trunk Flexion	Channel 5	18	0,70	122	15,20	0.001
	Channel 7	99	16,80	185	17,70	0.046
	Channel 8	25	3,30	88	13,30	0.003
	Channel 12	605	71,40	177	10,10	0.004
	Channel 15	182	10,80	411	59,80	0.036
	Channel 17	583	47,10	1714	214,20	0.014

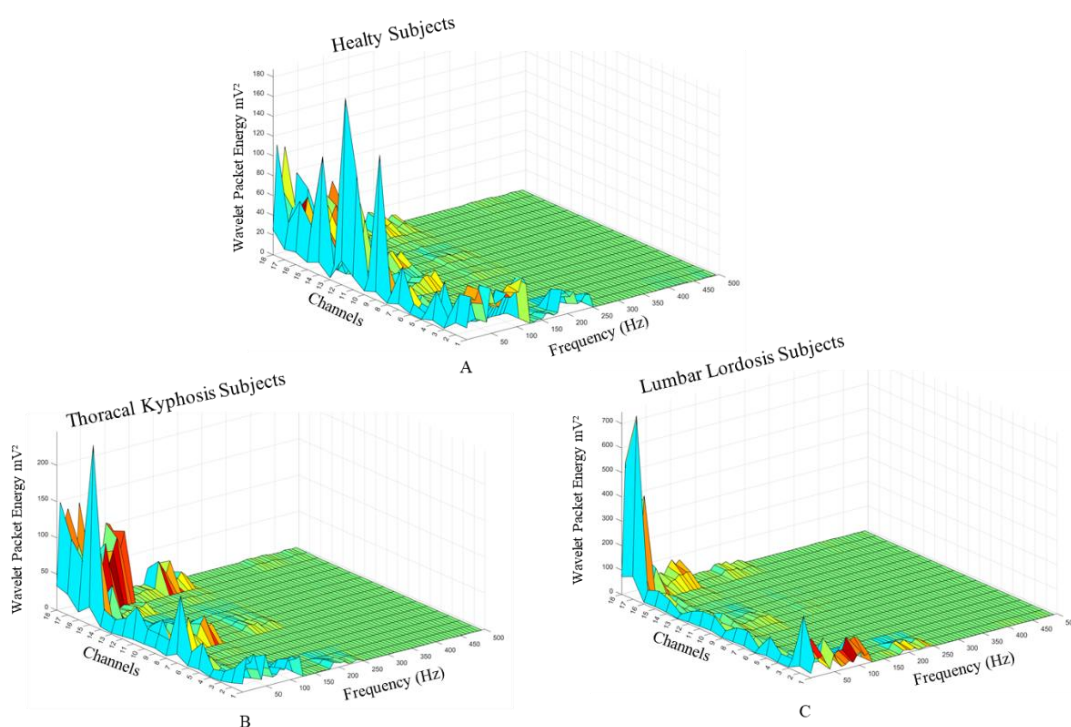


Figure 3. Trunk flexion movement WPE results (3A. Healty Subjects, 3B. Thoracal Kyphosis Subjects, 3C. Lumbar Lordosis Subjects).

For the trunk flexion movement, Figure 3 shows the 3D plots of the WPE values corresponding to each node in the low and high frequency ranges with frequency and channel axis. Figure 3A shows the 3D plots of the analysis results for the trunk flexion motion of healthy subjects, Figure 3B for thoracal kyphosis subjects and Figure 3C for lumbar lordosis subjects. Table 2 shows the WPE mean, standard deviation and p-values of the statistical analysis results between healthy subjects and SPD subjects. The 3D plots in Figure 3 were evaluated in the light of the statistically significant difference channels in Table 2. In Table 2, the abdominal (5th channel p-value 0.001, 7th channel p-value 0.046 and 8th channel p-value 0.003), upper back (12th channel p-value 0.004), waist (15th channel p-value 0.036) and deltoid (17th channel p-value 0.014) muscle regions were found to have statistically significant differences between SPD subjects and healthy subjects. Figure 3A shows that WPE values from healthy subjects show activity up to the 235,375 Hz range. In Figure 3B, WPE values from thoracal kyphosis subjects showed activity up to the 251 Hz band. In Figure 3C, WPE values from lumbar lordosis subjects showed activity up to the 243,188 Hz band. When analysing the channels with a statistically significant difference, activity was detected in the upper back muscle region in healthy subjects. In thoracal kyphosis subjects, muscle activity was found in the waist muscle region and deltoid muscle regions. In lumbar lordosis subjects, activity was found in the deltoid muscle.

Statistically significant differences were found in the muscle dynamics of healthy subjects and SPD subjects in the trunk flexion movement.

Table 3. Statistical analysis of scapular retraction movement results with significant differences between healthy subjects and SPD subjects. (Mann-Whitney U test, n; Sample Size, X; Mean, SD; Standard Deviation; p; p Value).

Movement	Channels	Healthy Subjects (n=16)		Sagittal Plane Deformity Subjects (n=16)		p
		X	SD	X	SD	
Scapular Retraction	Channel 1	35	3.2	77	12.3	0.029
	Channel 6	23	1.3	12	0.9	0.003
	Channel 9	1050	89.6	1655	237.4	0.034
	Channel 10	738	68.0	1067	112.8	0.042
	Channel 11	248	21.3	1443	167.9	0.001
	Channel 12	800	96.1	1445	152.8	0.040
	Channel 14	32	5.1	54	4.5	0.044
	Channel 15	19	1.4	72	8.9	0.018

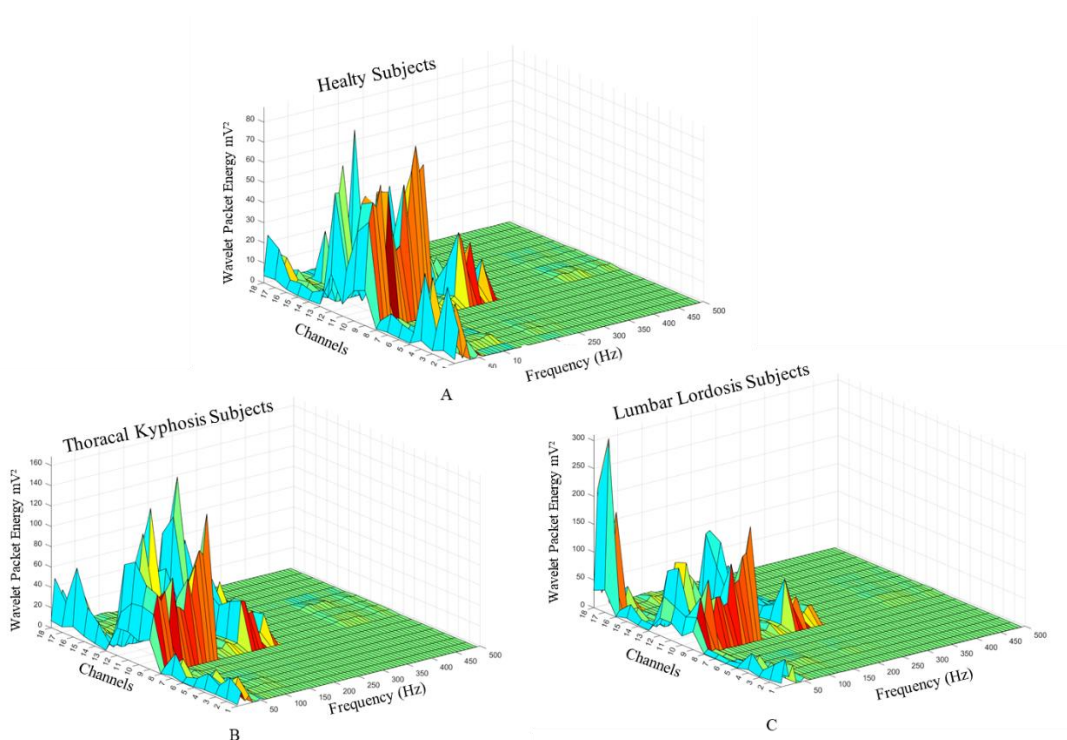


Figure 4. Scapular retraction movement WPE results (4A. Healty Subjects, 4B. Thoracal Kyphosis Subjects, 4C. Lumbar Lordosis Subjects).

For the scapular retraction movement, Figure 4 shows the 3D plots of the WPE values corresponding to each node in the low and high frequency ranges with frequency and channel axis. Figure 4A shows the 3D plot of the analysis results for the scapular retraction movement of healthy subjects, Figure 4B shows the 3D plot for thoracal kyphosis subjects and Figure 4C shows the 3D plot for lumbar lordosis subjects. The WPE mean, standard deviation and p-values of the results of the statistical analyses between healthy subjects and SPD subjects are shown in Table 3. The 3D plots in Figure 4 were evaluated in the light of the statistically significant difference channels in Table 3. When the muscle regions with statistically significant differences between SPD subjects and healthy subjects were analysed in Table 3, it was found that there were statistically significant differences in the pectoral muscle region (1st channel p value 0.029), upper back muscle region (9th channel p value 0.034, 10th channel p value 0.042, 11th channel p value 0.001 and 12th channel p value 0.040) and waist muscle region (14th channel p value 0.044 and 15th channel p value 0.018). Figure 4A shows that the WPE values of healthy subjects show activity up to the 243.88 Hz band. In Figure 4B, WPE values from thoracal kyphosis subjects showed activity up to the 227.562 Hz band. In Figure 4C, WPE values from lumbar lordosis subjects showed activity up to the 243.188 Hz band. When analysing the

channels with statistically significant difference, activity was detected in the upper back muscle region in healthy subjects and in SPD subjects. However, the WPE values were more dominant in SPD subjects than in healthy subjects. A statistically significant difference was found in the upper back muscles of SPD subjects during the scapular retraction movement, and it was found that SPD subjects performed the movement using more energy.

Table 4. Statistical analyses of right shoulder flexion movement results with significant differences between healthy subjects and SPD subjects. (Mann-Whitney U test, n; Sample Size, X; Mean, SD; Standard Deviation; p; p Value).

Movements	Channels	Healthy Subjects (n=16)		Sagittal Plane Deformity Subjects (n=16)		p
		X	SD	X	SD	
Right Shoulder Flexion	Channel 1	152	16.2	307	26.9	0.019
	Channel 9	20	0.6	83	7.8	0.002
	Channel 10	977	115.5	1759	139.6	0.038
	Channel 12	1228	317.1	1860	297.7	0.038
	Channel 15	21	1.6	116	14.7	0.000
	Channel 17	1306	123.3	635	167.7	0.029

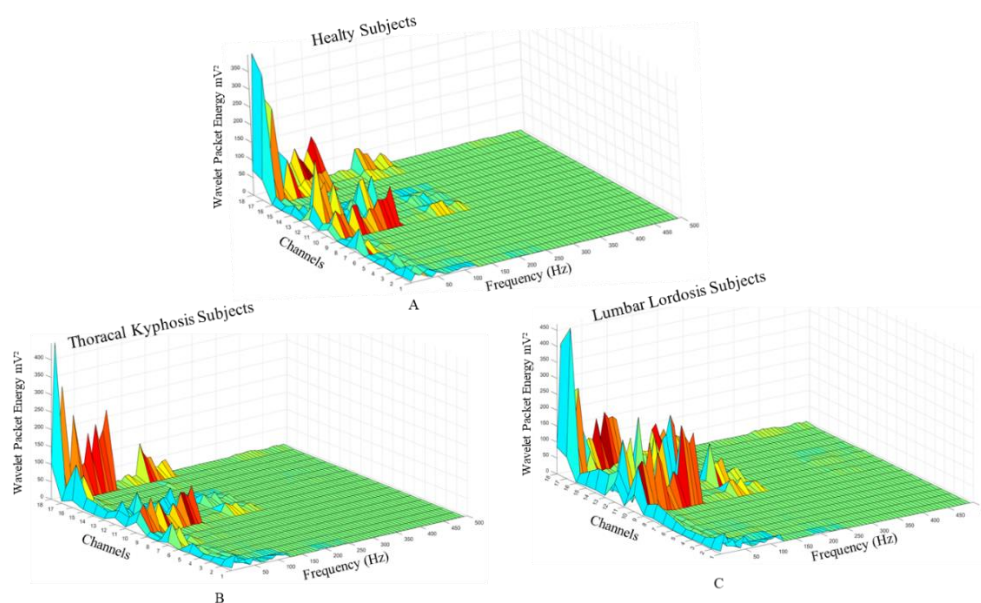


Figure 5. Right shoulder flexion WPE results (5A. Healthy Subjects, 5B. Thoracic Kyphosis Subjects, 5C. Lumbar Lordosis Subjects).

For the right shoulder flexion movement, Figure 5 shows the 3D plots of the WPE values corresponding to each node in the low and high frequency ranges with frequency and channel axis. Figure 5A shows the 3D plot of the analysis results for the right shoulder flexion movement of healthy subjects, Figure 5B for thoracic kyphosis subjects and Figure 5C for lumbar lordosis subjects. The mean WPE, standard deviation and p-values of the statistical analyses between healthy subjects and SPD subjects are shown in Table 4. The 3D plots in Figure 5 were evaluated using the channels with statistically significant differences in Table 4. When the muscle regions with statistically significant differences between SPD subjects and healthy subjects were analysed in Table 4, they were found in the pectoral muscle region (1st channel p-value 0.019), upper back muscle region (9th channel p-value 0.002, 10th channel p-value 0.038 and 12th channel p-value 0.038), waist muscle region (15th channel p-value 0.000) and deltoid muscle (17th channel p-value 0.029). Figure 5A shows that WPE values from healthy subjects show activity up to the 235,375 Hz band. In Figure 5B, WPE values from thoracic kyphosis subjects showed activity up to the 243,118 Hz band. In Figure 5C, WPE values in lumbar lordosis subjects showed activity up to the 251 Hz band. When the channels with statistically significant difference were examined, activity was detected in the right upper back and deltoid regions in healthy subjects, in the right upper back and deltoid regions in thoracic kyphosis subjects, and in the right upper back and deltoid regions in lumbar lordosis subjects. Although the muscle dynamic positions were present in the same muscle regions, the WPE value was higher in SPD subjects. It was found that SPD subjects performed the movement by using more energy.

Table 5. Statistical analysis of trunk left flexion movement results with significant differences between healthy subjects and SPD subjects. (Mann-Whitney U test, n; Sample Size, X; Mean, SD; Standard Deviation; p; p Value).

Movements	Channels	Healthy Subjects (n=16)		Sagittal Plane Deformity Subjects (n=16)		p
		X	SD	X	SD	
Trunk Left Flexion	Channel 4	272	39.6	64	5.8	0.018
	Channel 7	19	2.3	82	9.9	0.004

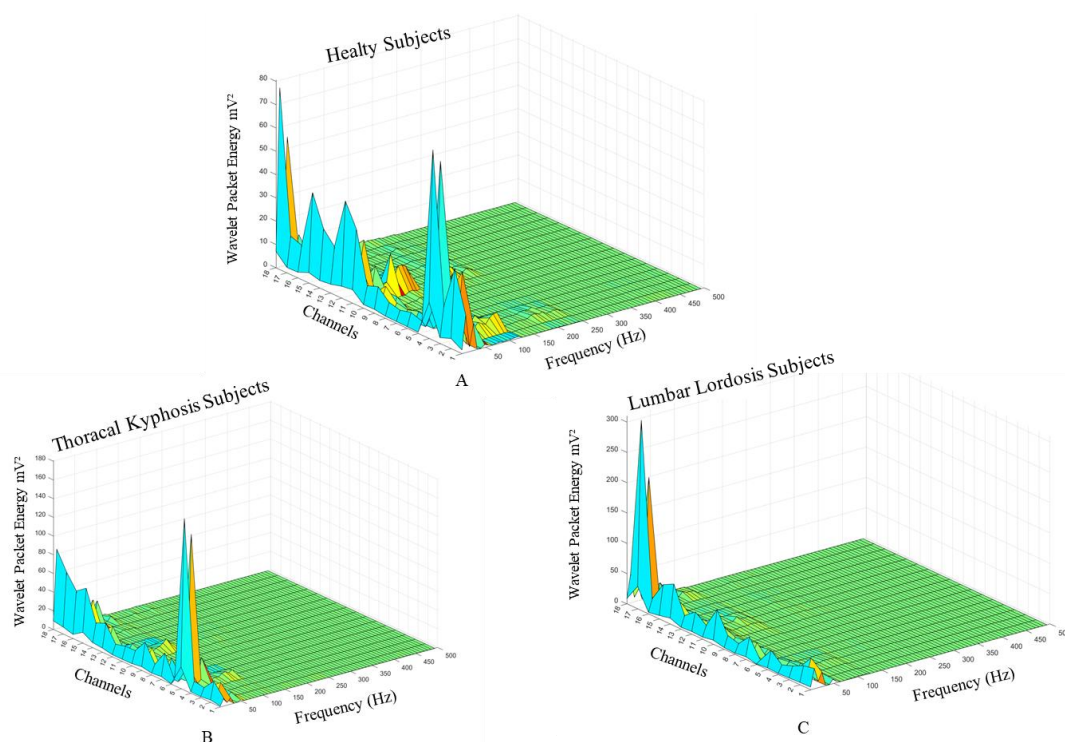


Figure 6. Left lateral flexion movement WPE results (6A. Healthy Subjects, 6B. Thoracal Kyphosis Subjects, 6C. Lumbar Lordosis Subjects).

For left lateral flexion, Figure 6 shows the 3D plots of the WPE values corresponding to each node in the low and high frequency ranges with frequency and channel axis. Figure 6A shows the 3D plot of the analysis results for the left lateral flexion motion for healthy subjects, Figure 6B for thoracal kyphosis subjects and Figure 6C for lumbar lordosis subjects. The mean WPE, standard deviation and p-values of the statistical analyses between healthy subjects and SPD subjects are shown in Table 5. The 3D plots in Figure 6 were evaluated in the light of the channels with statistically significant differences in Table 5. When the muscle regions with statistically significant differences between SPD subjects and healthy subjects were analysed in Table 5, the lateral abdominal muscle region (4th channel p-value 0.018) and the abdominal muscle region (7th channel p-value 0.004) were found. Figure 6A shows that the WPE values of healthy subjects show activity up to the 188.5 Hz band. In Figure 6B, WPE values from thoracal kyphosis subjects showed activity up to the 110.375 Hz band. In Figure 6C, WPE values from lumbar lordosis subjects showed activity up to the 94.75 Hz band. When the channels with statistically significant difference were analysed, activity was detected in the lateral abdominal muscle region and in the abdominal muscle region in healthy subjects. In thoracal kyphosis subjects, activity was detected in the lateral muscle region, while in lumbar lordosis subjects, muscle activity could not be detected in muscle regions with a statistically significant difference.

4. DISCUSSIONS

In this study, muscle dynamics of healthy subjects, subjects with thoracal kyphosis and lumbar lordosis were determined using sEMG data obtained from 18 channels during 15 movements. The results of the sEMG analysis and the statistical analysis of the data are presented in the results section.

When analysing the channels with a statistically significant difference in the trunk flexion movement, activity was detected in the upper back muscle region in healthy subjects, in the waist muscle region and deltoid muscle in thoracal kyphosis subjects and in the deltoid muscle in lumbar lordosis subjects. In the trunk flexion movement, the back muscles contract and try to stabilise the movement, while healthy subjects tilt their trunk forward. They complete the movement according to the kinematics of the movement. However, in SPD subjects, muscle activation is impaired due to the increased sagittal plane deformity, so they try to complete the movement with the support of the waist or shoulder muscle region to compensate. If we explain the compensatory mechanism [39], SPD subjects complete the movement with other muscle groups and supports instead of the upper back muscle region. In other words, it was observed that during trunk flexion movement, other muscle groups were used instead of extensor (back) muscle groups. The clinical significance of this is that by not being able to provide the correct muscle contraction dynamics, SPD subjects are at risk of increasing lordosis or kyphosis curvatures, requiring more energy than necessary, resulting in fatigue and musculoskeletal problems. It has been reported in the literature that the natural curvature of the spine in the sagittal plane is responsible for postural balance [11,12], and that musculoskeletal complaints such as postural affection, shoulder and cervical pain may occur when the natural curvature increases [3,4]. As a result of our study, the spatial variation of muscle dynamics in SPD subjects supports the findings of disease progression with the literature.

In the scapular retraction movement, when analysing the channels with a statistically significant difference, activity was detected in the upper back muscle region in healthy subjects and SPD subjects. However, the WPE values of SPD subjects were more dominant than healthy subjects. A statistically significant difference was found in the upper back muscles of SPD subjects in the scapular retraction movement. It was found that SPD subjects performed the movement with more energy. Particularly in thoracal kyphosis subjects, as the curvature of the thoracic region increases, the muscle activation required for postural control during this movement is more intense. For this reason, rehabilitation programmes are used to help these subjects use energy correctly and economically. Thoracal kyphosis subjects expend more energy than healthy subjects to increase the quality of movement and to perform it with the right combination. As in healthy subjects, maximum movement quality is aimed for with less energy. In addition, because the posterior group muscles (back muscles) are already in an abnormal muscle position in thoracal kyphosis subjects, they perform the movement with more energy in the scapular retraction movement. It has been suggested in the literature that musculoskeletal information for rehabilitation programmes applied to SPD subjects provides valuable information for the recovery process and that assessment of the musculoskeletal system together with the skeletal system is an important aspect of measuring thoracic kyphosis [5].

When analysing the statistical results of the right shoulder flexion movement, the muscle region with a statistically significant difference in the right shoulder flexion movement of SPD subjects and

healthy subjects was found to be the right upper back muscle region and the deltoid muscle. A statistically significant difference was found in the right shoulder flexion movement between healthy subjects and SPD subjects. For the right shoulder flexion movement, it was found that SPD subjects performed more activity than healthy subjects. This is because SPD subjects use more energy to stand upright and show more muscle activity and faster muscle fatigue. When analysing the channels with a statistically significant difference for the left lateral flexion movement, activity was detected in the lateral abdominal muscle region and in the abdominal muscle region in healthy subjects. In thoracic kyphosis subjects, activity was detected in the lateral muscle region, whereas in lumbar lordosis subjects, muscle activity was not detected in the muscle regions with statistically significant difference, although there was no statistically significant difference in lumbar lordosis subjects. Therefore, subject-specific muscle activation gives meaning to the advantages and disadvantages of lordotic posture. It may also contribute to rehabilitation programmes.

SPD subjects with isolated thoracic kyphosis or lumbar lordosis are not commonly encountered in clinics. Therefore, subjects with major pathology of thoracic kyphosis and subjects with major pathology of lumbar lordosis were considered. Statistical analyses were compared between healthy subjects and SPD subjects. One reason for this is to increase the statistical significance and the other reason is to look for a significant difference between SPD subjects and healthy subjects. This difference was used to determine the channels with different muscle activation. The sample of our current group of healthy subjects and SPD subjects was limited in number. This information constitutes the limitations of our study.

5. CONCLUSION

In this study, a multi-channel sEMG-based study was developed to investigate the effect of sagittal plane spinal deformity on muscle dynamics in adolescents during movement. It was found that muscle activation values and positions of muscle dynamics changed in SPD subjects compared to healthy subjects. In our study, our statistical results served as a filter to evaluate the muscle regions with significant differences. Although there was muscle activity in the same muscle group in some movements, SPD subjects showed more intense activity, and the activity of different muscle groups in some movements statistically supported that SPD subjects activated different muscle regions. It was found that SPD subjects use a lot of energy while performing the movements and compensate from other muscle regions to perform the movement with high quality. As they cannot provide the correct muscle contraction dynamics, SPD subjects are at risk of further increasing lordosis or kyphosis curvatures. The clinical significance of the results will provide a new perspective in the diagnosis and treatment process. In the treatment process of changing muscle dynamics, we believe that the evaluation of muscle dynamics together with radiological images when creating rehabilitation programmes for SPD subjects in the treatment process can be followed more effectively in the healing process. At the same time, this study has provided a movement-based assessment of the dynamics of the muscles responsible for upright posture in healthy adolescents. We believe that this study will contribute to the literature as a useful resource for biomechanical modelling and kinematic analysis studies. For future studies, we believe that muscle dynamics should be evaluated in subjects with sagittal plane deformity in the presence of scoliosis, which is a 3D deformity of the spine.

ACKNOWLEDGEMENT

There is no conflict of interest with any person/institution in the prepared article.

REFERENCES

- [1] Frost, B. A., S. Camarero-Espinosa and E. J. Foster (2019). "Materials for the spine: anatomy, problems, and solutions." *Materials* 12(2): 253.
- [2] Boseker, E. H., J. H. Moe, R. B. Winter and S. E. Koop (2000). "Determination of "normal" thoracic kyphosis: a roentgenographic study of 121 "normal" children." *Journal of Pediatric Orthopaedics* 20(6): 796-798.
- [3] Issahaku, S., E. Sackey, E. K. Tiburu and T. A. Sackey (2023). "Determination of the Lumbar Lordotic and Lumbosacral Angles in Normal Adults Ghanaian Population Using Radiologic Imaging Technique."
- [4] Gray, J. C. and O. Grimsby (2012). "Interrelationship of the spine, rib cage, and shoulder." *Physical therapy of the shoulder*: 87-130.
- [5] Barrett, E., K. McCreesh and J. Lewis (2014). "Reliability and validity of non-radiographic methods of thoracic kyphosis measurement: a systematic review." *Manual therapy* 19(1): 10-17.
- [6] Chaise, F. O., C. T. Candotti, M. L. Torre, T. S. Furlanetto, P. Pelinson and J. F. Loss (2011). "Validation, repeatability and reproducibility of a noninvasive instrument for measuring thoracic and lumbar curvature of the spine in the sagittal plane." *Brazilian Journal of Physical Therapy* 15: 511-517.
- [7] Perdriolle, R. and J. Vidal (1987). *Morphology of scoliosis: three-dimensional evolution*, SLACK Incorporated Thorofare, NJ. 10: 909-915.
- [8] Fletcher, N. D., H. Jeffrey, M. Anna, R. Browne and D. J. Sucato (2012). "Residual thoracic hypokyphosis after posterior spinal fusion and instrumentation in adolescent idiopathic scoliosis: risk factors and clinical ramifications." *Spine* 37(3): 200-206.
- [9] Parvaresh, K. C., E. J. Osborn, F. G. Reighard, J. Doan, T. P. Bastrom and P. O. Newton (2017). "Predicting 3D thoracic kyphosis using traditional 2D radiographic measurements in adolescent idiopathic scoliosis." *Spine Deformity* 5(3): 159-165.
- [10] Hayashi, K., V. V. Upasani, J. B. Pawelek, C.-É. Aubin, H. Labelle, L. G. Lenke, R. Jackson and P. O. Newton (2009). "Three-dimensional analysis of thoracic apical sagittal alignment in adolescent idiopathic scoliosis." *Spine* 34(8): 792-797.

- [11] Hwang, S. W., A. F. Samdani, M. Tantorski, P. Cahill, J. Nydick, A. Fine, R. R. Betz and M. D. Antonacci (2011). "Cervical sagittal plane decompensation after surgery for adolescent idiopathic scoliosis: an effect imparted by postoperative thoracic hypokyphosis." *Journal of Neurosurgery: Spine* 15(5): 491-496.
- [12] Adams, M., D. McNally, H. Chinn and P. Dolan (1994). "The clinical biomechanics award paper 1993 posture and the compressive strength of the lumbar spine." *Clinical Biomechanics* 9(1): 5-14.
- [13] Potvin, J., R. Norman and S. McGill (1991). "Reduction in anterior shear forces on the L4L5 disc by the lumbar musculature." *Clinical Biomechanics* 6(2): 88-96.
- [14] McGill, S. M., R. L. Hughson and K. Parks (2000). "Changes in lumbar lordosis modify the role of the extensor muscles." *Clinical biomechanics* 15(10): 777-780.
- [15] Ghorbani, L. and G. Ghasemi (2007). "Effects of eight weeks corrective exercises on lumbar lordosis." *Journal of research in rehabilitation sciences* 3(2).
- [16] Pace, N., L. Ricci and S. Negrini (2013). "A comparison approach to explain risks related to X-ray imaging for scoliosis, 2012 SOSORT award winner." *Scoliosis* 8(1): 1-7.
- [17] Farago, E., D. MacIsaac, M. Suk and A. D. Chan (2022). "A review of techniques for surface electromyography signal quality analysis." *IEEE Reviews in Biomedical Engineering* 16: 472-486.
- [18] Turker, H. (2013). *Electrodiagnosis in new frontiers of clinical research, BoD–Books on Demand*.
- [19] Gazzoni, M. (2010). "Multichannel surface electromyography in ergonomics: Potentialities and limits." *Human Factors and Ergonomics in Manufacturing & Service Industries* 20(4): 255-271.
- [20] Taborri, J., J. Keogh, A. Kos, A. Santuz, A. Umek, C. Urbanczyk, E. van der Kruk and S. Rossi (2020). "Sport biomechanics applications using inertial, force, and EMG sensors: A literature overview." *Applied bionics and biomechanics* 20-20
- [21] Li, G., O. W. Samuel, C. Lin, M. G. Asogbon, P. Fang and P. O. Idowu (2019). "Realizing efficient EMG-based prosthetic control strategy." *Neural Interface: Frontiers and Applications*: 149-166.
- [22] Topçu, Ç., H. Uysal, Ö. Özkan, Ö. Özkan, Ö. Polat, M. Bedeloğlu, A. Akgül, E. N. Döğer, R. Sever and Ö. H. Çolak (2018). "Recovery of facial expressions using functional electrical stimulation after full-face transplantation." *Journal of NeuroEngineering and Rehabilitation* 15: 1

- [23] Esposito, F., A. Veicsteinas, C. Orizio and D. Malgrati (1996). "Time and frequency domain analysis of electromyogram and sound myogram in the elderly." *European journal of applied physiology and occupational physiology* 73: 503-510.
- [24] Altan, E., K. Pehlivan and E. Kaplanoğlu (2019). Comparison of EMG based finger motion classification algorithms. 2019 27th Signal Processing and Communications Applications Conference (SIU), IEEE.
- [25] Ahamed, N. U., Z. Taha, M. Alqahtani, O. Altwijri, M. Rahman and A. Deboucha (2016). Age related differences in the surface EMG signals on adolescent's muscle during contraction. IOP Conference Series: Materials Science and Engineering, IOP Publishing.
- [26] Junior, J. J. A. M., M. L. Freitas, H. V. Siqueira, A. E. Lazzaretti, S. F. Pichorim and S. L. Stevan Jr (2020). "Feature selection and dimensionality reduction: An extensive comparison in hand gesture classification by sEMG in eight channels armband approach." *Biomedical Signal Processing and Control* 59: 101920.
- [27] Ferdjallah, M., J. J. Wertsch and R. Shaker (2000). "Spectral analysis of surface electromyography (EMG) of upper esophageal sphincter-opening muscles during head lift exercise." *Journal of rehabilitation research and development* 37(3): 335-340.
- [28] Chowdhury, R. H., M. B. Reaz, M. A. B. M. Ali, A. A. Bakar, K. Chellappan and T. G. Chang (2013). "Surface electromyography signal processing and classification techniques." *Sensors* 13(9): 12431-12466.
- [29] Camata, T. V., J. L. Dantas, T. Abrão, M. A. Brunetto, A. C. Moraes and L. R. Altimari (2010). Fourier and wavelet spectral analysis of EMG signals in supramaximal constant load dynamic exercise. 2010 Annual International Conference of the IEEE Engineering in Medicine and Biology, IEEE.
- [30] Sparto, P. J., M. Parnianpour, E. A. Barria and J. M. Jagadeesh (2000). "Wavelet and short-time Fourier transform analysis of electromyography for detection of back muscle fatigue." *IEEE Transactions on rehabilitation engineering* 8(3): 433-436.
- [31] Zhang, X., Y. Wang and R. P. Han (2010). Wavelet transform theory and its application in EMG signal processing. 2010 Seventh International Conference on Fuzzy Systems and Knowledge Discovery, IEEE.
- [32] Strang, G. and T. Nguyen (1996). *Wavelets and filter banks*, SIAM.
- [33] Rong, Y., D. Hao, X. Han, Y. Zhang, J. Zhang and Y. Zeng (2013). "Classification of surface EMGs using wavelet packet energy analysis and a genetic algorithm-based support vector machine." *Neurophysiology* 45: 39-48.

- [34] Wallen, R. D. (2004). "The illustrated wavelet transform handbook." Biomedical Instrumentation & Technology 38(4): 298-298.
- [35] Daubechies, I. (1992). Ten lectures on wavelets, SIAM.
- [36] Englehart, K., B. Hudgin and P. A. Parker (2001). "A wavelet-based continuous classification scheme for multifunction myoelectric control." IEEE Transactions on Biomedical Engineering 48(3): 302-311.
- [37] Tombak, K. (2021). Adölesan idiyopatik skolyozda kontrollü schroth egzersiz ve ev programlarının gövde simetrisi, deformite algısı ve yaşam kalitesi üzerindeki etkilerinin karşılaştırılması (Doctoral dissertation), Eastern Mediterranean University, Cyprus
- [38] Daryabor, A., Arazpour, M., Sharifi, G., Bani, M. A., Aboutorabi, A., & Golchin, N. (2017). Gait and energy consumption in adolescent idiopathic scoliosis: A literature review. Annals of physical and rehabilitation medicine, 60(2), 107-116.
- [39] Wilczyński, J., Habik, N., Paprocki, M. J., Rychter, P., Wilczyński, I., & Dworakowska, D. (2017). Scoliosis compensation and postural responses in school girls. Journal of Education, Health and Sport, 7(8), 218-232.



RESEARCH ARTICLE

ALTERED NUMBERS OF LUCAS NUMBER SQUARED

Fikri KÖKEN^{1,*}, Emre KANKAL²

¹Necmettin Erbakan University, Seydisehir Ahmet Cengiz Faculty of Engineering, Department of Computer Engineering, Konya, TURKEY. fkoken@erbakan.edu.tr, ORCID: 0000-0002-8304-9525

²Necmettin Erbakan University, Institute of Science and Technology, Department of Mathematics, Konya, TURKEY. kangalemre56@gmail.com, ORCID: 0000-0002-2707-5323

Receive Date: 15.02.2023

Accepted Date: 16.05.2023

ABSTRACT

We investigate two types altered Lucas numbers denoted $G_{L(n)}^{(2)}(a)$ and $H_{L(n)}^{(2)}(a)$ defined by adding or subtracting a value $\{a\}$ from the square of the n^{th} Lucas numbers. We achieve these numbers form as the consecutive products of the Fibonacci numbers. Therefore, consecutive sum-subtraction relations of altered Lucas numbers and their Binet-like formulas are given by using some properties of the Fibonacci numbers. Also, we explore the gcd sequences of r -successive terms of altered Lucas numbers denoted $\{G_{L(n),r}^{(2)}(a)\}$ and $\{H_{L(n),r}^{(2)}(a)\}$, $r=1,2$, $a \in \{1,9\}$ according to the greatest common divisor (gcd) properties of consecutive terms of the Fibonacci numbers. We show that these sequences are periodic or Fibonacci sequences.

Keywords: *Altered Lucas numbers, Greatest common divisor (gcd) sequences, Fibonacci sequence.*

1. INTRODUCTION

One can produce the Lucas sequence by using a recurrence relation $L_n = L_{n-1} + L_{n-2}$ $n \geq 2$ with initial conditions $L_0 = 2$ and $L_1 = 1$. The Lucas sequence $\{L_n\}_{n=0}^{\infty}$ consists of the numbers $\{2, 1, 3, 4, 7, 11, 18, \dots\}$ (Lucas numbers are sequence number A000032 in OEIS [1]). Also, the n^{th} Lucas number can be presented with the Binet formula $L_n = \alpha^n + \beta^n$, $\alpha, \beta = (1 \pm \sqrt{5})/2$, $n \in \mathbb{Z}^+$. The Binet formula is used to generalize indices from $n \in \mathbb{Z}^+$ to $n \in \mathbb{Z}$ such as $L_{-n} = (-1)^n L_n$, and to prove some properties of the Lucas numbers, such as the Cassini identity $L_{n+1}L_{n-1} - L_n^2 = 5(-1)^{n-1}$, subscript sum $F_{m+1}L_n + F_mL_{n-1} = L_{m+n}$, and subscript subtraction $(-1)^n (F_{m+1}L_n - F_mL_{n+1}) = L_{m-n}$ identities. Similarly,

let $F_0 = 0$ and $F_1 = 1$ be initial conditions, then a n^{th} Fibonacci number is defined by the recurrence relation $F_n = F_{n-1} + F_{n-2}$, $n \in \mathbb{Z}$. The Fibonacci sequence $\{F_n\}_{-\infty}^{\infty}$ consists of numbers $\{\dots, 2, -1, 1, 0, 1, 1, 2, \dots\}$ (A147316). The n^{th} Fibonacci number is given with the Binet formula $F_n = (\alpha^n - \beta^n) / \sqrt{5}$, $\alpha, \beta = (1 \pm \sqrt{5}) / 2$, $n \in \mathbb{Z}$. In addition, the following equations that can act as any bridge between the Fibonacci F_n and Lucas L_n numbers, $F_{n+1} + F_{n-1} = L_n$, $2F_{n+m} = F_m L_n + F_n L_m$, $L_{n+1} + L_{n-1} = 5F_n$, $2L_{n+m} = L_m L_n + 5F_n F_m$ are valid as well-known properties in the literature. The proof of many equations belonging to the Fibonacci and Lucas numbers can be given by using the Fibonacci and Lucas Binet formulas [2].

Now, we give a lot of sum properties as examples of sequences produced from the Lucas numbers. A sum of the Lucas numbers is $\sum_{i=1}^n L_i = L_{n+2} - 3$ (Concerned with sequence A027961 in OEIS [1]). A sum of single-indices Lucas numbers is found as $\sum_{i=1}^n L_{2i-1} = L_{2n} - 2$ (A004146). A sum of the even-indices Lucas numbers is $\sum_{i=1}^n L_{2i} = L_{2n+1} - 1$. A sum of the square of the Lucas numbers is $\sum_{i=1}^n L_i^2 = L_n L_{n+1} - 2$ (A005970) [2]. In [3,4], the authors consider these results as any sequence, and these sequences are studied as altered Lucas sequences.

In [3], the author defined the shifted Lucas numbers $\{L_n + a\}_{n \geq 0}$ derived from the Lucas sequences and established a gcd sequence denoted $\{l_n(a)\}_{n \geq 0} = \{gcd(L_n + a, L_{n+1} + a)\}_{n \geq 0}$ by taking their greatest common divisor of them. The sequence $\{l_n(a)\}_{n \geq 0}$ is bounded by its values $\{|a^2 \pm 5|\}$ as $l_{2n-1}(a) \leq a^2 + 5$, $l_{2n}(a) \leq |a^2 - 5|$. When $a = 1$, the sequence $\{l_n(1)\}_{n \geq 0}$ is a periodic sequence that appears to take the following values $l_{4n-1}(1) = \{3, 1, 6, 1, 3, 2\}$, $n \in \mathbb{Z}_6$; $l_{4n}(1) = \{1, 4, 1\}$, $l_{4n+1}(1) = \{2, 1, 1\}$, $l_{4n+2}(1) = \{1, 1, 4\}$, $n \in \mathbb{Z}_3$. He compared the bounded inequalities according to the values found for the sequence $\{l_n(1)\}$.

F. Köken study on the altered sequences $\{L_n^+\}_{n > 0}$ and $\{L_n^-\}_{n > 0}$; these consist of numbers L_n^+ and L_n^- , are defined as when n is odd, $L_n^+ = L_n - 1$ and $L_n^- = L_n + 1$; when n is even, $L_n^+ = L_n + 3$ and $L_n^- = L_n - 3$. Let L_n^+ be the n^{th} altered numbers, $L_{4k}^+ = 5F_{2k+1}F_{2k-1}$, $L_{4k+1}^+ = 5F_{2k+1}F_{2k}$, $L_{4k+2}^+ = L_{2k+2}L_{2k}$ and $L_{4k+3}^+ = L_{2k+2}L_{2k+1}$ are given. The entities of the $\{L_n^-\}$ have shown the numbers

$L_{4k}^- = L_{2k+1}L_{2k-1}$, $L_{4k+1}^- = L_{2k+1}L_{2k}$, $L_{4k+2}^- = 5F_{2k+2}F_{2k}$ and $L_{4k+3}^- = 5F_{2k+2}F_{2k+1}$. In addition, let $L_{n,r}^\pm = (L_n^\pm, L_{n+r}^\pm)$ denote r -successive gcd numbers, the sequence $\{L_{4k,1}^+\}_{k \geq 1}$ is equal to the subsequence $\{5F_{2k+1}\}_{k \geq 1}$, and the $\{L_{4k-2,1}^+\}_{k \geq 1}$ is equal to the subsequence $\{L_{2k}\}_{k \geq 1}$. Also, the numbers $L_{n,1}^-$ has been given with equalities $L_{4k,1}^- = L_{2k+1}$ and $L_{4k+2,1}^- = 5F_{2k+2}$. Also, according to values $r = 2, 3, 4$, the gcd numbers $L_{n,r}^+$ and $L_{n,r}^-$ are obtained in [4].

We establish this paper as follows. In Section 2, we give a brief overview of necessary definitions and identities. In Section 3.1, we define two altered sequences, and explore properties of sums, difference, Binet's formula and closed forms for the numbers $G_{L(n)}^{(2)}(a)$ and $H_{L(n)}^{(2)}(a)$. In Section 3.2, we establish two types r -successive altered Lucas gcd sequences denoted with $G_{L(n),r}^{(2)}(a)$ and $H_{L(n),r}^{(2)}(a)$ for the values $G_{L(n)}^{(2)}(a)$ and $H_{L(n)}^{(2)}(a)$, and investigate these sequences according to the cases $r = 1, 2$.

2. MATERIAL AND METHOD

The gcd property of integer sequences can be given as $(F_m, F_n) = (F_n, F_r)$ for $m = qn + r$ all $m, n, r, q \in \mathbb{N}$, where F_n is the n^{th} Fibonacci number. Thus, it is seen that the greatest common divisor of two Fibonacci numbers is a Fibonacci number such as $(F_m, F_n) = F_{(m,n)}$. For example, two successive Fibonacci numbers are relatively prime, $(F_n, F_{n+1}) = (F_n, F_{n+2}) = 1$ in [1,2].

According to whether n is odd or even in Lucas identities known as the Cassini identity $L_n^2 - 5(-1)^n = L_{n+1}L_{n-1}$ and $L_n^2 - 4(-1)^n = 5F_n^2$, we can obtain the equations $L_{2k+1}^2 + 5 = L_{2k+2}L_{2k}$, $L_{2k}^2 - 5 = L_{2k+1}L_{2k-1}$, $L_{2k+1}^2 + 4 = 5F_{2k+1}^2$ and $L_{2k}^2 - 4 = 5F_{2k}^2$ [2]. We inspire by these equations for this question, "Can any altered Lucas sequences such as $\{L_n^2 \pm a\}$ be defined?"

Also, in the literature, there have been a great many papers studying sums of l -consecutive products of the Lucas numbers; $\sum_{i=1}^{2n} L_i L_{i+1} = L_{2n+1}^2 - 1$ or $\sum_{i=0}^{2n} L_i L_{i+1} = L_{2n+1}^2 + 1$ and $\sum_{i=1}^{2n+1} L_i L_{i+1} = L_{2n+2}^2 - 6$ or $\sum_{i=0}^{2n+1} L_i L_{i+1} = L_{2n+2}^2 - 4$ [2,5,6]. We can consider the results of these sums as altered Lucas numbers motivated by these sums.

Now, we will develop a theory using the following equations:

$$L_{m+n+1}^2 + L_{m-n}^2 = 5F_{2m+1}F_{2n+1}, \tag{1}$$

$$L_{m+n}^2 - L_{m-n}^2 = 5F_{2m}F_{2n}. \tag{2}$$

The identities in Eq. 1 and Eq. 2 can be proved using Binet’s formula. We have mainly used the identities in Eq. 1 and Eq. 2 to obtain the following equations, but one can use Binet’s formula for their proofs.

Lemma 1. Let F_n and L_n be the n^{th} Fibonacci and Lucas number, then

$$L_{2k}^2 + 1 = 5F_{2k-1}F_{2k+1}, \tag{3}$$

$$L_{2k+1}^2 - 1 = 5F_{2(k+1)}F_{2k}, \tag{4}$$

$$L_{2k+1}^2 + 9 = 5F_{2k+3}F_{2k-1}, \tag{5}$$

$$L_{2k}^2 - 9 = 5F_{2(k+1)}F_{2(k-1)}. \tag{6}$$

Proof: For $m = k + 1$ and $n = k$ in Eq. 1, we have obtained $L_{2k+2}^2 + L_1^2 = 5F_{2k+3}F_{2k+1}$. Let $m = k + 2$ and $n = k$ in Eq. 2, then we have achieved $L_{2k+2}^2 - L_2^2 = 5F_{2k+4}F_{2k}$. The others are given in similar ways. ■

In [7], [8], the identities in Eq. 3 and Eq. 4 given within the preliminary information section are again shown in Lemma 1 with a different proof method. In [7], [8], the authors have investigated solutions of the diophantine equation of the form $A_{n_1}A_{n_2} \dots A_{n_k} \pm 1 = B_m^2$, where A_n and B_n are either the n^{th} Fibonacci number or Lucas number.

The problem of finding all integral solutions to this diophantine equation is known as the Brocard–Ramanujan problem. These studies show that altered Lucas numbers $\{L_n^2 \pm 1\}$ will play a significant part in the Diophantine equations applications of the numbers theory. That is, one can explore solutions of some diophantine equations of form $A_{n_1}A_{n_2} \dots A_{n_k} \pm a = L_m^2$.

3. ALTERED SEQUENCES OF LUCAS NUMBERS SQUARED

In this section, let's define two types of altered numbers derived from the n^{th} Lucas number squared for a value $\{a\}$ according to whether their indices are even or odd, respectively.

3.1. $G_{L(n)}^{(2)}(a)$ and $H_{L(n)}^{(2)}(a)$ Altered Lucas Numbers

Let L_n be the n^{th} Lucas number. Altered Lucas numbers are defined as

$$G_{L(n)}^{(2)}(a) = L_n^2 + (-1)^n a, \tag{7}$$

$$H_{L(n)}^{(2)}(a) = L_n^2 - (-1)^n a, \tag{8}$$

and also, the altered Lucas sequences are denoted as $\{G_{L(n)}^{(2)}(a)\}_{n=0}^{\infty}$ and $\{H_{L(n)}^{(2)}(a)\}_{n=0}^{\infty}$.

For example, the numbers $G_{L(n)}^{(2)}(1) = H_{L(n)}^{(2)}(-1)$ and $H_{L(n)}^{(2)}(9) = G_{L(n)}^{(2)}(-9)$ are given in Table 1.

Table 1. $G_{L(n)}^{(2)}(1)$ and $H_{L(n)}^{(2)}(9)$, altered Lucas numbers.

n	0	1	2	3	4	5	6	7	8	9	10	11	12
$G_{L(n)}^{(2)}(1)$	5	0	10	15	50	120	325	840	2210	5775	15130	39600	103685
$H_{L(n)}^{(2)}(9)$	-5	10	0	25	40	130	315	850	2200	5785	15120	39610	103675

Table 1 shows that they are any increasing sequences with special values except for the first values, and also, these numbers are divisible by the Fibonacci number $F_5 = 5$. Thus, some sums of l -

consecutive products of the Lucas numbers are divisible by $F_5 = 5$ such as $\sum_{i=1}^{2n} L_i L_{i+1} = G_{L(2n+1)}^{(2)}(1)$,

$\sum_{i=2}^{2n+1} L_i L_{i+1} = H_{L(2n+2)}^{(2)}(9)$ and $\sum_{i=0}^{2n+1} L_i L_{i+1} = H_{L(2n+2)}^{(2)}(4)$. It is clearly seen from the Fibonacci identities

$L_n^2 - 5(-1)^n = L_{n+1}L_{n-1}$ and $L_n^2 - 4(-1)^n = 5F_n^2$, we have

$$H_{L(n)}^{(2)}(4) = G_{L(n)}^{(2)}(-4) = 5F_n^2, \tag{9}$$

$$H_{L(n)}^{(2)}(5) = G_{L(n)}^{(2)}(-5) = L_{n+1}L_{n-1}. \tag{10}$$

But, we give the closed forms of the altered sequences $\{G_{L(n)}^{(2)}(1)\}$ and $\{H_{L(n)}^{(2)}(9)\}$ as follows.

Theorem 1. Let $G_{L(n)}^{(2)}(1)$ and $H_{L(n)}^{(2)}(9)$ denote the n^{th} altered numbers of the Lucas numbers squared, then they are valid:

$$G_{L(n)}^{(2)}(1) = 5F_{n+1}F_{n-1}, \tag{11}$$

$$H_{L(n)}^{(2)}(9) = 5F_{n+2}F_{n-2}. \tag{12}$$

Proof: If we use the identity given in Eq. 3 for $a=1$ and $n=2k$ at the definition in Eq. 7 then $G_{L(2k)}^{(2)}(1)$ is given as $G_{L(2k)}^{(2)}(1) = 5F_{2k-1}F_{2k+1}$, and if we use the Eq. 4 for $a=1$ and $n=2k+1$ in Eq. 7, $G_{L(2k+1)}^{(2)}(1)$ is given $G_{L(2k+1)}^{(2)}(1) = 5F_{2(k+1)}F_{2k}$. Therefore, the number $G_{L(n)}^{(2)}(1) = 5F_{n+1}F_{n-1}$ is obtained by considering according to $n=2k$ and $n=2k+1$ situations. If we use the Eq. 5 for $a=9$ and $n=2k+1$ at the definition in Eq. 8, then $H_{L(2k+1)}^{(2)}(9)$ equal $5F_{2k+3}F_{2k-1}$. And if we use the identity in Eq. 6 for $a=9$ and $n=2k$ in Eq. 8, $H_{L(2k)}^{(2)}(9)$ equal $5F_{2(k+1)}F_{2(k-1)}$. We have $H_{L(n)}^{(2)}(9) = 5F_{n+2}F_{n-2}$ is seen from $n=2k$ and $n=2k+1$ situation. ■

Now, let's research about some sum and subtraction identities of the numbers $G_{L(n)}^{(2)}(1)$ and $H_{L(n)}^{(2)}(9)$

Theorem 2. $G_{L(n)}^{(2)}(1)$ and $H_{L(n)}^{(2)}(9)$ are the n^{th} altered numbers of the Lucas numbers squared, then

$$G_{L(n)}^{(2)}(1) + G_{L(n+1)}^{(2)}(1) = H_{L(n)}^{(2)}(9) + H_{L(n+1)}^{(2)}(9) = 5F_{2n+1}, \tag{13}$$

$$G_{L(n+1)}^{(2)}(1) - G_{L(n-1)}^{(2)}(1) = H_{L(n+1)}^{(2)}(9) - H_{L(n-1)}^{(2)}(9) = 5F_{2n}, \tag{14}$$

$$2G_{L(n+1)}^{(2)}(1) + G_{L(n)}^{(2)}(1) - G_{L(n-1)}^{(2)}(1) = 5F_{2n+2}, \tag{15}$$

$$2H_{L(n+1)}^{(2)}(9) + H_{L(n)}^{(2)}(9) - H_{L(n-1)}^{(2)}(9) = 5F_{n+1}L_{n+1}. \tag{16}$$

Proof If we have rewritten identities in Eq. 13 and Eq. 14 using the identities in Eq. 11 and Eq. 12, then, $G_{L(n)}^{(2)} + G_{L(n+1)}^{(2)} = 5(F_{n+1}(F_{n-1} + F_n) + F_n^2) = 5F_{2n+1}$ and $H_{L(n+1)}^{(2)} - H_{L(n-1)}^{(2)} = 5F_n(F_{n+1} + F_{n-1}) = 5F_n L_n$ are obtained by the identities $F_n^2 + F_{n+1}^2 = F_{2n+1}$ and $F_n L_n = F_{2n}$. Since the other relations are made similarly, they are not given for brevity. If we sum identities in Eq. 13 and Eq. 14 side-to-side collection, we get identities in Eq. 15 and Eq. 16. ■

As a result, the sum of two successive altered Lucas numbers equals the Fibonacci number. Using the Fibonacci Binet formula, a Binet-like formula for the numbers $G_{L(n)}^{(2)}(1)$ and $H_{L(n)}^{(2)}(9)$ can be obtained.

Theorem 3. Let $G_{L(n)}^{(2)}(1)$ and $H_{L(n)}^{(2)}(9)$ be the n^{th} altered numbers of the Lucas numbers squared, then

$$G_{L(n)}^{(2)}(1) = (\alpha^{n+1} - \beta^{n+1})(\alpha^{n-1} - \beta^{n-1}), \tag{17}$$

$$H_{L(n)}^{(2)}(9) = (\alpha^{n+2} - \beta^{n+2})(\alpha^{n-2} - \beta^{n-2}). \tag{18}$$

Proof: They appear as an application of the Fibonacci Binet formula from closed forms in Eq. 11 and Eq. 12. ■

The identities in Eq. 16 and Eq. 17 are referred to as Binet-like formulas for the numbers $G_{L(n)}^{(2)}(1)$ and $H_{L(n)}^{(2)}(9)$. They can be utilized to establish various properties of the numbers $G_{L(n)}^{(2)}(1)$ and $H_{L(n)}^{(2)}(9)$. Additional information and applications of these formulas in sequences $a(n) = F_n F_{n+2}$ and $b(n) = F_n F_{n+4}$ can be found in the sequences (A059929) and (A192883).

Theorem 4. Let $G_{L(n)}^{(2)}(L_t^2)$ and $H_{L(n)}^{(2)}(L_t^2)$ be the n^{th} altered numbers of the Lucas numbers squared, then

$$G_{L(n)}^{(2)}(L_t^2) = 5F_{n+t} F_{n-t}, \quad t \text{ is odd}, \tag{19}$$

$$H_{L(n)}^{(2)}(L_t^2) = 5F_{n+t} F_{n-t}, \quad t \text{ is even}, \tag{20}$$

where L_t^2 is the square of the t^{th} Lucas numbers used in place of $\{a\}$.

Proof. If we have rewritten values of $m = k + (t+1)/2$ and $n = k - (t-1)/2$ in Eq. 1 for t is odd, then $G_{L(2k+1)}^{(2)}(L_t^2) = 5F_{2k+t+1}F_{2k-t+1}$ is given with according to $a = L_t^2$ and $n = 2k+1$ in Eq. 7. Also, if they are taken $m = k + (t+1)/2$ and $n = k - (t-1)/2$ in Eq. 2, the $G_{L(2k)}^{(2)}(L_t^2) = 5F_{2k+t}F_{2k-t}$ is $a = F_t^2$ and $n = 2k$ in Eq. 7.

Similarly, if we consider values of $m = k + t/2$ and $n = k - t/2$ in Eq. 1 and Eq. 2 when t is even, according to $a = L_t^2$ in Eq. 8, they are obtained as the $H_{L(2k+1)}^{(2)}(L_t^2)$ and $H_{L(2k)}^{(2)}(L_t^2)$, which are produce the identity in Eq. 20. ■

Also, the general terms of the altered sequences $\{G_{L(n)}^{(2)}(L_1^2)\}$ and $\{H_{L(n)}^{(2)}(L_1^2)\}$ can be given by the Fibonacci identities as $G_{L(n)}^{(2)}(9) = 5F_n^2 + 13(-1)^n$ and $H_{L(n)}^{(2)}(1) = 5F_n^2 + 3(-1)^n = F_{3n}/F_n$ (A047946). But, they are the form of other altered Fibonacci sequences. In addition, they could not be generalized as the product of Fibonacci or Lucas numbers.

3.2. $G_{L(n),r}^{(2)}(1)$ and $H_{L(n),r}^{(2)}(9)$ Altered Lucas Gcd Sequences

We have examined properties related to the greatest common divisor (gcd) of two numbers whose indices differ r from the altered sequences, definitions of whose are given

$$G_{L(n),r}^{(2)}(a) = (G_{L(n)}^{(2)}(a), G_{L(n+r)}^{(2)}(a)), \tag{21}$$

$$H_{L(n),r}^{(2)}(a) = (H_{L(n)}^{(2)}(a), H_{L(n+r)}^{(2)}(a)), \tag{22}$$

where $G_{L(n)}^{(2)}(a)$ and $H_{L(n)}^{(2)}(a)$ be the n^{th} altered Lucas numbers. The sequences $\{G_{L(n),r}^{(2)}(a)\}$ and $\{H_{L(n),r}^{(2)}(a)\}$ formed by these numbers are called the r -successive altered Lucas gcd sequences.

Now, the numbers $G_{L(n),1}^{(2)}(1)$ and $H_{L(n),1}^{(2)}(9)$ are sampled in Table 2.

Table 2. $G_{L(n),1}^{(2)}(1)$ and $H_{L(n),1}^{(2)}(9)$, 1-successive altered Lucas gcd numbers.

n	0	1	2	3	4	5	6	7	8	9	10	11	12
$G_{L(n),1}^{(2)}(1)$	5	10	5	5	10	5	5	10	5	5	10	5	5

$H_{L(n),1}^{(2)}(9)$	5	10	25	5	10	5	5	50	5	5	10	5	25
-----------------------	---	----	----	---	----	---	---	----	---	---	----	---	----

The special values in Table 2 show that the sequences $\{G_{L(n),1}^{(2)}(1)\}$ and $\{H_{L(n),1}^{(2)}(9)\}$ are not increasing or decreasing. But, they can be periodic. Thus, we have studied whether or not the l -successive altered Lucas gcd sequences take special values in certain periods.

Theorem 5. Let $G_{L(n),1}^{(2)}(1)$ and $H_{L(n),1}^{(2)}(9)$ be the n^{th} l -successive altered Lucas gcd numbers, then

$$G_{L(n),1}^{(2)}(1) = \begin{cases} 10, & n \equiv 1 \pmod{3} \\ 5, & \text{otherwise} \end{cases}, \quad (23)$$

$$H_{L(n),1}^{(2)}(9) = \begin{cases} 50, & n \equiv 7 \pmod{15} \\ 25, & k \equiv 2, 12 \pmod{15} \\ 10, & k \equiv 1, 4, 10, 13 \pmod{15} \\ 5, & \text{otherwise} \end{cases}. \quad (24)$$

Proof: We have rewritten the number $G_{L(2k),1}^{(2)}(1) = (G_{L(2k)}^{(2)}(1), G_{L(2k+1)}^{(2)}(1)) = 5(F_{2k+1}F_{2k-1}, F_{2k+2}F_{2k})$, according to the closed form in Eq. 11 and the definition in Eq. 21. By using the property $(F_n, F_{n+1}) = 1$, we have $(F_{2k+1}, F_{2k+2}) = (F_{2k+1}, F_{2k}) = (F_{2k-1}, F_{2k}) = 1$. So, we should examine the situation (F_{2k-1}, F_{2k+2}) . By using the property $2|F_{3n}$, if we have $2k-1 \equiv 0 \pmod{3}$ and $2k+2 \equiv 0 \pmod{3}$ then $k \equiv 2 \pmod{3} \Leftrightarrow (F_{2k-1}, F_{2k+2}) = 2$. Otherwise, $(F_{2k-1}, F_{2k+2}) = 1$. It is seen that

$$G_{L(2k),1}^{(2)}(1) = 5(F_{2k+1}F_{2k-1}, F_{2k+2}F_{2k}) = \begin{cases} 10, & k \equiv 2 \pmod{3} \\ 5, & \text{otherwise} \end{cases}. \quad (25)$$

Also, we have $G_{L(2k+1),1}^{(2)}(1) = 5(F_{2(k+1)}F_{2k}, F_{2k+1}F_{2k+3})$, according to the identities in Eq. 11 and Eq. 21. Since $(F_n, F_{n+1}) = 1$, we can write $(F_{2k+2}, F_{2k+3}) = (F_{2k+2}, F_{2k+1}) = (F_{2k}, F_{2k+1}) = 1$. So, we should examine the situation (F_{2k}, F_{2k+3}) . So, if we have $2k \equiv 0 \pmod{3}$ and $2k+3 \equiv 0 \pmod{3}$ then $k \equiv 0 \pmod{3} \Leftrightarrow (F_{2k}, F_{2k+3}) = 2$ by using the property $2|F_{3n}$. Otherwise, $(F_{2k}, F_{2k+3}) = 1$. It is obtained as

$$G_{L(2k+1),1}^{(2)}(1) = 5(F_{2(k+1)}F_{2k}, F_{2k+1}F_{2k+3}) = \begin{cases} 10, & k \equiv 0 \pmod{3} \\ 5, & \text{otherwise} \end{cases} \quad (26)$$

Whether the index is even or odd from the identities found in Eq. 25 and Eq. 26, it is seen that $k \equiv 2 \pmod{3}$ for $n = 2k$; and $k \equiv 0 \pmod{3}$ for $n = 2k + 1$. Thus, we find $G_{L(n),1}^{(2)}(1) = 10$ for $n \equiv 1 \pmod{3}$. In the other cases, then $G_{L(n),1}^{(2)}(1) = 5$.

Similarly, we have $H_{L(2k),1}^{(2)}(9) = (H_{L(2k)}^{(2)}(9), H_{L(2k+1)}^{(2)}(9)) = 5(F_{2k+2}F_{2k-2}, F_{2k+3}F_{2k-1})$, according to identity in Eq. 12 and the definition in Eq. 22. We consider $H_{L(2k),1}^{(2)}(9) = 5(F_{2k-2}, F_{2k+3})(F_{2k+2}, F_{2k-1})$ since $(F_{2k+2}, F_{2k+3}) = (F_{2k-2}, F_{2k-1}) = 1$. Using the property $(F_x, F_y) = F_{(x,y-x)}$, we rewrite their identities

$$(F_{2k-2}, F_{2k+3}) = F_{(2k-2, 2k+3)} = F_{(2k-2,5)} = F_5, \quad 2k-2 \equiv 0 \pmod{5}, \quad (27)$$

$$(F_{2k+2}, F_{2k-1}) = F_{(2k+2, 2k-1)} = F_{(3, 2k-1)} = F_3, \quad 2k-1 \equiv 0 \pmod{5}. \quad (28)$$

It is seen if $k \equiv 1 \pmod{5}$, then $(F_{2k-2}, F_{2k+3}) = 5$; and if $k \equiv 2 \pmod{3}$ then $(F_{2k+2}, F_{2k-1}) = 2$. According to the Chinese remainder theorem, we obtain $H_{L(2k),1}^{(2)}(9) = 50$ for $k \equiv 11 \pmod{15}$. The desired results for the products of the two expressions in their possible cases are obtained as

$$H_{L(2k),1}^{(2)}(9) = 5(F_{2k-2}, F_{2k+3})(F_{2k+2}, F_{2k-1}) = \begin{cases} 50, & k \equiv 11 \pmod{15} \\ 25, & k \equiv 1, 6 \pmod{15} \\ 10, & k \equiv 2, 5, 8, 14 \pmod{15} \\ 5, & \text{otherwise} \end{cases} \quad (29)$$

Same way, according to identities in Eq. 12 and Eq. 22, we have $H_{L(2k+1),1}^{(2)}(9) = 5(F_{2k+3}F_{2k-1}, F_{2k+4}F_{2k})$. Because of $(F_{2k+3}, F_{2k+4}) = (F_{2k-1}, F_{2k}) = 1$, we can rewrite $H_{L(2k+1),1}^{(2)}(9) = 5(F_{2k+3}, F_{2k})(F_{2k-1}, F_{2k+4})$. Using the properties $(F_x, F_y) = F_{(x,y-x)}$, we have $(F_{2k}, F_{2k+3}) = F_{(2k,3)} = F_3$, $2k \equiv 0 \pmod{3}$ and $(F_{2k+4}, F_{2k-1}) = F_{(5, 2k-1)} = F_5$, $2k-1 \equiv 0 \pmod{5}$. It is seen that if $k \equiv 0 \pmod{3}$ then $(F_{2k}, F_{2k+3}) = 2$; and if $k \equiv 3 \pmod{5}$ then $(F_{2k+4}, F_{2k-1}) = 5$. According to the Chinese remainder theorem, we obtain

as $H_{L(2k+1),1}^{(2)}(9) = 50$ for $k \equiv 3 \pmod{15}$. The desired results for the products of the two expressions in their possible cases are obtained as

$$H_{L(2k+1),1}^{(2)}(9) = 5(F_{2k}, F_{2k+3})(F_{2k+4}, F_{2k-1}) = \begin{cases} 50, & k \equiv 3 \pmod{15} \\ 25, & k \equiv 8, 13 \pmod{15} \\ 10, & k \equiv 0, 6, 9, 12 \pmod{15} \\ 5, & \text{otherwise} \end{cases} \quad (30)$$

According to whether the indices are $n = 2k$ and $n = 2k + 1$ even or odd from the values found in Eq. 29 and Eq. 30, respectively we consider $H_{L(2k),1}^{(2)}(9) = 50$ for $k \equiv 11 \pmod{15}$ and $H_{L(2k+1),1}^{(2)}(9) = 50$ for $k \equiv 3 \pmod{15}$. Thus, we find $H_{L(n),1}^{(2)} = 50$ for $n \equiv 7 \pmod{15}$. When it's appropriate case in Eq. 29 and Eq. 30, it is follow $k \equiv 1, 6 \pmod{15}$ for $n = 2k$ and $k \equiv 8, 13 \pmod{15}$ for $n = 2k + 1$, it is $H_{L(n),1}^{(2)} = 25$, $n \equiv 2, 12 \pmod{15}$. If the other cases are written in their place, desired results are obtained similar way. ■

For terms of the 2-successive altered gcd sequences, let's create Table 3:

Table 3. $G_{L(n),2}^{(2)}(1)$ and $H_{L(n),2}^{(2)}(9)$, 2-successive altered Lucas gcd numbers.

n	0	1	2	3	4	5	6	7	8	9	10	11	12
$G_{L(n),2}^{(2)}(1)$	5	15	10	15	25	120	65	105	170	825	445	720	1165
$H_{L(n),2}^{(2)}(9)$	5	5	40	5	5	10	5	5	40	5	5	10	5

In Table 3, it is seen that the 2-successive altered Lucas gcd sequence $\{G_{L(n),2}^{(2)}(1)\}$, $n \geq 2$ takes values according to a specific increasing sequence. The sequence $\{H_{L(n),2}^{(2)}(9)\}$ is periodic. Now let's give the properties of these sequences.

Theorem 6. Let $G_{L(n),2}^{(2)}(1)$ and $H_{L(n),2}^{(2)}(9)$ be the n^{th} 2-successive altered Lucas gcd numbers, then

$$G_{L(n),2}^{(2)}(1) = \begin{cases} 15F_{n+1}, & n \equiv 1 \pmod{4} \\ 5F_{n+1}, & \text{otherwise} \end{cases}, \quad H_{L(n),2}^{(2)}(9) = \begin{cases} 40, & k \equiv 2 \pmod{6} \\ 10, & k \equiv 5 \pmod{6} \\ 5, & \text{otherwise} \end{cases} \quad (31)$$

Proof: According to the identity in Eq. 11, we write $G_{L(n),2}^{(2)}(1) = 5F_{n+1}(F_{n-1}, F_{n+3})$. So, we have $(F_{n-1}, F_{n+3}) = F_{(n-1,4)} = F_4$, $n \equiv 1 \pmod{4}$ by using the property $(F_x, F_y) = F_{(x,y-x)}$ and $G_{L(n),2}^{(2)}(1) = 5F_4F_{n+1} = 15F_{n+1}$ for $n \equiv 1 \pmod{4}$. Otherwise, $(F_{n-1}, F_{n+3}) = F_{(n-1,4)} = F_2$ or F_1 . Since $F_1 = F_2 = 1$, we have $G_{L(n),2}^{(2)}(1) = 5F_{n+1}$ for $n \not\equiv 1 \pmod{4}$.

According to the identity in Eq. 12, we write $H_{L(n),2}^{(2)}(9) = 5(F_{n+2}F_{n-2}, F_{n+4}F_n)$. Since $(F_{2k+2}, F_{2k}) = (F_{2k+2}, F_{2k+4}) = (F_{2k-2}, F_{2k}) = 1$, we can take as $H_{L(n),2}^{(2)}(9) = 5(F_{n-2}, F_{n+4})$. Thus, we get $H_{L(n),2}^{(2)}(9) = 5F_{(n-2,6)} = 5F_6$, $n \equiv 2 \pmod{6}$. Otherwise, the others are $H_{L(n),2}^{(2)}(9) = 5F_{(n-2,6)} = 5F_3$, $n \equiv 5 \pmod{6}$; or $5F_2$, $n \equiv 0, 4 \pmod{6}$; or $5F_1$, $n \equiv 1, 3 \pmod{6}$. ■

Theorem 7. Let $G_{L(n),2}^{(2)}$ be the n^{th} 2-successive altered Lucas gcd number, then

$$G_{L(n+1),2}^{(2)}(1) + G_{L(n),2}^{(2)}(1) = \begin{cases} 5(F_{n+1} + L_{n+2}), & n \equiv 1 \pmod{4} \\ 5L_{n+3}, & n \equiv 0 \pmod{4} \\ 5F_{n+3} & \text{otherwise} \end{cases} \quad (32)$$

Proof: We know the number $G_{L(n),2}^{(2)}(1) = 15F_{n+1}$ for $n \equiv 1 \pmod{4}$, otherwise it is $5F_{n+1}$. Thus,

$$G_{L(n+1),2}^{(2)}(1) + G_{L(n),2}^{(2)}(1) = \begin{cases} 5(F_{n+2} + 3F_{n+1}), & n \equiv 1 \pmod{4} \\ 5(3F_{n+2} + F_{n+1}), & n \equiv 0 \pmod{4} \\ 5(F_{n+1} + F_{n+2}), & \text{otherwise} \end{cases} \quad (33)$$

By using the identity $F_{n+1} + F_{n-1} = L_n$, we have

$$G_{L(n+1),2}^{(2)}(1) + G_{L(n),2}^{(2)}(1) = \begin{cases} 5(F_{n+3} + 2F_{n+1}), & n \equiv 1 \pmod{4} \\ 5(F_{n+2} + F_{n+4}), & n \equiv 0 \pmod{4} \\ 5F_{n+3}, & \text{otherwise} \end{cases} \quad (34)$$

The desired result is achieved. ■

We will continue our work according to the particular values of these numbers given in Table 4, since closed-form expressions cannot be found for the numbers $G_{L(n)}^{(2)}(9) = H_{L(n)}^{(2)}(-9)$ and $H_{L(n)}^{(2)}(1) = G_{L(n)}^{(2)}(-1)$ for the value of $a = \{9, 1\}$ in identities given Eq. 7 and Eq. 8, respectively.

Table 4. $G_{L(n)}^{(2)}(9)$ and $H_{L(n)}^{(2)}(1)$, altered Lucas numbers.

n	0	1	2	3	4	5	6	7	8	9	10	11	12
$G_{L(n)}^{(2)}(9)$	13	-8	18	7	58	112	333	832	2218	5767	15138	39592	103693
$H_{L(n)}^{(2)}(1)$	3	2	8	17	48	122	323	842	2208	5777	15128	39602	103683

Table 4 shows that the sequences $G_{L(n),1}^{(2)}(9) = H_{L(n),1}^{(2)}(1) = \{1, 2, 1\}$, $n \in Z_3$; $H_{L(n),2}^{(2)}(1) = \{1, 1, 8, 1, 1, 2\}$, $n \in Z_6$; $G_{L(n),3}^{(2)}(9) = \{1, 2, 2\}$, $n \in Z_3$ and $H_{L(n),3}^{(2)}(1) = \{1, 2, 2, 17, 2, 2, 1, 2, 2\}$, $n \in Z_9$ are periodic [9]. But, the proofs for these values have not been provided. Thus, these values have been determined through a computer program up to 100 for the numbers $G_{L(n),r}^{(2)}(9)$ and $H_{L(n),r}^{(2)}(1)$, $r = 1, 2, 3$. In [9], it is the numbers $G_{L(n),2}^{(2)}(9) = \{1, 1, 2, 7, 1, 16, 1, 1, 2, 1, 1, 56, 1, 1, 2, 1, 1, 16, 1, 7, 2, 1, 1, 8\}$, $n \in Z_{24}$.

4. CONCLUSION AND RECOMMENDATIONS

In our study, two types of altered Lucas numbers denoted $G_{L(n)}^{(2)}(a)$ and $H_{L(n)}^{(2)}(a)$ are derived with values $\{a\}$. We have shown that the numbers $G_{L(n)}^{(2)}(1)$ and $H_{L(n)}^{(2)}(9)$ equal some consecutive products of the Fibonacci numbers. Thus, r -successive altered Lucas gcd sequences $\{G_{L(n),r}^{(2)}(1)\}$ and $\{H_{L(n),r}^{(2)}(9)\}$ are studied for $r = 1, 2$. We have obtained these sequences are either periodic and bounded or primefree and unbounded. Also, we have generalized the value $\{a\}$ as the square of Lucas number such as

$$G_{L(n)}^{(2)}(L_t^2) = 5F_{n+t}F_{n-t}, \quad t \text{ is odd}, \tag{35}$$

$$H_{L(n)}^{(2)}(L_t^2) = 5F_{n+t}F_{n-t}, \quad t \text{ is even}. \tag{36}$$

Other properties of these sequences and their r -successive gcd sequences are left to the interested readers for future research. Nevertheless, we will consider some matrix and graph theory applications in the next articles.

ACKNOWLEDGEMENT

This study is a part of Ms. thesis of Emre KANKAL in [9]. The authors thank the anonymous referee for carefully reading the manuscript and for their suggestions which helped improve its presentation.

REFERENCES

- [1] OEIS Foundation Inc. (2011). The on-line encyclopedia of integer sequences. <http://oeis.org>.
- [2] Koshy T. (2001). Fibonacci and Lucas numbers with applications. John Wiley and Sons Inc, NY.
- [3] Chen, K.W. (2011). Greatest common divisors in shifted Fibonacci sequences. Journal of Integer Sequences, 14, 11.4.7.
- [4] Köken, F. (2020). The gcd sequences of the altered Lucas sequences. Annales Mathematicae Silesianae, 34, 2, 222-240. DOI: 10.2478/amsil-2020-0005.
- [5] Cerin, Z. (2013). On factors of sums of consecutive Fibonacci and Lucas numbers. Annales Mathematicae et Informaticae, 41, 19–25.
- [6] Tekcan, A., Gezer, B. and Bizim, O. (2007). Some relations on Lucas numbers and their sums. Advanced Studies in Contemporary Mathematics, 15, 195–211.
- [7] Szalay, L. (2012). Diophantine equations with binary recurrences associated to the Brocard–Ramanujan problem. Portugaliae Mathematica, 69, 3, 213–220.
- [8] Pongsriiam, P. (2017). Fibonacci and Lucas numbers associated with Brocard-Ramanujan equation. Communications of the Korean Mathematical Society, 32, 3, 511-522.
- [9] Kankal E. (2023). The thesis of master of science, Necmettin Erbakan University. The Graduate School of Natural And Applied Science, Konya.



RESEARCH ARTICLE

**ALAMOUTI SPACE-TIME CODING FOR VEHICULAR COMMUNICATIONS IN THE
PRESENCE OF CHANNEL ESTIMATION ERRORS**

Serdar Özgür ATA

TÜBİTAK BİLGEM, P.K. 74, 41470 Gebze, Kocaeli, serdar.ata@tubitak.gov.tr, ORCID: 0000-0003-2902-6282

Receive Date: 04.07.2023

Accepted Date: 12.07.2023

ABSTRACT

In this paper, the error performance of the Alamouti space-time coding (STC) scheme is investigated for vehicle-to-vehicle (V2V) communication systems over imperfect cascaded fading channels. In vehicular communication systems, perfect knowledge of the channel state information is not available to the users at all times due to the rapid movement of communicating vehicles and fast change of the rich scattering environment which makes the fading effects in wireless channels more severe. Therefore, in the analysis, we consider the erroneous estimation of the channel gain, which is more realistic for practical scenarios. For this purpose, we first derive the moment-generation function (MGF) of the channel fading coefficient with estimation error in the case of the cascaded Nakagami- m fading conditions. Then, using the MGF, we obtain the closed-form symbol-error-rate (SER) expressions of Alamouti STC with two transmitting and L receiving antennas for the M-PSK and M-QAM modulation schemes. Then, the exact ergodic capacity expression is derived for the proposed system. Furthermore, the analytical results are verified through Monte-Carlo simulations. Numerical results show that the SER performance of V2V communication systems can be improved significantly by using Alamouti STC even in case of harsh fading conditions and full channel-state information is not available due to estimation errors.

Keywords: *Alamouti Space-Time Coding, Cascaded Fading Channels, Channel Estimation Error, Ergodic Capacity, Symbol-Error Rate, Vehicular Communications*

1. INTRODUCTION

Vehicular communication is a rapidly growing research field of wireless communication applications with the potential to sustain safety, efficiency, and reliability in high-mobility environments in 5G networks. The focus on communications among vehicles or between vehicles and the infrastructure has been achieving high data rates, besides lower energy consumption and lower latency in 5G networks [1-3]. With the ultra-connectivity objective of 6G communications, seamless and secure communications is also aimed for intelligent transportation systems. Thus the internet of vehicles (IoV) is emerging as an advanced vehicular networking technology [4-6]. Moreover, the presence of dense and high-speed vehicles and the need for reliable and secure communication of a very high

number and density of communication nodes will increase the effective usage of artificial intelligence techniques in next-generation vehicular communication systems [7-8].

As the number of connected autonomous vehicles grows, vehicle-to-everything (V2X) communication technologies including vehicle-to-infrastructure communications (V2I), vehicle-to-vehicle (V2V) communications, vehicle-to-pedestrian (V2P) communications present intrinsic challenges for ensuring continuous and seamless connectivity [9]. The main challenge is the severe fading channel effects limiting the channel capacity. The channel effects become much more challenging in V2X systems as the receivers and transmitters are almost always in motion [10-11]. In addition, the presence of tall buildings and structures in urban areas or natural elevations and tall trees in rural areas cause shading effects. On the other hand, frequency spread due to Doppler shift at high speeds is another disturbance factor in V2X systems [12].

The channel fading effect in vehicular communication systems is modelled as cascaded channel models including Nakagami- m fading model because the channel gains resulting from independent scattering fields are multiplied by each other to characterize the relevant statistical properties [13-14]. Several studies have been done to enhance the performance of V2V systems under Nakagami- m fading. Two-way half-duplex amplify-and-forward (AF) relaying in vehicular communications was analysed in [15]. The fixed-gain AF relaying over cascaded Nakagami- m channels with physical layer network coding was introduced in [16]. The performance analysis of full-duplex AF relaying over cascaded Nakagami- m fading channels incorporating self-interference (SI) at the relay is studied in [17] for V2V communications.

In vehicular communications, due to the high-speed environment and insufficient pilot subcarriers in the symbols, channel estimation becomes a challenging task in practice for fast time-varying channels. Conventional channel estimation methods may not overcome error propagation problems and new compensation schemes are designed [18]. Moreover, channel estimation for high mobility systems is considered in [19] to extensively analyse the channel estimation performance where reconfigurable intelligent surfaces (RISs) are incorporated into the environment.

Moreover, space-time coding (STC) is a powerful technique used in wireless networks with multiple transmit antennas to improve the reliability of data transmission under severe channel conditions. Alamouti space-time coding has been extensively studied for wireless communication systems in urban environments [20]. The performance analysis on symbol-error-probability (SEP) in a multiple-relay AF cooperative communication system with Alamouti-type orthogonal STC at the transmitter and Alamouti's space-time-decoder at the receiver is investigated in [21] with imperfect channel-state-information (CSI). In [22], a new differential space-time block coded spatial modulation (STBC-SM) technique is introduced for multi-user massive multiple-input multiple-output (MIMO) communications in the uplink, where STBC-SM and differential coding is combined to strengthen the diversity gains in the absence of the CSI.

Hence, to fill in the gap in the investigation of how channel estimation errors affect the system performance of vehicular communication systems and to advance the error performance of V2V communication systems over cascaded fading channels in the presence of channel estimation errors,

we propose to use the Alamouti STBC technique using M -ary modulation schemes, then examine the performance of the proposed systems. The contributions of this paper are listed as follows.

- The MGF of erroneously estimated fading gain in the cascaded Nakagami- m channels is derived in the closed form. Thus, for the first time in literature, we investigate the performance analysis of the V2V communication system subject to imperfect cascaded fading channels, which is more suitable for realistic wireless vehicular communication scenarios.
- A closed-form expression for the symbol-error-rate (SER) of Alamouti STC for M-PSK modulation over imprecise cascaded Nakagami- m fading channels is obtained.
- The closed-form SER formulation of Alamouti STC for M-QAM modulation over imprecise cascaded Nakagami- m fading channels is obtained.
- The closed-form average capacity expression of Alamouti STC over imprecise cascaded Nakagami- m fading channels is obtained.

The rest of the paper is organized as follows. Section 2 introduces the proposed V2V communication system model. Section 3 presents the imperfect cascaded Nakagami- m fading channel model. In Section 4, the derivation of the MGF of the channel gain with estimation errors and the MGF of the end-to-end SNR over imperfect cascaded Nakagami- m fading channels are performed. Then, using these MGFs, SER expressions for the M-PSK and M-QAM modulation schemes are provided. In Section 5, ergodic capacity analysis is given. Section 6 represents the numerical and Monte-Carlo simulation results to verify the analytical derivations and discusses the performance of the proposed system. Finally, the contributions and findings of the paper are summarized in Section 7.

2. SYSTEM MODEL

Due to reasons such that the rapidly changing physical environment which consists of too many scattering obstacles, high mobility of the communicating nodes, and their lower antenna heights, fading conditions in V2V communication systems are much more severe compared to the classical wireless communication systems. Therefore, to enhance the error performance of these systems, the usage of diversity techniques is inevitable in designing the V2V communication infrastructures. At this point, as there is no space limitation on the vehicles, using the space-time diversity techniques by deploying multi-antennas on the nodes is a very reasonable choice. Providing full-rate and full diversity gain, no need for CSI or knowledge of channel coefficients at the transmitter, and having low implementation complexity with a simple decoding scheme, Alamouti STC can be very useful from a practical point of view to be used in vehicular communication systems illustrated in Figure 1. Additionally, since it requires just two consecutive time slots to transmit the source's signals, it also offers an adequate solution against the changeable characteristics of the vehicular channels. Thus, we examine a V2V communication system in Figure-1 where the $2 \times L$ Alamouti STC is employed between the source with two transmitting antennas and the destination with L receiving antennas. Hence the source transmits two symbols s_1 and s_2 in the form of Alamouti code at time t and $t + T$ by using two antennas as

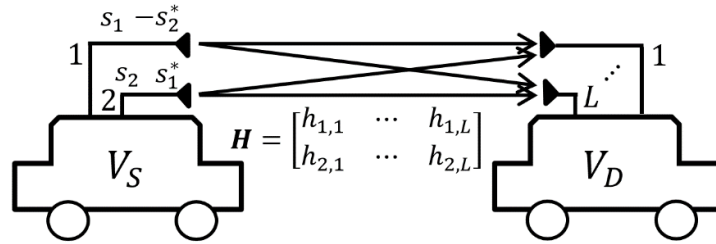


Figure 1. V2V communication system employing $2 \times L$ Alamouti Space-Time Coding scheme, where V_S is the source vehicle, V_D is the destination vehicle, and \mathbf{H} is the channel gain matrix.

$$\mathbf{S} = \begin{bmatrix} s_1 & s_2 \\ -s_2^* & s_1^* \end{bmatrix}, \quad (1)$$

where \mathbf{S} is the code matrix for STC of Alamouti type and $*$ denotes the complex conjugate operator. In \mathbf{S} , row indices indicate the transmitting time interval while column indices indicate which antenna is used to transmit the corresponding symbol in a given time interval [23]. Since the number of transmitting antennas n_T is 2 and receiving antennas n_R is L , the channel gain matrix, \mathbf{H} , becomes

$$\mathbf{H} = \begin{bmatrix} h_{1,1} & \dots & h_{1,L} \\ h_{2,1} & \dots & h_{2,L} \end{bmatrix}, \quad (2)$$

where $h_{i,l}$ is the channel's fading coefficient between the i^{th} transmitting antenna of the source and the l^{th} receiving antenna of the destination, where $i = 1, 2$ and $l = 1, \dots, L$. Therefore, after the transmission phase, signals received by the l^{th} antenna of the destination node at time t and $t + T$ become

$$r_1^l = h_{1,l}s_1 + h_{2,l}s_2 + n_1^l, \quad (3a)$$

$$r_2^l = -h_{1,l}s_2^* + h_{2,l}s_1^* + n_2^l, \quad (3b)$$

respectively, where n_1^l and n_2^l denote the additive white Gaussian noise (AWGN) modelled as Gaussian random variables with zero mean and double-sided power spectral density of $N_0/2$. Then the receiver constructs two decision statistics \tilde{s}_1 and \tilde{s}_2 by combining the received signals with channels state information as [23]

$$\tilde{s}_1 = \sum_{l=1}^L h_{1,l}^* r_1^l + h_{2,l} (r_2^l)^* = \sum_{l=1}^L \sum_{k=1}^2 |h_{k,l}|^2 s_1 + \sum_{l=1}^L h_{1,l}^* n_1^l + h_{2,l} (n_2^l)^*, \quad (4)$$

$$\tilde{s}_2 = \sum_{l=1}^L h_{2,l}^* r_1^l - h_{1,l} (r_2^l)^* = \sum_{l=1}^L \sum_{k=1}^2 |h_{k,l}|^2 s_2 + \sum_{l=1}^L h_{2,l}^* n_1^l - h_{1,l} (n_2^l)^*. \quad (5)$$

After applying the maximum-combining-ratio (MRC) scheme to the received symbols, the instantaneous SNR per symbol becomes

$$\gamma = \sum_{l=1}^L \gamma_l = \sum_{l=1}^L \gamma_{1,l} + \gamma_{2,l} = \frac{P_s}{2N_0} \sum_{l=1}^L |h_{1,l}|^2 + |h_{2,l}|^2, \quad (6)$$

where P_s is the total transmitting power of the source node.

3. CHANNEL MODEL

In cascaded fading channel models, the channel gain h is modeled as the multiplication of several random variables $\{h_n\}_{n=1}^N$, which correspond to the multiple scattering effects in the medium as [13]

$$h = \prod_{n=1}^N h_n, \quad (7)$$

where N denotes the cascading degree of the wireless channel. For the case of h_n being a Nakagami- m distributed random variable with the fading parameter of m_n , it is called as N^* Nakagami- m fading channel and probability density function (PDF) besides cumulative distribution function (CDF) of h are given as [13]

$$f_h(h) = 2h^{-1} \delta G_{0,N}^{N,0} \left[h^2 \Delta \mid \begin{matrix} (-), (-) \\ (m_1, \dots, m_N), (-) \end{matrix} \right], \quad (8a)$$

$$F_h(h) = \delta G_{1,N+1}^{N,1} \left[h^2 \Delta \mid \begin{matrix} (1), (-) \\ (m_1, \dots, m_N), (0) \end{matrix} \right], \quad (8b)$$

where $\delta = \prod_{n=1}^N (1/\Gamma(m_n))$ and $\Delta = \prod_{n=1}^N (m_n/\Omega_n)$ while $\{\Omega_n\}_{n=1}^N$ is the average power of the corresponding multiplicative channel gain as $\Omega_n = E[h_n^2]$, where $E[\cdot]$ denotes the expectation operator. Here $\Gamma(\cdot)$ is Gamma function [24, 8.310] and $G_{v,u}^{s,t} \left[\cdot \mid \begin{matrix} \underline{a}_t, \underline{a}_v \\ \underline{b}_s, \underline{b}_u \end{matrix} \right]$ is the Meijer's G function [24, 9.301], where $\underline{a}_t \triangleq (a_1, \dots, a_t)$, $\underline{a}_v \triangleq (a_{t+1}, \dots, a_v)$, $\underline{b}_s \triangleq (b_1, \dots, b_s)$, and $\underline{b}_u \triangleq (b_{s+1}, \dots, b_u)$.

In vehicular communications, due to the rapid movement of the communicating nodes and rich scattering environment, fading characteristics of the wireless channels may vary fast in time and therefore the perfect estimation of the channel statistics may not be possible. For these reasons, assuming imperfect channel estimation is much more reasonable in practical V2V application scenarios. In that case, the erroneously estimated channel gain \hat{h} can be modelled as a summation of the perfectly estimated channel gain h and an error term n_h , and mathematically given as [21]

$$\hat{h} = \rho h + \sqrt{1 - \rho^2} n_h, \quad (9)$$

where ρ is the correlation coefficient between h and \hat{h} , holding $0 \leq \rho \leq 1$, which determines the accuracy of the estimation. Furthermore, the estimation error n_h is normally distributed with zero mean and σ_h^2 variance, $n_h \sim N(0, \sigma_h^2)$.

4. PERFORMANCE EVALUATION

In the letter, the performance analysis of the proposed system is evaluated by exploiting the moment generation function (MGF) approach. With the definitions of $\alpha \triangleq \rho h$ and $\beta \triangleq \sqrt{1 - \rho^2} n_h$, then $\hat{h} = \alpha + \beta$, it can be written that

$$\gamma \triangleq \hat{h}^2 = \alpha^2 + 2\alpha\beta + \beta^2. \quad (10)$$

Thus, the MGF of Y , which is denoted by $\mathcal{M}_Y(s)$, becomes

$$\mathcal{M}_Y(s) = E[e^{-sY}] = E[e^{-s\alpha^2} e^{-s\beta^2} e^{-2s\alpha\beta}]. \quad (11)$$

By using the $K - th$ order Taylor expansion of the term $e^{-2s\alpha\beta}$, $\mathcal{M}_Y(s)$ can be written as

$$\begin{aligned} \mathcal{M}_Y(s) &= E \left[e^{-s\alpha^2} e^{-s\beta^2} \sum_{k=0}^K \frac{(-2s)^k}{k!} \alpha^k \beta^k \right] \\ &= \sum_{k=0}^K \frac{(-2s)^k}{k!} E[e^{-s\alpha^2} \alpha^k] E[e^{-s\beta^2} \beta^k] \\ &= \sum_{k=0}^K \frac{(-2s)^k}{k!} I_\alpha(s) I_\beta(s), \end{aligned} \quad (12)$$

where

$$I_\alpha(s) = E[e^{-s\alpha^2} \alpha^k] = \int_0^\infty e^{-s\alpha^2} \alpha^k f_\alpha(\alpha) d\alpha \quad (13)$$

and

$$I_\beta(s) = E[e^{-s\beta^2} \beta^k] = \int_{-\infty}^\infty e^{-s\beta^2} \beta^k f_\beta(\beta) d\beta. \quad (14)$$

Since $f_\alpha(\alpha) = \rho^{-1} f_h(\alpha/\rho)$, by using (8a), $I_\alpha(s)$ can be written as

$$I_\alpha(s) = 2\delta \int_0^\infty e^{-s\alpha^2} \alpha^{k-1} G_{0,N}^{N,0} \left[\alpha^2 \frac{\Delta}{\rho^2} \mid \begin{matrix} (-),(-) \\ (m_1, \dots, m_N), (-) \end{matrix} \right] d\alpha. \quad (15)$$

Then, by applying $z = \alpha^2$ transformation, this integral can take the form of

$$I_\alpha(s) = \delta \int_0^\infty e^{-sz} z^{\frac{k}{2}-1} G_{0,N}^{N,0} \left[z \frac{\Delta}{\rho^2} \mid \begin{matrix} (-),(-) \\ (m_1, \dots, m_N), (-) \end{matrix} \right] dz \quad (16)$$

and exploiting the integral property of Meijer's G function [25, 2.24.3.1], $I_\alpha(s)$ is obtained as

$$I_\alpha(s) = \delta S^{\frac{k}{2}} G_{1,N}^{N,1} \left[\frac{\Delta}{s\rho^2} \mid \begin{matrix} (1-\frac{k}{2}),(-) \\ (m_1, \dots, m_N), (-) \end{matrix} \right]. \quad (17)$$

After that, by following a similar approach, using the relation of $f_{\beta}(\beta) = f_{n_h}(\beta/\sqrt{1-\rho^2})/\sqrt{1-\rho^2}$ and after several algebraic manipulations, $I_{\beta}(s)$ may be reformulated as

$$I_{\beta}(s) = \xi \int_{-\infty}^{\infty} e^{-(s+\Xi)\beta^2} \beta^k d\beta, \quad (18)$$

where $\xi = 1/\sqrt{2\pi\sigma^2(1-\rho^2)}$ and $\Xi = (2\sigma^2(1-\rho^2))^{-1}$. Then, with the help of [24, 3.383.11], $I_{\beta}(s)$ is obtained as

$$I_{\beta}(s) = \frac{\xi}{(s+\Xi)^{\frac{k+1}{2}}} \Gamma\left(\frac{k+1}{2}\right). \quad (19)$$

Hence, by substituting (17) and (19) into (12), $M_{\gamma}(s)$ is obtained as

$$\mathcal{M}_{\gamma}(s) = \xi \delta \sum_{k=0}^K \frac{(-2s)^k}{k!} \frac{\Gamma\left(\frac{k+1}{2}\right)}{(s+\Xi)^{\frac{k+1}{2}}} S^{\frac{k}{2}} G_{1,N}^{N,1} \left[\frac{\Delta}{s\rho^2} \mid \begin{matrix} (1-\frac{k}{2}), (-) \\ (m_1, \dots, m_N), (-) \end{matrix} \right]. \quad (20)$$

Now, by defining the instantaneous SNR in the imperfect cascaded fading channel as $\gamma \stackrel{\Delta}{=} \bar{\gamma}Y$, it holds that

$$\mathcal{M}_{\gamma}(s) = E[e^{-s\gamma}] = E[e^{-s\bar{\gamma}Y}] = \mathcal{M}_{\gamma}(s\bar{\gamma}), \quad (21)$$

where $\bar{\gamma}$ is denoting the average SNR at a fading channel and defined as $\bar{\gamma} = P/2N_0$, while P is the total transmitting power of the source node. Hence, by substituting $s\bar{\gamma}$ into (20), the MGF of γ is obtained as

$$\mathcal{M}_{\gamma}(s) = \xi \delta \sum_{k=0}^K \frac{(-2)^k \Gamma\left(\frac{k+1}{2}\right)}{k!} \frac{(s\bar{\gamma})^{\frac{3k}{2}}}{(s\bar{\gamma}+\Xi)^{\frac{k+1}{2}}} G_{1,N}^{N,1} \left[\frac{\Delta}{s\bar{\gamma}\rho^2} \mid \begin{matrix} (1-\frac{k}{2}), (-) \\ (m_1, \dots, m_N), (-) \end{matrix} \right]. \quad (22)$$

4.1. 2 × 1 Alamouti STC Scheme

In the case of the systems consisting of a source with two transmitting antennas and a destination with a single receiving antenna, $L = 1$, end-to-end SNR denoted by γ_T at the destination is

$$\gamma_T = \gamma_1 + \gamma_2, \quad (23)$$

therefore, the MGF of γ_T becomes

$$\mathcal{M}_{\gamma_T}(s) = \mathcal{M}_{\gamma_1}(s) \mathcal{M}_{\gamma_2}(s), \quad (24)$$

where the $\mathcal{M}_{\gamma_i}(s)$, for $i \in \{1, 2\}$, is calculated with the help of (22) by using the corresponding channel parameters as $(\rho, N, m_n, \Omega_n, \sigma, \xi, \delta, \Xi, \Delta) \rightarrow (\rho_i, N_i, m_{n,i}, \Omega_{n,i}, \sigma_i, \xi_i, \delta_i, \Xi_i, \Delta_i)$.

4.2. $2 \times L$ Alamouti STC Scheme

In case of L receiving antennas installed at the destination vehicle, the instantaneous SNR at the l^{th} antenna is

$$\gamma_l = \gamma_{l,1} + \gamma_{l,2} \quad (25)$$

and the corresponding MGF becomes

$$\mathcal{M}_{\gamma_l}(s) = \mathcal{M}_{\gamma_{l,1}}(s)\mathcal{M}_{\gamma_{l,2}}(s). \quad (26)$$

Thus, the end-to-end SNR acquired by the destination after employing the MRC scheme is obtained as

$$\gamma_T = \sum_{l=1}^L \gamma_l \quad (27)$$

and the MGF of γ_T can be calculated as

$$\mathcal{M}_{\gamma_T}(s) = \prod_{l=1}^L \mathcal{M}_{\gamma_l}(s). \quad (28)$$

Yet again, while evaluating (28) via (26), calculation of $\mathcal{M}_{\gamma_{l,i}}(s)$, for $i \in \{1, 2\}$ is performed by using (22) with the corresponding channel parameters as $(\rho, N, m_n, \Omega_n, \sigma, \xi, \delta, \Xi, \Delta) \rightarrow (\rho_i^l, N_i^l, m_{n,i}^l, \Omega_{n,i}^l, \sigma_i^l, \xi_i^l, \delta_i^l, \Xi_i^l, \Delta_i^l)$ between the i^{th} transmitting and the l^{th} receiving antennas.

4.3. Symbol-Error-Rate for M-PSK Modulation

When considering an L -branch MRC receiver, the average SER for M-PSK modulation over generalized fading channels is given by

$$P_e^{M-PSK} = \frac{1}{\pi} \int_0^{\pi-\pi/M} \mathcal{M}_{\gamma_T}(\theta_M) d\theta = \frac{1}{\pi} \int_0^{\pi-\pi/M} \prod_{l=1}^L \mathcal{M}_{\gamma_l}(\theta_M) d\theta, \quad (29)$$

where $\theta_M = \frac{\sin^2(\pi/M)}{\sin^2\theta}$ [26]. Even though an explicit solution of (29) in terms of elementary functions has not been derived due to the integral expression of the multiplication of L Meijer's G functions, which is not tabulated in the current literature, a tight approximation for SER of the M-PSK modulation can be effectively calculated as [27]

$$P_e^{M-PSK} \approx \left(\frac{1}{3} - \frac{1}{2M}\right) \mathcal{M}_{\gamma_T}\left(\sin^2\left(\frac{\pi}{M}\right)\right) + \frac{1}{4} \mathcal{M}_{\gamma_T}\left(\frac{4}{3} \sin^2\left(\frac{\pi}{M}\right)\right) + \left(\frac{1}{4} - \frac{1}{2M}\right) \mathcal{M}_{\gamma_T}\left(\frac{\sin^2\left(\frac{\pi}{M}\right)}{\sin^2\left(\pi - \frac{\pi}{M}\right)}\right). \quad (30)$$

Thus, by substituting (28) into (30) and using the MGF expression of the instantaneous SNR in cascaded fading channels with estimation errors in (22), the average symbol error rate of Alamouti STC using M-PSK modulation is obtained for V2V communication systems over N^* Nakagami- m fading channels with channel estimation error.

4.4. Symbol-Error-Rate for M-QAM Modulation

The average SER for a coherent M-QAM modulation scheme with multi-channel reception is given as

$$P_e^{M-QAM} = \frac{4\alpha}{\pi} \int_0^{\pi/2} \mathcal{M}_{\gamma_T}(\phi_M) d\phi - \frac{4\alpha^2}{\pi} \int_0^{\pi/4} \mathcal{M}_{\gamma_T}(\phi_M) d\phi, \quad (31)$$

where $\alpha = \left(1 - \frac{1}{M}\right)$ and $\phi_M = \frac{3/(2(M-1))}{\sin^2 \phi}$ [26]. Using the relation between the expectation operation and the MGF function, (31) can be written as

$$P_e^{M-QAM} = E[I_1] - E[I_2], \quad (32)$$

where I_1 and I_2 are the integral expressions of

$$I_1 = \frac{4\alpha}{\pi} \int_0^{\pi/2} e^{-\phi_{M\gamma_T}} d\phi, \quad (33a)$$

$$I_2 = \frac{4\alpha^2}{\pi} \int_0^{\pi/4} e^{-\phi_{M\gamma_T}} d\phi, \quad (33b)$$

respectively. With the help of [27, Eq.8], I_1 can be approximated as

$$I_1 \approx 4\alpha \left(\frac{1}{12} e^{-\phi_{M\gamma_T}} + \frac{1}{4} e^{-\frac{4}{3}\phi_{M\gamma_T}} \right) = \frac{\alpha}{3} e^{-\phi_{M\gamma_T}} + \alpha e^{-\frac{4}{3}\phi_{M\gamma_T}}, \quad (34)$$

therefore $E[I_1]$ becomes

$$E[I_1] \approx \frac{\alpha}{3} \mathcal{M}_{\gamma_T} \left(\frac{3}{2(M-1)} \right) + \alpha \mathcal{M}_{\gamma_T} \left(\frac{2}{M-1} \right). \quad (35)$$

For the derivation of $E[I_2]$, we can write

$$E[I_2] = E[I_{21}] - E[I_{22}], \quad (36)$$

where

$$I_{21} = \frac{4\alpha^2}{\pi} \int_0^{\pi/2} e^{-\phi_{M\gamma_T}} d\phi, \quad (37a)$$

$$I_{22} = \frac{4\alpha^2}{\pi} \int_{\pi/4}^{\pi/2} e^{-\phi_{M\gamma_T}} d\phi. \quad (37b)$$

Similarly, with the help of [27, Eq.8], I_{21} can be approximated as

$$I_{21} \approx 4\alpha^2 \left(\frac{1}{12} e^{-\phi_{M\gamma_T}} + \frac{1}{4} e^{-\frac{4}{3}\phi_{M\gamma_T}} \right) = \frac{\alpha^2}{3} e^{-\phi_{M\gamma_T}} + \alpha^2 e^{-\frac{4}{3}\phi_{M\gamma_T}}, \quad (38)$$

then

$$E[I_{21}] \approx \frac{\alpha^2}{3} \mathcal{M}_{\gamma_T} \left(\frac{3}{2(M-1)} \right) + \alpha^2 \mathcal{M}_{\gamma_T} \left(\frac{2}{M-1} \right). \quad (39)$$

In the evaluation of $E[I_{22}]$, by following the similar approach in [27] and using the trapezoid rule of the definite integrals, the integral expression of I_{22} can be approximated to the $\left(\frac{4\alpha^2}{\pi}\right)$ times the area of a trapezoid having parallel sides of length with $e^{-\frac{3}{2M-1}\frac{\gamma_T}{M-1}}$ and $e^{-3\frac{\gamma_T}{M-1}}$, and height with $\left(\frac{\pi}{4}\right)$ as

$$I_{22} \approx \frac{4\alpha^2}{\pi} \left(e^{-\frac{3}{2M-1}\frac{\gamma_T}{M-1}} + e^{-3\frac{\gamma_T}{M-1}} \right) \frac{\pi}{8} = \frac{\alpha^2}{2} \left(e^{-\frac{3}{2M-1}\frac{\gamma_T}{M-1}} + e^{-3\frac{\gamma_T}{M-1}} \right) \quad (40)$$

and therefore $E[I_{22}]$ is obtained as

$$E[I_{22}] \approx \frac{\alpha^2}{2} \mathcal{M}_{\gamma_T} \left(\frac{3}{2(M-1)} \right) + \frac{\alpha^2}{2} \mathcal{M}_{\gamma_T} \left(\frac{3}{M-1} \right). \quad (41)$$

By substituting (39) and (41), $E[I_2]$ becomes

$$E[I_2] \approx \alpha^2 \mathcal{M}_{\gamma_T} \left(\frac{2}{M-1} \right) - \frac{\alpha^2}{2} \mathcal{M}_{\gamma_T} \left(\frac{3}{M-1} \right) - \frac{\alpha^2}{6} \mathcal{M}_{\gamma_T} \left(\frac{3}{2(M-1)} \right). \quad (42)$$

Finally, substituting (35) and (42) in (31), the average SER for a coherent M-QAM modulation scheme with multi-channel reception is obtained as

$$P_e^{M-QAM} \approx \left(\frac{1}{2} + \frac{1}{6M^2} \right) \mathcal{M}_{\gamma_T} \left(\frac{3}{2(M-1)} \right) + \frac{(M-1)^2}{2M^2} \mathcal{M}_{\gamma_T} \left(\frac{3}{M-1} \right) + \left(\frac{M-1}{M^2} \right) \mathcal{M}_{\gamma_T} \left(\frac{2}{M-1} \right). \quad (43)$$

Hence, by substituting (28) into (43) and then using (22), the average SER of Alamouti STC using M-QAM modulation is obtained for V2V communication systems that are subject to cascaded Nakagami- m fading channels with channel estimation errors.

5. ERGODIC CAPACITY ANALYSIS

The exact ergodic capacity of L -branch diversity combiner over mutually not-necessarily independent or identically distributed fading channels is given by [28]

$$C_{avg} = \frac{W}{\log(2)} \sum_{n=1}^N w_n C_1(s_n) \frac{d}{ds} \mathcal{M}_{\gamma_T}(s) \Big|_{s \rightarrow s_n}, \quad (44)$$

where W is the channel's bandwidth, $s_n = \tan\left(\frac{\pi}{4} \cos\left(\frac{2n-1}{2N}\pi\right) + \frac{\pi}{4}\right)$, and $w_n = \frac{\pi^2 \sin\left(\frac{2n-1}{2N}\pi\right)}{4N \cos^2\left(\frac{\pi}{4} \cos\left(\frac{2n-1}{2N}\pi\right) + \frac{\pi}{4}\right)}$.

Using (26) and (28), it may be written that

$$\begin{aligned} \frac{d}{ds} \mathcal{M}_{\gamma_T}(s) &= \sum_{l=1}^L \prod_{j=1, j \neq l}^L \mathcal{M}_{\gamma_j}(s) \frac{d}{ds} \mathcal{M}_{\gamma_l}(s) \\ &= \sum_{l=1}^L \prod_{j=1, j \neq l}^L \mathcal{M}_{\gamma_j}(s) \times \left(\mathcal{M}_{\gamma_{l,2}}(s) \frac{d}{ds} \mathcal{M}_{\gamma_{l,1}}(s) + \mathcal{M}_{\gamma_{l,1}}(s) \frac{d}{ds} \mathcal{M}_{\gamma_{l,2}}(s) \right). \end{aligned} \quad (45)$$

By using (21), it may be written that $\frac{d}{ds} \mathcal{M}_{\gamma_{l,i}}(s) = \bar{\gamma} \frac{d}{ds} \mathcal{M}_{\gamma}(s\bar{\gamma})$ where $\bar{\gamma} = E[\gamma_{l,i}]$ for $i \in 1,2$. Therefore, $\frac{d}{ds} \mathcal{M}_{\gamma}(s)$ should be derived to calculate (45). Hence, by using (21)

$$\begin{aligned} \frac{d}{ds} \mathcal{M}_{\gamma}(s) &= \sum_{k=0}^K \frac{(-2s)^k}{k!} I_{\alpha}(s) I_{\beta}(s) \\ &= \sum_{k=0}^K \frac{(-2)^k}{k!} s^{k-1} \left(k I_{\alpha}(s) I_{\beta}(s) + s I_{\beta}(s) \frac{d}{ds} I_{\alpha}(s) + s I_{\alpha}(s) \frac{d}{ds} I_{\beta}(s) \right), \end{aligned} \quad (46)$$

where $I_{\alpha}(s)$ and $I_{\beta}(s)$ are given by (16) and (19), respectively. By using (16) it may be written as

$$\begin{aligned} \frac{d}{ds} I_{\alpha}(s) &= \frac{d}{ds} \delta \int_0^{\infty} e^{-sz} z^{\frac{k}{2}-1} G_{0,N}^{N,0} \left[z \frac{\Delta}{\rho^2} \mid \begin{matrix} (-), (-) \\ (m_1, \dots, m_N), (-) \end{matrix} \right] dz \\ &= -\delta \int_0^{\infty} e^{-sz} z^{\frac{k}{2}} G_{0,N}^{N,0} \left[z \frac{\Delta}{\rho^2} \mid \begin{matrix} (-), (-) \\ (m_1, \dots, m_N), (-) \end{matrix} \right] dz. \end{aligned} \quad (47)$$

Hence, with the help of the integral property of Meijer's G function [25, 2.24.3.1], (47) is obtained as

$$\frac{d}{ds} I_{\alpha}(s) = -\delta s^{\frac{k}{2}+1} G_{1,N}^{N,1} \left[\frac{\Delta}{s\rho^2} \mid \begin{matrix} (-\frac{k}{2}), (-) \\ (m_1, \dots, m_N), (-) \end{matrix} \right]. \quad (48)$$

After that, by using (19) $\frac{d}{ds} I_{\beta}(s)$ may be derived as

$$\frac{d}{ds} I_{\beta}(s) = \xi \Gamma\left(\frac{k+1}{2}\right) \frac{d}{ds} (s + \Xi)^{-\frac{k+1}{2}} = -\frac{k+1}{2} \xi \Gamma\left(\frac{k+1}{2}\right) (s + \Xi)^{-\frac{k+3}{2}}. \quad (49)$$

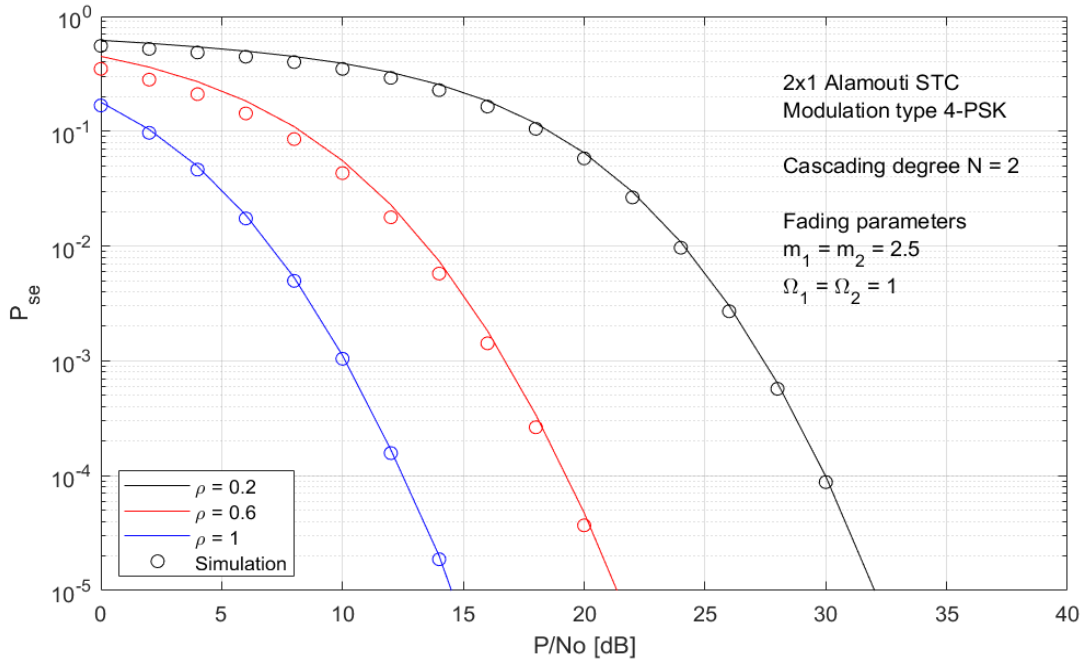


Figure 2. Performance of 2x1 Alamouti STBC over imprecise 2*Nakagami- m fading channels with $m_1 = m_2 = 2.5$ for $\rho = 0.2, 0.6,$ and 1 .

Thus, by substituting (48) and (49) into (46), then by calculating (45) with the help of (46) and substituting it into (44), the average capacity of the Alamouti STBC errors is obtained in the closed-form for MIMO V2V communication systems over cascaded fading channels with the channel estimation.

6. NUMERICAL RESULTS AND SIMULATIONS

Throughout this section, numerical results and simulations are provided comparatively to validate the analytic results derived in the paper. During calculations, it is assumed that the transmitter transmits the symbols with unit power per antenna. Also, the fading coefficients for the cascaded channels have unit power as $\Omega = E[h^2]$. In figures, the analytic plots are represented by solid lines while the simulation results are marked by circles.

In Figure 2, the SER performance of 2x1 Alamouti STBC using 4-PSK modulation over cascaded Nakagami- m fading channels is presented for the miscellaneous degrees of channel estimation errors. For this figure, the cascading degree and the related fading parameters are set as $N = 2$ and $m_1 = m_2 = 2.5$, respectively. The correlation coefficient between a channel gain h and its erroneous estimation \hat{h} is chosen as $\rho \in \{0.2, 0.6, 1\}$. As is seen from the figure, the presence of channel

estimation errors significantly worsens the SER performance of the system. For example, to achieve 10^{-3} error rate, an extra 7dB SNR is required for $\rho = 0.6$ in comparison with the perfect estimation of the channel statistics which corresponds to $\rho = 1$.

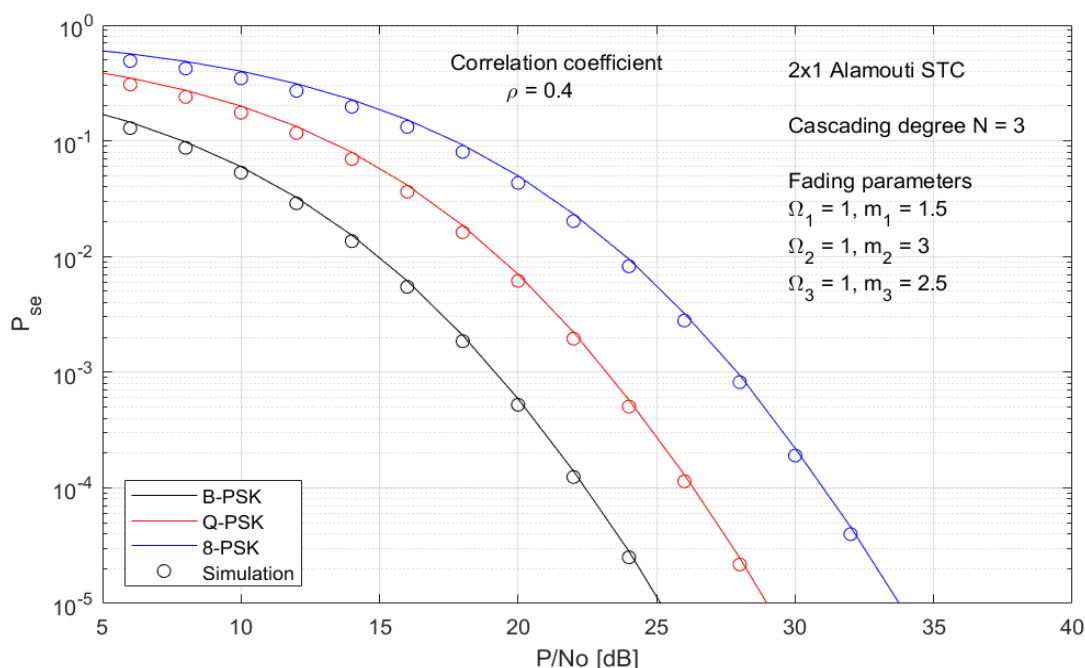


Figure 3. SER performances of vehicular communication systems employing Alamouti STC scheme with B/Q/8-PSK modulations over 3*Nakagami- m channels with $m_1 = 1.5, m_2 = 3$ and $m_3 = 2.5$ in the presence of channel estimation errors for $\rho = 0.4$.

Figure 3 represents the effect of modulation order on the SER performance of Alamouti STC scheme over cascaded fading channels. The plots are given for the BPSK, QPSK, and 8-PSK modulation schemes over 3*Nakagami- m fading channels, $N=3$, with $m_1 = 1.5, m_2 = 3$, and $m_3 = 2.5$. The correlation coefficient related to the estimation error is set as $\rho = 0.4$. As seen from the figure, the SER performance of the system decreases by increasing modulation order, which makes the maximum-likelihood decision-making process becomes more vulnerable to estimation errors since the distances among the symbols in the constellation are getting closer. For example, the figure shows that the SNR gap between BPSK and QPSK modulations is approximately 5dB at 10^{-3} SER value. It is also seen that the 8-PSK modulation scheme requires extra 8dB SNR to provide the same SER value for the proposed system when compared with using BPSK modulation.

In Figure 4, the effect of the channel's cascading degree on the SER performances is presented when the cascading degree is as $N = 1, 2$, and 4 , which are corresponding to Rayleigh, 2^* Rayleigh, and 4^* Rayleigh fading channels, respectively, in V2V communication systems employing Alamouti's space-time coding scheme using 8-PSK modulation. Here, the correlation coefficient between h and \hat{h} is set as $\rho = 0.3$. The figure reveals that the increasing cascading degree of the fading channels significantly degrades the SER performance of the system. For example, the SNR gap between $N = 1$ and $N = 2$ (Rayleigh and 2^* Rayleigh channels) is approximately 5dB while it is about 8dB in the case of $N = 2$ and $N = 4$ (2^* Rayleigh and 4^* Rayleigh channels) to reach the 10^{-3} SER value.

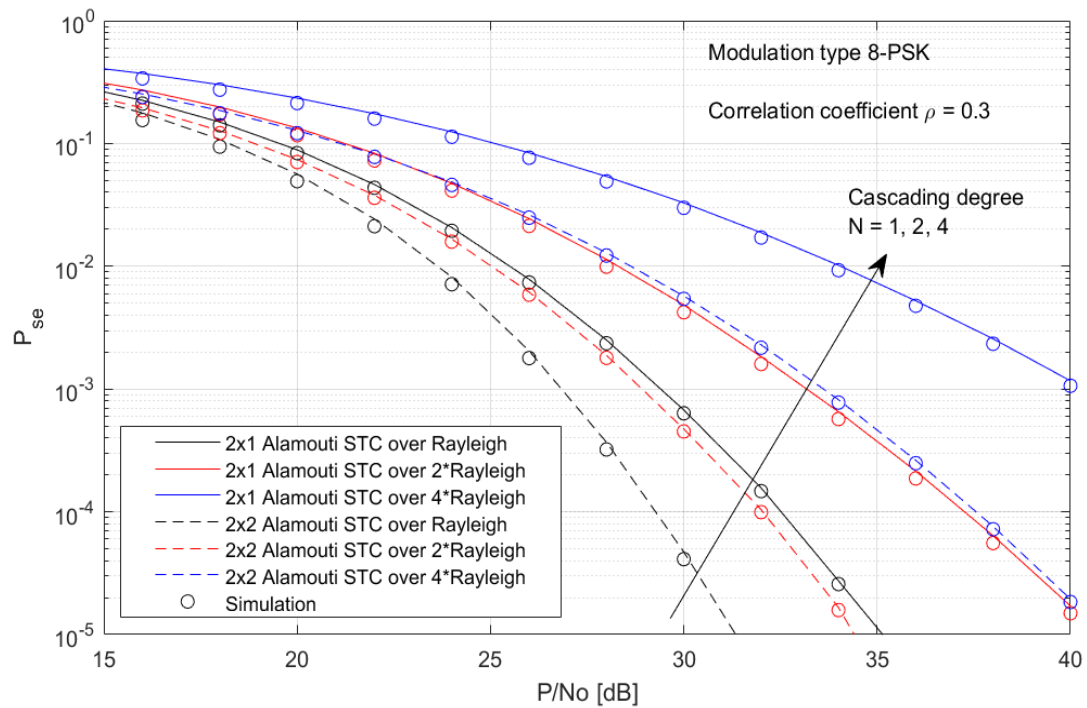


Figure 4. SER performances of vehicular communication systems employing Alamouti STBC using 8-PSK modulation for different vehicular fading channel models for $\rho = 0.3$.

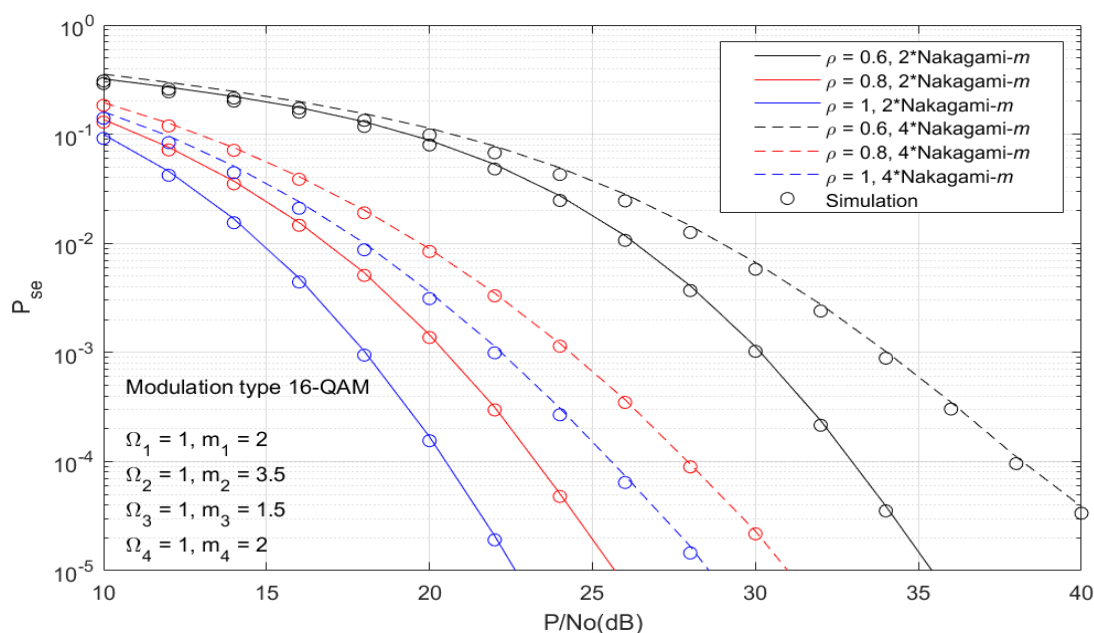


Figure 5. Performances of Alamouti STC scheme using 16-QAM modulation over 2*Nakagami- m and 4*Nakagami- m fading channels for $\rho = 0.6, 0.8,$ and 1 .

Additionally, Figure 4 represents the SER performance comparison for SIMO (2x1) and MIMO (2x2) configurations of Alamouti STBC over the imprecise cascaded Nakagami- m fading channels. The figure reveals that the system performance may be significantly enhanced by using multiple receiving antennas. For example, an extra receiving antenna provides 10 times better SER at 30dB SNR.

The performance of Alamouti STC scheme using 16-QAM modulation for V2V communication systems is presented in Figure 5. The plots are given for 2*Nakagami- m with $m_1 = 2, m_2 = 3.5,$ and 4*Nakagami- m with $m_1 = 2, m_2 = 3.5, m_3 = 1.5, m_4 = 2$ fading channels and $\rho = 0.6, 0.8, 1$ values of the correlation coefficient between h and its erroneous estimation \hat{h} . The figure reveals that the presence of channel estimation errors severely worsens the SER performance of vehicular communication systems. For example, to achieve the error rate of 10^{-3} over 2*Rayleigh fading channels, extra 13dB SNR is required for $\rho = 0.6$ in comparison with the perfect estimation case in which $\rho = 1$. It is also seen that the PSK modulation provides better SER performance than the QAM modulation does in V2V communication systems employing Alamouti STBC over imprecise cascaded fading channels. Finally, it is shown by the figures that the analytical and simulation results tightly match, which is because of the analytical SER expressions are approximations to the exact ones.

7. CONCLUSIONS

In this letter, we proposed to use the Alamouti STC to enhance the SER performance of V2V communication systems over cascaded fading channels where the perfect knowledge of the channel state information is not available to the users all the time due to the rapid movement of the communicating vehicles and fast-changing characteristics of the rich scattering environment which makes the fading effects in wireless channels more severe. Therefore, in investigating the SER profile of the proposed system, we consider the erroneous estimation of the fading channels' gains which is much more realistic for the practical scenarios. During the analysis, we first derive the moment-generation function (MGF) of the erroneously estimated channel fading coefficient in the case of the cascaded Nakagami- m fading conditions. Then, using this MGF, SER expressions of Alamouti STC with two transmitting and L receiving antennas for the M-PSK and M-QAM modulation schemes are obtained. After that the ergodic capacity analysis for the proposed system is examined and a closed-form expression of it is derived. Furthermore, the analytical results are verified by Monte-Carlo simulations. The results reveal that the SER performance of V2V communication systems is severely degraded in case of full channel-state information is not available due to estimation errors but it can be improved significantly by using the Alamouti STC method. It is also presented that using PSK modulation provides better SER performance than using QAM modulation in the vehicular communication systems employing Alamouti STC over imprecise cascaded fading channels.

ACKNOWLEDGEMENT

This research received no specific grants from any public, commercial or non-profit funding agencies.

REFERENCES

- [1] Gyawali, S., Xu, S., Qian, Y. and Hu, R.Q., (2021). Challenges and Solutions for Cellular Based V2X Communications, *IEEE Communications Surveys and Tutorials*, 23-1, 222-255.
- [2] Kim, J., Choi, Y.-J., Noh, G. and Chung, H., (2023). On the Feasibility of Remote Driving Applications Over mmWave 5G Vehicular Communications: Implementation and Demonstration, *IEEE Transactions on Vehicular Technology*, 72-2, 2009-2023.
- [3] Guo, C., Liang, L. and Li, G.Y., (2019). Resource Allocation for Vehicular Communications with Low Latency and High Reliability, *IEEE Transactions on Wireless Communications*, 18-8, 3887-3902.
- [4] Liu, R., Liu, A., Qu, Z. and Xiong, N.N., (2023). An UAV-Enabled Intelligent Connected Transportation System with 6G Communications for Internet of Vehicles, *IEEE Transactions on Intelligent Transportation Systems*, 24-2, 2045-2059.
- [5] Lv, Z., Qiao, L. and You, I., (2021). 6G-Enabled Network in Box for Internet of Connected Vehicles, *IEEE Transactions on Intelligent Transportation Systems*, 22-8, 5275-5282.

- [6] Xu, X., Yao, L., Bilal, M., Wan, S., Dai, F. and Choo, K.-K.R., (2022). Service Migration Across Edge Devices in 6G-Enabled Internet of Vehicles Networks, *IEEE Internet of Things Journal*, 9-3, 1930-1937.
- [7] Pan, Q., Wu, J., Nebhen, J., Bashir, A.K., Su, Y. and Li, J., (2022). Artificial Intelligence-Based Energy Efficient Communication System for Intelligent Reflecting Surface-Driven VANETs, *IEEE Transactions on Intelligent Transportation Systems*, 23-10, 19714-19726.
- [8] Tang, F., Kawamoto, Y., Kato, N. and Liu, J., (2020). Future Intelligent and Secure Vehicular Network Toward 6G: Machine-Learning Approaches, *Proceedings of the IEEE*, 108-2, 292-307.
- [9] Noor-A-Rahim, M., Liu, Z., Lee, H., Khyam, M.O., He, J., Pesch, D., Mousser, K. and Poor, H.V., (2022). 6G for Vehicle-to-Everything (V2X) Communications: Enabling Technologies, Challenges, and Opportunities, *Proceedings of the IEEE*, 110-6, 712-734.
- [10] Boulogeorgos, A.-A.A., Sofotasios, P.C., Selim, B., Muhaidat, S., Karagiannidis, G.K. and Valkama, M., (2016). Effects of RF Impairments in Communications Over Cascaded Fading Channels, *IEEE Transactions on Vehicular Technology*, 65-11, 8878-8894.
- [11] Zhang, H., Liao, Z., Shi, Z., Yang, G., Dou, Q. and Ma, S., (2022). Performance Analysis of MIMO-HARQ Assisted V2V Communications with Keyhole Effect, *IEEE Transactions on Communications*, 70-5, 3034-3046.
- [12] Aliev, R., Hehn, T., Kwoczek, A. and Kürner, T., (2018). Predictive Communication and Its Application to Vehicular Environments: Doppler-Shift Compensation, *IEEE Transactions on Vehicular Technology*, 67-8, 7380-7393.
- [13] Karagiannidis, G.K., Sagias, N.C., and Mathiopoulos, P.T., (2007). N*Nakagami: A novel stochastic model for cascaded fading channels, *IEEE Transactions on Communications*, 55-8, 1453-1458.
- [14] Jaiswal, N. and Purohit, N., (2021). Performance Analysis of NOMA-Enabled Vehicular Communication Systems with Transmit Antenna Selection Over Double Nakagami-m Fading, *IEEE Transactions on Vehicular Technology*, 70-12, 12725-12741.
- [15] Zhang, C., Ge, J., Li, J. and Hu, Y., (2013). Performance analysis for mobile relay-based M2M two-way AF relaying in N* Nakagami-m fading, *Electronics Letters*, 49-5, 344-346.
- [16] Ata, S.Ö. And Altunbaş, I., (2016). Fixed-gain AF PLNC over cascaded Nakagami-m fading channels for vehicular communications, *AEU-International Journal of Electronics and Communications*, 70-4, 510-516.

- [17] Eshteiwi, K., Sleim, B. and Kaddoum, G., (2020). Full Duplex of V2V Cooperative Relaying over Cascaded Nakagami-m Fading Channels, International Symposium on Networks, Computers, and Communications, Montreal, Canada, 1-5.
- [18] Baek, S., Lee, I. and Song, C., (2019). A New Data Pilot-Aided Channel Estimation Scheme for Fast Time-Varying Channels in IEEE 802.11p Systems, IEEE Transactions on Vehicular Technology, 68-5, 5169-5172.
- [19] Xu, C., An, J., Bai, T., Sugiura, S., Maunder, R.G., Wang, Z., Yang, L.L., Hanzo, L., (2023). Channel Estimation for Reconfigurable Intelligent Surface Assisted High-Mobility Wireless Systems, IEEE Transactions on Vehicular Technology, 72-1, 718-734.
- [20] Liu, T.-H., (2015). Analysis of the Alamouti STBC MIMO System with Spatial Division Multiplexing Over the Rayleigh Fading Channel, IEEE Transactions on Wireless Communications, 14-9, 5156-5170.
- [21] Khattabi, Y.M. and Matalgah, M.M., (2018). Alamouti-OSTBC Wireless Cooperative Networks With Mobile Nodes and Imperfect CSI Estimation, IEEE Transactions on Vehicular Technology, 67-4, 3447-3456.
- [22] Zhu, J., Xiao, L., Xiao, P., Quddus, A., He, C. and Lu, L., (2021). Differential STBC-SM Scheme for Uplink Multi-User Massive MIMO Communications: System Design and Performance Analysis, IEEE Transactions on Vehicular Technology, 70-10, 10236-10251.
- [23] Alamouti, S.M., (1998). Simple Transmit Diversity Technique for Wireless Communications, IEEE Journal on Selected Areas in Communications, 16-8, 1451-1458.
- [24] Gradshteyn, I.S. and Ryzhik, I.M., (2015). Table of Integrals, Series, and Products, 8th ed., Academic Press, New York.
- [25] Prudnikov, A.P., Brychkov, Y.A. and Marichev, O.I., (1986). Integrals and Series - Vol. 3 - More Special Functions. CRC Press.
- [26] Simon, M. K. and Alouini, M.S., (2005). Digital Communication over Fading Channels, 2nd ed., Wiley & Sons.
- [27] Mckay, M.R., Zanella, A., Collings, I.B. and Chiani, M., (2009). Error probability and SINR analysis of optimum combining in rician fading, IEEE Transactions on Communications, 57-3, 676-687.
- [28] Yilmaz, F. and Alouini, M.S., (2012). A Unified MGF-Based Capacity Analysis of Diversity Combiners over Generalized Fading Channels, IEEE Transactions on Communications, 60-3, 862-875.



RESEARCH ARTICLE

EFFECTS OF WIND SPEED AND MOUNTING TYPE ON PV MODULE IN UNBALANCED DISTRIBUTION SYSTEMS

Salman Ahmed NUR^{1,*}, Selçuk EMİROĞLU²

¹Sakarya University, Electrical and Electronics Engineering, Sakarya, salmaanahmednuur@gmail.com,
ORCID: 0000-0002-8391-1170

²Sakarya University, Electrical and Electronics Engineering, Sakarya, selcukemiroglu@sakarya.edu.tr,
ORCID: 0000-0001-7319-8861

Receive Date: 01.05.2023

Accepted Date: 03.07.2023

ABSTRACT

This paper assesses the effects of wind speed and mounting type on the performance of photovoltaic (PV) modules in the three phase unbalanced IEEE 34 node distribution system. The study was conducted in OpenDSS considering ZIP load model and residential load shape. The module temperature was calculated considering the wind speed and mounting type of the PV panel. The impact of wind speed on PV has been analyzed using three different wind data sets. Furthermore, free standing and flat roof mounting types were considered to evaluate the effect of mounting configuration. It was found that integrating PV into the distribution system reduced substation demand and energy losses. Results also show that the PV produced more power in high wind speed scenarios than in low wind speed scenarios. Regarding the mounting configuration, the PV incorporated with free standing configuration generated more power than the flat roof mounting type.

Keywords: *Photovoltaic Systems, Wind Speed, Mounting Type, Ambient Temperature, Unbalanced Distribution System*

1. INTRODUCTION

The rising concerns about the impact of fossil fuel energy on climate change and global warming have led to increasing demand for clean and renewable energy sources. With the advancement of technology, industrial development and the increase in the world population, the need for energy is also increasing rapidly. In fact, the total amount of primary energy consumed in the world in 2022 reached 595 EJ [1]. Photovoltaics (PVs) is among the various renewable energy sources seen as to solution to these problems and it is expected to become one of the major energy resources due to the learning and cost reductions, large potential for solar PV expansion, and integration strategies that allow penetration of PV into the power grid [2]. Despite the significant advancements in PV technology, there is still a great deal of interest in studying external factors such as weather conditions that may impact the PV output. It is well understood that the cell temperature impacts the efficiency

and electrical output of PV cells [3]–[6]. Various factors affect this temperature including wind speed, ambient temperature, and irradiance [7]. In particular, the temperature of the PV module is highly sensitive to wind speed and to a lesser extent to wind direction [8]. Numerous studies have discussed the impact of wind on cell temperature in different environmental conditions. Al-Bashir et al [9] analysed the effects of cell temperature, solar irradiance and wind speed on PV system's performance. They found a linear relation between the irradiance, cell temperature, wind speed and the PV power. Because of the low wind speed in the area where the experiment was conducted, the impact of the wind speed was not significant. Goverde *et al.*[10] investigated the influence of wind on the temperature of PV mini-modules. They found that the module's surface temperature decreased on average by 11 °C, 16 °C, and 21 °C at a wind speed of 1 m/s, 2 m/s, and 5 m/s at an illumination of 400 W/m². Tahir et al [11] examined the Impact of wind speed and temperature on five types of PV panels for various regions in Pakistan. The obtained results observed a decrease in PV efficiency when considering only the effect of temperature. However, the efficiency increased when was considered the impact of both wind speed and temperature. Even though PV module efficiency is determined based on standard test conditions (STC), it is crucial to observe how these modules perform in actual field conditions to accurately predict their efficiency and power output [12]. Although solar irradiance and ambient temperature are commonly used as the sole parameters to calculate the PV module operating temperature in the literature, studies [13]–[15] indicate that wind speed may also have a significant impact on increasing efficiency by lowering PV cell temperature because of its cooling effect. Ambient wind speed has positive and negative aspects. In the USA, a wind speed of 10 m/s can reduce the operating temperature by 3.5°C. However, in a hot place like Saudi Arabia, a 10°C drop is possible at a wind flow of 2.8-5.3 m/s [16]. Therefore, accurate solar cell temperature estimations are required for reliable energy yield simulations. Various researchers ([7], [17], [18], [19]) proposed models incorporating wind's effect on PV module performance. Skoplaki *et al* [7] proposed simple mathematical equations for calculating the temperature and electrical efficiency of PV modules considering wind effect and arbitrary mounting. The PV mounting design, whether free standing, BIPV, BIPV/T, or BAPV, is a further factor to consider because it has a big impact on cell temperature and the passing air flow across the PV sides [20]. A solar system's energy output can be maximized by selecting the proper solar mounting system and installing it correctly, as this will ensure structural support and determine the best orientation and elevation for the system [21]. Various approaches exist for integrating solar PVs into buildings. Two techniques used to mount PV arrays are roof-mounted systems and ground-mounted systems [22]. Awan et al. [23] compared ground-mounted and rooftop PV with optimal interrow distance between parallel arrays, and found that rooftop systems performed better and had more economic advantages than ground-mounted systems in urban environments. Cura [24] evaluated the economical and technical considerations of PV plants operating under various environmental conditions. Various case studies were conducted at two different solar plants with ground mounted and roof mounted installation. The results of the simulation demonstrated that ground-mounted PV arrays had higher efficiency than the those with roof-mounted PV arrays. Tamoor [25] investigated the design and energy estimation of a ground mounted PV with interrow spacing and optimal tilt angle installation. The study assessed the efficiency of the solar system and aided in determining how to make the best use of the space that is available, both of which are critical for the financial viability of the PV power plants. Kazim [26] has also compared the performance of PV panels mounted on flat surfaces and roof tops in UAE and found that the flat surface mounting structure had a lower efficiency due to the tilt angle, but also a lower temperature and dust

accumulation than the roof top mounting structure. The author also reported that the flat surface mounting structure had a higher power output per unit area than the roof top mounting structure.

The impact of wind speed is frequently disregarded when modeling PV systems, but it is crucial to determine the modules' temperature and, consequently, their efficiency [7]. The literature review [24] revealed that the potential of solar energy systems is more than the other renewable energy systems. The installation of PV plants has grown steadily due to lower costs of equipment, higher government subsidies and increased public consciousness of the fossil fuel related environmental issues. Moreover, estimating the energy production of PV plants during real climate conditions is important both for researchers and investors. For this purpose, this study aims to investigate the effects of wind speed and the mounting type on the PV module performance under real environmental conditions. To test this, a PV is connected to the IEEE 34 test feeder and power flow analyses were performed using OpenDSS (Open Distribution System Simulator)[27]. Various case studies have been conducted by using three wind speed data namely high, moderate, and low along with free standing and flat roof mounting configurations. Moreover, 10-minute temperature data and irradiance have been used to model the PV in OpenDSS. It should be noted that the time resolution of 10-minute was considered based on the ground measurements of solar radiation, wind speed, and ambient temperature that were available. To assess the influence of wind alone on the output of the PV, the same temperature and irradiance have been used for all case studies. By comparing the case studies, the impact of wind speed and mounting type on the power output of the PV has been observed. The contribution of this paper is to study the effect of wind speed and mounting type on the PV system integrated into the distribution network. The sections of this paper are organized as follows: in Section 2, the meteorological data of solar irradiance, temperature, and wind speed to calculate panel temperature is presented. The design of the PV system, the distribution test system, the load modelling, and the cell temperature calculation considering wind speed are also covered in this section. In Section 3, Several case studies are created to analyze the impact of wind speed and mounting types on PV power output. This section also discusses daily energy generation and power losses of the PV system at free standing and flat roof mounting configurations. Finally, the conclusions which highlight the main findings of this study are presented in Section 4.

2. MODELLING APPROACH

2.1. Meteorological Sample Data

As a sample input, data from [28] has been used. These data have been recorded by nine automated solar stations in Pakistan from 2014 to 2017 and it consists of daily 10-minute values of wind speed, solar irradiance, and temperature. In order to evaluate the influence of wind speed on the output of the PV power, the data measured in the station in Lahore has been used and three different days (23/10/2014, 21/02/2015, and 20/06/2015) with an average wind speed of (1.18 m/s, 4.1 m/s, and 6.9 m/s, respectively) has been selected. The wind speed graph for these days is given in Figure 1.

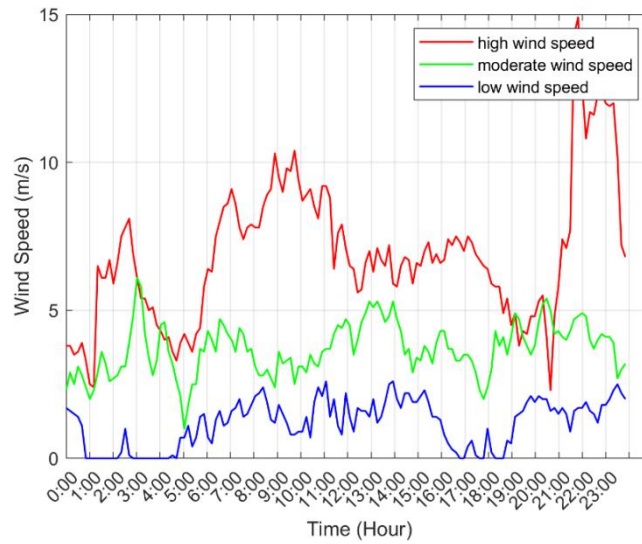


Figure 1. The wind speed data [28].

As the study aims to evaluate the influence of wind speed on PV power output, the same temperature, and irradiance have been used for all scenarios. The irradiance and the temperature are shown in figures (2) and (3) respectively.

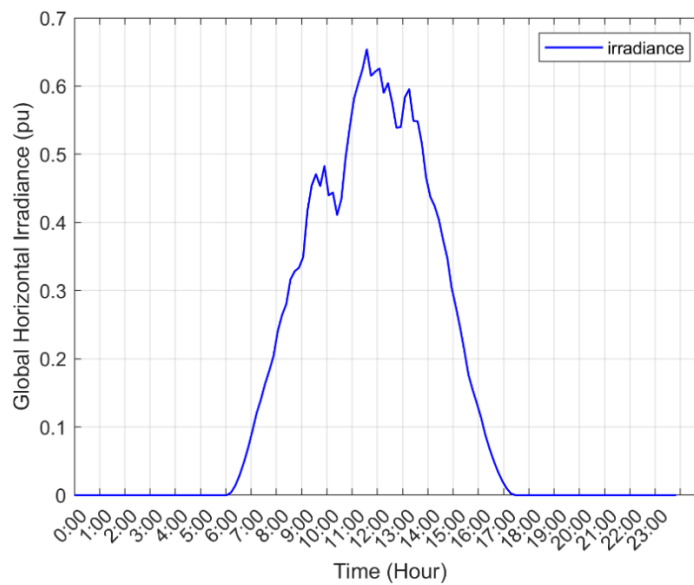


Figure 2. The irradiance data [28].

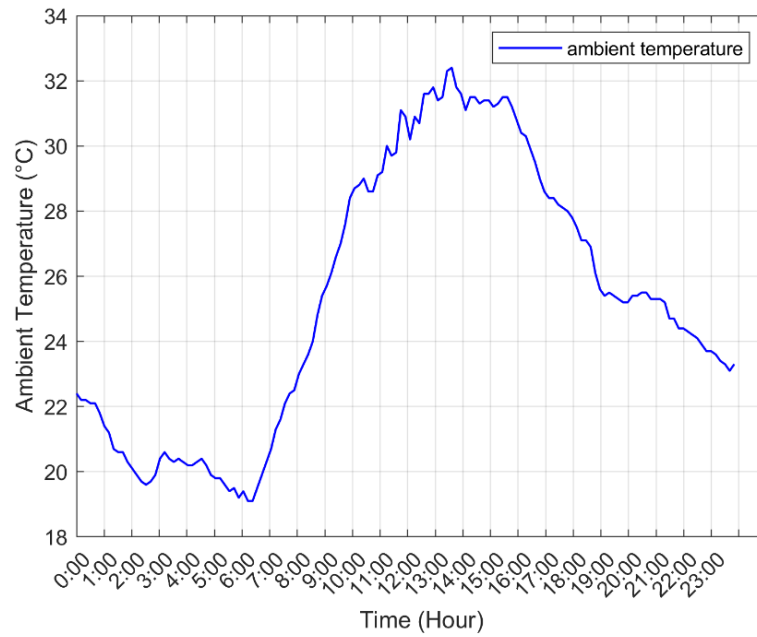


Figure 3. The ambient temperature data [28].

2.2. Test System and Load Modelling

The IEEE 34 node test feeder has been used in this study as a base network. It consists of light and unbalanced loads, an inline transformer, two voltage regulators, and shunt capacitors [29]. The modified IEEE 34 with a PV connected to node 858 is shown in Figure 4.

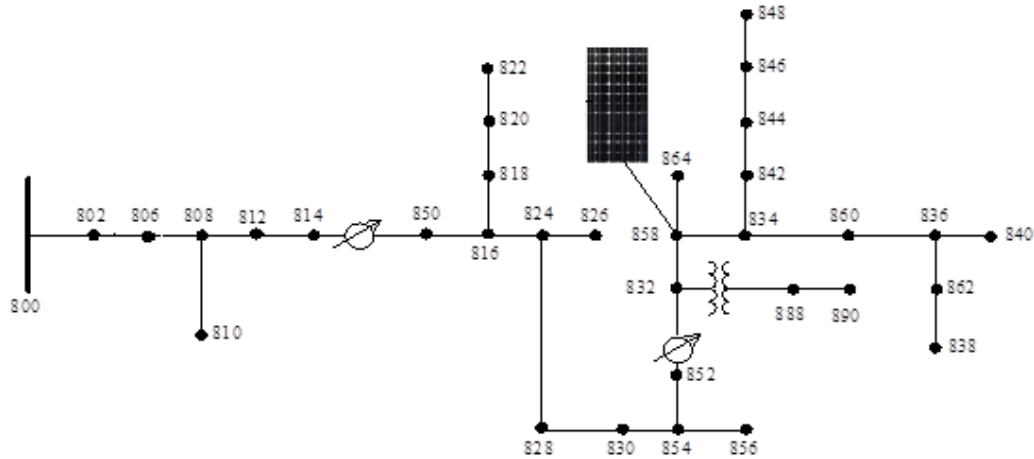


Figure 4. The modified IEEE 34 node feeder [29].

Load modelling has a significant impact on the results of the analysis performed. To accurately characterize the system, a ZIP model load has been used. ZIP stands for the three defined load types: constant impedance (Z), constant current (I), and constant power (P) [30]. The ZIP model considers the voltage dependency of loads. The ZIP coefficients for a residential customer used in this study are given in Table I.

Table 1. The residential ZIP coefficients [30].

Class	Zp	Ip	Pp	Zq	Iq	Pq
Residential	0.85	-1.12	1.27	10.96	-18.73	8.77

In order to precisely model the consumption behavior of network customers, a 10-minute interval of a residential load shape obtained from [31] has been used. The daily residential load curve is shown in Figure 5.

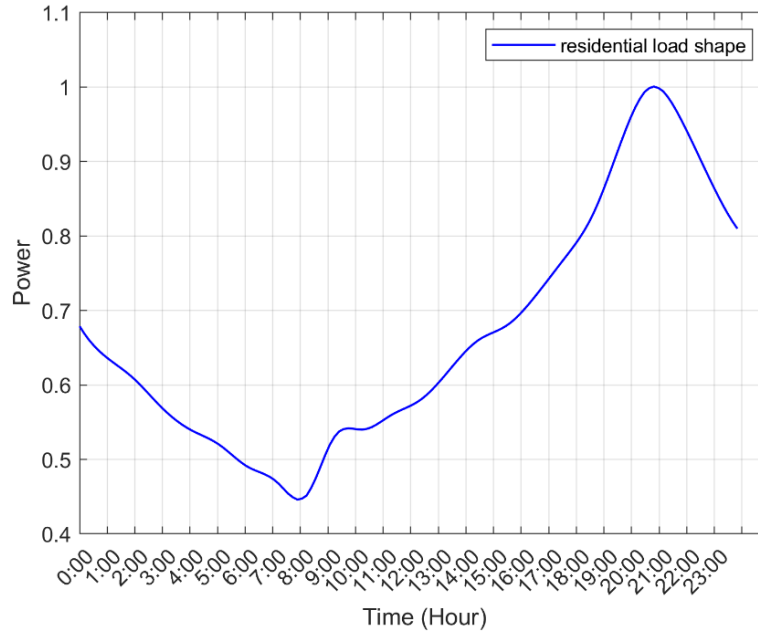


Figure 5. The 24-h load shape of residential customers [31].

2.3. PV Modeling in OpenDSS

The Open Distribution System Simulator (OpenDSS) is a powerful simulation tool for electrical distribution systems. It supports almost all steady state analyses commonly performed for utility distribution systems. The key advantage of OpenDSS is that it supports unbalanced multi-phase power flow analysis and distributed generation integration. In OpenDSS, the PV model consists of a PV panel and an inverter element with an ideal maximum power point (MPP) tracker. This model injects an active power (P_{out}) into the network. To calculate $P_{out}(t)$, the model requires the data of module/cell temperature, irradiance, inverter efficiency, and the rated power. The active power $P_{out}(t)$ injected into the grid is given in Equations (1) and (2).

$$P_{out}(t) = P(t) \times \text{eff}(P(t)) \quad (1)$$

$$P(t) = P_{mpp} \times \text{irradiance} \times \text{factor}(T(t)) \quad (2)$$

Where $P(t)$ is PV array power output, $P_{mpp}(1kW/m^2)$ is the rated power at the MPP, $\text{irrad}(t)$ is per unit irradiation value, $\text{factor}(T(t))$ is the Pmpp correction factor as a function of the temperature and $\text{eff}(P(t))$ is the inverter efficiency. The PV system has a P_{mpp} of 1000 kW and a power factor of 1 and is connected to node 858 of the IEEE 34 node test feeder.

2.4. Modeling of Cell Temperature

The cell temperature is affected by the local wind speed, ambient temperature, and irradiance on the plane of the array [7]. The OpenDSS uses the module temperature when modeling the PV element. However, the obtained temperature data is ambient temperature. Therefore, the cell/module temperature T_c is calculated using Equation (3) proposed by [7]. Equation (3) calculates the operating temperature for any mounting type and wind speeds higher than 0 m/s.

$$T_c = T_a + \omega \left(\frac{0.32}{8.91 + 2 \times V_f} \right) G_T \quad (3)$$

Where T_c is the cell/module temperature, T_a is the ambient temperature, ω is the mounting coefficient, V_f is the wind speed and G_T is the irradiance on the panel. In this study, two mounting types have been used namely, free standing and flat roof. The values of ω presented in Table II were obtained from [7].

Table 2. Values of mounting coefficient for two mounting types [7].

PV panel mounting type	ω
Free standing	1
Flat roof	1.2

3. SIMULATIONS AND RESULTS

As the study aims to demonstrate the impact of wind speed and mounting types on PV output, various scenarios are created. The same ambient temperature and irradiance are used for all case studies to evaluate the effect of wind speed and mounting type. The scenarios analyzed in this study are presented in Table III. The simulation scenarios are divided into seven case studies, as follows:

- Base Case: The simulation was conducted on IEEE 34 node test feeder using a residential ZIP load, and no PV connection to the network.
- Case A: The PV is connected to node 858 and simulated with high wind speed data and free standing mounting coefficient.
- Case B: The PV is connected to node 858 and simulated with moderate wind speed data and free standing mounting coefficient.
- Case C: The PV is connected to node 858 and simulated with low wind speed data and free standing mounting coefficient.
- Case D: The PV is connected to node 858 and simulated with high wind speed data and flat roof mounting coefficient.
- Case E: The PV is connected to node 858 and simulated with moderate wind speed data and flat roof mounting coefficient.
- Case F: The PV is connected to node 858 and simulated with low wind speed data and flat roof mounting coefficient.

Table 3. Case studies.

Wind speed	Mounting type	
	Free standing	Flat roof
High	Case A	Case D
Moderate	Case B	Case E
Low	Case C	Case F

The simulation results of substation demand, PV panel output, load consumption, and the total power losses over a 24-hour period for all case studies are given in Table IV. The results show that in the free standing mounting case studies, Case A had the highest power production at the highest wind speed, followed by Case B and Case C. The PV panel generated 2.21% more power in the scenario simulated with the high wind speed data set (Case 1) than in the scenario simulated with the low wind speed data set (Case C). Also, relative to the Base Case, the substation power demand reduced by 12.44 %, 12.33%, and 12.17% in Case A, Case B, and Case C respectively. When the active power at node 858 is compared to the power measured at the PV panel output, it was observed a 69 kWh energy loss due to the inverter. The highest loss reduction was achieved by 12.66% in the free standing high wind speed scenario (Case A).

Table 4. The simulation results for all case studies.

	Substation Demand (kWh)	Panel Output (kWh)	Energy at Node 858 (kWh)	Load Consumption (kWh)	Network Losses (kWh)
Base case	31502	-	-	28478	3025
Case A	27582	3612	3543	28485	2640
Case B	27617	3578	3509	28484	2642
Case C	27666	3532	3463	28483	2645
Case D	27600	3595	3526	28484	2641
Case E	27643	3555	3486	28484	2644
Case F	27702	3500	3431	28485	2648

Using the flat roof mounting coefficient for the panel temperature, Case D had the highest power output of 3595 kWh due to the high wind speed. Conversely, Case E and Case F had lower power outputs of 3555 kWh and 3500 kWh respectively. It is worth noting that the PV panel power output was 2.64% higher in the case with the high wind speed (Case D) than in the case with the law wind speed (Case F). This demonstrates the impact of wind speed on PV production since the wind cools the cell temperature and thus reduces the power loss due to temperature. In addition, as the power

produced by the PV module increased, the substation power demand decreased by 12.38%, 12.25%, and 12.06% for Case D, Case E, and Case F, respectively, compared to Base Case.

The results show that the mounting type affects the PV power output, as the free standing mounting configuration produced more power than the flat roof mounting configuration by 0.47%, 0.64%, and 0.9% for high, moderate, and low wind speed conditions, respectively. This is due to the higher mounting coefficient of the flat roof than that of free standing (see Table II), which results in a higher cell temperature as shown in equation 3. The daily PV panel output for Case A, Case B, and Case C is presented in Figure 6, while Figure 7 displays the daily PV power output for Case D, Case E, and Case F.

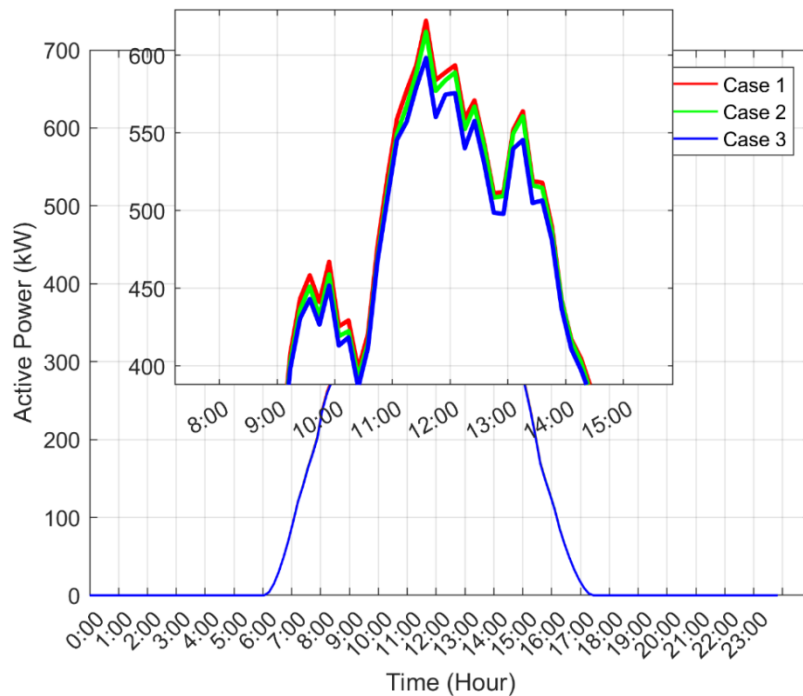


Figure 6. The 24-h PV panel output for Case A, Case B, and Case C.

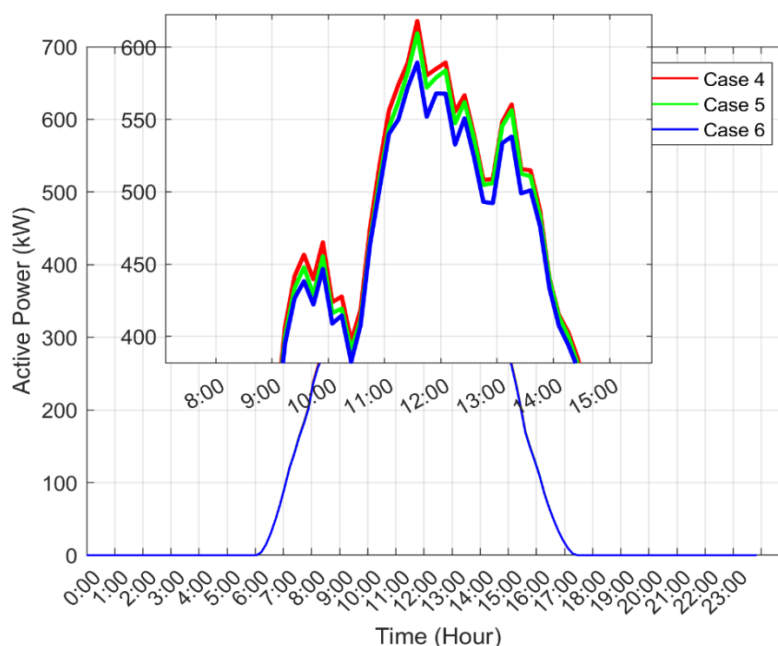


Figure 7. The 24-h PV panel output for Case D, Case E, and Case F.

4. CONCLUSION

This paper has investigated the effects of wind speed and mounting type on the output performance of photovoltaic modules in an unbalanced distribution network. The analyses of the PV system was conducted on the unbalanced IEEE 34 node feeder. No load consists entirely of constant power, constant impedance, or constant current. Therefore, in order to represent the actual system loads, the loads in the IEEE 34 distribution test system are modeled as ZIP load model, which is a voltage dependent load model. In addition, a residential ZIP coefficient and residential load curve were used. For the three-phase unbalanced power flow solution, the OpenDSS software, which is open source, was used. The PV conversion process is strongly influenced by the operating temperature, which affects the PV power output and the efficiency in a nearly linear way, making them decrease with it. A simple equation (Eq. (3)) that uses three environmental variables (solar irradiance, wind speed, and ambient temperature) and a dimensionless mounting parameter that indicates the integration level of a specific installation was applied to estimate the PV operating temperature. Two mounting configurations (free standing and flat roof) and three wind speed data namely, high, moderate, and low have been used in the present study. To assess the effect of the wind speed alone on PV power output, the same ambient temperature and irradiance have been used for each case study. The simulated scenarios show that the substation demand and network losses decreased when the PV was integrated into the distribution network. The highest loss reduction was achieved by 12.66% in the free standing high wind speed scenario (Case A). The results also indicate that module temperature was influenced by wind speed. The PV output power was higher for high wind speed cases than for low wind speed

for both mounting types. In the case study simulated with the high wind speed data set (Case 1), the PV panel generated 2.21% more power than in the scenario simulated with the low wind speed data set (Case C). This is because the wind cools the cell temperature and consequently reduces the PV power loss due to temperature. Moreover, the present study also assessed the impact of PV mounting configuration on PV performance. Under high, medium, and low wind speed conditions, the PV module generated 0.47%, 0.64%, and 0.9% more energy in free standing mounting than in flat roof mounting, respectively. The accurate selection of mounting type for solar system projects is crucial for the overall production, efficiency, and lifespan of solar panels. Since it is a costly investment, the selection of mounting systems should not be overlooked as a minor consideration. It is concluded that it would be useful to take wind speed into account when assessing PV energy production, particularly in the areas with higher wind speeds.

ACKNOWLEDGEMENT

This research has received no external funding.

REFERENCE

- [1] Petroleum, B. (2022). BP Statistical Review of World Energy, (71), 60.
- [2] Victoria, M., Haegel, N., Peters, I. M., Sinton, R., Jäger-Waldau, A., del Canizo, C., Breyer, C., Stocks, M., Blakers, A., Kaizuka, I., Komoto, K. (2021). Solar photovoltaics is ready to power a sustainable future. *Joule*, 5(5), 1041-1056.
- [3] Dash, P. K., Gupta, N. C. (2015). Effect of temperature on power output from different commercially available photovoltaic modules. *International Journal of Engineering Research and Applications*, 5(1), 148-151.
- [4] Dubey, S., Sarvaiya, J. N., Seshadri, B. (2013). Temperature dependent photovoltaic (PV) efficiency and its effect on PV production in the world—a review. *Energy procedia*, 33, 311-321.
- [5] Rahman, M. M., Hasanuzzaman, M., Rahim, N. A. (2015). Effects of various parameters on PV-module power and efficiency. *Energy Conversion and Management*, 103, 348-358.
- [6] Kawajiri, K., Oozeki, T., Genchi, Y. (2011). Effect of temperature on PV potential in the world. *Environmental Science & Technology*, 45(20), 9030-9035.
- [7] Skoplaki, E., Boudouvis, A. G., Palyvos, J. A. (2008). A simple correlation for the operating temperature of photovoltaic modules of arbitrary mounting. *Solar energy materials and solar cells*, 92(11), 1393-1402.
- [8] Griffith, J. S., Rathod, M. S., Paslaski, J. (1981). Some tests of flat plate photovoltaic module cell temperatures in simulated field conditions. In *15th Photovoltaic Specialists Conference*, 822-830.

- [9] Al-Bashir, A., Al-Dweri, M., Al-Ghandoor, A., Hammad, B., Al-Kouz, W. (2019). Analysis of effects of solar irradiance, cell temperature and wind speed on photovoltaic systems performance.
- [10] Goverde, H., Goossens, D., Govaerts, J., Dubey, V., Catthoor, F., Baert, K., Poortmans, J. Driesen, J., (2015). Spatial and temporal analysis of wind effects on PV module temperature and performance. *Sustainable Energy Technologies and Assessments*, 11, 36-41.
- [11] Tahir, Z.R., Kanwal, A., Asim, M., Bilal, M., Abdullah, M., Saleem, S., Mujtaba, M.A., Veza, I., Mousa, M. Kalam, M.A., (2022). Effect of Temperature and Wind Speed on Efficiency of Five Photovoltaic Module Technologies for Different Climatic Zones. *Sustainability*, 14(23), 15810.
- [12] Gökmen, N., Hu, W., Hou, P., Chen, Z., Sera, D., Spataru, S. (2016). Investigation of wind speed cooling effect on PV panels in windy locations. *Renewable Energy*, 90, 283-290.
- [13] Schwingshackl, C., Petitta, M., Wagner, J.E., Belluardo, G., Moser, D., Castelli, M., Zebisch, M. Tetzlaff, A. (2013). Wind effect on PV module temperature: Analysis of different techniques for an accurate estimation. *Energy Procedia*, 40, 77-86.
- [14] Kaplani, E., Kaplanis, S. (2014). Thermal modelling and experimental assessment of the dependence of PV module temperature on wind velocity and direction, module orientation and inclination. *Solar Energy*, 107, 443-460.
- [15] Said, S. A., Al-Aqeeli, N., Walwil, H. M. (2015). The potential of using textured and anti-reflective coated glasses in minimizing dust fouling. *Solar Energy*, 113, 295-302.
- [16] Hasan, K., Yousuf, S. B., Tushar, M. S. H. K., Das, B. K., Das, P., Islam, M. S. (2022). Effects of different environmental and operational factors on the PV performance: A comprehensive review. *Energy Science & Engineering*, 10(2), 656-675.
- [17] Koehl, M., Heck, M., Wiesmeier, S., Wirth, J. (2011). Modeling of the nominal operating cell temperature based on outdoor weathering. *Solar Energy Materials and Solar Cells*, 95(7), 1638-1646.
- [18] Mattei, M., Notton, G., Cristofari, C., Muselli, M., Poggi, P. (2006). Calculation of the polycrystalline PV module temperature using a simple method of energy balance. *Renewable energy*, 31(4), 553-567.
- [19] Kurtz, S., Whitfield, K., TamizhMani, G., Koehl, M., Miller, D., Joyce, J., Wohlgemuth, J., Bosco, N., Kempe, M. Zgonena, T. (2011). Evaluation of high- temperature exposure of photovoltaic modules. *Progress in photovoltaics: Research and applications*, 19(8), 954-965.
- [20] Kaplanis, S., Kaplani, E., Kaldellis, J. K. (2022). PV temperature and performance prediction in free-standing, BIPV and BAPV incorporating the effect of temperature and inclination on the heat transfer coefficients and the impact of wind, efficiency and ageing. *Renewable Energy*, 181,

235-249.

- [21] Wijeratne, W. P. U., Yang, R. J., Too, E., Wakefield, R. (2019). Design and development of distributed solar PV systems: Do the current tools work?. *Sustainable cities and society*, 45, 553-578.
- [22] Stapleton, G., Neill, S. (2012). *Grid-connected solar electric systems: the earthscan expert handbook for planning, design and installation*. Routledge..
- [23] Awan, A. B., Alghassab, M., Zubair, M., Bhatti, A. R., Uzair, M., Abbas, G. (2020). Comparative analysis of ground-mounted vs. rooftop photovoltaic systems optimized for interrow distance between parallel arrays. *Energies*, 13(14), 3639.
- [24] Cura, D., Yilmaz, M., Koten, H., Senthilraja, S., Awad, M. M. (2022). Evaluation of the technical and economic aspects of solar photovoltaic plants under different climate conditions and feed-in tariff. *Sustainable Cities and Society*, 80, 103804.
- [25] Tamoor, M., Habib, S., Bhatti, A. R., Butt, A. D., Awan, A. B., Ahmed, E. M. (2022). Designing and energy estimation of photovoltaic energy generation system and prediction of plant performance with the variation of tilt angle and interrow spacing. *Sustainability*, 14(2), 627.
- [26] Kazim, W. (2015). Performance of PV Panel Mounting Structure for Flat Surface and Roof-Top in UAE Climatic Conditions. *Int. J. of Sustainable Water & Environmental Systems*, 7(1), 37-40.
- [27] Dugan, R. C., McDermott, T. E. (2011). An open source platform for collaborating on smart grid research. 2011 IEEE power and energy society general meeting, 1-7.
- [28] World Bank. World Bank via ENERGYDATA.info under a project funded by the Energy Sector Management Assistance Program (ESMAP). Retrieved march 9, 2023, from <https://energydata.info/dataset/pakistan-solar-radiation-measurement-data>.
- [29] Kerting, W. H. (1991). Radial distribution test feeders IEEE distribution planning working group report. *IEEE Trans. Power Syst*, 6(3), 975-985.
- [30] Diaz-Aguiló, M., Sandraz, J., Macwan, R., De Leon, F., Czarkowski, D., Comack, C., Wang, D. (2013). Field-validated load model for the analysis of CVR in distribution secondary networks: Energy conservation. *IEEE Transactions on Power Delivery*, 28(4), 2428-2436.
- [31] Emiroglu, S., Uyaroglu, Y., Ozdemir, G. (2017). Distributed Reactive Power Control based Conservation Voltage Reduction in Active Distribution Systems. *Advances in Electrical & Computer Engineering*, 17(4), 99-106.



RESEARCH ARTICLE

**DETECTION AND CHARACTERIZATION OF SOME GLAZE FAULTS ENCOUNTERED
IN SANITARYWARES**

Eray ÇAŞIN¹, Nihal DERİN COŞKUN^{2*}, C. Eren IŞIK³

¹Nevtec Ar-Ge, Design Logistics Inc., Çorum, eraycasin@nevtec.com.tr, ORCID: 0000-0003-3698-2248

^{2*}Ordu University, Faculty of Fine Arts, Dept. Of Ceramics and Glass, Ordu, nihalderincoskun@odu.edu.tr,
ORCID: 0000-0002-3024-9443

³Kütahya Dumlupınar University, Faculty of Fine Arts, Kütahya, eren.isik@dpu.edu.tr,
ORCID: 0000-0002-1129-2497

Receive Date: 17.02.2023

Accepted Date: 20.08.2023

ABSTRACT

The use of suitable glaze compositions, which enable ceramic sanitaryware (such as sink, toilet bowl, toilet bowl, etc.) to have better hygienic, aesthetic and technical properties, is of great importance as in other ceramic products. Glaze compositions, which provide durability to sanitaryware materials, reduce impact resistance and give ceramic material a hygienic appearance, are produced as ~97% white color depending on the preferences of the consumers, therefore, surface defects attract more attention in glazing and post-glazing process applications. When faults occurred during the different stages of manufacture detected on the final product, failure to detect faults on the final product by passing many production stages poses a problem in terms of intervention in the process. Faults that occur during glaze preparation are important in terms of cost. Since it is a stage in which many economic evaluations have been made in production, eliminating the faults caused from glaze preparation prevents further financial loss.

In this study, the appearance of the faults in the sanitaryware items and the change in their regions (occured as a result of the oils contaminations from the machinery and components used in the preparation of glaze, the pipes of the tanks used in the glaze transport tanks and the glaze transfer or the impurities contaminated from the environment, the splashing of the impurities by the colored glazes in the glazing cabinets etc.) were characterized by means of SEM (Scanning Electron Microscopy), XRF (X-ray fluorescence spectrometry), XRD (X-Ray Diffractometry) and color measurement (L a* b*) analyses. According to the data derived from the final defected products, the faulty products were imitated by using the same components and methods on the plates under the laboratory conditions. Finally, the solutions for the problems were determined on the basis of faulty products obtained in the laboratory.

Keywords: *Glaze Faults, Sanitaryware, Characterization*

1. INTRODUCTION

The glaze covering the surfaces of ceramic products is among the main elements of ceramic production in terms of its visual effect on ceramic products, as well as in terms of protecting the product and ensuring its use for many years [1,2]. Moreover, since it is easy to clean and comes into contact with water, glaze becomes a more important production step in vitrified products with low water absorption (<1%) [2,3]. When the studies on sanitaryware production are examined in the literature, considering the problems experienced in the sector due to raw material supply, it is important to make seger calculations of different regional raw materials, to add them to the recipe or to reduce the ratio of high-cost raw materials in the recipe and to substitute alternative raw materials [4,5]. In addition, the precursor materials used in the glaze composition affect sintering temperature, microstructure, crystal development, energy costs, gas emissions and ultimately the effects on the final product properties [6,7]. However, the problems encountered in daily production in the factories currently working in the sector are solved by the R&D units, but these data remain individually within the industry. This study, unlike the literature, aims to create original and sectoral data in that it includes the examination of the problems encountered in production at the laboratory scale. As seen in Figure 1, since the sanitaryware products coming out of the kiln are large in size and the number of production is less than other ceramic products (such as porcelain, tile, etc.); therefore, the cost of the faults occurring in their production is relatively higher. Especially, it is more difficult to repair for the faults taking place in the products after firing, and this fault rate makes it as a waste product, because it disrupts the aesthetic and/or structure in use [8].



Figure 1. Kiln outlets of vitrified products [4].

In 2020, it is reported that in Italy, one of the important prominent ceramics manufacturers, the work done to reduce the costs by reducing the mass of the products produced in the industry has still not reached an adequate level [8,9]. The glaze, which is the most important factor in ensuring hygiene in such costly products, becomes even more important. While glazes are produced primarily from SiO₂, alkali metal oxides (Na₂O, K₂O, etc.), stabilizer alkaline earth metal oxides (CaO, BaO, MgO etc.),

zircon silicate, opacifiers such as zircon oxide and crystallizing raw materials such as ZnO; it is a production stage where parameters such as compatibility with the body, melting and surface expansion are important [10]. When the ceramic defects occurring after glaze firing are examined, they can be grouped mainly under general headings such as cracking, pinholes, color changes, deformation, consolidation, pits or bumpy surfaces, spalling, etc. [11,12]. However, it has stages that cannot be produced by machine due to its very intricate and large size. This increases the manual processes in sanitaryware, and even requires manual touches in machine-made processes. These processes let the occurrence of pollution caused by external factors apart from general faults. Examples of some vitrified products are given in Figure 2.

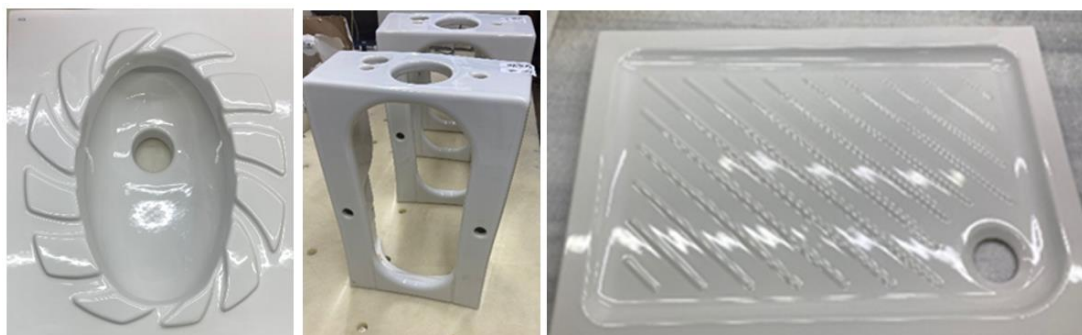


Figure 2. Some vitrified products.

In the study, after the detection of defects, which are generally included in the concept of pollution, but whose exact cause is unknown, these faults are imitated on a laboratory basis and the stages that need to be controlled in production in this direction are examined. The data obtained through the study are an addition to the main glaze, raw materials, precursors and energy etc. problems studies in the literature also it will contribute to production problems in terms of solution methods in industry.

2. METHOD

In the study, slip and glaze of the product called as vitreous china (VC), which is used in production in Isvea Sanitaryware factories, was used. The sources of faults in production line have been identified. The faulted samples obtained by applying them on specimen of 10x10 cm under the laboratory conditions were characterized. Scanning electron microscope (SEM) and chemical composition analyses (EDX) images were obtained with Zeiss Supra 50VP Brand device. The faults detected at this stage are classified as follows.

2.1. Faults Originated From Glaze Preparation

2.1.1. Tank pipe end

In order for the glaze suspension prepared in glaze preparation to be used in the process, it must be transported via tanks [3]. Although the inner parts of the tanks are made of plastic material, metallic pipes made of chrome-plated steel materials are generally used to transfer the glaze to the robot or

glazing cabinets. The inner parts of these pipes are caused by the friction of the glaze suspension, the upper parts are worn by the removal and installation of the clamps, and the abraded metallic particles mix into the glaze and cause staining on the glaze. The tank pipe end and its stain fault are given in Figure 3.

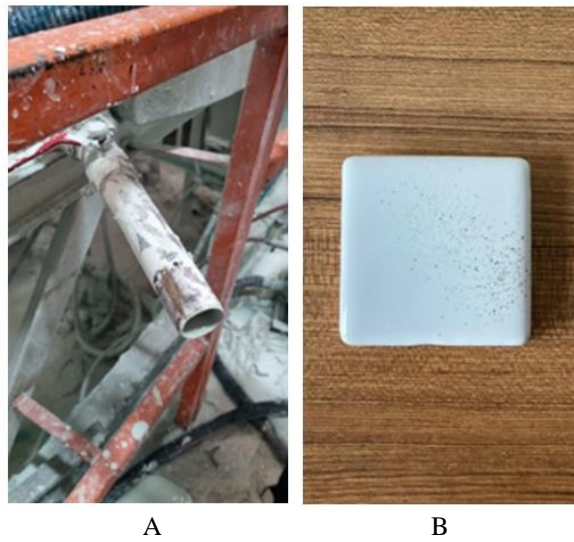


Figure 3. Tank pipe end (A) and faults due to tank pipe end (B).

2.1.2. Glaze preparation mixers

There are mixers used in glaze preparation and mixing glazes. These mixers are generally used in rheological adjustments of glaze suspension. Meanwhile, dried machine oil contaminations in the chain and bearing parts of these mixers, which have up and down moving parts, mix into the glaze. The glaze preparation mixer and its stain defects are given in Figure 4.

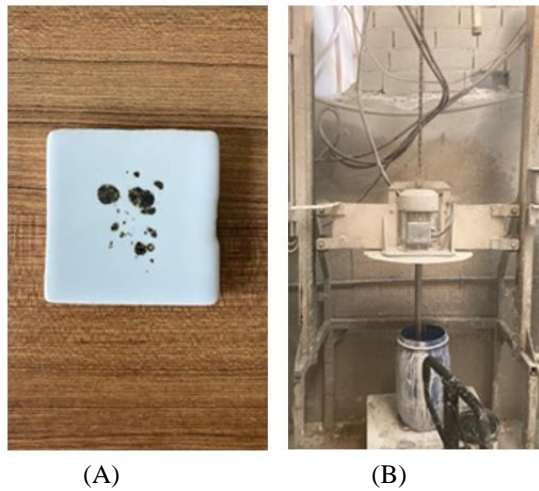


Figure 4. Faults caused by glaze mixers (A) and glaze preparation mixer (B).

2.1.3. Colored glaze splashing

In the recent years, many colored sanitaryware products have been manufactured by ceramic companies. Although these production rates do not usually exceed 2%, there are some production difficulties in manufacturing them. In cases where the colored glaze needs to be changed, the system is completely washed with water. However, if the washing is not done properly, the glazes of different colors remaining in the system smear on the other colors and cause staining defects. Colored glaze splash stain defects is given in Figure 5.



Figure 5. Faults due to splash of colored glaze.

2.1.4. Funnel for raw material addition

The raw materials that make up the glaze suspension are loaded into the mill from the weighing silo. Such faults can be prevented by using automatic systems while dosing to the mill. However, some glaze suspensions cannot be made with an automatic system in line with glaze consumption. The reason for this is that the glaze suspension cannot be passed through the system as tonnage or some raw materials that are not in the system are thrown manually. Some raw materials, which are proportionally less in glaze suspensions, are dosed manually. The raw material funnel, which is placed in the mouth of the mill when the workers do the dosing manually, is a metallic material made throughout the enterprise. Abrasions occur over time due to the contact of the metallic material with the raw materials, and these worn parts cause stain defects. The raw material chamber (funnel) and its stains faults are given in Figure 6.



Figure 6. Hopper for raw material addition.

2.1.5. Glaze preparation ceiling, glazing ceiling coating materials

Insulations are made in some places so that the production units are less affected by the weather conditions in summer and winter months. The materials from which these insulations are made are porous materials such as rock wool. Ceramic powders in the process can also accumulate in such porous materials and cause stains such as spilling after a long time. In addition, when the ceilings are not properly insulated or when cleaning is done on an upper floor, the water leaking from the gaps between the metal plates or the concrete flooring causes the metal parts to rust and the paint on the metal to spill. The images of the rust defects caused by the ceiling coating material of the glaze preparation line and glazing and the moisture on the ceiling are given in Figure 7.

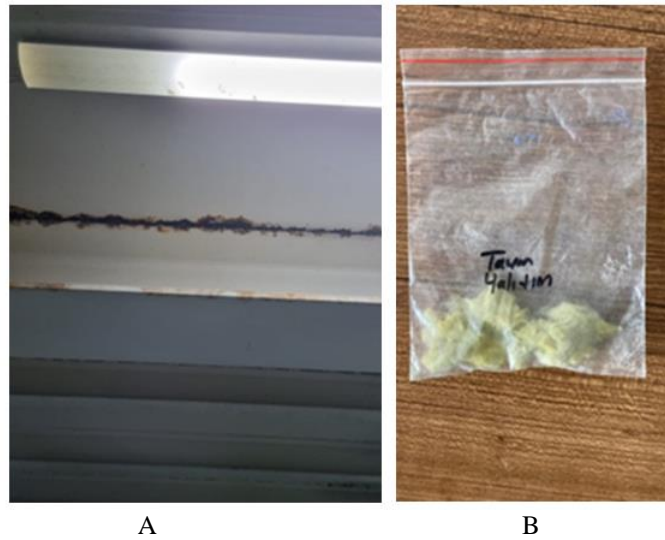


Figure 7. Ceiling of glaze preparation (A) and defects originated from glaze ceiling coating materials (B).

3. RESULTS AND DISCUSSION

3.1. SEM/EDX Analysis of Tank Pipe End Faults

The pipes of the tanks are made of metallic materials. Since these materials are iron in their content, it is seen that there are iron stains when these materials are worn. When SEM analyses are examined, it is observed that a layered structure is formed in a hollow form in the region of iron stains. As seen in Figures 8 and 9, Fe^{+2} in the structure causes a regional deterioration by damaging the area around it as a result of melting with heat, as well as the place where it is poured. The iron region formed in the crystal phase disrupts the crystal formation in the structure. In the regional SEM analyses, it was determined that there are Fe_2O_3 phases on the crystal structure.

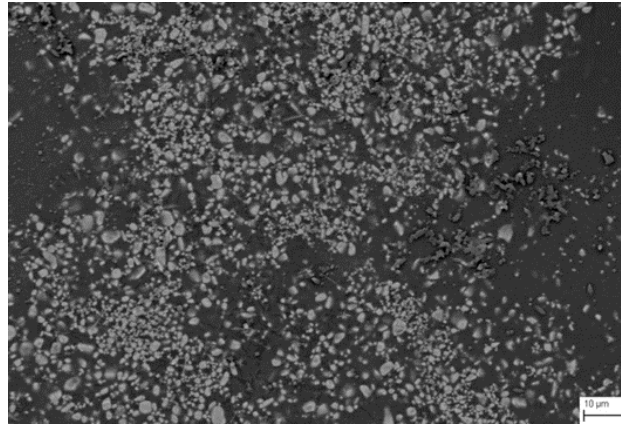


Figure 8. SEM image of the faults caused by the end of the glaze tank pipe.

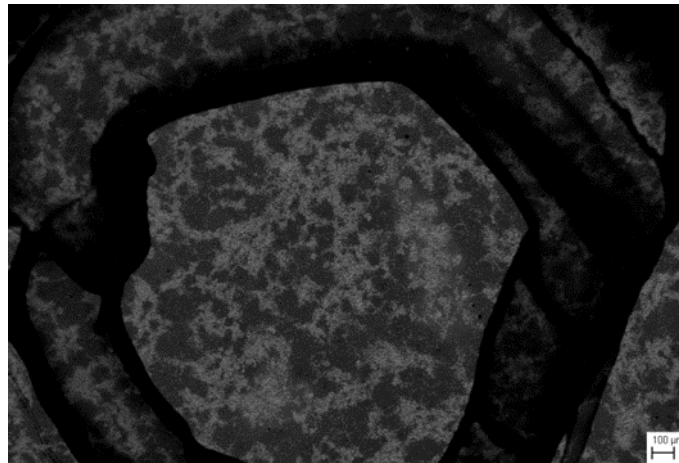


Figure 9. Sem image of iron phase fault caused by glaze tank pipe end defect.

According to the EDX analyses, the values in the Fe_2O_3 are compatible the SEM analyses (Table 1). The zircon-based calcium alumina silicate structure, which forms the basic structure of the glaze, defines the formation of the glaze in all EDX studies. Apart from this, it is seen that the pieces that can break off from the pipe end are simulated in the experimental studies where the Fe_2O_3 ratio is relatively high. These defects cause brown iron stains after firing [11,13].

Table 1. The results of the SEM/ EDX analysis for Glaze Tank pipe end defects.

	MgO	Al ₂ O ₃	CaO	Fe ₂ O ₃	SiO ₂	Na ₂ O	ZrO ₂	Total
1	2.87	8.96	14.93	10.83	57.71	4.69	0	99.99
2	0	5.01	4.87	3.83	41.2	2.68	42.41	100

3	0	4.84	7.37	6.42	41.24	3.14	36.98	99.99
4	1.26	5.46	6.75	7.72	44.9	3.02	30.89	100
5	2.08	7.37	6.64	0	55.74	2.31	25.86	100

3.2. SEM / EDX Analysis of Glaze Preparation Mixers Based Faults

Since the need for production is continuous, glaze preparation tanks are changed frequently depending on the product manufactured. Glaze tanks, which are changed due to rheological changes, are mixed in production mixers after adding binders. In the meantime, impurities are mixed with the structure, and the staining that occurs as a result of this, as it is organic based, removes many components from the structure at $\sim 450^{\circ}\text{C}$, thus causing black or dark staining in the structure. Although the mixer ends are made of chrome-plated steel material, the hard particles in the glaze (such as quartz and alumina, etc.) break the coating on the mixer blades and cause such staining. As seen in Figures 10 and 11, the particles are disseminated in the whole sample [14].

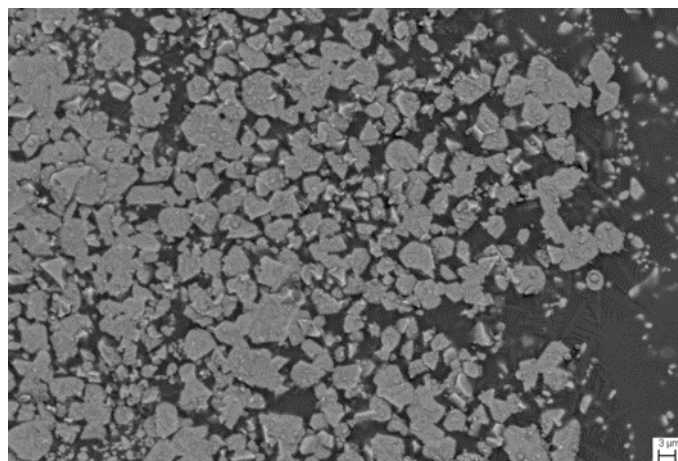


Figure 10. SEM image of the faults caused by the glaze mixer.

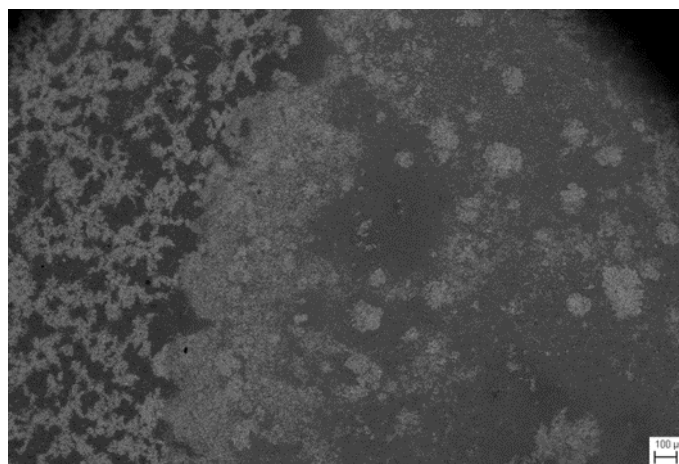


Figure 11. SEM image of the faults caused by the glaze mixer.

As seen in the EDX analysis in Table 2, the stains transmitted from the bearing in the glaze preparation mixers are mainly chromium and iron content. Particularly iron-bearing particles were found. It is seen that the defect color is black and brown. As seen in Table 2, these rates increase due to the thinness of the chrome plating and the fact that the material at the bottom of the chromium plating consists of ferrous metallics.

Table 2. Sem/edx results of defects originating from glaze mixers.

	MgO	Al ₂ O ₃	CaO	Cr ₂ O ₃	Fe ₂ O ₃	ZnO	SiO ₂	NiO	Na ₂ O	ZrO ₂	Total
1	8.04	4.12	0.95	1.58	64.29	21.03	0	0	0	0	100.01
2	12.36	6.9	3.21	1.42	50.01	17.44	8.65	0	0	0	99.99
3	7.07	0	0	1.53	66.47	24.2	0	0.73	0	0	100
4	1.68	6.35	8.54	0	4.36	1.88	46.16	0	2.78	28.25	100
5	0.86	7.85	5.47	0	0	1.38	59.89	0	4.11	20.44	100

3.3 SEM/EDX Analysis of Color Glaze based Splashes

Glaze spatter formation is the faults that may occur due to not washing the pumps used in the transfer of glazes in the process to the airbrush (pistole). Although the glazing colors are separated according to the production planning, sometimes colored and white glazes can be glazed in the same cabinets. In these cases, pumps and cabinets are washed. However, the particles remaining on the edges of the pumps or cabinets may appear on the glaze surfaces as a stain defect with the effect of compressed air. When the SEM analysis in Figures 12 and 13 are examined, it is seen that the impurities are in light gray tones and with less density compared to the SEM's of iron-bearing structures. It is seen that some pigments melt in the body, reducing the color formation in the glaze layer and there are small regional densities.¹⁵

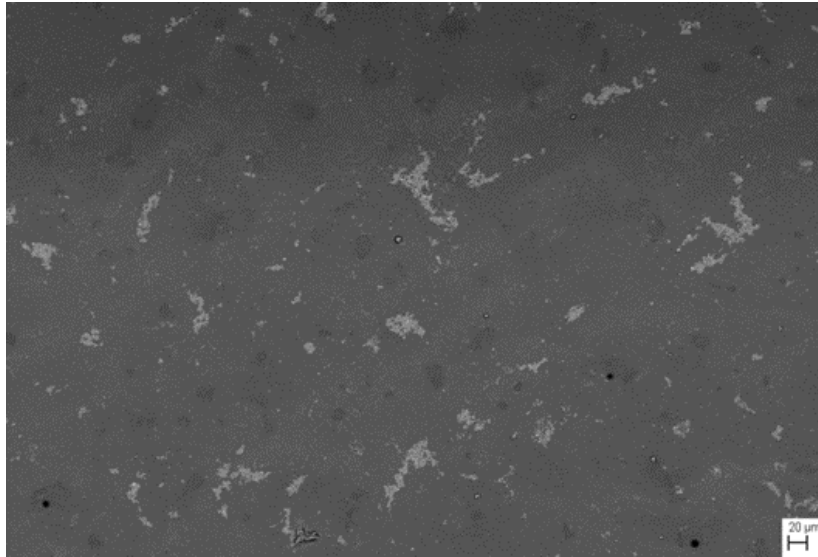


Figure 12. Sem image of the defects due to colored glaze splash.

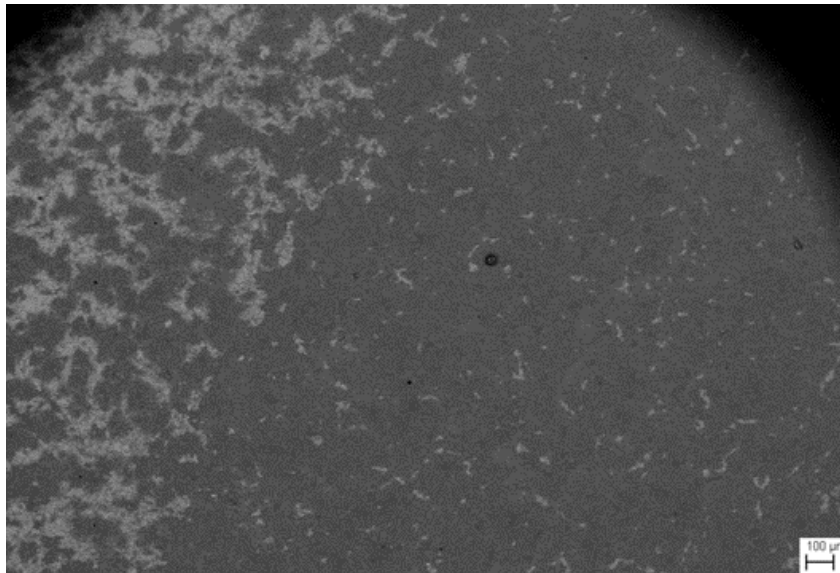


Figure 13. Sem image of the defects due to colored glaze splash.

It has been observed that the dulled glazes come in the same color as in the stained areas. Due to the dull of glazes, Al ratios are high. It was observed that the structure of glossy glazes was targeted in the

regions with high zircon ratio, while the alumina ratios were high and the matte glazes stained when the faulty regions were targeted with a low ratio (Table 3).

Table 3. Sem/edx results of defects caused by colored glaze splash.

	MgO	Al ₂ O ₃	CaO	ZnO	SiO ₂	Na ₂ O	K ₂ O	ZrO ₂	Total
1	3.5	6.78	5.32	0	42.92	3.15	1.69	36.64	100
2	2.72	14.72	5.29	0	70.53	4.41	2.23	0	99.9
3	2.5	14.19	5.09	2.1	67.37	4.39	2.65	1.7	99.99
4	0.82	9.25	5.85	1.16	61.6	3.51	0.7	17.11	100

3.3. SEM/EDX Analysis of Raw Material Adding Funnel Sourced Defects

Since this tool is made of metallic materials in the operating workshops, iron stains have been observed. The fact that it is less than the other raw materials given in the study causes the glassy phase to be observed predominantly in the SEM images, while the impurities can be clearly examined in dark black in Figure 15. It has been observed that there are iron stains in the light gray areas, micro pinhole defects occur in the SEM images of these spots, the iron particles formed in these areas are separated from the environment by burning out and they leave stains in the structure together with the pinhole defect. In Figures 14 and 15, SEM images of the defect originating from the raw material chamber are given.

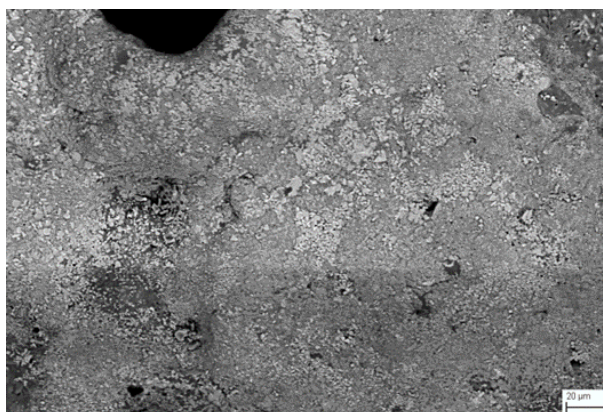


Figure 14. Sem image of the defect originated from the raw material hopper.

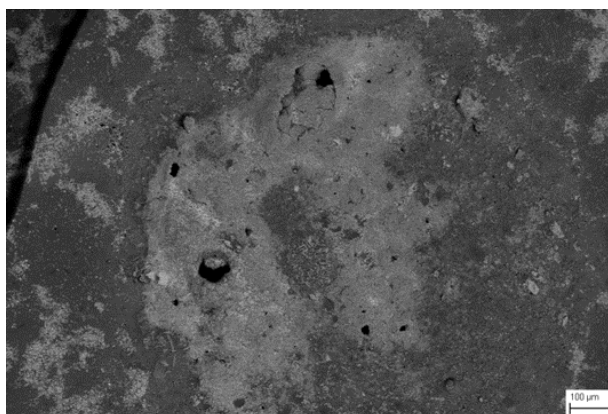


Figure 15. SEM image of the defect originated from the raw material hopper.

Since the iron rate is determined by the EDX analysis done for the black spots, the Fe_2O_3 's rate can increase up to ~62% and these results are given in Table 4. The results obtained from the spot EDX analysis done for the iron points support this determination. The deterioration of the glassy structure in these regions is associated with relatively low SiO_2 ratios.

Table 4. SEM/EDX results of raw material hopper defects (% by weigh).

	MgO	Al ₂ O ₃	CaO	Cr ₂ O ₃	Fe ₂ O ₃	ZnO	SiO ₂	Na ₂ O	K ₂ O	ZrO ₂	TiO ₂	Total
1	5.66	15.74	4.16	0	45	7.32	18.74	0	0	0	3.38	100
2	6.33	10.28	0	1	62.39	4.39	8.67	0	0	0	6.94	100
3	0	33.23	0	0	44.23	0	22.54	0	0	0	0	100
4	6.04	21.68	2.2	0.33	29.36	9.16	26.83	0	0.57	0	3.84	100.01
5	4.9	22.04	4.35	0	21.14	6.36	36.62	0	0	0	4.59	100
6	2.8	7.37	6.64	0	0	0	55.74	2.31	0	25.86	0	100

3.4. SEM /EDX Analysis of faults originated Glaze Preparation Ceiling and Glaze Ceiling Coating Materials

Ece Banyo factory operates as a two-story production facility. Glaze preparation and glazing sections are located at the bottom of the drying kilns. Since this platform is metal, stone wool materials are used in the interstices of the ceiling. These materials can deform over time with the effect of temperature and humidity, and they can break off from the structure and mix into the glaze tanks. It was determined that the materials used for insulation, other than iron, were poured in the particles poured from the ceiling due to the changes in ambient temperature, and Ca ions were high in these materials. In SEM analyses, this ratio is observed to be scattered regionally. Compared to the SEM analyses of the previous faults, it is observed that there is a more homogeneous structure and dark colored glaze structures are deteriorated, although it is not as effective as iron in the glassy phase. SEM images of the defects caused by glaze preparation ceiling and ceiling insulation materials are given in Figures 16 and 17.

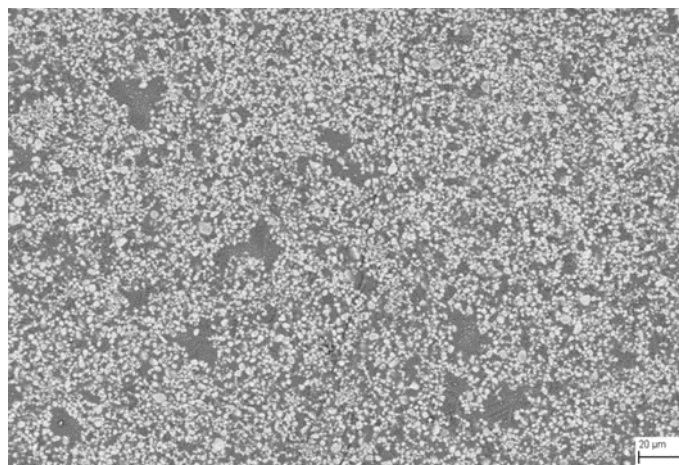


Figure 16. Sem image of defects caused by glaze preparation ceiling insulation material.

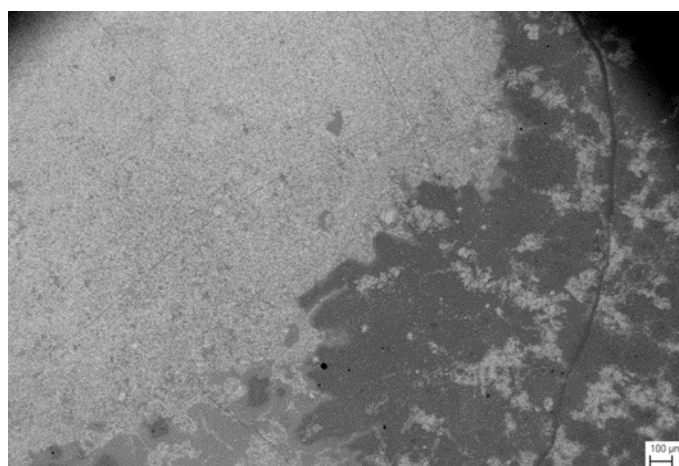


Figure 17. Sem image of defects caused by glaze preparation ceiling insulation material.

The fact that CaO in the EDX analyses varies between ~22% and 3% in the structure shows that this is due to different spills. The SiO₂ ratio, which indicates the glassy phase, also varies due to the mixed material, and this change can be examined proportionally in both the impurities and the main building raw materials in Table 5.

Table 5. Sem/edx results of the defects caused by glaze preparation ceiling insulation material (% by weight).

	MgO	Al ₂ O ₃	CaO	Fe ₂ O ₃	ZnO	SiO ₂	Na ₂ O	K ₂ O	ZrO ₂	Total
1	0	9.66	22.11	8.04	0	55.32	4.88	0	0	100.01
2	0	0	2.85	0	0	34.56	0	0	62.59	100
3	0.99	4.92	9.46	5.84	0	38.53	2.21	0	38.06	100.01
4	2.28	8.97	16.23	9.64	0.83	52.46	5.48	0.35	3.77	100.01
5	2.08	7.37	6.64	0	0	55.74	2.31	0	25.86	100

3.5. XRD Analysis

As seen from the XRD analyses below, the analyses of the samples listed as 3.1-3.5 from bottom to top show that the quartz peak is seen apart from the defects caused by the ceiling covering materials, but the structure is deteriorated due to the Zr content of the ceiling material. XRD analysis are given in Figure 18.

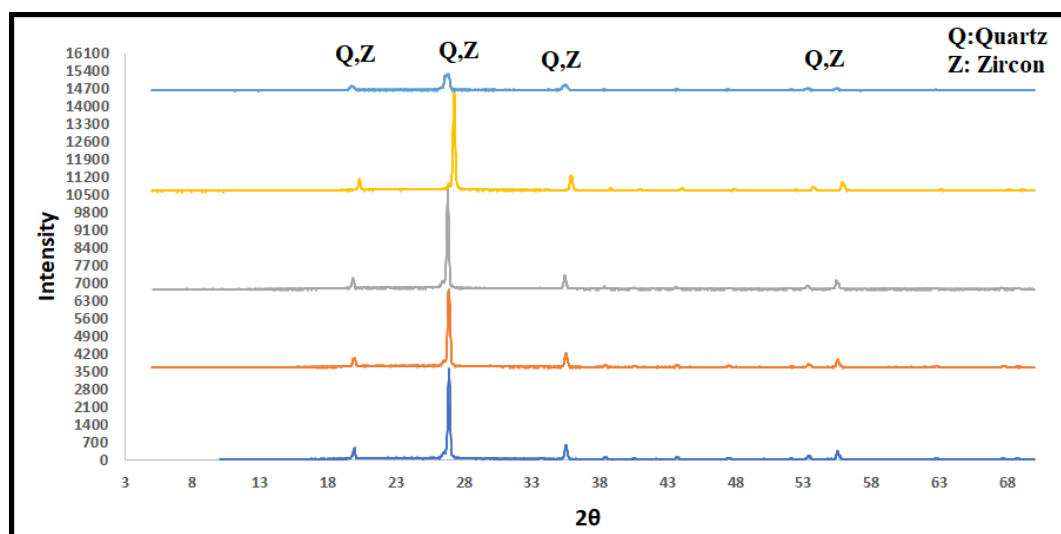


Figure 18. Xrd analysis results of the defects.

4. CONCLUSIONS

According to the results of the analysis, it was observed that Fe₂O₃ ratios were generally high in EDX spot analysis due to the iron content of the materials used in the process. In addition, it was observed that the crystal structure of the glaze was deteriorated in the point analysis where the Fe₂O₃ ratio was high, and the ZrO₂ ratio was low or not found at all in the SEM/EDX analysis. As known, vitrified glazes are mostly opaque glazes-based Zircon Silicate. There are very few studies in the literature in the field of vitrified ceramic materials. Especially glaze studies are carried out on products with high

visual effects such as wall tiles, floor tiles and porcelain products. In addition, the main glaze defects are emphasized. With this study, scientific explanations of faults caused by different process components were made and some deficiencies in the field of vitreous ware were tried to be solved. The fact that R&D studies are not adequate in the sanitary ware industry causes engineers to not find answers to the defects. These causes time and product losses in the process. By focusing on the main cause of the problem, it will show a scientific way to understand the numerical analyses used in production more clearly and to make the right interventions in production by carrying out such studies in order to offer a solution and make the chief cause analysis right. The intense observation of Fe-containing point analysis in the findings is due to the fact that the materials used in the production units are metallic-based. In these regions, it was observed that the crystal structures of the glazes were also deteriorated with stain defects. For this reason, in the processes where these defects occurred, the sources of fault were eliminated and the products were recycled.

ACKNOWLEDGEMENT

We would like to thank the managers and employees of Ece Bathroom Gereçleri Sanayi ve Ticaret A.Ş. for giving us opportunities at their factory sites and the Ceramic Research Center (SAM) for their assistance in the characterization studies.

REFERENCES

- [1] Gol, F., Saritas, Z., G., Cıbuk, S., Ture, C., Kacar, E., Yilmaz, A., Arslan, M., and Sen, F. (2022). Coloring effect of iron oxide content on ceramic glazes and their comparison with the similar waste containing materials. *Ceramics International*, 48(2), 15 January, 2241-2249.
- [2] Wang, S., Li, X., Wang, C., Bai, M., Zhou, X., Zhang, X., and Wang, Y. (2022). Anorthite-based transparent glass-ceramic glaze for ceramic tiles: Preparation and crystallization mechanism, *Journal of the European Ceramic Society*, 42(3), March, 1132-1140.
- [3] Hasanuzzaman, M., and Islam, F., Rashid, A. (2022). Investigation of methods to prevent pin-holing defect in tableware ceramic industry, *Int J Ceramic Eng Sci.*, 1–10.
- [4] Öztürk, Z. B. and Can, A. (2023). The use of micronized pumice in the production of ceramic sanitaryware glazes with sustainable industrial characteristics, *Journal of the Faculty of Engineering and Architecture of Gazi University*, 38(3), 1967–1977.
- [5] Kaplan, A.E. ve Binal, G. (2017). Vitrikiye Seramik Beyaz Opak Sırlarda Zirkonyum Silikat Miktarının Azaltılması, *Bilecik Şeyh Edebali Üniversitesi Fen Bilimleri Dergisi*, 4(1).
- [6] Aydın, T. and Casin, E. (2021). Mixed Alkali and Mixed Alkaline-Earth Effect in Ceramic Sanitaryware Bodies Incorporated with Blast Furnace Slag, *Waste and Biomass Valorization*, 12(5), 2685–2702.

- [7] Bernasconi, A., Diella, V., Pavese, A., Marinoni, N., and Francescon, F. (2012). Characterization of traditional sanitary-ware glazes using classical and unconventional analytical methods, European Mineralogical Conference 1, EMC2012-473.
- [8] Fortuna, A., Fortuna, D.M, and Martini, E., (2017). An industrial approach to ceramics: Sanitaryware, Plinius n. 43.
- [9] Silvestri, L. (2020). Life cycle assessment of sanitaryware production: A case study in Italy, Journal of Cleaner Production, 251, 1 April 2020, 119708.
- [10] Mete, Z. (2020). Seramik Kimyası, Tibyan Yayıncılık, İzmir.
- [11] Fraser, H. (2005). Ceramic Faults and Their Remedies, A & C Black Publishers Ltd.
- [12] Kartal, A. (1998). Sır ve Sırlama Tekniği, Banaz.
- [13] Topateş, G., Alıcı, B., Tarhan, B., and Tarhan, M. (2020). The effect of zircon particle size on the surface properties of sanitaryware glaze, Materials Research Express 7, 015203.
- [14] Arcasoy, A., and Başkırkan, H. (2020). Seramik Teknolojisi, İstanbul.
- [15] Öztürk, Z.B., Atabey, İ.İ. (2022). Mechanical and microstructural characteristics of geopolymer mortars at high temperatures produced with ceramic sanitaryware waste, Ceramics International, Volume 48, Issue 9, 1 May, Pages 12932-12944.



RESEARCH ARTICLE

**EXPERIMENTAL THERMAL PERFORMANCE ANALYSIS OF NANOFLUID ASSISTED
SLINKY GROUND HEAT EXCHANGER IN SPACE COOLING APPLICATION**

Abdullah KAPICIOĞLU^{1*}, Tahsin YÜKSEL²

^{1*}Sivas Cumhuriyet University, Faculty of Technology, Department of Production Engineering, Sivas,
akapicioglu@cumhuriyet.edu.tr, ORCID: 0000-0003-2982-0312

²Sivas Cumhuriyet University, Faculty of Technology, Department of Production Engineering, Sivas,
tyuksel@cumhuriyet.edu.tr, ORCID: 0000-0003-3238-9113

Receive Date: 22.06.2023

Accepted Date: 20.08.2023

ABSTRACT

Ground source heat pump has made a severe breakthrough in space conditioning applications due to their high energy efficiency, and expectations for these systems have increased due to using renewable energy. Concerning the increasing expectation, researchers and engineers have increased their research on these systems and focused on cost and efficiency. The efficiency of the ground source heat pump system is directly related to the ground heat exchanger loop, which provides the thermal connection between the heat pump and the ground, and increasing the effectiveness of the ground heat exchanger can be achieved with a nanofluid-based heat transfer fluid. On the other hand, as a ground source heat pump system component, ground heat exchangers have very different design configurations. Among the various configurations, slinky ground heat exchangers are of great interest due to their higher heat transfer efficiency and reduced installation space requirements compared to traditional straight pipe configurations. In this study, the effect of nanofluids on increasing the effectiveness of slinky ground heat exchangers was experimentally investigated and compared with the results obtained using conventional heat transfer fluids. The results obtained from the experimental study determined that using nanofluid at a rate of 0.1% as a heat transfer fluid in slinky ground heat exchangers in cooling applications increased the average effectiveness by about 20%.

Keywords: *Slinky Ground Heat Exchanger, Nanofluid, Effectiveness, Experimental Analysis*

1. INTRODUCTION

The demand for efficient and sustainable space conditioning systems has increased significantly in recent years due to rising energy costs and environmental concerns [1]. Conventional space cooling systems such as air conditioning consume a significant amount of energy and contribute to greenhouse gas emissions. Researchers and engineers have increased their research to develop energy-efficient cooling systems in this context. The use of ground source heat pump (TKIP) in conditioning

applications is one of the innovative approaches when energy saving and environmental concerns are taken into consideration [2,3].

There are many studies in the literature on different application areas on the subject [4-7]. GSHP systems use the stable thermal properties of the earth with the help of components called soil heat exchanger (GHE). Basically, GHEs are components that effectively exchange heat between the soil and a fluid circulating in buried pipes. Regarding application diversity, GHEs are divided into two as vertical and horizontal [8,9]. Although horizontal GHEs have lower performance compared to verticals, they have a low cost and relatively easy installation [10]. Horizontal GHEs, on the other hand, are classified according to various pave forms. Among these configurations, slinky ground heat exchangers (SGHE) are of great interest due to their higher heat transfer efficiency and reduced installation space requirements compared to traditional straight pipe configurations [11]. Wu et al. [12] reported that the use of SGHE saves up to 30% of installation space.

On the other hand, the performance of GHEs varies depending on many components, such as installation depth, design parameters, and the fluid used in the pipe. The thermal performance improvement of fluids can be achieved with nanofluids (NF), which has recently attracted great interest in the literature. In this context, NAs have the potential to improve the general heat transfer properties of TIDs [7]. NFs are suspensions of nanoparticles dispersed in a base fluid. The addition of nanoparticles changes the thermophysical properties of the base fluid, such as thermal conductivity and convective heat transfer coefficient. Studies conducted on MVCNT [13], Al₂O₃ [14], TiO [15] and SiO [16] reported that suspensions formed with different nanoparticles provide an increase in thermal capacity compared to the base fluid. However, despite extensive theoretical research on NFs, limited experimental data are available regarding their GHE performance, especially in the context of space cooling applications. Including NFs in these systems can reduce energy consumption and the environmental impact associated with space cooling. In summary, it can promote sustainable and efficient cooling technologies.

This study aimed to experimentally investigate the thermal efficiency of NF supported SGHE in space cooling applications and compared with the results obtained using conventional heat transfer fluid (ethylene glycol-water/base fluid) to determine the effect of NF. Investigating the effect of NF under real ambient conditions will shed light on the practical feasibility and potential benefits of incorporating nanofluids into GSHP systems.

2. MATERIALS AND METHODS

While the overall performance of the GSHP system depends on many external and internal parameters, the performance of GHE generally depends on more specific parameters, such as ground temperature-and specific heat capacity of the fluid. In this context, thermal performance tests should be carried out to determine GHE performance. In this context, the heat exchange rate can be calculated by measuring the inlet, outlet temperatures, and flow rate of the fluid passing through the heat exchanger for the cooling mode:

$$\dot{Q} = mC_p (T_{out} - T_{in}) \quad (1)$$

or

$$\dot{Q} = q\dot{V}C_p (T_{out} - T_{in}) \quad (2)$$

Another important parameter that we encounter in GHEs is GHE effectiveness. The concept of effectiveness here can be defined as the ratio of the actual heat transfer rate to the maximum amount of heat that can be transferred. The effectiveness of the GHE can be calculated using the following equation:

$$\varepsilon = \frac{mC_p (T_{GHE,in} - T_{GHE,out})}{mC_p (T_{GHE,in} - T_{ground})} \quad (3)$$

or

$$\varepsilon = \frac{(T_{GHE,in} - T_{GHE,out})}{(T_{GHE,in} - T_{ground})} \quad (4)$$

3. EXPERIMENTAL SETUP

The experimental setup consists of the SGHE buried 2.5 m below the ground surface, a heat pump system, and the cooling area. As mentioned earlier, the SGHE configuration improves the system's overall performance by allowing the heat transfer surface area to increase compared to other GHEs installed in a similar area [17,18].

The space to be conditioned has dimensions of 3 m x 7 m x 2.3 m and the heat load of the area was calculated as 2.2 kW using the HeatCAD package program according to Sivas province. The heat loss value per unit area has been calculated as approximately 104 W/m². Estimating the GHE length to meet the heating and cooling demand of the space is an important step in the GSHP system setup. Different methodologies have been proposed in the literature to calculate the GHE length. In this study, a methodology suggested by Chiasson was used [19]. According to the calculated heat load, the required pipe length was calculated as 75 m in total. The SGHE is placed on the ground in 20 spirals with a radius of 0.3 m. The pipe used in SGHE is SDR 11 polyethylene pipe with an outer diameter of 40 mm and a wall thickness of 3 mm. Temperature measurements were carried out with the help of T-type thermocouples from different points, SGHE inlet, outlet and over the pipe. SGHE is integrated into the heat pump with the aid of a 245 L heat exchange tank. NF with 0.1% concentration, prepared by dispersing 8 nm Al₂O₃ nanoparticles in a base fluid (ethylene glycol-water), was used as the heat

transfer fluid in the ground loop. The mass flow rate of the fluid circulating in the system was kept at 0,450kg/s with the help of an inverter circulation pump. Heating experiments of the related experimental setup were previously carried out by Kapıcıoğlu [20]. The schematic view of the system is given in Figure 1.

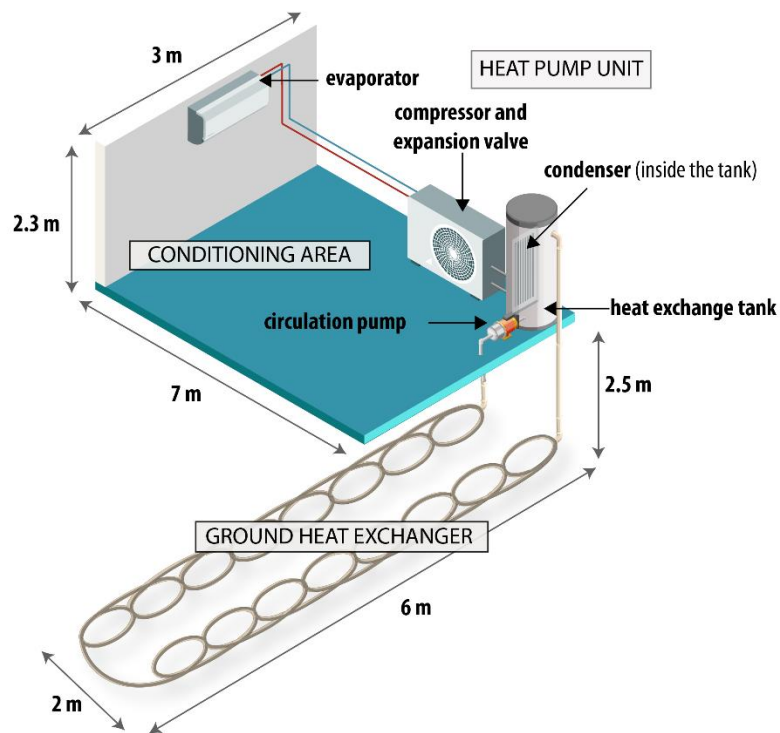


Figure 1. Schematic view of the experimental setup.

The experimental study was carried out in July 2021. In the experimental study, the temperature values for both the base fluid and the NF were monitored during the eight-hour operating period. In order to evaluate the thermal equilibrium in the ground for both fluids, temperatures around the ground were recorded from the beginning of the experiments. The ground temperature change during the experiment period is given in Figure 2.

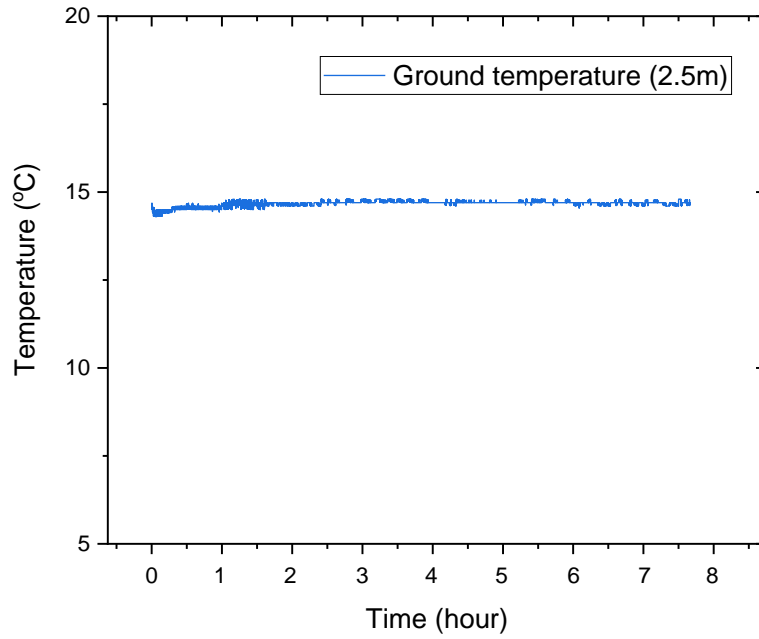


Figure 2. The ground temperature change during the experiment.

Similar working conditions were tried to be achieved in experimental studies and these values were meticulously recorded with the help of a data recorder. During the experimental period, temperature data were taken, one data per second. Some typical data recorded are shown in Table 1.

Table 1. Inlet and outlet temperatures of Al₂O₃ nanofluid with base and 0.1% concentration into SGHE.

Time (min)	Base fluid		Al ₂ O ₃ (%0,1)	
	GHE inlet (°C)	GHE outlet (°C)	GHE inlet (°C)	GHE outlet (°C)
30	20.79	20.49	20.14	19.68
60	23.86	23.10	23.81	23.02
120	26.37	25.43	25.73	24.90
180	28.09	27.08	27.62	26.67
240	29.00	27.99	28.33	27.31
300	30.10	29.17	29.32	28.44
360	29.83	29.08	28.87	28.13
420	29.04	28.45	28.30	27.64

480	28.37	27.85	27.44	26.86
-----	-------	-------	-------	-------

The experimental uncertainty in this study includes the uncertainties in temperature and flow measurements. Uncertainty analysis was performed using the uncertainty analysis method defined by Kline-McClintock [21]. The overall uncertainty of the measurements is estimated at $\pm 1.46\%$ for mass flow rate and ± 0.5 for temperatures.

4. RESULT AND DISCUSSION

The temperature of the fluid circulating in a GHE is directly related to parameters such as ground temperature and load amount of the system. Figure 3 shows the inlet and outlet temperatures of the base fluid to the SGHE. From the beginning of the experiments, it is seen that both the inlet and outlet fluid temperatures begin to increase over time. The fluctuation in the initial phase is due to the uneven temperature distribution during the transfer of the fluid in the tank to the ground. This situation ends with the balancing of the ground temperature and the fluid temperature in the first fifteen minutes. In addition, fluctuations were observed during the first ninety minutes due to the amount of heat transfer required by the system during the first operation. The inlet and outlet temperatures of the fluid circulating in the GHE were determined as $27.06\text{ }^{\circ}\text{C}$ ($\pm 3.72\text{ }^{\circ}\text{C}$) and $26.42\text{ }^{\circ}\text{C}$ ($\pm 3.77\text{ }^{\circ}\text{C}$), respectively.

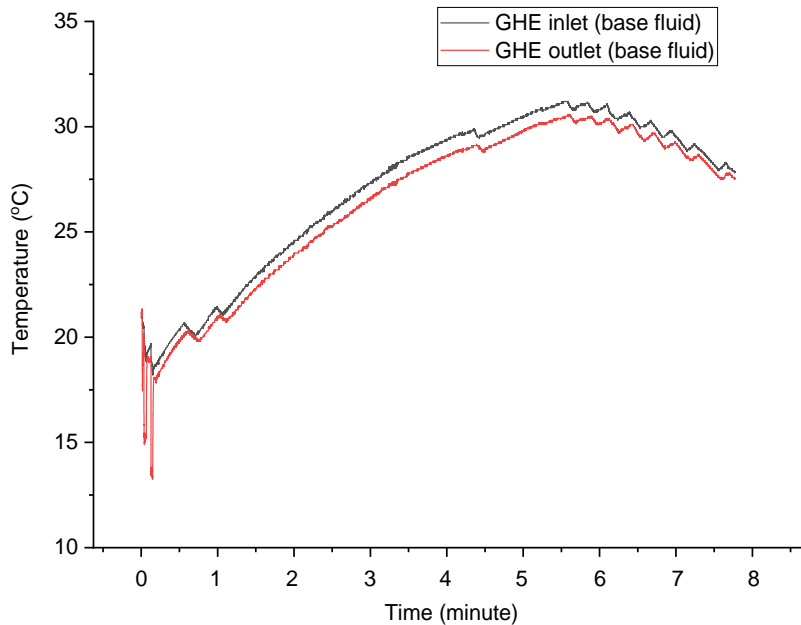


Figure 3. Temperature profile of base fluid in SGHE.

The experiments for the base fluid were carried out in NF under similar conditions, and the SGHE inlet and outlet temperatures are presented in Figure 4. The temperature value of the fluid in the SGHE shows an increasing trend during the day, similar to the base fluid. The inlet and outlet temperatures of the NF circulating in the SGHE were calculated on average as 26.58 °C (± 3.74 °C) and 25.87 °C (± 3.67 °C), respectively. Compared to the base fluid, the average temperature values calculated here are also at lower levels. Also, similar initial conditions were observed for both fluids. Both fluids (base and NF) draw heat from the ground in the first 15 minutes instead of giving it to the ground. This is due to the fact that the fluid in the tank is initially at a lower temperature than the ground. This situation ends with reversing the flow direction of the heat at the end of the fifteen-minute period. However, the fluctuation in NF is lower than in the base fluid. This situation can be associated with the high thermal capacity of NF.

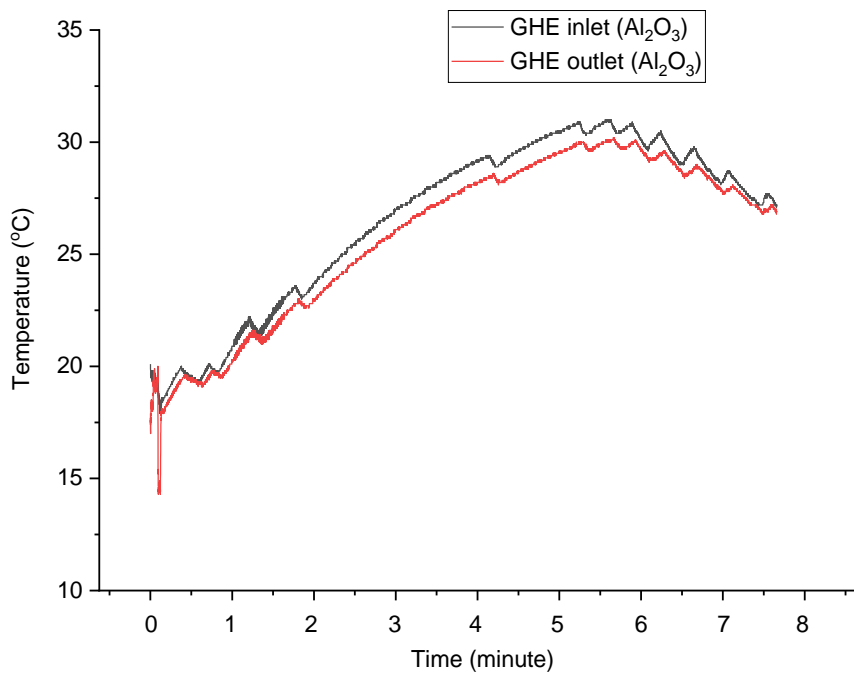


Figure 4. Temperature profile of NF with 0.1% concentration in SGHE.

Figure 5 shows the SGHE effectiveness changes for the use of base fluid and NF as the heat transfer fluid over the eight-hour operating period. The average effectiveness of SGHEs using base fluid and NA is 0.114 (0.061) and 0.137 (0.09), respectively. Due to the heating of the ground due to the increase in the operating time of the system, the performance of the SGHE decreases, so the effectiveness decreases over time. This situation can be explained as follows: the temperature difference between the inlet and outlet fluid temperatures occurs in an almost similar range, so the

variation in heat transfer is relatively limited. However, the inlet fluid temperature continues to increase with time so that the maximum possible heat transfer increases with time. These two effects cause the effectiveness of GHE to decrease over time. While the difference between base fluid and ground temperature is 11.8 °C on average, this value is around 11.1 °C in NF.

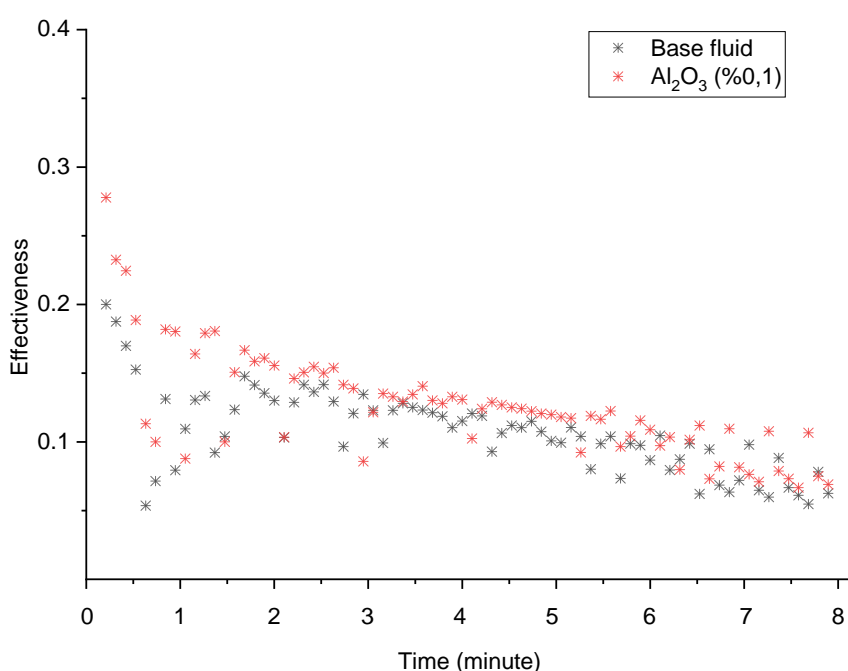


Figure 5. GHE effectiveness of base fluid and nanofluid with 0.1% concentration.

5. CONCLUSIONS

In this study, the effectiveness of using NF in a GHE with a slinky design integrated into a ground source heat pump system in space cooling applications was investigated. NF, which is used as the heat transfer fluid in the system, is prepared from 8 nm Al₂O₃ nanoparticles and has a concentration value of 0.1%. Experimental results showed that the nanofluid supported SGHE exhibited improved thermal performance compared to the base system. The important findings obtained as a result of the study can be listed as follows:

The use of NF in the SGHE system resulted in an improvement of 1.77% in inlet temperatures and 2.08% in outlet temperatures. With these values, the use of NF can be accepted as an indication that it will provide improved cooling performance by improving the SGHE heat transfer properties.

When the GHE effectiveness depending on ground temperature was examined, the average effectiveness of SGHEs using base fluid and NF was 0.114 and 0.137, respectively. With these results, it can be said that the use of NF as a heat transfer fluid increases the effectiveness by nearly 20%.

As a result, it has been observed that NF provides better heat exchange between the ground and the heat transfer fluid, thanks to its enhanced heat transfer properties attributed to the high thermal conductivity of nanoparticles. As a result of this situation, it can be said that it will increase the cooling efficiency by leading to lower fluid outlet temperatures and higher heat transfer rates.

Finally, it should be noted that more research is needed to investigate the economic viability and environmental impacts, as well as the long-term stability and reliability of NFs in GHEs. However, the experimental results provide valuable information for the development and optimization of nanofluid assisted cooling systems.

ACKNOWLEDGEMENTS

Sivas Cumhuriyet University supported this study with the project no TEKNO-025 within the scope of the BAP program (CUBAP). It was also partially supported by the Scientific and Technological Research Council of Turkey (TUBITAK) with project no 118M140.

REFERENCES

- [1] Wang, X., Zhou, C., Ni, L., (2022). Experimental investigation on heat extraction performance of deep borehole heat exchanger for ground source heat pump systems in severe cold region. *Geothermics* 105, 102539. <https://doi.org/10.1016/J.GEOTHERMICS.2022.102539>
- [2] Kaneko, C., Yoshinaga, M., (2023). Long-term operation analysis of a ground source heat pump with an air source heat pump as an auxiliary heat source in a warm region. *Energy Build* 289, 113050. <https://doi.org/10.1016/J.ENBUILD.2023.113050>
- [3] Violante, A.C., Donato, F., Guidi, G., Proposito, M., (2013). Experimental evaluation of using various renewable energy sources for heating a greenhouse. *Energy Build* 65, 340–351. <https://doi.org/10.1016/j.enbuild.2013.06.018>
- [4] Kapicioğlu, A., Esen, H., (2022). Economic and environmental assessment of ground source heat pump system: The case of Turkey. *Sustainable Energy Technologies and Assessments* 53. <https://doi.org/10.1016/j.seta.2022.102562>
- [5] Dehghan B., B., (2017). Experimental and computational investigation of the spiral ground heat exchangers for ground source heat pump applications. *Appl Therm Eng* 121, 908–921. <https://doi.org/10.1016/j.applthermaleng.2017.05.002>

- [6] Kapıcıoğlu, A., Esen, H., (2019). Experimental investigation on using Al₂O₃/ethylene glycol-water nano-fluid in different types of horizontal ground heat exchangers. *Appl Therm Eng* 165, 114559. <https://doi.org/10.1016/j.applthermaleng.2019.114559>
- [7] Esen, H., Inalli, M., (2009). Modelling of a vertical ground coupled heat pump system by using artificial neural networks. *Expert Syst Appl* 36, 10229–10238. <https://doi.org/10.1016/j.eswa.2009.01.055>
- [8] Coşkun, S., Güler, F., Fazlıç, M.A., Ergün, E.H., (2018). Dikey Tip Toprak Kaynaklı Bir Isı Pompasının Simülasyonu. *Uludağ University Journal of The Faculty of Engineering* 23, 155–168. <https://doi.org/10.17482/uumfd.467169>
- [9] Esen, H., İnallı M., Sengur A., Esen M. (2008). Modelling a ground-coupled heat pump system using adaptive neuro-fuzzy inference systems, *International Journal of Refrigeration*,31,65-74. <https://doi.org/10.1016/j.ijrefrig.2007.06.007>
- [10] Florides, G., Kalogirou, S., (2007). Ground heat exchangers-A review of systems, models and applications. *Renew Energy*. <https://doi.org/10.1016/j.renene.2006.12.014>
- [11] Wu, Y., Gan, G., Verhoef, A., Vidale, P.L., Gonzalez, R.G., (2010). Experimental measurement and numerical simulation of horizontal-coupled slinky ground source heat exchangers. *Appl Therm Eng* 30, 2574–2583. <https://doi.org/10.1016/J.APPLTHERMALENG.2010.07.008>
- [12] M'hamed, B., Che Sidik, N.A., Akhbar, M.F.A., Mamat, R., Najafi, G., (2016). Experimental study on thermal performance of MWCNT nanocoolant in Perodua Kelisa 1000cc radiator system. *International Communications in Heat and Mass Transfer* 76, 156–161. <https://doi.org/10.1016/j.icheatmasstransfer.2016.05.024>
- [13] Elias, M.M., Mahbulul, I.M., Saidur, R., Sohel, M.R., Shahrul, I.M., Khaleduzzaman, S.S., Sadeghipour, S., (2014). Experimental investigation on the thermo-physical properties of Al₂O₃ nanoparticles suspended in car radiator coolant. *International Communications in Heat and Mass Transfer* 54, 48–53. <https://doi.org/10.1016/j.icheatmasstransfer.2014.03.005>
- [14] Mukherjee, S., Chakrabarty, S., Mishra, P.C., Chaudhuri, P., (2020). Transient heat transfer characteristics and process intensification with Al₂O₃-water and TiO₂-water nanofluids: An experimental investigation. *Chemical Engineering and Processing - Process Intensification* 150, 107887. <https://doi.org/10.1016/j.cep.2020.107887>
- [15] Hussein, A.M., Bakar, R.A., Kadirgama, K., (2014). Study of forced convection nanofluid heat transfer in the automotive cooling system. *Case Studies in Thermal Engineering* 2, 50–61. <https://doi.org/10.1016/j.csite.2013.12.001>
- [16] Tadepalli, R., Gadekula, R.K., Reddy, K.V., Goud, S.R., Nayak, S.K., Saini, V., Dondapati, R.S., (2018). Characterization of Thermophysical properties of Al₂O₃, TiO₂, SiO₂, SiC and CuO

- Nano Particles at Cryogenic Temperatures. *Mater Today Proc* 5, 28454–28461. <https://doi.org/10.1016/j.matpr.2018.10.132>
- [17] Fujii, H., Nishi, K., Komaniwa, Y., Chou, N., (2012). Numerical modeling of slinky-coil horizontal ground heat exchangers. *Geothermics* 41, 55–62. <https://doi.org/10.1016/J.GEOTHERMICS.2011.09.002>
- [18] Sangi, R., Müller, D., (2018). Dynamic modelling and simulation of a slinky-coil horizontal ground heat exchanger using Modelica. *Journal of Building Engineering* 16, 159–168. <https://doi.org/10.1016/J.JOBE.2018.01.005>
- [19] Chiasson, A.D., (2016). *Geothermal heat pump and heat engine systems: Theory and practice*. John Wiley & Sons.
- [20] Kapicioğlu, A., (2022). Energy and exergy analysis of a ground source heat pump system with a slinky ground heat exchanger supported by nanofluid. *J Therm Anal Calorim* 147, 1455–1468. <https://doi.org/10.1007/s10973-020-10498-0>
- [21] Holman, J.P., (2012). *Experimental Methods for Engineers*, 8th ed. McGraw-Hill.

NOMENCLATURE

SYMBOLS

<i>GHE</i>	ground heat exchanger
GSHP	ground source heat pump
NF	nanofluid
<i>Q</i>	heat capacity, kW
<i>SGHE</i>	slinky ground heat exchanger
<i>T</i>	temperature, K or °C
\dot{V}	flow rate (L/s)
<i>C_p</i>	specific heat at constant pressure (kJ kg ⁻¹ K ⁻¹)
ϵ	effectiveness
ρ	fluid density kg m ⁻³
\dot{m}	mass flow rate, kg s ⁻¹

SUBSCRIPTS

<i>in</i>	inlet
<i>GHE</i>	ground heat exchanger
<i>out</i>	outlet



RESEARCH ARTICLE

INFLUENCE OF Ti MICROALLOYING ON ZAMAK-5

Melih KOCYIGIT¹, H. Erdem CAMURLU^{2*}

¹Akdeniz University, Department of Mechanical Engineering, Antalya, melihkocyigit@outlook.com,
ORCID: 0000-0003-2933-0436

²Akdeniz University, Department of Mechanical Engineering, Antalya, erdemcamurlu@gmail.com,
ORCID: 0000-0003-3170-4492

Receive Date: 05.03.2023

Accepted Date: 05.07.2023

ABSTRACT

ZAMAK-5 is a Zn-Al alloy which contains 3.9-4.3 % Al, 0.75-1.25 % Cu and 0.03-0.06 % Mg. Low melting temperature and good castability are some of the advantages of ZAMAK-5. In the present study, the composition of ZAMAK-5 alloy was modified by microalloying it with Ti. Alloying was accomplished by melting ZAMAK-5 at 450 and 650 °C and introducing Ti as Al10Ti master alloy. It was found by ICP analyses that modified alloys contained 0.01 and 0.03 wt.% Ti. Re-melting and casting of the alloyed samples were conducted at 650 °C under argon atmosphere. The modified alloy that contained 0.03 % Ti had near eutectic Zn-Al composition due to the increased amount of Al. The increase in the Al content was caused by master alloy addition. According to microstructural and solidification analyses, the modified alloy that contained 0.03 % Ti had lower liquidus temperature and less primary (η) dendrites in its microstructure. Alloying with Ti was found to increase hardness and bending strength of the base alloy. Alloy that was modified with 0.03 % Ti exhibited the highest hardness (102.3 ± 2.8 HB₁₀), compressive yield strength (290.0 ± 5.0 MPa) and bending strength (661.4 ± 30.5 MPa).

Keywords: ZAMAK-5, Ti addition, Zinc-aluminum alloys, Casting.

1. INTRODUCTION

Zn-Al alloys have been used in automotive applications, mechanical parts, and decorative areas due to their advantages such as good castability, long mold life and low melting point [1, 2]. They exhibit superior properties at cutting, drilling, reaming, tapping, turning, etc. and provide ease of use at machining applications due to advantages such as surface quality after heat treatment, low cutting forces and wear [3]. Nowadays, ZAMAK-2, ZAMAK-3 and ZAMAK-5 are the most popular Zn-Al alloys. ZAMAK-5 is a Zn-Al alloy which contains 3.9-4.3 % Al, 0.75-1.25 % Cu and 0.03-0.06 % Mg. ZAMAK-2, ZAMAK-3 ve ZAMAK-5 alloys have hypo-eutectic composition according to the Al-Zn phase diagram [4].

Azizi et. al. (2015), mechanically alloyed ZAMAK-2 via powder metallurgy (PM) method and a maximum hardness value of 101 HB was obtained. In the study, die cast and sand-cast product hardness values were compared to the hardness values of the PM products. It was found that while die

cast samples exhibited better hardness value (130 HB) than the PM products, hardness values of the sand-cast samples (85 HB) were lower than the PM products [5].

Altınsoy and Kızıllarslan (2016), investigated the effect of the Ti addition to ZAMAK-3 on microstructure, hardness and fracture toughness. They suggested that the amount of eutectic structure increased when Ti amount increased in the composition. Furthermore, it was reported that Ti addition did not affect the hardness and fracture toughness values of the main alloy (ZAMAK-3) [6].

Sandlöbes et. al. (2016) conducted studies to understand the aging processes of the (Zn_{4.3}Al_{10.59}Cu_{0.31}Mg) Zn-Al-Cu-Mg alloys which contain almost the same amount of Al, Cu and Mg in their compositions as ZAMAK-5. In the study, tensile strength of the alloys was investigated at room temperature and at 85 °C. It was reported that the alloys exhibited better tensile strength (157 MPa) at 85 °C, than that at room temperature (133 MPa) [7].

Wu et. al. (2016), determined that increasing Mg amount in the Zn-Al alloys resulted in precipitation of the Mg₂Zn₁₁ phase in a lamellar fashion in the eutectoid structure. Moreover, it was indicated that, Zn-Al alloys which had moderate amount of Mg (0.21 wt.%), had the highest yield strength at a room temperature and at high temperatures [8].

Recently, there have been studies on modifying Zn-Al alloys with different elements such as B, Ni, Mn, by different researchers [9-11]. Ayday et al. [9] examined the effects of boron addition on mechanical and thermophysical properties of ZA12 alloy. It was reported that B addition enhanced hardness and tensile strength, along with ductility. Moreover, thermal conductivity of ZA12 alloy was seen to decrease by B addition [9]. Ti was added previously to Zn-Al alloys to modify the structure [12]. Ti has limited diffusion rate in Zn and it has anti-grain growth effect on as cast Zn. [13]. It was reported that, Ti addition improved strength of pure Zn-Al alloys. In addition, it increased creep resistance of Zn alloys [14].

Although there are remarkable studies in the literature that investigate the microalloy additions to ZAMAK and Zn-Al alloys, no study that investigated the effect of the Ti addition to the ZAMAK-5 alloy was encountered. Ti has a limited solubility in Zn and forms Zn-TiZn₁₅ eutectic at %0.11 Ti in Zn. It is expected that TiZn₁₅ intermetallic plays a role in increasing the hardness and strength of the zinc alloys [4,14]. In the studies of Türk (1996) [15] and Durman (1996) [16], 0.01 % Ti addition was reported to increase the strength and 0.03 % Ti addition was reported to increase the hardness of ZA-8 alloy. Therefore, in the present study, chemical composition of commercial ZAMAK-5 was modified by microalloying it with Ti in the vicinity of these percentages. Solidification behavior, microstructure, hardness, bending and compressive strength of the modified alloy were investigated.

2. MATERIAL AND METHODS

2.1. Preparation of Alloys and Casting

Commercial ZAMAK-5 (3.5-4.5 %Al, 0.75-1.25 % Cu, 0.03-0.08 % Mg) was alloyed with Al10Ti master alloy at 450 and 650°C. The percentages given in this text are weight % (wt.%). It can be seen in the Zn-Al phase diagram that there is a eutectic melting at 380 °C at 5 wt.% Al composition [4]. In the vicinity of this composition, the alloys are completely liquid state above 400 °C. For this reason, for microalloying of ZAMAK-5 the first selected temperature was 450 °C. It was reported in literature that the alloying elements deteriorate when ZAMAK alloys are heated to above 650 °C [17].

Therefore, for microalloying of ZAMAK-5 the second selected temperature was 650 °C, which can be suggested as the highest allowable temperature.

Two sets of Ti microalloyed ZAMAK-5 samples were prepared. In the first set, calculated amount of Al10Ti to yield 0.05 % Ti was mixed with the ZAMAK-5 melt at 450 °C. In the second set, calculated amount of Al10Ti to yield 0.10 % Ti was mixed with the ZAMAK-5 melt at 650 °C. Alloying process was conducted in a Protherm muffle furnace for 6 hours. Obtained Ti modified alloys were cast into a steel mold having 14 mm diameter.

For the preparation of the samples, which were utilized in the microstructural examinations and in the mechanical tests, the alloys were re-melted at 650 °C and cast in an induction furnace (Indutherm MC 20 V, max. Power 3.5 kW). Re-melting/casting was applied for reducing porosity and obtaining better surface quality of the test samples. The utilized induction furnace contained a tiltable melting/casting chamber with protective atmosphere. There were the induction coils in which the melting crucible was placed inside the chamber. A steel mold (8 mm inside diameter) which was preheated to 150 °C was also placed inside the chamber, in line with the crucible. Two consecutive vacuum-argon filling cycles were applied prior to melting the alloy. Melting was conducted in argon atmosphere at 1 atm. Casting was accomplished by tilting the chamber 90 degrees so that the molten metal was poured from the melting crucible into the mold inside the chamber. The furnace was programmed so that the argon pressure inside the chamber increased to 3 atm. when the chamber was tilted for casting. In order to avoid adhesion between mold and the molten alloy, inner side of the mold was coated with hexagonal boron nitride spray (Ekamold). Same casting process was applied to non-modified base alloy (ZAMAK-5) for comparison of the results.

2.2. Microstructural and Elemental Analyses

Cast samples were cut and ground with 800, 1200, 3000 grit emery paper, polished with 1-micron diamond paste and etched with nital (2 % nitric acid in ethanol) solution. Microstructure was investigated by optical and scanning electron microscopy (SEM). An optical microscope (Nikon Eclipse LV150) and Clemex image analysis software was used for microstructural analyses. The secondary dendrite arm spacing (SDAS) size values were obtained by the measure tool of the software. The SDAS sizes were determined according to method E, which was described in [18]. In this method, SDAS sizes were determined by measuring the distance from center to center of two neighboring secondary dendrite arms. Average and standard deviation of 100 measurements were reported. In addition, the areal fractions of the phases or structures were measured by the area measurement tool of Clemex software. FESEM-EDS analyses were done by ZEISS- SUPRA 40VP.

For elemental analysis, 2 g of sawdust was removed from the samples and ICP-OES (Inductively Coupled Plasma - Optical Emission Spectrometry) analyses were performed at Meta Nickel Cobalt Company, Manisa Gördes Plant.

2.3. Mechanical Testing

Three-point bending and compressive strength tests were carried out by Shimadzu Autograph AG-IC model 50 kN universal mechanical tester. The diameters of the samples which were utilized for three-point bending tests were 8 mm. In bending tests, a span length of 25 mm was applied. Three-point bending tests were conducted according to the procedure in ASTM B528-05 standard. The diameter and the height values of the samples which were used for the compression tests, were 8 mm and 15mm, respectively. To calculate the compressive yield strength of the samples, 0.2 % offset method

was used according to E9- 89a ASTM standard. It is indicated in this standard that the compressive strength of the ductile materials can be determined from the stress-strain diagram at a specified total strain. Therefore, in the present study, compressive strength values of the samples were determined at 50% strain and they were reported as compressive strength at 50% strain. 50% strain was selected since after this value the stress-strain curve was seen to lose linearity. Hardness tests were performed by Brinell hardness tester (Bulut Makina – Digirock) with 2.5 mm diameter steel ball tip and 62.5 kg load (HB10 scale).

2.4. Cooling Curves

In order to investigate effect of Ti addition on solidification, a set of samples was cast into a sand mold (Heraeus - Quick Cup) having 35mm x 35mm bottom sizes and 45mm height. During cooling and solidification of the samples, temperature was measured with a K-type thermocouple that was placed in the middle of the sand mold. Cooling curves were obtained by recording the temperature data via an ORDEL PC991 step control device and ORDEL SBA200 converter interface.

3.RESULTS AND DISCUSSION

3.1. Microstructural and Elemental Analyses

According to the ICP-OES analyses, 0.05 % Ti added alloy (alloyed at 450 °C) had 0.01 % Ti, and 0.10 % Ti added alloy (alloyed at 650 °C) contained 0.03 wt. % Ti in its composition (Table 1). It was determined that modified alloys contained lower quantity of Ti than the added amount. This can be originated due to the retaining of some of the added alloy in the slag. Amount of Ti in the modified ZAMAK-5 was seen to increase with the increase in the master alloy amount and alloying temperature. In accordance with the ICP-OES analysis results, ZAMAK-5 alloy that contained 0.01 wt. % Ti was coded as Z5-0.01Ti and the alloy that contained 0.03 wt. % Ti was coded as Z5-0.03Ti.

The amount of Al in the modified ZAMAK-5 was seen to increase with the increase in the master alloy amount. It was determined that Z5-0.01Ti contained 4.43 wt. % Al and Z5-0.03Ti contained 5.1 wt. % Al (Table 1). The Al amounts in the modified ZAMAK-5 samples were near the eutectic composition (5.0 %).

Table 1. Amounts of Ti and Al in the samples, according to ICP-OES analyses.

Alloy/ Element (Wt.%)	ZAMAK- 5	Z5-0.01Ti	Z5-0.03Ti
Al	4.43	4.57	5.10
Ti	-	0.01	0.03

The eutectic Zn-Al alloys solidifies at 382 °C by eutectic transformation ($L \rightarrow \eta + \beta$). On the other hand, in the hypo-eutectic base alloy (ZAMAK-5), primary η dendrites are formed in the liquid first. Later on, $L \rightarrow \eta + \beta$ eutectic transformations takes place. Lamellar eutectic phase ($\eta + \beta$) is formed around the η dendrites via eutectic transformation. After that, β in the eutectic structure transforms to Zn rich (η) phase and Al rich (α) phases via eutectoid transformation that occurs at 275 °C (transformed eutectic). As a result of the eutectoid transformation there are primer η dendrites and ($\eta + \alpha$) phases (transformed β) in the microstructure at a room temperature. According to the EDS analyses and results in the literature, the light colored areas are primary η dendrites (shown as A in

Figure 1(b)) and dark colored areas are transformed eutectic $\eta + \alpha$ phases (shown as B in Figure 1(c)) in the microstructure of the samples given in Figure 1 [4,8]. A greater amount of $\eta + \alpha$ phase mixture was detected visually in the microstructure of the Z5-0.03Ti. This is believed to be a result of its composition being in close to the eutectic composition (Figure 1(c)). The fraction of primary η dendrites in the microstructure of the base ZAMAK-5 and Z5-0.01Ti was higher than that in Z5-0.03Ti, because of their hypo-eutectic compositions (Figure 1 (a, b)). According to the areal calculations performed through the image analyses of the microstructures given in Table 2, the area covered by the pre-eutectic η phase was 67% in base ZAMAK-5, whereas it decreased to 38 % in Z5-0.03Ti sample (the amounts of transformed eutectic structure were complementary of these values to 100%).

Effect of Ti addition on secondary dendrite arm spacing (SDAS) values of η dendrites were measured during the image analyses of the microstructures by Clemex software. The results are presented in Table 2. The SDAS values in ZAMAK-5 and Z5.01Ti sample were similar, whereas there was a decrease in the SDAS values of Z5.03Ti sample. Addition of Ti appears to have resulted in a decrease in the SDAS values of ZAMAK-5. After alloying, all the samples which were subjected to microstructural examinations and mechanical tests were obtained by melting at 650 °C and then casting. Therefore, the same cooling rate was accomplished in all the samples. As a result, the cooling rate did not have an effect on the differences in the microstructure of the samples. All the differences in the microstructure can be attributed to the effect of alloying. The reduction in the SDAS size as a result of the addition of Al10Ti master alloy may be related with the increase in the Al content of the alloy or the presence of Ti (Table 1).

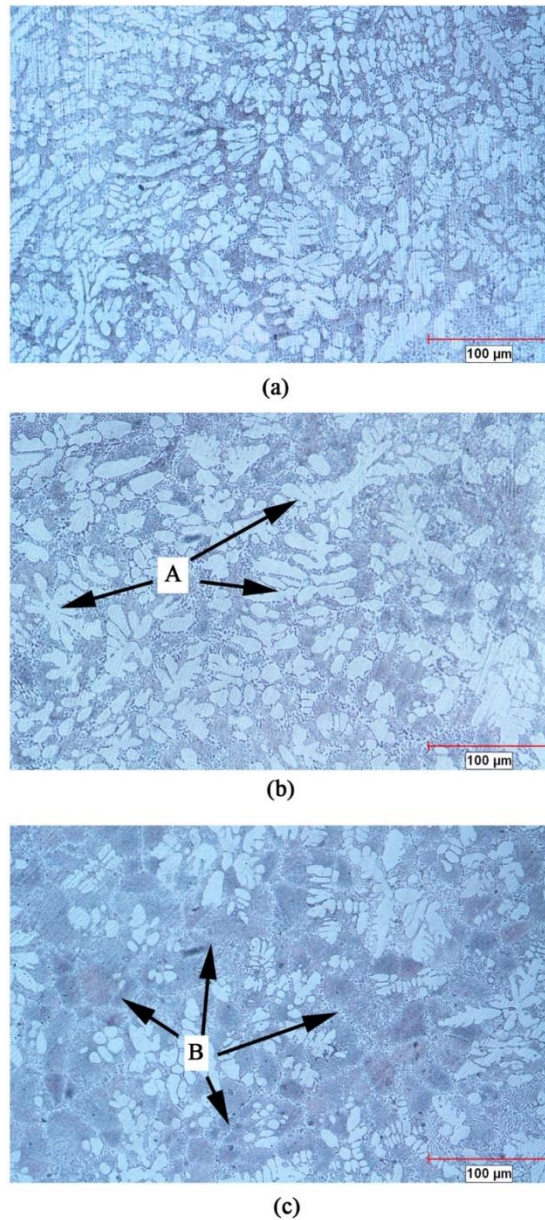


Figure 1. Microstructure images of the samples (Optical Microscope, magn. 200X), (a) Base alloy, (b) Z5-0.01Ti (Alloyed at 450 °C and re-melted and cast at 650 °C), (c) Z5-0.03Ti (Alloyed at 650 °C and re-melted and cast at 650 °C).

Table 2. Secondary dendrite arm spacing (SDAS) and area percentages of the structure in the microstructure of the samples.

Sample	SDAS (μm)	Area %	
		Pre-eutectic η	(Transformed) Eutectic Structure
ZAMAK-5	7.8 \pm 1.16	67	33
Z5-0.01Ti	7.6 \pm 1.20	56	44
Z5-0.03Ti	6.5 \pm 1.13	38	62

The magnified portion of a transformed eutectic region (which was marked as B in Figure 1(c)) is presented in Figure 2. According to the SEM-EDS analyses that was conducted on this region (Figure 2), 5 times more Ti than the overall composition was detected (Table 3). Therefore, it is considered that Ti was mostly located on the eutectic regions. This finding is in agreement with the data given in the literature, since Ti has a limited solubility in Zn [4,14].

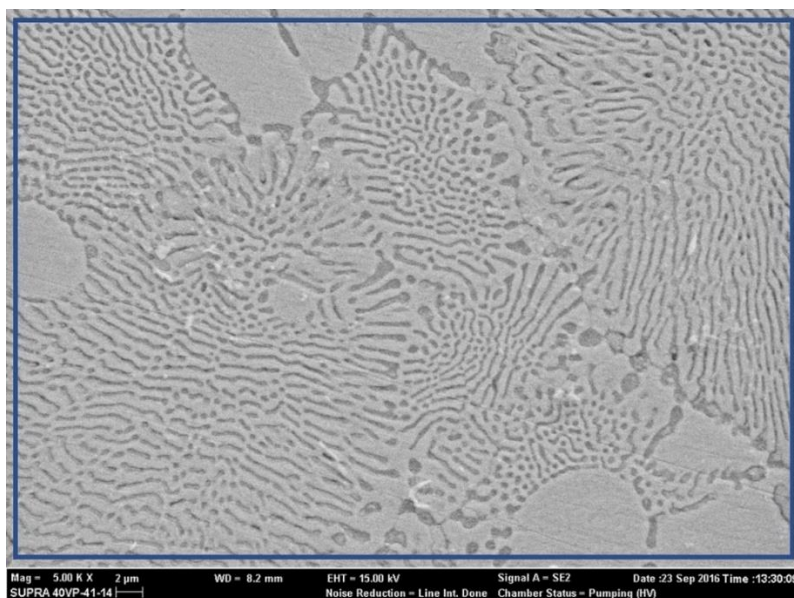


Figure 2. SEM image of transformed eutectic region of 0.03 % Ti modified ZAMAK-5 (magn. 5 kX).

Table 3. EDS result of the Ti modified ZAMAK-5 given in Figure 2 (transformed eutectic region).

	Wt. % Al	Wt. % Cu	Wt. % Ti	Wt. % Zn
Selected Region (Blue Frame)	7.49	1.25	0.15	91.11

3.2. Solidification Process of the Ti Modified and Base ZAMAK-5 Alloys

When solidification curves were examined, it was determined that the liquidus temperatures of the Ti modified alloys are lower than that of base ZAMAK-5 alloy (Figure 3). During solidification, primary η phase start to occur at 389 °C for ZAMAK-5, at 386 °C for Z5-0.01Ti and at 384 °C for Z5-0.03Ti samples. These values are in accordance with the Al contents of the samples.

It can be seen at Figure 3. that, Z5-0.03Ti has the lowest liquidus point. This validates the less amount of the primer η dendrites formed in this sample. This result is in accordance with the microstructure images (Figure 1). In addition, it might be suggested that Z5-0.03Ti has the shortest transformation time, which is caused by its near eutectic composition.

It was determined that the solidus temperatures of all the samples were at 380-381 °C. These values agree well with the data given in the literature, since the eutectic temperature of Zn-Al alloys is at 380 °C [4].

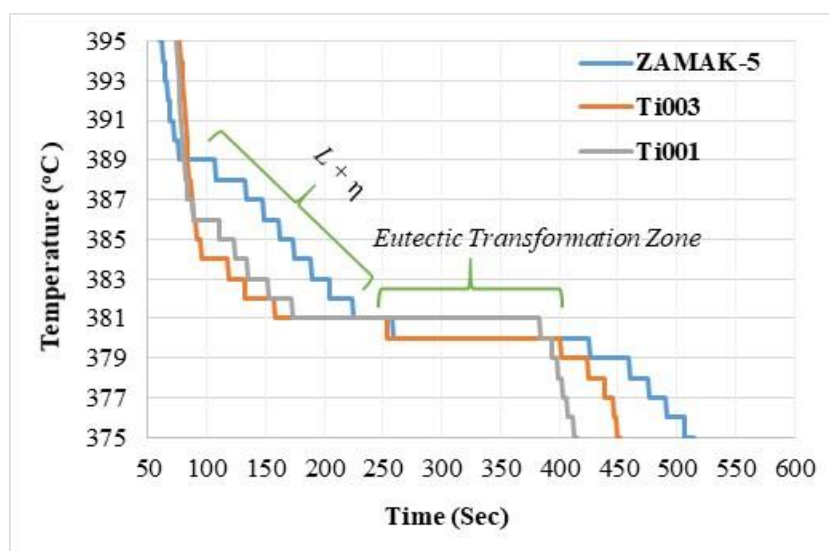


Figure 3. Cooling curves of the samples.

3.3. Hardness Test Results

According to the hardness test results, it was determined that hardness values of Ti modified alloys were higher than that of base ZAMAK-5 alloy (Figure 4.). It can be suggested that Ti presence in the eutectic regions in the microstructure may be effective on these results. In addition, the higher fraction of the eutectic structure in the of the Ti modified samples may be suggested for enhancing the hardness. While hardness value of the base ZAMAK-5 alloy was 96.9 ± 2.4 HB₁₀, hardness of Z5-0.01Ti was 100.2 ± 1.8 HB₁₀ and that of Z5-0.03Ti was 102.3 ± 2.8 HB₁₀.

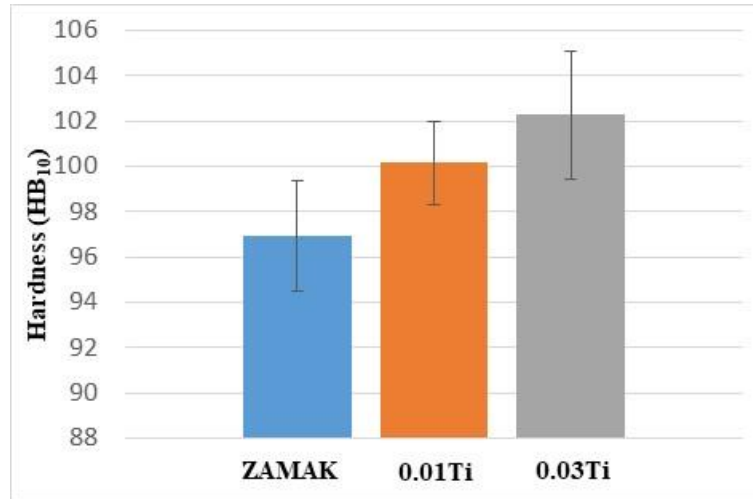


Figure 4. Hardness values of the samples.

3.4. Three-Point Bending Strength

Average and standard deviation values of the bending test results are presented in Figure 5 and Table 4. These values were obtained by averaging the results of 3 tests. It can be seen that Ti addition results in a slight difference in the 3-point bending stress-strain curves of the samples. Bending strength was determined as the highest stress attained in the bending test. Base sample and Z5-0.01Ti exhibited similar bending strength values. Bending strength of Z5-0.03Ti was higher than the bending strength values of the other samples. In the study of Ayday, ZA12 zinc alloy was microalloyed with B. The increase in the hardness and strength was attributed to the finer structure that was formed upon microalloying with B [9]. In the present study, the increase in the bending strength can be attributed to the decrease in the SDAS values and also to the increase in the amount of the eutectic structure, as a result of Al10Ti master alloy addition, as shown in Section 3.1. In addition, formation of TiZn₁₅ phase may have played a role in increasing the hardness and strength, as suggested in the literature [4,14]. However, this phase was not detected in the present study, most probably due to its low amount. Strain at maximum stress values appeared to be not dependent on the Ti amount of the samples.

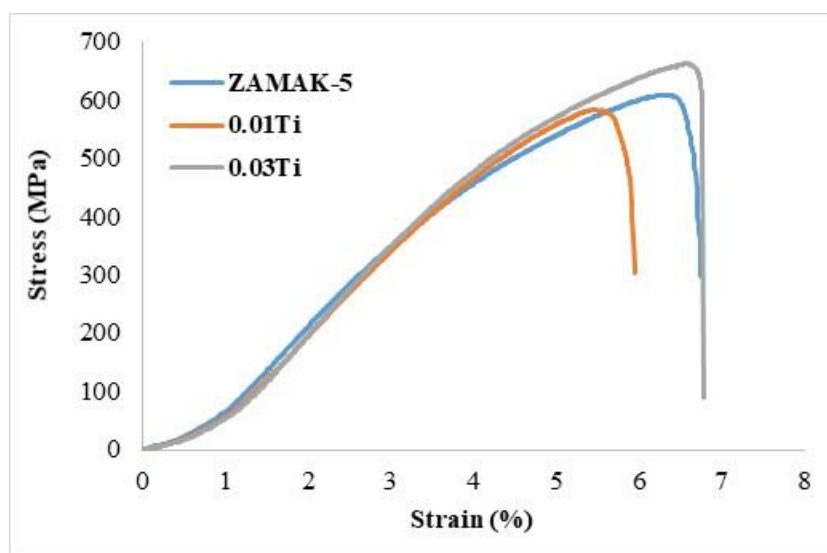


Figure 5. Stress-strain curves of the samples obtained by 3-point bending tests.

Table 4. Three-point bending strength and strain values of the samples.

Sample	Bending Strength (BS) (MPa)	Standard Deviation (BS)	Strain at Max. Stress (SaMS) (%)	Standard Deviation (SaMS)
ZAMAK-5	608.0	31.0	6.4	0.9
Z5-0.01Ti	583.3	48.4	5.5	1.3
Z5-0.03Ti	661.4	30.5	6.6	0.6

3.5. Compressive Strength

Average and standard deviation values of the compression test results are presented in Figure 6 and Table 5. These values were obtained by averaging the results of 3 tests. Compressive strength values of the samples were determined as described in E9- 89a ASTM standard. In the present study, they were determined at 50% strain from the stress-strain curves given in Figure 6 and reported as compressive strength at 50% strain in Table 5. Base alloy and Z5-0.01Ti sample exhibited similar values of 729.7 ± 8.0 and 719.6 ± 11.9 MPa, respectively. Z5-0.03Ti sample had a compressive strength at 50% strain value of 779.8 ± 7.5 MPa.

Compressive yield strength values of the samples were determined according to 0.02% offset method described in E9- 89a ASTM standard by using the enlarged initial portion of the stress-strain plot given in Figure 6. Z5-0.01Ti and Z5-0.03Ti had similar compressive yield strength (about 290MPa) which was higher than that of ZAMAK-5 (about 280MPa) (Figure 6 and Table 5). It can be considered that Ti presence provides this slight increase in the compressive strength. The higher slope of the curves in the Ti modified samples can be taken as an indication of higher elastic modulus of these samples, as compared to base ZAMAK-5.

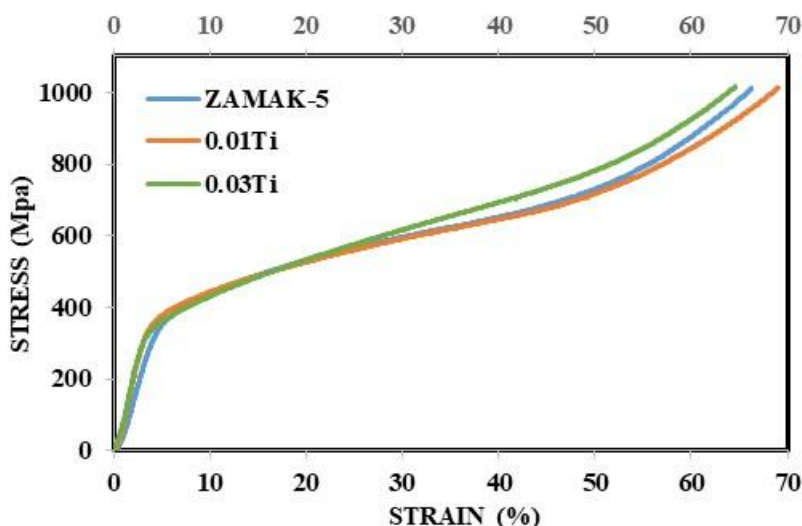


Figure 6. Stress-strain curves of the samples obtained by compression tests.

Table 5. Compressive yield strength and compressive strength at 50% strain values of the samples.

Sample	Compressive Yield Strength (CSY) (MPa)	Standard Deviation (CSY)	Compressive Strength at 50% Strain (CS50) (MPa)	Standard Deviation (CS50)
ZAMAK-5	280.3	4.5	729.7	8.0
Z5-0.01Ti	289.6	2.6	719.6	11.9
Z5-0.03Ti	290.0	5.0	779.8	7.5

4. CONCLUSION

In this study, effects of Ti microalloying on solidification temperature, microstructure, hardness, and bending and compressive strength of commercial ZAMAK-5 alloy were investigated. Modified alloys contained lower quantity of Ti than the added amount. Ti in the modified ZAMAK-5 was seen to increase with the increase in the added master alloy amount and alloying temperature. Liquidus temperature was 389 °C for ZAMAK-5, 386 °C for Z5-0.01Ti and 384 °C for Z5-0.03Ti samples. The amount of eutectic structure in the microstructure of the samples was found to increase with increasing amount of Al10Ti master alloy addition. The Al content of the samples was believed to be effective on the liquidus temperatures and on the amount of eutectic structure. As a result of EDS analyses, it was considered that Ti was mostly located on the eutectic regions. Addition of Ti resulted in a decrease in the SDAS values of ZAMAK-5. Z5-0.03Ti sample had higher bending strength than the other samples. Hardness and compressive strength values of samples which contained Z5-0.03 % Ti were higher than those of the base alloy. Obtained results show that with Ti-Al modification, ZAMAK-5 may be used for applications that require higher hardness and strength.

ACKNOWLEDGEMENTS

Authors thank to Akdeniz University Scientific Research Projects Coordination Unit for supporting this study with Project No: FYL-2015-587. Help of Prof. Dr. Yavuz Topkaya and Meta Nickel Cobalt Company on elemental analyses is acknowledged.

REFERENCES

- [1] Goodwin, E. F., and Pnikvar A. L. (1998). Engineering Properties of Zinc Alloys (3rd edition). USA: International Lead Zinc Research Organization, Inc., 1-9.
- [2] Campbell, J. (2011). Casting Handbook (1st edition). England: Elsevier Ltd., 255-260.
- [3] Barnhurst, R. J. (1990). ASM Handbook Volume 02 - Properties and Selection: Nonferrous Alloys and Special-Purpose. USA: ASM International, 1619.
- [4] Murray, J. L. (1983). The Al–Zn (aluminum-zinc) system. Bulletin of Alloy Phase Diagrams, 4, 55-73.
- [5] Azizi, A., and Haghghi, G. (2015). Fabrication of ZAMAK 2 alloys by powder metallurgy process. The International Journal of Advanced Manufacturing Technology, 77, 2059-2065.
- [6] Altınsoy, İ., and Kızılarıslan, A. (2016). Effect of Ti addition on microstructure of zamak-3 alloy. Proceedings of the 18th International Metallurgy & Materials Congress.
- [7] Sandlöbes, S., Wu, Z., Pradeep, K.G., and Korte-Kerzel, S. (2016). Precipitation and decomposition phenomena in a Zn-Al-Cu-Mg alloy. Materials Letters, 175, 27-31.
- [8] Wu, Z., Sandlöbes, S., Wu, L., Hu, W., Gottstein, G., and Korte-Kerzel S. (2016). Mechanical behavior of Zn–Al–Cu–Mg alloys: Deformation mechanisms of as-cast microstructures. Materials Science and Engineering A, 651, 675-687.
- [9] Ayday, A., Kurnaz, S. C., Uysal, Ü., and Pehlivan, H. (2023). Effect of boron addition on thermal and mechanical properties of cast ZA12 alloy. International Journal of Metalcasting, 17, 1-12.
- [10] Umashankar, M., and Annamalai, K. (2017). Investigation on Ni-modified ZA alloy for damping properties. Materials Today: Proceedings, 4, 10134-10137.
- [11] Veerabhadrapa, A., Kabadi, V. R., Genechari, S. M., and Chavan, V. R. (2017). Influence of Mn content on tribological wear behaviour of ZA-27 alloy. Materials Today: Proceedings, 4, 10927-10934.
- [12] Abdel-Hamid, A. A. (1992). Structure modification of the α' phase in Zn - Al cast alloys by microalloying. International Journal of Materials Research, 83, 314-320.
- [13] Morgan, S. W. K. (1985). Zinc and its alloys and compounds (1st edition). England: Ellis Horwood, 245.

- [14] Houghton, M.E., and Murray, M.T. (1983). An introduction to zinc alloys. *Metals Forum*, 6, 211-255.
- [15] Türk, A. (1996). Çinko-alüminyum esaslı ZA-8 alaşımında alaşım elementlerinin mekanik özelliklere ve mikroyapıya etkisi, Yayınlanmamış Doktora Tezi, İTÜ Fen Bilimleri Enstitüsü.
- [16] Durman, M., and Türk, A. (1996). Yeni çinko-alüminyum esaslı alaşımların geliştirilmesi, Tübitak, Proje No: Misag 41.
- [17] Aktuna, İ. (2019). İkincil eritmenin zamak alaşımlarının mikroyapı ve mekanik özellikleri üzerindeki etkilerinin incelenmesi, Yayınlanmamış Yüksek Lisans Tezi, Akdeniz Üniversitesi Fen Bilimleri Enstitüsü.
- [18] Vandersluis, E., and Ravindran, C. (2017). Comparison of measurement methods for secondary dendrite arm spacing. *Metallography Microstructure & Analysis* 6, 89-94.



RESEARCH ARTICLE

**ANTIBACTERIAL, ANTIFUNGAL, ANTIBIOFILM, ANTIOXIDANT, AND ANTICANCER
PROPERTIES OF METHANOL EXTRACTS OF SOME *ACANTHOLIMON BOISS*
(PLUMBAGINACEAE) SPECIES**

Maside Temiz BOSTANCI¹, Ali Savas BULBUL², Cihangir UYGUN³, Muhammed BEKMEZCI⁴,
Ramazan BAYAT⁵, Fatih SEN^{6,*}

¹Kahramanmaraş Sutcu Imam University, Faculty of Science and Letters, Department of Biology, Kahramanmaraş, Türkiye.
maside_temiz_bostanci@gmail.com, ORCID: 0000-0002-2625-6974

²Bayburt University, Faculty of Applied Sciences, Emergency and Disaster Management Division Bayburt, Türkiye
asavasbulbul@gmail.com, ORCID: 0000-0002-2200-7348

³Akedas Primary School, Kahramanmaraş, Türkiye. cihangiruygun3@gmail.com, ORCID: 0009-0000-0916-734X

⁴Sen Research Group, Department of Biochemistry, University of Dumlupınar, 43000 Kutahya, Türkiye
muhammedbekmezci42@gmail.com, ORCID: 0000-0003-3965-6333

⁵Sen Research Group, Department of Biochemistry, University of Dumlupınar, 43000 Kutahya, Türkiye
ramazanbayat@yandex.com, ORCID: 0000-0002-9763-1591

⁶Sen Research Group, Department of Biochemistry, University of Dumlupınar, 43000 Kutahya, Türkiye
fatihsen1980@gmail.com, ORCID: 0000-0001-6843-9026

Receive Date: 12.05.2023

Accepted Date: 26.07.2023

ABSTRACT

Therapeutic properties of plants have been used since the existence of mankind. To benefit from this feature, the discovery of the active components of plants has gained momentum today. One of these plant species is *Acantholimon Boiss*. This plant extract has antifungal, antimicrobial, and anticancer properties. In this article, antimicrobial, antifungal and antioxidant capacities and antibiofilm properties of *Acantholimon Boiss* plant extract on 15 bacterial and 2 fungal species were evaluated. Antimicrobial properties were evaluated by Agar Well Diffusion method. It was observed that the plants formed a zone diameter of 12-18 cm. Minimum Inhibition Concentration (MIC) and Minimum Bactericidal Concentration (MBC) tests were used to determine the minimum active property. Biofilms of almost all bacteria were reduced by 10-50% by *Acantholimon* species at doses of 8 mg/ml-16 mg/ml. For MCF-7 cells, the IC50 values for *A. acerosum subsp. brachystachyum* (Boiss.), *A. acenum var. balansae*, *A. armenum var. balansae* and *A. kotschyi* were 0.143 mg/ml, 0.63 mg/ml, 0.63 mg/ml, 0.63 mg/ml, 0.63 mg/ml, 0.63 mg/ml and 0.107 mg/ml, respectively. The same doses did not show a cytotoxic effect on HUVEC cell lines. With this article, it has given important results in terms of having a wide range of bacterial studies and examining its activities in fungi and cell lines. These findings suggest that extracts of *Acantholimon Boiss* species may be a potential source of natural medicines and antibacterial, antifungal, antibiofilm, antioxidant, and anticancer activities may support their therapeutic use.

Keyword: *Acantholimon* species; Anticancer activity; Antimicrobial activity; Antioxidant activity.

1. INTRODUCTION

Plants are highly valued in various businesses due to their fragrant, medicinal, aromatic, or therapeutic capabilities. Medical plants supply fundamental raw ingredients for a variety of businesses, including medicine, cosmetics, fragrance, and food [1]. The ancient scriptures and customary wisdom of numerous cultures demonstrate that people's search for plant benefits dates back to ancient times [2,3]. Most of the medications used today are derived from plants. Aspirin and quinine are two examples of common medications derived from plants. These medications are created by extracting active compounds in plants or by enhancing these components [3–5]. Almost every compound contains compounds with medical content. One of the plant species to be used for this purpose is *Plumbaginaceae* family. This family is a family of perennial (rarely annual) plants that prefer cold, dry, and saline habitats, usually in mountainous and coastal areas. Plants in the family may be herbs, shrubs, or semi-shrubs. The diversity and endemism of the plants in the family are highest in the cold and dry mountainous regions of Central Asia [6,7]. There are six breeds representative of the family in Türkiye and the East Aegean islands [8]. *Acantholimon* species is a plant of the genus *Plumbaginaceae*, which forms spiny cushions, flowers are simple or branched, flowers are arranged in two rows and leaves are almost always spiny [9]. The arid mountainous regions of southwest and northeast Asia are the most dominant regions of this genus. The genus contains many plants as endemic species [6,10]. Extracts of this plant species are known to exhibit very good inhibitory effects on a wide variety of bacteria, fungi, and different cell lines [11–14].

When the literature studies are examined, *Acantholimon austroiranicum*, *Acantholimon bracteatum* (Girard) Boiss., *Acantholimon gilliati*, *Acantholimon longiscapum*, *Acantholimon serotinum*, *Acantholimon scorpius*, and *Acantholimon chlorostegium* plants were tested for antimicrobial, antitumor, insecticide, cytotoxicity, liver protective, and antioxidant activity. Studies have shown that *Acantholimon* species have therapeutic properties [15–17].

The activity of these plants on various fungi is also frequently observed in the literature. One of the fungal species used in the study was *Candida albicans*. *Candida* species cause the majority of fungal-associated systemic bloodstream infections in intensive care units worldwide. Although *Candida albicans* is the most common and invasive species, non-*albicans* *Candida* species have become more prevalent in the last 20 years, leading to a decrease in the dominance of *Candida albicans*. However, there is still a significant risk of pathogens [18,19]. Another fungus, *Candida parapsilosis*, can build biofilms on central venous catheters and other surgically implanted devices. Additionally, when critical care patients get complete parenteral nutrition, *C. parapsilosis* grows quickly. Particularly in underweight newborns and malnourished youngsters, this poses a danger of mortality. Although infections with *C. parapsilosis* typically have lower rates of morbidity and mortality than infections with *C. albicans*, some clinical isolates of this species are known to be less susceptible to echinocandins, and in some regions, resistance to azole therapy has also been recorded [19–21].

Although some studies with *Acantholimon* species are included in the literature, they have generally covered a limited area. Accordingly, Karimzadeh et al. (2020) reported that the *Acantholimon serotinum* plant showed very strong cytotoxic activity on Breast cancer (MDA-MB231). It is reported to have a medically traditional use among people in Asia [22,23]. The biological activities of extracts and some fractions of the species *Acantholimon lycopodioides* were studied by Parvez et al. (2020)[24]. In the study, they reported that *Acantholimon* species have important biological activities in terms of antimicrobial, antioxidant, anticancer, and hepatoprotective properties. Soltanian et al.

(2020) evaluated the cytotoxicity, free radical scavenging activity, and antimicrobial activity against some bacterial species of three species belonging to the genus *Acantholimon* on various cell lines and found quite ambitious results [14]. Parvez et al. (2020) emphasized that *Acantholimon lycopodioides* have important biological activities in terms of antimicrobial, antioxidant, and anticancer properties [13].

Within the framework of these aims, in this study, the activities of *Plumbaginaceae* family members on various bioactive and anticancer properties on a wide variety of bacterial groups, fungal groups, and cell lines were monitored. The fact that a wide range of bacterial groups was tested in the study, as well as the experiments with fungi and cell lines, were carried out in the same study, the results of the study will have a wide range of effects. In addition, since biological activity and cell culture studies on *Acantholimon* species are rare, the study is intended to fill a very important gap in the scientific literature.

2.MATERIAL AND METHOD

2.1. Plant Samples

Acantholimon species which are used in this study were collected by Dr. Cihangir Uygun from different locations on Ahir Mountain in Kahramanmaras (**Table:1**).

Table 1. Features, Locations, and Photos of Plants.

Plants	Morphological Features	Location
<i>Acantholimon acerosum</i> subsp. <i>brachystachyum</i>	Monomorphic leaf, 7-8 mm in the outer bracte and the inner bracte are equal. Calix is in the form of a 12-14 mm long pillow [9].	Kahramanmaras Ahir Mountain, Transmitter Antenna Zone.1800m Altitude, Habitat properties Alpin region, step, intense windy hill.
<i>Acantholimon armenum</i> var. <i>balansae</i>	In the outer bracte, it is 8-9 mm long. Leaf width 1.5 mm, exterior bracte is equal to the internal bracte or slightly shorter [25].	Kahramanmaras Ahir Mountain, Sulutarla around the region. 1600m altitude. Habitat properties Step, sub- alpin- alpin.
<i>Acantholimon kotschyi</i>	Linear 1.5-4 cm x 1-2 mm leaf, bracte equal 5-6 mm, calix 1-1.4 mm [26].	Kahramanmaras Ahir Mountain Summit, Karagol around the region,1600m altitude. Habitat properties, Step.
<i>Acantholimon libanoticum</i>	Monomorphic, 1.5-2.5 cm leaf, calix lop, and funnel-like form of 12-13 mm [9,26].	Kahramanmaras Ahir Mountain, Kucukgol around the region, 1650m altitude. Habitat Properties Step.

2.2. Extract Preparation

The technology developed by Comlekcioglu and Aygan in 2020 was modified to create plant extracts. [27]. The above-ground parts of the plants were crushed into a powder with a magnetic grinder. The powder was added to the sample at 1g/10 ml of methanol. After this period, the mixture was applied in an ultrasonic water bath for 30 minutes. After half an hour, the extracts were filtered into another

container, the filtered portion was returned to the bottle, and 1g/10ml methanol was added. There have been three iterations of these actions. After the extraction process, the liquid extracts were centrifuged and allowed to dry.

2.3. Antimicrobial Activity

Revitalized bacteria in the range of 0.5-1 were utilized. Bacteria were seeded into Muller Hilton Agar using sterile exchanges. 50 µl from each plant sample, *A.armenum* var. *balansae*, *A.libanoticum* together, *A.kotschyi*, and *A.acerosum* subsp. *brachystachyum* together were tested. Bacteria inoculated on the Petri plate were incubated at 25 °C for two days and fungi at 37 °C for 18 to 24 hours. After incubation, the zone diameters on the Petri plates were measured with a ruler and recorded with an acetate pen.

2.4. Minimum Inhibition Concentration (MIC)

MIC was used to determine the lowest concentration of a material that would inhibit bacterial growth. 96 Well plates were used for this test. Nutrient Broth 100µl is put on each well of Well plates. Then 100 µL extracts were placed in the first well and mixed homogeneously. By taking 100 µl, this technique was repeated up to 6 wells. Wells 7 and 8 served as controls. OD values (600 nm) were obtained after 18 to 24 hours of incubation at 37 °C.

2.5. Minimum Bactericidal Concentration (MBC)

The MIC test was used to determine minimum inhibitory concentrations (MBC). After incubation, samples from plate wells without bacterial growth for MBC were zigzag injected into Muller Hilton. After injection, the plates were incubated at 37 °C for 18 to 24 hours. As a result of the experiment, minimal bactericidal doses that killed 99.9% of the microorganisms were obtained.

2.6. Antibiofilm Activity

Literature was taken into consideration for the determination of antibiofilm activity [28]. Plate wells were empty after incubation. The distilled water was then cleaned and allowed to air dry. The dried wells received 130 µl of 95 percent methanol, which was then poured into them and allowed to fix for 15 minutes before the methanol was drained and the plates were allowed to dry once again. The dry microplate wells were filled with 125 µl of 0.1 percent crystal violet solution and left at room temperature for 10 minutes. The plate was given a second distilled water washing after drying for ten minutes. Gram-positive bacteria were present in the drying wells, therefore, to dissolve the adhering bacteria, 200 µl of a 33 percent glacial acetic acid solution was applied. 200 µl of a 33 percent glacial acetic acid solution and 200 µl of a 95 percent ethanol solution, correspondingly, were poured into the wells containing gram-positive bacteria and gram-negative bacteria, respectively, and allowed for 15 minutes to dissolve the adhering bacteria (eq. 1).

$$\% \text{ Decrease: } ((C-Co)/C) \times 100 \quad (1)$$

C: Positive control sample. Co: Test sample.

2.7. Antioxidant Activity

Using the Blois (1958) [29] approach, a 0.1 mM DPPH (2,2-diphenyl-1-picrylhydrazil) solution was made and added to the antioxidant test apparatus. We prepared and vortexed plant extracts with concentrations of 1 mg/ml, 0.1 mg/ml, 0.01 mg/ml, and 0.001 mg/ml. 150 µl of DPPH and 50 µl of extract were applied to the wells of a 96 cm plate. The wells received 200 µl of DPPH as a blank, 50

µl of methanol, and 150 µl of DPPH. An ELISA reader was used to read the sample at 517 nm after it had been incubated for 30 minutes at room temperature and in the dark. The percentage of radical scavenging was estimated from the absorbance values obtained after the spectrophotometric tests using the following formula. The GraphPad Prism 8 software and IC₅₀ values were used to determine the percentage findings of the three repeats (eq. 2).

$$\text{Radical sweep \%} = (A_0 - A) / A_0 \times 100 \quad (2)$$

A: AbsSample517nm A₀: AbsBlank517nm

2.8. Anticancer Activity (MTT Method)

The study was also tested in comparison with the MCF-7 Breast cancer cell line and Human Umbilical Vein Endothelial Cells (HUVEC).

2.8.1. Preparing the medium

The completed medium was prepared by adding the components in the following ratio to the medium required to culture the cells.

- 1- 445 ml DMEM (Dulbecco's Modified Eagle's Medium),
- 2- 50 ml FBS (Fatal Bovine Serum),
- 3- 5 ml PS(Penicillin-Streptomycin).

The media content prepared for MCF-7 cells was added to the content of 0.05 mg of insulin. The prepared completed medium was filtered through a 0.20 µm filter before use and stored in the refrigerator at +4 °C.

2.8.2. Cell passage and freezing

Cells stored at 80°C were thawed under laboratory conditions for use. The media and cells were transferred to falcon tubes of 15 cm³ volume and centrifuged at 1000 rpm for 5 minutes. After centrifugation, the supernatant was aspirated to remove dead cells and wastes and 2 ml of the completed medium suitable for each cell was carefully pipetted onto the pellet. Cells were transferred to 75 cm² flasks and 10 ml of complete medium was added. The flask was placed in an incubator containing 5% CO₂ at 37°C. The morphological structure and density of the cells were monitored and the cell media was changed 2-3 times during the week. The passage was performed to cover the cell density of the flask surface. In the incubation step of this procedure, the medium was first aspirated from the cell flask. After PBS was added, the flask surface was washed and aspirated, the flask was filled. Following this step, 2/3 ml trypsin was injected and the live cells adhering to the flask surface were incubated for 5 minutes and separated. After incubation, a microscope was used to examine the detachment of the cells. The mixture was poured into a 3 ml flask and centrifuged at 1000 rpm for 5 minutes to separate the cells. From the absorbance values obtained after spectrophotometric tests, the percentage of radical scavenging was estimated using the following formula. A further 10 ml of prepared medium was poured into a new flask containing the cells and then placed in an incubator containing 5% CO₂ at 37 °C. After this procedure, the cell density for transplantation was determined.

2.8.3. Cell counting and transplantation

The completed medium was added after the cells had been incubated, and they were then withdrawn, centrifuged, and treated with PBS and Trypsin at rates appropriate for counting the cells during the passage process. To count the cells in the Thoma slide, 50 µl of Trypan Blue dye was added to 50 µl of Eppendorf and 50 µl of cell suspension. We counted the divisions on the slide and computed the average number of cells. Each well of the Well Plate would hold 5,000 cells for the duration of the experiment. From the prepared suspension, the necessary cell was obtained, and it was then added to the working volume with the prepared medium. A 100 µl plate's wells are occupied by the cells. After being placed on the plate, the cells were incubated for 24 hours at 37°C with 5 percent CO₂.

2.8.4. Preparation of plant concentrations and application to cells

By diluting with the finished medium, concentrations of 10, 10-1, 10-2, and 10-3 from the plant extract were created. The respective wells were filled with vortexed plant concentrations, 100 µl was added and then the plate was incubated once more. This technique was repeated three times with three different controlled analyses of the experiments.

2.8.5. Control of cell vitality by MTT method

Before staining, MTT stain was made up at a rate of 5 mg/ml. By limiting direct light in the cabin, the prepared paint is filtered. The remaining Well plate cabinet from the incubator was stolen, and the functional supplies within were sucked. Then, 10 µl of the ready-made MTT paint was added to each well, and the mixture was allowed to incubate for 3–4 hours. 100 µl of DMSO was added to the wells after the paint had been aspirated during incubation. An ELISA reader operating at a wavelength of 570 nm read the plate after it had been incubated for 5 minutes. Using the GraphPad Prism 8 application, the study results were assessed.

2.8.6. Statistical analysis

Statistical analyzes were performed using the software application GraphPad Prism version 8. Statistical differences between cell proliferation and apoptosis studies were calculated using the two-way ANOVA test. IC₅₀ values were determined using the GraphPad tool. P values below 0.05 were considered statistically significant.

3. RESULTS AND DISCUSSION

3.1. Antimicrobial Activity, MIC-MBC Results

Plant extracts in terms of antibacterial properties *Enterobacter aerogenes* ATCC 13048, *Salmonella infantis*, *Klebsiella pneumoniae*, *Pseudomonas aeruginosa* DSMZ 50071, *Salmonella kentucky*, *Enterococcus faecalis* ATCC 29212, *Listeria innocua*, *Salmonella enteritidis* ATCC 13075, *Enterococcus durans*, *Salmonella typhimurium*, *Staphylococcus aureus* ATCC 25923, *Staphylococcus epidermidis* DSMZ 20044, *Bacillus subtilis* DSMZ 1971, *Escherichia coli* CFAI ATCC 25922 and *Serratia marcescens* ATCC 13048 bacteria tested against strains. It has also been tested on antifungal properties *Candida parapsilosis* and *Candida albicans*. In line with the findings; *Acantholimon kotschy* and *Acantholimon acerosum* subsp. *brachystachyum* methanol extracts showed a zone diameter effect of 12-17 mm on *Pseudomonas aeruginosa*, *Salmonella enteritidis*, and *Escherichia coli* species. *Acantholimon libanoticum* and *Acantholimon armenum* var. *balansae* methanol extracts showed a zone diameter of 14-18 mm on *Klebsiella pneumoniae*, *Listeria innocua*, *Enterococcus durans*, and *Salmonella typhimurium* species in addition to *Pseudomonas aeruginosa*, *Salmonella enteritidis* and *Escherichia coli* species (Table:2).

Table 2. Antibacterial activity zone diameters of *Acantholimon* plant extracts (mm).

Bacteria	<i>A. kotschy</i>	<i>A. libanoticum</i>	<i>A. acerosum</i> subsp. <i>brachystachyum</i>	<i>A. armenum</i> var. <i>balansae</i>	AZM 10
<i>Enterobacter aerogenes</i> ATCC 13048	-	-	-	-	17
<i>Salmonella infantis</i>	-	-	-	-	19
<i>Klebsiella pneumoniae</i>	-	17±1	-	18±1,73	14
<i>Pseudomonas aeruginosa</i> DSMZ 50071	15,33±0,57	16,66±0,57	14,66±0,57	15,66±2,08	20
<i>Salmonella kentucky</i>	-	-	-	-	18
<i>Enterococcus faecalis</i> ATCC 29212	-	-	-	-	17
<i>Listeria innocua</i>	-	16±0	-	15,33±0,57	20
<i>Salmonella enteritidis</i> ATCC 13075	12,66±0,57	15,33±0,57	14,33±0,57	16±0	15
<i>Enterococcus durans</i>	-	15±1	-	14,33±0,57	18
<i>Salmonella typhimurium</i>	-	15,33±0,57	-	15,33±1,15	20
<i>Staphylococcus aureus</i> ATCC 25923	-	-	-	-	19
<i>Staphylococcus epidermidis</i> DSMZ 20044	-	-	-	-	18
<i>Bacillus subtilis</i> DSMZ 1971	-	-	-	-	13
<i>Escherichia coli</i> CFAI ATCC 25922	17±1	18,33±1,52	17±1	18±1	13

<i>Serratia marcescens</i> ATCC 13048	-	-	-	-	17
--	---	---	---	---	----

(-): No inhibition zone was formed. AZM: Azithromycin 10 mg/ml

Plant extracts have been tested on *Candida albicans* and *Candida parapsilosis*. The tests were studied 3 times and the arithmetic means of the findings and the standard deviation value were shown in the tables. All the extracts yielded near-control findings on both species. Among the species, the most effective antifungal effects were *A.acerosum* subsp. *brachystachyum* and *A.armenum* var. *balansae* plants (Table: 3).

Table 3. Antifungal activity zone diameters (mm) in fungal species of plant extracts.

Fungus	<i>A. kotschyi</i>	<i>A.libanoticum</i>	<i>A. acerosum</i> subsp. <i>brachystachyum</i>	<i>A.armenum</i> var. <i>balansae</i>	K
<i>Candida albicans</i>	17,66±0,57	18,66±1,15	19,33±0,57	19,33±0,57	25
<i>Candida parapsilosis</i>	19,66±1,15	20,33±1,15	21,33±0,57	21,33±0,57	18

(K): Control Fungus Syrup

Dilution laws were used in conjunction with the MIC technique to determine the lowest inhibitory concentrations. Decreasing concentrations of the same amount of bacteria were tested. The MIC was calculated as the first concentration to inhibit colony formation. Bacteria can be inhibited by some *Acantholimon species*, usually at doses of 2 mg/ml to 4 mg/ml. In the inhibitory concentration test results on fungi, two *Candida species* were inhibited by *Acantholimon species* at concentrations between 2 and 4 mg/ml. At doses of 4 mg/ml to 8 mg/ml, *Candida* fungal species have demonstrated a fatal impact on *Acantholimon* plants.

3.2. Antibiofilm Activity Results

Antibiofilm; Biofilm creation is characterized as an activity blocking feature. The biofilm surface reduction percentages of the plants were tested by the crystal violet method.

Acantholimon kotschyi showed biofilm reduction activity most on *Enterococcus durans* at a concentration of 16 mg/ml. While *Acantholimon kotschyi* extract did not exert any effect on the bacteria *Salmonella kentucky*, *Listeria innocua*, *Staphylococcus epidermidis*, *Escherichia coli*, and *Staphylococcus aureus*, it did act on other microorganisms in proportion to concentrations. The highest concentration used, 16 mg/ml plant concentration, was capable of blocking more than 50% biofilm areas on *Enterobacter aerogenes*, *Salmonella infantis*, *Klebsiella pneumoniae*, *Enterococcus durans* and *Bacillus subtilis* bacteria.

Acantholimon libanoticum showed a directly proportional reduction effect on biofilm field formation at concentrations of 16 mg/ml and 8 mg/ml. *Salmonella enteridis*, *Enterococcus durans*, *Salmonella typhimurium*, and *Staphylococcus epidermidis* species have shown approximately 50% biofilm surface reduction efficacy. *Salmonella infantis*, *Listeria innocua*, *Escherichia coli*, and *Serratia marcescens*

did not show any reduction effect on bacterial species, and no effect was observed in all bacterial species at a concentration of 4 mg/ml.

All concentrations on *Acantholimon armenum var. balansae*, *Escherichia coli*, and *Serratia marrescens* bacteria also showed no biofilm surface reduction effect. It had a reduction effect of close to 40% on *Salmonella kentucky*, *Salmonella typhimurium*, *Salmonella enteritidis*, *Staphylococcus epidermidis* bacteria, and about 30% on *Enterobacter aerogenes*, *Salmonella infantis*, *Klebsiella pneumoniae*, *Listeria innocua*, and *Enterococcus durans* bacteria.

Acantholimon acerosum subsp. brachystachyum showed an effect on biofilm field formation in microorganisms tested other than *Salmonella infantis* and *Listeria innocua* bacteria at 16 mg/ml, 8 mg/ml, 4 mg/ml, and 2 mg/ml concentrations. The tested concentration of 16 mg/ml showed the highest reduction effect with 63.45% on *Escherichia coli*, followed by 57.26% on *Salmonella kentucky*. The concentration of 16 mg/ml shows effects between 40-10% in other bacteria. It tended to reduce biofilm on the bacterium *Bacillus subtilis* by over 30% at all concentrations. All the findings were directly proportional to the concentrations tested, and *Acantholimon acerosum subsp. brachystachyum* was the plant that gave the most reduction tendency to microorganisms tested among the *Acantholimon* species.

3.3. Antioxidant Activity Results

4 different concentrations (1 mg/ml, 0.1 mg/ml, 0.01 mg/ml, and 0.001 mg/ml) were tested 3 times by DPPH (2,2-diphenyl-1-picrylhydrazyl) Radical Sweep Method. The plants whose antioxidant capacities were tested by the DPPH method created graphs by calculating the average values of the three studies studied and IC_{50} values were calculated using the GraphPad program. Ascorbic Acid data from the antioxidant activity findings of Tozyilmaz et al. were taken as a reference as the standard substance [30]. Figure 1 shows the graph of IC_{50} values of antioxidant activity of *Acantholimon* species.

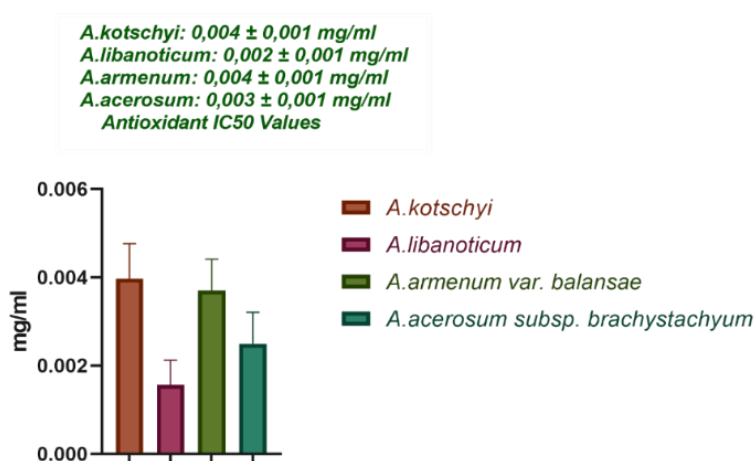


Figure 1. Graphic of IC_{50} values of antioxidant activity of *Acantholimon* species.

When the DPPH radical scavenging percentage values of *Acantholimon kotschyi* concentrations were examined, the concentrations of 1 mg/ml and 0.1 mg/ml used showed 73% and 75% effects. Compared to these two concentrations, which had an effect of over 70%, the other two concentrations tested (0.01 mg/ml and 0.001 mg/ml) also showed similar values despite the decrease in the plant extract. When the antioxidant capacity of *Acantholimon kotschyi* is examined by considering the effect values of 41% and 32%.. When the DPPH Radical sweep percentage values of *Acantholimon libanoticum* methanol extract were examined, the plant tested at a concentration of 1 mg/ml showed a 100% effect. The concentration of 0.1, 0.01 mg/ml, and 0.001 mg/ml showed a radical sweeping effect in direct proportion to the decrease in plant concentration. These findings obtained as a result of repetitions show that the antioxidant capacity of the *Acantholimon libanoticum* plant is high.

When the DPPH radical sweeping percentage values of *Acantholimon armenum* var. *balansae* methanol extracts are examined, it is seen that the first two high concentrations of the plant used (1 mg/ml and 0.1 mg/ml) show an average radical sweeping effect of 75%. At concentrations of 0.01 and 0.001, it gave a radical sweep percentage directly proportional to plant concentration. An examination of the *Acantholimon armenum* var. *balansae* DPPH radical sweep chart showed that the plant had a good antioxidant capacity.

When the DPPH radical sweep percentage values of *Acantholimon acerosum* subsp. *brachystachyum* methanol extracts were examined, 1 mg/ml concentration showed 76% radical sweeping effect, while 0.001 mg/ml concentration showed 34% sweeping effect. In line with this proportion, *Acantholimon acerosum* subsp. *brachystachyum* extract shows that the antioxidant capacity is good.

3.4. Anticancer Activity Results

Acantholimon kotschyi, *Acantholimon libanoticum*, *Acantholimon armenum* var. *balansae*, and *Acantholimon acerosum* subsp. *brachystachyum* methanol extracts on HUVEC and MCF-7 cell lines were tested by the MTT method in the concentration range of 0.01-10 mg/ml in a cell culture medium. The test results were calculated statistically using the GraphPad Prism 8 program ($p < 0.05$). IC_{50} values of cell viability rates of plant extracts of *Acantholimon* species at different concentrations to HUVEC cells in Figure 2a and Figure 2b.

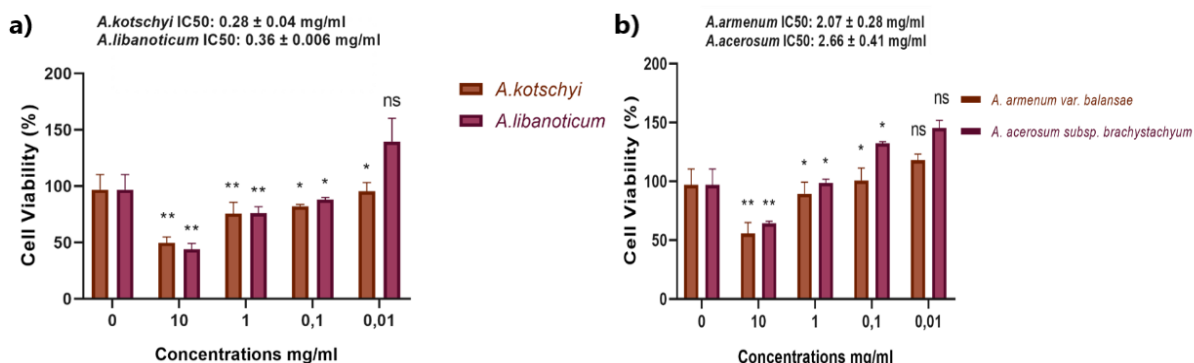


Figure 2. a) *Acantholimon kotschyi* and *Acantholimon libanoticum* HUVEC Cell Line Vitality Graph and IC_{50} Values. b) *Acantholimon armenum* var. *balansae* and *Acantholimon acerosum* subsp. *brachystachyum* HUVEC Cell Line Vitality Graph and IC_{50} Values.

Figure 2a. and Figure 2b. show the cell viability rates of plant extracts of *Acantholimon* species applied to HUVEC cells at different concentrations (0.01-10 mg/ml). The decrease in cell viability appears to be associated with concentrations. HUVEC cell line IC₅₀ values were calculated as 0.28 mg/ml for *A.kotschyi*, 0.36 mg/ml for *A.libanoticum*, 2.07 mg/ml for *A.armenum* var. *balansae* and 2.66 mg/ml for *A.acerosum* subsp. *brachystachyum*. IC₅₀ values of cell viability rates of plant extracts of *Acantholimon* species at different concentrations to HUVEC cells in Figure 3a and Figure 3b.

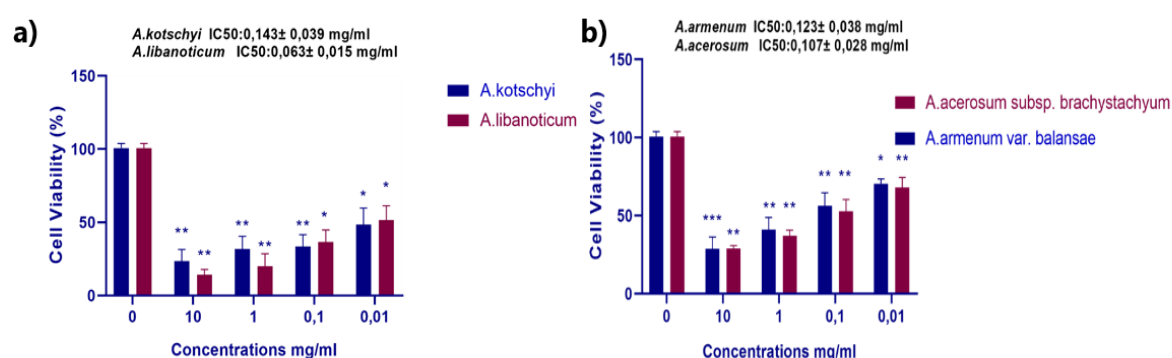


Figure 3. a) *Acantholimon kotschyi* and *Acantholimon libanoticum* MCF-7 Cell Line Vitality Graph and IC₅₀ Values. **b)** *Acantholimon armenum* var. *balansae* and *Acantholimon acerosum* subsp. *brachystachyum* MCF-7 Cell Line Vitality Graph and IC₅₀ Values.

Figure 3a. and Figure 3b. show the cell viability rates of plant extracts of *Acantholimon* species applied to MCF-7 cells at different concentrations (0.01-10 mg/ml). Analysis of the IC₅₀ values on the HUVEC and MCF-7 cell lines revealed that the tested *Acantholimon* species exhibited cytotoxicity on the MCF-7 cell line but not on the HUVEC cell line.

4. CONCLUSION

Plants are increasingly being used as therapeutic agents, and their significance in this area is rising. Very significant research has been conducted on the use of plants as microbiological agents and as one of the active ingredients in anti-cancer medications. In this study, the use of *Acantholimon Boiss.* species as biologically active agents were investigated. According to the results, according to the findings of the antibiofilm activity test by crystal violet method; *Acantholimon kotschyi* showed a biofilm surface reduction effect on *Enterococcus durans* at a concentration of 16 mg/ml. It blocked more than 50% biofilm area on *Enterobacter aerogenes*, *Salmonella infantis*, *Klebsiella pneumoniae*, *Enterococcus durans*, and *Bacillus subtilis* bacteria. *Acantholimon libanoticum* also reduced the biofilm surface by approximately 50% on *Salmonella enteridis*, *Enterococcus durans*, *Salmonella typhimurium*, and *Staphylococcus epidermidis* species. In addition, all concentrations reduced the biofilm surface on *Acantholimon armenum* var. *balansae*, *Escherichia coli* and *Serratia marrescens* bacteria. However, on other bacteria, it decreased by 30-40% in proportion to the concentrations. *Acantholimon acerosum* subsp. *brachystachyum* formed biofilms on microorganisms other than *Salmonella infantis* and *Listeria innocua* in the tested concentration range of 2 to 16 mg/ml. In

addition to this effect obtained in bacterial species, its activity in cell lines was also observed quite well. It was observed that the decrease in cell viability was related to the concentrations of plant extracts of *Acantholimon species* in the range of 0.01-10 mg/ml applied to HUVEC cells. Analysis of the IC50 values on the HUVEC and MCF-7 cell lines revealed that the tested *Acantholimon species* exhibited cytotoxicity on the MCF-7 cell line but not on the HUVEC cell line.

In line with these data, it was determined that the study plants within the *Acantholimon species* have important biological activities and show similar properties to other species. In this study, antibacterial, antifungal, and cell line assays of local plant sources were carried out together and biological agent activities were emphasized. The results provided important contributions to the literature to emphasize the biological activity of *Acantholimon* plant species.

ETHICS APPROVAL AND CONSENT TO PARTICIPATE

This article does not contain any studies with human participants or animals performed by any of the authors.

CONSENT FOR PUBLICATION

Authors accept the publication policy of the journal.

AVAILABILITY OF DATA AND MATERIAL

None

COMPETING INTERESTS

None

FUNDING

None

AUTHORS' CONTRIBUTIONS

M.T.B, A.S.B., C.U.,M.B., R.B., and F. S. organized all experiments and wrote the manuscript. M.T.B., and A.S.B. performed all experiments and characterizations.

ACKNOWLEDGMENTS

This article is derived from Maside Temiz Bostanci's master's thesis accepted at Kahramanmaraş Sütçü İmam University in 2021.

REFERENCES

- [1] Jaleel, C.A., Sathiya, S., Karthikeyan, B., Jaleel, A., Azooz, M.M., and Iqbal, M., (2008). Antibiogram of *Catharanthus roseus* Extracts. *Global Journal of Molecular Sciences*. 3 (1), 1–07.

- [2] Saroya, A.S., (2011). Herbalism, phytochemistry and ethnopharmacology. *Herbalism, Phytochemistry and Ethnopharmacology*. 1–430.
- [3] Bagetta, G., (2012). Herbal medicines : development and validation of plant-derived medicines for human health. 478.
- [4] Saad, B., Zaid, H., Shanak, S., and Kadan, S., (2017). Introduction to Medicinal Plant Safety and Efficacy. *Anti-Diabetes and Anti-Obesity Medicinal Plants and Phytochemicals*. 21–55.
- [5] Pandey, M., Debnath, M., Gupta, S., and Chikara, S.K., (2011). Phytomedicine: An ancient approach turning into future potential source of therapeutics. *Journal of Pharmacognosy and Phytotherapy*. 3 (3), 27–37.
- [6] Kubitzki, K., (1993). *Plumbaginaceae. Flowering Plants, Dicotyledons*. 523–530.
- [7] Chrtek, J., (1984). P. H. Davis (ed.) *Flora of turkey and the east aegean Islands*. Vol. 7. *Folia Geobotanica et Phytotaxonomica*. 19 (3), 322–322.
- [8] Bokhary, H.A., Suleiman, A.A.A., Basalah, M.O., and Parvez, S., (1987). Chemical Composition of Desert Truffles from Saudi Arabia. *Canadian Institute of Food Science and Technology Journal*. 20 (5), 336–341.
- [9] Doğan, M. and Akaydin, G., (2005). A new species of *Acantholimon* Boiss. sect. *Glumaria* Boiss. (*Plumbaginaceae*) from Elaziğ, Turkey. *Botanical Journal of the Linnean Society*. 149 (3), 351–356.
- [10] Alev Ateş, M., Kaptaner İğci, B., Selçuk Körüklü, T., Fişne, A., and Aytaç, Z., (2019). Morphologic, Palynologic, and Phylogenetic Relationships of *Acantholimon* Species (*Plumbaginaceae*) Sharing Similar Habitats. *Comm. J. Biol.* 3 (1), 48–52.
- [11] Parvez, M.K., Basudan, O.A., Noman, O.M., Al-Dosari, M.S., and Alqasoumi, S.I., (2020). The first bioactivity studies of *Acantholimon lycopodioides* from high altitude Karakoram-Himalayan desert. *Saudi Journal of Biological Sciences*. 27 (10), 2514–2520.
- [12] Pasdaran, A., Sarker, S.D., Nahar, L., and Hamed, A., (2019). Chemical Composition, Antibacterial, Insecticidal and Anti-Oxidant Activities of Three *Acantholimon* Species (*A. atropatanum*, *A. gilliatii* and *A. tragacanthium*). *The Natural Products Journal*. 10 (3), 272–278.
- [13] Parvez, M.K., Basudan, O.A., Noman, O.M., Al-Dosari, M.S., and Alqasoumi, S.I., (2020). The first bioactivity studies of *Acantholimon lycopodioides* from high altitude Karakoram-Himalayan desert. *Saudi Journal of Biological Sciences*. 27 (10), 2514–2520.
- [14] Soltanian, S., Sheikhabaei, M., Mirtadzadini, M., and Khandani, B.K., (2020). Evaluation of anticancer, antioxidant and antibacterial properties of methanol extract of three *Acantholimon* Boiss. species. *Avicenna Journal of Phytomedicine*. 10 (6), 641.

- [15] Goorani, S., Shariatifar, N., Seydi, N., Zangeneh, A., Moradi, R., Tari, B., et al., (2019). The aqueous extract of *Allium saralicum* R.M. Fritsch effectively treat induced anemia: experimental study on Wistar rats. *Oriental Pharmacy and Experimental Medicine*. 19 (4), 403–413.
- [16] Nasiri, E., Naserirad, S., Lashgari, A.P., Gazor, R., Mohammadghasemi, F., and Roushan, Z.A. (2016). Hepatoprotective effect of *Acantholimon bracteatum* (Girard) Boiss. on formaldehyde-induced liver injury in adult male mice. *Research Journal of Pharmacognosy (RJP)*. 3 (3), 55–61.
- [17] Gazor, R., Asgari, M., Pasdaran, A., Mohammadghasemi, F., Nasiri, E., and Roushan, Z.A., (2017). Evaluation of Hepatoprotective Effect of *Acantholimon Gilliati* Eerial Part Methanolic Extract. *Iranian Journal of Pharmaceutical Research : IJPR*. 16 (Suppl), 135.
- [18] Tóth, R., Nosek, J., Mora-Montes, H.M., Gabaldon, T., Bliss, J.M., Nosanchuk, J.D., (2019). *Candida parapsilosis*: From genes to the bedside. *Clinical Microbiology Reviews*. 32 (2).
- [19] Mayer, F.L., Wilson, D., and Hube, B., (2013). *Candida albicans* pathogenicity mechanisms. 4 (2), 119–128.
- [20] Bonassoli, L.A., Bertoli, M., and Svidzinski, T.I.E., (2005). High frequency of *Candida parapsilosis* on the hands of healthy hosts. *Journal of Hospital Infection*. 59 (2), 159–162.
- [21] Tóth, R., Nosek, J., Mora-Montes, H.M., Gabaldon, T., Bliss, J.M., Nosanchuk, J.D., et al. (2019) *Candida parapsilosis*: From genes to the bedside. *Clinical Microbiology Reviews*. 32 (2).
- [22] Angmo, K., Adhikari, B.S., and Rawat, G.S., (2012). Changing aspects of traditional healthcare system in western Ladakh, India. *Journal of Ethnopharmacology*. 143 (2), 621–630.
- [23] Abbas, Z., Khan, S.M., Alam, J., Khan, S.W., and Abbasi, A.M., (2017). Medicinal plants used by inhabitants of the Shigar Valley, Baltistan region of Karakorum range-Pakistan. *Journal of Ethnobiology and Ethnomedicine*. 13 (1), 1–15.
- [24] Parvez, M.K., Basudan, O.A., Noman, O.M., Al-Dosari, M.S., and Alqasoumi, S.I., (2020). The first bioactivity studies of *Acantholimon lycopodioides* from high altitude Karakoram-Himalayan desert. *Saudi Journal of Biological Sciences*. 27 (10), 2514–2520.
- [25] Doğan, S., Turan, P., Doğan, M., Arslan, O., and Alkan, M., (2007). Partial characterization of peroxidase from the leaves of thymbra plant (*Thymbra spicata* L. var. *spicata*). *European Food Research and Technology*. 225 (5–6), 865–871.
- [26] Cullen, J. (James), Knees, Sabina., Cubey, H.S., and Shaw, J.M.H., (2011). *The European garden flora, flowering plants : a manual for the identification of plants cultivated in Europe, both out-of-doors and under glass.*
- [27] Çömlekcioğlu, N. and Aygan, A., (2020). Farklı Tekniklerle Elde Edilen *Hibiscus sabdariffa* L. Özüünün Yağ Asitleri, Biyoaktif İçeriği ve Antimikrobiyal Aktivitesi. *Turkish Journal of Agriculture - Food Science and Technology*. 8 (12), 2723–2728.

- [28] Merritt, J.H., Kadouri, D.E., and O'Toole, G.A., (2006). Growing and Analyzing Static Biofilms. *Current Protocols in Microbiology*. 00 (1),.
- [29] Blois, M.S., (1958). Antioxidant Determinations by the Use of a Stable Free Radical. *Nature*. 181 (4617), 1199–1200.
- [30] Tozyılmaz, V., Bülbül, A.S., and Ceylan, Y., (2020). Anadolu Florasına Ait Bazı Alyssum L. Türlerinin Antimikrobiyal, Antioksidan ve Antibiyofilm Aktivitesinin Belirlenmesi. *Kahramanmaraş Sütçü İmam Üniversitesi Tarım ve Doğa Dergisi*.



RESEARCH ARTICLE

**THE EFFECT OF QUERCETIN ON SOME HEMATOLOGICAL PARAMETERS AGAINST
BISPHENOL-A EXPOSURE IN STREPTOZOCIN-INDUCED RATS**

Yılmaz KOÇAK^{1*}, Gökhan OTO², Seray ALPARSLAN³

^{1*}Van Yuzuncu Yil University, Faculty of Health Sciences, Physical Therapy and Rehabilitation, Van,
yilmazkocak@yyu.edu.tr, ORCID: 0000-0002-8364-4826

²Van Yuzuncu Yil University, Faculty of Medicine, Department of Pharmacology, Van,
gokhanoto@yyu.edu.tr, ORCID: 0000-0002-8492-4846

³Van Yuzuncu Yil University, Faculty of Medicine, Department of Pharmacology, Van,
serayertaskin@gmail.com, ORCID: 0009-0008-8568-4427

Receive Date: 27.06.2023

Accepted Date: 03.08.2023

ABSTRACT

Bisphenol-A (BPA) is an endocrine-disrupting environmental toxin widely used in the composition of plastics. Today, the widespread use of BPA in preserving and packaging food and beverages increases BPA exposure. Therefore, recent research has focused on the health effects of continuous exposure to BPA. This study aimed to investigate the protective effect of quercetin (QUE) on different hematologic variables in rats induced by the environmental toxin BPA and streptozocin (STZ). Wistar albino rats were administered BPA orally (p.o.) at 10 mg/kg and QUE intraperitoneally (i.p.) at 15 mg/kg for 14 days. STZ was administered subcutaneously (s.c.) in a single dose of 50 mg/kg at the beginning of the experiment. 72 rats were randomly selected for the experimental procedure and divided into 9 groups with 8 animals in each group. The groups were created as follows; Group 1: Control (Saline); Group 2: Corn oil (0.5 ml, solvent); Group 3: STZ (50 mg/kg); Group 4: BPA (10 mg/kg); Group 5: QUE (15mg/kg); Group 6: STZ (50 mg/kg) + QUE (15mg/kg); Group 7: BPA (10 mg/kg) + QUE (15mg/kg); Group 8: STZ (50 mg/kg) + BPA group (10 mg/kg); Group 9: STZ (50 mg/kg) + BPA (10 mg/kg) + QUE (15mg/kg). STZ and BPA-treated rats showed functional variability in all hematologic parameters. The combination of STZ and BPA significantly reduced erythrocytes, leukocytes, and their associated parameters. However, QUE treatment alone or in combination corrected the altered hematologic parameters. The results of this study demonstrated that exposure to BPA in combination with STZ may alter hematologic indices, while QUE may be a therapeutic agent to correct the altered blood profile.

Keywords: *Bisphenol-A, Quercetin, Streptozocin, RBCs, WBCs.*

1. INTRODUCTION

Bisphenol A (BPA) is a chemical synthetic substance used in food and beverage packaging that disrupts the function of the endocrine system. People can be exposed to BPA through inhalation, dermal absorption, or orally [1]. BPA exposure may have harmful effects on human health [2]. Indeed, studies have reported that BPA may contribute to obesity, diabetes (DM), cancer, urogenital and immune system disorders [3]. In addition, there is a relationship between BPA and diabetes, and the active form of the estrogen hormone estradiol plays an important role. It has been suggested that

estradiol provides energy balance and glucose homeostasis and contributes to the maintenance of insulin sensitivity [4]. One Epidemiologic study reported that exposure to BPA may contribute to the etiology of Type 2 DM [5]. Furthermore, BPA has been shown to disrupt body functions, affect human and animal health even at low doses [1]. Indeed, BPA has been found in human blood, urine, milk, and urine, suggesting that it may pose risks to the metabolic function of the organism.

Flavonoids are a member of the polyphenolic class found in natural sources and have a variety of properties. Flavonoids are abundant in vegetables and fruits and are known to be the most effective antioxidants in nature. They protect the body against damage from reactive oxygen species. Quercetin (QUE) is one of the best-known polyphenols and is found in vegetables and fruits such as cabbage, apples, grapes, and broccoli. QUE is rich in vitamin C and has strong antioxidant activity, and previous studies have reported that QUE has anticancer, antibacterial, antidiabetic, and antiviral activities [6].

Streptozotocin (STZ) is one of the most widely used diabetogenic agents to create an experimental model of diabetes in animals. STZ blocks insulin release in the pancreas, leading to insulin-dependent DM. This is a toxic effect of STZ on beta cells. This cytotoxic effect is explained by the impairment of glucose-induced insulin secretion by inhibiting the signaling ability of mitochondrial metabolism in the cell [7]. STZ is a compound that damages organs by suppressing the immune system in the body. STZ injection also decreased white blood cells (WBC) and other hematologic parameters. It has been reported that this may be due to an inadequate defense system against inflammation and bone marrow depression [8].

Environmental toxins (BPA) may contribute to the pathogenesis of various diseases in the organism. There is also evidence that flavonoids such as quercetin may prevent the development of these diseases due to their antioxidant properties. This study aimed to investigate the effects of quercetin on some hematologic parameters against BPA exposure in STZ-induced rats.

2. MATERIALS AND METHODS

2.1. Chemicals

The chemicals used in the experiment, STZ (Merck) and Quercetin were obtained from Sigma-Aldrich, taking into account their purity ratios. Sodium citrate was purchased from Turkey. Blood was analyzed by following the procedures in the automatic hematology device.

2.2. Animal Material

This study was carried out using 72 female Wistar albino rats with a live weight of 200-250 g. The rats were housed in plastic cages at 22±2 degrees Celsius and 12 hours of darkness/light. The animals were allowed free access to feed and water and were fed with pellet feed.

2.3. Experimental Groups

Rats were randomly divided into 9 groups with 8 animals in each group. Control received only saline (s.c.). BPA was dissolved in corn oil and administered by oral (po) gavage [9]. STZ was administered subcutaneously (s.c.) in a freshly prepared solution in 20 mM sodium citrate buffer (pH: 4.5) [10]. QUE was dissolved in saline and given i.p. at a dose of 15mg/kg [11]. The experimental procedure was established as follows.

Group 1: (n=8) Control (Saline),

- Group 2: (n=8)** Corn oil (0.5 ml, solvent)
Group 3: (n=8) STZ (50 mg/kg),
Group 4: (n=8) BPA (10 mg/kg),
Group 5: (n=8) QUE (15mg/kg),
Group 6: (n=8) STZ (50 mg/kg) + QUE (15mg/kg),
Group 7: (n=8) BPA (10 mg/kg) + QUE (15mg/kg),
Group 8: (n=8) STZ (50 mg/kg) + BPA group (10 mg/kg),
Group 9: (n=8) STZ (50 mg/kg) + BPA (10 mg/kg) + QUE (15mg/kg).

2.4. Hematological Analysis

Blood samples were collected from the hearts of rats under anesthesia and transferred into anticoagulant (EDTA) tubes. In blood samples, Red blood cells (RBCs), hemoglobin (HGB) hematocrit (HCT), mean corpuscular volume (MCV), mean corpuscular hemoglobin (MCH), mean cell hemoglobin concentration (MCHC), platelet (PLT), white blood Cells (WBC), neutrophils (NEUT), lymphocytes (LYMPH), monocytes (MONO), and eosinophils (EO) hematological variables were measured. These measurements were performed in the microbiology laboratory of Van Yüzüncü Yıl University Dursun Odabaş Medical Center.

2.5. Statistical Analysis

The statistical assessment of the collected data was expressed as the mean \pm standard deviation ($X \pm SD$). Continuous variables were compared among groups using One-way Analysis of Variance (ANOVA). Subsequently, post-analysis, the Duncan test was applied to identify distinctions between various groups. Significance levels were set at 5%, and the calculations were performed using the SPSS software program (IBM SPSS for Windows, version 26).

3. RESULTS

The hematological values obtained in the study were analyzed. RBC levels decreased in STZ and STZ+BPA groups, whereas increased in QUE-treated groups (STZ+QUE, BPA+QUE, and STZ+BPA+QUE) ($P < 0.05$, Table 1, Figure 1). HGB levels were in parallel with RBC levels. The control group and QUE-treated groups were significantly higher than STZ ($7.8 \pm 0.80 \times 10^3/\mu\text{L}$) and STZ+BPA ($7.2 \pm 0.45 \times 10^3/\mu\text{L}$) groups ($P < 0.05$). HGB decreased with STZ and BPA and increased with QUE treatment. STZ+BPA group ($12.7 \pm 1.70 \text{ g/dL}$) had the lowest HGB value, while STZ+BPA+QUE group ($16.8 \pm 1.43 \text{ g/dL}$) had the highest value. In MCV, the STZ+BPA+QUE combination ($64.5 \pm 7.90 \text{ fL}$) had higher values compared to control ($59.4 \pm 1.39 \text{ fL}$) ($P < 0.05$). There was no significant difference between the other groups ($P > 0.05$). MCH and MCHC levels decreased in STZ+BPA and STZ+BPA+QUE groups compared to control groups. In MCH, the corn oil ($18.1 \pm 0.68 \text{ pg}$) group had the highest value, while STZ+BPA ($17.2 \pm 0.76 \text{ pg}$) and STZ+BPA+QUE ($17.4 \pm 0.31 \text{ pg}$) group had the lowest value. It was statistically significant when these groups were compared ($P < 0.05$). PLT increased in QUE-treated groups and decreased in STZ and BPA-treated groups. While the PLT level showed a significant decrease in the STZ-only ($643.0 \pm 88.87 \times 10^3/\mu\text{L}$) group, it surprisingly increased in the QUE-only ($1298.1 \pm 173.8 \times 10^3/\mu\text{L}$) group ($P < 0.05$, Table 1). WBC levels decreased in STZ ($6.3 \pm 1.6 \times 10^3/\mu\text{L}$) and STZ+BPA ($6.1 \pm 1.3 \times 10^3/\mu\text{L}$) groups, whereas increased in corn oil ($8.9 \pm 0.5 \times 10^3/\mu\text{L}$) and STZ+QUE ($8.2 \pm 1.1 \times 10^3/\mu\text{L}$) groups ($P < 0.05$). HCT level was parallel with HGB and RBC values. HCT decreased in STZ and BPA-treated groups, whereas it increased with QUE treatment ($P < 0.05$, Table 2, Figure 2). NEUT levels decreased in the STZ+BPA ($14.8 \pm 0.5\%$) group and increased in the STZ+QUE ($28.8 \pm 4.7\%$) group and were found

significant compared to the other groups ($P < 0.05$). LYMPHs were significantly lower in STZ ($60.7 \pm 2.09\%$) and STZ+BPA ($61.8 \pm 2.57\%$) groups ($P < 0.05$). MONO levels were higher in STZ-treated groups ($1.13 \pm 0.6\%$). EO was decreased in the BPA ($0.21 \pm 0.07\%$) and STZ+BPA ($0.18 \pm 0.07\%$) groups and significantly higher in the STZ+BPA+QUE ($0.47 \pm 0.08\%$) group ($P < 0.05$). Changes in hematologic findings and comparisons between groups are shown in detail in Table 1-2 and Figure 1-2.

Table 1. The effect of STZ, BPA, and QUE singly and in combination on different hematologic variables (RBC, HGB, MCV, MCH, MCHC, and PLT).

Groups	RBC ($10^3/L$)	HGB (g/dL)	MCV (fL)	MCH (pg)	MCHC (g/dL)	PLT ($10^3/\mu L$)
Control	8.5 ± 0.7^{bc}	15.5 ± 1.1^{abc}	59.4 ± 1.3^b	17.9 ± 0.1^{ab}	30.7 ± 1.0^a	938.8 ± 109.7^{bc}
Corn oil	8.4 ± 1.1^{bc}	14.5 ± 0.8^c	61.9 ± 1.3^{ab}	18.1 ± 0.6^a	28.4 ± 3.1^{ab}	871.5 ± 105.3^{bcd}
STZ	7.8 ± 0.8^{cd}	13.2 ± 0.7^d	60.7 ± 2.0^{ab}	17.7 ± 0.4^{ab}	29.1 ± 0.6^{ab}	643.0 ± 88.8^d
BPA	8.4 ± 0.9^{bc}	14.9 ± 1.3^{bc}	61.0 ± 1.8^{ab}	17.9 ± 0.6^{ab}	29.3 ± 0.6^{ab}	944.6 ± 71.6^{bc}
QUE	10.3 ± 1.3^a	14.5 ± 0.5^c	60.4 ± 2.9^{ab}	17.8 ± 0.6^{ab}	29.4 ± 0.5^{ab}	1298.1 ± 173.8^a
STZ+QUE	8.3 ± 0.3^{bc}	16.2 ± 0.8^{ab}	61.3 ± 3.2^{ab}	17.5 ± 0.3^{ab}	28.7 ± 0.4^{ab}	996.0 ± 186.8^{bc}
BPA+QUE	9.3 ± 0.3^b	14.8 ± 0.6^c	61.2 ± 3.2^{ab}	17.6 ± 0.3^{ab}	28.9 ± 1.4^{ab}	1114.0 ± 239.6^{ab}
STZ+BPA	7.2 ± 0.4^d	12.7 ± 1.7^d	61.8 ± 2.5^{ab}	17.2 ± 0.7^b	28.2 ± 0.9^b	771.8 ± 136.1^{cd}
STZ+BPA+QUE	9.1 ± 0.8^b	16.8 ± 1.4^a	64.5 ± 7.9^a	17.4 ± 0.3^b	28.1 ± 0.7^b	975.2 ± 176.9^{bc}

Data are Mean \pm SE; N = 8. Abbreviations: STZ= Streptozotocin; BPA= Bisphenol A; QUE= Quercetin; RBCs= Red blood cells; HGB= hemoglobin; MCV= mean corpuscular volume; MCH= mean corpuscular hemoglobin; MCHC= mean cellular hemoglobin concentration; PLTs= Platelets; ^{a,b,c,d} p: values with different letters are significant when compared with each other ($p < 0.05$).

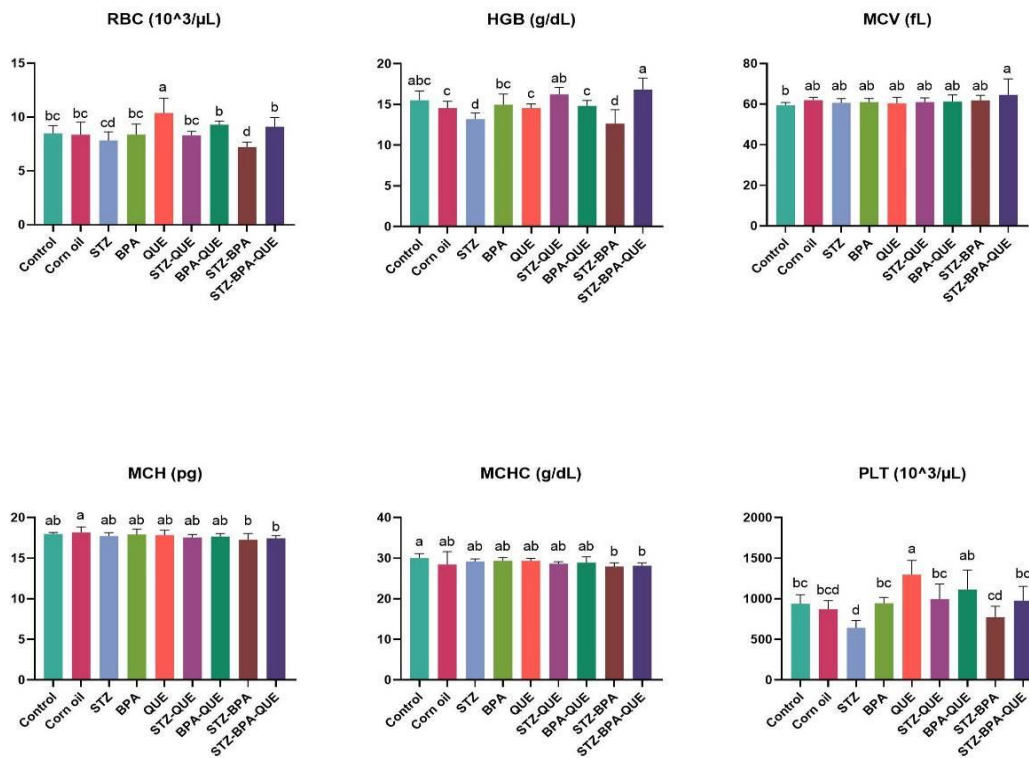


Figure 1. Effect of STZ, BPA, and QUE singly and in combination, on different hematologic variables. Data are Mean \pm SE; N = 8. Abbreviations: STZ= Streptozotocin; BPA= Bisphenol A; QUE= Quercetin; RBCs= Red blood cells; HGB= hemoglobin; MCV= mean corpuscular volume; MCH= mean corpuscular hemoglobin; MCHC= mean cellular hemoglobin concentration; PLT= Platelet; ^{a,b,c,d} p: values with different letters are significant when compared with each other (p<0.05).

Table 2. The effect of STZ, BPA, and QUE singly and in combination on different hematologic variables (WBC, HCT, NEUT, LYMPH, MONO, and EO).

Groups	WBC (10 ³ /L)	HCT (%)	NEUT (%)	LYMPH (%)	MONO (%)	EO (%)
Control	7.9 \pm 1.3 ^a	64.0 \pm 8.0 ^a	18.2 \pm 2.9 ^b	80.0 \pm 3.2 ^a	0.98 \pm 0.5 ^c	0.35 \pm 0.1 ^b
Corn oil	8.9 \pm 0.5 ^a	53.9 \pm 9.3 ^{ab}	19.4 \pm 1.2 ^b	80.7 \pm 5.4 ^a	0.67 \pm 0.4 ^c	0.30 \pm 0.08 ^{bc}
STZ	6.3 \pm 1.6 ^b	49.1 \pm 1.8 ^c	19.2 \pm 2.4 ^b	60.7 \pm 2.0 ^b	1.13 \pm 0.6 ^{bc}	0.28 \pm 0.09 ^{bcd}
BPA	7.9 \pm 1.6 ^a	51.2 \pm 2.8 ^{ab}	19.5 \pm 1.8 ^b	61.0 \pm 1.8 ^a	0.63 \pm 0.2 ^c	0.21 \pm 0.07 ^{cd}
QUE	8.0 \pm 1.5 ^a	53.0 \pm 4.6 ^{ab}	20.4 \pm 1.5 ^b	60.4 \pm 2.9 ^a	0.63 \pm 0.5 ^c	0.31 \pm 0.07 ^{bc}
STZ+QUE	8.2 \pm 1.1 ^a	56.7 \pm 3.4 ^b	28.8 \pm 4.7 ^a	61.3 \pm 3.2 ^a	1.10 \pm 0.6 ^{bc}	0.35 \pm 0.05 ^b
BPA+QUE	7.5 \pm 1.0 ^{ab}	50.0 \pm 2.8 ^{ab}	21.7 \pm 5.0 ^b	61.2 \pm 3.2 ^a	1.01 \pm 0.5 ^c	0.18 \pm 0.11 ^d
STZ+BPA	6.1 \pm 1.3 ^b	46.9 \pm 2.7 ^c	14.8 \pm 0.5 ^c	61.8 \pm 2.5 ^c	2.20 \pm 0.6 ^a	0.18 \pm 0.07 ^d
STZ+BPA+QUE	7.4 \pm 0.6 ^{ab}	53.0 \pm 5.7 ^{ab}	20.7 \pm 3.2 ^b	64.5 \pm 7.9 ^a	1.60 \pm 0.2 ^{ab}	0.47 \pm 0.08 ^a

Data Mean \pm SE; N = 8. Abbreviations: STZ= Streptozotocin; BPA= Bisphenol A; QUE= Quercetin; WBCs= White blood cells; NEUTs= Neutrophils; LYMPHs= Lymphocytes; MONOs= Monocytes;

Eosinophils= Eosinophils; ^{a,b,c,d}p: values with different letters are significant when compared with each other (p<0.05).

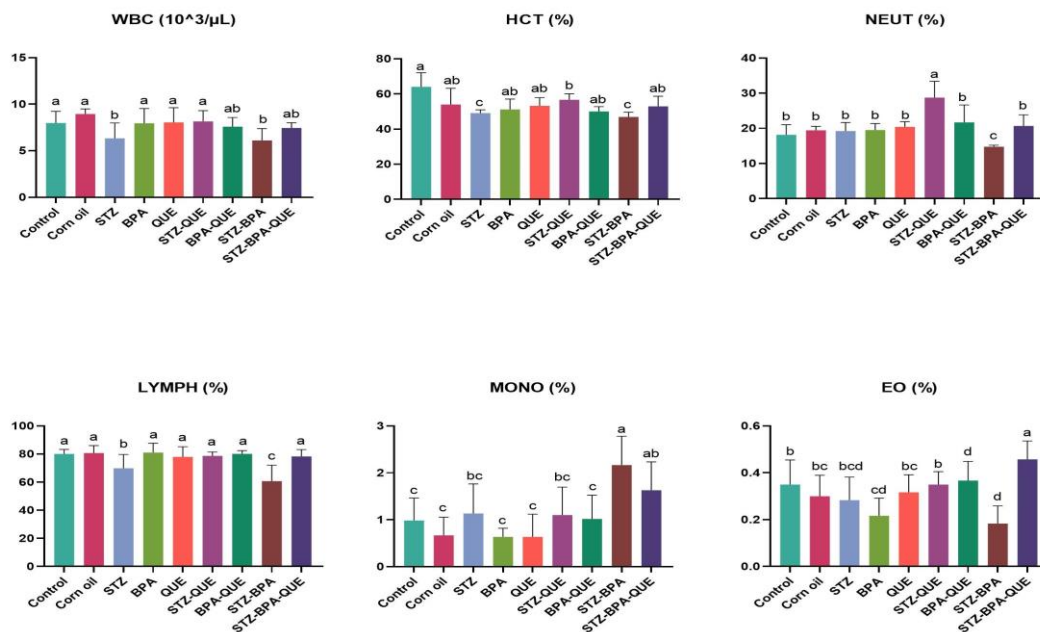


Figure 2. Effect of STZ, BPA, and QUE, singly and in combination, on different hematologic variables. Data are Mean ± SE; N = 8. Abbreviations: STZ= Streptozotocin; BPA= Bisphenol A; QUE= Quercetin; WBCs= White blood cells; NEUTs= Neutrophils; LYMPHs= Lymphocytes; MONOs= Monocytes; Eosinophils= Eosinophils; ^{a,b,c,d}p: values with different letters are significant when compared with each other (p<0.05).

4. DISCUSSION

The expansion of industrial production and increasing environmental toxins have had negative effects on the health of humans and animals. BPA is found in the structure of cheap plastic and polycarbonate products that are frequently used today and is an endocrine-disrupting environmental toxin. This toxin is thought to have many negative effects on health. Therefore the current study focused on the administration of STZ, BPA, and QUE either singly or in combination. STZ-treated rats induced changes in hematologic parameters. The results of this study support previous findings suggesting that STZ induces proliferation and apoptosis, especially in beta-cells [12, 13]. The basic mechanism of STZ in the body is antibody formation. These antibodies lead to degeneration of pancreatic beta cells and impaired insulin secretion [14]. Pancreatic damage leads to decreased insulin release and increased glucose in the blood [15]. The increase in circulating blood sugar can trigger oxidative stress and lead to a decrease in RBC and HGB values [16]. STZ has been found to decrease RBC and HGB levels. Because STZ-induced hyperglycemia causes dysfunction in the bone marrow. Accordingly, decreased HGB production may result in anemia. Furthermore, oxidation of membrane proteins leads to lipid peroxidation. This leads to hemolysis and shortened lifespan of the RBC [17]. In this study, it was found that the STZ+BPA combination decreased RBC and HGB

levels, while QUE treatment significantly restored them. BPA is an endocrine disruptor with estrogenic properties [18]. In a study conducted in male rats, it was reported to decrease erythropoiesis [19]. Walaa et al. (2015) suggested that BPA decreased RBC and HGB levels and increased anemia [20]. However, QUE is a flavonoid with potent antioxidant activity scavenging reactive oxygen species. This property of QUE has been reported to reduce the risk of several chronic diseases [21]. In addition, the oxidative stress-reducing effect of QUE has been reported to have positive effects on hematologic parameters [22]. HCT is expressed as a percentage of whole blood volume in relation to RBC. Increased HCT can cause polycythemia or dehydration. Decreased HCT may be due to renal failure, inflammation, and anemia [23]. STZ and BPA administration decreased the HCT level and QUE restored it. The decrease in the HCT index as a result of exposure to toxic agents is attributed to impaired hemostasis in blood and plasma osmolarity due to anemia [14]. The present results, in agreement with the literature, showed that STZ and BPA interacted to decrease RBC, HGB and HCT, while QUE normalized these values. STZ-treated rats exhibited a significant decrease in PLT levels. BPA administration did not produce a significant result on PLT levels. However, QUE treatment significantly increased PLT levels. Chronic diseases have been suggested to be markers for microvascular complications in diseases such as diabetes in which platelet indices are affected [24]. The decrease in STZ-administered rats indicates the effect of hyperglycemia as well as immune-induced suppression of hemopoiesis [22, 25, 26]. The low PLT level seen in STZ and BPA suggests that it may be due to a suppressed immune system. Although MCV, MCH, and MCHC levels were partially decreased in STZ and BPA groups compared to the control, it was not significant. However, the STZ+BPA+QUE combination was found to increase MPV levels compared to the other groups. These results are consistent with previous findings [20, 27]. STZ and STZ+BPA administration caused decreases in WBC and LYMPH counts. This is consistent with studies showing that STZ and BPA administration decreased these values [8, 20]. Decreased WBC and LYMPH may be related to the inhibition of leukocytosis due to increased inflammation with weakening of the immune system [14]. QUE supplementation significantly increased WBC and LYMPH counts to near control values. QUE is pleiotropic and reduces glucose absorption, insulin secretory, and insulin-sensitizing activities in the intestines [28]. QUE probably achieved this effect by controlling STZ-induced hyperglycemia and oxidative stress. NEUTs, EOs, and MONOs are blood cells that help the body maintain its immune system in various chronic diseases and inflammation. Decreased numbers of NEUTs and EOs result in delayed wound healing and prolonged inflammation resulting in morbidity and mortality in chronic diseases such as diabetes [14]. NEUTs have been associated with decreased production of reactive oxygen species, protein glycosylation, and hyperglycemia [14]. EO is a multifunctional leukocyte involved in bacterial and viral infections, allergic and parasitic infections [29]. MONOs are cells involved in the synthesis and release of proinflammatory and oxidant cytokines in the organism. These cells are thought to contribute to the formation of microvascular diseases [30, 31]. STZ+BPA-treated rats showed a significant decrease in the number of NEUTs and EOs. However, MONOs were significantly increased in STZ and STZ+BPA-treated rats, whereas QUE treatment was found to decrease MONO levels. This result is in agreement with the previous study [22]. Rats receiving QUE exhibited a significant increase in these immune cells by preventing oxidative stress, and protein glycosylation. This study is in agreement with studies reporting an immune modulatory and potent radical scavenging effect of QUE [32, 33]. Therefore, QUE may have strengthened the body's defense system by increasing the formation of immune system cells.

5. CONCLUSION

This study focused on the possible changes in hematologic parameters of BPA, the most widely produced chemical in the world to which humans are constantly exposed, and the effect of QUE on these changes. STZ and BPA administration were found to decrease RBC, WBC, HGB, HCT, PLT, NEUT, LYMPH, and EO levels. However, QUE administration increased the decreased hematologic parameters. The findings show that STZ and BPA may interact synergistically and cause changes in hematological parameters. The negative impact of these toxic agents on hematological parameters can affect many physiological processes such as impairment of the body's defense system, anemia, decreased oxygen-carrying capacity of the blood, and coagulation factors. However, QUE possesses potent antioxidant activity, which may have contributed to its ability to restore STZ and BPA-induced changes in hematologic parameters. In conclusion, co-administration of BPA with STZ negatively affects hematologic parameters. QUE exhibited therapeutic activity to correct these parameters. More detailed studies are needed to understand the effects of BPA exposure on human health and the pharmacological efficacy of QUE.

ACKNOWLEDGMENT

This study was carried out by Van Yuzuncu Yil University Scientific Research Projects Coordination Unit within the scope of the project numbered TYL-2023-10480.

ETHICS APPROVAL

This study was conducted with the approval of the local ethics committee of Van Yuzuncu Yil University (decision date 27.04.2023 and numbered 2023/06-07).

REFERENCES

- [1] Abraham, A., Chakraborty, P., Staples, C., van der Hoeven, N., Clark, K., Mihaich, E., Woelz, J., Hentges, S. (2018). Distributions of concentrations of bisphenol A in North American and European surface waters and sediments determined from 19 years of monitoring data. *Chemosphere*, 201(8), 448–458.
- [2] Hwang, M., Park, S.-J., and Lee, H.-J. (2023). Risk assessment of bisphenol a in the korean general population. *Applied Sciences*, 13(6), 3587.
- [3] Ma, Q., Deng, P., Lin, M., Yang, L., Li, L., Guo, L., Zhang, L., He, M., Lu, Y., Pi, H., Zhang, Y., Yu, Z., Chen, C., and Zhou, Z. (2021). Long-term bisphenol-A exposure exacerbates diet-induced prediabetes via TLR4-dependent hypothalamic inflammation. *Journal of Hazardous Materials*, 402, 123926.
- [4] Çelik, Y., and Şahin, S. (2021). Health effects of bisphenol-A as an endocrine disrupting chemical. *Journal of Continuing Medical Education*, 29(6), 439–445.
- [5] Rancière, F., Botton, J., Slama, R., Lacroix, M. Z., Debrauwer, L., Charles, M. A., Roussel, R., Balkau, B., Magliano, D. J., and Vol, S. (2019). Exposure to bisphenol -A and bisphenol s and incident type 2 diabetes: A case-cohort study in the French cohort D.E.S.I.R. *Environmental Health Perspectives*, 127(10), 1–9.

- [6] Azeem, M., Hanif, M., Mahmood, K., Ameer, N., Chughtai, F. R. S., and Abid, U. (2023). An insight into anticancer, antioxidant, antimicrobial, antidiabetic and anti-inflammatory effects of quercetin: a review. *Polymer Bulletin*, 80(1), 241–262.
- [7] Lenzen, S. (2008). The mechanisms of alloxan- and streptozotocin-induced diabetes. *Diabetologia*, 51(2), 216–226.
- [8] Amra, E. A., Abd, S. A., Raheem, E., Habib, T. N., and Aboelkhair, H. A. (2022). Protective effect of bradykinin potentiating factor on haematological parameters of diabetic male albino rats. *Sohag Journal of Sciences*, 114(2), 105–114.
- [9] Moselhy, W., Ahmed, W. M. S., Moselhy, W. A., and Nabil, T. M. (2015). Bisphenol A toxicity in adult male rats: Hematological, biochemical and histopathological approach. *Global Veterinaria*, 14(2), 228–238.
- [10] Anwar, M., Shousha, W. G., El-mezayen, H. A., Wadallah, R. A., El-Wassef, M., Nazif, N. M., and El-bana, M. A. (2013). Antiatherogenic effect of almond oil in streptozotocin induced diabetic rats. *Journal of Applied Pharmaceutical Science*, 3(10), 59–65.
- [11] Abdelmoaty, M. A., Ibrahim, M. A., Ahmed, N. S., and Abdelaziz, M. A. (2010). Confirmatory studies on the antioxidant and antidiabetic effect of quercetin in rats. *Indian Journal of Clinical Biochemistry*, 25(2), 188–192.
- [12] Prud'homme, G. J., Glinka, Y., Kurt, M., Liu, W., and Wang, Q. (2017). The anti-aging protein Klotho is induced by GABA therapy and exerts protective and stimulatory effects on pancreatic beta cells. *Biochemical and Biophysical Research Communications*, 493(4), 1542–1547.
- [13] Khan, D., Vasu, S., Moffett, R. C., Irwin, N., and Flatt, P. R. (2017). Influence of neuropeptide Y and pancreatic polypeptide on islet function and beta-cell survival. *Biochimica et Biophysica Acta (BBA) - General Subjects*, 1861(4), 749–758.
- [14] Hajam, Y. A., Rai, S., Ghosh, H., and Basheer, M. (2020). Combined administration of exogenous melatonin and insulin ameliorates streptozotocin induced toxic alteration on hematological parameters in diabetic male Wistar rats. *Toxicology Reports*, 7, 353–359.
- [15] Zhang, Q., Cui, Q., Hou, Y., Wang, H., Xu, Y., and Pi, J. (2017). The impairment of glucose-stimulated insulin secretion in pancreatic β -cells caused by prolonged glucotoxicity and lipotoxicity is associated with elevated adaptive antioxidant response. *Food and Chemical Toxicology*, 100, 161–167.
- [16] Zhang, W., Meng, J., Liu, Q., Makinde, E. A., Lin, Q., and Olatunji, O. J. (2020). Shorea roxburghii leaf extract Ameliorates hyperglycemia induced abnormalities in high fat/fructose and streptozotocin induced diabetic rats. *Chemistry & Biodiversity*, 17(3), e1900661.
- [17] Kolanjiappan, K., Manoharan, S., and Kayalvizhi, M. (2002). Measurement of erythrocyte lipids, lipid peroxidation, antioxidants and osmotic fragility in cervical cancer patients. *Clinica Chimica Acta*, 326(1–2), 143–149.
- [18] Schönemann, A. M., Moreno Abril, S. I., Diz, A. P., and Beiras, R. (2022). The bisphenol-A



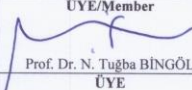
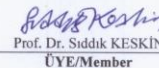
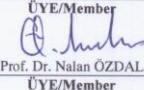

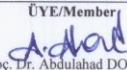
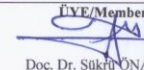
metabolite MBP causes proteome alterations in male *Cyprinodon variegatus* fish characteristic of estrogenic endocrine disruption. *Environmental Pollution*, 300, 118936.

- [19] Karnam, S. S., Ghosh, R. C., Mondal, S., and Mondal, M. (2015). Evaluation of subacute bisphenol -A toxicity on male reproductive system. *Veterinary World*, 8(6), 738–744.
- [20] Moselhy, W., Ahmed, W. M. S., Moselhy, W. A., and Nabil, T. M. (2015). Bisphenol -A toxicity in adult male rats: Hematological, biochemical and histopathological approach. *Global Veterinaria*, 14(2), 228–238.
- [21] Bhutada, P., Mundhada, Y., Bansod, K., Bhutada, C., Tawari, S., Dixit, P., and Mundhada, D. (2010). Ameliorative effect of quercetin on memory dysfunction in streptozotocin-induced diabetic rats. *Neurobiology of Learning and Memory*, 94(3), 293–302.
- [22] Keskin, E., Dönmez, N., Kılıçarslan, G., and Kandır, S. (2016). Beneficial effect of quercetin on some haematological parameters in streptozotocin-induced diabetic rats. *Bulletin of Environment, Pharmacology and Life Sciences*, 5(6), 65-8.
- [23] Kundrapu, S., and Noguez, J. (2018). Laboratory assessment of anemia. In G. S. Makowski (Ed.), *Advances in Clinical Chemistry* (1st ed., Vol. 83, pp. 197–225). Cambridge: Elsevier.
- [24] Dörtbudak, M. Y., Çadırcı, M. Ş., and Karakılıç, A. Z. (2013). Effects of vitamin E and selenium on erythrocyte and platelet indices and pancreatic histopathology in experimental diabetes. *Journal of Harran University Medical Faculty*, 10(2), 54–59.
- [25] Omoba, O. S., Olagunju, A. I., Akinrinlola, F. O., and Oluwajuyitan, T. D. (2022). Shallot-enriched amaranth-based extruded snack influences blood glucose levels, hematological parameters, and carbohydrate degrading enzymes in streptozotocin-induced diabetic rats. *Journal of Food Biochemistry*, 46(11), e14098.
- [26] Gayathri, M., and Kannabiran, K. (2009). The effects of oral administration of an aqueous extract of *Ficus bengalensis* stem bark on some hematological and biochemical parameters in rats with streptozotocin-induced diabetes. *Turkish Journal of Biology*, 33(1), 9–13.
- [27] Konsue, A., Picheansoonthon, C., and Talubmook, C. (2017). Fasting blood glucose levels and hematological values in normal and streptozotocin-induced diabetic rats of *mimosa pudica* L. extracts. *Pharmacognosy Journal*, 9(3), 315–322.
- [28] M. Eid, H., and S. Haddad, P. (2017). The antidiabetic potential of quercetin: underlying mechanisms. *Current medicinal chemistry*, 24(4), 355–364.
- [29] Hogan, S. P., Rosenberg, H. F., Moqbel, R., Phipps, S., Foster, P. S., Lacy, P., Kay, A.B., and Rothenberg, M. E. (2008). Eosinophils: biological properties and role in health and disease. *Clinical & Experimental Allergy*, 38(5), 709–750.
- [30] Galli, F., Varani, M., Trapasso, F., Tetti, S., and Signore, A. (2022). Radiolabeling of monocytes, NK cells and dendritic cells and quality controls. *Nuclear Medicine and Molecular*

Imaging, 299–304.

- [31] Monie, T. P. (2017). A Snapshot of the Innate Immune System. (T. P. Monie, Ed.)The innate immune system (1st ed.). Cambridge: Academic Press.
- [32] Ravikumar, N., and Kavitha, C. N. (2020). Immunomodulatory effect of quercetin on dysregulated Th1 / Th2 cytokine balance in mice with both type 1 diabetes and allergic asthma, 10(03), 80–87.
- [33] Wiyono, T., Nisa, K., Handayani, S., Windarsih, A., Hayati, S. N., Wulanjati, M. P., Sholikhahb, E. N., and Pratiwi, W. R. (2023). Ameliorative effect of quercetin on pancreatic damage in rodent: a meta-analysis. Egyptian Journal of Basic and Applied Sciences, 10(1), 433–446.

APPENDIX

		VAN YÜHADYEK VAN YÜZÜNCÜ YIL ÜNİVERSİTESİ Hayvan Deneyleri Yerel Etik Kurulu	
ÇALIŞMA ONAY BELGESİ			
VAN YUZUNCU YIL UNIVERSITY (TURKEY) ANIMAL RESEARCHES LOCAL ETHIC COMMITTEE APPROVAL CERTIFICATE			
Araştırmanın Adı:	Diyabetik ratlarda Bisfenol A maruziyetine karşı kuersetinin bazı hematolojik parametreler üzerine etkisi.		
Research Title:	The effect of quercetin on some haematological parameters against Bisphenol A exposure in diabetic rats. İngilizce başlık buraya yazılmalıdır.		
Araştırmacı(lar): Investigator(s)	Yürütücü / Chief investigator:	Dr. Öğr. Ü. Yılmaz KOÇAK	
	Yardımcı Araştırmacı(lar) / Co-investigator(s):	Prof. Dr. Gokhan OTO Seray ALPARSLAN	
Araştırmada kullanılacak hayvanlar / Animals to be used in the research:			
Tür / species: Wistar albino sıçan/ Wistar albino rat	Sayı / Numbers: 72	Cinsiyet / Sex: Dişi/ Female	
Yaş / Age: 3-4 aylık/3-4 months old			
Araştırmanın Öngörülen Başlama Tarihi / Proposed Research Starting Date: 30.04.2023			
Araştırmanın Öngörülen Bitiş Tarihi / Proposed Research Completion Date: 14.05.2025			
Karar:			
Yukarıda bilgileri verilen planlanan araştırma projesi için Hayvan Deneyleri Etik Kurul Onayı gerekmemektedir.			
Tarih: 27/04/2023; Karar No: 2023/06-07			
Decision:			
The proposed research project detailed above does not need Animal Researches Ethic Committee Approval. Date 27/04/2023 Decision number 2023/06-07			
	BAŞKAN V./CHAIR		
	 Prof. Dr. Yıldırım BAŞBUĞAN		
ÜYE/Member	ÜYE/Member	ÜYE/Member	
 Prof. Dr. N. Tuğba BİNGÖL ÜYE	 Prof. Dr. Süddik KESKİN ÜYE/Member	 Prof. Dr. Nalan ÖZDAL ÜYE/Member	
Prof. Dr. Atilla DURMUŞ	Prof. Dr. Semiha DEDE	Doç. Dr. Ferda KARAKUŞ	
ÜYE/Member	ÜYE/Member	ÜYE/Member	
 Doç. Dr. Caner Yılmaz DEMİR ÜYE/Member	 Doç. Dr. Abdulahad DOĞAN ÜYE/Member	 Doç. Dr. Şükrü ONALAN ÜYE/Member	
Dr. Öğr. Üyesi Dicle ALTINDAL	Vet. Hek. İsmail Hakkı BEHÇET	Zir. Müh. Kenan YILDIRIMOĞLU	



RESEARCH ARTICLE

**NUMERICAL MODELING OF BACKWARD-FACING STEP FLOW VIA
COMPUTATIONAL FLUID DYNAMICS**

Ilker GOKTEPELI^{1*}, Ulas ATMACA²

^{1*}Konya Technical University, Faculty of Engineering and Natural Sciences, Department of Mechanical Engineering, Konya, igoktepe@ktun.edu.tr, ORCID: 0000-0002-2886-8018

²Konya Technical University, Faculty of Engineering and Natural Sciences, Department of Mechanical Engineering, Konya, suatmaca@ktun.edu.tr, ORCID: 0000-0002-9265-1446

Receive Date: 21.05.2023

Accepted Date: 18.08.2023

ABSTRACT

As a fundamental case for problems of fluid mechanics, examination of flow separation and its reattachment is important for engineering applications. Considering the significance of the subject, backward-facing step flow has been modeled via Computational Fluid Dynamics (CFD) based on an experimental study previously done at $Re = 5000$. Steady simulations have been conducted by $k-\varepsilon$ Renormalization Group (RNG) considering the same flow conditions of the reference study. Pressure distributions, streamwise and cross-stream velocity components, velocity magnitude values with streamline patterns and turbulence kinetic energy values have been presented by using contour graphics. Furthermore, the stations for pressure distributions, velocity profiles for streamwise components and turbulence kinetic energy values have been defined for evolution of related data. Lower pressure zone for the wake region of the backward-facing step has been attained due to flow separation. Separation of the upstream boundary layer has been seen and it became a curved one. Moreover, turbulence level of the step wake has been obtained as higher than those of any other points. Transition to core flow has been attained at $y^* = 1.1$ that is above the step height. Flow oscillations have been observed for $x^* \geq 2$ and $y^* \leq 1$ since the fluctuations for these values were effective in the wake region. To sum up, the dimensionless reattachment length has been numerically obtained as 5.92 which is very good agreement with the experimental results at same Reynolds number. The deviation from the reference results is from 0.34 % to 1.33 %.

Keywords: *Backward-facing step, Flow separation, $k-\varepsilon$ RNG, Reattachment length, Turbulence*

1. INTRODUCTION

Flow separation and its reattachment is a fundamental phenomenon for fluid mechanics and heat transfer problems. These problems are considered as significant for modern engineering applications. Backward-facing step flow is one of the cases that flow separation and flow reattachment are noteworthy. These flow structures are influenced by geometric design, expansion ratio, flow

characteristics as well as thermal conditions [1-2]. This type of flow is frequently observed in the studies related to aerodynamics and hydrodynamics. For this reason, backward-facing step flow is encountered in aeronautical, civil, mechanical and naval engineering disciplines such as airfoils, buildings, heat exchangers, hydrofoils, spoilers [1]. What is more, the present case is related to turbine blades, combustor flame-holder and engine inlets [3]. Furthermore, it is possible to associate this subject to ecological, hydrological and also meteorological issues [4]. Several designs are also used to decrease the velocity of fluid flow [5]. A micro combustor has also been presented as a backward-facing step [6-7]. Based on these usage examples, controlling shear flows is very important for industrial applications [8]. At the upstream of a backward-facing step, there is detached boundary layer. However, recirculation region including one or more vorticities occurred at the downstream due to the backward-facing step. Then, separated flow owing to this step reattaches at a point in the wake region [9].

Over the decades, the present problem has been researched in the experimental, numerical and theoretical studies of open literature. In terms of experimental studies, Jovic and Driver [10] have examined the influence of Reynolds number on skin friction measurements for $5000 \leq Re \leq 37200$. They have used Laser-Oil Flow Interferometry (LOI) method for backward-facing step flow. Kasagi and Matsunaga [11] have used particle tracking velocimeter for three-dimensional backward-facing step flow at $Re = 5540$. They have compared experimental results with the ones obtained via Direct Numerical Simulation (DNS) from open literature. Scarano et al. [12] have implemented a pattern recognition technique for flow past a backward-facing step. For $Re = 5000$, Digital Particle Image Velocimetry (DPIV) has been used. Wengle et al. [13] have examined backward-facing step flow by the wind tunnel experiments and compared these results with the numerical ones of DNS at $Re = 3000$. Kostas et al. [14] have experimentally studied on backward-facing step flow by using Particle Image Velocimetry (PIV) at $Re = 4660$. Furuichi et al. [15] have measured velocity fields of separated shear layer and flow reattachment zone for a backward-facing step. They have used Laser Doppler Velocimetry (LDV) in terms of two-dimensional case at $Re = 5000$. It was concluded that large-scale fluctuations could be modeled via a model proposed by the authors. Same method has also been utilized by Nie and Armaly [16]. Three-dimensional backward-facing step flow has been investigated from $Re = 100$ to $Re = 8000$. The aim of their study is to capture the boundaries of reverse flow zones. Schram et al. [17] have done PIV experiments for flow over a backward-facing step at $Re = 5100$. Bouda et al. [18] have used Laser Doppler Anemometry (LDA) for turbulent jet flow past a backward-facing step at $Re = 7600$. Experimental results have been compared with the numerical ones of RANS simulations. Wu et al. [19] have conducted experiments about backward-facing step flow via PIV at $Re = 3450$. They have examined the effect of smooth and rough surfaces on flow characteristics. Nadge and Govardhan [20] have experimentally investigated flow structure for the wake region of a backward-facing step via PIV. For different Reynolds numbers, the results have been presented. Yamada and Nakamura [21] have measured heat transfer and flow characteristics in the wake region of a backward-facing step from $Re = 2500$ to $Re = 5200$.

When it comes to numerical studies about backward-facing step flow, Le et al. [22] have utilized DNS to examine turbulent flow of a backward-facing step at $Re = 5100$. Chiang et al. [23] have conducted numerical analyses for backward-facing step flow at $50 \leq Re \leq 2500$. Avancha and Pletcher [24] have numerically studied on the same problem for $Re = 5540$. In a study including the case of heat transfer,

LES turbulence model has been implemented. Dejoan and Leschziner [25] have used LES turbulence model for the same case at $Re = 3700$. Aider and Danet [26] have performed numerical analyses by using LES model for flow over a backward-facing step at $Re = 5100$. Barri et al. [27] have numerically studied on flow past a backward-facing step. DNS has been used in their study for Reynolds number of 5600. El Khoury et al. [28] have utilized DNS to consider backward-facing step flow at $Re = 5200$. Jürgens and Kaltenbach [29] have employed LES turbulence model for backward-facing step flow of $Re = 3000$. LES turbulence model has also been used by Kanchi et al. [30] for backward-facing step flow for varying Reynolds numbers from 5000 to 28000. Togun et al. [31] have numerically studied on backward-facing step flow for laminar and turbulent flow of heat transfer problem. In their study for turbulent flow, they have used $k-\omega$ Shear Stress Transport (SST) turbulence model. Amiri et al. [32] have presented a study with experimental and numerical parts for heat transfer of backward-facing step flow in terms of various Reynolds number values. Xu et al. [33] have established a numerical model for three-dimensional backward-facing step flow. Several Reynolds numbers have been considered for the case including heat transfer.

The aim of the study is to examine the backward-facing step flow that is very important for engineering applications owing to flow separation and its reattachment. It is well known that flow behavior is affected by the change of channel height for flow direction. Therefore, this effect should be considered and investigated by using experimental and numerical techniques. Due to non-availability of experimental facilities, numerical modeling with reliable methods is crucial. At the present Reynolds number for the present case, various turbulence models have been tested. As a result, $k-\varepsilon$ Renormalization Group (RNG) turbulence model has been implemented for the numerical study since the numerical results have been validated with respect to the experimental outcomes of the literature.

2. NUMERICAL METHOD

Backward-facing step flow has been numerically investigated at $Re = 5000$. Turbulence models based on $k-\varepsilon$ and $k-\omega$ methods have been compared. After the comparison of these models, $k-\varepsilon$ RNG turbulence model has been used for numerical simulations conducted in ANSYS-Fluent 21. As a reference study, research presented by Furuichi et al. [15] has been considered and the numerical results have been compared and validated.

2.1. Turbulence Model

Continuity and momentum equations have been solved. In this process, Reynolds-Averaged Navier-Stokes (RANS) equations are utilized. In case of incompressible flow conditions, aforementioned equations have been considered with Eqs. 1-2, respectively [34-35]:

$$\frac{\partial \rho}{\partial t} + \frac{\partial}{\partial x_i} (\rho u_i) = 0 \quad (1)$$

$$\frac{\partial}{\partial t} (\rho u_i) + \frac{\partial}{\partial x_i} (\rho u_i u_j) = -\frac{\partial \rho}{\partial x_i} + \frac{\partial}{\partial x_j} \left[\mu \left(\frac{\partial u_i}{\partial x_j} + \frac{\partial u_j}{\partial x_i} - \frac{2}{3} \delta_{ij} \frac{\partial u_l}{\partial x_l} \right) \right] + \frac{\partial}{\partial x_j} (-\rho \overline{x'_i x'_j}) \quad (2)$$

Turbulent stresses have to be included for the solution process. Turbulence models are the methods providing these terms for the solution. As a k-ε based method, k-ε RNG turbulence model has been used in the present study. The difference between the k-ε RNG model and standard k-ε model is related to analytical derivation for the technique with the constants, the additional terms and the functions in the equations of transport as in Eqs. 3-4 [34].

$$\frac{\partial}{\partial t}(\rho k) + \frac{\partial}{\partial x_i}(\rho k u_i) = \frac{\partial}{\partial x_i} \left[\mu_{eff} \alpha_k \frac{\partial k}{\partial x_j} \right] + G_k - \rho \varepsilon + S_k \quad (3)$$

$$\frac{\partial}{\partial t}(\rho \varepsilon) + \frac{\partial}{\partial x_i}(\rho \varepsilon u_i) = \frac{\partial}{\partial x_i} \left[\mu_{eff} \alpha_k \frac{\partial \varepsilon}{\partial x_j} \right] + C_{1\varepsilon} G_k \frac{\varepsilon}{k} - C_{2\varepsilon} \rho \frac{\varepsilon^2}{k} - R_\varepsilon + S_\varepsilon \quad (4)$$

The RNG turbulence model could be considered as the refinement of its standard method. Moreover, it shows more sensitivity for the estimation of the effects of rapid strain and streamlines curvature compared to the properties of the standard model [34].

2.2. Flow Domain

Flow domain has been defined as three-dimensional with respect to a study experimentally done by Furuichi et al. [15]. Its dimensions are $-12.5 \leq x^* = x/h \leq 12.5$ in streamwise direction and $-6 \leq z^* = z/h \leq 6$ in spanwise direction. What is more, these are $0 \leq y^* = y/h \leq 2$ and $0 \leq y^* = y/h \leq 3$ for the upstream ($-12.5 \leq x^* \leq 0$) and the downstream ($0 \leq x^* \leq 12.5$) regions of the step height in cross-stream direction, respectively. These dimensions are non-dimensional by considering the step height which is $h = 0.02$ m. Schematic view of the model has been given in Figure 1.

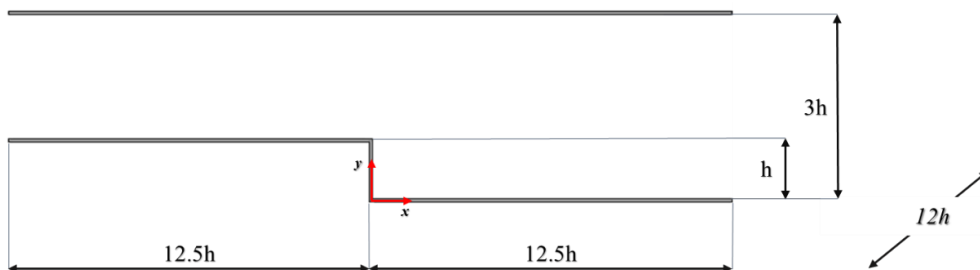


Figure 1. Schematic view of the model.

For the inlet, $U_\infty = 0.25$ m/s has been defined as uniform velocity at Reynolds number of $Re_h = U_\infty h / \nu = 5000$ based on a step height. Kinematic viscosity of water is considered. Pressure outlet has been used as boundary condition to provide gauge pressure at the channel exit that is open to atmosphere. No-slip boundary condition has been applied for the channel walls.

Numerical solution is performed via uniform or non-uniform grid elements covering the geometry of the problem [36-37]. Therefore, grid independence study is very crucial for the reliability of the numerical simulations. For the present study, the numbers of grid elements of 4 500 000, 6 000 000 and 8 200 000 have been contrasted via reattachment length ($x_r^* = x_r/h$) presented in the reference

study. After the flow separation from the backward-facing step, flow reattaches to the bottom surface of the duct downstream. The reattachment length is measured between the flow separation from the step and the reattachment point. When the value for wall shear stress (τ) is zero at any point, the difference between the origin and this point indicates the reattachment length. By the way, wall shear stress has also been given in non-dimensional form as $\tau^* = \tau / (\rho U_{in}^2)$ where water density and uniform inlet velocity are used. As an example, the downstream results obtained by the k- ϵ RNG turbulence model have been presented in Figure 2.

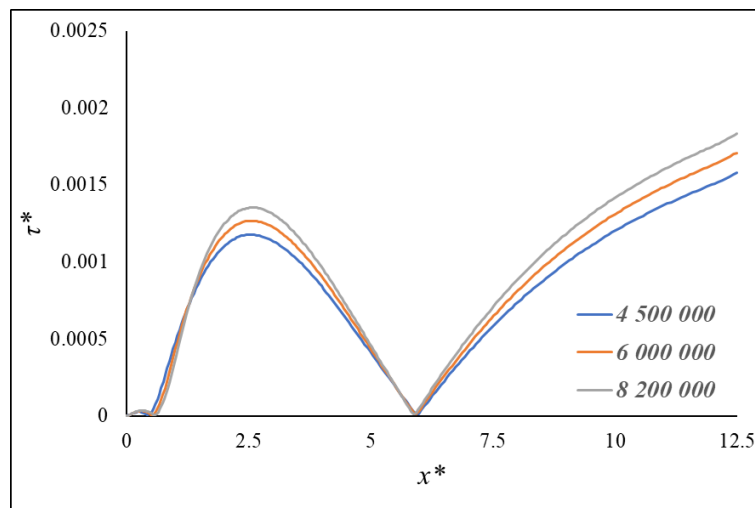


Figure 2. Grid independence test for wall shear stress at $y^* = z^* = 0$.

The experimental result for the reattachment length has been obtained as $x_r^* = 6$ by Furuichi et al. [15]. For this reason, this value has been accepted as the reference value for grid independence test. The closest value to the experimental result has been attained as $x_r^* = 5.92$ by using the number of grid elements as 6 000 000 with respect to the results. The grid system has been presented in Figure 3.

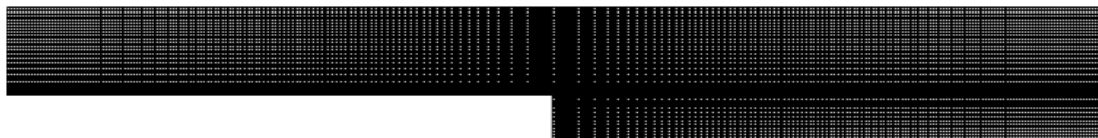


Figure 3. The grid structure on x-y plane.

What is more, the residuals of all equations have been taken as 10^{-6} throughout the steady simulations. Moreover, the turbulence models based on k- ϵ and k- ω methods have been compared in terms of wall shear stress values. As an example, the results obtained via the number of grid elements as 6 000 000 have been shown. In Figure 4, the comparison chart has been given for Standard k- ϵ , k- ϵ RNG, k- ϵ Realizable, Standard k- ω and k- ω SST turbulence models.

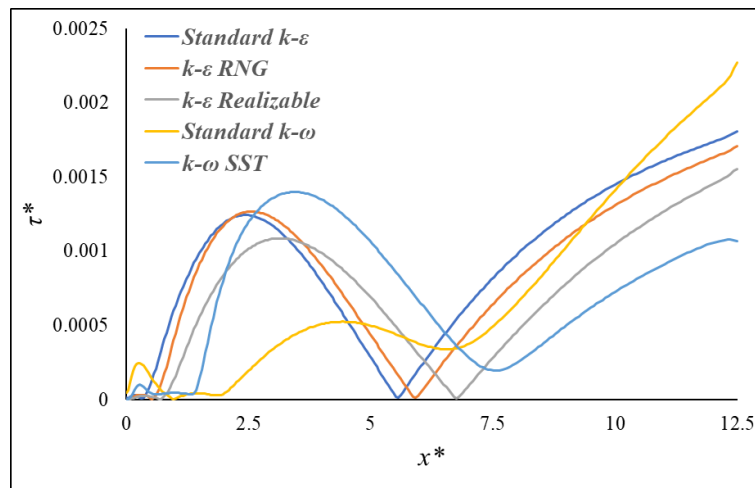


Figure 4. Wall shear stress for various turbulence models at $y^* = z^* = 0$.

With respect to these results, the turbulence models based on $k-\omega$ are failed to capture the reattachment length when it is compared to the result of the reference study. Relatively, the turbulence models based on $k-\epsilon$ are more successful. Nonetheless, $k-\epsilon$ Realizable turbulence model is the third one among the investigated ones in case of reattachment length. As a result, the closest result to the reference value has been attained by using $k-\epsilon$ RNG turbulence model.

2.3. Validation

Hydrodynamic flow characteristics for a backward-facing step has been investigated via $k-\epsilon$ RNG turbulence model. The aspect ratio is obtained by the division of spanwise length to the step height as $AR = 12$ while the expansion ratio is given by the ratio of the duct height of downstream to the duct height of upstream as $ER = 1.5$ as in the reference experimental study. The flow domain has been established by considering the dimensions with those used by Furuichi et al. [15]. Dimensionless values for reattachment length have been given in Table 1.

Table 1. Dimensionless reattachment length values at similar Reynolds numbers.

	Method	Re	AR	ER	x_r^*
Scarano et al. [12]	PIV	5000	10	1.2	5.9
Furuichi et al. [15]	LDV	5000	12	1.5	6

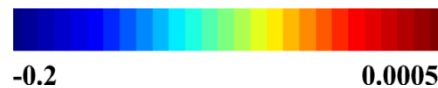
Aider and Danet [26]	LES	5100	4	1.2	5.8
Kang and Choi [38]	LES	5100	4	1.2	6.2
Present study	k-ε RNG	5000	12	1.5	5.92

The value has been obtained with percentage error of 1.33 % compared to the reference result given by Furuichi et al. [15]. Furthermore, the reattachment length of the present study has been attained by with percentage error of 0.34 % with respect to the value presented by Scarano et al. [12] in terms of same Reynolds number. In case of similar Reynolds number, the numerical result is also close to the values obtained by Aider and Danet [26] and Kang and Choi [38]. With respect to these results, the present result is in good agreement.

3. RESULTS AND DISCUSSION

Flow characteristics over a backward-facing step have been numerically examined via k-ε RNG turbulence model for $Re = 5000$. Numerical results including pressure distributions, streamwise and cross-stream velocity components, velocity magnitude values with streamline patterns and turbulence kinetic energy values have been given for planes at $z^* = 0$, respectively. Moreover, the contour graphics for streamwise velocity components have been presented for planes in a row at $0 \leq x^* \leq 7$. Pressure values have been shown for eight stations in a row. The stations have been given for $x^* = 0, 1, 2, 3, 4, 5, 6$ and 7 , respectively. Same stations have been used for the exhibitions of streamwise velocity components and turbulence kinetic energy values.

Pressure distributions have been presented for $-0.2 \leq P^* = P / (\rho U_\infty^2) \leq 0.0005$ as depicted in Figure 5 at $z^* = 0$. Pressure values indicated decrement owing to effect of backward-facing step flow and the pressure drop was clearly observed for the downstream. Flow separation from the edge of the step has been obtained and pressure values have changed. Lower pressure zone for the wake region has been attained. Rotational flow structure has been seen as anticipated. Gradual pressure distributions have been provided for the channel as stated by Goktepe et al. [39]. Due to flow recovery, increasing pressure values have been seen. This situation is effective after the flow reattachment point. Since the cross-sectional area of the duct increases, fluid velocity decreases and pressure value reversely increases as expected.



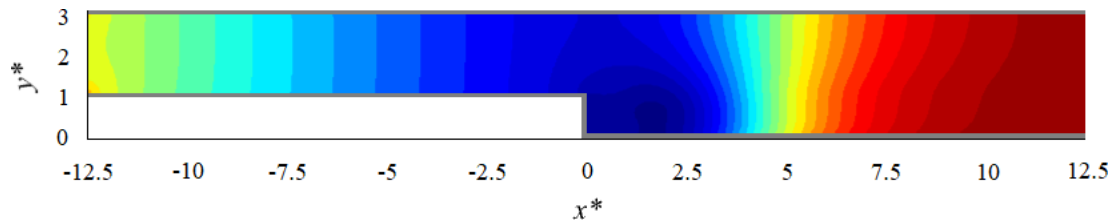


Figure 5. Pressure distributions along the channel.

Streamwise velocity component values of $-0.2 \leq u^* = u / U_\infty \leq 1.08$ have been shown in Figure 6 for $z^* = 0$. The peak value for this component has been attained around the channel axis. However, minimum value has been obtained in the wake region. Before the flow reattachment, negative values have been observed. Rotational flow structures have been observed with the negative velocity values as in the study done by Goktepe et al. [40]. The upstream boundary layer has indicated separation from the edge and became a curved one as quasi-boundary. A large vorticity has occurred inside the aforementioned zone. Furthermore, a smaller one through the step depth has been spotted.

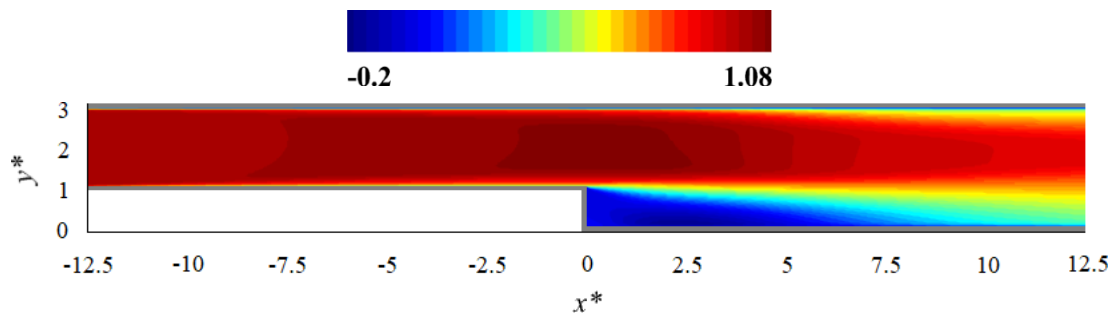


Figure 6. Streamwise velocity components along the channel.

Cross-stream velocity components have been given in Figure 7 for the range of $-0.056 \leq v^* = v / U_\infty \leq 0.056$ as shown. The peak value has been attained in the wake region of the backward-facing step. Flow separation is responsible for this distribution. Nevertheless, minimum value of this component has been observed for $3 \leq x^* \leq 7$ and $0.5 \leq y^* \leq 1.5$. The size of the cluster with negative values is larger than that of the cluster with positive values. Approximately average values have been attained for the rest of the duct.



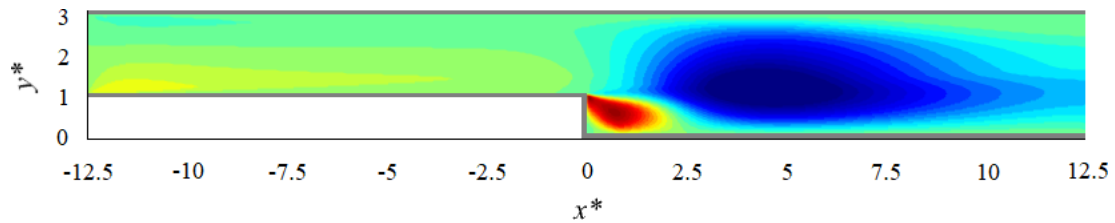


Figure 7. Cross-streamwise velocity components along the channel.

Velocity magnitude values with streamline patterns have been presented for the plane at $z^* = 0$ as in Figure 8. The vorticity for the wake in terms of $x^* < 5.92$ has been seen. This vorticity has occurred because of separated flow. As expected, flow separation triggers a lower pressure region [41, 42]. A small vorticity has been observed in the wake region close to the bottom edge. It is called as a secondary eddy.

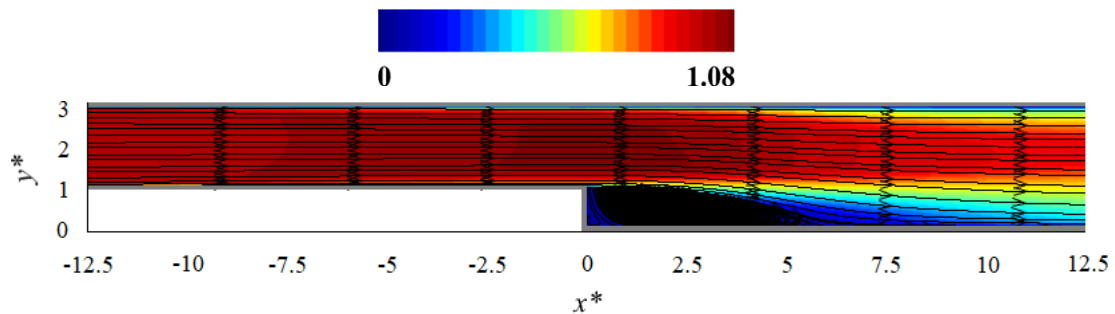


Figure 8. Velocity magnitude values with streamline patterns along the channel.

Turbulence kinetic energy values have been exhibited for $0.0016 \leq TKE^* = TKE / U_\infty^2 \leq 0.048$ in Figure 9. Kinetic energy is defined for the mean flow conditions. When attaining kinetic energy of the turbulent flow structure, turbulence kinetic energy (TKE) is utilized as a term, and it depends on turbulence density of the flow field [39]. Minimum value has been affected via core flow around the duct axis. However, it is not clearly valid for maximum value. With influence of turbulence triggered by flow separation, the highest value has been obtained in the wake region. It is a deduction that turbulence level of the step wake is higher than those of any other points.

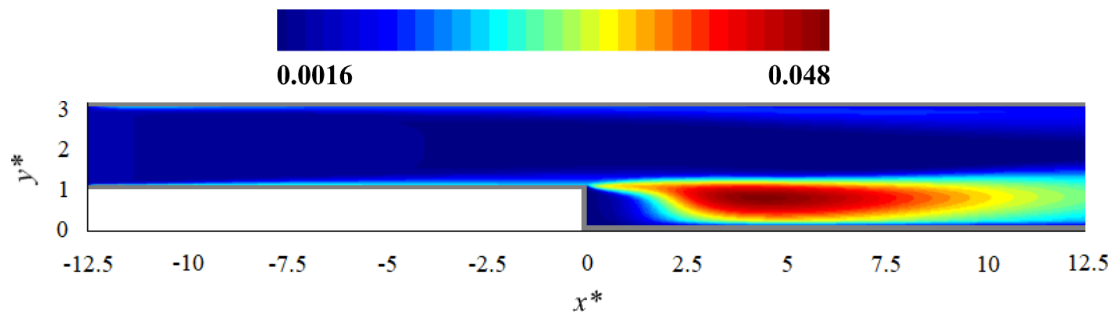


Figure 9. Turbulence kinetic energy values along the channel.

Streamwise velocity components of $-0.2 \leq u^* = u / U_\infty \leq 1.08$ have also been indicated on the planes in a row for $x^* = 0, 1, 2, 3, 4, 5, 6$ and 7 as in Figure 10. Maximum value has been attained around the channel axis. However, minimum value for this component has been attained in the wake region of the step. Negative values have been observed before the flow reattachment point at $x^* = 5.92$ as seen. Rotational flows were effective as stated previously. The upstream boundary layer has separated from the surface and formed as a curved one via quasi-boundary. A large vorticity has occurred and a smaller one through the step depth has also been detected. Moreover, symmetrical flow patterns have been spotted with respect to the line crossing through $z^* = 0$.

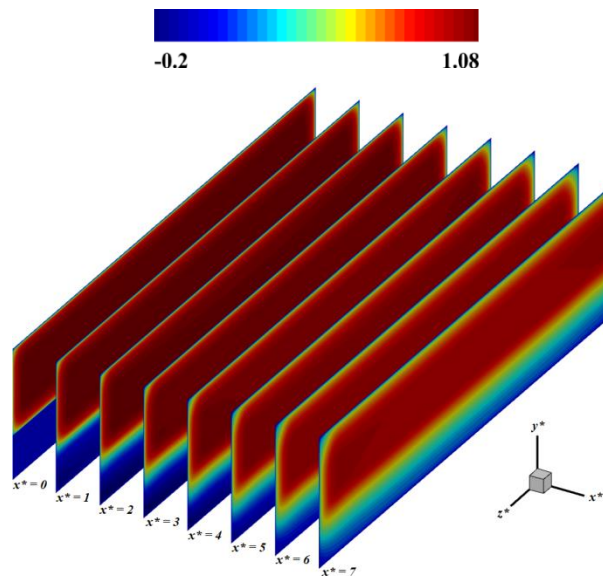


Figure 10. Streamwise velocity components on various stations.

Pressure distributions along the x -axis have been given for $y^* = 1$ and $y^* = 2$ at $z^* = 0$ as in Figure 11. For the upstream region of the backward-facing step, pressure drop has been obtained. The reason is that cross-sectional area is narrower. Depending on this case, velocity value for fluid flow is higher. However, pressure tends to increase for the downstream zone of the backward-facing step. Because there is an expansion for the cross-section. For this reason, velocity value is getting lower. On the other hand, pressure values have been increased. When the pressure difference between $y^* = 1$ and $y^* = 2$ is investigated, pressure values of $y^* = 1$ are lower than those of $y^* = 2$ for the first part of the downstream. However, it is vice versa for the second part of the downstream. This trend has been affected by interaction between flow separation and wake flow.

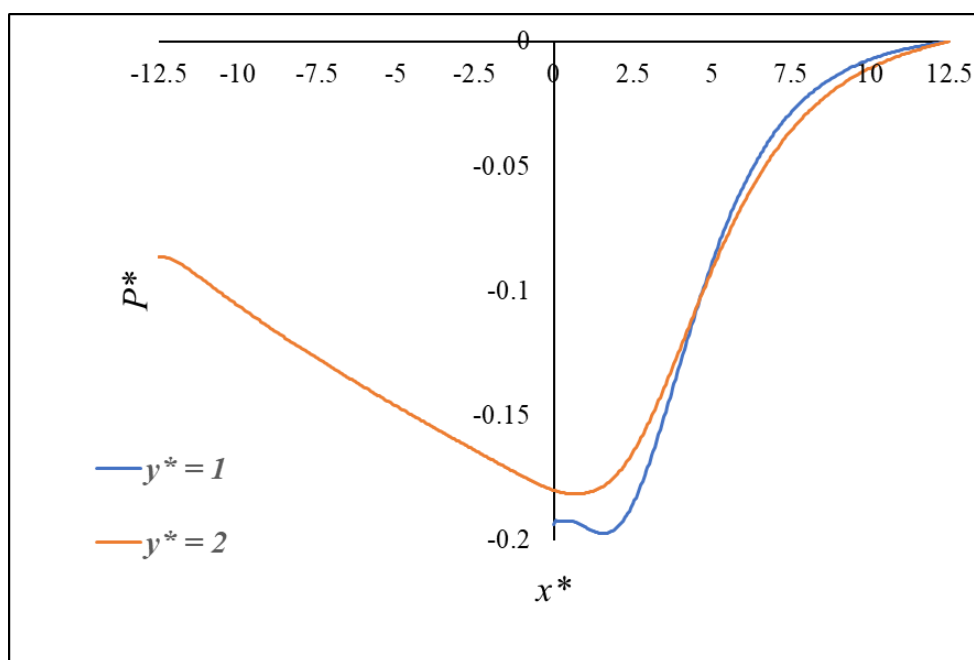


Figure 11. Pressure distributions for different stations.

Velocity profiles of streamwise components have been presented for $0 \leq x^* \leq 7$ at $z^* = 0$ as in Figure 12. Evolution of velocity profiles has been observed in a row in terms of the region covering flow separation and its reattachment inside the step wake. For the investigated part of the duct, streamwise velocity components are in the range of $-0.2 \leq u^* \leq 1.1$ as seen. Rotational flows are indicated by negative values which are dominant for $1 \leq x^* \leq 5$ in the chart. Since there is not any element disrupting the flow at the upstream, all values are positive as expected. Same situation has also been detected for $x^* > 6$ as flow reattachment is completed. In addition to the first reason, the effect of the wake region has also disappeared. Transition to core flow has been obtained at $y^* = 1.1$ which is above the step height. In that point, same velocity value of $u^* = 0.75$ has been provided.

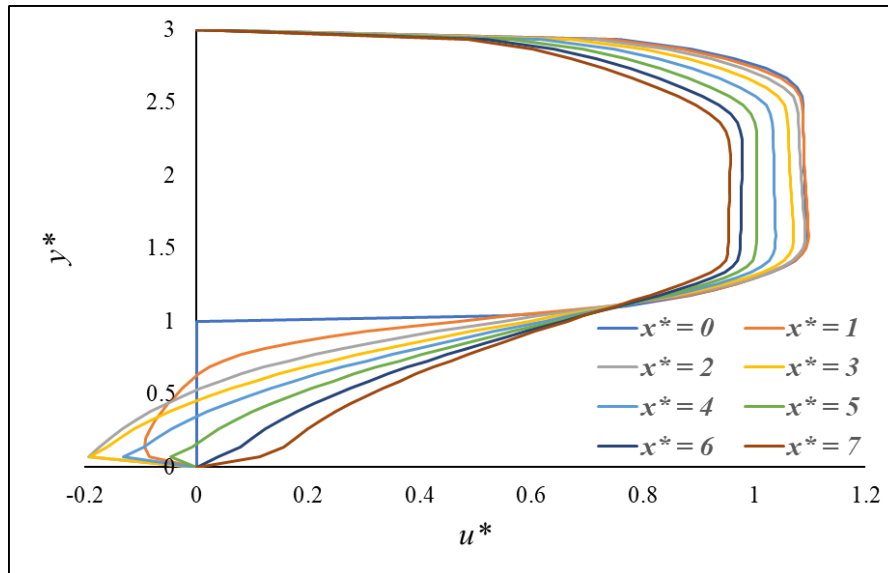


Figure 12. Velocity profiles of streamwise components for different stations.

Turbulence kinetic energy values have also been given for $0 \leq x^* \leq 7$ at $z^* = 0$ as in Figure 13. As explained previously, kinetic energy is valid in case of average flow conditions. When obtaining kinetic energy of the turbulent flow field, turbulence kinetic energy (TKE) is the required terms based on turbulence density of the flow structure. Change of these values has been presented in a row and the zone for separated and reattached flow in the wake region has been defined. Turbulence kinetic energy values have been given for $0 \leq TKE^* \leq 0.05$ for the related section of the channel. Flow oscillations have been observed for $x^* \geq 2$ and $y^* \leq 1$ since the fluctuations for these values are effective in the wake region.

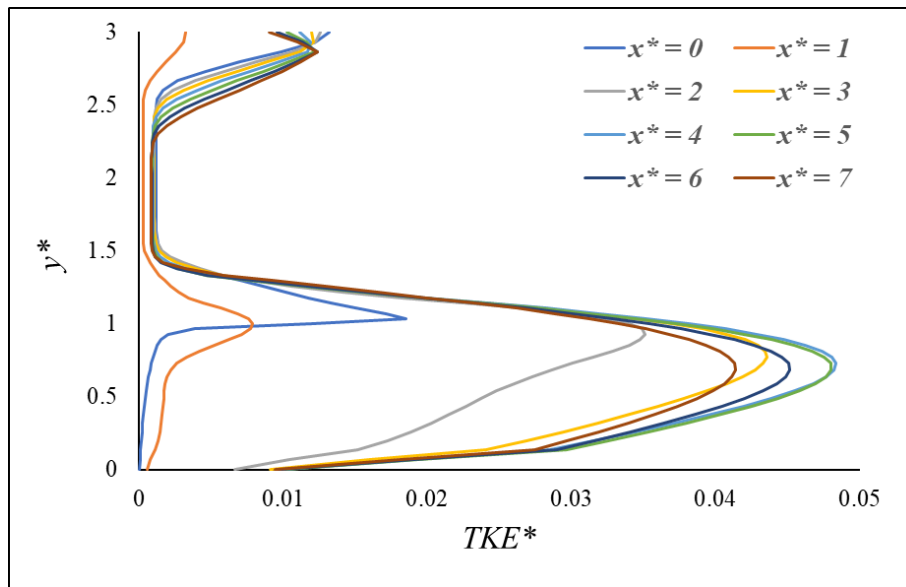


Figure 13. Turbulence kinetic energy values for different stations.

There is difference between the values from neighbor points. It is the indicator that turbulence intensity is higher at any related points. As there is not any element disrupting the core flow, the fluctuations in these values are limited.

4. CONCLUSIONS

In the present study, backward-facing step flow has been modeled with respect to an experimental study done at $Re = 5000$. Steady simulations have been conducted regarding the same flow conditions of the reference study. Pressure distributions, streamwise and cross-stream velocity components, velocity magnitude values with streamline patterns and turbulence kinetic energy values have been presented by using contour graphics. Furthermore, the stations for pressure distributions, velocity profiles for streamwise components and turbulence kinetic energy values have been defined for evolution of related data. The obtained results could be outlined as followings:

- The turbulence models of Standard $k-\epsilon$, $k-\epsilon$ RNG, $k-\epsilon$ Realizable, Standard $k-\omega$ and $k-\omega$ SST have been tested. In terms of reattachment length, $k-\epsilon$ RNG turbulence model has been chosen and numerical solutions have been done.
- Lower pressure zone for the wake region of the backward-facing step has been attained due to flow separation.
- Separation of the upstream boundary layer has been seen and it became a curved one.
- What is more, turbulence level of the step wake has been obtained as higher than those of any other points.

- Transition to core flow has been attained at $y^* = 1.1$ that is above the step height.
- Flow oscillations have been observed for $x^* \geq 2$ and $y^* \leq 1$ since the fluctuations for these values are effective in the wake region.
- The dimensionless reattachment length has been numerically obtained as 5.92 which is very good agreement with the experimental results at same Reynolds number. The deviation from the reference results is from 0.34 % to 1.33 % in terms of percentage errors.

Since the backward-facing step flow including flow separation and its reattachment, it is very significant for engineering applications as airfoils, buildings, heat exchangers, hydrofoils, spoilers, turbine blades, combustor flame-holder and engine inlets, micro combustors. Flow behavior is influenced owing the change of channel height for flow direction. For this reason, the expansion effect should be considered and investigated via experimental and numerical methods. Considering the non-availability of experimental facilities, numerical modeling with reliable methods is very important. Use and comparison of other turbulence models is recommended for future studies on the backward-facing step flow.

ACKNOWLEDGMENT

The present study has been supported by Konya Technical University Academic Staff Training Program with the project number of 2018-OYP-046.

REFERENCES

- [1] Chen, L., Asai, K., Nonomura, T., Xi, G. and Liu, T., (2018). A review of backward-facing step (BFS) flow mechanisms, heat transfer and control, *Thermal Science and Engineering Progress*, 6, 194-216.
- [2] Teso-Fz-Betoño, D., Juica, M., Portal-Porras, K., Fernandez-Gamiz, U. and Zulueta, E., (2021). Estimating the reattachment length by realizing a comparison between URANS k-omega SST and LES WALE models on a symmetric geometry, *Symmetry*, 13(9), 1555.
- [3] Arthur, J.K., (2023). A narrow-channeled backward-facing step flow with or without a pin-fin insert: Flow in the separated region, *Experimental Thermal and Fluid Science*, 141, 110791.
- [4] Detto, M., Katul, G.G., Siqueira, M., Juang, J.Y. and Stoy, P., (2008). The structure of turbulence near a tall forest edge: The backward-facing step flow analogy revisited, *Ecological Applications*, 18(6), 1420-1435.
- [5] Deepa, G. and Murali, G., (2014). Effects of viscous dissipation on unsteady MHD free convective flow with thermophoresis past a radiate inclined permeable plate, *Iranian Journal of Science and Technology*, 38(3.1), 379-388.

- [6] Jiaqiang, E., Cai, L., Li, J., Ding, J., Chen, J. and Luo, B., (2022). Effects analysis on the catalytic combustion and heat transfer performance enhancement of a non-premixed hydrogen/air micro combustor, *Fuel*, 309, 122125.
- [7] Zuo, W., Zhao, H., Jiaqiang, E., Li, Q. and Li, D., (2022). Numerical investigations on thermal performance and flame stability of hydrogen-fueled micro tube combustor with injector for thermophotovoltaic applications, *International Journal of Hydrogen Energy*, 47(39), 17454-17467.
- [8] Giannopoulos, A. and Aider, J.L., (2020). Prediction of the dynamics of a backward-facing step flow using focused time-delay neural networks and particle image velocimetry data-sets, *International Journal of Heat and Fluid Flow*, 82, 108533.
- [9] Oder, J., Shams, A., Cizelj, L. and Tiselj, I., (2019). Direct numerical simulation of low-Prandtl fluid flow over a confined backward facing step, *International Journal of Heat and Mass Transfer*, 142, 118436.
- [10] Jovic, S. and Driver, D., (1995). Reynolds number effect on the skin friction in separated flows behind a backward-facing step, *Experiments in Fluids*, 18, 464-467.
- [11] Kasagi, N. and Matsunaga, A., (1995). Three-dimensional particle-tracking velocimetry measurement of turbulence statistics and energy budget in a backward-facing step flow, *International Journal of Heat and Fluid Flow*, 16(6), 477-485.
- [12] Scarano, F., Benocci, C. and Riethmuller, M.L., (1999). Pattern recognition analysis of the turbulent flow past a backward facing step, *Physics of Fluids*, 11(12), 3808-3818.
- [13] Wengle, H., Huppertz, A., Bärwolff, G. and Janke, G., (2001). The manipulated transitional backward-facing step flow: an experimental and direct numerical simulation investigation, *European Journal of Mechanics-B/Fluids*, 20(1), 25-46.
- [14] Kostas, J., Soria, J. and Chong, M., (2002). Particle image velocimetry measurements of a backward-facing step flow, *Experiments in Fluids*, 33, 838-853.
- [15] Furuichi, N., Hachiga, T. and Kumada, M., (2004). An experimental investigation of a large-scale structure of a two-dimensional backward-facing step by using advanced multi-point LDV, *Experiments in Fluids*, 36, 274-281.
- [16] Nie, J.H. and Armaly, B.F., (2004). Reverse flow regions in three-dimensional backward-facing step flow, *International Journal of Heat and Mass Transfer*, 47(22), 4713-4720.
- [17] Schram, C., Rambaud, P. and Riethmuller, M.L., (2004). Wavelet based eddy structure eduction from a backward facing step flow investigated using particle image velocimetry, *Experiments in Fluids*, 36, 233-245.

- [18] Bouda, N.N., Schiestel, R., Amielh, M., Rey, C. and Benabid, T., (2008). Experimental approach and numerical prediction of a turbulent wall jet over a backward facing step, *International Journal of Heat and Fluid Flow*, 29(4), 927-944.
- [19] Wu, Y., Ren, H. and Tang, H., (2013). Turbulent flow over a rough backward-facing step, *International Journal of Heat and Fluid Flow*, 44, 155-169.
- [20] Nadge, P.M. and Govardhan, R.N., (2014). High Reynolds number flow over a backward-facing step: structure of the mean separation bubble, *Experiments in Fluids*, 55, 1-22.
- [21] Yamada, S. and Nakamura, H., (2016). Construction of 2D-3C PIV and high-speed infrared thermography combined system for simultaneous measurement of flow and thermal fluctuations over a backward facing step, *International Journal of Heat and Fluid Flow*, 61, 174-182.
- [22] Le, H., Moin, P. and Kim, J., (1997). Direct numerical simulation of turbulent flow over a backward-facing step, *Journal of Fluid Mechanics*, 330, 349-374.
- [23] Chiang, T.P., Sheu, T.W. and Fang, C.C., (1999). Numerical investigation of vortical evolution in a backward-facing step expansion flow, *Applied Mathematical Modelling*, 23(12), 915-932.
- [24] Avancha, R.V. and Pletcher, R.H., (2002). Large eddy simulation of the turbulent flow past a backward-facing step with heat transfer and property variations, *International Journal of Heat and Fluid Flow*, 23(5), 601-614.
- [25] Dejoan, A. and Leschziner, M.A., (2004). Large eddy simulation of periodically perturbed separated flow over a backward-facing step, *International Journal of Heat and Fluid Flow*, 25(4), 581-592.
- [26] Aider, J.L. and Danet, A., (2006). Large-eddy simulation study of upstream boundary conditions influence upon a backward-facing step flow, *Comptes Rendus Mécanique*, 334(7), 447-453.
- [27] Barri, M., El Khoury, G.K., Andersson, H.I. and Pettersen, B., (2010). DNS of backward-facing step flow with fully turbulent inflow, *International Journal for Numerical Methods in Fluids*, 64(7), 777-792.
- [28] El Khoury, G.K., Andersson, H.I., Barri, M. and Pettersen, B., (2010). Massive separation of turbulent Couette flow in a one-sided expansion channel, *International Journal of Heat and Fluid Flow*, 31(3), 274-283.
- [29] Jürgens, W. and Kaltenbach, H.J., (2012). The effect of sweep on the forced transitional flow over a backward-facing step, *Computers and Fluids*, 59, 1-10.

- [30] Kanchi, H., Sengupta, K. and Mashayek, F., (2013). Effect of turbulent inflow boundary condition in LES of flow over a backward-facing step using spectral element method, *International Journal of Heat and Mass Transfer*, 62, 782-793.
- [31] Togun, H., Safaei, M.R., Sadri, R., Kazi, S.N., Badarudin, A., Hooman, K. and Sadeghinezhad, E., (2014). Numerical simulation of laminar to turbulent nanofluid flow and heat transfer over a backward-facing step, *Applied Mathematics and Computation*, 239, 153-170.
- [32] Amiri, A., Arzani, H.K., Kazi, S.N., Chew, B.T. and Badarudin, A., (2016). Backward-facing step heat transfer of the turbulent regime for functionalized graphene nanoplatelets based water-ethylene glycol nanofluids, *International Journal of Heat and Mass Transfer*, 97, 538-546.
- [33] Xu, J.H., Zou, S., Inaoka, K. and Xi, G.N., (2017). Effect of Reynolds number on flow and heat transfer in incompressible forced convection over a 3D backward-facing step, *International Journal of Refrigeration*, 79, 164-175.
- [34] Yagmur, S., Dogan, S., Aksoy, M.H. and Goktepe, I., (2020). Turbulence modeling approaches on unsteady flow structures around a semi-circular cylinder, *Ocean Engineering*, 200, 107051.
- [35] Goktepe, I. and Atmaca, U., (2023). Examination of air flow characteristics over an open rectangular cavity between the plates, *International Journal of Aeroacoustics*, 22(3-4), 351-370.
- [36] Murali, G., Paul, A.J.I.T. and Narendrababu, N.V., (2015). Numerical study of chemical reaction effects on unsteady MHD fluid flow past an infinite vertical plate embedded in a porous medium with variable suction, *Electronic Journal of Mathematical Analysis and Applications*, 3(2), 179-192.
- [37] Murali, G. and Narendrababu, N.V., (2021). Convective MHD jeffrey fluid flow due to vertical plates with pulsed fluid suction: A numerical study, *Journal of Computational Applied Mechanics*, 54(1), 36-48.
- [38] Kang, S. and Choi, H., (2002). Suboptimal feedback control of turbulent flow over a backward-facing step, *Journal of Fluid Mechanics*, 463, 201-227.
- [39] Goktepe, I., Atmaca, U. and Cakan, A., (2020). Investigation of heat transfer augmentation between the ribbed plates via Taguchi approach and computational fluid dynamics, *Journal of Thermal Science*, 29, 647-666.
- [40] Goktepe, I., Atmaca, U. and Yagmur, S., (2021). Visualization of flow characteristics between the ribbed plates via Particle Image Velocimetry, *Thermal Science*, 25(1), 171-179.
- [41] Goktepe, I. and Atmaca, U., (2020). Numerical examination of heat transfer augmentation between the plates with square cross-sectional ribs for the staggered arrangement, *Kocaeli Journal of Science and Engineering*, 3(2), 33-40.

- [42] Goktepe, I. and Atmaca, U., (2021). Computational study on the effect of the staggered ribs on heat transfer phenomena between the horizontal plates, Hittite Journal of Science and Engineering, 8(1), 7-17.



RESEARCH ARTICLE

**EVALUATION OF THE MONITORING OF SURFACE DEFORMATIONS IN OPEN-PIT
MINES WITH SENTINEL-1A SATELLITE RADAR DATA**

Bekir POYRAZ^{1*}, Yavuz GÜL², Fatih POYRAZ³

¹Sivas Cumhuriyet University, Division of Mining Engineering, bpoyraz@cumhuriyet.edu.tr,
ORCID: 0000-0003-2832-4632

²Sivas Cumhuriyet University, Engineering Faculty, Civil Engineering, ygul@cumhuriyet.edu.tr,
ORCID: 0000-0002-2969-577X

³Sivas Cumhuriyet University, Engineering Faculty, Geomatics Engineering, fpoyraz@cumhuriyet.edu.tr,
ORCID: 0000-0001-9471-7261

Receive Date: 28.07.2023

Accepted Date: 25.08.2023

ABSTRACT

Accidents and loss of life can occur in surface mines due to large mass displacements (landslides). In order to prevent these irreversible situations, it is very important to identify displacements in advance or to take necessary measures by obtaining early warning signs. Within the scope of this study, satellite radar images (SAR, Synthetic Aperture Radar) obtained from the European Space Agency (ESA) Sentinel-1A satellite were used to reveal the traceability and monitoring sensitivity of deformations and possible mass displacements in the dump area of a mining operation. The results obtained from 2 Global Positioning Systems (GPS) installed in the field were compared with the results obtained from satellite radar data and their compatibility with each other was evaluated. When the horizontal/vertical velocity values obtained by decomposing the Sentinel-1A ascending and descending satellite line of sight (LOS, Line Of Sight) velocities were compared with the horizontal/vertical velocity values of GPS, the results were statistically equal. GPS-based vertical velocities were -131.5 mm/year at GPS1 and -20.7 mm/year at GPS2, while Sentinel-1A-based velocities were -94.5 mm/year at GPS1 and -7.8 mm/year at GPS2. While both GPS and satellite-based vertical deformations show the same direction (in the form of subsidence), the deformation velocity values obtained from satellite radar data are lower than GPS results. Horizontal deformations obtained with satellite radar data could not be determined in the north/south direction due to satellite orbital motions, while they could be partially determined in the east/west direction. GPS-based east/west horizontal velocities were +2.8 mm/year in GPS1 and insignificant velocity was found in GPS2. Satellite-based east/west horizontal velocity values were +6.8 mm/year at GPS1 and +8.4 mm/year at GPS2.

Keywords: GPS, InSAR, LOS, SBAS, Sentinel-1A, Surface mining

1. INTRODUCTION

Today, deformation determination studies in open pit mines are generally carried out on a point basis and landslide risk is tried to be determined according to the general movements of these points. If the locations of the points are not within the deformation zones, it is assumed that there is no risk in the study area [1]. This situation prevents measures from being taken against possible landslides. Discontinuity and stress directions change due to the ongoing excavation works in mining operations. When determining deformation areas, not only certain areas but the entire working area and its surroundings should be considered as possible deformation areas. Therefore, deformation monitoring studies should be areal rather than point-based and should cover the entire study area.

The two best methods for monitoring deformation on an areal basis are remote sensing and aerial photogrammetry. In recent years, the Interferometric Synthetic Aperture Radar (InSAR) method, which utilizes satellite data to determine surface deformations and movements over vast areas, has emerged as a prominent technique [2]. In this method, delays in the signals reflected and returned from the satellite are detected, enabling the generation of high-resolution images through signal processing.

While point-based deformations can be monitored very effectively with GPS, deformations over large areas can be monitored using satellite radar data [3-5]. GPSs are capable of determining the three-dimensional position of points with mm accuracy. While GPSs can be easily used to monitor slow landslides in small areas, monitoring large areas requires the tracking of a large number of points. On the other hand, the InSAR method is capable of reliably measuring daily or longer-term displacements in the earth's surface with mm accuracy, using satellite radar imagery to monitor deformations and tectonic movements over extensive areas [3,6-10]. These two methods have their respective advantages and disadvantages. The most important shortcomings of this system are the necessity to select an appropriate model to correct ionospheric errors in GPS measurements and the fact that data acquisition is limited to the point of installation [11]. When continuously monitoring a large number of points with GPS networks, high costs can be incurred [10]. However, the biggest advantage of GPS measurement is that it provides mm-accurate values for east/west, north/south, and up/down directions on a point-by-point basis [12]. On the other hand, the InSAR method offers significant advantages such as monitoring large areas, high temporal resolution, and all-weather monitoring [13]. Nevertheless, the main disadvantages of this method include limitations in deformation tracking due to satellite transit times [5], the impact of atmospheric effects on measurement results [13,14], and the inability to determine north/south direction deformations [5,8-10,15,16]. Considering these factors together, it is suggested that more accurate surface displacement estimates can be achieved by using GPS and InSAR methods together, providing results with both high temporal and spatial resolution [2,8]. Additionally, by utilizing both methods, the disadvantages associated with point-based tracking and satellite transit times are expected to be overcome.

Within the scope of this study, satellite radar data (SAR, Synthetic Aperture Radar), and GPS data were utilized to detect horizontal and vertical deformations in a specific region at a mine site. Simultaneously with the provision of SAR data, 2 GPS units were installed in the field, and measurements were conducted. Horizontal and vertical deformation velocity values determined from

both SAR and GPS measurements were compared, revealing the similarities and differences between them.

2. MATERIAL AND METHODOLOGY

The horizontal and vertical deformation rates determined from Sentinel-1A satellite SAR data, considering the date of installation of the GPSs, were determined by taking into account the nearest Distributed Scatterer (DS) value at the points where the GPSs were installed. These results were then compared with the horizontal and vertical deformation velocities obtained from the GPSs.

2.1. Study Area

The studied area is the Kalburçayırı coal open-pit area where the coal needs of the Kangal Thermal Power Plant are met (Figure 1). The operation site is located within the borders of the Kangal district of Sivas province, Turkey. Kalburçayırı, situated in the southern part of the district center and approximately 30 km away from the district, features coal deposits of 7 m thickness in two seams. The cover on the upper vein measures 42 m in thickness, while an intermediate cover of 20 m separates the two veins. The coal is accompanied by limestone, clayey limestone, and marl as side rocks. The area comprises small hills, presenting a high plateau appearance. Due to erosions, the south of the area is more hilly than the north [17].

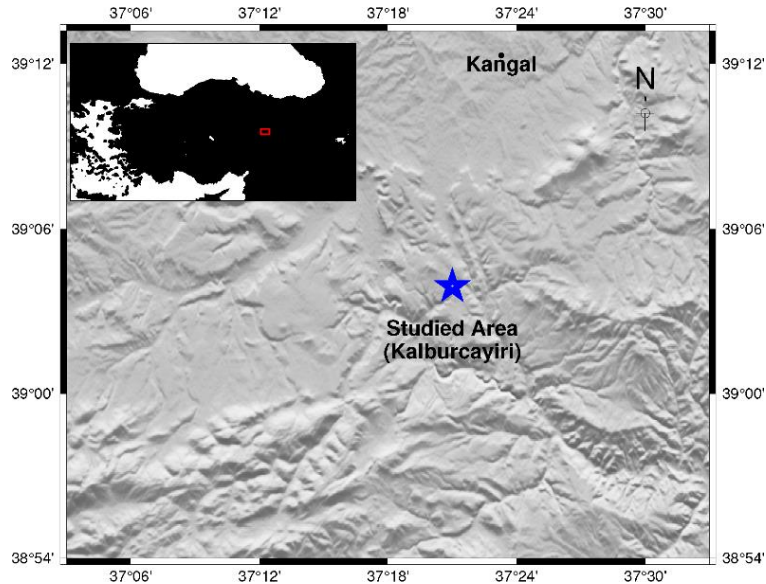


Figure 1. Studied area.

2.2. Methodology And Data Set

In line with the workflow plan given in Figure 2, the studies outlined below were carried out.

- Installation of 2 GPS units in the field to compare whether satellite radar imagery-based studies produce reliable results.
- Providing satellite radar images in descending and ascending orbit from Sentinel-1A satellite of the European Space Agency (ESA).
- Determination of horizontal and vertical deformation velocities by decomposing method from deformation velocities in the satellite line-of-sight (LOS) direction obtained from SAR data,
- Comparison of horizontal and vertical deformation velocity values determined from Sentinel-1A satellite radar data with horizontal and vertical deformation velocity values estimated from GPS results.

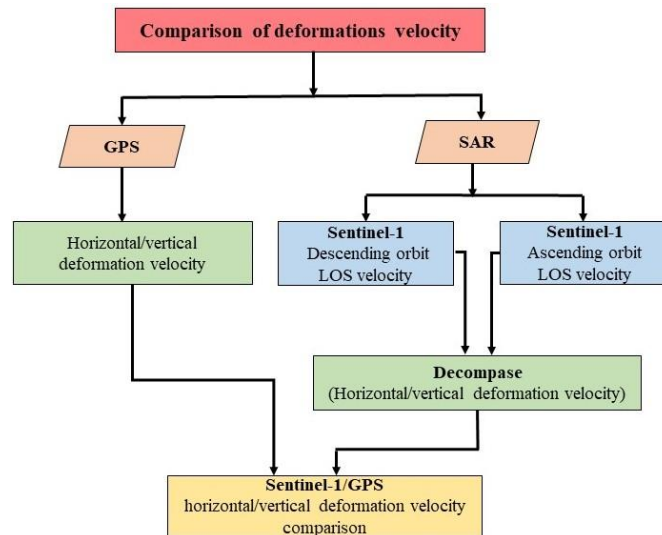


Figure 2. Work flow plan.

Within the scope of the study, 19 SAR data of the Sentinel 1A (IW, Interferometric Wide Swath Mode) satellite in descending (10) and ascending (9) orbits were used, taking into account the data acquisition date of the GPS installed in Kangal Kalburçayırı field (June 01, 2022 - October 31, 2022). The satellite image data set used is given in Table 1.

Table 1. Time range and image numbers of the satellite radar data.

Sentinel-1A				
	Image ID	Date	Frame	Product Modes
Ascending	1	20220715	116	IW
	2	20220727	116	IW
	3	20220808	116	IW
	4	20220820	116	IW
	5	20220901	116	IW
	6	20220913	116	IW

	7	20220925	116	IW
	8	20221007	116	IW
	9	20221019	116	IW
Descending	1	20220709	21	IW
	2	20220721	21	IW
	3	20220802	21	IW
	4	20220814	21	IW
	5	20220826	21	IW
	6	20220907	21	IW
	7	20220919	21	IW
	8	20221001	21	IW
	9	20221013	21	IW
	10	20221025	21	IW

2.3. SAR Calculations

For the Sentinel-1A satellite, 9 ascending orbital radar images from July 15, 2022, to October 19, 2022, and 10 descending orbital radar images from July 9, 2022, to October 25, 2022, are used as datasets in Table 1. The deformation velocity values in the LOS direction were determined by GMTSAR [18,19], StaMPS/MTI (Stanford Method for Persistent Scatterers) [20] programs, and SBAS technique, and the interferogram pairs are shown in Figure 3. GMTSAR is an open-source InSAR processing system based on Generic Mapping Tools (GMT).

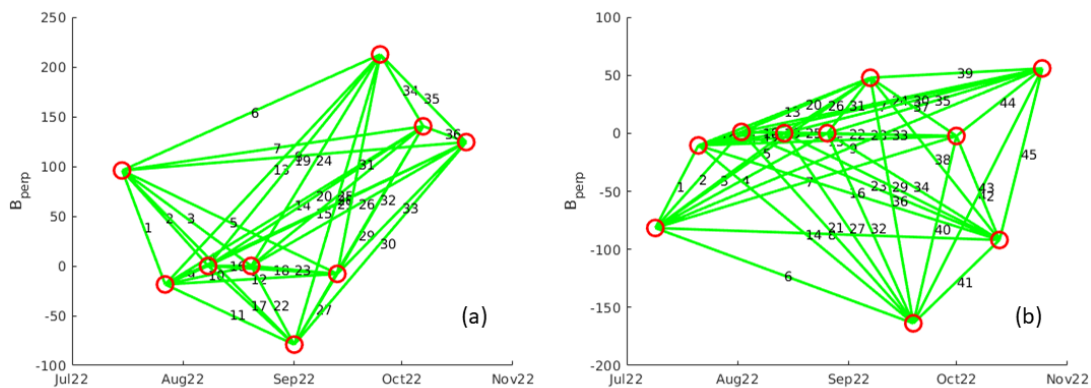


Figure 3. Spatial and temporal distribution of the Sentinel-1A image relative to SBAS (Green lines indicate interferogram pairs). a) 116 track numbers ascending. b) 21 track numbers descending.

The MineSAR program was used for the determination and detailed evaluation of the horizontal and vertical deformation velocities of the DS points around the GPS locations using the decomposing method. MineSAR software supported by the Small and Medium Enterprises Development Organization of Turkey (KOSGEB) within the scope of the R & D, Innovation and Industrial Application Support Program was developed by Geomine R&D Software Company. With MineSAR

software, a limited region can be encircled from the entire deformation area and the DSs at that location can be seen.

LOS deformation velocities are converted to horizontal and vertical directions using the following equations in MineSAR software. Surface deformations are expressed as $V=(V_E, V_N, V_{UP})^T$ in three dimensions in the east, north, and up directions. The transformation of the surface displacement vector to the V_{LOS} satellite line of sight is written as in Eq. 1. In Eq. 1, V_{LOS} , s , and V are the LOS displacement, satellite unit vector, and three-dimensional surface displacement vectors, respectively. Eq. 2 shows the satellite unit vector in detail. For ascending and descending transitions, α_h in Eq. 2 is the angle of heading, and θ is the angle of incidence [3,21,22]. In the last stage, the LOS displacement values of the descending and ascending satellites were converted into east and up components using Eq. 3 [23].

$$V_{LOS}=s^T.V \quad (1)$$

$$s=(-\cos\alpha_h\sin\theta \quad \sin\alpha_h \sin\theta \quad \cos\theta)^T \quad (2)$$

$$\begin{pmatrix} -\cos(\alpha_{ASC}) & \sin(\alpha_{ASC}) \cos(\delta_{ASC}) \\ -\cos(\alpha_{DSC}) & \sin(\alpha_{DSC}) \cos(\delta_{DSC}) \end{pmatrix} \begin{pmatrix} V_{UP} \\ V_{EW} \end{pmatrix} = \begin{pmatrix} V_{LOS,ASC} \\ V_{LOS,DSC} \end{pmatrix} \quad (3)$$

In Eq. 3, for ascending and descending satellites, α_{ASC} , α_{DSC} denotes the angles of heading, and δ_{ASC} , $\cos(\delta_{DSC})$ denotes the angles of incidence (Figure 4). V_{UP} is the velocity for the up component, V_{EW} is the velocity for the east component, $V_{LOS,ASC}$ is the velocity in the ascending satellite LOS direction, $V_{LOS,DSC}$ is the velocity in the descending satellite LOS direction. Vertical and horizontal deformation velocity maps are given in Figures 5 and 6.

From the LOS data, vertical up/down and east/west horizontal displacements can be detected, while north/south horizontal displacements cannot be detected due to the satellite's orbit motion. [2,9,15,16].

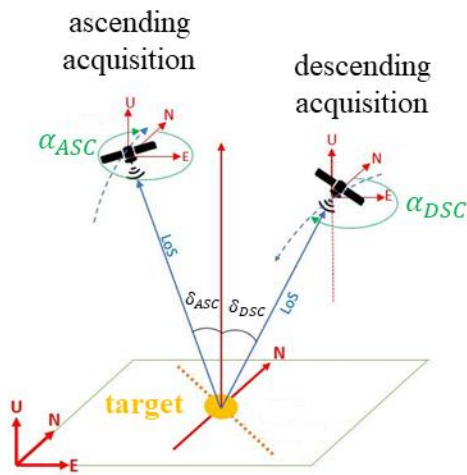


Figure 4. Schematic overview of the imaging geometry of a satellite in ascending and descending orbits [24].

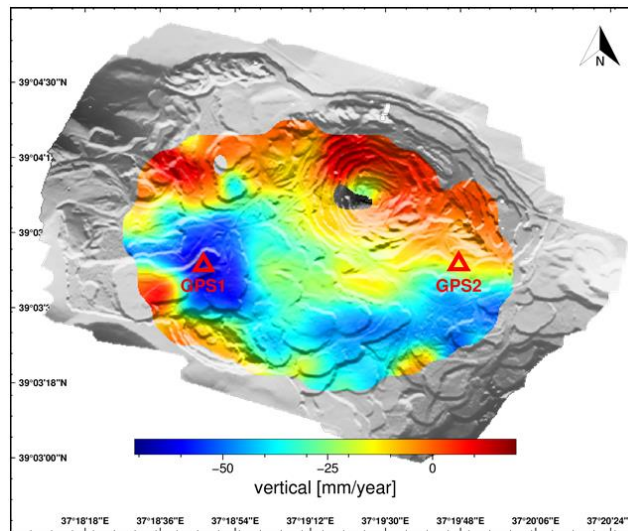


Figure 5. Spatial distribution maps of vertical deformation velocities.

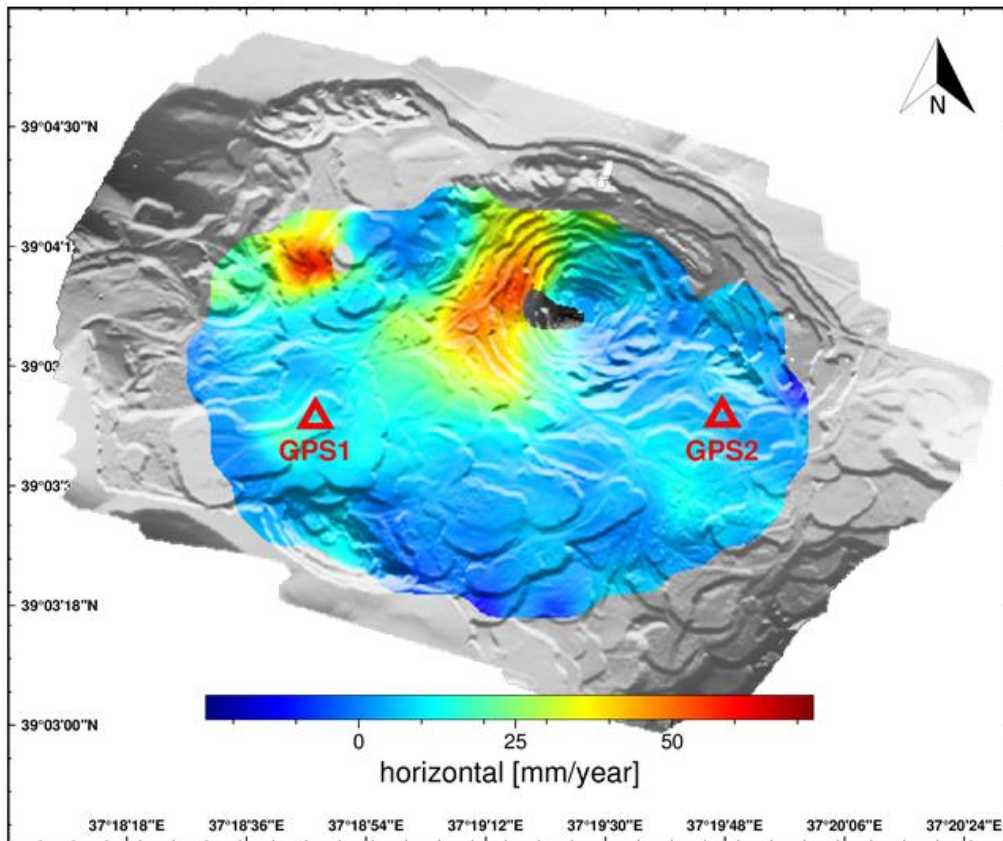


Figure 6. Spatial distribution maps of horizontal deformation velocities.

In order to compare the horizontal/vertical deformation velocities determined from Sentinel-1A satellite radar data with the horizontal/vertical deformation velocities obtained from GPS1 and GPS2 data, the DS points closest to the point where GPS1 and GPS2 were installed were considered (Figure 7).

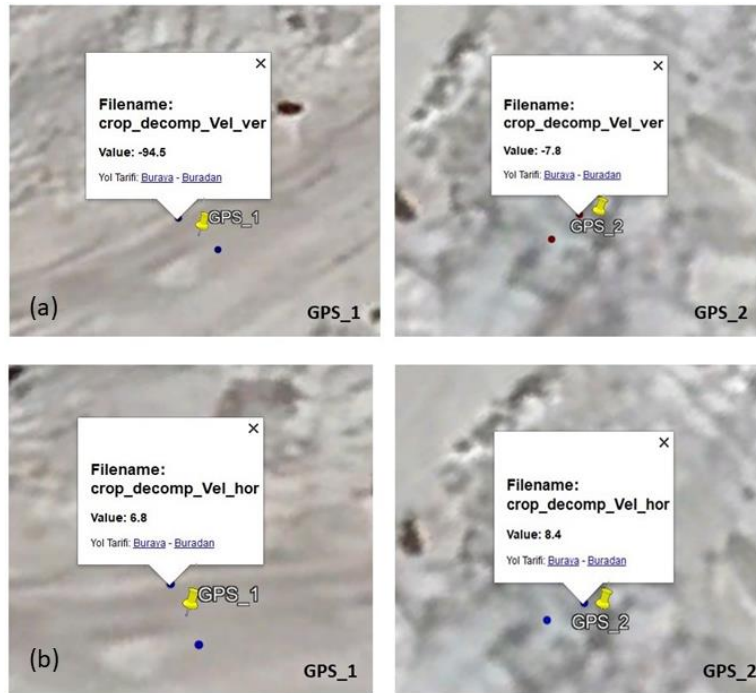


Figure 7. DS point nearest to GPS point. a) vertical deformation. b) horizontal deformation.

Velocity values of DS points in horizontal and vertical directions were calculated according to Eq. 3. The standard deviation values of the DS points in horizontal and vertical directions were obtained by applying the error propagation rule to Eq. 3 (Table 2). The reason for choosing one DS point closest to the GPS points is that the error propagation rule can only be applied to the first measurements when calculating the standard deviation values of the DS points. Since the error propagation rule is applied to the first measurement values, the closest DS point is chosen instead of the average of the DSs around the GPS point.

As a result of the decomposition process according to Eq. 3, the velocity values of the up and east components were estimated, while the standard deviation values were obtained using the "Error propagation rule." It is inevitable that inaccuracies in the measurements will result in inaccuracies in the calculated magnitudes. The process of determining the effects of errors in the measurements on the functions calculated from these measurements is carried out according to the Error Propagation Rule. We assume that the measurements L_1 , L_2 , and L_3 , with known variances and covariances, have x and y functions (Eq. 4 and 5) as follows,

$$x = g(L_1, L_2, L_3) \quad (4)$$

$$y = h(L_1, L_2, L_3) \tag{5}$$

The effect of errors in the measurements on the x, y functions can be determined by taking the differential of these functions with respect to the measurements (Eq. 6 and 7). The error propagation rule applies only to the first measurements [25].

$$dx = \frac{\partial g}{\partial L_1} dL_1 + \frac{\partial g}{\partial L_2} dL_2 + \frac{\partial g}{\partial L_3} dL_3 \tag{6}$$

$$dy = \frac{\partial h}{\partial L_1} dL_1 + \frac{\partial h}{\partial L_2} dL_2 + \frac{\partial h}{\partial L_3} dL_3 \tag{7}$$

Table 2. The amount of horizontal/vertical deformation at the DS point nearest to GPS1 and GPS2

	GPS1 point (mm/year)	std	GPS2 point (mm/year)	std
Vertical deformation	-94.5	18.1	-7.8	5.4
Horizontal deformation	6.8	17.0	8.4	5.2

Considering the DSs at the closest distance to the GPS points, the vertical deformation rate at the GPS1 location was -94.5 mm/year and the horizontal deformation rate was +6.8 mm/year, while the vertical deformation rate at the GPS2 location was -7.8 mm/year and the horizontal deformation rate was +8.4 mm/year.

2.4. GPS Calculations

In order to compare the horizontal and vertical deformation velocity values obtained from SAR data, 2 "Z-MAX THALES" brand GPS devices were installed within the boundaries shown in Figure 8 in the area we call the deformation area. GPS devices have been continuously powered by solar panels and batteries. The deformation area has been tracked with GPS devices for approximately 4 months.

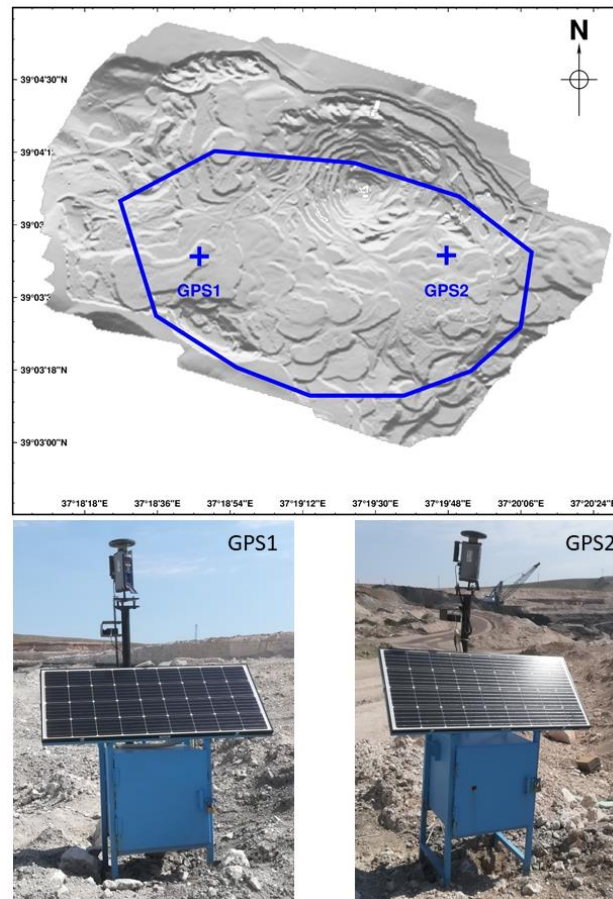


Figure 8. GPS's installed in the field.

GPS1 and GPS2 devices were installed in the field on June 01, 2022. The measurement results were evaluated on the website of the Geodetic Research Center of Canada [26], and the horizontal and vertical positions of the GPSs on the earth's surface were determined. Horizontal and vertical deformation velocity values were estimated from the time series (Figure 9) produced with the help of these data. There were interruptions in the time series given in Figure 9, due to a lack of data. This is due to the low data storage capacity of the device in question. However, as seen in Figure 9, this lack of data did not affect the general trend.

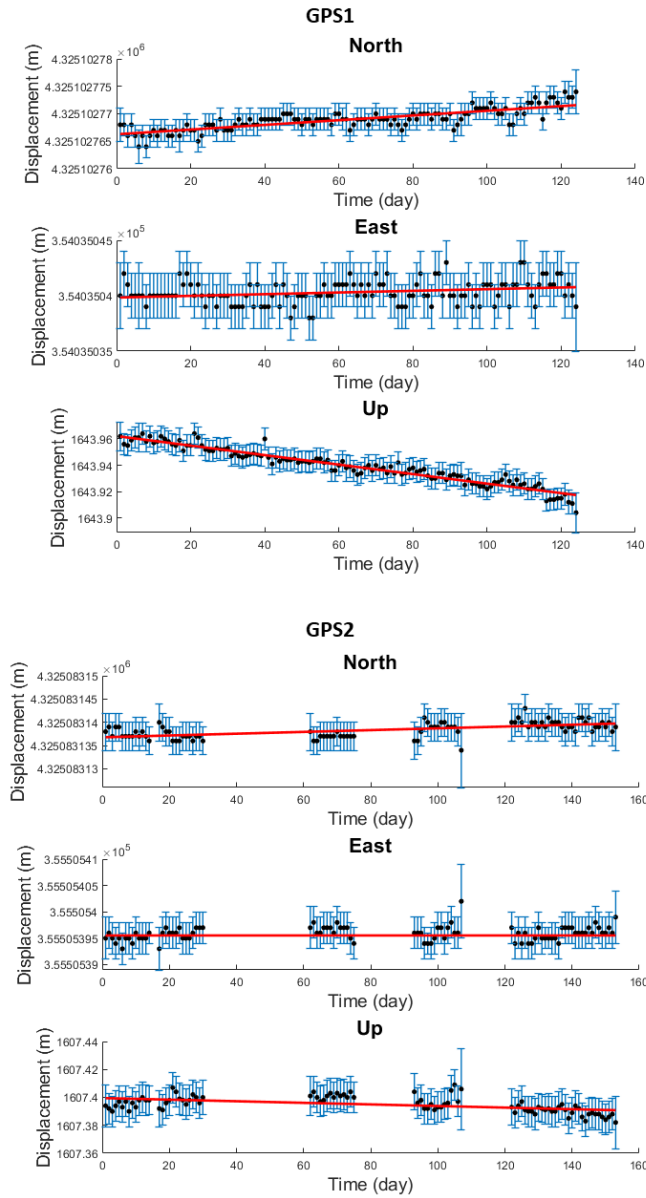


Figure 9. Time series for GPS1 and GPS2 points.

The velocity values obtained from the time series of GPS1 and GPS2 were analyzed using a t-test (at $\alpha = 0.05$ confidence interval, t-test value; 1.9796 for GPS1 and 1.9876 for GPS2). Significant velocity values were determined and the obtained numerical quantities are presented in Table 3.

Table 3. GPS horizontal/vertical deformation estimated velocity values.

	GPS1				GPS2			
	V (mm/year)	SV _{Std}	t-test	Decision	V (mm/year)	SV _{Std}	t-test	Decision
North	15.6	1.05	14.83	significant	7.0	0.93	7.60	significant
East	2.8	0.95	2.89	significant	1.3	0.91	1.42	unsignificant
Up	-131.5	3.27	40.28	significant	-20.7	3.64	5.70	significant

- Vertical deformations in the form of collapse were determined as -131.5 mm/year at GPS1 and -20.7 mm/year at GPS2.
- For the horizontal deformations in the east/west direction, the velocity value was +2.8 mm/year at the GPS1 point, while unsignificant velocity value was found at the GPS2 point.
- The horizontal deformation values in the north/south direction were +15.6 mm/year at GPS1 and +7.0 mm/year at GPS2.

Based on the t-test results, the velocities in the directions of North, East, and Up at GPS1, and North and Up at GPS2 were found to be significant. However, the velocity value in the east/west direction at GPS2 was found to be unsignificant.

3. DISCUSSIONS

Horizontal/vertical velocity values were determined by decomposing Sentinel-1A data. F-test and t-test analyses were performed to determine whether the horizontal/vertical velocity values of Sentinel-1A and GPSs can be considered equal. Firstly, the equality of variances was checked with the F-test, and accordingly, the variance of the difference to be used in the t-test was calculated. The results obtained are presented in Table 4.

Table 4. GPS and Sentinel-1A horizontal/vertical deformation velocity comparison.

ID	Vertical deformation							F test		t-test	
	GPS (mm/year)			Sentinel-1A (mm/year)			Velocity difference	GPS1 F limit :2.086	GPS2 F limit :3.282	GPS1 t limit :2.364	GPS2 t limit :2.322
	n	V	std	n	V	std	Vd	F test	Decision	t-test	Decision
GPS1	124	-131.5	3.27	9	-94.5	18.1	-37	2.22	not equal	2.01	Equal
GPS2	89	-20.7	3.64	9	-7.8	5.4	-12.9	4.49	not equal	1.98	Equal
ID	Horizontal deformation							F test		t-test	
	GPS (mm/year)			Sentinel-1A (mm/year)			Velocity difference	GPS1 F limit :2.086	GPS2 F limit :2.117	GPS1 t limit :2.365	GPS2 t limit :2.364
	n	V	std	n	V	std	Vd	F test	Decision	t-test	Decision
GPS1	124	2.8	0.95	9	6.8	17.0	4.0	23.24	not equal	0.23	Equal

GPS2	89	1.3	0.91	9	8.4	5.2	7.1	3.30	not equal	1.34	Equal
-------------	----	------------	------	---	------------	-----	-----	------	-----------	------	--------------

**n: Number of measures; V: LOS velocity (mm/year); std: Standard deviation*

As a result of the comparisons made by considering the horizontal/vertical velocity values given in Table 4. the following findings were made.

Although the variances of the satellite and GPS-based velocities obtained at GPS1 and GPS2 points for vertical and horizontal deformations were not equal, the velocity values were found to be equal according to the statistical analysis results. Therefore, the velocities obtained can be considered equal.

GPS-based vertical velocities were -131.5 mm/year at GPS1 and -20.7 mm/year at GPS2, while Sentinel-1A-based velocities were -94.5 mm/year at GPS1 and -7.8 mm/year at GPS2. While GPS and satellite-based vertical deformations show the same direction (in the form of subsidence), the deformation velocity values obtained from satellite radar data are lower at both GPS1 and GPS2 points compared to GPS results. Similar results were observed in studies [9]. It is stated that the horizontal/vertical velocity values obtained from satellite radar images are lower than the velocity values obtained with GPS. This study also presents similar findings. The difference in deformation velocity magnitudes is believed to be due to the fact that Distributed Scatterers (DS) could not be found at the exact GPS points, and therefore, the deformation velocity value at the DS point closest to the GPS point was taken into account. However, the use of fewer data and larger standard deviations when estimating velocity values from SAR data compared to GPS (Table 4) is considered to be an important factor in the different results. The number of data for velocity estimation is 124 for GPS1, 89 for GPS2, and only 9 for Sentinel-1A. Moreover, while the standard deviation values for GPS are around 3.5 mm/year, the standard deviation of SAR data reaches up to 18 mm/year.

Horizontal deformations obtained with satellite radar data could not be determined in the north/south direction due to satellite orbital motions, while they could be partially determined in the east/west direction. These values were determined as +2.8 mm/year at the GPS1 point, and insignificant velocity was found at the GPS2 point. Additionally, the horizontal deformation values in the east/west direction were +6.8 mm/year at the GPS1 point and +8.4 mm/year at the GPS2 point.

Although north/south deformation velocities of +15.6 mm/year at GPS1 and +7.0 mm/year at GPS2 were determined based on GPS, these velocities/movements could not be detected with satellite-based data. In studies on the subject, it is stated that approximately 7% to 11% of the deformations in the north/south direction can be determined by the decomposition method from satellite radar data [2,9]. In light of this information and considering the small of number values, the reason for not obtaining a satellite-based north/south directional result can also be explained. This situation is confirmed in the literature.

According to these determinations; since the horizontal/vertical deformation velocity values obtained from GPS and Sentinel-1A data are statistically equal according to the t-test, the results are compatible. The deformation directions determined from both GPS and SAR data are the same. In this study, vertical and horizontal deformations obtained using GPS and satellite radar data gave similar results to previous studies [2,3,9,27-29].

4. CONCLUSIONS AND RECOMMENDATIONS

In this study, the dump site of a coal mine was selected as the study area. Horizontal and vertical deformation velocities in the area were determined using data from the Sentinel-1A satellite over a specific time interval. To validate and compare the satellite radar data, GPS devices were installed at 2 points within the deformation area, and deformations were measured over approximately 4 months. The horizontal and vertical deformations determined by both SAR images and GPS data were compared and the results are given below.

The directions of horizontal and vertical deformations determined from GPS and Sentinel-1A data are consistent. Velocity values are consistent according to the t-test. Although the vertical and horizontal deformation velocities obtained by the decomposition method based on Sentinel-1A are lower than the GPS-based velocities, they generally show the same direction (in the form of collapse). These results are consistent with the literature.

Although a north/south directional movement was determined based on GPS, these velocities/movements could not be detected with satellite-based data. In studies on the subject, it is stated that approximately 10% of the north/south deformations can be determined using satellite radar data. Considering that the numbers are very small, it is an expected result that a satellite-based north/south deformation could not be obtained. This situation also supports the observation in the previous point.

Satellite-based velocity values were found to be lower than GPS-based velocity values. This is thought to be due to the use of fewer data and larger standard deviations when estimating velocity values from SAR data compared to GPS. On the other hand, despite the differences in magnitudes, the deformation directions obtained from GPS data and the directions obtained from SAR data were found to be the same.

When the above-mentioned points are evaluated as a whole, it is useful to consider the following recommendations and suggestions.

In satellite radar-based deformation monitoring, a significant problem is that deformation detection times are limited to the acquisition dates of satellite imagery. Deformations that occur between satellite passes cannot be monitored until the next acquisition. The most crucial advantage of GPS over satellite-based techniques is its capability to determine horizontal deformations in the north/south direction. However, since GPS allows only point-based assessments, monitoring large areas by establishing GPS networks can be costly and workforce.

The comparison of GPS and Sentinel-1A velocity values was statistically equal. The velocity magnitudes determined by the InSAR/SBAS technique were lower than those determined by GPS. Nevertheless, the InSAR/SBAS technique provided consistent results in terms of deformation directions and continuity. The study's results suggest that the InSAR/SBAS technique can be effectively used to monitor deformations in mining areas with sufficient sensitivity for early warning purposes.

With the combination of the InSAR technique and GPS systems, it is thought that the deformations can be monitored more effectively by overcoming the problems caused by the waiting times caused by the satellite transit time. Especially with the GPS units to be installed in the deformation zones determined from the satellite data, the tracking process can be improved significantly.

This approach can enable real-time and continuous deformation monitoring, especially at mine sites, which can lead to a more comprehensive understanding of ground motions at mine sites. Since the method requires minimum field application, it will stand out as an approach that takes occupational health and safety into account at the highest level.

ACKNOWLEDGEMENT

The authors would like to thank Prof. Dr. Kemal Özgür Hastaoğlu, who works at Sivas Cumhuriyet University, Faculty of Engineering, Survey Engineering, for his support. The authors would like to thank the Kangal Coal Enterprise officials for their cooperation and Geomine R & D company for MineSAR software support.

REFERENCES

- [1] Hastaoğlu, K. Ö., Gül, Y., Poyraz, F., and Kara, B. C. (2019). Monitoring 3D areal displacements by a new methodology and software using UAV photogrammetry. *International Journal of Applied Earth Observation and Geoinformation*, 83, 101916.
- [2] Poyraz, F., Gül, Y., and Duymaz, B. (2020). Determination of deformations by using the PSI technique at a common dump site of three different open-pit marble mines in Turkey. *Turkish J. Earth Sci.* 29, 1004–1016.
- [3] Hastaoğlu, K.O. (2016). Comparing the results of PSInSAR and GNSS on slow motion landslides, Koyulhisar, Turkey. *Geomatics, Nat. Hazards Risk* 7, 786–803
- [4] Carlà, T., Tofani, V., Lombardi, L., Raspini, F., Bianchini, S., Bertolo, D., Thuegaz, P., and Casagli, N. (2019). Combination of GNSS, satellite InSAR, and GBInSAR remote sensing monitoring to improve the understanding of a large landslide in high alpine environment. *Geomorphology* 335, 62–75.
- [5] Poyraz, B. (2023). Maden işletmelerinde yüzey deformasyonlarının yapay açıklıklı uydu radar görüntüleriyle izlenebilirliğinin araştırılması. (Tez No. 802631) [Doktora Tezi, Sivas Cumhuriyet Üniversitesi], Yükseköğretim Kurulu Tez Merkezi (in Turkish), Sivas.
- [6] Casu, F., Manzo, M., and Lanari, R. (2006). A quantitative assessment of the SBAS algorithm performance for surface deformation retrieval from DInSAR data. *Remote Sens. Environ.* 102, 195–210.

- [7] Ferretti, A., Savio, G., Barzaghi, R., Borghi, A., Musazzi, S., Novali, F., Prati, C., and Rocca, F. (2007). Submillimeter accuracy of InSAR time series: Experimental validation. *IEEE Trans. Geosci. Remote Sens.*, 45, 1142–1153
- [8] Fuhrmann, T., Garthwaite, M., Lawrie, S., and Brown, N. (2018). Combination of GNSS and InSAR for future Australian datums. In: *IGNSS Symposium 2018 - International Global Navigation Satellite Systems Association*, pp. 1–13.
- [9] Poyraz, F., and Hastaoğlu, K.O. (2020). Monitoring of tectonic movements of the Gediz Graben by the PSInSAR method and validation with GNSS results. *Arab. J. Geosci.*, 13, 1–11.
- [10] Bányai, L., Bozsó, I., Szűcs, E., Gribovszki, K., and Wertzergom, V. (2023). Monitoring strategy of geological hazards using integrated three-dimensional InSAR and GNSS technologies with case study. *Period. Polytech. Civ. Eng.*
- [11] Rovira-Garcia, A., Juan, J.M., Sanz, J., González-Casado, G., and Ibáñez, D. (2016). Accuracy of ionospheric models used in GNSS and SBAS: methodology and analysis. *J. Geod.*, 90, 229–240.
- [12] Del Soldato, M., Confuorto, P., Bianchini, S., Sbarra, P., and Casagli, N. (2021). Review of works combining GNSS and InSAR in Europe. *Remote Sens.* 13, 1684.
- [13] Hu, B., Chen, J., and Zhang, X. (2019). Monitoring the land subsidence area in a coastal urban area with InSAR and GNSS. *Sensors* 19, 3181.
- [14] Parizzi, A., Gonzalez, F.R., and Brcic, R. (2020). A covariance-based approach to merging InSAR and GNSS displacement rate measurements. *Remote Sens.* 12, 300.
- [15] Pawluszek-Filipiak, K., and Borkowski, A. (2020). Integration of DInSAR and SBAS techniques to determine mining-related deformations using Sentinel-1 Data: The case study of Rydułtowy Mine in Poland. *Remote Sens.* 2020, Vol, 12, Page 242 12, 242.
- [16] Kim, J., Lin, S.Y., Singh, R.P., Lan, C.W., and Yun, H.W. (2021). Underground burning of Jharia coal mine (India) and associated surface deformation using InSAR data. *Int. J. Appl. Earth Obs. Geoinf.* 103, 102524.
- [17] Gül, Y. (2006). Bazı açık işletmelerdeki değişik kaya birimlerinin taşıma kapasitelerinin araştırılması ve kayaç özellikleri ile ilişkilendirilmesi. (Tez No. 181739) [Doktora Tezi, Sivas Cumhuriyet Üniversitesi], Yükseköğretim Kurulu Tez Merkezi (in Turkish), Sivas.
- [18] Sandwell, D., Mellors, R., Tong, X., Wei, M., and Wessel, P. (2011). Open radar interferometry software for mapping surface deformation. *Eos, Trans. Am. Geophys. Union* 92, 234–234.
- [19] Sandwell, D., Mellors, R., Tong, X., Xu, X., Wei, M., and Wessel, P. (2016). GMTSAR: An InSAR processing system based on generic mapping tools (second edition). Scripps institution of oceanography technical report. Livermore, CA (United States).

- [20] Hooper, A., Bekaert, D., Hussain, E., and Spaans, K. (2018). StaMPS/MTI manual version 4.1b. School of Earth and Environment University of Leeds, United Kingdom.
- [21] Arikan, M., Hooper, A., and Hanssen, R. (2010). Radar time series analysis over west Anatolia. In: Lacoste Francis H (editor). Fringe 2009 Proceedings. ESA SP 677. Noordwijk, Netherlands: ESA, pp. 1-6.
- [22] Fuhrmann, T., and Garthwaite, M. C. (2019). Resolving three-dimensional surface motion with InSAR: Constraints from multi-geometry data fusion. *Remote Sensing*, 11(3), 241. [https://doi: 10.3390/rs11030241](https://doi.org/10.3390/rs11030241)
- [23] Hanssen, R.F. (2001). Radar interferometry: Data interpretation and error analysis. *Remote Sensing and Digital Image Processing*. Springer Dordrecht, Dordrecht.
- [24] Brouwer, W. (2021). An analysis of the InSAR displacement vector decomposition: InSAR fallacies and the strap-down solution. Delft University of Technology. Master thesis, 140pp, Netherlands
- [25] Bektaş, S. (2005). Endirekt ve koşullu ölçülerle dengeleme hesabı. OMÜ yayınlari, Yayın No:118, ISBN 975- 7636-54-1, 208 sayfa, OMÜ Basımevi,
- [26] <https://webapp.csrscs.nrcan-rncan.gc.ca/geod/tools-outils/ppp.php?locale=en> (accessed date: 7.11.23).
- [27] Bayık, Ç. (2018). Çok zamanlı ve çok frekanslı SAR-GNSS verileri ile heyelanların araştırılması: Beylikdüzü-Esenyurt örneği. Bülent Ecevit Üniversitesi; Fen Bilimleri Enstitüsü (Doktora Tezi); 137s; Zonguldak
- [28] Çınar, O. (2019). Yapay açıklıklı radar ve GPS/GNSS verileri ile düşey yönlü yüzey deformasyonlarının modellenmesi. Çanakkale Onsekiz Mart Üniversitesi, Fen Bilimleri Enstitüsü (Yüksek Lisans Tezi), 91s, Çanakkale
- [29] Cigna, F., Esquivel Ramírez, R., and Tapete, D. (2021). Accuracy of Sentinel-1 PSI and SBAS InSAR displacement velocities against GNSS and geodetic leveling monitoring data. *Remote Sensing*, 13(23), 4800.



RESEARCH ARTICLE

INVESTIGATION OF MECHANICAL PROPERTIES OF AL 7075 ALLOY SOLIDIFIED UNDER VIBRATION

Mustafa GÜLMEZ¹, Ağah AYĞAHOĞLU^{2,*}

¹Kütahya Vocational and Technical Anatolian High School, Machine and Design Technology, Kütahya, gulmez42@hotmail.com, ORCID: 0000-0003-4508-7894

²Kütahya Dumlupınar University, Faculty of Engineering, Department of Mechanical Engineering, Kütahya, agah.aygahoglu@dpu.edu.tr, ORCID: 0000-0002-6556-8663

Receive Date: 04.07.2023

Accepted Date: 05.09.2023

ABSTRACT

Al 7075 alloy is a material with high mechanical properties and limited plastic formability at room temperature. In some special applications, it may need to be obtained by casting. In this study, it is aimed to increase the strength of the Al 7075 alloy by solidification which has a wide range of applications in sectors such as automotive, aircraft and space defense industry, under mechanical vibration applied at different frequencies after casting. Microstructure examination, compression test and hardness measurement tests are conducted to determine the changes in the mechanical properties of Al 7075 alloy in different frequencies by after solidification under mechanical vibration. Maximum hardness value is obtained at 30 Hz frequency in mechanical vibrations applied at frequencies between 10-50 Hz. This hardness value is lower than the hardness values that can be obtained by precipitation hardening, but considerably higher than the material without heat treatment.

Keywords: Al 7075, Mechanical Vibration, Solidification.

1. INTRODUCTION

Vibration treatment is a common additional approach to materials during metal solidification, aimed at improving their macrostructure and microstructure, consequently enhancing their mechanical properties. Most studies on this subject explain the effects of the vibration process and its relation to the cavitation phenomenon. [1, 2].

Among aluminium alloys, Al 7075 is the most preferred material due to its high strength value. If an even higher strength value is desired, precipitation hardening can be employed. However, the application of this process is limited due to several factors: the high cost associated with precipitation hardening, the requirement for large furnaces when dealing with sizable components, and the formation of different thermal gradients at different cross-section thicknesses in complex shaped parts. For Al 7075 work pieces to be produced with casting process, if a slight strength increase from the

current strength is desired, grain size reduction, which is another strength increasing method, can be applied. Strength value increase can be achieved in the material by applying the solidification method under vibration (mechanical or ultrasonic vibrations), which can be applied for grain reduction, at different frequencies.

The technique of solidifying metallic materials under mechanical vibration is discovered by Sokoloff. Compared to other techniques, this technique is used more because of its convenience and cheapness. Campbell [3], stated that grain refinement occurs in castings due to the application of vibration during casting, thus improving the mechanical properties, so that the production of high-strength structural materials is mainly based on the development of a product in which the grain size is as small as possible. He also observed that, the corrosion resistance of the alloys improved along with their mechanical properties. Guo et al. [4] observed that during solidification, the energy resulting from the excess heat and latent heat of the molten alloy is mainly absorbed by the die and that the mechanical vibration is indirectly given back to the molten alloy by vibrating the die. On the other hand, Southgate concluded in their study that eutectic formations are promoted, resulting in a 10% increase in tensile stress. Freedman and Wallace have found in their study that small grains with coarse eutectic components are formed. Also, as reported by Pillai, the same components have reduced in grain size under vibration treatment and become coarser only when modified with 0.05 wt% Na to the alloy [5]. Jiang et al. [6] used vibration in A356 aluminium alloy. They determined that, the mechanical properties of A356 aluminium alloy obtained from conventional casting decreased continuously with the increase of the wall thickness, and the mechanical properties and density of A356 aluminium alloy obtained by mechanical vibration are greatly increased. They also observed that, the tensile strength, yield strength, elongation and hardness of the sample with a wall thickness of 40 mm are 35%, 42%, 63% and 29% higher, respectively, than the sample obtained from conventional casting under T6 condition. Fisher used the vibration process on LM6 alloy (Al- 12.3%Si) and as a result, he reported the reduction of secondary dendrites and grain size on LM6 alloy. Along with this study, Burbure also reported a reduction in grain size for thick and short needle-shaped Al 12% Si as the vibration amplitude is increased. According to the report, the tensile stress decreased due to the coarsening of the silicon. However, no effect on ductility is observed [5]. Al-Ethari et al. [7] investigated the effect of mechanical and thermo mechanical treatment on the microstructure, grain size, porosity and hardness of Al-Zn-Mg alloy. As a result, they observed a 45% decrease in the grain size of the samples cast using mold vibration and hot forming. Additionally, the heat-treated and hot-shaped samples exhibited a 57% reduction in grain size. Along with these, they found that the porosity of these samples is decreased by 58% and 98%, respectively, while their hardness is increased by 11% and 81%, respectively.

In Al-Si alloys, when low-frequency vibration is applied depending on the effect of frequency, modification is observed in the alloy, and it has been determined that the porosities are more involved in low vibration than in high vibration. Kocatepe and Burdett applied vibration to two types of LM6 alloys. In the results, they found that the grain size of the unmodified alloy was reduced by 52% due to vibration (while the modified alloy exhibited 76% grain purification/refinement). As a consequence of the vibration treatment, the eutectic silicon in each alloy became coarser. Additionally, they observed that the coarsening of silicon increases as both the vibration amplitude and frequency increase [5, 8].

By examining the studies given above, it can be said that, the application of vibration has led to both the eutectic composition of aluminium and the microstructural change of its dendritic structure.

Vibration can improve ordered structures when the amplitude is wide enough. As a result, severe radial segregation is lost, as is the case with samples that solidify under microgravity conditions [9]. Deshpande's study also concluded that the grains in Al-Si alloy are tighter, denser and more uniform throughout the casting as a result of mechanical mold vibration [10]. Mehda et al. [11] studied the effect of mechanical vibration on Al4.5Cu (LM11) alloy during permanent die casting. They found that increasing mold vibration amplitude raises casting density due to improved fluidity from α -Al dendrite fragmentation and spherical structure formation. They also investigated the formation of α -Al dendrites during solidification prevents the molten metal from flowing easily into the mold, consequently causing shrinkage porosity. Additionally, their findings revealed that while gas porosity is observed in castings produced in fixed molds, there is no evidence of gas porosity in castings produced by mold vibration. This suggests that mechanical vibration is effective in degassing the melt. Vorozhtsov et al. [12] suggested that vibration has no effect when applied above the liquidus temperature, which is related to the duration of mechanical vibration. It may even be the source of unwanted gas retention events, so vibration should be initiated at the very beginning of solidification and terminated by full metal solidification.

In this work, apart from the studies in the literature, the microstructure variation and its effect on mechanical properties of the Al 7075 alloy solidified under mechanical vibration applied at different frequencies are investigated.

2. EXPERIMENTS AND EVALUATION

At the first stage of the study, samples are placed in a specially designed vibrating mold (Figure 1) with an average weight of 20 g (± 2 g). Then, based on the relation $T_m = T + 0.2T$ [13], the samples are melted in the furnace at 735 °C for about an hour, and after that, they are taken to the mechanical vibration mechanism (Figure 2) together with the mold. The dimensions of the molds containing the samples solidified by vibration are $\varnothing 15 \times 50$ mm.

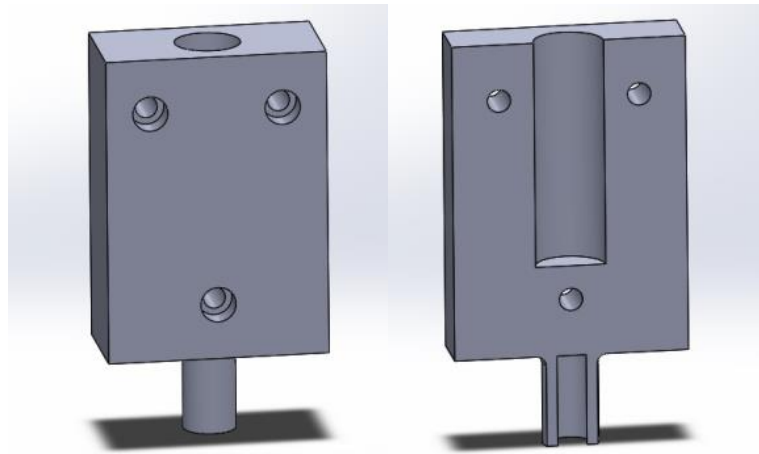


Figure 1. Mechanical vibration molds.

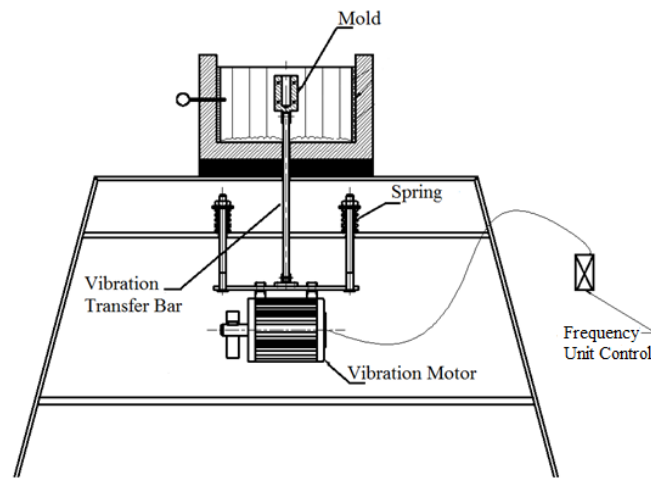


Figure 2. Solidification test setup under mechanical vibration.

A total of 27 samples are manufactured at frequencies between 10 and 50 Hz (10, 15, 20, 25, 30, 35, 40, 45, 50 Hz), adjusted in the mechanical vibration mechanism, with the same cooling criteria at each frequency. The vibration applied to the samples taken from the furnace continued until the solidification of the material is achieved.

Among the samples examined after the process, especially those that are solidified between 30 – 50 Hz, macro-sized porosities and slag are formed on the upper parts of the samples. For this reason, the samples are cut by using cooling liquid in an abrasive cutting machine by taking very few areas from

the lower part and the upper part. As a result, samples with a diameter of $\varnothing 15$ and a height of approximately 30 mm are obtained.

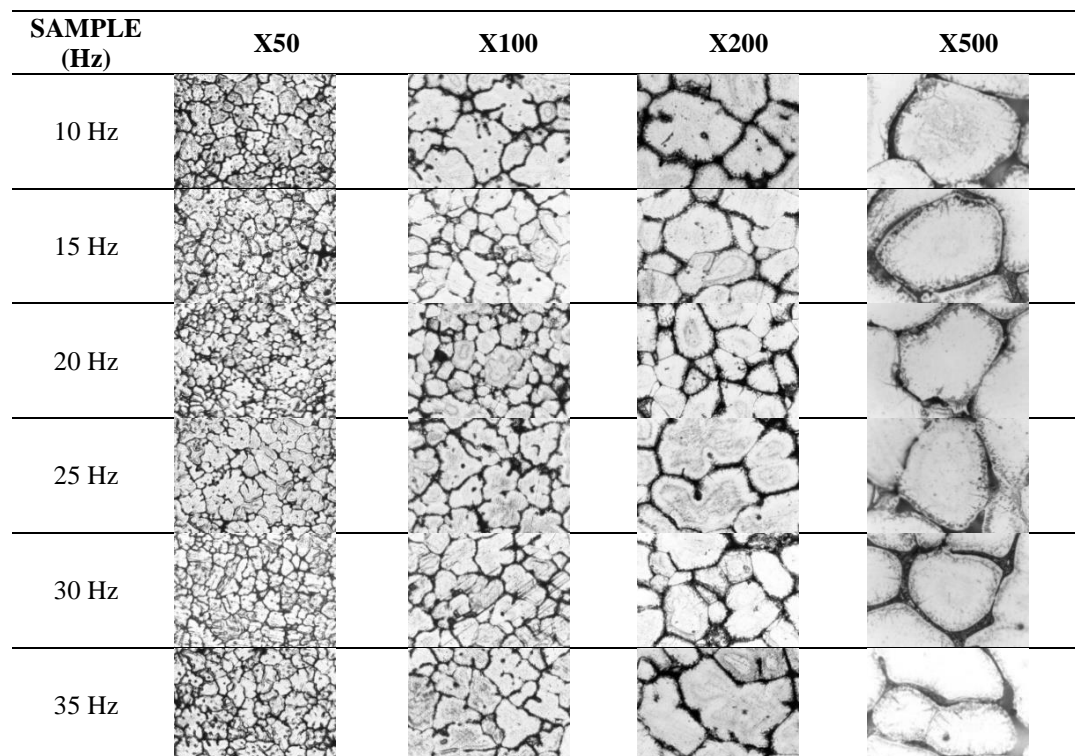
Samples are etched with Keller's reagent for metallographic examination. After etching, microstructure photos of the samples are taken at 5X, 10X, 20X, 50X magnifications, and grain sizes are measured.

The hardness of the samples prepared for Brinell Hardness method is measured using a ball diameter of $\varnothing 2.5$ mm and a load of 67.5 kgf. Compression test is carried out to determine the mechanical properties of AL 7075 materials such as compressive yield strength, compressive strength, compressive elasticity modulus and strain under static loading conditions. Compression test is carried out by applying 10 mm compression distance to the samples.

3. RESULTS

3.1. Microstructure Observations

The microstructure photos at different magnification ratios taken from the surfaces of each etched sample after metallographic preparations are shown in Figure 3.



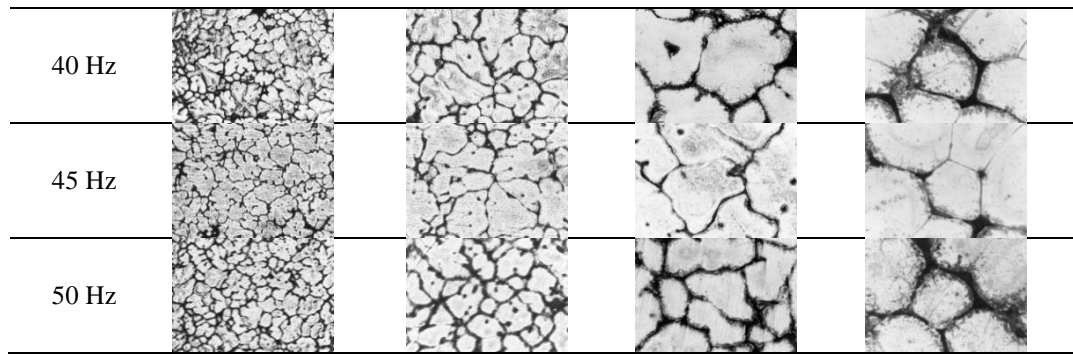


Figure 3. Microstructure photos of samples at different magnification ratios.

Upon optical microscope examinations following the application of mechanical vibrations, it is determined that grain shrinkage did not occur uniformly across all grains forming the structure. Instead, small-sized grains are observed to form in random locations.

As seen in Figure 4, obtained through optical microscope measurements, the grain size decreases with increasing vibration frequency, consistent with findings in the literature. With these results, it can be said that it is possible to obtain fine grained structures in solidification with high frequency ultrasonic vibration.

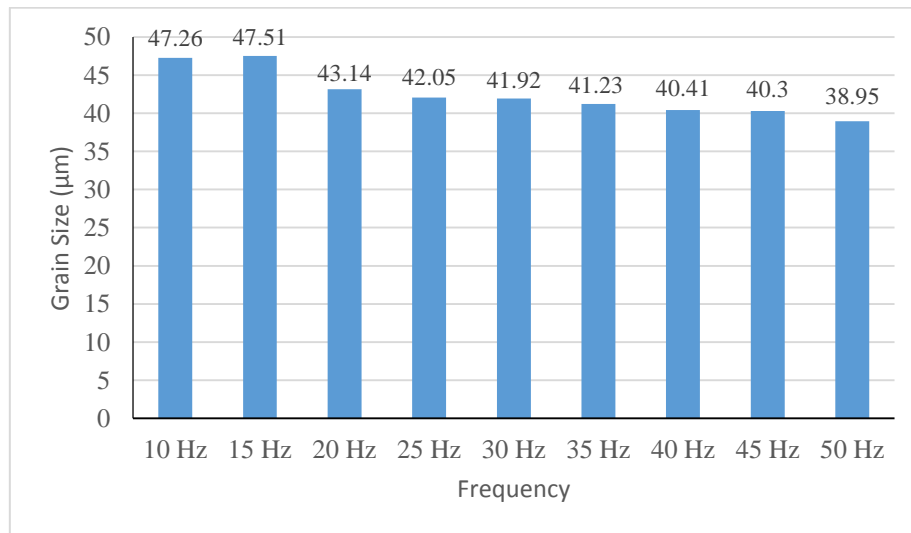


Figure 4. Grain size measurements.

3.2. Hardness Measurement

In the examined studies in the literature, it is stated that the hardness values of the lower parts close to the vibration source are higher than the upper parts in the samples solidified under vibration. Hardness measurements (HB) are made on both the upper and lower parts of the 30 mm long samples obtained from this point of view. The obtained hardness values are given in Figure 5.

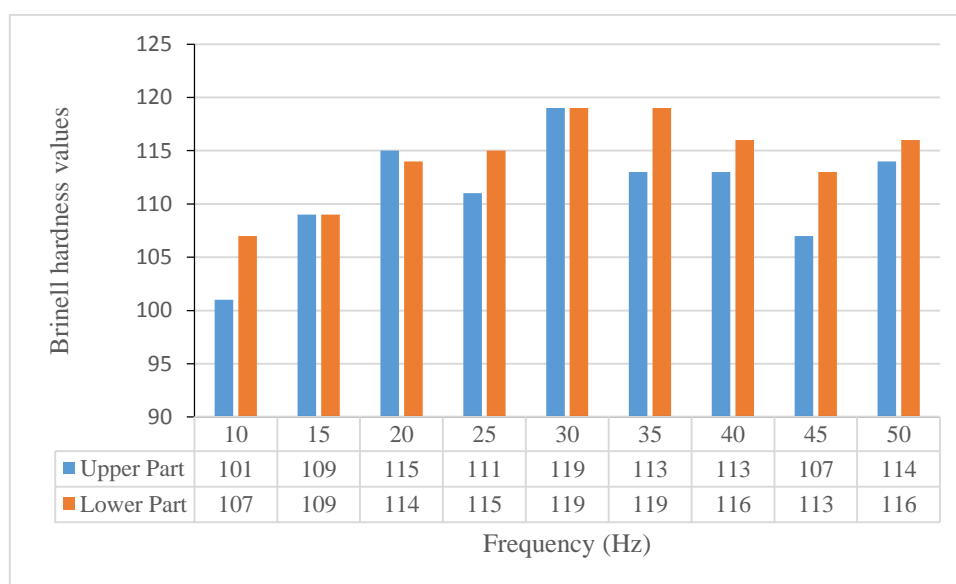


Figure 5. Brinell hardness values of upper and lower parts of samples between 10-50 Hz.

In the hardness measurements made, the hardness values taken from the lower part of the sample increases up to 30 Hz. After 30 Hz, a decrease is observed, and at 50 Hz, an increase is detected again. In general, the hardness values taken from the upper side of all samples are partially lower than the hardness values taken from the lower side. However, as can be seen in Figure 5, the mechanical vibration applied at a frequency of 30 Hz reached the maximum hardness value (119 HB) in both the upper and lower parts of the sample. This shows that 30 Hz frequency value can be determined as a critical value in solidification under mechanical vibration for Al 7075 alloy.

3.3. Compression Tests

Compression tests are applied to the samples, which are solidified by mechanical vibration at all frequencies and applied precipitation hardening, with a feed rate of 3 mm/min and a maximum compression distance of 10 mm. Stress - % Strain graphs obtained as a result of the tests are given in Figure 6, and Stress - % Strain values according to mechanical vibration frequencies are given in Table 1.

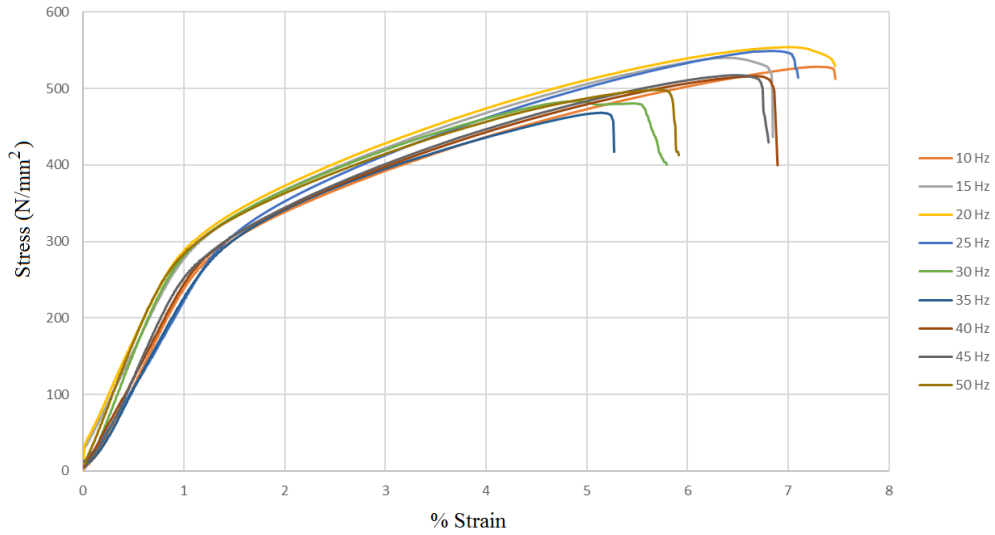


Figure 6. Stress - % Strain graph of samples according to mechanical vibration frequencies.

Table 1. Stress-% Strain values according to mechanical vibration frequencies.

Sample	σ_{\max} (N/mm ²)	% ϵ_{\max}
10 Hz	528,4	7,28
15 Hz	540,1	6,40
20 Hz	554,1	7,01
25 Hz	549,0	6,85
30 Hz	483,3	4,90
35 Hz	468,3	5,13
40 Hz	516,1	6,68
45 Hz	517,4	6,45
50 Hz	498,3	5,70

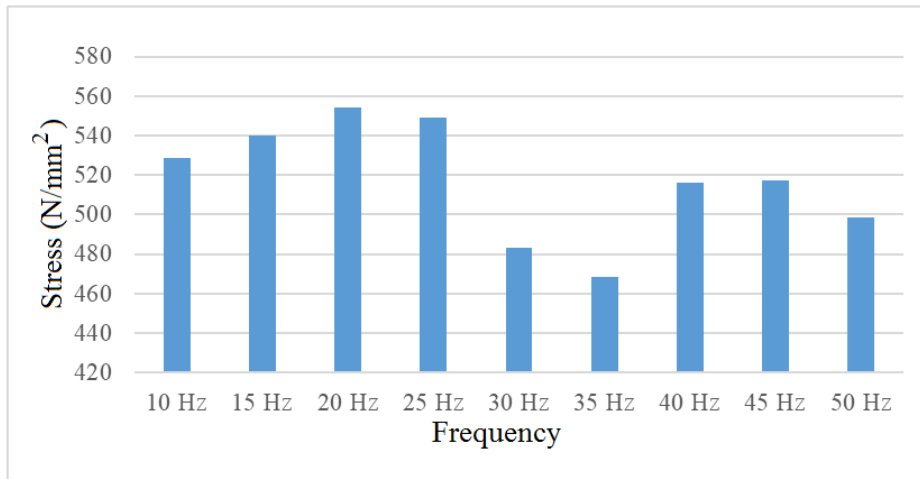


Figure 7. Stress - mechanical vibration graph.

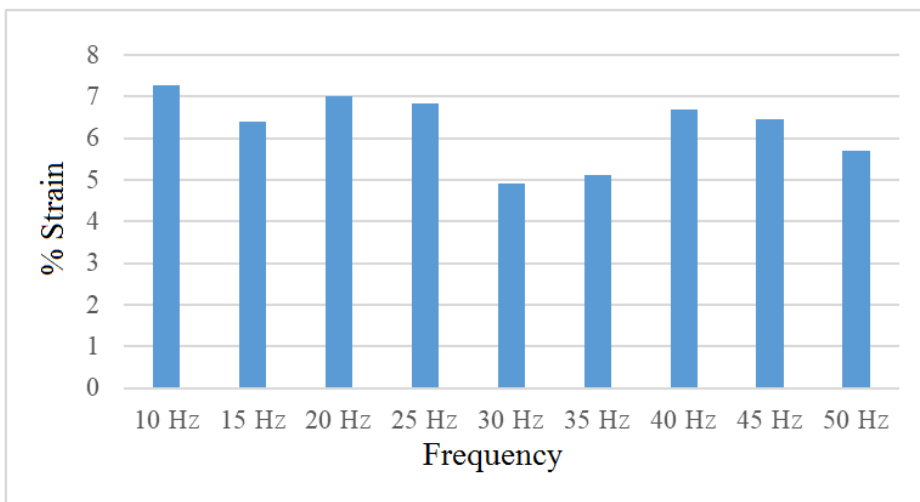


Figure 8. Mechanical vibration - % strain graph.

When the graphs obtained as a result of the compression tests and the maximum compressive strength and maximum strain amounts obtained from the graphs are examined (Figure 7), a homogeneous stress increase is detected in the samples applied with 10 – 15 – 20 Hz vibration. However, a relationship could not be determined between the stress values obtained at higher frequencies (25-50 Hz). Although the lowest compressive stress values are obtained in the samples manufactured at 30 Hz and 35 Hz, where the highest hardness value is measured, it is noteworthy that their strain values

are also the lowest (Figure 8). As it is known, the strength of the materials increases as the deformation capacity decreases. To investigate this difference at 30 Hz and 35 Hz, the samples are cut vertically and examined for any cracks or porosities in the internal structure. As a result of visual inspection and penetrant fluid application, no capillary cracks are detected, but it is determined that there are significant number of porosities in the sample as seen in Figure 9.

These determined porosities explain the inconsistency of the data obtained in the compression test plots.

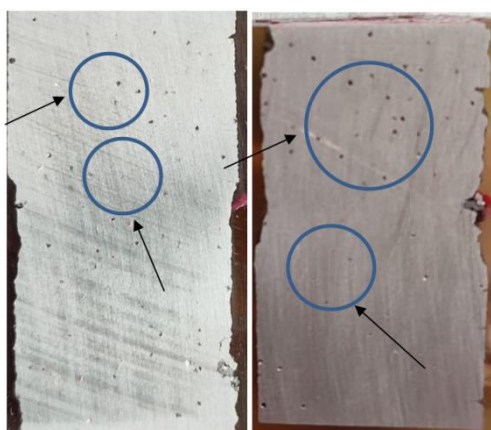


Figure 9. The porosities in the samples.

4. CONCLUSION

At the results of the experiments, we observed that, by applying mechanical vibration to Al 7075 alloy at different frequencies during the solidification, partially smaller sized grains are obtained in the microstructure, and it is determined that the hardness values of the samples increased. It has also been determined that the frequency of 30 Hz among the different frequencies applied in the current experimental setup provides the best hardness value for the Al 7075 material. It has been proven by many studies in the literature that solidification under vibration has a grain size reducing effect on the material microstructure. As it is commonly known, reducing the grain size of a material leads to an enhancement in both its strength and hardness. However, findings of this study reveal an interesting insight. While the grain size is observed to decrease with an increase in vibration frequency, it is noted that the change in hardness isn't directly proportional to the grain size change. Considering this, the solidification of Al 7075 alloy under vibration might trigger various material changes beyond grain size, such as precipitate and phase formation. These anomalies will be subjects of investigation in forthcoming studies by authors.

The increase in the hardness values of the samples obtained as a result of the mechanical vibration applied during solidification is lower than the hardness values obtained by the precipitation hardening

process. However, if a product made from Al 7075 material is intended to be obtained through casting and will be used in an application area where an increase in strength value isn't necessary, solidification under mechanical vibration will be more advantageous in terms of both cost and time compared to precipitation hardening.

On another side of view, the compression test results of the samples are not as favorable as anticipated due to the porosities formed in the casting materials as a consequence of the applied mechanical vibrations. In this study, there is a potential to eliminate material porosities by implementing appropriate conditions for applying mechanical vibrations in an open atmosphere. These conditions include applying mechanical vibrations to the material under vacuum or pressure and designing mechanisms capable of vibrating within the furnace before material solidification is achieved. Furthermore, with the implementation of these conditions, a rise in compressive strength equivalent to the increase in hardness values can be attained.

ACKNOWLEDGEMENT

This research received no specific grant from any funding agency in the public, commercial or not-for-profit sectors.

REFERENCES

- [1] Vorozhtsov et al., (2016). Theoretical and experimental investigations of the process of vibration treatment of liquid metals containing nanoparticles. *JOM*, 68, 3094–3100.
- [2] Taghavi, F.; Saghafian, H.; Kharrazi, Y.H.K. (2009). Study on the effect of prolonged mechanical vibration on the grain refinement and density of A356 aluminum alloy. *Materials & Design*, 30, 1604–1611.
- [3] Campbell, J.,(1981). Effect of vibration during solidification, *International Metals Review*, V:26, 71-108.
- [4] GUO et al., (2014). Grain refinement of Al–5%Cu aluminum alloy under mechanical vibration using melttable vibrating probe, *Transactions of Nonferrous Metals Society of China* V:24, 2489-2496.
- [5] Abu-Dheir et al., (2005). Silicon morphology modification in the eutectic Al-Si alloy using mechanical mold vibration. *Materials Science and Engineering A*. 393, 109–117.
- [6] Jiang et al., (2014). Combined effects of mechanical vibration and wall thickness on microstructure and mechanical properties of A356 aluminum alloy produced by expendable pattern shell casting, *Materials Science and Engineering: A* V: 619, 228-237

- [7] Al-Ethari et al., (2020). Influence of Mechanical and Thermo Mechanical Treatment on Micro Structure and Hardness of Al-ZnMg Alloy, Test Engineering and Management, V:83 , 11133 – 11141.
- [8] Kocatepe, K. (2007). Effect of low frequency vibration on porosity of LM25 and LM6 alloys. Materials and Design. 28, 1767–1775.
- [9] Nguyen-Thi et al., (2004). Tailoring of dendritic microstructure in solidification processing by crucible vibration. Journal of Crystal Growth. 275, 1579–1584.
- [10] Deshpande, J. U. (2006). Effect of mold vibration on the performance and casting characteristics of aluminum alloys (Unpublished Master's Thesis). Worcester Polytechnic Institute, Massachusetts.
- [11] Mehta et al., (2019) Effects of Amplitude of Die Vibration on Cast Structure of Al4.5Cu Alloy, Inter Metalcast, V:13, 438–449.
- [12] Kudryashova et al., (2019) Optimizing the Conditions of Metal Solidification with Vibration, Metals , 9(3), 366
- [13] Alüminyum dökümde tane incelticiler, <http://www.aluminyumdokum.org/aluminyum-dokumde-tane-incelticiler/>



RESEARCH ARTICLE

ENERGY-POPULATION EVALUATION AND PROJECTION OF KÜTAHYA PROVINCE

Oğuz Ozan YOLCAN^{1*}, Ramazan KÖSE²

^{1*}Kütahya Dumlupınar University, Faculty of Engineering, Department of Mechanical Engineering, Kütahya, oguzozan.yolcan@dpu.edu.tr, ORCID: 0000-0002-6664-5675

²Kütahya Dumlupınar University, Faculty of Engineering, Department of Mechanical Engineering, Kütahya, ramazan.kose@dpu.edu.tr, ORCID: 0000-0001-6041-6591

Receive Date: 23.11.2022

Accepted Date: 19.09.2023

ABSTRACT

Examination of the energy situation is essential, especially for countries that are dependent on foreign Energy terms of Energy. Energy consumption, which increases indirectly with population and technology, needs to be evaluated in the short, medium, and long term. Energy projections are one of the most critical issues in the development planning of states. In this study, the population and energy status of the Kütahya province of Turkey were examined in detail, and the population and Energy projections were evaluated. While reviewing the population projection, predictions have been prepared depending on the population changes of the last five years, the last ten years, the last 15 years, and the previous 20 years, together with the projection prepared by the Turkish Statistical Institute. While preparing the electrical energy consumption projection of Kütahya province, evaluations were made according to three different scenarios prepared by the Ministry of Energy and Natural Resources of the Republic of Turkey. Accordingly, the electricity consumption of Kütahya province in 2039; has been determined as 2.71 billion kWh according to the 1st scenario, 2.96 billion kWh according to the 2nd scenario, and 3.27 billion kWh according to the 3rd scenario.

Keywords: *Energy, population, electricity projection*

1. INTRODUCTION

Energy consumption and short- and long-term energy projections are essential considerations for governments' investment and savings plans. This study examined the energy status of Kütahya province of Turkey and evaluated energy consumption projections.

According to the International Atomic Energy Agency, world electrical energy consumption will reach 104 EJ (28,889 TWh) in 2030, 127 EJ (35,278 TWh) in 2040, and 152.7 EJ (42,417 TWh) in 2050 [1]. In addition, the Ministry of Energy and Natural Resources of the Republic of Turkey has predicted Turkey's electrical energy consumption as 370 TWh for 2025 and 591 TWh for 2040 [2].

Şişman et al. modeled Turkey's energy consumption using Artificial Neural Networks. The model created was developed for 1975-2016, and the electricity consumption for Turkey until the end of 2023 was accurately estimated with the model created [3]. Kan et al., while modeling electricity demand, also referred to techno-economic criteria. Seasonal and daily variations were considered while designing the demand model [4]. Wu et al. developed a new model for electricity demand forecasting. The developed model has been evaluated for simulating and predicting the electricity consumption of the Hubei region of China in a specific time period. It has been stated that the model has high performance [5]. Belançon evaluated Brazil's electricity needs in 2030 under four different scenarios. To determine the electricity need, Brazil's 20-year electricity load curves were examined [6]. Cekinir et al. evaluated Turkey's 2050 energy projection under four different scenarios. Turkey's electricity production values for the year 2050 are modeled with Artificial Neural Networks. In addition, it has been evaluated how much the production from Turkey's domestic resources should increase to meet the consumption in 2050 [7]. Zhang et al. evaluated the electricity consumption for the Jiangsu region of China, considering socioeconomic criteria. For the electricity consumption estimation, the period 2018-2100 has been evaluated [8]. Soummane and Ghersi have developed a model to determine Saudi Arabia's electricity needs by 2030. Considering the cost and efficiency criteria, modeling was applied under various scenarios [9]. Da Silva et al. have developed a methodology for the estimation of electricity consumption in an industrial sector. The developed method was evaluated to estimate the electricity consumption of the Brazilian paper industry until 2050 [10]. Perez-Garcia and Moral-Carcedo developed a methodology for long-term forecasting of electricity demand. The developed methodology was applied to Spain [11]. Roberts et al. have developed a model for the United States that predicts hourly electricity demand based on thermal conditions [12].

Kütahya is a province in the Aegean Region of Turkey, with 13 districts, including the central district [13]. The representation of Kütahya on the map of Turkey is given in Figure 1 [14]. The district borders of Kütahya province and the annual total solar radiation are shown in Figure 2 [14].

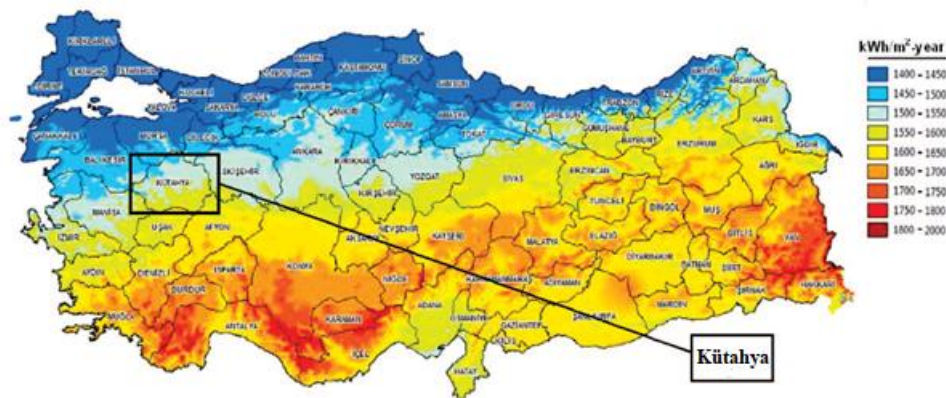


Figure 1. Location of Kütahya province in Turkey [14].

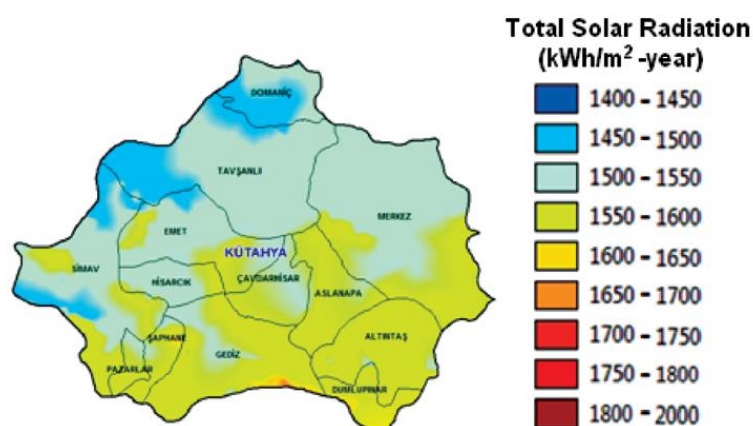


Figure 2. Kütahya district borders and annual solar radiation [14].

For district centers of Kütahya province, General information such as latitude, longitude, altitude, average daily solar radiation, average daily sunshine duration, and annual average temperature are given in Table 1 [15]–[17].

Table 1. General information of Kütahya districts [15]–[17].

	Latitude	Longitude	Altitude	Average temperature (°C)	Wind speed (m/s)
Merkez	39.4	30	960	10.50	2.79
Altıntaş	39.1	30.1	1030	10.84	2.98
Aslanapa	39.2	29.9	1030	10.61	2.92
Çavdarhisar	39.2	29.6	1010	10.96	2.87
Domaniç	39.8	29.6	880	10.49	2.74
Dumlupınar	39.9	30	1225	10.33	2.99
Emet	39.3	29.3	900	11.21	2.84
Gediz	39	29.4	750	12.57	2.77
Hisarcık	39.3	29.2	760	11.92	2.69
Pazarlar	39	29.1	925	11.69	2.63
Simav	39.1	29	820	11.78	2.68
Şaphane	39	29.2	980	11.40	2.61
Tavşanlı	39.5	29.5	845	10.83	3.01

2. POPULATION AND ENERGY OUTLOOK OF KÜTAHYA

As of the end of 2020, the total population of Kütahya is 576 688. [18]. The population view of Kütahya by years is given in Figure 3 [18]. While the people of Kütahya was approximately 593 thousand in 2000, it decreased to 564 thousand in 2011.

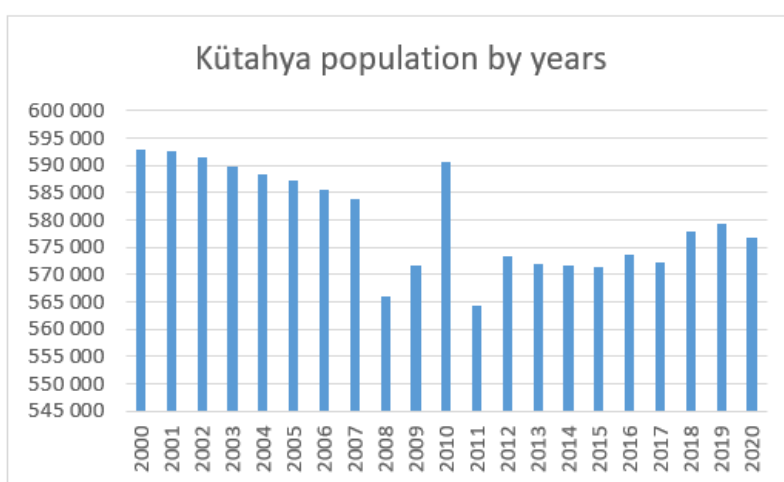


Figure 3. Kütahya population by years [18].

The population growth rate of Kütahya by years is shown in Figure 4 [18]. In the given date range, the highest increase in the population of Kütahya was realized in 2009 – 2010 with 3.2%. The highest population decline occurred in 2010 – 2011, with 4.5%.

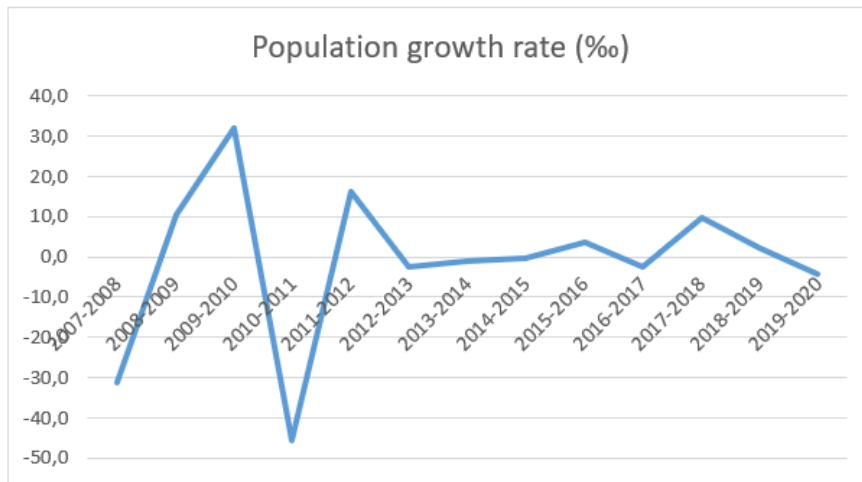


Figure 4. Kütahya population growth rate by years [18].

As of the end of March 2022, the licensed electrical Energy installed power in Kütahya is 1067.82 MW, and the unlicensed electrical energy installed power is 118.93 MW [19]. The unlicensed installed power consists of 2.61 MW of biomass and 116.32 MW of solar Energy. The development of unlicensed installed capacity by years is given in Figure 5 [19]. While unlicensed solar installed power was 1 MW in January 2016, this value increased to 116.32 MW by the end of March 2022.

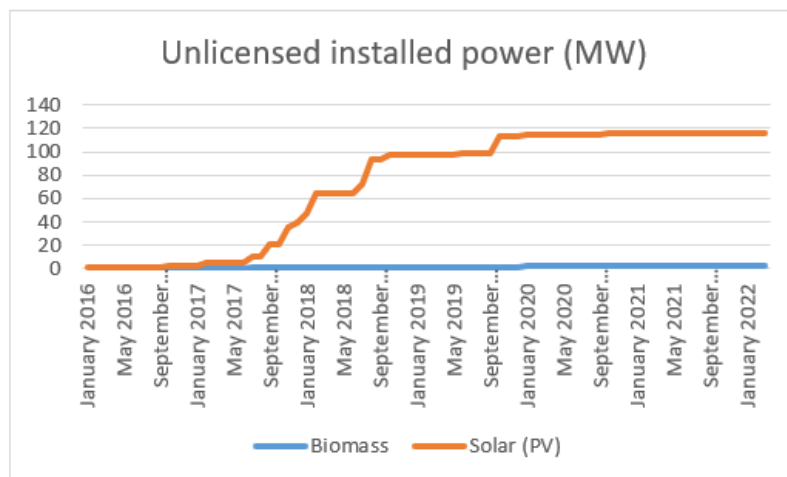


Figure 5. Kütahya unlicensed electrical energy installed capacity [19].

The licensed electricity generation of Kütahya province was 384 million kWh in March 2022. Licensed electricity production of Kütahya by years is shown in Figure 6 [19]. The highest generation was realized in February 2018 with 633.6 million kWh in the given date range.

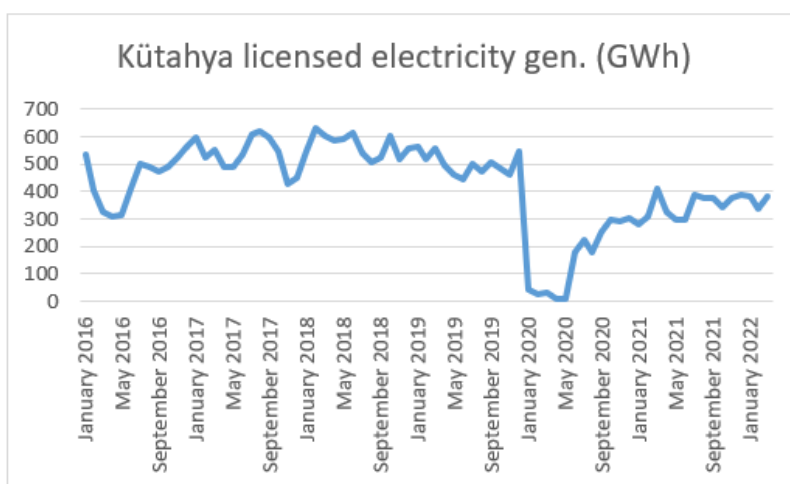


Figure 6. Kütahya licensed electricity generation [19].

Unlicensed electricity generation in Kütahya province was realized as 15.1 million kWh in March 2022. The unlicensed electricity production of Kütahya by years is shown in Figure 7 [19]. The highest generation was realized in July 2020 with 26.4 million kWh in the given date range.

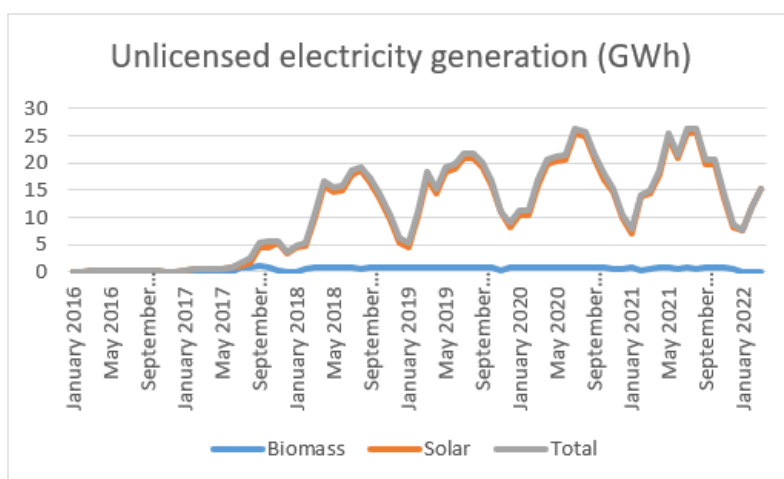


Figure 7. Kütahya unlicensed electricity generation [19].

The total electricity generation (licensed and unlicensed) of Kütahya province was realized as 399.1 million kWh in March 2022 [19]. The graph of total electrical energy production of Kütahya province by years is given in Figure 8.

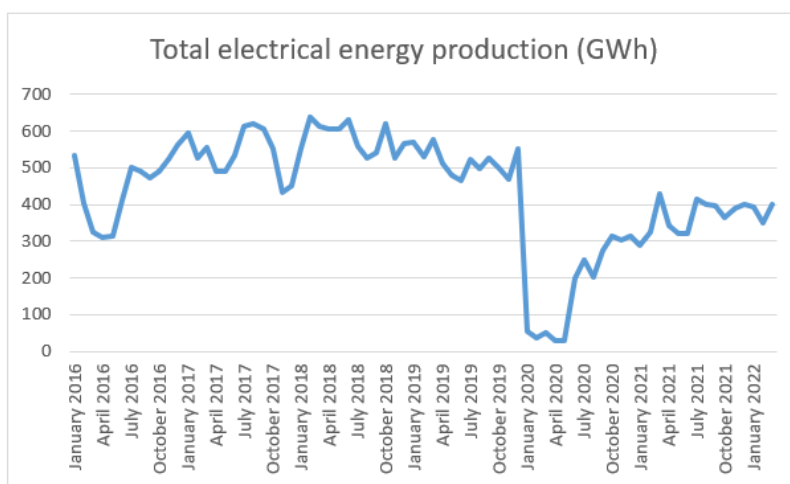


Figure 8. Total electrical energy production of Kütahya province [19].

The number of electricity consumers in the province of Kütahya is 421,762 as of the end of March 2022 [19]. The change in the number of electricity consumers in Kütahya province by years is given in Figure 9.

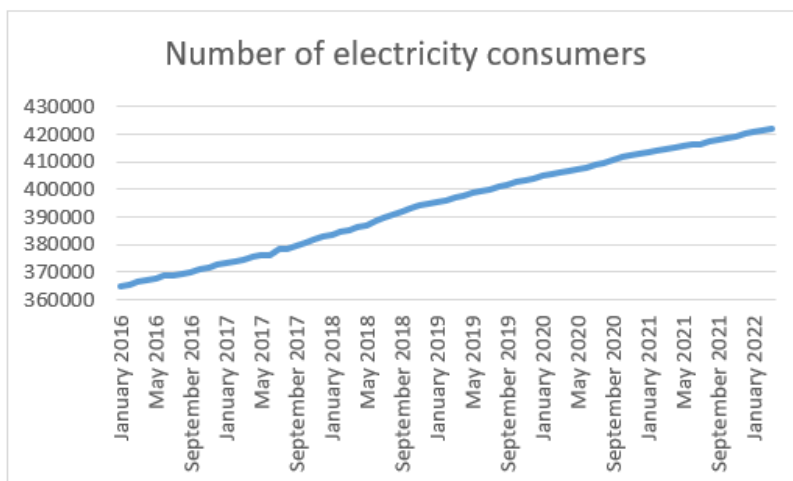


Figure 9. The number of electricity consumers in the province of Kütahya [19].

Electricity consumption in Kütahya province was 169.2 million kWh in March 2022. [19]. The electricity consumption of Kütahya province by year is given in Figure 10. The lowest electricity consumption in the given date range was 107.7 million kWh in February 2016, and the highest was 171.4 million kWh in December 2021.

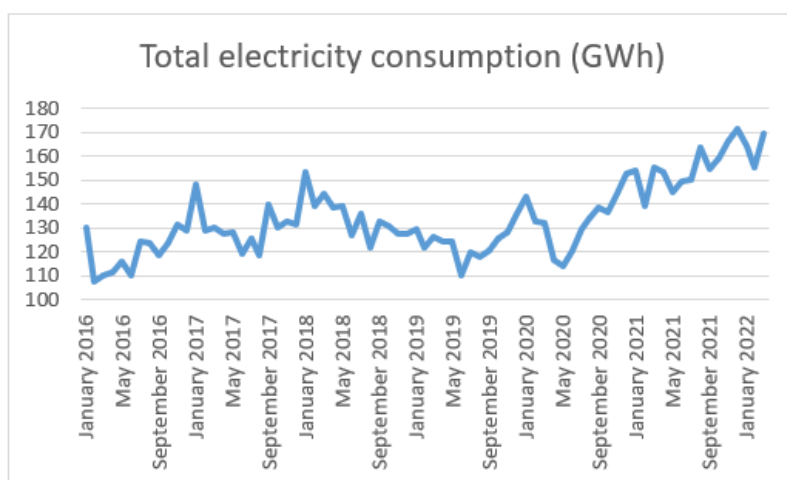


Figure 10. Electricity consumption in Kütahya [19].

The electricity consumption graph of Kütahya province according to sectors is given in Figure 11 [19]. When the electricity consumption graph of Kütahya province is analyzed, it is seen that the highest share in consumption belongs to the Industry sector, followed by Residential and Commercial consumption.

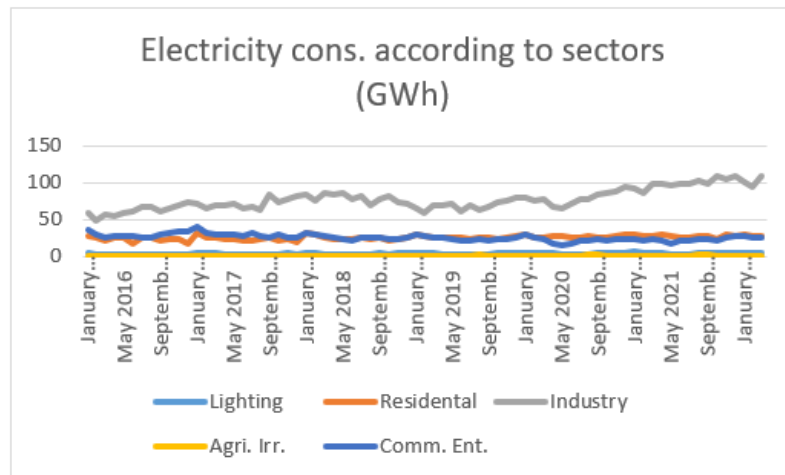


Figure 11. Electricity consumption according to sectors [19].

The average electricity consumption rates of Kütahya province in the given date range are shared in Figure 12. In the averages within the given date range, the highest share belongs to the Industry sector with 58%. The percentage of lighting is 3%, the share of residences is 19.2%, the share of agricultural irrigation is 0.5%, and the share of commercial enterprises is 19.3%.

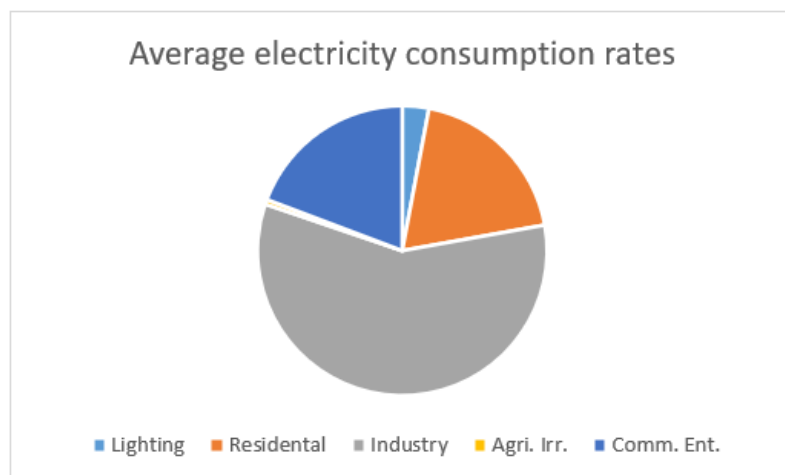


Figure 12. Average electricity consumption rates of Kütahya [19].

The graph of the ratio of total electricity generation (licensed and unlicensed) to consumption of Kütahya is shown in Figure 13. [19]. Except for the January 2020 – May 2020 date range, it is seen

that the electricity production of Kütahya province is higher than the electricity consumption. The average electricity generation to consumption ratio in the given date range is 328.8%. The main reason why production values are so high compared to consumption values is the thermal power plants located in the province of Kütahya.

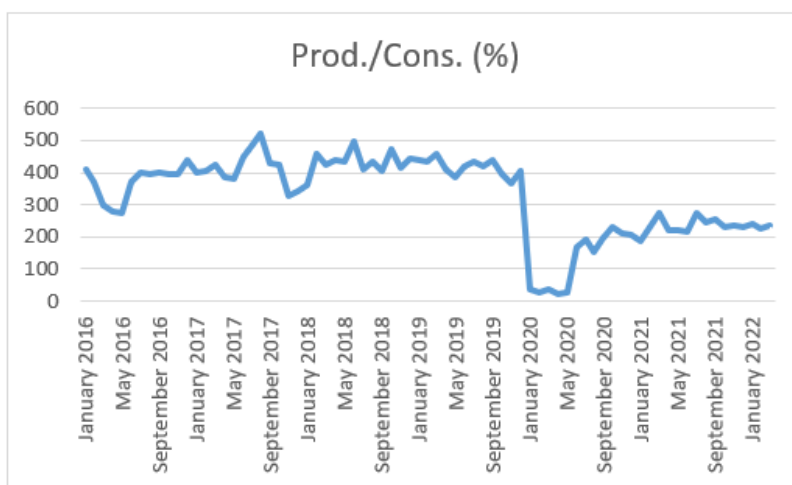


Figure 13. The ratio of total electricity generation to consumption of Kütahya [19].

The ratio of unlicensed solar power generation to total consumption in Kütahya is shown in Figure 14. [19]. Unlicensed solar power generation in July 2020 corresponds to 19.7% of total consumption. The average ratio of unlicensed solar energy generation to consumption in the given date range is 8%.

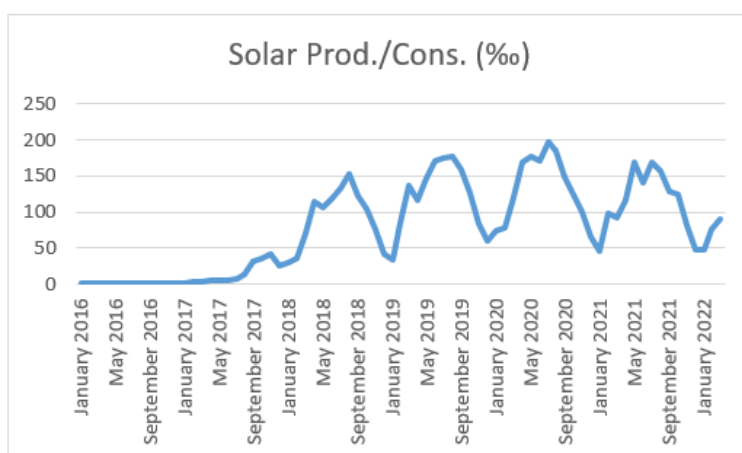


Figure 14. the ratio of unlicensed solar power generation to total consumption in Kütahya [19].

3. KÜTAHYA POPULATION AND ENERGY PROJECTIONS

Population projections by provinces from the end of 2017 to 2025 were shared by the Turkish Statistical Institute [20]. The population projection for the province of Kütahya until 2025 is shown in Figure 15. According to this projection, the population of Kütahya province in 2023 is estimated to be 577 125, and in 2025 the population of Kütahya province is expected to be 576 830.

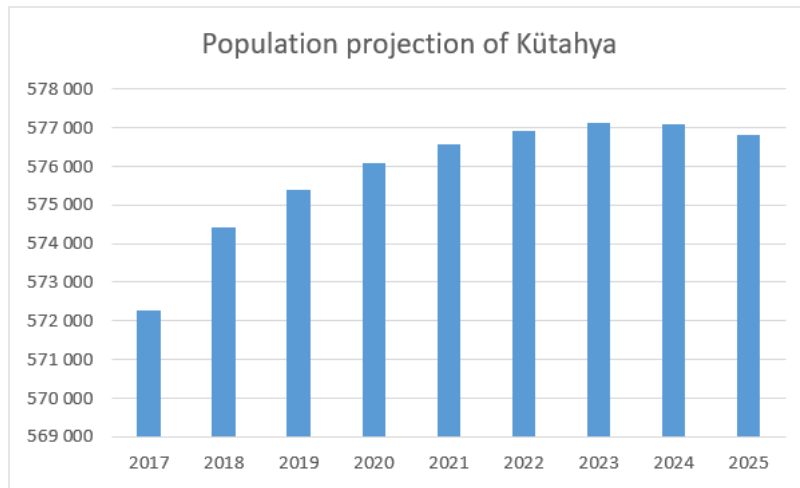


Figure 15. Kütahya province population projection prepared by TUIK [20].

One of the methods used to calculate population projections is the exponential increase method. This method can be calculated by the formula [21];

$$P = P_0 x e^{r \cdot t} \quad (1)$$

In this formula, P represents the projective population, P₀ represents the initial population, r represents the population growth rate, and t represents the time. Using the exponential increase method, the population projection of Kütahya province until 2025 was created. While creating the population projection, Population growth rates of the last five years, the last ten years, the last 15 years, and the last 20 years are used. The projection obtained is shared in Figure 16.

According to this graph, the population of Kütahya province in 2025; It reaches 576,830 in the TUIK projection, 588,750 in the calculation made according to the population growth rate of the last five years, 572,617 in the calculation made according to the population growth rate of the last ten years, 576,152 in the calculation made according to the population growth rate of the last 15 years, and 575,220 in the calculation made according to the population growth rate of the last 20 years.

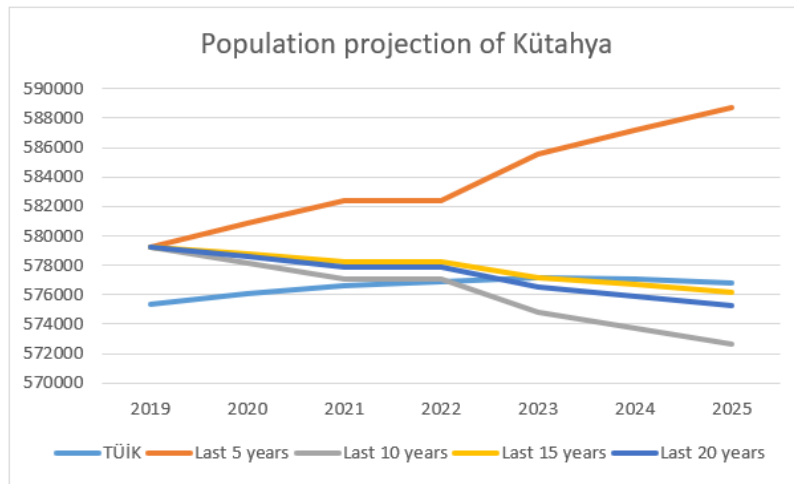


Figure 16. Population projection of Kütahya [20].

Three different scenarios have been prepared by the Ministry of Energy and Natural Resources of the Republic of Turkey for Turkey's 20-year electrical energy projection. [22]. These are the Low Scenario (Scenario 1), Reference Scenario (Scenario 2), and High Scenario (Scenario 3). These scenarios are adapted to the electrical energy consumption of Kütahya province and are shared in Figure 17.

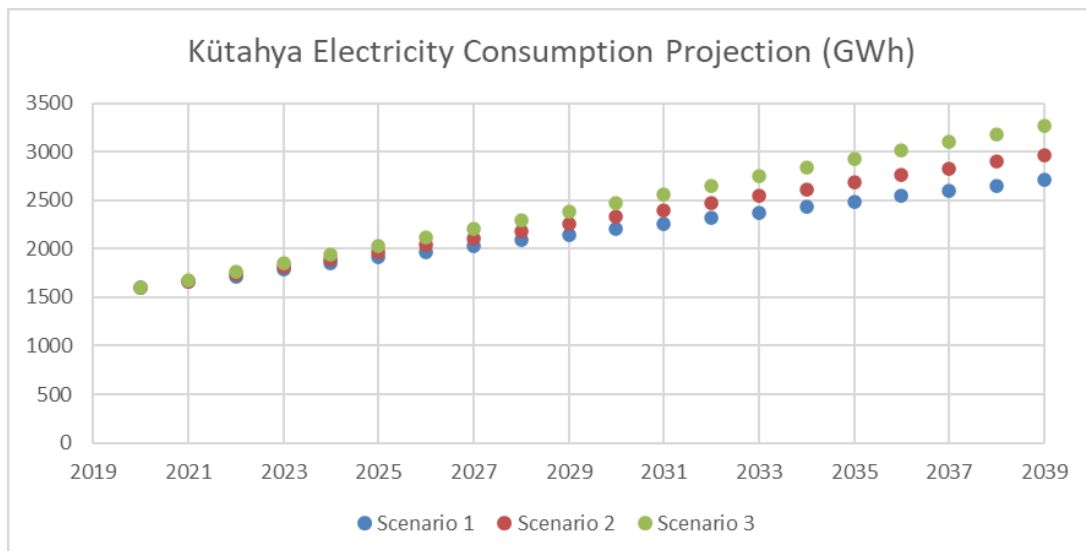


Figure 17. Electric energy consumption projection of Kütahya province [22].

According to these prepared scenarios, the electrical energy consumption of Kütahya province in 2039;

According to scenario 1, 2.71 billion kWh (70% more than 2020),

According to scenario 2, 2.96 billion kWh (86% more than 2020)

According to scenario 3, it will be 3.27 billion kWh (105% more than 2020).

4. ASSESSMENTS

Energy efficiency, reducing foreign dependency on Energy by utilizing domestic resources, and increasing the rate of utilization of renewable energy resources are critical issues in terms of the development plans of states. In terms of the evaluation and planning of energy resources, energy projections need to be evaluated.

In this study, the population and energy status of the Kütahya province of Turkey were examined in detail, and the population and Energy projections were evaluated. While examining the population projection, projections have been prepared depending on the population changes of the last five years, the last ten years, the last 15 years, and the last 20 years, together with the projection prepared by the Turkish Statistical Institute. While preparing the electrical energy consumption projection of Kütahya province, evaluations were made according to three different scenarios prepared by the Ministry of Energy and Natural Resources of the Republic of Turkey. Accordingly, the electricity consumption of Kütahya province in 2039; has been determined as 2.71 billion kWh according to the 1st scenario, 2.96 billion kWh according to the 2nd scenario, and 3.27 billion kWh according to the 3rd scenario.

ACKNOWLEDGMENT

There is no conflict of interest with any person/institution in the paper.

REFERENCES

- [1] International Atomic Energy Agency. (2019). Energy, electricity and nuclear power estimates for the period up to 2050, reference data series no. 1.
- [2] Republic of Turkey Ministry of Energy and Natural Resources. (2022). Republic of Turkey Ministry of Energy and Natural Resources – electricity.
- [3] Şişman, N., Sofuoğlu, M. A., Aras, N. and Aras, H. (2022). Modelling of Turkey's energy consumption using artificial neural networks. *Advanced Engineering Forum*, 44 (1), 73-86.

- [4] Kan, X., Reichenberg, L. and Hedenus, F. (2021). The impacts of the electricity demand pattern on electricity system cost and the electricity supply mix: A comprehensive modeling analysis for Europe. *Energy*, 235 (1), 121239.
- [5] Wu, W. Z., Pang, H., Zheng, C., Xie, W. and Liu, C. (2021). Predictive analysis of quarterly electricity consumption via a novel seasonal fractional nonhomogeneous discrete grey model: a case of Hubei in China. *Energy*, vol. 229 (1), 120714.
- [6] Belançon, M. P. (2021). Brazil electricity needs in 2030: trends and challenges. *Renewable Energy Focus*, 36 (1), 89–95.
- [7] Cekinir, S., Ozgener, O. and Ozgener, L. (2022). Türkiye’s energy projection for 2050. *Renewable Energy Focus*, 43 (1), 93–116.
- [8] Zhang, M., Cheng, C. H. and Ma, H. Y. (2020). Projection of residential and commercial electricity consumption under SSPs in Jiangsu province, China. *Advances in Climate Change Research*, 11 (2), 131–140.
- [9] Soummane, S. and Ghersi, F. (2022). Projecting Saudi sectoral electricity demand in 2030 using a computable general equilibrium model. *Energy Strategy Reviews*, 39 (1), 100787.
- [10] da Silva, F. L. C., Cyrino Oliveira, F. L. and Souza, R. C. (2019). A bottom-up bayesian extension for long term electricity consumption forecasting. *Energy*, 167 (1), 198–210.
- [11] Pérez-García J, Moral-Carcedo J (2016) Analysis and long term forecasting of electricity demand through a decomposition model: A case study for Spain. *Energy* 97:127–143.
- [12] Roberts, M. J., Zhang, S., Yuan, E., Jones, J., and Fripp, M. (2022). Using temperature sensitivity to estimate shiftable electricity demand. *iScience* 25 (9), 104940.
- [13] Republic of Türkiye Kutahya Governorship. (2021). Information about Kütahya.
- [14] Ozgur, M. A. and Köse, G. (2013). A technoeconomic analysis of solar photovoltaic power systems: Kütahya case study. *Energy Sources, Part A: Recovery, Utilization and Environmental Effects*, 35 (1), 42–57.
- [15] Ministry of Energy and Natural Resources of the Republic of Turkey. (2020). *Solar Energy Potential Atlas*.
- [16] European Commission. (2017). JRC photovoltaic geographical information system (PVGIS).
- [17] Climate-data.org. (2021). İklim: Türkiye.
- [18] Turkish Statistical Institute. (2021). Population results based on address.

- [19] Republic of Türkiye Energy Market Regulatory Authority EPDK. (2021). Electricity market monthly sector reports.
- [20] Turkish Statistical Institute. (2021). Türkiye population and demography.
- [21] Suddhendu, B. (1988). Stochastic Processes in Demography and Applications, John Wiley & Sons.
- [22] Republic of Türkiye Energy Market Regulatory Authority EPDK. (2021). General Directorate of Energy Affairs reports.



RESEARCH ARTICLE

VALORIZATION OF TURKISH COFFEE WASTE AS A BIODIESEL FEEDSTOCK

Ayşe Hilal ULUKARDEŞLER^{1*}

^{1*} Bursa Uludağ University, Vocational School of Technical Sciences, Bursa, ulukardesler@uludag.edu.tr,
ORCID: 0000-0001-6563-5785

Receive Date: 12.06.2023

Accepted Date: 04.09.2023

ABSTRACT

Increasing industrialization and population increase demand to fossil fuels. Fossil fuels are limited all over the world. This causes the supply of these fuels to deplete and at the same time increase greenhouse gas emissions. Biodiesel is a good alternative to fossil fuels. Researchers are looking for products with high oil content as a feedstock for biodiesel production. Since the average oil content of coffee is 15% by weight and the annual coffee consumption in the world is approximately 1.5-2 million tons, it is possible to contribute to the economy by producing biodiesel from the waste coffee oil. Turkish coffee is a special coffee due to its preparation and cooking methods and has an important place in Turkish culture. Its consumption between the other coffee types is above 80% in Turkey, so it should be evaluated differently. In this study, the oil amount of Turkish coffee waste was investigated and it was discussed as a raw material for biodiesel. 16.8% wt. oil was obtained as a result of soxhlet extraction of Turkish coffee waste. This study suggests 8.44 million L of biodiesel production from Turkish coffee waste annually.

Keywords: *Biodiesel, Coffee, Turkish Coffee, Turkish Coffee Waste, Renewable Energy*

1. INTRODUCTION

Energy consumption which is mainly based on fossil fuels increases in parallel with the rapidly increasing population around the world. According to the World Energy Statistics the share of fossil fuels in the global energy supply in 2020 is 78% [1,2]. In Turkey it was determined that fossil fuels had the highest share among the total energy supply sources with a share of 87% and 13% share was created by renewable energy sources. In Turkey, main energy sources in power generation are as follows: coal 37%, natural gas 30%, hydroelectric 19.7%, wind 6.5%, solar 2.6%, geothermal 2.4%, and renewable waste 1.2% in 2018 [3]. Since the dependence on fossil resources in energy continues in the global arena, the tendency to renewable energy is on the rise. Today the policies adopted by the countries for energy saving are seen as an extremely critical area in ensuring energy supply security, reducing foreign dependency, protecting the environment and combating climate change. In particular, the Paris Climate Agreement was accepted as a milestone in the fight against climate change, and in this direction, the European Union Renewable Energy Directive was updated in 2018. According to

this directive, it is aimed to increase the share of renewable energy sources to 32% and to reduce greenhouse gas emissions by 40% until 2030 [4].

Biodiesel is an alternative fuel produced from renewable resources such as animal and vegetable oils and can be used in diesel engines. It is a sustainable, environmentally friendly, non-toxic alternative fuel. Global biodiesel production is estimated to reach 23 billion liters by 2025. Biodiesel can also reduce CO₂ emissions by 50% which is a valuable incentive given the role of the transport sector in increasing greenhouse gases [5-7].

Population growth, urbanization and industrialization led to an increase in the amount of production and consumption on one hand, and on the other hand, it caused an increase in the amount of waste generated. With this increase, there have been many discussions about managing the wastes. Although the removal of wastes from the living area was considered sufficient at first, requirement and finding of new areas for the removal of wastes due to the increasing amount became a big problem. The constant search for new areas for waste and the existence of reusable materials in the resulting solid wastes have caused a radical change in the understanding of waste management. With this change, the management of solid waste, which has a large share in the total amount of waste produced, has also come to the fore, and it has been determined that solid wastes are not items to be disposed of but inputs that can be used in other activities [8-11]. Many environmental and financial benefits can be achieved by recycling wastes. Considering this situation, large amounts of waste cooking oil, used coffee grounds, food wastes and used tea wastes may be recycled which supplied from restaurants, cafes etc. Converting huge amounts of waste into energy and value-added products is one of the effective ways to solve the problems of many countries that struggle to cope with these wastes generated every day [12,13].

Coffee is the most popular and most consumed beverage in the world. It is the second product with the highest trade volume in the world after oil [14]. Approximately 1.6 billion cups of coffee are consumed every day and this large industry produces a large amount of waste with spent coffee grounds. Recycling such wastes into fuels and products through biorefineries is a promising way to solve the waste problem. Coffee waste or spent coffee grounds are among the hopeful raw materials for biodiesel production. It is a high quality raw material with an average oil content of 15% by weight, similar to soybean and palm oil, which are among the first generation raw materials [7,12,15-17]. Different roasting and extraction processes of coffee bring about remarkable biological differences in its structure. Turkish coffee is a blend of moderately roasted and finely ground high quality Arabian-type coffee beans that originating from Brazil and Central America. The way of its making distinguishes Turkish coffee from others. Since new preparation technique was invented by the Turks, it was called Turkish coffee and boiled in copper pots. Unlike the filter coffee, it is extremely finely ground, is prepared by slowly boiling the coffee in water. Turkish coffee is an important part of Turkish culture and is known as one of the traditional drinks. Under this name, it spread to the world and became a part of the cultural and social history and lifestyle of the Turks. It has been determined that Turkish coffee contains biologically active components and caffeine at a higher rate than other coffee types and preparations [18-21].

In this current study, the potential use of the Turkish coffee waste in biodiesel production was investigated. Although there are many studies about the spent coffee grounds in the production of biodiesel, Turkish coffee waste is not found. Since Turkish coffee plays major role in coffee industry in Turkey, it should be evaluated separately. This work is especially about the Turkish coffee waste and as a case study for Turkey.

2. COFFEE CONSUMPTION IN WORLD AND TURKEY

2.1. World

Coffee is the second product with the largest trade share after oil and has a serious consumer base in the world [14]. Coffee first began to grow on Arabica coffee trees in the Kaffa region in Ethiopia. Although there are various shapes and flavors of coffee beans in the world, there are mainly two groups called Robusta and Arabica. World consumption of Robusta coffee bean is 25 percent, while Arabica coffee bean is around 75 percent. Generally, Arabica coffee is considered superior to robusta due to its delicate aroma, highly acidic nature, and wine like taste [22]. Its acidity is also higher than Robusta. Robusta coffee beans, on the other hand, have stronger aromas and intense flavors compared to Arabica. Robusta beans have a more intense aroma than Arabica beans. At the same time, the caffeine content is twice as high as Arabian. Both varieties have high volatile organic contents. Processing different coffees at different stages causes diversity in spent coffee grounds [8].

The latest data showed that more than 9.98 million tons (166.34 million 60 kg bags) of coffee products were consumed between 2020 and 2021 worldwide. According to the International Coffee Organization (ICO), Europe (33%), Asia and Oceania (22%), and North America (19%) are the main coffee consumers. United States (26.98 million 60 kg bags) and Brazil (22.4 million 60 kg bags) are the main consumers of coffee [23]. Figure 1 shows the consumption of coffee values for the years 2020-2021.

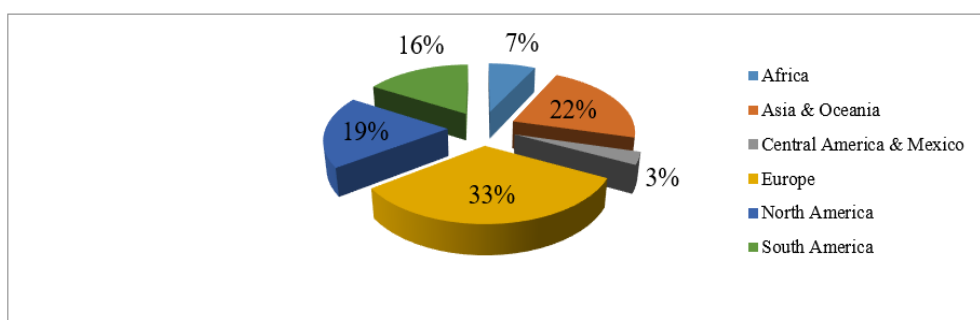


Figure 1. The consumption of coffee in world [23].

2.2. Turkey

Turkish coffee culture started in 1517 and soon after, coffee houses were opened where people came together and drank coffee. In the 17th century, the popularity of Turkish coffee spread to different

countries. Coffee is not just a consumption item in Turkish cuisine and culture. It has been an effective element of national identity that reflects the history, culture, traditions and cuisine and it differs from modern coffees with its preparation, drinking, presentation and special equipment applied. For Turkish coffee, the highest quality Arabica coffee beans are selected and used. After grounding the beans in a coffee mill and getting the thinnest possible form, coffee is cooked as Turkish coffee by the method prepared in a small boiling pot with a narrow top developed by the Turks [24,25]. Although traditionally "Arabica" type beans are used, different beans can also be used, provided that they are of very high quality. Finely ground Turkish coffee is prepared with water by boiling the coffee slowly. Roasting degree is between the important factors in the taste of Turkish coffee. In order to achieve the characteristic flavor and fine texture of Turkish coffee, the coffee beans must be kept moist after roasting and not be completely dried [20,21]. Turkish coffee is the only type of coffee served with its grounds. It would be unfair to say that the difference of Turkish coffee from other coffees due to its many characteristics is only due to its cooking. Turkish coffee is a value that was included in the Intangible Cultural Heritage List of Humanity by UNESCO in 2013 due to its many features such as the history it gives to the place where it is drunk, being based on a rich cultural foundation, and its place in social life [26,27]. Figure 2 shows the filter coffee and Turkish coffee.



Figure 2. (a) Filter coffee.

(b) Turkish coffee.

Turkey is one of the most exciting markets in the world. Turkish coffee itself has a long and deep-rooted tradition. Since 2010, consumption has grown at a steady 15% year-on-year. Coffee consumption in Turkey in 2020/2021 was approximately 106 million kg and is increasing every year which means 1.2 kg of coffee per person per year [23]. In Turkey, Turkish coffee accounts for 40% of outdoor beverage preference whereas this value is around 65% at homes [28]. Table 1 shows the coffee consumption values for last four years for the importing countries. Turkey has the maximum change between these countries.

Table 1. Coffee consumption* of importing countries [23].

Countries	2017/18	2018/19	2019/20	2020/21	Change (%)
Turkey	1376	1740	1711	1754	8.4

Russian Federation	4324	4691	4631	4681	2.7
Algeria	1911	2150	2110	2131	3.7
Republic of Korea	2371	2476	2471	2513	2.0
Switzerland	1013	1079	1060	1074	2.0
Australia	1854	1961	1939	1962	1.9
Canada	3829	4020	3929	4011	1.6
USA	26112	27759	26651	26982	1.1
Saudi Arabia	1275	1266	1241	1253	-0.6
Japan	7750	7561	7355	7386	-1.6

* In thousand 60 kg bags

3. VALORIZATION AND POTENTIAL OF COFFEE WASTE

3.1. Filter Coffee

Coffee is one of the most common global beverages, with approximately 10 million tons consumed annually and it produces more than 99% of coffee waste as a by-product after brewing. If not properly managed, high coffee waste production rates cause adverse environmental impacts. Waste coffee grounds have attracted a lot of attention in recent years due to its components such as fiber, amino acids, polyphenols, and saturated fatty acids. The recovery of these organic compounds could be very beneficial. Approximately 650 kg of waste coffee grounds formed from 1 ton of coffee, and this value is about 6 million tons yearly [14,29,30]. According to Brand et al. (2000), only 6% by weight of harvested fresh coffee reaches the consumer as a beverage. Therefore, considering the water from by-product or drying of used coffee grounds, it leaves around 94% waste [31]. This makes it the largest contributor to coffee biowaste, with around six million tonnes produced annually worldwide [32].

Coffee grounds contain C (59.5%), H (7.3%), N (2.5%) and O (30.7%). Mussatto (2011) stated that the grounds are rich in semi-cellulosic and cellulose polymerized sugar (from hemicelluloses; mannose, galactose, arabinose and celluloses; glucose), while galactan and mannan are the main sugars in the grounds. Its chemical composition and the minerals in the coffee structure can take the values in Table 2 [33,34].

Table 2. Chemical composition and minerals of coffee grounds.

Components	Dry weight (g/100 g)	Minerals	mg/kg
Cellulose	8.6	Potassium	3549
Hemicellulose	36.7	Phosphorus	1475.1
Arabinan	1.7	Magnesium	1293.3
Galactan	13.8	Calcium	777.4
Mannan	21.2	Aluminum	279.3
Proteins	13.6	Iron	118.7

Acetyl groups	2.2	Manganese	40.1
Ashes	1.6	Copper	32.3
		Zinc	15.1

There are many studies that have focused on the production of biodiesel from used coffee grounds. Visak (2017) investigated the kinetics of oil extraction from used coffee grounds using n-hexane as solvent. They found that oil extraction can be carried out in 10 minutes because of the higher diffusion coefficients of oils from used coffee grounds. For the first time, successful in situ transesterification of spent coffee grounds was demonstrated using sodium hydroxide as catalyst at different methanol/oil molar ratios [35]. In addition, Uddin (2019) used waste coffee grounds and the oil was obtained from waste coffee grounds using n-hexane in extraction. Since the crude oil has higher acidity, a two-stage acid-base catalyst transesterification process was used to produce biodiesel. They produced biodiesel within the limit of standards [36]. Nguyen (2020) studied used coffee grounds for biodiesel synthesis using 1,8-diazabicyclodec-7-ene as both a green solvent and catalyst. They found optimal reaction conditions using the response surface methodology. They found the maximum biodiesel yield 97.18% [29]. Rocha (2014) studied the production of biodiesel and ethanol from used coffee grounds. They studied ultrasound-assisted extraction of fat from spent coffee ground. They produced biodiesel with a yield of 97% into fatty acid methyl esters [37]. The conversion of a binary mixture of waste cooking oil and used coffee grounds oil (50/50% by volume) into biodiesel was investigated by Atabani (2019). This study reinforces that the blending of waste cooking oil and spent coffee ground oil improves biodiesel properties and contributes to its economy. Atabani (2018) studied the recycling of used coffee grounds as a potential raw material for alternative fuel production [12,13,38].

3.2. Turkish Coffee

In case for Turkey, Turkish coffee is the most consumed coffee type in cafes and homes. Considering that Turkish coffee is consumed with its grounds, it can be thought that it is more than enough to be evaluated as waste, since it will be for each cup. Considering the average Turkish coffee consumption is around 84% of the total coffee consumed in Turkey, Turkish coffee waste generated annually is around 57 million kg [39-42].

In order to obtain the potential of Turkish coffee waste potential, spent Turkish coffee waste grounds were collected from the cafes. Its brand was Kurukahveci Mehmet Efendi which uses Arabica beans. Approximately 1 kg of waste was used as a sample. The grounds were dried at 105°C to remove moisture. The oil was then extracted by using a Soxhlet process which brand is Gerhardt Analytical Systems. The extraction process was carried out at Tubitak BUTAL (Bursa Test and Analysis Laboratory) in Bursa, Turkey. Ether was used as an organic solvent. The Soxhlet temperature was maintained at 65-70 °C. Rotary vacuum evaporator was applied to separate oil from the organic solvent. The yield was calculated on dry weight basis. The oil amount of coffee grounds is found as 16.8±0.1% (on a dry weight basis). Table 3 shows the oil percentage amounts of the spent coffee grounds found in literature.

Table 3. Oil yields on a dry weight basis in literature and this study.

Study	Oil yield (w/w %)	Coffee type
Efthymiopoulos et al., 2019 [43]	13.4-14.8	Spent coffee grounds
Haile, 2014 [44]	15.6	Spent coffee grounds
Deligiannis, 2011 [45]	10-15	Spent coffee grounds
Al-Hamamre, 2013 [46]	15.3	Spent coffee grounds
Atabani, 2017 [38]	13	Spent coffee grounds
Ahangari and Sargolzaei, 2013 [47]	16.7	Spent coffee grounds
This study	16.8	Turkish coffee waste

4. RESULTS AND DISCUSSION

Coffee, which has been an inevitable part of daily life and culture for centuries and consumed heavily by all segments of society, has an important place in both commercial and social life.

Every year millions of tonnes of coffee waste are generated in the food and beverage market all over the world. The massive amount of coffee waste generated daily could result a significant part of biodiesel production. Coffee consumption in the world has been estimated as 9.98 million tonnes in 2021. Its 65% can be assumed as waste. When the average oil content is assumed as 15% and the specific gravity is assumed as 0.92, 1057 million L of coffee oil can be obtained from waste coffee per year [44,46,48]. If the biodiesel conversion efficiency is approximately 85%, approximately 900 million L of waste coffee biodiesel can be produced annually in the world.

In Turkey, increasing the number of branches in the market and facilitating accessibility through the creation of new local and boutique coffee brands are one of the real indicators of the growth of the coffee sector. While per capita coffee consumption per capita was 200 grams in 2002, it has increased to over 1.1 kilogram today. Growth is noticeably higher than other countries on an annual basis. As it is previously highlighted, Turkish coffee is the most consumed coffee in Turkey. When coffee consumption value in Turkey, which is 106 million kg is taken into account, 84% which means 89 million kg is used by Turkish coffee yearly. If 65% is assumed as coffee waste, Turkish coffee waste value becomes 57 million kg. If the oil content of Turkish coffee waste is taken as 16.8% and specific gravity is assumed as 0.92; 10.4 million L of coffee oil may be obtained. As a result, 8.44 million L of biodiesel could be produced from Turkish coffee waste annually.

5. CONCLUSION

Global biodiesel production is expected to reach 39.3 billion liters by 2027, an increase of 9% from the 2017 level. In particular, it is predicted that the European Union will be the largest biodiesel producer. Undoubtedly, the development direction of the biofuels market will be determined by macroeconomic indicators, nationally adopted policies and crude oil prices. When an examination was made according to the types of raw materials used in the production of the biodiesel sector, it was determined that 30% of the waste vegetable oil and 70% of the vegetable oil seeds were used.

Using coffee waste as a raw material for biodiesel production seems like a perfect solution. Because it's free waste and high quality. Coffee residues contain between 11% and 20% by weight oil as much as traditional biodiesel raw materials such as soybean, rapeseed and palm oil.

Although Turkish coffee is not a type of coffee it is a method of a preparation, it should be assessed separately from the other coffee types in Turkey. It has been determined that Turkish coffee contains caffeine and biologically active components at higher rates than other coffee types and preparation methods [49]. As it is seen on Table 3, the oil content of the Turkish coffee waste is also higher than the other coffee waste oil results. This shows the importance of the Turkish coffee waste in Turkey. The main disadvantage of Turkish coffee waste with respect to filter coffee waste is, it should be taken from each cup. It may take time and may be tiring.

When it comes the negative effect of coffee waste on environment, the amount of coffee waste sent to landfills can be 43,000 tons per day (15.7 million tons per year). Disposal of one ton of used coffee grounds produces 682 kg of CO₂ per year, equivalent to 28.64 million tons of CO₂. Therefore, the CO₂ from the disposal of used coffee grounds is equal to that from burning 10.7 million L of diesel fuel per year. With this viewpoint, 39.42 million kg of CO₂ is being generated by Turkish coffee waste.

ACKNOWLEDGEMENT

No funding, grants, or other support was received.

REFERENCES

- [1] International Energy Agency. www.iea.org (accessed on 15.07.2022)
- [2] Estevez, R., Aguado-Deblas, L., Lopez-Tenllado, F.J., Luna, C., Calero, J., Romero, A.A., Bautista, F.M. and Luna, D., (2022). Biodiesel is dead: long life to advanced biofuels-A comprehensive critical review, *Energies*, 15, 3173.
- [3] Turkish Electricity Transmission Corporation, teias.gov.tr (accessed on 02.07.2022).
- [4] Biyodizel Sanayi Raporu I, www.biyodizel.org.tr (accessed on 01.07.2022)
- [5] Okolie, J.A., Escobar, J.I., Umenweke, G., Khanday, W. and Okoya, P.U., (2022). Continuous biodiesel production: A review of advances in catalysis, microfluidic and cavitation reactors, *Fuel*, 307, 121821, 1-22.
- [6] da Silva, C.A., dos Santos, R.N., Oliveira, G.G., de Souza Ferreira, T.P., de Souza, N.L.G.D., Soares, A.S., de Melo, J.F., Colares, C.J.G., de Souza, U.J.B. and de Araújo-Filho, R.N., (2022). Biodiesel and bioplastic production from waste-cooking-oil transesterification: An environmentally friendly approach, *Energies*, 15, 1073.

- [7] Kamil, M., Ramadan, K.M., Olabi, A.G., Al-Ali, E.I., Ma, X. and Awad, O.I., (2020). Economic, technical, and environmental viability of biodiesel blends, *Renewable Energy*, 147, 1880-1894.
- [8] Banu, J.R., Kavitha, S., Kannah, R.Y., Kumar, M.D., Preethi, Atabani, A.E. and Kumar, G., (2020). Biorefinery of spent coffee grounds waste: Viable pathway towards circular, *Bioresource Technology*, 302, 122821, 1-15.
- [9] Deshmukh, G.K., Rehman, A. and Gupta, R., (2021). Combustion and emission characteristics of a compression-ignition engine fuelled with transesterified-jatropha biodiesel-diesel blends, *International Journal of Renewable Energy Research*, 11(2), 899-907.
- [10] Jayakumar, M., Karmegam, N., Gundupalli, M.P., Gebeyehu, K.B., Asfaw, B.T., Chang, S.W., Ravindran, B. and Awasthi, M.K., (2021). Heterogeneous base catalysts: synthesis and application for biodiesel production - A review, *Bioresource Technology*, 331, 125054, 1-12.
- [11] Abomohra, A.E., Zheng, X., Wang, Q., Huang, J. and Ebaid, R., (2021). Enhancement of biodiesel yield and characteristics through in-situ solvo-thermal co-transesterification of wet microalgae with spent coffee grounds, *Bioresource Technology*, 323, 124640, 1-11.
- [12] Atabani, A.E., Al-Muhtaseb, A.H., Kumar, G., Saratale, G.D., Aslam, M., Khan, H.A., Said, Z. and Mahmoud, E., (2019). Valorization of spent coffee grounds into biofuels and value-added products: pathway towards integrated bio-refinery, *Fuel*, 254, 115640, 1-20.
- [13] Atabani, A.E., Shobana, S., Mohammed, M.N., Uğuz, G., Kumar, G., Arvindnarayan, S., Aslam, M. and Al-Muhtaseb, A.H., (2019). Integrated valorization of waste cooking oil and spent coffee grounds for biodiesel production: Blending with higher alcohols, FT-IR, TGA, DSC and NMR characterizations, *Fuel*, 244, 419-430.
- [14] Colantoni, A., Paris, E., Bianchini, L., Ferri, S., Marcantonio, V., Carnevale, M., Palma, A., Civitarese, V. and Gallucci, F., (2021). Spent coffee ground characterization, pelletization test and emissions assessment in the combustion process, *Scientific Reports*, 11:5119, 1-14.
- [15] Wu, C.T., Agrawal, D.C., Huang, W.Y., Hsu, H.C., Yang, S.J., Huang, S.L. and Lin, Y.S., (2019). Functionality analysis of spent coffee ground extracts obtained by the hydrothermal method, *Journal of Chemistry*, 4671438, 1-8.
- [16] Vanyan, L., Cenian, A. and Trchounian, K., (2022). Biogas and biohydrogen production using spent coffee grounds and alcohol production waste, *Energies*, 15, 5935.
- [17] Chen, C.Y., Shih, C.H., Lin, T.C., Zheng, J.H., Hsu, C.C., Chen, K.M., Lin, Y.S. and Wu, C.T., (2021). Antioxidation and tyrosinase inhibitory ability of coffee pulp extract by ethanol, *Journal of Chemistry*, 8649618, 1-8.

- [18] Altundağ, Ö.Ö., (2019). Health dimensions of Turkish Coffee and its effects, İzmir Democracy University Health Sciences Journal, 2(3), 183-193.
- [19] Temeloğlu, E. and Akdeniz, D., (2020). Tüketicilerin Türk Kahvesi hakkında bilgiye sahip olma algı seviyelerinin demografik özelliklere göre karşılaştırılması, Uluslararası Türk Dünyası Turizm Araştırmaları Dergisi, 5(1), 116-126.
- [20] Süren, T. and Kızıleli, M., (2021). Geleneksel Türk içecekleri, AHBVÜ Turizm Fakültesi Dergisi, 24 (1), 46-71.
- [21] Kefeli, E., Şahin, Ö. and Yarmacı, N., (2020). Üçüncü nesil kahve işletmelerinde Türk Kahvesinin yeri: İstanbul örneği, Uluslararası Batı Karadeniz Sosyal ve Beşeri Bilimler Dergisi, 4(2), 130-147.
- [22] Saratale, G.D., Bhosale, R., Shobana, S., Banu, J.R., Pugazhendhi, A., Mahmoud, E., Sirohi, R., Bhatia, S.K., Atabani, A.E., Mulone, V., Yoon, J.J., Shina, H.S. and Kumar, G., (2020). A review on valorization of spent coffee grounds (SCG) towards biopolymers and biocatalysts production, Bioresource Technology, 314, 123800, 1-12.
- [23] International Coffee Organization, www.ico.org, (accessed on 09.07.2022)
- [24] Küçükkömürler, S. and Özgen, L., (2009). Coffee and Turkish Coffee culture, Pakistan Journal of Nutrition, 8(10), 1693-1700.
- [25] Akşit, N.A., (2017). Değişen kahve tüketim alışkanlıkları ve Türk Kahvesi üzerine bir araştırma, Journal of Tourism and Gastronomy Studies, 5(4), 310-325.
- [26] Karhan, J., (2021). Toplumsal ve kültürel bir içecek: "Türk Kahvesi", Karadeniz Uluslararası Bilimsel Dergi, 52, 149-165.
- [27] Bir Kahveden Daha Fazlası, "Türk Kahvesi", www.brewmood.com.tr/blog/ (accessed on 01.07.2022).
- [28] Yüksel, A.N., Barut, K.T.Ö. and Bayram, M., (2020). The effects of roasting, milling, brewing and storage processes on the physicochemical properties of Turkish Coffee, LWT-Food Science and Technology, 131, 109711, 1-8.
- [29] Nguyen, H.C., Nguyen, M.L., Wang, F.M., Juan, H.Y. and Su, C.H., (2020). Biodiesel production by direct transesterification of wet spent coffee grounds using switchable solvent as a catalyst and solvent, Bioresource Technology, 296, 122334, 1-7.
- [30] Boğa, T. and Dertli, E., (2021). Kullanılmış kahve telvesinin lif kaynağı olarak değerlendirilme potansiyeli, European Journal of Science and Technology, 31(1), 114-120.

- [31] Brand, D., Pandey, A., Roussos, S. and Soccol, C.R., (2000). Biological detoxification of coffee husk by filamentous fungi using a solid state fermentation system, *Enzyme and Microbial Technology*, 27(1-2), 127-133.
- [32] La Scalia, G., Saeli, M., Miglietta, P.P. and Micale, R., (2021). Coffee biowaste valorization within circular economy: an evaluation method of spent coffee grounds potentials for mortar production, *The International Journal of Life Cycle Assessment*, 26, 1805–1815.
- [33] Mussatto, S.I., Carneiro, L.M., Silva, J.P.A., Roberto, I.C. and Teixeira, J.A., (2011). A study on chemical constituents and sugars extraction from spent coffee grounds, *Carbohydrate Polymers*, 83, 368-374.
- [34] Silva, M.A., Nebra, S.A., Silva, M.M.J. and Sanchez, C.G., (1998). The use of biomass residues in the Brazilian soluble coffee industry, *Biomass and Bioenergy*, 14(5/6), 457-467.
- [35] Najdanovic-Visak, V., Lee, F.Y.L, Tavares, M.T., and Armstrong, A., (2017). Kinetics of extraction and in situ transesterification of oils from spent coffee grounds, *Journal of Environmental Chemical Engineering*, 2017, 5, 2611–2616.
- [36] Uddin, M.N., Techato, K., Rasul, M.G., Hassan, N.M.S. and Mojifur, M., (2019). Waste coffee oil: a promising source for biodiesel production, *Energy Procedia*, 160, 677-682.
- [37] Rocha, M.V.P., de Matos, L.J.B.L., de Lima, L.P., Figueiredo, P.M.S., Lucena, I.L., Fernandes, F.A.N. and Gonçalves, L.R.B., (2014). Ultrasound-assisted production of biodiesel and ethanol from spent coffee grounds, *Bioresource Technology*, 167, 343-348.
- [38] Atabani, A.E., Mercimek, S.M., Arvindnarayan, S., Shobana, S., Kumar, G., Cadir, M. and Al-Muhateb, A.H., (2018). Valorization of spent coffee grounds recycling as a potential alternative fuel resource in Turkey: an experimental study, *Journal of the Air & Waste Management Association*, 68:3, 196-214.
- [39] Acar, N., Çakırbaş, A. and Çizmeçi, B., (2019). Determination of factors affecting the selection of turkish coffee places: an example of Nevşehir, *Anemon Muş Alparslan Üniversitesi Sosyal Bilimler Dergisi*, 7(1), 135-143.
- [40] Karaman, N., Kılıç, A. and Avcıkurt, C., (2019). Tüketicilerin kahve kafeleri ziyaret eğilimlerinin ve değişen kahve tüketim alışkanlıklarının belirlenmesi: geleneksel Türk kahvesi üzerine bir araştırma, *Türk Turizm Araştırmaları Dergisi*, 3(3), 612-632.
- [41] Akşit Aşık, N., (2017). A research on changing coffee consumption habits and Turkish coffee, *Journal of Tourism and Gastronomy Studies*, 5(4), 310-325.
- [42] Kahve Tüketim Alışkanlıkları, [twenty.com](https://www.twentify.com), (accessed on 05.07.2022).

- [43] Efthymiopoulos, I., Hellier, P., Ladommatos, N., Kay, A. and Mills-Lampsey, B., (2019). Effect of solvent extraction parameters on the recovery of oil from spent coffee grounds for biofuel production, *Waste Biomass Valorization*, 10, 253-264.
- [44] Haile, M., (2014). Integrated valorization of spent coffee grounds to biofuels, *Biofuel Research Journal*, 2, 65-69.
- [45] Deligiannis, A., Papazafeiropoulou, A., Anastopoulos, G. and Zannikos, F., (2011). Waste coffee grounds as an energy feedstock, *Proceedings of the 3rd International CEMEPE & SECOTOX Conference Skiathos, June 19-24*, 617-622.
- [46] Al-Hamamre, Z., Foerster, S., Hartmann, F., Kröger, M. and Kaltschmitt, M., (2012). Oil extracted from spent coffee grounds as a renewable source for fatty acid methyl ester manufacturing, *Fuel*, 96, 70-76.
- [47] Ahangari, B. and Sargolzaei, J., (2013). Extraction of lipids from spent coffee grounds using organic solvents and supercritical carbon dioxide, *Journal of Food Processing and Preservation*, 37, 1014-1021.
- [48] Ariga, S.R., Aisyah, Y., Patria, A., Arpi, N. and Yunita, D., (2018). Physicochemical characterization of oil from roasted coffee, *Proceeding of The 8th AIC: Health and Life Sciences, Syiah Kuala University*, 94-102.
- [49] Tan, A. and Hocaoğlu, E., (2017). Türkiye’de hazır kahve satın alma ve tüketim alışkanlıkları, *Gaziantep University Journal of Social Sciences*, 16(4), 950-962.



RESEARCH ARTICLE

**INVESTIGATION OF RECENTLY ABUSED DRUGS IN DRIED BLOOD SPOTS USING
FTA CARDS BY LIQUID CHROMATOGRAPHY TANDEM MASS SPECTROMETRY:
VALIDATION AND APPLICATION TO REAL SAMPLES**

Yeter EROL ÖZTÜRK^{1*}

^{1*}Council of Forensic Medicine, Chemistry Department, Ankara, yetererol@hotmail.com, ORCID: 0000-0001-9503-7057

Receive Date: 13.08.2023

Accepted Date: 06.09.2023

ABSTRACT

A robust and selective liquid chromatography-tandem mass spectrometry (LC-MS/MS) method was established for the analysis of 19 illicit drugs and metabolites in whole blood dried blood spots (DBS) using FTA cards. Samples prepared using Ahlstrom Munksjö Gensaver™ Colorcards were extracted with methanol. Analytical separation of the analytes was maintained using an Agilent Poroshell column with mobile phase A (0.1% formic acid in water) and B (methanol). Multiple Reaction Monitoring (MRM) with positive ionisation on LC-MS/MS was used to develop the method. The method was validated and met the acceptance criteria with acceptable results for carry-over, linearity, specificity, sensitivity, accuracy, precision, matrix effect and recovery. The method was applied to positively reported whole blood samples from patients suspected of drug abuse. Good quantitative agreement was obtained between the DBS and whole blood methods. Application to real DBS samples showed that this method is a good alternative and useful technique for the detection of drugs of abuse in forensic toxicology and appears to provide a good alternative storage condition.

Keywords: *DBS, LC-MS/MS, drug abuse, real samples, illicit drugs*

1. INTRODUCTION

DBS is commonly used as a sampling procedure that involves taking a significantly small volume of blood from the fingertip or heel [1]. DBS is commonly used to collect, store, transport and analyse a variety of human body fluids, and its use has primarily focused on the diagnosis of infections, generally used in the systematic screening of diseases in newborns [2].

DBS provides significant advantages over traditional whole-blood sampling techniques. It is a simple sample collection technique using non-specialist personnel, allowing blood samples to be collected at the point and time of need, a minimally invasive collection procedure, small sample size and integrity of storage and transport. DBS minimizes sample preparation procedures inclusively and simplifies the automation of processes. DBS samples from closed cases can be stored for long periods for clinical and forensic purposes because of the small sample sizes. DBS can also be useful in monitoring

addiction treatment, preventing the risk of infection with chronic diseases and the risk of viruses such as hepatitis, HIV and blood-borne viruses. The short stability of drugs in biological samples during transport and storage makes interpretation of results difficult. It can also stabilise a wider range of analytes than whole blood samples, even when stored in uncontrolled environmental conditions. [3]. DBS provides a stabilising effect by reducing the hydrolysis reactions of drugs that have ester groups in their chemical structure, such as cocaine and 6-AM [4-5]. Owing to these many benefits, DBS has been accepted for toxicokinetic studies, drug detection and monitoring, analysis of illicit drugs and their metabolites, doping, and assays of molecules with high weight, such as therapeutic proteins, antibodies, biomarkers, and proteomics [1, 5-20].

Since the 1950s, its benefits have been noticed long before [6], preclinical [7] and clinical trials [8, 9] and for drug investigation, drugs or their metabolites abuse [10-31]. Blood is a common biological sample for the detection and quantification of abused drugs and their metabolites in forensic toxicology. DBS has been applied to tetrahydrocannabinol and its main metabolites [18], natural and synthetic cannabinoids [19], cocaine and opiates [21], amphetamines [25] and methadone [28]. However, no validated methods have been published for the detection and quantification of these illicit drugs and/or their metabolites in DBS using ginsaver color cards (FTA) with real samples. FTA cards are used to purify and extract nucleic acids for genetic profiling and have never been used in forensic toxicology for the investigation of abused drugs. These cards are only used for genetic profiling and there is no other application to date. The study aims to provide genetic profiling and drug testing in one DBS sample. This is because in some cases it is not possible to take a whole blood sample for drug testing. This study presents a robust, rapid and cost-effective liquid chromatography method for the quantitative detection of 19 illicit drugs and/or their metabolites in DBS using FTA cards. The results were analysed and examined for correlation with those obtained using a validated solid phase extraction whole blood method [32], which was also used to quantify positive results.

2. MATERIAL AND METHODS

2.1. Chemicals and Reagents

ADB-BUTINACA N-butanoic acid, Amphetamine, Methamphetamine, 6-MAM (6-Monoacetylmorphine), ADB-BUTINACA, ADB-BUTINACA N-(4-hydroxybutyl), Benzoylcegonine, Buprenorphine, Cocaine, Codeine, MDMA, MDEA, MDA, MDMB-4en-PINACA, MDMB-4en-PINACA butanoic acid, Methadone, Morphine, THC and THC-COOH were purchased from Chiron (Trondheim, Norway) at concentrations of 1 mg/mL and the internal standard (Diazepam-d5) obtained from Cerilliant (Paloma, TX, USA) at concentrations of 1 mg/mL. All reagents, solutions, and solvents were ammonium acetate, formic acid, methanol, ethyl acetate, and VWR Chemicals (Gibbstown, NJ, USA). Ginsaver Color cards were obtained from Ahlstrom Munksjö (Barenstein, Germany).

2.2. LC-MS/MS

The liquid chromatography system included of a Shimadzu liquid chromatography module with a combined column oven (Shimadzu, Kyoto, Japan) maintained at 40 °C and an Agilent Poroshell column (150×4.6 mm, 2.7 µm). The mobile phase included A (5mM ammonium acetate and 0.1 % v/v formic acid in water) and B (methanol). The gradient was set as follows 10% B for 0-0.3 min and then

B was increased from 10% to 80% within 3 min; between 3-7 min. B was increased from 80% to 95%; B was held at 95% for 7-11 min and decreased from 95% to 10% B for 11.1-15 min. The flow rate, the injection volume and autosampler temperature were set to 0.6 mL/min, 5 μ L and 8 $^{\circ}$ C, respectively. Electrospray ionisation (ESI+) and MRM mode were used for detection. The source voltage was set at 1.5 kV. Nebulizing, heating and drying gas flows were set at 3 L/min, 10 L/min and 10 L/min respectively. The interface, desolvation line, heat block and desolvation temperatures were set at 300 $^{\circ}$ C, 250 $^{\circ}$ C, 400 $^{\circ}$ C and 526 $^{\circ}$ C respectively. CID gas was set at 270 kPa. The pause time and polarity switching times were set to 1 ms. ms and 5 ms, respectively, and the dwell time for the analytes was set between 5 and 13 ms. The MRM transitions and collision energies were optimized for each transition with infusion. The total run time was 15 minutes.

2.3. Preparation of Standard Solutions

Stock solutions of primary analytes at a concentration of 1 mg/ml were dissolved in methanol and stored at -20° C, and other solutions were prepared daily. The IS was prepared in methanol at a concentration of 200 ng/mL.

2.4. Human Samples

Blank blood samples were used to develop and validate the method and were provided by a regional blood donation centre. Authentic samples were provided from samples collected for routine drug abuse analysis and samples not collected for this study. Thirty samples with 103 positive results for the analytes included in this study and stored at -20° C prior to analysis.

2.5. Sample Preparation

To prepare the samples, 100 μ L of sample was applied to Gensaver cards, dried overnight at room temperature and the DBS was then analysed. The whole spot was cut out and placed on a glass slide. Five millilitres of methanol and 50 μ L of each deuterated IS working mixture were added. After vortexing for 2 minutes, the tube was gently shaken in a homogeniser for 20 minutes and centrifuged at 4000 rpm for 10 minutes. The extract was evaporated gently at 40 $^{\circ}$ C under a stream of nitrogen. The residue was reconstituted in 250 μ L of a mixture of A (90) and B (10) mobile phases. The sample was vortexed for 2 min, centrifuged at 14,000 rpm for 10 min, transferred to a vial and a 10 μ L aliquot was injected into the system.

2.6. Method Validation

The method validation was performed for linearity in terms of selectivity, matrix effect, carryover limit of detection (LOD), limit of quantification (LOQ), linearity, inter and intra-assay precision, recovery, matrix effects and process efficiency. The method has been validated in accordance with international guidelines on forensic toxicology and DBS technique [33, 34]. Six blank blood samples were analysed to investigate the selectivity for potential interferences at the expected retention times of the analytes and IS. Seven calibration points were analyzed between 0.1-50 ng/mL, with three replicates at each concentration. The coefficient of determination (R^2) was expected to be greater than 0.995 and the calibrators were expected to quantify within $\pm 10\%$. The LOD ($S/N \geq 3$) and LOQ ($S/N \geq 10$) were estimated with six fortified samples at the lowest concentrations with acceptable precision and accuracy of $<20\%$. Intra-assay precision was evaluated with six replicates per level concentration at 5 ng/mL (low) and 50 ng/mL (high). Inter-assay precision was assessed over five consecutive days

using three replicates for each concentration. Carryover was investigated by injecting extracted blanks after five injections of the highest concentration level of the recovery experiment. Recovery, matrix effect and process efficiency were investigated at two different concentrations (n=6, 5 ng/mL (low) and 50 ng/mL (high)) and calculated according to Matuszewski et al. [35].

2.7. Real Sample Analysis

Thirty authentic samples were analysed using the DBS technique and 103 positive results were reported for the analytes included in the study and the results of DBS method were compared with data obtained using the routine whole blood method. In the routine method, the sample volume was 500 µL and the solid phase extraction (SPE) used for sample preparation and analysis was set up by LC-MS/MS analysis [32]. Linear regression analysis, the paired t-test (with a significance level of 0.05) and the Bland-Altman difference plot (with a 95% limit of agreement) were used to investigate the agreement between the results [36-38]. The differences between the two methods and the acceptability of the suitability of the interval were analysed [37].

3. RESULT AND DISCUSSION

3.1. Method Validation Results

The method validation parameters are given in Tables 1 and 2. Selectivity was investigated with six samples. No significant interfering peaks were found. The calibration curve was constructed using the (1/x; x, concentration) linear regression model with a coefficient of determination (R²) of not less than 0.995 and was found to be linear between 0.1-50 ng/mL. The intra- and inter- assay precisions of the method were found to be 1.2-9.9% and 2.1-10.1%, respectively. The accuracy of the method was 91-108%. All precision and accuracy were acceptable. The LODs were 0.3-2.9 ng/mL and the LOQs were 0.4-3.9 ng/mL. No relevant peaks were observed in the blanks used to investigate carryover. Extraction recoveries ranged from 21.1-115.3% at the two concentrations. Matrix effect and process efficiency values were in the range of 83.0-116.0% and 78.0-109.0% at the two concentrations, respectively.

Table 1. Validation data of the developed method (LOD, LOQ, Recovery, Linear Range and Correlation Coefficient values of analytes).

Analyte	LOD (ng/ mL)	LOQ (ng/ mL)	Recovery (5 ng/mL)	Recovery (50 ng/mL)	Linear Range (ng/mL)	Corr. Coeff. (R ²)
6-MAM	0.8	1.1	78.3	77.4	0.1-50	0.999
ADB-BUTINACA	0.3	0.5	102.8	93.8	0.1-50	0.998
ADB-BUTINACA N-(4-hydroxybutyl)	0.3	0.4	98.9	83.7	0.1-50	0.998
ADB-BUTINACA N-butanoic acid	0.3	0.5	97.3	92.2	0.1-50	0.997
Amphetamine	2.6	3.9	25.9	28.3	0.1-50	0.996
Benzoylcegonine	0.7	1.1	115.3	109.2	0.1-50	0.999
Buprenorphine	2.9	3.7	75.8	69.0	0.1-50	0.996

Cocaine	0.6	0.8	75.0	67.5	0.1-50	0.999
Codeine	0.7	0.8	105.5	101.9	0.1-50	0.996
MDA	1.6	1.9	67.6	62.9	0.1-50	0.996
MDEA	0.6	0.8	63.6	55.8	0.1-50	0.999
MDMA	0.7	1.0	67.1	63.0	0.1-50	0.996
MDMB-4en-PINACA	0.3	0.5	87.0	93.1	0.1-50	0.999
MDMB-4en-PINACA	0.3	0.5	95.9	98.3	0.1-50	0.998
butanoic acid						
Methadone	0.7	1.2	74.6	64.8	0.1-50	0.997
Methamphetamine	2.0	3.1	24.7	21.1	0.1-50	0.996
Morphine	0.5	0.7	85.3	84.5	0.1-50	0.996
THC	2.3	2.9	63.5	52.0	0.1-50	0.996
THC-COOH	1.0	2.0	91.3	87.3	0.1-50	0.996

Table 1. Validation data of the developed method (recovery and precision values).

Analyte	Recovery (%) (5 ng/mL)	Recovery (%) (50 ng/mL)	Intra-assay precision (%) (5 ng/mL)	Intra-assay precision (%) (50 ng/mL)	Inter-assay precision (%) (5 ng/mL)	Inter-assay precision (%) (50 ng/mL)
6-MAM	78.3	77.4	4.8	2.8	5.6	3.1
ADB-BUTINACA	102.8	93.8	3.3	1.9	4.8	2.3
ADB-BUTINACA N-(4-hydroxybutyl)	98.9	83.7	3.8	2.1	4.2	2.5
ADB-BUTINACA N-butanoic acid	97.3	92.2	3.2	2.3	4.1	2.6
Amphetamine	25.9	28.3	5.3	4.5	6.5	5.3
Benzoylecgonine	115.3	109.2	4.3	2.2	5.8	4.3
Buprenorphine	75.8	69.0	5.7	3.0	6.5	5.1
Cocaine	75.0	67.5	4.1	3.0	4.9	3.2
Codeine	105.5	101.9	3.0	2.6	4.1	2.7
MDA	67.6	62.9	4.7	3.7	5.5	2.8
MDEA	63.6	55.8	4.4	2.4	4.9	2.5
MDMA	67.1	63.0	4.3	1.2	6.0	3.4
MDMB-4en-PINACA	87.0	93.1	2.6	1.8	3.8	2.3
MDMB-4en-PINACA	95.9	98.3	2.5	1.7	3.9	2.4
butanoic acid						
Methadone	74.6	64.8	2.4	1.8	5.6	4.4
Methamphetamine	24.7	21.1	4.1	2.3	4.8	2.1
Morphine	85.3	84.5	3.6	3.3	4.5	3.8
THC	63.5	52.0	9.9	8.8	10.1	9.2
THC COOH	91.3	87.3	3.2	2.3	4.5	2.8

3.2. Analysis of Real Sample Results

Thirty authentic real collected as part of the Council of Forensic Medicine's drug abuse screening activities, resulting in a total of 103 positive analyte was reported: 6-MAM (n=3), ADB-BUTINACA (n=3), ADB-BUTINACA N-(4-hydroxybutyl) (n=4), ADB-BUTINACA N-butanoic acid (n=4), Amphetamine (n=12), Benzoylcegonine (n=6), Buprenorphine (n=3), Cocaine (n=3), codeine (n=8), MDA (n=5), MDEA (n=3), MDMA (n=5), MDMB-4en-PINACA (n=3), MDMB-4en-PINACA butanoic acid (n=3), methadone (n=4), methamphetamine (n=12), morphine (n=3), THC (n=3), THC-COOH (n=11). The results of DBS and whole blood analyses are shown in Table 3.

Table 2. Concentrations of analytes on DBS and classical whole blood method.

Compound	DBS Concentration (ng/mL)	Case	Classical Whole Blood Method (ng/mL)	Case
6-MAM	0.9-2.7	3	1.3-3.2	3
ADB-BUTINACA	0.9-1.2	3	1.1-1.4	3
ADB-BUTINACA N-(4-hydroxybutyl)	2.3-3.9	4	2.8-4.1	4
ADB-BUTINACA N-butanoic acid	8.3-11.2	4	9.1-12.3	4
Amphetamine	9.5-68.9	12	3.0-75.8	12
Benzoylcegonine	1.4-101.6	6	2.0-121.3	6
Buprenorphine	6.3-7.8	3	7.1-9.3	3
Cocaine	3.2-4.6	3	4.3-5.9	3
Codeine	0.9-5.1	8	0.8-4.3	8
MDA	6.4-15.5	5	7.4-14.6	5
MDEA	2.7-4.3	3	2.3-4.1	3
MDMA	70.7-107.1	5	65.9-103.4	5
MDMB-4en-PINACA	0.6-1.8	3	0.7-1.7	3
MDMB-4en-PINACA butanoic acid	2.8-10.3	3	3.1-9.7	3
Methadone	6.9-14.8	4	8.3-14.8	4
Methamphetamine	4.6-195.2	12	3.2-183.6	12
Morphine	0.7-10.7	8	1.7-8.9	8
THC	3.1-4.9	3	5.6-7.3	3
THC COOH	4.5-43.1	11	6.6-39.2	11

All positive analytes were detected by routine methods and DBS. DBS was found to be completely reliable when compared with the routine whole blood method and no false negatives or false positives were observed. The total ion chromatograms and product ion spectra of DBS and whole blood from the same sample are shown in Figure 1.

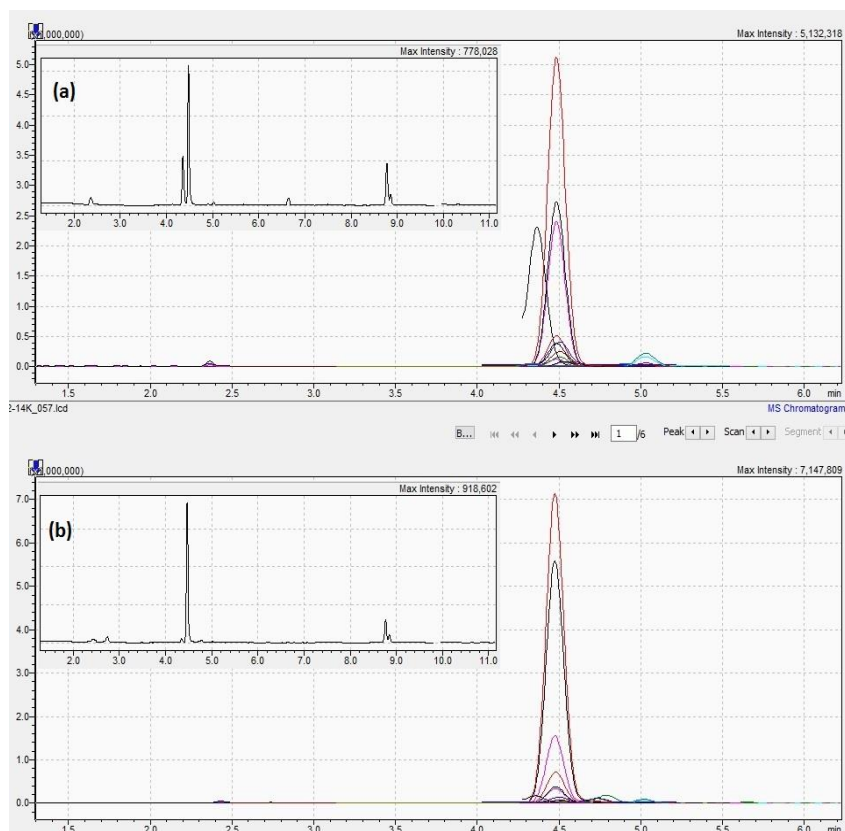


Figure 1. The total ion chromatogram and extracted ion chromatograms of whole blood method (a) and DBS method (b) of the same case sample.

The analyte concentrations obtained by the DBS method were found to be compatible with the routinely analysed whole blood method and a strong correlation was found between the results (Pearson's $r = 0.9650$). In addition, a significant correlation was found using least squares regression analysis ($p < 0.05$), with $r^2 = 0.9406$. A paired two-tailed t-test with a significance level of 0.05 was also used to test for differences between the two methods and no significant difference was found ($t_{\text{calculated}} < t_{\text{table}}$). Finally, the Bland-Altman analysis was also performed between the two groups (limits of agreement of 95%; lower and upper limits, median $\pm 1.96 \times \text{sd}$ (standard deviation)). The plot shows a good agreement between the two methods. The differences between the THC-COOH values were examined between two methods using the Bland-Altman difference plot (Figure 2).

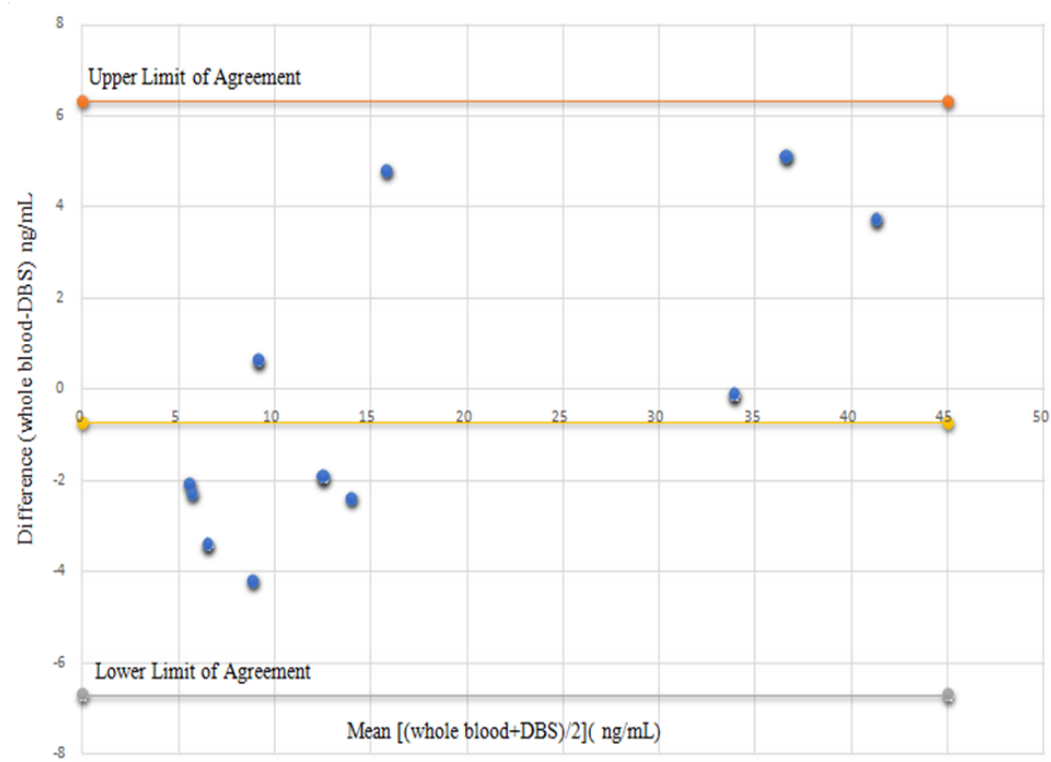


Figure 2. Bland-Altman difference plots of the differences between DBS and whole blood assays against the average obtained by the two assays (Upper Limit Agreement=median+1.96×sd and Lower Limit Agreement=median-1.96×sd).

This study confirms and extends the findings of previously published methods [2, 3, 4, 18, 19, 20, 23, 25, 27, 28, and 29]. In particular, an evaluation of the stability of analytes between the two methods showed that the DBS method produced more reliable quantitative results than the classical methods, even though the cards were stored at room temperature after sampling [19, 20, 23, 25, 27, 28, and 29].

DBS samples provide a compatible alternative for the detection of abused drugs. The method is fast, reliable and selective. It can be a good alternative to complex sample preparation methods such as solid phase extraction (SPE). Material and solvent consumption can be reduced, and smaller sample volumes (100 μ L or less) can be easily handled. This study proved that analyses by DBS technique are as sensitive and reliable as classical methods and can be a good alternative method.

4. CONCLUSION

The LC-MS/MS method developed and validated successfully for the determination and quantification of 19 abused drugs in DBS using FTA cards. Method validation results showed compliance with the guidelines. This study is the first to investigate classical abused drugs and emerging synthetic cannabinoids in authentic whole blood samples of drug abuse suspects collected on DBS. This study confirmed that DBS cards are robust and safe sample storage for the analysis of most drugs analyzed in whole blood. The results obtained from 30 authentic cases showed a promising qualitative and quantitative compliance between the whole blood and the same blood samples dried on DBS cards. In this study, the developed method represents a good complementary alternative to forensic sample analysis by providing a uncomplicated, inexpensive and easy-to-maintain method for determination and quantification simultaneously of abused drugs in the field of forensic toxicology. According to the literature, the stability of most drugs in DBS, even without the addition of preservatives, allows for robust and accurate quantitative results after sample collection and storage at room temperature. With these promising technical, sampling, storage and stability advantages, new research is needed in relation to different applications such as occupational and clinical toxicology and therapeutic monitoring.

CONFLICT OF INTEREST

The author declares no conflict of interests.

ACKNOWLEDGMENTS

The author would like to thank MD. Hızır Aslıyüksel, President of the Council of Forensic Medicine.

REFERENCES

- [1] Sadler Simões, S., Castañera Ajenjo, A., and Dias, M.J. (2018). Dried blood spots combined to an UPLC-MS/MS method for the simultaneous determination of drugs of abuse in forensic toxicology. *J Pharm Biomed Anal*, 5,147,634-644.
- [2] Grüner, N., Stambouli, O., and Ross, R.S. (2015). Dried blood spots preparing and processing for use in immunoassays and in molecular techniques. *J Vis Exp*, 13(97), 52619.
- [3] Quraishi, R., Jain, R., and Ambekar, A. (2013). The use of dried blood spot samples in screening drugs of abuse. *Pharmacology & Pharmacy*, 4(2), 152-159.
- [4] Alfazil, A.A., and Anderson, R.A. (2008). Stability of benzodiazepines and cocaine in blood spots stored on filter paper. *J Anal Toxicol*, 32(7), 511-515.
- [5] Garcia Boy, R., Henseler, R., Mattern, R., and Skopp, G. (2008). Determination of morphine and 6-acetylmorphine in blood with use of dried blood spots. *Ther Drug Monit*, 30(6), 733-739.

- [6] Beaudette, P., and Bateman, K.P. (2004). Discovery stage pharmacokinetics using dried blood spots, *J Chromatogr B Analyt Technol Biomed Life Sci.* 809(1), 153-158.
- [7] Barfield, M., Spooner, N., Lad, R., Parry, S., and Fowles, S. (2008). Application of dried blood spots combined with HPLC-MS/MS for the quantification of acetaminophen in toxicokinetic studies. *J Chromatogr B Analyt Technol Biomed Life Sci.* 870(1), 32-37.
- [8] Spooner, N., Lad, R., and Barfield, M. (2009). Dried blood spots as a sample collection technique for the determination of pharmacokinetics in clinical studies: considerations for the validation of a quantitative bioanalytical method. *Anal Chem*, 81(4), 1557-1563.
- [9] Dainty, T.C., Richmond, E.S., Davies, I., and Blackwell, M.P. (2012). Dried blood spot bioanalysis: an evaluation of techniques and opportunities for reduction and refinement in mouse and juvenile rat toxicokinetic studies. *Int J Toxicol*, 31, 4.
- [10] Velghe, S., Troyer, R.D., and Stove, C. (2018). Dried blood spots in therapeutic drug monitoring and toxicology. *Expert Opin Drug Metab Toxicol*, 14, 1-3.
- [11] Edelbroek, P.M., Van der Heijden, J., and Stolk, L.M. (2009). Dried blood spot methods in therapeutic drug monitoring: methods, assays, and pitfalls. *Ther Drug Monit*, 31, 327.
- [12] McDade, T.W., Williams, S., and Snodgrass, J.J. (2007). What a drop can do: dried blood spots as a minimally invasive method for integrating biomarkers into population-based research. *Demography*, 44, 899.
- [13] Den Burger, J.C., Wilhelm, A.J., Chahbouni, A., Vos, R.M., Sinjewel, A., and Swart, E.L. (2012). Analysis of cyclosporin A, tacrolimus, sirolimus, and everolimus in dried blood spot samples using liquid chromatography tandem mass spectrometry. *Anal Bioanal Chem*, 404, 1803.
- [14] Versace, F., Déglon, J., Lauer, E., Mangin, P., and Staub, C. (2013). Automated DBS extraction prior to HILIC/RP LC-MS/MS target screening of drugs. *Chromatographia*, 76(19-20), 1281-1293.
- [15] Thomas, A., Deglon, J., Steimer, T., Mangin, P., Daali, Y., and Staub, C. (2010). On-line desorption of dried blood spots coupled to hydrophilic interaction/reversed-phase LC/MS/MS system for the simultaneous analysis of drugs and their polar metabolites. *J Sep Sci*, 33(6-7), 873-879.
- [16] Moretti, M., Freni, F., Tomaciello, I., Vignali, C., Groppi, A., Visonà, S.D., Tajana, L., Osculati, A.M.M., and Morini, L. (2019). Determination of benzodiazepines in blood and in dried blood spots collected from post-mortem samples and evaluation of the stability over a three-month period. *Drug Test Anal*, 11, 1403-1411.

- [17] Moretti, M., Freni, F., Tomaciello, I., Vignali, C., Groppi, A., Visonà, S.D., Osculati, A.M.M., and Morini, L. (2019). Determination of antidepressants and antipsychotics in dried blood spots (DBSs) collected from post-Mortem samples and evaluation of the stability over a three-month period. *Molecules*, 24, 3636.
- [18] Mercolini, L., Mandrioli, R., Sorella, V., Somaini, L., Giocondi, D., Serpelloni, G., and Raggi, M.A. (2013). Dried blood spots: liquid chromatography-mass spectrometry analysis of Δ^9 -tetrahydrocannabinol and its main metabolites. *J Chromatogr A*, 4, 1271(1), 33-40.
- [19] Protti, M., Rudge, J., Sberna, A.E., Gerra, G., and Mercolini, L. (2017). Dried haematic microsamples and LC-MS/MS for the analysis of natural and synthetic cannabinoids. *J Chromatogr B Analyt Technol Biomed Life Sci*, 1044-1045, 77-86.
- [20] Ambach, L., Redondo, A.H., König, S., and Weinmann, W. (2013). Rapid and simple LC-MS/MS screening of 64 novel psychoactive substances using dried blood spots. *Drug Test Anal*, 6(4), 367-375.
- [21] Antelo-Domínguez, A., Cocho, J.A., Taberner, M.J., Bermejo, A.M., Bermejo-Barrera, P., and Moreda-Piñero, A. (2013). Simultaneous determination of cocaine and opiates in dried blood spots by electrospray ionization tandem mass spectrometry. *Talanta*, 117, 235-241.
- [22] Jantos, R., Veldstra, J.L., Mattern, R., Brookhuis, K.A., and Skopp, G. (2011). Analysis of 3,4-methylenedioxymethamphetamine: whole blood versus dried blood spots. *J Anal Toxicol*, 35(5), 269-273.
- [23] Clavijo, C.F., Hoffman, K.L., Thomas, J.J., Carvalho, B., Chu, L.F., Driver, D.R., Hammer, G.B., Christians, U., and Galinkin, J.L. (2011). A sensitive assay for the quantification of morphine and its active metabolites in human plasma and dried blood spots using high performance liquid chromatography-tandem mass spectrometry. *Anal Bioanal Chem*, 400(3), 715-728.
- [24] Mommers, J., Mengerink, Y., Ritzen, E., Weusten, J., Van der Heijden, J., and Van der Wal, S. (2013). Quantitative analysis of morphine in dried blood spots by using morphine-d3 pre-impregnated dried blood spot cards. *Anal Chim Acta*, 774, 26-32.
- [25] Saussereau, E., Lacroix, C., Gaulier, J.M., and Gouille, J.P. (2012). On-line liquid chromatography/tandem mass spectrometry simultaneous determination of opiates, cocaine and amphetamines in dried blood spots. *J Chromatogr B Analyt Technol Biomed Life Sci*, 885(886), 1-7.
- [26] Sosnoff, C.S., Ann, Q., Bernert, J.T., Powell, M.K., Miller, B.B., Henderson, L.O., Hannon, W.H., Fernhoff, P., and Sampson, E.J. (1996). Analysis of benzoylecgonine in dried blood spots

by liquid chromatography– atmospheric pressure chemical ionization tandem mass spectrometry. *J Anal Toxicol*, 20(3), 179–184.

- [27] Thomas, A., Geyer, H., Schänzer, W., Crone, C., Kellmann, M., Moehring, T., and Thevis, M. (2012). Sensitive determination of prohibited drugs in dried blood spots (DBS) for doping controls by means of a benchtop quadrupole/Orbitrap mass spectrometer. *Anal Bioanal Chem*, 403(5), 1279-1289.
- [28] Saracino, M.A., Marcheselli, C., Somaini, L., Pieri, M.C., Gerra, G., Ferranti, A., and Raggi, M.A. (2012). A novel test using dried blood spots for the chromatographic assay of methadone. *Anal Bioanal Chem*, 404(2), 503-511.
- [29] Moretti, M., Visonà, S.D., Freni, F., Tomaciello, I., Vignali, C., Groppi, A., Tajana, L., Osculati, A.M.M., and Morini, L. (2018). A liquid chromatography-tandem mass spectrometry method for the determination of cocaine and metabolites in blood and in dried blood spots collected from postmortem samples and evaluation of the stability over a 3-month period. *Drug Test Anal*, 10, 1430–1437.
- [30] Moretti, M., Manfredi, A., Freni, F., Previderé, C., Osculati, A.M.M., Grignani, P., Tronconi, L., Carelli, C., Vignali, C., and Morini, L. (2021). A comparison between two different dried blood substrates in determination of psychoactive substances in postmortem samples. *Forensic Toxicol*, 39, 385–393.
- [31] Kacargil, C.U., Daglioglu, N., and Goren, I.E. (2020). Determination of illicit drugs in dried blood spots by lc–ms/ms method: validation and application to real samples. *Chromatographia*, 83(7), 885-892.
- [32] Yeter, O., and Erol Öztürk, Y. (2019). Detection and quantification of 5F-ADB and its methyl ester hydrolysis metabolite in fatal intoxication cases by liquid chromatography-high resolution mass spectrometry. *Forensic Sci Int*, 302, 109866.
- [33] Scientific Working Group for Forensic Toxicology. (2013). Standard practices for method validation in forensic toxicology. *J Anal Toxicol*, 37(7), 452-74.
- [34] Timmerman, P., White, S., Globig, S., Lüdtke, S., Bruner, L., and Smeraglia, J. (2011). EBF recommendation on the validation of bioanalytical methods for dried blood spots. *Bioanalysis*, 3(14), 1567-1575.
- [35] Matuszewski, B.K., and Constanzer, M.L. (2003). Strategies for the assessment of matrix effect in quantitative bioanalytical methods based on HPLC – MS/MS. *Anal Chem*, 75, 3019–3030.
- [36] Bland, J.M., and Altman, D.G. (1986). Statistical methods for assessing agreement between two methods of clinical measurement. *Lancet*, 1(8476), 307-310.

- [37] Stockl, D., Dewitte, K., and Thienpont, L. (1998). Validity of linear regression in method comparison studies: is it limited by the statistical model or the quality of the analytical input data? *Clin Chem*, 44(11), 2340–2346.
- [38] Dewitte, K., Fierens, C., Stockl, D., and Thienpont, L. (2002). Application of the Bland-Altman plot for interpretation of method- comparison studies: a critical investigation of its practice. *Clin Chem*, 48(5), 799–801.



RESEARCH ARTICLE

ANTIMICROBIAL ACTIVITY OF PROTON SALTS OF 3-(SULFAMOYLPHENYL CARBAMOYL)ACRYLIC ACID DERIVATIVES WITH AMINOPYRIDINE DERIVATIVES

Halil İlkimen¹, Cengiz YENİKAYA², Aysel GÜLBANDILAR³

¹Kütahya Dumlupınar University, Faculty of Art and Sciences, Department of Chemistry, Kutahya, Türkiye, halil.ilkimen@dpu.edu.tr, ORCID: 0000-0003-1747-159X,

²Kütahya Dumlupınar University, Faculty of Art and Sciences, Department of Chemistry, Kutahya, Türkiye, cengiz.yenikaya@dpu.edu.tr, ORCID: 0000-0002-5867-9146

³Eskişehir Osmangazi University, Department of Food Engineering, Faculty of Agricultural Engineering, Eskişehir, Türkiye, aysel.gulbandilar@ogu.edu.tr, ORCID: 0000-0001-9075-9923

Receive Date: 08.06.2023

Accepted Date: 19.07.2023

ABSTRACT

Ten proton transfer salts (**9-18**) were synthesized from the reaction of 2-aminopyridine (**1**), 2-amino-3/4/5/6-methylpyridines (**2-5**) and 3-aminomethylpyridine (**6**) with (*E*)-3-(3/4-sulfamoylphenylcarbamoyl)acrylic acid (**7** and **8**), respectively. *Bacillus subtilis* (wild culture), *Candida albicans* (ATCC 14053) (yeast), *Enterococcus faecalis* (ATCC 29212) (Gram positive), *Escherichia coli* (ATCC 25922), *Listeria monocytogenes* (ATCC 7644), *Pseudomonas aeruginosa* (ATCC 27853), *Staphylococcus aureus* (NRRL B-767) (Gram negative) bacterial microorganisms have been tested against the antimicrobial evaluation of compounds (**1-18**). Vancomycin, Cefepime, Levofloxacin and the antifungal substance Fluconazole were used as antibacterial reference compounds for comparing the MIC values of **1-18**. Compounds **1**, **3-6**, **8-13**, **15**, **17** and **18** for *E. faecalis*, **5** for *B. subtilis*, **1**, **3-12**, **15**, **17** and **18** for *S. aureus*, **3**, **9**, **10**, **13**, **15** and **17** for *L. monocytogenes*, **16** for *E. Coli* and **4** for *P. aeruginosa* the best effect are observed. Proton transfer salts {**9**, **14**, **15** and **17**} were showed higher effect than Fluconazole while other compounds (except compounds **2** and **4**) had similar effects with Fluconazole. The compounds **2** and **4** showed less activity than Fluconazole.

Keywords: 2-Aminopyridine derivatives, 3/4-(Sulfamoylphenylcarbamoyl) acrylic acid, Proton transfer salt, Antibacterial and antifungal activity.

1. INTRODUCTION

Proton transfer is one of the most fundamental processes that plays an important role in many chemical and biochemical reactions [1-7]. Proton transfer reactions are unique among numerous chemical processes in which a proton is transferred from one binding site to another, either intermolecular or intramolecular. These only involve the transport of a nucleus without any auxiliary

electrons. Such reactions can occur without serious disorder in the bonding electrons and without introducing repulsive forces between the non-bonding electrons [8]. Recently, research on proton transfer has been mainly focused on crystal engineering [9,10], catalytic reactions [11,12], organic ferroelectrics [13,14], energetic materials [15-17], nonlinear optical materials [18,19], hydrogen storage [20-23] and pharmaceutical industry [24,25] focused on other related areas. Aromatic/aliphatic carboxylic acids and aromatic/aliphatic bases are generally used in the synthesis of proton transfer salts. In these reactions, the proton of the acid is transferred by the base to form compounds with (+) and (-) charges. These compounds are water-soluble compounds [26].

The biological activity of acrylic acid derivatives which are the acid compound of this study are known such as anti-inflammatory [27], dielectric properties [28], antimicrobial activity [28,29], virus type 1 (HIV-1) [30] and antiglaucoma [31,32]. In the literature, 2-amino-3/4/5/6-methylpyridines [34], 2-aminopyridine [33], 2-aminobenzothiazole and 2-amino-6-ethoxybenzothiazole [35] proton transfer salts with (*E*)-3-(3-sulfamoylphenylcarbamoyl)acrylic acid (**7**) while 1*H*-benzimidazole, 2-aminopyridine [32], 2-amino-3/4/5/6-methylpyridine, 3-aminopyridine [36] proton transfer salts are synthesized with (*E*)-3-(4-sulfamoylphenylcarbamoyl)acrylic acid (**8**) have been synthesized. The antimicrobial properties of metal complexes of **8** are investigated [37].

2-Aminopyridine derivatives which are the basic components of this study, have known biological activities such as antiviral, antiparasitic, antibacterial, anticonvulsant, antihistamine, antifungal, anti-inflammatory, antidiabetic, analgesic and anti-Alzheimer's. In the literature, abundant salts of 2-aminopyridine derivatives with other compounds continue to be synthesized.

In this study, salts **9-13** of between **7** and **1-5**, and **14-18** of between **8** and **1-6** were synthesized by methods found in the literature [32-36]. The antimicrobial activities of the compounds **1-6** and **8** [37] and **9-18** were tested against *C. albicans* (yeast) and *E. coli*, *L. monocytogenes*, *B. subtilis*, *P. aeruginosa*, *E. faecalis*, and *S. aureus* bacterial microorganisms. The antimicrobial test results of all compound substances (**1-18**) were compared with the control compounds.

2. EXPERIMENTAL

2. 1. Synthesis of 9-18.

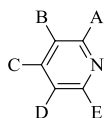
Proton transfer salts **9-18**, which we synthesized and characterized in our previous studies [32-36]. The structures of free ligands (**1-8**) and proton transfer salts (**9-18**) are given in Figure 1.

The ethanol solution of 10 mmol **7** (50 mL) was added to 10 mmol **1** for **9**, **2** for **10**, **3** for **11**, **4** for **12** and **5** for **13** (50 mL). The ethanol solution of 10 mmol **8** (50 mL) was added to 10 mmol **1** for **14**, **3** for **15**, **4** for **16**, **5** for **17** and **6** for **18** (50 mL). The white solids resulting from the reaction mixture were filtered and dried (m.p 207 °C for **7**, d.p 189 °C for **9**, d.p 190 °C for **10**, d.p 182 °C for **11**, d.p 200 °C for **12**, d.p 180 °C for **13**, m.p 209 °C for **8**, d.p 191 °C for **14**, d.p 210 °C for **15**, d.p 180 °C for **16**, d.p 190 °C for **17** and d.p 145 °C for **18**).

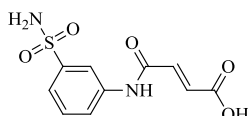
2. 2. Microbiological Test

In this study, Eskişehir Osmangazi University, Faculty of Medicine provided the *E. faecalis* and *E. coli* bacteria utilized and the biology department of Eskişehir Technical University provided the *C. albicans*, *B. subtilis*, *L. monocytogenes*, *S. aureus* and *P. aeruginosa* microorganisms. All compounds (1–18) had their antibacterial activity assessed using a microdilution susceptibility test. In DMSO solution, the sample solutions had previously been separated.

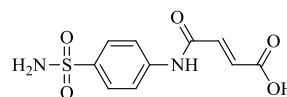
The compounds' antibacterial investigation was conducted using a microbroth dilution susceptibility test [38]. The samples' stock solutions in DMSO were created. In 4 mL of DMSO solution, antibiotics (8 mg) and synthesized substances (8 mg) were dissolved. Using McFarland No. 0.5 standard solution, overnight-grown bacterial and yeast suspensions in double-strength Mueller-Hinton broth were standardized to 10^8 Colony Forming Units/mL. The wells then received 100 μ L of each microbe suspension. As a negative control, the last well chain without a microorganism was employed. The medium and sterile distilled water acted as a positive growth control. The first well without turbidity was chosen as the MIC following an 18–24 h incubation period at 37 °C [39,40].



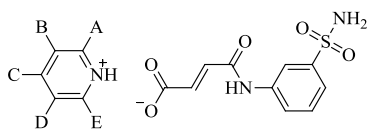
- A = NH₂, B = H, C = H, D = H, E = H (1)
 A = NH₂, B = CH₃, C = H, D = H, E = H (2)
 A = NH₂, B = H, C = CH₃, D = H, E = H (3)
 A = NH₂, B = H, C = H, D = CH₃, E = H (4)
 A = NH₂, B = H, C = H, D = H, E = CH₃ (5)
 A = H, B = CH₂NH₂, C = H, D = H, E = H (6)



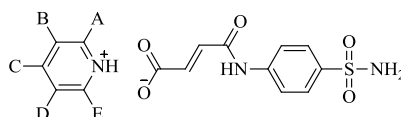
7



8



- A = NH₂, B = H, C = H, D = H, E = H (9)
 A = NH₂, B = CH₃, C = H, D = H, E = H (10)
 A = NH₂, B = H, C = CH₃, D = H, E = H (11)
 A = NH₂, B = H, C = H, D = CH₃, E = H (12)
 A = NH₂, B = H, C = H, D = H, E = CH₃ (13)



- A = NH₂, B = H, C = H, D = H, E = H (14)
 A = NH₂, B = H, C = CH₃, D = H, E = H (15)
 A = NH₂, B = H, C = H, D = CH₃, E = H (16)
 A = NH₂, B = H, C = H, D = H, E = CH₃ (17)
 A = H, B = CH₂NH₂, C = H, D = H, E = H (18)

Figure 1. Structures of 1-18.

3. RESULTS AND DISCUSSION

In this work, antimicrobial activity of **1-18** were tested by microdilution method. MIC values of **1-18** are given in Table 1. According to MIC values it was observed that the all compounds have antibacterial and antifungal activity properties.

It was determined that compound **5** (7.80 µg/mL) had the highest activity against *B. subtilis* bacteria. All compounds found to have higher efficacy against this bacterium than the Vancomycin control compound. The compounds **5, 8, 9, 12** and **17** were more effective than Levofloxacin, and Cefepime control compounds while the compounds **1-4, 6, 7, 10, 11, 13-15** and **18** were showed similar effects with the compounds. The compound **16** showed less activity than Levofloxacin, and Cefepime.

Table 1. Antimicrobial activity values of compounds (µg/mL).

Compound	<i>S. aureus</i>	<i>E. faecalis</i>	<i>E. coli</i>	<i>B. subtilis</i>	<i>P. aeruginosa</i>	<i>L. monocytogenes</i>	<i>C. albicans</i>
Vancomycin	31.25	62.50	31.25	250	62.50	125.00	-
Levofloxacin	31.25	62.50	31.25	62.50	31.25	31.25	-
Cefepime	62.50	31.25	62.50	62.50	31.25	31.25	-
Fluconazole	-	-	-	-	-	-	62.50
1	62.50	62.50	15.60	62.50	62.50	62.50	62.50
2	125.00	125.00	125.00	62.50	62.50	62.50	125.00
3	62.50	62.50	31.25	62.50	62.50	31.25	62.50
4	62.50	62.50	31.25	62.50	15.60	62.50	125.00
5	62.50	62.50	62.50	7.80	62.50	62.50	62.50
6	62.50	62.50	62.50	62.50	125.00	62.50	62.50
7	62.50	125.00	62.50	62.50	62.50	62.50	62.50
8	62.50	62.50	31.25	31.25	62.50	62.50	62.50
9	62.50	62.50	62.50	31.25	31.25	31.25	15.60
10	62.50	62.50	125.00	62.50	62.50	31.25	62.50
11	62.50	62.50	31.25	62.50	62.50	62.50	62.50
12	62.50	62.50	31.25	31.25	62.50	62.50	62.50
13	125.00	62.50	62.50	62.50	62.50	31.25	62.50
14*	125.00	125.00	31.25	62.50	125.00	62.50	31.25
15	62.50	62.50	31.25	62.50	62.50	31.25	31.25
16	125.00	125.00	7.80	125.00	62.50	62.50	62.50
17	62.50	62.50	31.25	31.25	62.50	31.25	31.25
18	62.50	62.50	62.50	62.50	62.50	62.50	62.50

*[37]

Against *E. faecalis* bacteria, all compounds (except compounds **2, 7, 14** and **16**) were determined to have similar effects (62.50 µg/mL) with Vancomycin and Levofloxacin. The compounds **2, 7, 14** and

16 showed less activity (125.00 µg/mL) than Vancomycin and Levofloxacin. The all showed less activity (62.50-125.00 µg/mL) than Cefepime.

Against *S. aureus* bacteria, the compounds **1, 3-12, 15, 17** and **18** were determined to have similar effects (62.50 µg/mL) with Cefepime while the compounds **2, 14** and **16** showed less activity (125.00) than Cefepime. The all compounds showed less activity (62.50-125.00 µg/mL) than Vancomycin and Levofloxacin (31.25 µg/mL).

Against *E. coli* bacteria, compounds **1** (15.60 µg/mL) and **16** (7.80 µg/mL) had higher activity than all control compounds. Compounds **3, 4, 8, 11, 12, 14, 15** and **17** for Vancomycin and Levofloxacin and **5, 6, 7, 9, 13** and **18** for Cefepime have similar effects with control compounds.

Against *L. monocytogenes*, the compounds **3, 9, 10, 13, 15** and **17** showed the same effect as Levofloxacin and Cefepime, and all other substances were found to be more effective against this bacterium than the Vancomycin control compound.

Against *P. aeruginosa* bacteria, the compound **4** showed a higher effect (15.60 µg/mL) than the control compounds. The compounds **1-3, 5, 7, 8, 10-13** and **15-18** were determined to have similar effects (62.50 µg/mL) with Vancomycin while the compound **9** showed similar activity (31.25 µg/mL) than Levofloxacin and Cefepime. The compounds **6** and **14** showed less activity (125.00 µg/mL) than all the control compounds.

Against *C. albicans* yeast species, the compounds **9** (15.60 µg/mL), **14, 15** and **17** (31.25 µg/mL) showed a higher effect than Fluconazole (62.50 µg/mL) while other compounds (except compounds **2** and **4**) had similar effects (62.50 µg/mL) with Fluconazole. The compounds **2** and **4** showed less activity (125.00 µg/mL) than Fluconazole.

In the antimicrobial activity studies of compounds containing sulphanilamide and maleic acid, only studies conducted by our group were found in the literature as salt [37]. In addition, the activities of some monomeric or polymeric structures were examined and it was observed that they showed activity against bacteria and yeasts [28,29]. When the antimicrobial activities of the synthesized salts were compared with similar compounds found in the literature, it was observed that they had similar activity [28,29,37].

4. CONCLUSIONS

All compounds showed antimicrobial activity against *E. coli*, *B. subtilis*, *P. aeruginosa*, *S. aureus*, *E. faecalis*, *L. monocytogenes* and *C. albicans* microorganisms. In general, the synthesized compounds showed similar properties with the control compounds against bacteria (*P. aeruginosa*, *S. aureus*, *E. coli*, *L. monocytogenes*, *B. subtilis* and *E. faecalis*). Compounds **1, 3-6, 8-13, 15, 17** and **18** for *E. faecalis*, **5** for *B. subtilis*, **1, 3-12, 15, 17** and **18** for *S. aureus*, **3, 9, 10, 13, 15** and **17** for *L. monocytogenes*, **16** for *E. Coli* and **4** for *P. aeruginosa* the best effect are observed. Proton transfer salts {**9, 14, 15** and **17**} were showed higher effect than Fluconazole while other compounds (except compounds **2** and **4**) had similar effects with Fluconazole. The compounds **2** and **4** showed less activity than Fluconazole.

ACKNOWLEDGEMENT

The Kütahya Dumlupnar University Research Foundation provided funding for this investigation (Grant Nos. 2013/36 and 2019/12).

REFERENCES

- [1] Root, M.J. and MacKinnon, R. (1994). Two identical noninteracting sites in an ion channel revealed by proton transfer. *Science*, 265, 1852-1856.
- [2] Armentano, D., De Munno, G., Mastropietro, T. F., Julve, M. and Lloret, F. (2005). Intermolecular proton transfer in solid phase, a rare example of crystal-to-crystal transformation from hydroxo-to oxo-bridged iron (III) molecule-based magnet. *Journal of the American Chemical Society*, 127, 10778-10779.
- [3] Chen, K. (2000). Atomically defined mechanism for proton transfer to a buried redox centre in a protein. *Nature*, 405, 814-817.
- [4] Chen, K. Y., Lai, C. H., Hsu, C. C., Ho, M. L., Lee, G. H. and Chou, P. T. (2007). Ortho green fluorescence protein synthetic chromophore; excited-state intramolecular proton transfer via a seven-membered-ring hydrogen-bonding system. *Journal of the American Chemical Society*, 129, 4534-4535.
- [5] Dellago, C. and Hummer, G. (2006). Kinetics and mechanism of proton transport across membrane nanopores. *Physical Review Letters*, 97, 245901.
- [6] Luecke, H., Richter, H.T. and Lanyi, J. K. (1998). Proton transfer pathways in bacteriorhodopsin at 2.3 angstrom resolution. *Science*, 280, 1934-1937.
- [7] Heberle, J., Riesle, J., Thiedemann, G., Oesterhelt, D. and Dencher, N. A. (1994). Proton migration along the membrane surface and retarded surface to bulk transfer. *Nature*, 370, 379-382.
- [8] Gupta, S. K. S. (2016). Proton transfer reactions in apolar aprotic solvents. *Journal of Physical Organic Chemistry*, 29, 251-264.
- [9] Park, S., Kwon, O. H., Kim, S., Park, S., Choi, M. G., Cha, M., Park, S. Y. and Jang, D. J. (2005). Imidazole-based excited-state intramolecular proton-transfer materials, synthesis and amplified spontaneous emission from a large single crystal. *Journal of the American Chemical Society*, 127, 10070-10074.
- [10] Moghimi, A., Alizadeh, R., Shokrollahi, A., Aghabozorg, H., Shamsipur, M. and Shockravi, A. (2005). First anionic 1,10-phenanthroline-2,9-dicarboxylate containing metal complex obtained

from a novel 1:1 proton-transfer compound, Synthesis, characterization, crystal structure, and solution studies. *Inorganic Chemistry*, 42, 1616-1624.

- [11] Nichols, D. A., Hargis, J. C., Sanishvili, R., Jaishankar, P., Defrees, K., Smith, E. W., Wang, K. K., Prati, F., Renslo, A. R., Woodcock, H. L. and Chen, Y. (2015). Ligand-induced proton transfer and low-barrier hydrogen bond revealed by x-ray crystallography. *Journal of the American Chemical Society*, 137, 8086-8095.
- [12] Gerlits, O., Wymore, T., Das, A., Shen, C. H., Parks, J. M., Smith, J. C., Weiss, K. L., Keen, D. A., Blakeley, M. P., Louis, J. M., Langan, P., Weber, I. T. and Kovalevsky, A. (2016). Long-range electrostatics-induced two-proton transfer captured by neutron crystallography in an enzymecatalytic site. *Angewandte Chemie*, 55, 4924-4927.
- [13] Horiuchi, S. and Tokura, Y. (2008). Organic ferroelectrics. *Nature Materials*, 7, 357-366.
- [14] Horiuchi, S., Kumai, R. and Tokura, Y. (2007). A supramolecular ferroelectric realized by collective proton transfer. *Angewandte Chemie*, 46, 3497-3501.
- [15] Bolton, O. and Matzger, A. J. (2011). Improved stability and smart-material functionality realized in an energetic cocrystal. *Angewandte Chemie*, 50, 8960-8963.
- [16] Yoon, M., Suh, K., Natarajan, S. and Kim, K. (2013). Proton conduction in metal-organic frameworks and related modularly built porous solids. *Angewandte Chemie*, 52, 2688-2700.
- [17] Shimizu, G. K., Taylor, J. M. and Kim, S. (2013). Proton conduction with metal-organic frameworks. *Science*, 341, 354-355.
- [18] Jayanalina, T., Rajarajan, G., Boopathi, K. and Sreevani, K. (2015). Synthesis, growth, structural, optical and thermal properties of a new organic nonlinear optical crystal, 2-amino-5-chloropyridinium-L-tartrate. *Journal of Crystal Growth*, 426, 9-14.
- [19] Asselberghs, I., Zhao, Y., Clays, K., Persoons, A., Comito, A. and Rubin, Y. (2002). Reversible switching of molecular second-order nonlinear optical polarizability through proton-transfer. *Chemical Physics Letters*, 364, 279-283.
- [20] Adamson, A., Guillemin, J.C. and Burk, P. (2015). Proton transfer reactions of hydrazineboranes. *Journal of Physical Organic Chemistry*, 28, 244-249.
- [21] Cochlin, D. (2014). Graphene's promise for proton transfer in fuel cell membranes. *Fuel Cells Bulletin*, 2014, 12-12.
- [22] Lototsky, M. V., Tolj, I., Davids, M. W., Klochko, Y. V., Parsons, A., Swanepoel, D., Ehlers, R., Louw, G., Westhuizen, B., Smith, F., Pollet, B.G., Sita, C. and Linkov, V. (2016). Metal hydride hydrogen storage and supply systems for electric forklift with low-temperature proton

- exchange membrane fuel cell power module. *International Journal of Hydrogen Energy*, 41, 13831-13842.
- [23] Spry, D.B. and Fayer, M. D. (2009). Proton transfer and proton concentrations in protonated Nafion fuel cell membranes. *Journal of Physical Chemistry B*, 113, 10210-10221.
- [24] Steed, J. W. (2013). The role of co-crystals in pharmaceutical design. *Trends in Pharmacological Sciences*, 34, 185-193.
- [25] Bica, K., Shamshina, J., Hough, W. L., MacFarlane, D. R and Rogers, R. D. (2011). Liquid forms of pharmaceutical co-crystals, exploring the boundaries of salt formation. *Chemical Communications*, 47, 2267-2269.
- [26] Aghabozorg, H., Sadrkhanlou, E., Shokrollahi, A., Ghaedi, M. and Shamsipur, M. (2009). Synthesis, characterization, crystal structures, and solution studies of Ni(II), Cu(II) and Zn(II) complexes obtained from pyridine-2,6-dicarboxylic acid and 2,9-dimethyl-1,10-phenanthroline. *Journal of the Iranian Chemical Society*, 6(1), 55-70.
- [27] Jan, M. S., Ahmad, S., Hussain, F., Ahmad, A., Mahmood, F., Rashid, U., Abid, O.R., Ullah, F., Ayaz, M. and Sadiq, A. (2020). Design, synthesis, in-vitro, in-vivo and in-silico studies of pyrrolidine-2,5-dione derivatives as multitarget anti-inflammatory agents. *European Journal of Medicinal Chemistry*, 186, 111863.
- [28] Bapna, S., Hiran, B. L. and Jain, S. (2015). Antimicrobial evaluation of maleimide monomers, homopolymers and copolymers containing azo, sulfonamide and thiazole groups. *Journal of Advances in Chemistry*, 11(1), 3404-3415.
- [29] Erol, I. (2022). Synthesis and characterization of novel sulfonamide functionalized maleimide polymers, Conventional kinetic analysis, antimicrobial activity and dielectric properties. *Journal of Molecular Structure*, 1255, 132362.
- [30] Nicklaus, M. C., Neamati, N., Hong, H., Mazumder, A., Sunder, S., Chen, J., Milne, G. W. A. and Pommier, Y. (1997). HIV-1 integrase pharmacophore, discovery of inhibitors through three-dimensional database searching. *Journal of Medicinal Chemistry*, 40(6), 920-929.
- [31] Oktay, K., Kose, L. P., Sendil, K., Gultekin, M. S., Gulcin, I. and Supuran, C. T. (2016). The synthesis of (Z)-4-oxo-4-(arylamino)but-2-enoic acids derivatives and determination of their inhibition properties against human carbonic anhydrase I and II isoenzymes. *Journal of Enzyme Inhibition and Medicinal Chemistry*, 31(6), 939-945.
- [32] Yenikaya, C., Ilkimen, H., Demirel, M. M., Ceyhan, B., Bulbul, M. and Tunca, E. (2016). Preparation of two maleic acid sulfonamide salts and their copper(II) complexes and antiglaucoma activity studies. *Journal of the Brazilian Chemical Society*, 27(10), 1706-1714.

- [33] İlkimen, H., Yenikaya, C., İmdat, G., Tunca, E. and Bülbül, M. (2017). Synthesis and characterization of proton transfer salts between 2-aminopyridine derivatives and maleamic acid derivate containing sulfonamide and their Cu(II) complexes, and investigation of their effects on human erythrocyte carbonic anhydrase isoenzymes. *Suleyman Demirel University Journal of Natural and Applied Sciences*, 21(2), 480-494.
- [34] İlkimen, H., Yenikaya, C., Bülbül, M. and İmdat, G. (2017). Synthesis and characterization of proton transfer salt between maleamicacid derivative including sulfonamide moiety and 2-aminopyridine and preparation of their Co(II) and Cu(II) complexes and investigation of inhibition properties on carbonic anhydrase isoenzymes. *Celal Bayar University Journal of Science*, 13(1), 211-225.
- [35] İlkimen, H. and Yenikaya, C. (2022). Synthesis and characterization of proton transfer salts of 2-aminobenzothiazole derivatives. *Bayburt University Journal of Science*, 5(1), 52-68.
- [36] İlkimen, H. and Yenikaya, C. (2022). Synthesis and characterization of proton salts of aminopyridine derivatives and (*E*)-3-(4-sulfamoylphenylcarbamoyl)acrylic acid. *Sinop University Journal of Natural Sciences*, 7(1), 57-50.
- [37] İlkimen, H., Yenikaya, C. and Gülbandılar A. (2023). Antimicrobial activity of (*E*)-3-(4-sulfamoylphenylcarbamoyl)acrylic acid derivatives. *Journal of Scientific Reports-A*, 52, 365-375.
- [38] Koneman, E. W., Allen, S. D. and Winn, W. C. (1997). *Colour atlas and textbook of diagnostic microbiology* (Lippincott Raven Pub, Philadelphia).
- [39] Kaplancıklı, Z. A., Zitouni, G. T., Ozdemir, A., Revial, G. and Güven, K. (2007). Synthesis and antimicrobial activity of some thiazolyl-pyrazoline derivatives. *Phosphorus, Sulfur, and Silicon and the Related Elements*, 182, 749-764.
- [40] Seferoglu, Z., Ertan, N., Yılmaz, E. and Uraz, G. (2008). Synthesis, spectral characterisation and antimicrobial activity of new disazo dyes derived from heterocyclic coupling components. *Coloration Technology*, 124, 27-35.



RESEARCH ARTICLE

**THE FIRST LIGHT CURVE ANALYSIS OF V1010 CAS USING GROUND-BASED AND
TESS DATA**

Neslihan ALAN^{1*}

¹Istanbul University, Faculty of Science, Department of Astronomy and Space Sciences, Istanbul, neslihan.alan@gmail.com,
ORCID: 0000-0001-9809-7493

Receive Date: 21.08.2023

Accepted Date: 18.09.2023

ABSTRACT

Eclipsing binary systems play a pivotal role in quantifying the absolute parameters of stars, such as the mass (M), the radius (R), and the luminosity (L), offering invaluable laboratories for astronomical research and enhancing our comprehension of stellar evolution as well as galaxy dynamics. These systems provide a unique opportunity to precisely ascertain these crucial parameters. The simultaneous analyses of high-quality space observations, combined with ground-based photometric data, have allowed more sensitive detection of fundamental stellar parameters by multicolour photometry. In the paper, the absolute parameters of the component stars for the V1010 Cas binary system were sensitively obtained by a simultaneous analysis of the Transiting Exoplanet Survey Satellite (*TESS*) light curve, and new CCD observations in *BVRI* filters obtained with 60 cm Robotic telescope (T60) at the TUBITAK National Observatory. Thereby, the radii and masses of the primary and secondary components were determined as $R_1 = 2.46 \pm 0.01 R_{\odot}$, $R_2 = 1.78 \pm 0.03 R_{\odot}$, and $M_1 = 2.06 \pm 0.05 M_{\odot}$, $M_2 = 1.83 \pm 0.04 M_{\odot}$, respectively. The distance of V1010 Cas was also calculated as 444 ± 42 pc. Furthermore, the system's overall age was approximated at about 570 ± 60 Myr.

Keywords: *Eclipsing binary stars, photometry, absolute parameters, V1010 Cas*

1. INTRODUCTION

Eclipsing binary stars are very significant in astrophysics, as they are the only way to determine fundamental stellar parameters from direct observations. These parameters can be obtained more precisely, especially by utilizing high-resolution photometric data provided by space telescopes like *TESS* [1]. Increasing the sensitivity of the absolute parameters of stars allows theoretical models to be tested and more realistic models to be built by comparing evolutionary models with observational findings. Detached eclipsing binary systems are very useful for this aim due to the relatively little interaction between the components. With fundamental stellar parameters calculated from observations of detached eclipsing binaries, evolutionary models for single stars can be investigated, and the agreement of observations to the theoretical evolution models can be tested. In addition, it is also important in this context to bring the fundamental stellar parameters to the literature with light

curve analyses of detached eclipsing binaries, which have not been investigated in detail before. For this reason, the detached eclipsing binary system V1010 Cas with only times of minima reported and no light curve analysis performed up to now, was selected in this study.

V1010 Cas is categorized as an Algol-type eclipsing binary system [2]. A detailed study of the system has not been performed until now. Thus, the absolute parameters of the V1010 Cas components remained elusive. The light curve analysis of the system is essential to reveal its fundamental stellar parameters. In this work, the first light curve solution of V1010 Cas was performed utilizing *TESS* and T60 data, and the fundamental stellar parameters of the system were derived. General information about V1010 Cas is listed in Table 1.

Table 1. Catalogue information of V1010 Cas.

RA *	00 ^h 57 ^m 56 ^s .98
DEC *	+60° 06' 14".98
Type *	EA
Spectral Type [2]	A2
Magnitude (V) *	9 ^m .1
Period (day) *	2.398

(*) represents the data taken from SIMBAD (<https://simbad.unistra.fr/simbad>)

The paper presenting the findings of the first light curve analysis of V1010 Cas is organized as below. Observational data and a description of the calculation of the new light elements are presented in Section 2. Simultaneous light curve analysis of the *TESS* and ground-based photometric data are explained in Section 3. Findings of the photometric analysis and determination of the astrophysical parameters of the V1010 Cas are introduced in Sec. 4. At the end, in Sec. 5, the conclusions and discussion of the research are summarized.

2. PHOTOMETRIC DATA

New CCD multicolour observations of V1010 Cas were made at the TUBITAK National Observatory (TUG) over 152 nights between July 2018 and October 2019. A 60 cm RC Robotic (T60) telescope is controlled by the OCAAS open source software, officially called TALON (see [3]), equipped with FLI ProLine 3041-UV CCD until 23 July 2019, and after this date, Andor iKon-L 936 BEX2-DD model camera, was used. The FLI ProLine 3041-UV CCD gives an observable field of view (FoV) of 17'.4 and image scales of 0".51 per pixel, while the Andor iKon-L 936 BEX2-DD camera provides image scales of 0".456 per pixel and an observable FoV of 15'.6.

Observations were performed by means of Bessell *BVRI* filters (see [4]). For each filter, the exposure time was set to 5 seconds. In order to correct for on-chip pixel-to-pixel inconsistencies, calibration images including sky flats and bias frames were acquired at intervals throughout the observations. TYC 3680-1229-1 was used as the comparison star, while TYC 3680-71-1 was utilized as the check

star. In addition, data from the *TESS* were also used in the light curve solution. With an observing time of 27.4 days per sector, *TESS* is able to observe the majority of the entire sky in sectors. The wavelength range of *TESS* observations is 600-1000 nm [1]. Photometric *TESS* data of V1010 Cas included in the light curve analyses were acquired between October 8th and 2nd November 2019 with an exposure time of 120 seconds. *TESS* data of V1010 Cas were retrieved from the Mikulski Archive for Space Telescopes (MAST) database. For the analysis, light curves obtained with Pre-search Data Conditioning Simple Aperture Photometry [1] were selected. Photometric data had an average error of approximately 0.1% (~ 9 mmag).

Reduction of the data for the T60 observations includes several steps. First, bias and dark frames were removed from the science frames, followed by a flat-fielding correction. Subsequently, these CCD images that had undergone reduction were employed to calculate the target stars' differential magnitudes. The IRAF aperture photometry GUI tool, MYRaf software [5], was used for this specific procedure. No significant light variations were found in the comparison and check stars throughout the observation nights. For the comparison minus check stars magnitudes, the external uncertainties were quantified to be about 30 mmag in *B*, 15 mmag in *V*, 17 mmag in *R*, and 18 mmag in *I* filters. These values were derived based on the standard deviation of differential magnitude variation between the comparison and check stars observed on the same night. The observational data remained unconverted to the standard Bessell *BVRI* system and differential magnitudes were used in light curve analyses.

The minima times were determined based on *TESS* data. The primary times of minima were obtained from the first, middle and last parts, and the secondary minima time was procured middle part of *TESS* observations. Totally, four *TESS* minima times were obtained, and then transformed from *BJD* to *HJD*. The minima times of V1010 Cas in the literature were also obtained from the O-C Gateway (<http://var2.astro.cz/ocgate>). A total of 18 minima times were used for analysis, and an investigation into the system's period changes was conducted. Despite this analysis, no parabolic or cyclical period variations were detected. Consequently, new light elements for V1010 Cas were established by applying a linear fit to all the times of minima. These new light elements are presented by the equation below:

$$HJD(MinI) = 2458767.0492(9) + 2^d.397766 (1) \times E \quad (1)$$

The values given inside the parentheses in the equation represent the errors at the last digit for the light elements.

3. LIGHT CURVE MODELLING

The normalized *BVRI* and *TESS* photometric data were used simultaneously in the light curve solution. On the other side, due to the scattering ground-based data before the simultaneous solution, the *TESS* light curve was first analyzed and the corresponding parameters were obtained. This prevented the scattered ground-based data from contaminating the analysis results. Subsequently, ground-based data was included in the solution to calculate color-dependent flux contributions and to increase the accuracy of the temperature, and a simultaneous solution was performed. To accurately

estimate uncertainties in the adjusted parameters, the solution done via the Wilson-Devinney [6] (W-D) code integrated with Monte Carlo simulation [7, 8]. Within the W-D code, certain parameters were held constant, based on prior research in the field and theoretical models. Meanwhile, others have been adjusted in later iterations. The parameters that were taken as the assumption and held constant are as follows. The unreddened colour index of $(B-V)_0 = 0.088 \pm 0.034$ mag, determined from the *Tycho-2* catalogue [9] using with $B-V=0^m.164 \pm 0.032$ and $E_d(B-V)=0^m.076 \pm 0.002$ according to the [10] calibration for V1010 Cas. The initial temperature of the primary component of the system was held constant at 8574 K in accordance with the $B-V$ colour index using the astrophysical parameters of main-sequence stars [11]. $BVRI$ filter light curves observed with ground-based T60 robotic telescope were solved simultaneously with the *TESS* data. In the analysis, mode 2 for detached binary systems was used, taking into account the character of the light variation. Using the square root law of limb darkening, limb darkening coefficients were obtained from van Hamme's tables [18], considering the temperatures of the V1010 Cas components and filter wavelengths. Due to the absence of *TESS* passband integration within the W-D code, the I -band was adopted in the light curve model as the *TESS* passband is centered at Cousins I -band. The constant coefficients are also selected by considering the I -band. According to [19], the bolometric gravity-darkening exponent of each component was fixed at 1.0 for radiative atmosphere ($T_{\text{eff}} > 7200$ K). Besides, in accordance with [20], the bolometric albedos of the components were held constant at 1.0 for radiative atmospheres. Both components were assumed to undergo synchronous rotation ($F_1=F_2=1$). At a phase of 0.5, the secondary minima of V1010 Cas is situated, and there seems to be an absence of asymmetry in the light curve. Moreover, the durations of ascent and descent are equivalent for both the primary and secondary minima. Therefore, it was assumed ($e = 0$) to be a circular orbit. The remaining parameters, including second component's effective temperature ($T_{\text{eff},2}$), orbital inclination (i), dimension-less surface potential of primary and secondary components ($\Omega_{1,2}$), primary component's fractional luminosity (L_1), phase shift, and mass ratio (q) were considered as adjustable parameters. To assess the potential contribution of a third body (l_3) to the overall light, l_3 was chosen as a free parameter in the analysis. In this way, a significant light contribution was detected in the V1010 Cas and l_3 was taken into account in the final solution. Table 2 lists the parameters derived from the best light curve model. It is depicted in Fig. 1 for a comparative comparison of observed and computed light curves. It is also illustrated the Roche geometry of the system in Fig. 2.

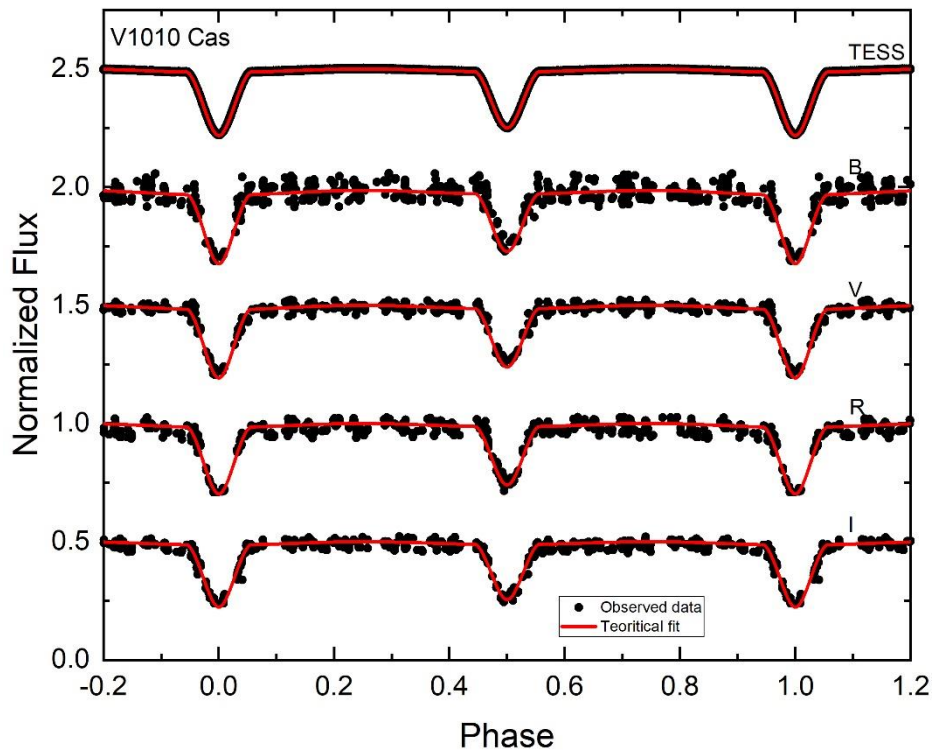


Figure 1. Contrasting the theoretical light curves (red line) and the observational data (black dot) for V1010 Cas.

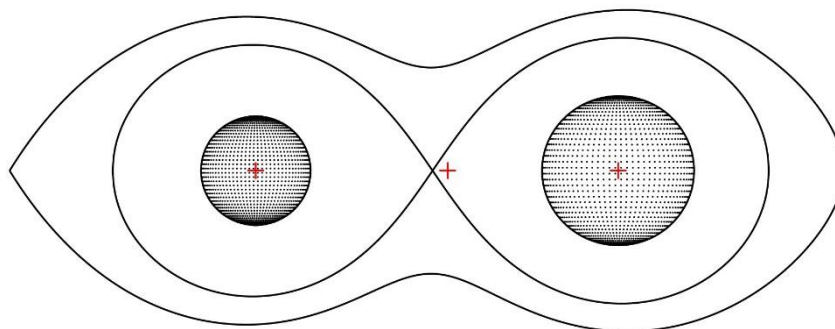


Figure 2. The Roche geometry of V1010 Cas, derived using the parameters of the best light curve model.

Table 2. The findings for V1010 Cas based on the light curve analysis. 1, 2 and 3 subscripts respectively correspond to the primary, secondary, and third components.

Parameter	Value
T_0 (HJD+2400000)	58767.0492
P_{orb} (days)	2.397766
i ($^\circ$)	83.508 ± 0.021
$T_{\text{eff},1}^a$ (K)	8574 ± 150
$T_{\text{eff},2}$ (K)	8196 ± 167
e	0.000
Ω_1	5.737 ± 0.014
Ω_2	6.982 ± 0.050
Phase shift	0.0002 ± 0.0001
q	0.889 ± 0.008
r_1^* (mean)	0.2074 ± 0.0002
r_2^* (mean)	0.1504 ± 0.0005
$L_1 / (L_1+L_2)$ (TESS)	0.683 ± 0.001
$L_1 / (L_1+L_2)$ (B)	0.701 ± 0.004
$L_1 / (L_1+L_2)$ (V)	0.691 ± 0.004
$L_1 / (L_1+L_2)$ (R)	0.682 ± 0.004
$L_1 / (L_1+L_2)$ (I)	0.683 ± 0.004
$L_2 / (L_1+L_2)$ (TESS)	0.317 ± 0.004
$L_2 / (L_1+L_2)$ (B)	0.299 ± 0.007
$L_2 / (L_1+L_2)$ (V)	0.309 ± 0.007
$L_2 / (L_1+L_2)$ (R)	0.318 ± 0.007
$L_2 / (L_1+L_2)$ (I)	0.317 ± 0.007
l_3 (TESS)	0.096 ± 0.001
l_3 (B)	0.037 ± 0.012
l_3 (V)	0.047 ± 0.012
l_3 (R)	0.058 ± 0.012
l_3 (I)	0.108 ± 0.013

^(a) stands for parameters held constant and (*) denotes fractional radii

4. ESTIMATED ABSOLUTE PARAMETERS AND EVOLUTIONARY STATUS

The radial velocity curves for V1010 Cas detached binary system components are currently non-existent, as no high-resolution spectral observations of the system have been performed. Nonetheless, it is possible to roughly estimate the absolute parameters for the component stars using the information determined from the photometric analysis. The absolute parameters are presented in detail in Table 3. Specifically, the primary component of V1010 Cas is treated as a main sequence star, characterized by an assumed $T_{\text{eff}} = 8574$ K, and then the primary component's mass (M_1) is designated as $2.06 M_{\odot}$, a value obtained through the correlation between T_{eff} and mass for main sequence stars, as indicated by [11]. Secondary component mass was calculated from the mass ratio obtained from the

photometric analysis. The fractional radii listed in Table 2, along with the semi-major axis derived using Kepler's third law, enabled the estimation of component radii. Solar values ($T_{\text{eff,Sun}} = 5777$ K, $M_{\text{Bol,Sun}} = 4^{\text{m.74}}$) and bolometric corrections from [11] were used to calculate the component luminosities and bolometric magnitudes. For the primary and secondary components, surface gravity values were determined as $\log g_1 = 3.971 \pm 0.015$ and $\log g_2 = 4.199 \pm 0.019$ in cgs unit, respectively. This finding reveals that each of the components has a different evolutionary status. On the basis of the apparent magnitude of V1010 Cas, light ratio of its components, listed in Table 2, interstellar extinction (see Table 3), and BC values ($\text{BC}_1 = -0.041$ and $\text{BC}_2 = 0.003$ computed via [11]) the distance of V1010 Cas was obtained to be 444 ∓ 42 pc. For the error propagation of the derived parameters, classical methods were applied by considering both the errors due to the assumptions and from the MC simulated light curve analysis in combination.

Table 3. Estimated absolute parameters of V1010 Cas.

Estimated Stellar Parameter	Value
$M_1 (M_{\odot})$	2.06 ± 0.05
$M_2 (M_{\odot})$	1.83 ± 0.04
$R_1 (R_{\odot})$	2.46 ± 0.01
$R_2 (R_{\odot})$	1.78 ± 0.03
$a (R_{\odot})$	11.84 ± 0.04
$\log L_1 (L_{\odot})$	1.47 ± 0.11
$\log L_2 (L_{\odot})$	1.11 ± 0.08
$\log g_1$ (cgs)	3.971 ± 0.015
$\log g_2$ (cgs)	4.199 ± 0.019
$M_{\text{Bol},1}$ (mag)	1.07 ± 0.20
$M_{\text{Bol},2}$ (mag)	1.96 ± 0.49
$M_{\text{V},1}$ (mag)	1.11 ± 0.21
$M_{\text{V},2}$ (mag)	1.96 ± 0.50
$A_{\text{V},d}$ (mag)	0.236 ± 0.006
Distance (pc)	444 ± 42

Obtaining absolute parameters of the system components has provided us with an understanding of the evolutionary status. To delve deeper into the evolutionary context, the MESA Isochrones & Stellar Tracks (MIST) framework, as referenced in several relevant studies [12, 13, 14, 15, 16 and 17] was employed. By plotting the estimated absolute parameters on the Hertzsprung Russell diagram, it was revealed that the best theoretical fit is along the evolutionary track characterized by a metallicity of $Z = 0.014 \pm 0.002$, as shown in Figure 3. According to the isochrones, the most representative age of the system is 570 ± 60 Myr.

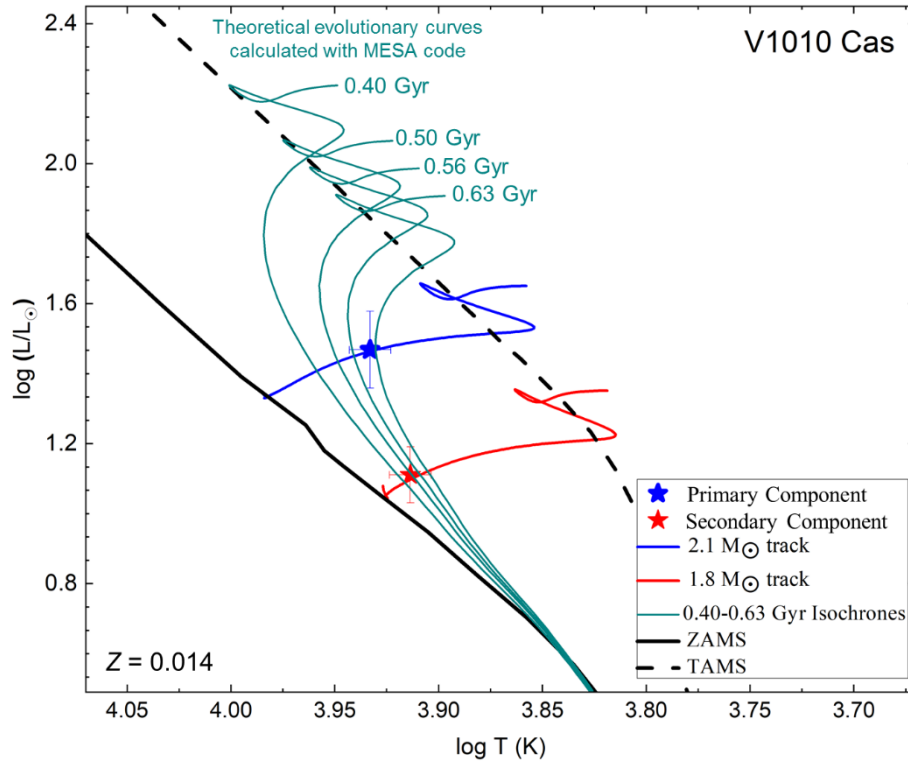


Figure 3. In the $\log L$ - $\log T$ plane, the positions of V1010 Cas components. Evolutionary tracks for a metallicity of $Z = 0.014$ are depicted with blue and red lines corresponding to respectively primary and secondary components.

5. RESULTS AND DISCUSSIONS

This paper presents the first light curve solution of ground-based CCD multicolour observational datasets in *BVRI* passbands and high-quality *TESS* data to estimate the fundamental parameters of the V1010 Cas components. Additionally, new light elements for the system were computed by utilizing the times of minima calculated from *TESS* data and those collected from the literature. Consequent to the photometric analysis, the mass for the primary component as $M_1 = 2.06 \pm 0.05 M_{\odot}$, and for secondary component as $M_2 = 1.83 \pm 0.04 M_{\odot}$ were determined. Regarding the primary and secondary components of V1010 Cas, the radii were found as follows: be $R_1 = 2.46 \pm 0.01 R_{\odot}$ and $R_2 = 1.78 \pm 0.03 R_{\odot}$, respectively. Furthermore, the light curve analysis indicates that the distance of V1010 Cas is approximately 444 ± 42 pc, a value in strong agreement with the Gaia-DR3 distance 436 ± 5 pc [21].

In this paper, the primary and secondary component temperatures of V1010 Cas were calculated as $T_{\text{eff},1} = 8574$ K and $T_{\text{eff},2} = 8196$ K, respectively, through photometric analysis of the system.

Comparing the obtained temperatures with the temperatures in the table given by [11] for main-sequence stars, it was found that the spectral types of V1010 Cas primary and secondary components are A4 and A5, respectively. Since no detailed photometric or spectral analysis of the system was previously available in the literature, the spectral types of the component stars could not be determined, but it was identified by [22] that V1010 Cas is a main-sequence star with spectral type A2. The mass ratio of V1010 Cas calculated in this study is $q = 0.889 \pm 0.008$, which is in strong agreement with the mean mass ratio value $\langle q \rangle = 0.88$ given for detached binary stars ([23]). Moreover, the mass values calculated for each component were substituted into the mass-luminosity relations given by [24] for main-sequence stars, and the mean luminosity values of the primary and secondary components were calculated as $\log L_1 = 1.37 L_\odot$ and $\log L_2 = 1.14 L_\odot$, respectively. The luminosity values ($\log L_1 = 1.47 \pm 0.11$, $\log L_2 = 1.11 \pm 0.08$) given in Table 3 for both components of V1010 Cas are in good agreement with those calculated from [24] relation within statistical uncertainties. This result supports that the system is still in the main-sequence band. The ages of components calculated on the basis of absolute parameters are consistent within statistical uncertainties, and the age of the system is estimated as 570 ± 60 Myr.

The absolute stellar parameters were calculated for the components of the V1010 Cas system using sensitive photometric data in this research. Detached binary systems like V1010 Cas provide a unique opportunity to directly measure stellar masses, radii, and luminosities, which are difficult to accurately determine for single stars. Overall, the V1010 Cas binary system provides a valuable laboratory for expanding our understanding of stellar evolution, binary interactions, and broader astrophysical phenomena. In order to calculate the mass ratios of the components and therefore their fundamental stellar parameters more precisely, radial velocity curves of the components are needed. For this purpose, it is essential that spectroscopic observations of V1010 Cas are also performed and used along with photometric data in the light curve solution. With future spectroscopic observations of the system, radial velocity curves of the components can be obtained and the light curve solution could be performed simultaneously with spectroscopic and photometric data to provide much more precise findings. Until spectral and photometric data for this system are evaluated simultaneously, the findings in this research will be the parameters most representative of V1010 Cas.

Author Contribution: Conception/Design of study, Conception/Design of study Data Analysis/Interpretation, Drafting Manuscript, Critical Revision of Manuscript, Final Approval and Accountability - N.A.

Conflict of Interest: The author declared no conflict of interest.

ACKNOWLEDGEMENT

Sincere thanks to the anonymous referees for their insightful and constructive suggestions that significantly improved the paper. This study was funded by the Scientific Research Projects Coordination Unit of Istanbul University. Project number: 37903. The author would like to thank TÜBİTAK for partial support towards using the T60 telescope via project 18BT60-1324. The author also thanks the observers and technical staff at the TÜBİTAK National Observatory for their support before and during the observations. A special thanks to Fahri ALIÇAVUŞ and Mehmet ALPSOY for

their valuable suggestions and contributions, and Selçuk BİLİR for the inspiration and helpful discussions.

REFERENCES

- [1] Ricker, G. R., Winn, J. N., Vanderspek, R., et al. (2015). Transiting Exoplanet Survey Satellite (TESS). *Journal of Astronomical Telescopes, Instruments, and Systems*, 1,014003.
- [2] Kazarovets, E. V., Samus, N. N., Durlevich, O. V., Kireeva, N. N., Pastukhova, E. N. (2008). The 79th Name-List of Variable Stars. *Information Bulletin on Variable Stars*, 5863, #1.
- [3] Parmaksizoglu, M., Dindar, M., Kirbiyik, H., Helhel, S. (2014). Software and electronic developments for TUG - T60 robotic telescope. *Revista Mexicana de Astronomia y Astrofisica Conference Series*, 45, 24.
- [4] Bessell, M. S. (1990). UBVRI passbands. *Publications of the Astronomical Society of the Pacific*, 102, 1181-1199.
- [5] Kilic, Y., Shameoni Niaei, M., Özeren, F. F., Yesilyaprak, C. (2016). MYRaf: A new Approach with IRAF for Astronomical Photometric Reduction. *Revista Mexicana de Astronomia y Astrofisica Conference Series*, 48, 38–39.
- [6] Wilson, R.E., Devinney, R.J. (1971). Realization of Accurate Close-Binary Light Curves: Application to MR Cygni. *The Astrophysical Journal*, 166, 605.
- [7] Zola, S., Rucinski, S.M., Baran, A., et. al. (2004). Physical Parameters of Components in Close Binary Systems: III. *Acta Astronomica*, 54, 299-312.
- [8] Zola, S., Gazeas, K., Kreiner, J.M., et. al. (2010). Physical parameters of components in close binary systems – VII. *Monthly Notices of the Royal Astronomical Society*, 408, 464-474.
- [9] Høg, E., Fabricius, C., Makarov, V. V., et al. (2000). The Tycho-2 catalogue of the 2.5 million brightest stars. *Astronomy and Astrophysics*, 355, L27–L30.
- [10] Schlafly, E. F. and Finkbeiner, D. P. (2011). Measuring Reddening with Sloan Digital Sky Survey Stellar Spectra and Recalibrating SFD. *The Astrophysical Journal*, 737, 103.
- [11] Eker, Z., Soydugan, F., Bilir, S., Bakis, V., et al. (2020). Empirical bolometric correction coefficients for nearby main-sequence stars in the Gaia era. *Monthly Notices of the Royal Astronomical Society*, 496, 3887–3905.

- [12] Choi, J., Dotter, A., Conroy, C., Cantiello, M., Paxton, B., Johnson, B. D. (2016). Mesa Isochrones and Stellar Tracks (MIST). I. Solar-scaled Models. *The Astrophysical Journal*, 823, 102.
- [13] Dotter, A. (2016). MESA Isochrones and Stellar Tracks (MIST) 0: Methods for the Construction of Stellar Isochrones. *The Astrophysical Journal Supplement Series*, 222, 8.
- [14] Paxton, B., Bildsten, L., Dotter, A., Herwig, F., Lesaffre, P., Timmes, F. (2011). Modules for Experiments in Stellar Astrophysics (MESA). *The Astrophysical Journal Supplement Series*, 192, 3.
- [15] Paxton, B., Cantiello, M., Arras, P., et al. (2013). Modules for Experiments in Stellar Astrophysics (MESA): Planets, Oscillations, Rotation, and Massive Stars. *The Astrophysical Journal Supplement Series*, 208, 4.
- [16] Paxton, B., Marchant, P., Schwab, J., et al. (2015). Modules for Experiments in Stellar Astrophysics (MESA): Binaries, Pulsations, and Explosions. *The Astrophysical Journal Supplement Series*, 220, 15.
- [17] Paxton, B., Schwab, J., Bauer, E. B., et al. (2018). Modules for Experiments in Stellar Astrophysics (MESA): Convective Boundaries, Element Diffusion, and Massive Star Explosions. *The Astrophysical Journal Supplement Series*, 234, 34.
- [18] van Hamme, W. (1993). New Limb-Darkening Coefficients for Modeling Binary Star Light Curves. *The Astronomical Journal*, 106, 2096.
- [19] von Zeipel, H. (1924). The radiative equilibrium of a rotating system of gaseous masses. *Monthly Notices of the Royal Astronomical Society*, 84, 665–683.
- [20] Rucinski, S. M. (1969). The Proximity Effects in Close Binary Systems. II. The Bolometric Reflection Effect for Stars with Deep Convective Envelopes. *Acta Astronomica*, 19, 245.
- [21] Gaia Collaboration, Vallenari, A., Brown, A. G. A., Prusti, T., et al. (2023). Gaia Data Release 3. Summary of the content and survey properties. *Astronomy and Astrophysics*, 674, A1.
- [22] Jaschek, C., Conde, H., de Sierra, A. C. (1964). Catalogue of stellar spectra classified in the Morgan-Keenan system. *Observatory Astronomical La Plata Series Astronomies*, 28, 1.
- [23] Eker, Z., Demircan, O., Bilir, S., Karataş, Y. (2006). Dynamical Evolution of Active Detached Binaries on the $\log J_0$ - $\log M$ Diagram and Contact Binary Formation. *Monthly Notices of the Royal Astronomical Society*, 373, 1483-1494.
- [24] Eker, Z., Bakış, V., Bilir, S., Soyduğan, F., Steer, I., Soyduğan, E., Bakış, H., Aliçavuş, F., Aslan, G., Alpsyoy, M. (2018). Interrelated Main-Sequence Mass-Luminosity, Mass-Radius, and

Mass-Effective Temperature Relations. Monthly Notices of the Royal Astronomical Society, 479, 5491-55111.



RESEARCH ARTICLE

**ENRICHMENT OF SİVAS/GEMEREK LIGNITE COAL BY OIL AGGLOMERATION
USING DIFFERENT VEGETABLE OILS**

Özlem KAYA^{1,*}, Neriman TAŞDÖĞEN CEBE²

Sivas Cumhuriyet University, Engineering Faculty, Metallurgy and Materials Engineering, Sivas, okaya@cumhuriyet.edu.tr,
ORCID: 0000-0001-7613-3609

²Sivas Cumhuriyet University, Engineering Faculty, Mining Engineering, Sivas, tasdogenneriman@gmail.com,
ORCID: 0000-0002-6555-5950

Receive Date: 28.07.2023

Accepted Date: 13.09.2023

ABSTRACT

The aim of this study was to investigate the use of various vegetable oils (almond oil, hazelnut oil, poppy oil, soybean (soya) oil, sunflower oil) for Sivas/Gemerek (in Turkey) lignite coal by oil agglomeration. The study examined the effect of bridging liquid type and dosage on oil agglomeration. Vegetable oil dosages of 2%, 5%, 10% and 20% were investigated in oil agglomeration experiments. The agglomeration of lignite coal with these bridging liquids was evaluated based on yield, combustible recovery and ash rejection. The agglomeration performances of these vegetable oils were compared. The highest ash rejection (70.30%) was observed by using soybean (soya) at 20% of the bridging liquid dosage. The yield and combustible recovery of lignite coal were achieved 36.46% yield and 38.05% combustible recovery in this soybean (soya) oil dosage, respectively. The lignite coal ash content was reduced from 19.08% to 15.54% under these optimum conditions.

Keywords: *Ash rejection, Combustible recovery, Lignite coal, Oil agglomeration, Vegetable oil, Yield.*

1. INTRODUCTION

Coal, petroleum and natural gas are fossil energy raw materials. Generally, rocks containing 50% combustible material are described as coal. Coal contains inorganic materials and moisture except organic materials. Coal is classified into four ranks by The American Society for Testing and Materials (ASTM): lignite, sub-bituminous, bituminous and anthracite. Lignite coal, also known as brown coal or low-rank coal, has the following characteristics: low calorific value, high moisture and ash content, proneness to spontaneous combustion, low friability.

Impurities in coal, which are important for both the use and cleaning of coal, are divided into three groups: moisture, ash and sulfur. The failure to reach the desired yield and ash ratios with classical

methods for cleaning fine coals (-500 μm) has led to the emergence of many physicochemical methods. Among these methods, oil agglomeration is a method with advantages such as high efficiency, low ash content, simple applicability and high selectivity. Oil agglomeration is a process for the enrichment of fine coals (-500 μm) and was developed as an alternative to flotation method. Also this method achieves beneficiation of low-quality coals such as lignite effectively [1,2].

In this method, differences in surface properties (hydrophobic (organic) and hydrophilic (inorganic)) between coal and gangue minerals are utilized to remove inorganic impurities. The oil agglomeration process involves intense mixing of an immiscible liquid (bridging liquid) and an aqueous suspension of fine coal. The hydrophobic (organic) coal particles readily coat with the bridging liquid, leading to the formation of agglomerates. On the other hand, hydrophilic (mineral matter) particles do not agglomerate upon collision. After the agglomeration process, the slurry is screened to separate the coal agglomerates (concentrate) from the non-agglomerated particles (tailings) [3,4].

Several studies have reported the use of various types of vegetable oils as bridging liquids in oil agglomeration. The study conducted by Alonso et al. [5] focused on obtaining high calorific value products from coal cleaning wastes. They achieved this by agglomerating the wastes with vegetable oils, including crude and refined sunflower and soybean oils. The study conducted by Asad et al. [6] focused on the beneficiation of Makarval coal. They investigated the use of soybean oil as an agglomerant in this process. The ash content of agglomerates has been reduced from 30% to 7.5% and sulfur content was reduced from 5.4% to 2.0%. The study conducted by Chakladar et al [7] found that turpentine oil is an effective bridging liquid for the beneficiation of Indian cooking coals by oil agglomeration. In the study, two high-ash coals of Indian origin, 26% and 34% ash, were selected. A wide range of particle sizes, pH, electrolyte type, agitation conditions and oil dosage were investigated. Both coals (-200 mesh) showed approximately 50% reduction in ash content. The study by Chary and Dastidar [8] examined the use of various oils as bridging liquids in the oil agglomeration of Indian bituminous coal. The oils investigated include: jatropha oil, karanja oil, rubber seed oil, cotton seed oil, sunflower oil, soya oil, castor oil, palm oil, sesame oil, coconut oil. The study conducted by Garcia et al. [9] found that refined sunflower and soybean oils were suitable for coal agglomeration with three Spanish anthracites. The study conducted by Ken and Nandi [10] focused on the desulfurization of high sulphur Indian coal by oil agglomeration using linseed oil. Experimental results showed that raw coal with 5.52% sulfur, 13.47% ash and GCV of 7038 kcal/kg can be beneficiated to produce clean coal with 2.18% sulfur along with 5.32% ash and 7769 kcal/kg GCV. The study by Malik et al. [11] investigated the use of edible and non-edible vegetable oils, including castor oil, soybean oil (soya oil), linseed oil, and mahua oil, for agglomerating five different types of Indian coals. Using different coal-oil combinations, agglomerate yields ranged from 40.0 to 87.5% and ash rejections from 13.5 to 62.0%. Valdés and Garcia [12] carried out agglomeration of coal fines cleaning wastes from two different Spanish coal cleaning plants with waste vegetable oils (WVO) from households. They recovered high calorific value and low ash coal with waste sunflower oil and olive oil.

The type and nature of the bridging liquid has a very important effect on the performance of the agglomeration process. It seems like various types of oils, such as diesel oil, fuel oil, kerosene, engine oil, vegetable oils and fish oil, have been effectively utilized as bridging liquids in the agglomeration

process. Considered renewable are vegetable oils with negligible sulphur, nitrogen and metal content. There are also several environmental benefits to using vegetable oils, too. In this work, different virgin vegetable oils (almond oil, hazelnut oil, poppy oil, soybean (soya) oil, sunflower oil) have been tested as bridging liquid in oil agglomeration. These vegetable oils have a high density of approximately 0.9 g/cm^3 and they are less expensive than compared to hydrocarbons. The usage of vegetable oils for oil agglomeration appears to be an attractive bridging liquid that should be considered. In the present study, the influence of different vegetable oil types and dosages on oil agglomeration of Sivas/Gemerek lignite coal was investigated and the agglomeration performances of these vegetable oils were compared.

2. MATERIAL AND METHOD

2.1. Material

The coal sample from the Sivas/Gemerek region in Turkey was used for the agglomeration experiments. The proximate and calorific value analysis of the coal sample has been completed (Table 1). The X-ray diffractometer can be used to analyze the composition of lignite coal. In this case, it detected the presence of quartz (SiO_2) and pyrite (FeS_2) in the lignite coal sample. The particle size distribution of the lignite coal ground to $-500 \mu\text{m}$ used in the agglomeration experiments is given in Table 2.

Table 1. Proximate and calorific value analyses of Sivas/Gemerek lignite coal.

Proximate Analysis		Calorific Value Analysis	
Parameters	(%)	Parameters	(kcal/kg)
Moisture in original coal	23.79	Upper calorific value of dry coal	3555
Moisture in air-dried coal	19.49		
Ash in dry coal	19.08		

Table 2. Particle size distribution of Sivas/Gemerek lignite coal.

Particle size (μm)	Weight (%)
-500 + 425	11.15
-425 + 300	12.70
-300 + 250	11.07
-250 + 180	10.54
-180 + 125	9.38
-125 + 90	8.92
-90 + 63	7.75
-63 + 45	6.32
-45	22.17
Total	100

The study used the following vegetable oils: almond oil, hazelnut oil, poppy oil, soybean (soya) oil and sunflower oil. The vegetable oils used in the oil agglomeration experiments were obtained from

the local market and used without any chemical or physical modification. The properties and densities of the bridging liquids used in this study are given in Table 3, where these are the data provided by the manufacturers.

2.2. Method

The coal sample was grinded using ball mill by closely controlled and sieved the particle size -500 μm . Heidolph RZR 2051 speed-controlled mechanical stirrer was used for performing the agglomeration tests. Agglomeration experiments were undertaken in 1000 mL glass beaker. Three-blade metal portable baffles were inserted to beaker as a turbulence generator. 15 g coal-400 mL distilled water mixtures were agitated to provide complete wetting of coal particles. Bridging liquid (vegetable oil) was then added, and mixture of coal-bridging liquid-water was agitated at 400 rpm for 15 min of agglomeration time. The experiments were carried out at the ambient pH of the mixture, which was measured to be pH 5.50. After agglomeration, the slurry was transferred to a sieve with an aperture of 500 μm . This separation process helps to separate the agglomerates from the tailings. The agglomerates were washed with distilled water. Then acetone washing was performed to remove the bridging liquid and again washed with distilled water. The oil agglomeration process schematic representation is shown in Figure 1.

Table 3. Bridging liquids used in this study and their properties.

Bridging Liquids	Properties	Density (g/cm³)
Almond oil	It is a yellowish vegetable oil that contains unsaturated oil acids of oleic and linoleic acid, saturated oil acids myristic and palmitic acid glycerides obtained by pressing Rosaceae seeds	0.912
Hazelnut oil	It is a vegetable oil that contains oil acids such as oleic acid and linoleic acid which is not chemically processed and is obtained by physical processes and extraction from hazelnut fruits	0.914
Poppy oil	It is a vegetable oil containing oleic acid, linoleic acid and lower amounts of stearic acid and palmitic acid glycerides which is obtained from pressing the seeds of <i>Papaver somniferum</i> varieties (containing 47-51% oil).	0.922
Soybean (soya) oil	It is a vegetable oil that is obtained by extraction or pressing from the seeds of soybean (<i>Glycine max</i>) species	0.917
Sunflower oil	It is a vegetable oil that contains oleic acid and linoleic acid obtained from the seeds of the plant <i>Helianthus annuus</i> with an oil content of 39-45%.	0.912

The agglomerates were dried at 105 ± 5 °C. At the end of drying, the agglomerates were weighed and analyzed for ash content. The standard ASTM-3174 method has been used for ash determination [13].

The yield (%), combustible recovery (%) and ash rejection (%) of the agglomerates were calculated by formulas as below:

$$Y(\%) = \frac{W_{t_a}}{W_{t_f}} * 100 \quad (1)$$

$$CR(\%) = \left(\frac{W_{t_a}}{W_{t_f}} \right) * \left(\frac{100 - A_a}{100 - A_f} \right) * 100 \quad (2)$$

$$AR(\%) = \left[\frac{A_f - \left(A_a * \frac{W_{t_a}}{W_{t_f}} \right)}{A_f} \right] * 100 \quad (3)$$

Where, Y= yield (%), W_{t_a} = weight of agglomerate (g); W_{t_f} = weigh of feed coal (g); CR= combustible recovery (%); A_a = ash of agglomerate (%); A_f = ash of feed coal (%); AR = ash rejection (%).

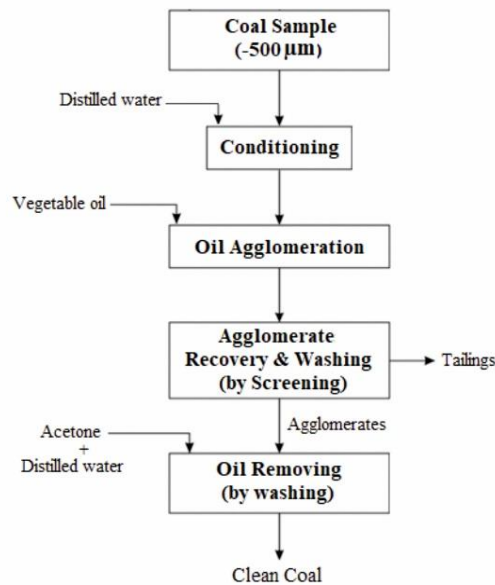


Figure 1. The oil agglomeration process schematic representation.

3. RESULTS AND DISCUSSION

The choice of liquids as bridging liquid in oil agglomeration is indeed crucial for the success of the process. It can significantly impact the efficiency and effectiveness of oil agglomeration. The bridging liquid acts as a medium to facilitate the agglomeration of coal particles. Bridging liquids have different properties, such as density, viscosity, surface tension and functional groups, which can

affect the agglomeration process. Therefore, careful consideration should be given to choosing the right liquid for successful oil agglomeration.

The study investigated the usage of five different vegetable oils (almond oil, hazelnut oil, poppy oil, soybean (soya) oil, and sunflower oil) in agglomeration experiments. The effects of these oils at different dosages (2%, 5%, 10%, and 20%) on the oil agglomeration process were examined.

Figure 2 illustrates the agglomeration performance of lignite coal with different almond oil dosages. Figure 3 illustrates the agglomeration performance of lignite coal with different sunflower oil dosages. Figure 4 illustrates the agglomeration performance of lignite coal with different poppy oil dosages.

As seen in Figures 2 and 3; the lowest yield and combustible recovery values in the examined vegetable oils were obtained at very low bridging liquid dosages (2% and 5%) for almond oil and sunflower oil. When almond oil and sunflower oil were used at low liquid dosages, an adequate liquid bridge could not form between the coal particles, resulting in low yield and combustible recovery. Increasing the doses of almond oil and sunflower oil resulted in higher yields and combustible recovery values of the agglomerates. Similarly, both yield and combustible recovery values of the agglomerates were increased by increasing the dosage of poppy oil. (Figure 4). This can be explained by the improved contact of coal pores with bridging liquids and the increased formation of larger spherical agglomerates due to an increase in the number of bridging liquid droplets [14]. However, the increase in combustible recovery is accompanied by a decrease in ash rejection. This can be explained to a reduced in the selectivity of the bridging liquid droplets. Similarly, Shukla and Venugopal [15] observed that there was a decrease in ash rejection as the oil dosage increased.

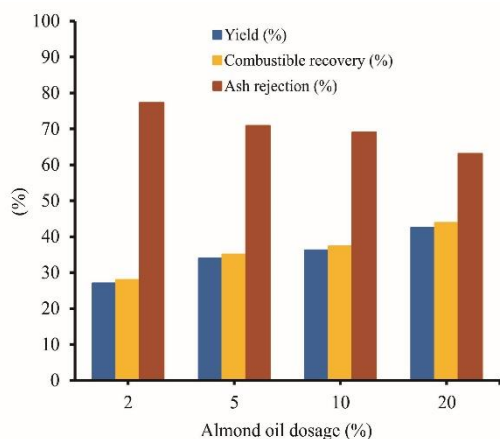


Figure 2. Agglomeration performance of lignite coal with different almond oil dosages.

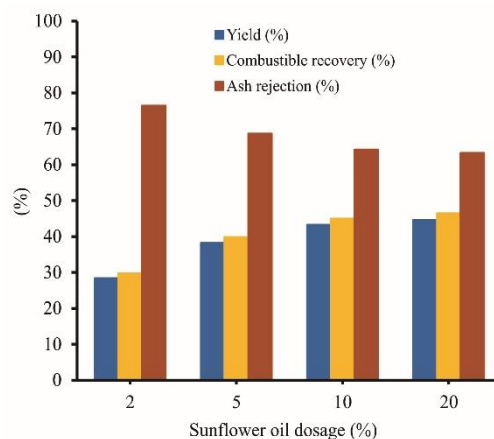


Figure 3. Agglomeration performance of lignite coal with different sunflower oil dosages.

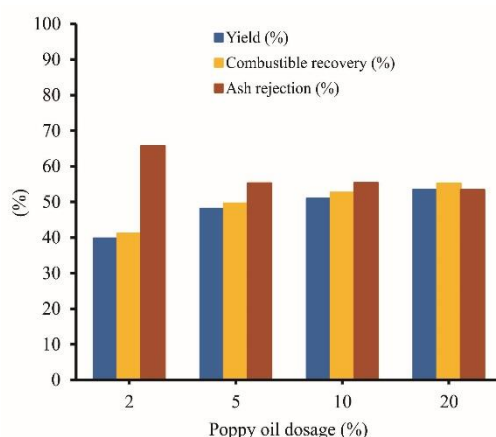


Figure 4. Agglomeration performance of lignite coal with different poppy oil dosages.

Figure 5 shows the agglomeration performance of lignite coal with different hazelnut oil dosages. As shown in Figure 5, the yield and combustible recovery values of hazelnut oil tended to decrease with increasing bridging liquid dosage. At lower dosages of hazelnut oil, i.e. 2% and 5%, this indicates that there is enough oil to coat all the coal particles. Increasing the dosage of hazelnut oil makes the agglomerates pasty, which in turn makes it difficult for them to agglomerate. This decrease in agglomerate formation leads to a lower yield and reduced recovery of combustible materials. However, the ash rejection values of hazelnut oil increase with an increasing dosage of bridging liquid. The high content of inorganic minerals in the agglomerates has caused a decrease in yield, resulting in increased ash rejection. Asad et al. [6] and Ken and Nandi [10] also reported that increasing the dosage of oil had a negative effect on ash rejection.

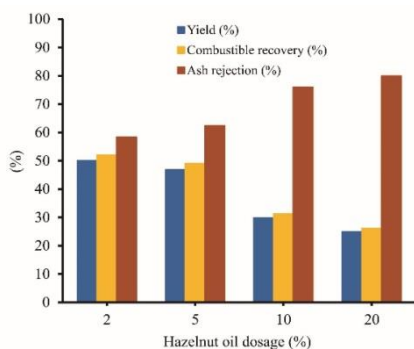


Figure 5. Agglomeration performance of lignite coal with different hazelnut oil dosages.

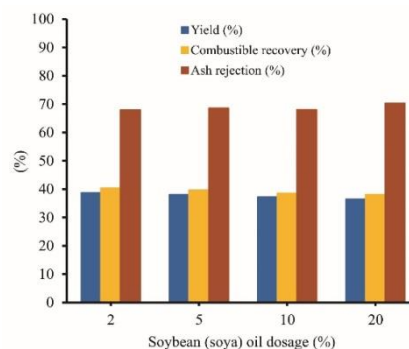


Figure 6. Agglomeration performance of lignite coal with different soybean (soya) oil dosages.

Figure 6 shows the agglomeration performance of lignite coal with different soybean (soya) oil dosages. As seen in Figure 6, the values for yield, combustible recovery, and ash rejection did not change significantly with increasing dosage of soybean (soya) oil. At all soybean (soya) oil dosages, the bridging liquid effectively covers the coal particles. Under these conditions, there is sufficient contact between hydrophobic coal particles and agglomerate formation, resulting in higher yield and combustible recovery. This also caused high ash rejection.

Figure 7 illustrates the results obtained with vegetable oil type and dosage for yield in oil agglomeration. Figure 8 illustrates the results obtained with vegetable oil type and dosage for combustible recovery in oil agglomeration. Figure 9 illustrates the results obtained with vegetable oil type and dosage for ash rejection in oil agglomeration.

As can be seen in Figure 7 and Figure 8, almond and sunflower oil dosages of 2% had the lowest yields and combustible recoveries. For example, using almond oil these values were 27% and 27.99%, using sunflower oil these values were 28.46% and 29.75%, respectively. By increasing the dosages of these oils, the yield and combustible recovery were improved but ash rejection was decreased. Similarly, when poppy oil dosages were increased from 2 to 20%, both the yield and the combustible yield increased, but the ash rejection decreased. As can be seen in Figure 9, the maximum ash rejection (79.97%) was achieved at a hazelnut oil concentration of 20%. However, as the hazelnut oil concentration increased from 2 to 20%, the yield decreased from 50.06% to 24.93% and the combustible recovery decreased from 52.03 to 26.08%.

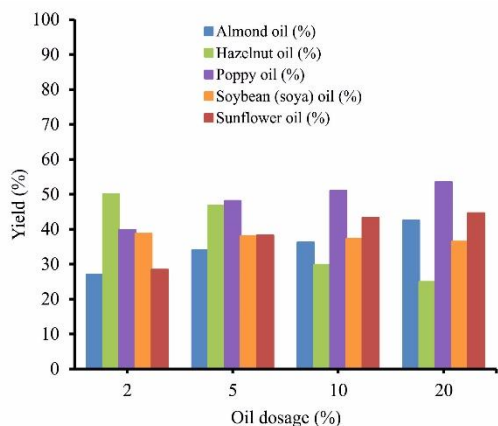


Figure 7. The results obtained with vegetable oil type and dosage for yield in oil agglomeration.

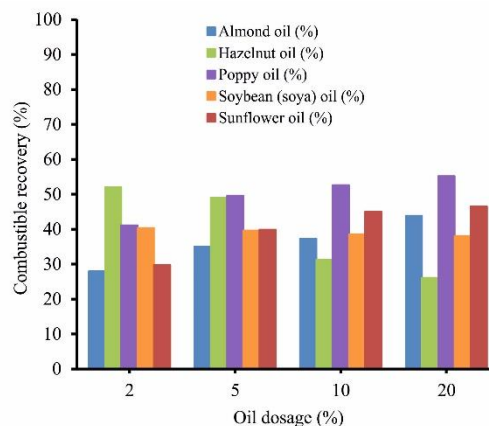


Figure 8. The results obtained with vegetable oil type and dosage for combustible recovery in oil agglomeration.

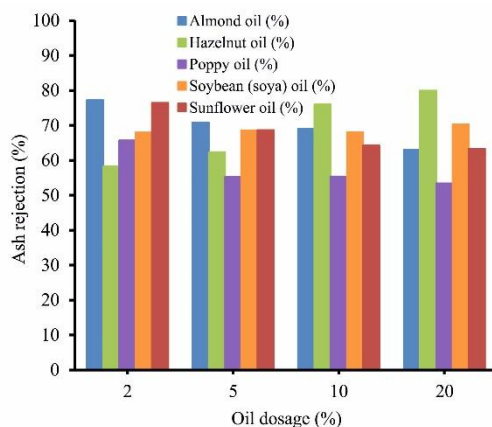


Figure 9. The results obtained with vegetable oil type and dosage for ash rejection in oil agglomeration.

As shown in Figure 9, the highest ash rejection of 70.30% was observed at a 20% soybean (soya) oil bridging liquid dosage. This bridging liquid achieved a yield of 36.46% and a combustible recovery of 38.05% (Figure 7 and Figure 8). Oil agglomeration experiments were evaluated together with yield, combustible recovery and ash rejection values to select the most suitable bridging liquid. The results of the present oil agglomeration study have shown that soybean (soya) oil has better bridging properties compared to other vegetable oils investigated. Based on the experimental results, soybean (soya) oil was selected as the most effective bridging liquid.

4. CONCLUSIONS

The focus of our present study is the enrichment of Sivas/Gemerek lignite by oil agglomeration using different vegetable oils. The following results have been reached:

- i. Almond oil, hazelnut oil, poppy oil, soybean (soya) oil, and sunflower oil were used as bridging liquids at different dosages.
- ii. The most effective results were obtained with a 20% dosage of soybean (soya) oil, which resulted in an ash rejection of 70.30%.
- iii. Using a 20% dosage of soybean (soya) oil, the agglomeration yield was 36.46% and the combustible recovery was 38.05% for lignite coal.
- iv. Under the optimum oil agglomeration conditions achieved, the ash content of the Sivas/Gemerek lignite was reduced from 19.08% to 15.54%.
- v. Experimental studies showed that Sivas/Gemerek lignite coal was enriched through the oil agglomeration process using soybean (soya) oil.

ACKNOWLEDGEMENT

This research has not received any grants.

REFERENCES

- [1] Laskowski, J.S. (2001). Coal Flotation and Fine Coal Utilization, Amsterdam. New York: Elsevier Science B.V.
- [2] Mehrotra, V.P., Sastry, K.V.S. and Morey, B.W. (1983). Review of oil agglomeration techniques for processing of fine coal. *International Journal of Mineral Processing*, 11, 175-201. [https://doi.org/10.1016/0301-7516\(83\)90025-X](https://doi.org/10.1016/0301-7516(83)90025-X)
- [3] Drzymala, J. (2007). *Mineral Processing, Foundations of theory and practice of minerallurgy*, 1st English ed. Wroclaw, Poland: Wroclow University of Technology, 464-467.
- [4] Fan, C.W., Hu, Y.C., Markuszewski, R. and Wheelock, T.D. (1989). Role of induction time and other properties in the recovery of coal from aqueous suspensions by agglomeration with heptane. *Energy&Fuels*, 3(3), 376-381. <https://doi.org/10.1021/ef00015a021>
- [5] Alonso, M.I., Valdés, A.F., Martínez-Tarazona, R.M. and Garcia, A.B. (1999). Coal recovery from coal fines cleaning wastes by agglomeration with vegetable oils: Effects of oil type and concentration. *Fuel*, 78, 753-759. [https://doi.org/10.1016/S0016-2361\(98\)00218-X](https://doi.org/10.1016/S0016-2361(98)00218-X)
- [6] Asad, M., Toqeer, A., Javaid, A., Khurram, S., Naseer, S. and Shahid, M. (2016). Agglomeration of Makarwal coal using soybean oil as agglomerants. *Energy Sources, Part A: Recovery, Utilization, and Environmental Effects*, 38 (24), 3733-3739. <http://dx.doi.org/10.1080/15567036.2016.1141268>
- [7] Chakladar, S., Banerjee, R., Mohanty, A., Chakravarty, S. and Patar, P.K. (2022). Turpentine oil: a novel and natural bridging liquid for agglomeration of coal fines of high ash coals. *International Journal of Coal Preparation and Utilization*, 42 (7), 2028-2040. <https://doi.org/10.1080/19392699.2020.1789976>
- [8] Chary, G.H.V.C. and Dastidar, G. (2013). Comprehensive study of process parameters affecting oil agglomeration using vegetable oils. *Fuel*, 106, 285-292. <https://doi.org/10.1016/j.fuel.2012.12.002>
- [9] Garcia, A.B., Martinez-Tarazona, M.R. and Vega, J.M.G. (1996). Cleaning of Spanish high-rank coals by agglomeration with vegetable oils. *Fuel*, 75, 885-890. [https://doi.org/10.1016/0016-2361\(96\)00012-9](https://doi.org/10.1016/0016-2361(96)00012-9)

- [10] Ken, B.S. and Nandi, B.K. (2019). Desulfurization of high sulfur Indian coal by oil agglomeration using Linseed oil. *Powder Technology*, 342, 690-697. <https://doi.org/10.1016/j.powtec.2018.10.045>
- [11] Malik, A., Singh, D.P., Sharma, S., Dastidar, M.G. and Roychoudhury, P.K. (1999). Oil agglomeration for recovery of coal fines: effect of vegetable oil and bacterial pretreatment. *Coal Preparation*, 20, 247-268. <https://doi.org/10.1080/07349349908945603>
- [12] Valdés, A.F. and Garcia, A.B. (2006). On the utilization of waste vegetable oils (WVO) as agglomerants to recover coal from coal fines cleaning wastes (CFCW). *Fuel*, 85(5-6), 607-614. <https://doi.org/10.1016/j.fuel.2005.08.011>
- [13] ASTM-3174 “Standard Test Method for Ash in the Analysis Sample of Coal and Coke from Coal”
- [14] Kaya, Ö. and Ari, M. (2020). Investigation of the factors affecting oil agglomeration using different reagent mixtures as a bridging liquid. *International Journal of Coal Preparation and Utilization*, 40 (7), 483-490. <https://doi.org/10.1080/19392699.2019.1568999>
- [15] Shukla, D. and Venugopal, R. (2019). Optimization of the process parameters for fine coal–oil agglomeration process using waste mustard oil. *Powder Technology*, 346, 316-325. <https://doi.org/10.1016/j.powtec.2019.02.001>



RESEARCH ARTICLE

CLASSIFICATION OF BRAIN TUMORS WITH DEEP LEARNING MODELS

Beyza Nur TÜZÜN^{1*}, Durmuş ÖZDEMİR²

^{1*}Kütahya Dumlupınar University, Institute of Graduate Education, Department of Computer Engineering, Kütahya, b.nur.tuzun@gmail.com, ORCID: 0000-0002-8289-6263

²Kütahya Dumlupınar University, Faculty of Engineering, Department of Computer Engineering, Kütahya, durmus.ozdemir@dpu.edu.tr, ORCID: 0000-0002-9543-4076

Receive Date: 05.05.2023

Accepted Date: 15.09.2023

ABSTRACT

This study aims to present a comparative analysis of existing (state-of-the-art) deep learning models to identify early detection of brain tumor disease using MRI (Magnetic Resonance Imaging) images. For this purpose, GoogleNet, Mobilenetv2, InceptionV3, and Efficientnet-b0 deep learning models were coded on the Matlab platform and used to detect and classify brain tumor disease. Classification has been carried out on the common Glioma, Meningioma, and Pituitary brain tumors. The dataset includes 7022 brain MRI images in four different classes, which are shared publicly on the Kaggle platform. The dataset was pre-processed and the models were fine-tuned, and appropriate parameter values were used. When the statistical analysis results of the deep learning models we compared were evaluated, the results of Efficientnet-b0 (%99.54), InceptionV3 (%99.47), Mobilenetv2 (%98.93), and GoogleNet (%98.25) were obtained, in the order of success. The study results are predicted to be useful in offering suggestions to medical doctors and researchers in the relevant field in their decision-making processes. In particular, it offers some advantages regarding early diagnosis of the disease, shortening the diagnosis time, and minimizing human-induced errors.

Keywords: *Deep Learning, Brain Tumor Detection, Image Classification, MRI processing*

1. INTRODUCTION

Artificial neural networks (ANN) are models that can derive and create new information by using previously learned or classified information with an artificial network structure and produce outputs that can make decisions [1]. The learning process in ANN is similar to the relationship between neurons (nerve cells) and neurons, as in the human brain, and certain adjustments are required. The first ANN cell model was developed by Warren McCulloch and Walter Pitts in 1943. They modeled a simple neural network using electrical circuits to explain how neurons in the brain work [2].

Deep learning is an artificial intelligence method that uses multi-layer artificial neural networks in the fields of image and sound processing [3]. Each layer in deep learning have more than one number of

neurons, the hidden layer; is the layer that has the most impact on learning ability [4]. Unlike machine learning, it can learn by automatically inferences from the symbols of the data in the image or sound without using external user-defined rules. Estimation accuracy rates increase according to the input data size and normalization processes [5], [6]. With the development and spread of deep learning models, studies have been carried out in many different fields, especially in the field of medicine [7], [9]. In the studies, factors such as solving the problems in the diagnosis and treatment process of time-consuming and complex diseases in the health sector, and determining how genetic variations cause disease are aimed.

The main visualization techniques used for the identification of diseases are CT (Computed Tomography) and MRI (Magnetic Resonance Imaging) imaging techniques [10]. With the CT technique, a clear image is obtained in the images of anatomical structures such as bones, but this clarity is lower in soft tissues and organs. The MR imaging technique can clearly reflect anatomical structures such as soft tissues, organs, and vessels [11]. For this reason, MRI imaging is used to detect brain tumors. In the phase of the regeneration of cells, mass or masses may occur in various parts of the body in cases caused by excessive proliferation, defects in the development, growth, and proliferation of the cell deviating from its average size, radiation exposure, genetic disorders [12]. These masses are called tumors. A brain tumor is a mass that results from the uncontrolled development and growth of brain cells within the skull [13]. Brain tumors are basically divided into benign and malignant. Benign tumors grow slowly and rarely spread. Their marginal structures can distinguish them. Malignant tumors grow and spread very quickly. They often threaten human life. Brain tumors with evolving medical imaging techniques and classification of findings in different patients are divided into two superclasses, primary and secondary, and 11 subclasses [14]. While primary brain tumor types originate from brain cells, secondary brain tumor types originate anywhere in the body and then spread to the brain. The 2016 American Association of Neurological Surgeons (AANS) classification of brain tumor types based on data from WHO (World Health Organization) is as follows [15], [16]:

I. Primary tumors of the brain

- Gliomas
- Meningioma
- Primitive neuroectodermal tumors (PNET)
- Pituitary tumors
- Pineal tumors
- Choroid plexus tumors
- Other, more benign primary tumors
- Tumors of nerves and/or nerve sheaths
- Cysts
- Other primary tumors, including skull base
- Primary Central Nervous System Lymphoma (PCNSL)

II. Metastatic brain tumors and carcinomatous meningitis

Glioma, Meningioma, and Pituitary brain tumor types commonly seen in this study were classified [17]. We also classified Brain MRI images using GoogleNet InceptionV3, MobileNetV2, and

Efficientnet-b0 deep learning models and compared the results with performance metrics for accuracy. In the study, fine-tuning and problem-oriented adaptation processes were carried out to obtain the best accuracy rate depending on parameters such as the number of training rounds and learning rate.

2. RELATED WORKS

Gürkahraman et al. [18] aimed to classify three different brain tumors (glioma, meningioma and pituitary gland tumor) using a convolutional neural network (CNN) on T1-weighted MR images and to determine the effectiveness of axial, coronal and sagittal MR sections in classification. They compared with DVM, k-NN, and Bayesian classifiers. The features existed extracted with the CNN model, and then the dataset was classified with SVM, k-NN, and Bayes classifiers. Noreen et al. [19] aimed to classify three different brain tumor MR images. In the final applications of pre-trained models, features were extracted from substrates that are different from natural images and medical images. They propose a multi-level feature extraction and merging method to solve this problem. They make changes to the Inception-v3 and DensNet201 model.

Sultan et al. [20] aimed to prove the ability of their new model to classify two different datasets with different labels. They performed classification on two separate datasets containing 3064 and 516 brain MRI images available to the public. They proposed a deep learning model based on CNN structure to classify different types of brain tumors. The second dataset aimed to differentiate between three grades of glioma, Stage 2, Stage 3, and Stage 4 tumor classes. Yerukalareddy and Pavlovskiy [21] proposed a new deep learning model for brain tumor classification in MRI images. They tested the proposed approach on two different MRI datasets and three types of brain tumors; It contains four different labels: glioma, meningioma, pituitary, and healthy. Divya et al. [22] used the ResNet50 model to classify MR brain images of tumor types such as glioma, meningioma, and pituitary. For a better result, they changed the layers and increased the number of layers from 174 layers to 181 layers. In the pieces of training, the Figshare MRI dataset consists of 3064 T1-weighted contrast-enhanced MR images of 233 patients with three different brain tumor types, including glioma, meningiomas, and pituitary tumors, containing 1426, 708, and 930 images, respectively, were utilized. Rehman et al. [23] used three convolutional neural network architectures to classify brain tumor types such as meningioma, glioma, and pituitary; Three studies were run using AlexNet, GoogLeNet, and VGGNet. The proposed studies observed that the fine-tuned VGG16 architecture achieved the highest accuracy of classification and detection, up to 98.69%. Deepak and Ameer [24] proposed the GoogleNet model to classify brain tumor types such as meningioma, glioma, and pituitary in their study. They created a system that followed a five-fold cross-validation process at the patient level on the MRI dataset from Figshare.

3. MATERIAL AND METHOD

3.1. Dataset

The dataset used in this study includes a total of 7022 brain MRI images in 4 different classes, shared openly by Masoud Nickparvar on the Kaggle platform. Examples from the dataset we used in the study are presented in Figure 1.

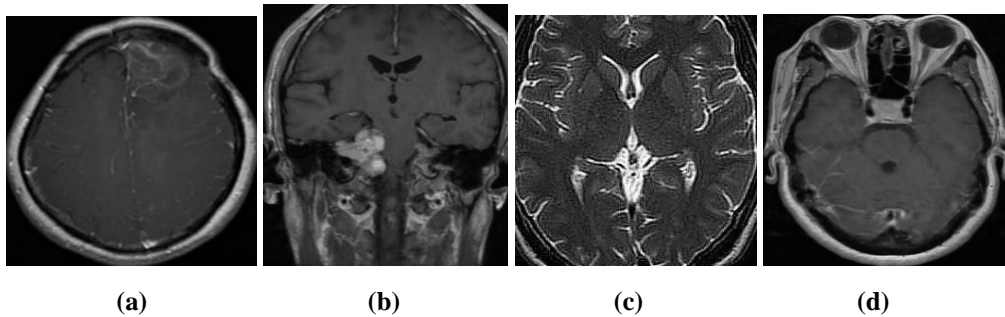


Figure 1. Examples from the data set are labeled as (a) glioma, (b) meningioma, (c) pituitary, and (d) no tumor, respectively.

Around 22% of the images were used as model tests and the rest as the training dataset. Data can be accessed from <https://www.kaggle.com/masoudnickparvar/brain-tumor-MRI-dataset> [25], [26]. The distribution of the images were Glioma (1645), Meningioma (1621), Pituitary (1757) ve No tumor (1600).

3.2. Preprocessing Stages and Fine-Tuning.

Brain MRI images were preprocessed using the OpenCV library. The endpoints in the image were found, and the margins were cropped. To apply the 45-threshold value threshold method to the images, grey coloring and blurring were made with the Gaussian Blur method. A series of erode and dilate methods were applied to eliminate small noise regions in the images equated with the Threshold method, and new images were obtained. Matlab imageDataAugmenter method RandRotation, RandXTranslation, and RandXTranslation parameters were applied in the [-20,20] rotation range before the models existed trained. Since the models use the RGB pixel color type, the images stand converted to RGB type. Unprocessed and preprocessed images in the data set used in the study were presented in Figure2.

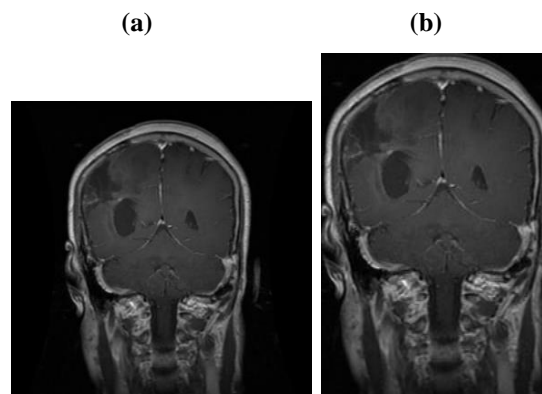


Figure 2. (a) Unprocessed image (b) Preprocessed image

3.3. Experimental Settings.

The blue markers in Figure 3 presented in show the space that the models occupy on the disk and the memory sizes. As the size of the models increases, the number of layers also increases. According to this figure, smaller-sized models were selected and their performances were compared in this study. The exact estimation and training iteration times depend on the hardware you use and the mini-batch size. Before the training phase the last fully connected layer (Fully Connected Layer) and classification (Classification Layer) layers were substituted with new ones to classify brain tumors. The training was assumed out in the Matlab R2021a application environment. A computer with 2.4GHz Intel(R)Core™ i7-3630QM CPU and Nvidia 950M GPU with 16 Ram was utilized for hardware. The parameter settings we applied in our model during the training phase are presented in Table 1.

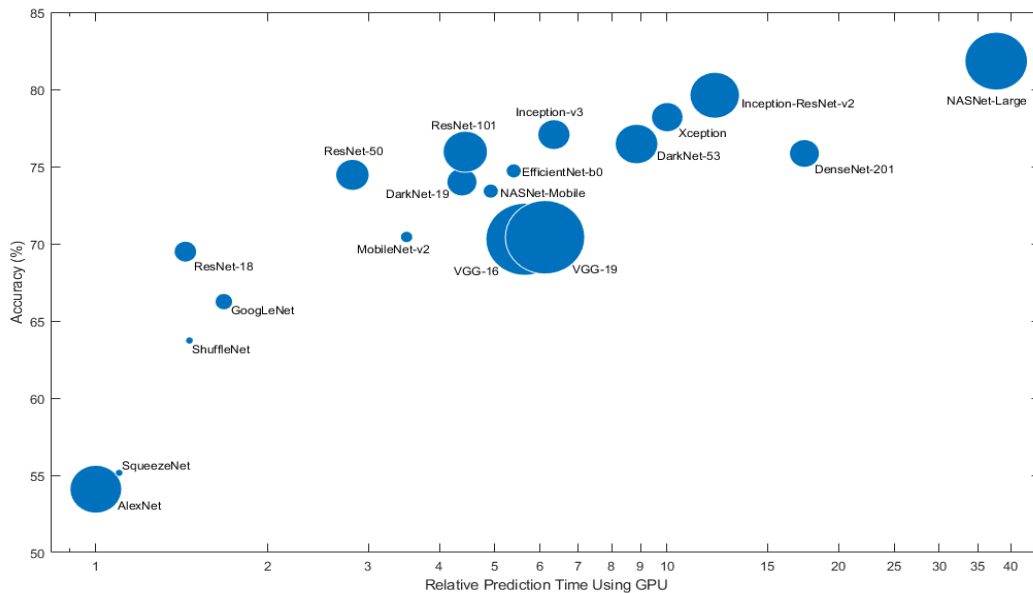


Figure 3. The relative training estimation time of models on GPU processor.

Table 1. Parameter Values

Epochs	30, 50, 100
Momentum	0.9
InitialLearnRate	0.1
Classes	4
Mini batch	16
Optimizer	'sgdm'
Verbose	False

L2Regularization	0.0001
GradientThresoldMethod	L2norm
GradientThresold	0.1
Learning rate schedule	Piecewise
Learning rate drop period	10
Learning rate drop factor	0.1

3.4. Evaluation with Performance Metrics.

The trained model is tested at the end of the training with different data reserved for the test, and a Confusion matrix is created with the results obtained. In this study we use the True Positive(TP), True Negative(TN), False Positive(FP), and False Negative(FN) performance metrics [27].

$$Accuracy = \frac{TP+TN}{TP+FN+TN+FP} \quad (1)$$

$$Recall = \frac{TP}{TP+FN} \quad (2)$$

$$Precision = \frac{TP}{TP+FP} \quad (3)$$

$$F1\ Score = 2 \times \frac{Precision \times Recall}{Precision + Recall} \quad (4)$$

The pieces of training were carried out with 100, 50, and 30 epochs, and the test results of the pieces of training were compared. In models trained with 100 epochs, the learn rate decreased by 0.01 every 10 epochs; in the last ten epochs, training was realized with a 1e-10 learn rate. Models trained with 50 epochs ended up with a learning rate of 1e-5, with the learn rate decreasing by 0.01 every ten epochs. Pieces of training made with 30 epochs started with 0.1 initial learning rate, and again in 10 epochs, the learning rate was reduced by 0.01 and ended with a learning rate of 0.0001. The accuracy, recall, precision, and f1 score values that change according to the test results of the models are shown in Table 2 below.

Table 2. The Test Results According to The Number of Training Epoch

Model	Epoch	Accuracy (%)	Recall (%)	Precision (%)	F1 Score (%)
GoogleNet	30	95.12	94.82	94.88	94.85
GoogleNet	50	98.93	98.84	98.87	98.86
GoogleNet	100	98.25	98.10	98.14	98.12
MobileNetV2	30	95.19	94.92	95.07	95
MobileNetV2	50	98.86	98.76	98.79	98.77
MobileNetV2	100	98.93	98.87	98.9	98.88
Efficientnet-b0	30	95.27	94.95	95.22	95.08

Efficientnet-b0	50	99.08	99.01	99.07	99.04
Efficientnet-b0	100	99.54	99.52	99.54	99.53
InceptionV3	30	96.80	96.56	96.76	96.66
InceptionV3	50	99.38	99.34	99.36	99.35
InceptionV3	100	99.47	99.42	99.45	99.43

As seen in Table 2, the training of the models, EfficientNet-b0, with 100 epochs, yielded the most successful results in the testing phase.

4. FINDINGS AND DISCUSSION

After Results of this study were presented to prevent overfitting, that is, excessive learning, while training epochs with piecewise different learn rate values with the piecewise parameter. However, parts trained with a high-value learn rate may not be fully trained. If it is low, the training may have slowed down, and the training period may have been prolonged. For this reason, retraining was done with different epoch values, and the results were compared. Among the GoogleNet, InceptionV3, MobileNetV2, and EfficientNet-b0 models, The best result values were obtained with the Efficientnet-b0 model, which was trained with 100 epochs. 99.54% accuracy, 99.52% recall, 99.54% precision and 99.53% f1-score values were obtained. However, results close to these values were obtained with other models as well. The Confusion Matrix of the EfficientNet-b0 model was given in Figure 4.

The results obtained from the test data of the model are as follows, respectively. The accuracy value for glioma-type tumors was obtained as 99.5%. In the glioma test data, 2 MRI images were incorrectly identified as meningioma, and 1 MRI image was defined as healthy (no tumor). The error rate value was found to be 1%. The predictive accuracy of meningioma type, which is one of the tumor types, was found to be 100%. A predictive accuracy of 99.3% was obtained in another tumor type, the pituitary. In the pituitary test results, 2 MRI images were wrong with an error rate of 0.7% and were defined as meningioma. As a result, the prediction accuracy for healthy MRI images of the brain is 99.8%. Among the healthy test data (no-tumor), 1 MRI brain image was misidentified as meningioma, and the error rate was 0.2%.

		Confusion Matrix					
Output Class	glioma	297 22.7%	0 0.0%	0 0.0%	0 0.0%	100% 0.0%	
	meningioma	2 0.2%	306 23.3%	1 0.1%	2 0.2%	98.4% 1.6%	
	notumor	1 0.1%	0 0.0%	404 30.8%	0 0.0%	99.8% 0.2%	
	pituitary	0 0.0%	0 0.0%	0 0.0%	298 22.7%	100% 0.0%	
		99.0% 1.0%	100% 0.0%	99.8% 0.2%	99.3% 0.7%	99.5% 0.5%	
		Target Class					
		glioma	meningioma	notumor	pituitary		

Figure 4. The Confusion Matrix of the EfficientNet-b0 model

Noreen et al. made changes in the InceptionV3 and DenseNet201 models in their study and obtained new models. These two new CNN models achieved an accuracy rate of 99.34% in the InceptionV3 model. When this result is compared with the training results made with the InceptionV3 model we used in this study, the test accuracy result of the training performed by setting 30 epochs was below the value obtained. However, in this study, it was observed that the test results of the pieces of training we performed with 50 and 100 epochs were more successful than the 99.34% accuracy rate. Again, Noreen et al. obtained an accuracy rate of 99.51% with the DenseNet201 model. In the Efficientnet-b0 model we suggested in the study, we achieved a test accuracy of 99.54% when 100 epochs were used, and it was observed that this ratio was more successful than the accuracy of the DenseNet201 model.

Deepak and Ameer [24] also achieved an accuracy rate of 98% with GoogleNet in their study. But in our study, as a result of the pieces of training carried out with GoogleNet, the accuracy rate of the training made by setting 30 epochs remained below this rate. However, it was observed that the test accuracy rates of the pieces of training performed by setting 50 and 100 epochs were more successful.

5. CONCLUSIONS AND SUGGESTION

As a result, this study uses deep learning models GoogleNet, InceptionV3, MobileNetV2, and Efficientnet-b0; It has been observed to be successful in classifying and detecting glioma meningioma and pituitary brain tumor types. The images and classes in the data set can be increased in future studies. Today, 3D techniques have begun to be used. Since this imaging method will increase in the future, it is recommended to work with these 3D images. This study used four deep learning models with faster training time. Apart from the four models used in the study, studies can be carried out with

other models or by creating a new model. By reusing the deep learning models used in the study, Apart from brain tumor types, classification and detection studies can be performed with MRI images of different disease type.

ACKNOWLEDGEMENT

The authors thank the reviewers for their valuable comments and suggestions, which improved the clarity and scope of the article.

ETHICAL APPROVAL

This study was carried out as part of the master thesis [ID: 720611] prepared by Beyza Nur TUZUN under the supervision of Assoc. Prof. Dr. Durmus OZDEMIR.

REFERENCES

- [1] Copeland, B. J., and Proudfoot, D. (2007). Artificial intelligence. *Philosophy of Psychology and Cognitive Science*, 429–482. <https://doi.org/10.1016/b978-044451540-7/50032-3>
- [2] Macukow, B. (2016). Neural Networks – State of Art, Brief History, Basic Models and Architecture. *Computer Information Systems and Industrial Management*, 3–14. https://doi.org/10.1007/978-3-319-45378-1_1
- [3] Seyyarer, E., Uçkan, T., Hark, C., Ayata, F., İnan, M., and Karcı, A. (2019). Applications and Comparisons of Optimization Algorithms Used in Convolutional Neural Networks. 2019 International Artificial Intelligence and Data Processing Symposium (IDAP). <https://doi.org/10.1109/idap.2019.8875929>
- [4] Kartal, M., and Duman, O. (2019). Ship Detection from Optical Satellite Images with Deep Learning. 2019 9th International Conference on Recent Advances in Space Technologies (RAST). <https://doi.org/10.1109/rast.2019.8767844>
- [5] Şeker, A., Diri, B., and Balık, H. H. (2017). Derin Öğrenme Yöntemleri Ve Uygulamaları Hakkında Bir İnceleme. *Gazi Mühendislik Bilimleri Dergisi*, 3(3), 47–64. Retrieved from <https://dergipark.org.tr/tr/pub/gmbd/issue/31064/372661>
- [6] Alzubaidi, L., Zhang, J., Humaidi, A. J., Al-Dujaili, A., Duan, Y., Al-Shamma, O., Fadhel, M. A., Al-Amidie, M., and Farhan, L. (2021). Review of deep learning: concepts, CNN architectures, challenges, applications, future directions. *Journal of Big Data*, 8(1). <https://doi.org/10.1186/s40537-021-00444-8>

- [7] Özdemir, D., and Arslan, N. N. (2022). Analysis of Deep Transfer Learning Methods for Early Diagnosis of the Covid-19 Disease with Chest X-ray Images. *Düzce Üniversitesi Bilim ve Teknoloji Dergisi*, 628–640. <https://doi.org/10.29130/dubited.976118>
- [8] Ravi, D., Wong, C., Deligianni, F., Berthelot, M., Andreu-Perez, J., Lo, B., and Yang, G.-Z. (2017). Deep Learning for Health Informatics. *IEEE Journal of Biomedical and Health Informatics*, 21(1), 4–21. <https://doi.org/10.1109/jbhi.2016.2636665>
- [9] Adeli, E., Rekik, I., Park, S. H., and Shen, D. (2020). Editorial: Predictive Intelligence in Biomedical and Health Informatics. *IEEE Journal of Biomedical and Health Informatics*, 24(2), 333–335. <https://doi.org/10.1109/jbhi.2019.2962852>
- [10] Kumamaru, K. K., Machitori, A., Koba, R., Ijichi, S., Nakajima, Y., and Aoki, S. (2018). Global and Japanese regional variations in radiologist potential workload for computed tomography and magnetic resonance imaging examinations. *Japanese Journal of Radiology*, 36(4), 273–281. <https://doi.org/10.1007/s11604-018-0724-5>
- [11] Yang, W., and Liu, J. (2013). Research and development of medical image fusion. <https://doi.org/10.1109/icmipe.2013.6864557>
- [12] Srikanth, B., and Venkata Suryanarayana, S. (2021). Multi-Class classification of brain tumor images using data augmentation with deep neural network. *Materials Today: Proceedings*. <https://doi.org/10.1016/j.matpr.2021.01.601>
- [13] Lavanyadevi, R., Machakowsalya, M., Nivethitha, J., and Kumar, A. N. (2017). Brain tumor classification and segmentation in MRI images using PNN. 2017 IEEE International Conference on Electrical, Instrumentation and Communication Engineering (ICEICE). <https://doi.org/10.1109/iceice.2017.8191888>
- [14] Julià-Sapé, M., Griffiths, J. R., Tate, R. A., Howe, F. A., Acosta, D., Postma, G., Underwood J., Majós C., and Arús, C. (2015). Classification of brain tumours from MR spectra: the INTERPRET collaboration and its outcomes. *NMR in Biomedicine*, 28(12), 1772–1787. <https://doi.org/10.1002/nbm.3439>
- [15] Louis, D. N., Perry, A., Wesseling, P., Brat, D. J., Cree, I. A., Figarella-Branger, D., Hawkins, C., Ng, H. K., Pfister, S. M., Reifenberger, G., Soffietti, R., von Deimling, A., and Ellison, D. W. (2021). The 2021 WHO Classification of Tumors of the Central Nervous System: a summary. *Neuro-Oncology*, 23(8). <https://doi.org/10.1093/neuonc/noab106>
- [16] Villa, C., Miquel, C., Mosses, D., Bernier, M., and Di Stefano, A. L. (2018). The 2016 World Health Organization classification of tumours of the central nervous system. *La Presse Médicale*, 47(11-12), e187–e200. <https://doi.org/10.1016/j.lpm.2018.04.015>

- [17] Zhou, Z., Wu, S., Chang, K.-J., Chen, W.-R., Chen, Y.-S., Kuo, W.-H., Lin, C.-C., and Tsui, P.-H. (2015). Classification of Benign and Malignant Breast Tumors in Ultrasound Images with Posterior Acoustic Shadowing Using Half-Contour Features. *Journal of Medical and Biological Engineering*, 35(2), 178–187. <https://doi.org/10.1007/s40846-015-0031-x>
- [18] Gürkahraman, K., and Karakış, R. (2021). Veri çoğaltma kullanılarak derin öğrenme ile beyin tümörlerinin sınıflandırılması. *Journal of the Faculty of Engineering and Architecture of Gazi University*, 36(2), 997–1012. <https://doi.org/10.17341/gazimmfd.762056>
- [19] Noreen, N., Palaniappan, S., Qayyum, A., Ahmad, I., Imran, M., and Shoaib, M. (2020). A Deep Learning Model Based on Concatenation Approach for the Diagnosis of Brain Tumor. *IEEE Access*, 8, 55135–55144. <https://doi.org/10.1109/access.2020.2978629>
- [20] Sultan, H. H., Salem, N. M., and Al-Atabany, W. (2019). Multi-Classification of Brain Tumor Images Using Deep Neural Network. *IEEE Access*, 7, 69215–69225. <https://doi.org/10.1109/access.2019.2919122>
- [21] Yerukalareddy, D. R., and Pavlovskiy, E. N. (2021). Brain Tumor Classification based on MR Images using GAN as a Pre-Trained Model. 2021 IEEE Ural-Siberian Conference on Computational Technologies in Cognitive Science, Genomics and Biomedicine (CSGB), 380–384. IEEE.
- [22] Divya, S., Padma Suresh, L., and John, A. (2020). A Deep Transfer Learning framework for Multi Class Brain Tumor Classification using MRI. 2020 2nd International Conference on Advances in Computing, Communication Control and Networking (ICACCCN). <https://doi.org/10.1109/icacccn51052.2020.9362908>.
- [23] Rehman, A., Naz, S., Razzak, M. I., Akram, F., and Imran, M. (2019). A Deep Learning-Based Framework for Automatic Brain Tumors Classification Using Transfer Learning. *Circuits, Systems, and Signal Processing*, 39(2), 757–775. <https://doi.org/10.1007/s00034-019-01246-3>
- [24] Deepak, S., and Ameer, P. M. (2019). Brain tumor classification using deep CNN features via transfer learning. *Computers in Biology and Medicine*, 111, 103345. <https://doi.org/10.1016/j.compbiomed.2019.103345>
- [25] Cheng, J. (2017, April 2). brain tumor dataset. Retrieved from Figshare website: https://figshare.com/articles/dataset/brain_tumor_dataset/1512427
- [26] Nickparvar, M. (2021). Brain Tumor MRI Dataset. Retrieved from Kaggle website: <https://www.kaggle.com/datasets/masoudnickparvar/brain-tumor-mri-dataset/metadata>
- [27] Luque, A., Carrasco, A., Martín, A., and de las Heras, A. (2019). The impact of class imbalance in classification performance metrics based on the binary confusion matrix. *Pattern Recognition*, 91, 216–231. <https://doi.org/10.1016/j.patcog.2019.02.023>



RESEARCH ARTICLE

**EFFECTS OF CYANIDE ON SOME ENZYME ACTIVITIES AND LIPID PEROXIDATION
IN SOME TISSUES OF CARP (*Cyprinus carpio*)**

Mustafa KAVASOĞLU^{1*}, Kazım UYSAL²

¹Kütahya Dumlupınar University, Gediz Vocational School, Department of Medical Services and Techniques, Kütahya, mustafa.kavasoglu@dpu.edu.tr, ORCID: 0000-0002-4136-6397

²Kütahya Dumlupınar University, Faculty of Arts and Sciences, Department of Biology, Kütahya, kazim.uyisal@dpu.edu.tr, ORCID: 0000-0001-6399-6616

Receive Date: 10.11.2022

Accepted Date: 11.09.2023

ABSTRACT

In this study, the changes in the catalase, superoxide dismutase, carbonic anhydrase activities, and the levels of malondialdehyde in the muscle, liver, gill, skin, brain, and intestinal tissues of carps (*Cyprinus carpio*), in which 0.1 mg/L and 0.2 mg/L concentrations cyanide were added, were investigated. It was determined that the catalase, superoxide dismutase, and carbonic anhydrase activities of fish exposed to cyanide were inhibited in some tissues and increased in some tissues. Especially in 15-day experiments statistically significant decreases were observed in enzyme activities. It was observed that malondialdehyde levels, which are one of the important markers of cell damage of tissues generally increased with cyanide exposure. In this study, malondialdehyde levels increased statistically significant in the liver and intestinal tissues in the 3-day experiment and the muscle tissue in the 15-day experiment.

Keywords: *Cyprinus carpio*, Cyanide, Enzyme, Lipid Peroxidation.

1. INTRODUCTION

Cyanide is a molecule formed by the triple bond of carbon and nitrogen atom. Cyanide and its compounds are used in various areas of industry like metal coating, rubber production, paint industry, and drug production. Cyanide is produced commercially to use in industry and it is also produced by some plant, insect, and bacteria species naturally. For instance, almond contains 297 mg/kg, wild cherry contains 140-370 mg/100g, and cassava contains 104 mg/100g cyanide [1]. Cyanide is released into the environment by natural means as well as industrial sources. After cyanide is used in industry, it is either chemically decomposed or stored in waste ponds. The discharge of cyanide as waste is also increasing day by day. Since cyanide is generally used with metal compounds, it also causes heavy metal pollution in the waters where it is discharged. In addition, high-bonding cyanide tends to form toxic complexes again [2].

Cyanide can enter the water sources from a variety of sources, such as wastewater from the metal plating and iron and steel industries, mining, and pesticides [3]. Efforts are made to reduce these rates by passing the wastewater through various processes. Although it is reduced, due to the highly toxic nature of cyanide, even low concentrations pose a danger to aquatic life in natural waters. Fish are the most sensitive group of aquatic organisms to pollutants. Therefore, even at low concentrations, fish are adversely affected by cyanide toxicity, causing permanent problems even if death does not occur. It has been reported in the literature that concentrations of 0.01 and 0.1 mg/L may be toxic to fish [4]. Wild et al. [5] reported that cyanide is in the range of 0.0001 - 0.05 mg/L in natural waters. EPA has also set the cyanide limit for freshwater environments as 0.052 mg/L [6].

Fish are the living species that are maximum affected by cyanide pollution in the aquatic environment. Being in the last link of the biological chain makes them so vulnerable. Cyanide causes various problems in fish, especially the lethal effect. When fish are exposed to 5-7.2 pg free CN/L cyanide, their swimming and reproductive systems are damaged, while they are at risk of death when exposed to 20-76 pg free CN/L cyanide [7]. David and Kartheek [8] found decreases in catalase, superoxide dismutase, glutathione peroxidase, and glutathione S-transferase activities in carp fish to which they applied sodium cyanide at a concentration of 0.1 mg/L for 10 and 20 days compared to the control group. For another freshwater fish species, *Labeo rohita*, it was reported that ATPase enzyme was inhibited in lethal (0,32 mg/L) and sublethal (0,064 mg/L) concentrations [9]; glycogen and pyruvate amounts decreased at sublethal (0,106 ve 0,064 mg/L) concentrations [10]; the levels of structural and soluble protein decreased at sublethal (0,2 mg/L) concentration [11]. Bonanno et al., found that blood thiocyanate levels in *Amphiprion clarkii*, to which they applied 50 ppm cyanide for 20 and 45 seconds, reached levels of 301 - 468 ppb [12]. In a previous study, in which we tried to reveal the acute toxic effect of 0.5 mg/L cyanide, it was observed that cyanide at this concentration caused cellular damage and affected some antioxidant enzyme activities in carp [13].

In this study, it was aimed to determine the toxic potential of cyanide in aquatic environments and aquatic organisms, taking into account its dangerous properties. For this purpose, catalase, superoxide dismutase, and carbonic anhydrase activities and changes in malondialdehyde levels in muscle, liver, gill, brain, skin, and intestinal tissues of carp were investigated in the presence of cyanide.

2. SUBJECTS AND METHODS

2.1. Test Environment, Fish Nutrition, and Anesthesia

In this study, sump systems consisting of 30x40x60 cm aquariums were used. Each system consisted of 5 aquariums, 4 aquariums, and 1 cleaning tank (Figure 1).

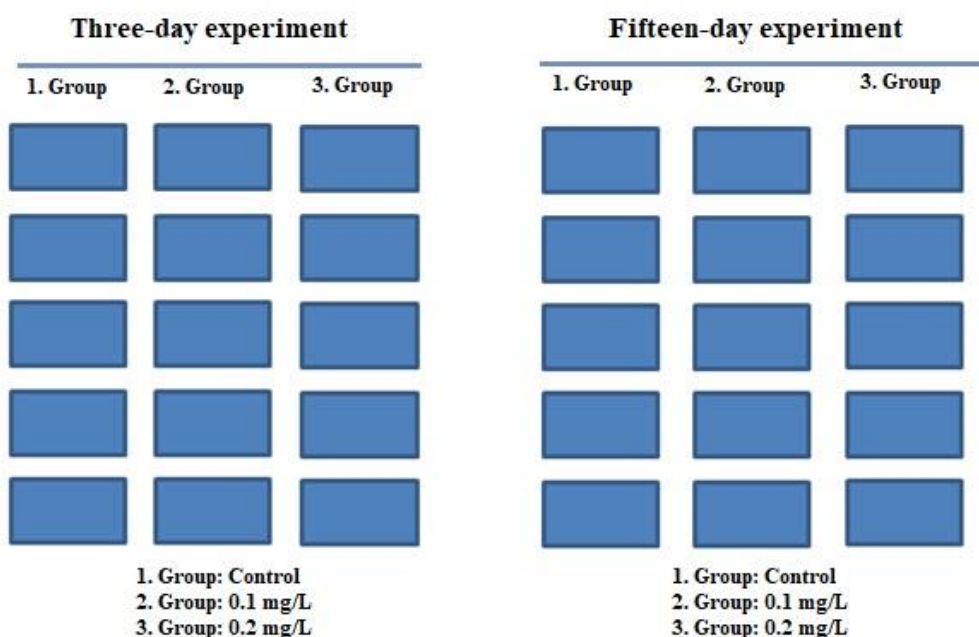


Figure 1. Experiment aquarium model (Each blue box means an aquarium).

The aquarium at the bottom of the system was determined as a cleaning tank and no fish were placed in this aquarium. A motor was added to the bottom aquarium and the circulation of the water in the system was ensured. Thus, aquariums with homogeneous water quality were obtained. Organic wastes were kept by the fiber material placed in the bottom aquarium. At the same time, an ultraviolet lamp was operated for 2 hours a day to clean the microorganisms in the water. The temperature of the waters in the aquariums is set at 22°C. To ensure the oxygenation of the water, an air stone was attached to each aquarium and the oxygen content of the aquarium water was not reduced below 6 mg/L. Aquarium maintenance was followed regularly. The water quality in the aquariums is kept at a level that does not adversely affect the health of the fish [14]. No fish died during the experiment.

Fish, whose height and weight were measured, were randomly placed in each aquarium as 4 fish. Since each system consisted of 4 aquariums, 16 fish were used in each group. Fish were fed with commercial feed at the rate of 1% of live weight. Sodium cyanide (NaCN) was used as the cyanide source (0.1 mg/L and 0.2 mg/L). The experiment continued for 3 days and 15 days.

At the end of the experiment, the fish were taken from the aquariums and transferred to the anesthesia pool. Clove oil (600 mg/L), which is both healthier and more effective than other chemical anesthetics, is used as an anesthetic agent [15, 16].

2.2. Biochemical Analysis

Fish taken from anesthesia were dissected and muscle, liver, gill, skin, brain, and intestinal tissues were removed. They were washed with physiological water and kept at the temperature of -80°C until the analysis are made. Before the biochemical analysis, the tissues were homogenized within $50\ \mu\text{M}$, $\text{pH} = 7.4$ cooled phosphate buffer at 8000 rpm for two minutes. The supernatant obtained after the homogenates were centrifuged at 9500 rpm at $+4^{\circ}\text{C}$ for 30 minutes was used for the biochemical analysis.

In the experiments, catalase (CAT) activity analysis was carried out according to the method determined by Aebi [17]. According to this method, the decrease of hydrogen peroxide in the presence of CAT was monitored spectrophotometrically at a wavelength of 240 nm. CAT analysis was carried out following the order specified in Table 1.

Table 1. CAT activity measurement procedure.

	Blind	Experiment
Phosphate buffer	0.01 ml	-
H ₂ O ₂ solution	3.00ml	3.00ml
Sample	-	0.01 ml

The specific catal activity calculation is as follows:

$$\frac{nkat}{mg\ protein} = \left[\left(\frac{\Delta A_c}{t} \right) \left(\frac{1}{\epsilon_{H_2O_2}} \right) \left(\frac{1}{\epsilon} \right) \left(\frac{V_T}{V_S} \right) \left(\frac{1000\mu L}{10\mu L} \right) \right] \frac{DC}{Protein\ concentration} \quad (1)$$

(ΔA_c : Absorbance change, ϵ H₂O₂ (molar absorption coefficient of H₂O₂) = $40,98\ \text{M}^{-1}\text{cm}^{-1}$, V_T : Total volume, V_S : Sample volume, DC : Dilution coefficient)

Measurement of superoxide dismutase (SOD) activity is based on spectrophotometric monitoring of the effect of SOD enzyme on the autoxidation of 6-hydroxy dopamine at wavelengths of 490 nm. [18, 19, 20, 21]. SOD analysis was carried out following the order specified in Table 2.

Table 2. SOD activity measurement procedure.

	Blind	Experiment
0.05 M phosphate buffer (pH 7.4)	740 μl	690 μl
Sample	-	50 μl
0.01 M 6-OHDA solution	10 μl	10 μl

The specific SOD activity calculation is as follows:

$$\frac{EU}{mg\ protein} = \frac{\left[\left(\frac{A_B - A_S}{A_K} \right) DC (V_T - V_S) \left(\frac{3\ mL}{V_S} \right) \right]}{Protein\ concentration} \quad (2)$$

(EU: Enzyme Unit, A_B: Blind absorbance, A_S: Sample absorbance, DC: Dilution coefficient, V_T: Total volume, V_S: Sample volume)

Carbonic anhydrase (CA) activity depends on the principle of having the ability to hydrolyze ester components by this enzyme. CA, p-nitrophenyl acetate, hydrolyzes to p-nitrophenol or p-nitrophenolate. This product indicates absorbance spectrophotometrically at 348 nm wavelength [22, 23]. CA analysis was carried out following the order specified in Table 3.

Table 3. CA activity measurement procedure.

	Blind	Experiment
0.05 M TRIS buffer (pH 7.4)	1.3 mL	1.3 mL
Sample	-	0.1 mL
Substrate	1 mL	1 mL
Pure water	0.7 mL	0.6 mL

The specific CA activity calculation is as follows:

$$\frac{EU}{mg\ protein} = \left(\frac{A_{last} - A_{first} - A_{blind}}{5} \right) \left(\frac{DC}{Protein\ concentration} \right) \quad (3)$$

A_{last}: Last absorbance, A_{first}: First absorbance, A_{blind}: Blind absorbance, DC: Dilution coefficient

The molar absorption coefficient of p-nitrophenol and p-nitrophenolate formed as a result of the activity of the CA enzyme (ε): 5.4x10⁻³M⁻¹cm⁻¹, the molar absorption coefficient of p-nitrophenyl acetate used as a substrate (ε): 0.4x10⁻³M⁻¹cm⁻¹. Dividing the absorption difference at 348 nm wavelength used in the formula by 5 gives the ion concentrations of p-nitrophenol and p nitrophenolate.

Malondialdehyde (MDA), is a product of lipid peroxidation and shows a colorful reaction with thiobarbituric acid (TBA). The reaction of MDA with TBA is read on a spectrophotometer at 532 nm wavelength [24]. MDA analysis was carried out following the order specified in Table 4.

Table 4. MDA activity measurement procedure.

	Blind	Experiment
TCA (10%)	2.5 ml	2.5 ml
Plasma	-	0.5 ml
Distilled water	0.5 ml	-

It was incubated in a 90°C water bath for 15 minutes. It was kept on ice for 15 minutes.

Supernatant	2 ml	2 ml
TBA (0.675%)	1 ml	1 ml

It was incubated in a 90°C water bath for 15 minutes. It was kept on ice for 15 minutes.

According to the results obtained, the concentration-absorbance graph was obtained. The concentration values of the samples were calculated by considering this graph. Protein determination was carried out using the Bradford method which is based on reading the complex at 595 nm wavelength [25]. In protein determination, firstly, a standard graph was obtained by using bovine serum albumin, which contains 1 mg of protein in 1 mL. In the calculation, the concentrations of the samples were determined from the standard graph. For the determination of protein in the tissue, the procedures were applied in the order indicated in the table below, and the absorbance was measured at 595 nm wavelength after a 10-minute waiting period.

Table 5. Protein amount measurement procedure.

	Blind	Experiment
Protein dye	5 mL	5 mL
Sample	-	0.1 mL
Pure water	0.1 mL	-

2.3. Statistical Analysis

In this study, SPSS 22 program was used for statistical analysis. Tables were created by calculating the mean and standard error values. The statistical difference between the groups which contain different concentrations of cyanide (0.1 mg/L and 0.2 mg/L) was determined by the One-Way ANOVA test. The statistical difference between the groups in which cyanide was applied at different times was determined by using Student's t-test. The results were analyzed at $p < 0.05$ significance level.

3. RESULTS AND DISCUSSION

3.1. Catalase Activities

Cyanide is a molecule that forms intracellular reactive oxygen species and leads to the accumulation of hydrogen peroxide and superoxide anion [26, 27]. CAT is a crucial enzyme that provides the defence of cells against oxidative stress. It converts the hydrogen peroxide molecule, which occurs in metabolic events such as phagocytosis and mitochondrial electron transport, into water and oxygen gas. Also, it tries to eliminate the loss of function that occurs because of various pollutants in the metabolism. In such circumstances, CAT activity could be inhibited. In this study, it was observed that the CAT activities of *C. carpio* exposed to cyanide at concentrations of 0.1 and 0.2 mg/L for three and fifteen days decreased compared to the control group (Table 6).

Table 6. CAT activities of fish used in the study.

	Catalase (nkat/mg protein)					
	3 Days			15 Days		
	C	0.1 mg/L	0.2 mg/L	C	0.1 mg/L	0.2 mg/L
Muscle	0.015±0.00	0.009±0.00	0.011±0.00	0.018±0.00 ^a	0.011±0.00 ^b	0.011±0.00 ^b
Liver	1.303±0.09	0.932±0.11	1.053±0.10	1.354±0.12	1.081±0.07	1.096±0.05
Gill	0.042±0.00	0.028±0.00	0.036±0.00	0.095±0.03	0.028±0.00	0.033±0.01
Skin	0.015±0.00	0.010±0.00	0.016±0.00	0.036±0.00	0.140±0.00	0.120±0.00
Brain	0.009±0.00	0.001±0.00	0.002±0.00	0.002±0.00	0.001±0.00	0.001±0.00
Intestine	0.192±0.03	0.080±0.01	0.062±0.02	0.092±0.03	0.122±0.04	0.175±0.05

(C: Control; Values shown with different letters contain statistical significance)

Only fish exposed to cyanide at concentrations of 0.1 and 0.2 mg/L for fifteen days increased their CAT activities in intestinal tissues compared to the control group. When the literature is examined, the studies are seen that CAT activities decrease depending on the applied chemical. David et al. [28] reported that NaCN decreased CAT activities in various tissues of fish in their study they carried out with fingerlings of common carp. When lethal and sublethal cyanide exposure, it was reported that the most significant decrease was seen in liver tissues, and then in gill, muscle, and brain tissues [28]. In another study, it was reported that exposure to 0.1 mg/L cyanide concentration for ten and twenty days decreased CAT activities in the liver tissues of carp fish compared to the control group [8]. When the related results in the literature are examined, it is understood that the findings of this study are coherent with the findings in the literature. When cyanide enters the living body, it forms a complex with the cytochrome c oxidase enzyme and prevents the functioning of enzymes such as CAT by blocking the antioxidant enzyme system. If this condition occurs at the acute level in high concentration, it is also reported to cause rapid death [28, 29].

3.2. Superoxide Dismutase Activities

SOD is another antioxidant enzyme that operates collectively with CAT. SOD catalyzes the free oxygen radical that formed in the cell to gaseous oxygen and hydrogen peroxide. In this study, while SOD enzyme was inhibited in muscle and skin tissues of *C. carpio* exposed to cyanide for three days, SOD activity increased in the liver, brain, gill, and intestinal tissues. SOD activities of muscle, liver, and intestinal tissues of *C. carpio* exposed to cyanide at concentrations of 0.1 mg/L and 0.2 mg/L for fifteen days decreased, and SOD activities of brain and gill tissues increased (Table 7).

Table 7. SOD activities of fish used in the study.

	Superoxide dismutase (EU/mg protein)					
	3 Days			15 Days		
	C	0.1 mg/L	0.2 mg/L	C	0.1 mg/L	0.2 mg/L
Muscle	48.92±1.84	45.27±1.18	44.03±1.5	46.84±1.06 ^a	46.17±1.02 ^{ab}	41.95±1.48 ^b
Liver	67.28±2.06	76.14±3.46	72.89±4.65	94.36±15.35	72.71±2.62	74.26±3.87
Gill	12.38±6.15	32.27±7.3	39.43±5.83	24.67±6.23 ^a	40.72±5.32 ^{ab}	50.3±3.68 ^b
Skin	79.66±2.66	69.28±5.38	71.26±2.37	89.61±1.30 ^a	108.96±3.95 ^b	79.11±4.06 ^a

Brain	85.57±3.71	91.89±1.84	95.43±1.66	75.13±1.04	80.65±0.91	84.36±6.14
Intestine	55.22±1.14	66.72±5.05	55.78±8.42	71.31±4.46 ^a	51.14±2.25 ^b	56.47±3.34 ^b

(C: Control; Values shown with different letters contain statistical significance)

Generally, SOD is inhibited by the joining of pollutants in the body. When the findings obtained in the study were examined, it was observed that the SOD enzyme was inhibited in only two tissues in a three-day exposure to cyanide, and more tissues in a fifteen-day exposure to cyanide. Accordingly, it can be said that the increase of cyanide exposure time mostly inhibits the SOD activity of *C. carpio* tissues. However, it was also determined that the SOD activities of some tissues of *C. carpio* increased with cyanide exposure. It may well be argued that the tissues that increase their activity do this as a reaction to cyanide exposure. David and Kartheek [8] reported that SOD activities were inhibited in the liver tissues of the *C. carpio* exposed to 0,1 mg/L cyanide. They related this condition to the deformation caused by reactive oxygen types in tissues after cyanide enters metabolism. In a previous study conducted by us, it was concluded that the SOD enzyme was inhibited in the liver tissue of *C. carpio* exposed to cyanide at a concentration of 0.5 mg/L for three days and increased its activity in the brain, muscle and gill tissue [13]. Responses of living things to pollutants vary according to many parameters such as exposure duration, temperature, pH, and metabolic condition. As a result, when we considered results derived from fish that were exposed to cyanide for 15 days, it could be seen that SOD activities were inhibited in more tissues. This condition shows that SOD inhibition can increase with higher concentrations and longer duration.

3.3. Carbonic Anhydrase Activities

CA is a metalloenzyme that contains zinc in its active site and catalyzes the hydrolysis of carbon dioxide and water. CA has particular importance for fish that have gill respiration. CA is responsible for the excretion of ammonia, ion regulation, osmoregulation, and acid-base balance in fish gills [30]. Besides, it is also known that the CA enzyme has the mission of destructing free oxygen radicals and preventing oxidative stress [31]. In this study, it was determined that the CA activities of *C. carpio* exposed to cyanide for three days increased in muscle, intestine, and skin tissues and decreased in liver and brain tissue (Table 8).

Table 8. CA activities of fish used in the study.

	Carbonic anhydrase (EU/mg protein)					
	3 Days			15 Days		
	C	0.1 mg/L	0.2 mg/L	C	0.1 mg/L	0.2 mg/L
Muscle	0.068±0.00	0.104±0.00	0.102±0.00	0.135±0.02 ^a	0.087±0.01 ^a	0.075±0.00 ^b
Liver	2.352±0.50	1.145±0.34	1.136±0.11	1.191±0.11	2.778±0.75	2.418±0.35
Gill	0.244±0.01	0.236±0.02	0.369±0.01	0.233±0.02	0.215±0.01	0.232±0.01
Skin	0.371±0.03	0.553±0.13	0.453±0.07	0.348±0.03	0.450±0.08	0.419±0.04
Brain	0.229±0.03	0.228±0.03	0.200±0.02	0.292±0.03	0.279±0.02	0.309±0.04
Intestine	1.078±0.17	1.088±0.16	1.119±0.29	1.079±0.19 ^a	0.716±0.24 ^{ab}	0.475±0.08 ^b

(C: Control; Values shown with different letters contain statistical significance)

In addition, it was determined that the CA activities of the gill tissues of fish exposed to 0.1 mg/L cyanide concentration decreased, while the CA activities of gill tissues of the fish exposed to 0.2 mg/L cyanide concentration increased. The results derived from the muscle, liver and intestine tissues of fish exposed to cyanide for 15 days are opposite of the ones exposed to cyanide for three days. The inhibition of CA activities in the muscle and intestine tissues is found to be statistically significant ($p < 0,05$) for the fish exposed to cyanide of 0.2 mg/L for 15 days. Alim et al. [32] purified the CA enzyme found in the gills of tuna (*Thunnus thynnus*) and analyzed the inhibition effect of various metals for the CA enzyme in vitro. As a result of the study, they determined that the inhibition effects of metals were in the form of $Ag^+ > Cu^{2+} > Pb^{2+} > Zn^{2+} > Cd^{2+} > Co^{2+}$ and that Ag^+ metal was a strong CA inhibitor. They also mentioned that CA activity can be a good toxicology biomarker. Ceyhun et al. [33] investigated the effects of 0.25, 1.0 and 2.5 $\mu\text{g/L}$ concentrations of deltamethrin, a pesticide, on CA activity in rainbow trout gill tissue and reported that it significantly inhibited CA activities within 24 to 48 hours.

While freshwater fish release ions such as H^+ , NH_4^+ and HCO_3^- by diffusion, they absorb Na^+ and Cl^- ions that form salt. This condition is known as osmoregulation and CA activity is vital for the regular occurrence. Literature findings and data obtained from this study show that various chemicals inhibit CA activity in metabolism. This condition can even result in the death of living things. However, in the findings obtained in this study, it was observed that the CA enzyme increased its activity in some tissues with the presence of cyanide. It could be said that the increase of CA enzyme in various tissues is for the reason of tolerating stress conditions resulted from cyanide.

3.4. Malondialdehyde Levels

Lipid peroxidation can be briefly defined as the degradation of fats as a result of oxidation. This event occurs in unsaturated fatty acids of cell membrane phospholipids [34]. Lipid peroxidation is one of the most significant indicators of cell injury. MDA that occurs during the lipid peroxidation process is frequently used today as a good biomarker of oxidative damage [35, 36]. Oxidative stress caused by cyanide in metabolism is primarily responsible for the formation of lipid peroxidation in the cell. In this study, *C. carpio* were exposed to cyanide of 0.1 mg/L and 0.2 mg/L concentrations. When the findings were examined, it was observed that MDA levels increased in all tissues except brain and gill tissues after exposure to cyanide for three days (Table 9).

Table 9. MDA amounts of fish used in the study.

	Malondialdehyde (nmol/mL)					
	3 Days			15 Days		
	C	0.1 mg/L	0.2 mg/L	C	0.1 mg/L	0.2 mg/L
Muscle	168.22±33.63	257.23±31.34	251.38±33.34	152.18±29.64 ^a	254.25±28.47 ^b	290.52±28.69 ^b
Liver	114.20±16.22 ^a	196.55±14.05 ^b	162.24±25.59 ^{ab}	83.29±13.39	124.00±4.19	148.47±9.44
Gill	176.20±9.45	173.56±17.10	168.87±21.12	135.72±15.59	157.24±11.62	167.24±12.03
Skin	58.94±21.46	94.18±7.42	75.76±17.12	38.00±19.36	70.72±15.78	76.53±16.03
Brain	99.80±19.34	99.65±21.03	86.12±10.34	100.28±14.32	102.09±16.27	111.86±18.09
Intestine	101.65±8.24 ^a	145.77±10.37 ^{ab}	166.35±18.23 ^b	134.82±14.78	179.53±35.75	167.29±19.83

(C: Control; Values shown with different letters contain statistical significance)

Especially in the liver, which is an organ with a high metabolic rate, MDA levels increased statistically significantly. Hermenean et al. [37] determined that the MDA amounts in the liver and kidney tissues of *Leuciscus cephalus* they caught from the parts of the Tur River rich in metals such as iron, zinc, copper, cadmium and lead in Romania were quite high. It was determined that MDA levels increased significantly in the liver and gill tissues of carp exposed to permethrin as a different toxic substance [38]. David and Kartheek [8] reported that 0.1 mg/L NaCN concentration significantly increased the amount of lipid peroxidation in carps. Fish contain polyunsaturated fatty acids, which have a very important role in the maintenance of cell membrane-bound functions. The high MDA ratio and lipid peroxidation obtained in this study may be due to the high content of polyunsaturated fatty acids in fish.

4. CONCLUSIONS

When the results obtained from this study were examined, it was seen that the degree of effect of cyanide in different tissues of *C. carpio* was not the same. It was determined that the liver, gill and skin tissues of *C. carpio* exposed to cyanide at concentrations of 0.1 mg/L and 0.2 mg/L were the most adversely affected. This condition indicates that even though cyanide does not show a vast amount of accumulation in metabolism, it generates tissue damage in the living things it enters.

The reaction of a tissue against a chemical agent may differ from organism to organism. In the same organism reaction of different tissues may also differ. In this study, it can be said that the different levels of enzyme activities in *C. carpio* exposed to cyanide at 0.1 mg/L and 0.2 mg/L concentrations for three and fifteen days may be due to the different biochemical effects of cyanide in different tissues.

Increased lipid peroxidation in the cell is one of the important markers of cell damage. In this study, a general inference can be drawn as cyanide can cause cell injury since the MDA level, which is a product of lipid peroxidation, is on the rise as a result of cyanide exposure.

ACKNOWLEDGEMENTS

This study was produced from Mustafa KAVASOĞLU's doctoral thesis. This study was presented at the "International Symposium on Fisheries and Aquatic Sciences" held in Antalya (Turkey) on 3 - 5 November 2016. This study was supported by Kütahya Dumlupınar University Scientific Research Projects Commission (Grant No: 2015 - 80). The authors would like to thank the Kütahya Dumlupınar University Scientific Research Projects Commission for funding the research.

REFERENCES

- [1] Kuyucak, N., and Akçıl, A. (2013). Cyanide and removal options from effluents in gold mining and metallurgical processes, *Minerals Engineering* 50-51, 13-29.

- [2] Patil, Y.B., and Paknikar, K.M. (2000). Biotoxification of silver-cyanide from electro-plating industry wastewater, *Letters in Applied Microbiology* 30, 33-37.
- [3] Dash, R.R., Gaur, A., and Balomajumder, C. (2009). Cyanide in industrial wastewaters and its removal: A review on biotreatment, *Journal of Hazardous Materials* 163, 1-11.
- [4] Prashant, M.S., and Neelagund, S.E. (2007). Free cyanide-induced biochemical changes in nitrogen metabolism of the indian major carp *Cirrhinus mrigala*, *Journal of Basic & Clinical Physiology & Pharmacology* 18(4), 277-287.
- [5] Wild, S.R., Rudd, T., and Neller, A. (1994). Fate and effects of cyanide during wastewater treatment processes, *Sci. Total Environ* 156, 93-107.
- [6] EPA (2002). National Recommended Water Quality Criteria: 2002.
- [7] Koçan, F. (2021). Environmental effects of cyanide gold production from ore, *International Journal of Engineering Research and Development*, 13(1), 250-264.
- [8] David, M., and Kartheek, R.M. (2016). In vivo studies on hepato-renal impairments in freshwater fish *Cyprinus carpio* following exposure to sublethal concentrations of sodium cyanide, *Environ Sci Pollut Res*, 23, 722-733.
- [9] Dube, P.N., and Hosetti, B.B. (2011). Inhibition of ATPase activity in the freshwater fish *Labeo rohita* (Hamilton) exposed to sodium cyanide, *Toxicology Mechanisms and Methods* 21(8), 591-595.
- [10] Dube, P.N., Shwetha, A., and Hosetti, B.B. (2013). Effect of exposure to sublethal concentrations of sodium cyanide on the carbohydrate metabolism of the Indian Major Carp *Labeo rohita* (Hamilton, 1822), *Pesq. Vet. Bras.* 33(7), 914-919.
- [11] Manjunatha, B., Mohiddin, G.J., Ortiz, J., and Selvanayagam, M. (2014). Effect of exposure to sublethal concentrations of sodium cyanide on the biochemical aspects in the liver of the freshwater fish, *Labeo rohita*, *International Journal of Pharmacology and Pharmaceutical Sciences* 2(1), 7-15.
- [12] Bonnano, J.A., Breen, N.E., Tlusty, M.F., Andrade, L., and Rhyne, A.L. (2021). The determination of thiocyanate in the blood plasma and holding water of *Amphiprion clarkii* after exposure to cyanide. *PeerJ*. 9:e12409.
- [13] Kavasoglu, M., Sarioğlu, Y., Uysal, K., Dönmez, M., Altıkat, S., Yetek, İ., and Kuru, H. İ. (2015). Effect of sodium cyanide on antioxidant enzyme activities and lipid peroxidation in some tissues of Mirror Carp (*Cyprinus carpio*). *Pakistan J. Zool.* 47(6). 1777-1782.
- [14] Lloyd, R. (1992). *Pollution and Freshwater Fish*, Fishing News Book, UK.

- [15] Han, M. C., Sağlıyan, A., and Polat, E. (2016). Akvaryum balıklarında karanfil yağının anestetik etkilerinin araştırılması, *Harran Üniversitesi Veteriner Fakültesi Dergisi*, 5 (1), 12 – 17.
- [16] Otay, T., Küçükgül, A., Pala, A., and Şeker, E. (2014). Sazan balıklarının anesteziinde karanfilin kullanımı, *Bilim ve Gençlik Dergisi*, 2, 43 – 50.
- [17] Aebi, H. (1974). *Catalase Methods of Enzymatic Analysis*, B. HU. New York and London, Academic, Press Inc, 673-677.
- [18] Aydemir, T., and Tarhan, L. (2001). Purification and partial characterization of superoxide dismutase from chicken erythrocytes, *Turkish Journal of Chemistry* 24, 451-459.
- [19] Crosti, N., Servidei, T., Bajer, J., and Serra, A. (1987). Modification of 6- hydroxydopamine technique for the correct determination of superoxide dismutase, *J.Clin. Chem. Clin. Biochem.* 25, 265-266.
- [20] Heikkila, R.E., and Cabbat, F. (1976). A sensitive assay for superoxide dismutase based on the autoxidation of 6-hydroxydopamine, *Analytical Biochemistry* 75, 356-362.
- [21] Tarhan, L., and Tüzmen, M.N. (2000). Some properties of Cu, Zn-superoxide dismutase from sheep erythrocyte, *Turkish Journal of Chemistry* 24, 109-116.
- [22] Armstrong, J., Mc, D., Myers, D.V., Verpoorte, J.A., and Edsall, J.T. (1966). Purification and properties of human erythrocyte carbonic anhydrase, *J. Biol. Chem.* 214, 5137.
- [23] Kandel, M., Gonall, A.G., Wong, S., and Kondel, S.I.. (1970). Some characteristics of human, bovine and horse carbonic anhydrase as revealed by inactivation studies, *J. Biol.Chem.* 245, 2444.
- [24] Draper, H.H., and Hadley, M. (1990). Malondialdehyde determination as index of lipid peroxidation, *Method Enzymol* 180, 421-431.
- [25] Bradford, M.M. (1976). A rapid and sensitive method for the quantitation of microgram quantities of protein utilizing the principle of protein-dye binding, *Anal. Biochem.* 72, 248.
- [26] Daya, S.S., Walker, R.B., and Anoopkumar-Dukie, S.S. (2000). Cyanide-induced free radical production and lipid peroxidation in rat brain homogenate is reduced by aspirin, *Metab. Brain Dis.* 15, 203-210.
- [27] Douglas, C.J., Krishnan, P., Li, L., Palur, G.G., Yan, S., Joseph, L.B., and Gary, E.I. (2003). Cyanide enhancement of dopamine-induced apoptosis in mesencephalic cells involves mitochondrial dysfunction and oxidative stress, *Neurotoxicology* 24, 333-342.

- [28] David, M., Munaswamy, V., Halappa, R., and Marigoudar, S.R. (2008). Impact of sodium cyanide on catalase activity in the freshwater exotic carp, *Cyprinus carpio* (Linnaeus), Pesticide Biochemistry and Physiology 92, 15-18.
- [29] Eisler, R. (1991). Cyanide Hazards to Fish, Wildlife, and Invertebrates: A Synoptic Review, Contaminant Hazard Reviews, Report 23.
- [30] Lionetto, M.G., Giordano, M.E., Vilella, S., and Schettino, T. (2000). Inhibition of eel enzymatic activities by cadmium, Aquat. Toxicol. 48, 561-571.
- [31] Raisanen, S.R., Lehenkari, P., Tasanen, M., Rahkila, P., Harkonen, P.L., and Vaananen, H.K. (1999). Carbonic anhydrase III protects cells from hydrogen peroxide-induced apoptosis. FASEB J. 13, 513-522.
- [32] Alim, Z., Çamur, B., Beydemir, Ş., and Küfrevioğlu, Ö.İ. (2014). The correlation between some metal concentrations and carbonic anhydrase activity in Tuna (*Thunnus Thynnus* Linnaeus, 1758) Gill, Hacettepe J. Biol. & Chem. 42(2), 219-224.
- [33] Ceyhun, S.B., Şentürk, M., Erdoğan, O., and Küfrevioğlu, Ö.İ. (2010). In vitro and in vivo effects of some pesticides on carbonic anhydrase enzyme from rainbow trout (*Oncorhynchus mykiss*) gills, Pesticide Biochemistry and Physiology 97, 177-181.
- [34] Yarsan, E. (1998). Lipid peroksidasyon olayı ve önlenmesine yönelik uygulamalar, Y. Y. Ü. Vet. Fak. Derg. 9(1-2), 89-95.
- [35] Hodgson, E. (2004). A textbook of modern toxicology, Wiley, Hoboken.
- [36] Paskerova, H., Hilscherova, K., and Blaha, L. (2012). Oxidative stress and detoxification biomarker responses in aquatic freshwater vertebrates exposed to microcystins and cyanobacterial biomass, Environ Sci Pollut Res 19, 2024-2037.
- [37] Hermenean, A., Damache, G., Albu, P., Ardelean, A., Ardelean, G., Ardelean, D.P., Horge, M., Nagy, T., Braun, M., Zsuga, M., Keki, S., Costache, M., and Dinischiotu, A. (2015). Histopathological alterations and oxidative stress in liver and kidney of *Leuciscus cephalus* following exposure to heavy metals in the Tur River, North Western Romania, Ecotoxicology and Environmental Safety 119, 198-205.
- [38] Uğurer, O. (2020). Investigation of antioxidant changes in common carps fish (*Cyprinus carpio* L. 1758) exposed to permethrin. Master thesis, Aksaray University Science Institute, Aksaray.

APPENDIX

T.C.
DUMLUPINAR ÜNİVERSİTESİ
HAYVAN DENEYLERİ YEREL ETİK KURULU
ARAŞTIRMA BAŞVURUSU ONAYI

BAŞVURU BİLGİLERİ	ARAŞTIRMANIN ADI	Kütahya İl'indeki bazı su kaynaklarında siyanür miktarlarının tespiti ve siyanür'ün sazan balığı (<i>Cyprinus carpio</i>) üzerine bazı etkilerinin araştırılması
	ARAŞTIRMA YÜRÜTÜCÜSÜ KURUMU	Doç. Dr. Kazım UYSAL DPU Fen Edebiyat Fakültesi Zooloji Anabilim Dalı
	PROJE YÜRÜTÜCÜSÜ KURUMU	Doç. Dr. Kazım UYSAL DPU Fen Edebiyat Fakültesi Zooloji Anabilim Dalı
	YARDIMCI ARAŞTIRICILAR	Doç. Dr. Kazım UYSAL Uzman Biyolog Mustafa KAVASOĞLU Uzman Biyolog Cemal YILDIZ
	ARAŞTIRMANIN TAHMİNİ SÜRESİ	12 Ay
	KULLANILACAK HAYVAN TÜRÜ VE SAYISI	Balık(Pallu Sazan-Cyprinus carpio) – 120 adet
DESTEKLEYİCİ KURULUŞ	TÜBİTAK	

DEĞERLENDİRİLEN İLGİLİ BELGELER	Belge Adı	Tarihi
	ARAŞTIRMA BAŞVURU FORMU	12.11.2014

KARAR BİLGİLERİ	Karar No : 2014.12.03	Tarih : 19.11.2014
	Yukarıda başvuru bilgileri verilen araştırma projesi gerekçe, amaç ve yöntemler dikkate alınarak görüşüldü ve ilgili belgeler incelendi. Projenin etik açıdan uygun olduğuna, çalışmanın aşağıdaki hususlar dikkate alınarak yürütülmesine ve sorumlu araştırmacıya iletmesine OY BİRLİĞİ ile karar verildi. 1) Projede herhangi bir değişiklik gerektiğinde kurulumuzdan onay alınması, 2) Projede çalışacağı bildirilen araştırmacılar değişikliği olduğunda kurulumuzdan onay alınması, 3) Deneysel hayvanları üzerinde yapılacak girişimin başlangıç ve bitiş tarihinin bildirilmesi, 4) Çalışma süresinde tamamlanamaz ise ek süre talebinde bulunulması, 5) Çalışma tamamlandığında sonuç raporunun gönderilmesi.	

ETİK KURUL BİLGİLERİ

ÜYELER

Unvanı / Adı / Soyadı EK Üyeliği	Uzmanlık Dalı	Kurumu	İlişki (*)	İmza
Doç. Dr. Aynur GÜLCAN Başkan	Mikrobiyoloji ve Klinik Mikrobiyoloji Anabilim Dalı	Tıp Fakültesi	<input type="checkbox"/> E <input checked="" type="checkbox"/> H	
Yrd. Doç. Dr. Ahmet KOÇAK Üye	Histoloji ve Embriyoloji Anabilim Dalı	Tıp Fakültesi	<input type="checkbox"/> E <input checked="" type="checkbox"/> H	
Yrd. Doç. Dr. Sezer AKÇER Üye	Anatomi Anabilim Dalı	Tıp Fakültesi	<input type="checkbox"/> E <input checked="" type="checkbox"/> H	
Yrd. Doç. Dr. Ceylan AYADA Üye	Fizyoloji Anabilim Dalı	Tıp Fakültesi	<input type="checkbox"/> E <input checked="" type="checkbox"/> H	
Yrd. Doç. Dr. Hasan METİNEREN Üye	Ortopedi ve Travmatoloji Anabilim Dalı	Tıp Fakültesi	<input type="checkbox"/> E <input checked="" type="checkbox"/> H	
Doç. Dr. M. Kasım ÇAYCI Üye	Biyoloji Anabilim Dalı	Fen-Edebiyat Fakültesi	<input type="checkbox"/> E <input checked="" type="checkbox"/> H	
Yrd. Doç. Dr. Muhammed OYLUMLU Üye	Kardiyoloji Anabilim Dalı	Tıp Fakültesi	<input type="checkbox"/> E <input checked="" type="checkbox"/> H	
Yrd. Doç. Dr. Zulfü BAYHAN Üye	Genel Cerrahi Anabilim Dalı	Tıp Fakültesi	<input type="checkbox"/> E <input checked="" type="checkbox"/> H	
Vet. HEKİM Aydın ARKILAR Üye	Veteriner HEKİM	Tıp Fakültesi DEHYUAM	<input type="checkbox"/> E <input checked="" type="checkbox"/> H	

* Araştırma ile ilişkisi

T.C.
DUMLUPINAR ÜNİVERSİTESİ
HAYVAN DENEYLERİ YEREL ETİK KURULU
ARAŞTIRMA BAŞVURUSU ONAYI

Erkan ERKOL Üye			<input type="checkbox"/> E <input checked="" type="checkbox"/> H	
--------------------	--	--	---	---

* Araştırma ile İlişkisi



RESEARCH ARTICLE

**ATTAINABLE SETS OF INTEGRAL CONSTRAINED SEIR CONTROL SYSTEM WITH
NONLINEAR INCIDENCE**

Ali. S. NAZLIPINAR^{1,*}, Farideh MOHAMMADIMEHR²

¹Kütahya Dumlupınar University, Faculty of Science and Letters, Department of Mathematics, Kütahya,
ali.nazlipinar@du.edu.tr, ORCID: 0000-0002-5114-208X

²Kütahya Dumlupınar University, Faculty of Science and Letters, Department of Mathematics, Kütahya,
moh.mehr68@gmail.com, ORCID: 0000-0003-0122-7920

Receive Date: 09.06.2023

Accepted Date: 15.09.2023

ABSTRACT

In this survey, we consider the dynamics of a contagious disease spread by employing a nonlinear dynamical control system of differential equations. It considers treatment and vaccination as key control parameters to discern their influence on disease control. The study, approximate the attainable sets of a given control system and presents visual results, while also discussing potential biological applications of their findings.

Keywords: *Attainable set, nonlinear incidence, SEIR model.*

1. INTRODUCTION

One of the core issues in control theory is the determination or estimation of attainable sets. Attainable set or reachable set is the set of all possible phase states of a system at different points in time and occurs in various applications, e.g in the existence of disturbances of parameters in control problems, in terminal point estimations of all solutions of a control problem, optimization, differential inclusions and differential games [16], [17]. Also, with this notion, an optimal control problem can be reduced to the construction or estimation of the sets in which the phase vector of the system lies. Thus, having approximate or exact knowledge about attainable set of a control system allows one to observe the limited capabilities of the control system to determine an optimal or suboptimal control.

The approaches developed to estimate the attainable sets of a specific control system depend on whether the function representing the system is linear or not, as well as on the limits that are a part of the control functions. Geometric constraints and integral constraints are both possible for control functions.

While the integral limitation of the controls is explained in such a way that the system is restricted and depleted when it is utilized, the control functions of the geometrical constraint of the system mean that

the effect of control is a kind of limited but not depleted amount. Thus, control systems with integral limitations on the control functions are used to represent the control problems involving finite and depleted sources.

Approximate computational techniques and some topological characteristics are present in attainable sets of affine control systems with integral limitations for control have been studied in [10], [11], [17]. In publications [12–15], these analyses are generalized for the fully nonlinear case, and [15] presents an approximation approach for computing the reachable sets in a specified terminal time.

The approximate calculation of attainable sets for control systems describing real physical or biological phenomena can be used for the in-depth study of such phenomena. For example, in biology, problems such as tumor development, changing populations of struggling species, and the spread of epidemics may need to calculate the points at which the state vector of the system can be brought with the use of limited resources.

In [18], the attainable sets of the SIR epidemic model with bilinear incidence and integral restriction of the control function are calculated approximately and shown graphically. The SIR (Susceptible-Infectious-Recovered) model is a basic compartmental epidemiological model widely used to understand the spread of infectious diseases. It assumes that individuals in a population can be classified into three compartments: Individuals who are susceptible to the disease and can become infected(S), individuals who are infected and capable of transmitting the disease to susceptible individuals(I), and people who have recovered from the disease and gained immunity, so they cannot be infected again(R).

Several infectious diseases can be reasonably modeled using the SIR system, especially those that exhibit a relatively straightforward transmission pattern and where immunity is acquired after infection. Some examples of diseases can be modeled as an SIR system include: Mumps, rubella, chickenpox, influenza etc.

The SEIR model is used instead of SIR model in diseases where there is an incubation period before the disease is contagious. By introducing the Exposed compartment(E), the SEIR model allows for a more detailed representation of disease transmission dynamics, making it more suitable for modeling diseases with incubation periods or other delays between infection and infectiousness. The SEIR model is particularly useful for diseases that have a significant latent period between exposure and becoming infectious. This includes diseases like COVID-19, where an individual may be exposed to the virus but may not show symptoms or be infectious immediately.

In this study, we will approximately calculate the points that a non-linear incidence SEIR control system can reach under the influence of limited and exhausted vaccination and treatment controls. The parameters of the system to be calculated are not produced from the actual data of the epidemics that have occurred before. The parameters have been chosen in accordance with the rapid spread of the epidemic in order to better show the points that the system can bring with the use of the control effect.

The paper is organised as follows: In Section 2, the SEIR system to be examined has been introduced, and a control system has been created by adding vaccination and treatment controls to the system. In Section 3, the main theorem used in the approximate calculation of attainable sets and the calculation algorithm obtained by this theorem are given. Section 4, calculates the reachable set of the epidemiological control system for various control stocks and presents the graphical results for specified parameters.

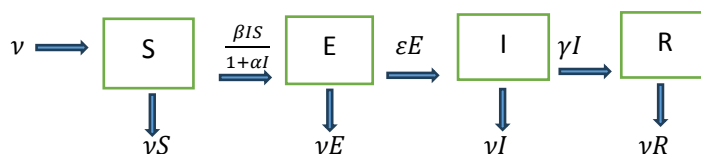
2. MODEL FORMULATION

There are numerous mathematical models that explain how infectious diseases spread and these models have been used to analyze a variety of diseases [2, 3, 4, 5, 6]. The 1927 publication of the Kermack-McKendrick model is one of the early epidemiology models [1]. Following this work, various mathematical models were created to study different types of infectious diseases. The basic rationale for constructing these models is to divide the population into various compartments and characterize the transitions from each compartment to the next over time. Therefore, models are named SI, SIS, SIR, SEIR, SEIRS and so on, considering the compartments in which the population is divided [2-6, 19,20].

In this work, we consider epidemic SEIR model with the nonlinear incidence rate $\beta SI/(1 + \alpha I)$. To formulate our model let $S(t)$, $E(t)$, $I(t)$ and $R(t)$ be the fractions of susceptible, exposed(infected but not yet infectious) and recovered individuals at time t . Also following assumptions are made:

1. Disease is assumed to transit horizontally that can be occurred by direct contact(licking, touching etc.) or indirect contact (vectors or fomites). All newborns are included in the susceptible class.
2. $\epsilon > 0$ is the rate of conversion ofexposed population to infectious, $\gamma > 0$ is the rate of conversion of infectious to recovered, $\nu > 0$ represents the birth (and death) rate.
3. $\beta > 0$ is the contact rate and $\alpha \geq 0$ represents the half saturation constant.

The dynamical transfer of the population is depicted in the following schema:



Under these assumptions, the model can be expressed as

$$\begin{aligned}
 \dot{S}(t) &= \nu - \beta \frac{I(t)S(t)}{1+\alpha I(t)} - \nu S(t), \\
 \dot{E}(t) &= \beta \frac{I(t)S(t)}{1+\alpha I(t)} - (\epsilon + \nu) E(t), \\
 \dot{I}(t) &= \epsilon E - (\gamma + \nu) I(t), \\
 \dot{R}(t) &= \gamma I(t) - \nu R(t)
 \end{aligned}
 \tag{2.1}$$

where the derivative d/dt is denoted by \bullet (dot).

Additionally, it observes that in the first three equations of (2.1), the compartment $R = R(t)$ is absent. The last equation of the system (2.1), $R = 1 - S - E - I$, can be used to determine R. Consequently, we can think about the sub-system provided by

$$\begin{aligned}
 \dot{S}(t) &= \nu - \beta \frac{I(t)S(t)}{1+\alpha I(t)} - \nu S(t), \\
 \dot{E}(t) &= \beta \frac{I(t)S(t)}{1+\alpha I(t)} - (\epsilon + \nu) E(t), \\
 \dot{I}(t) &= \epsilon E - (\gamma + \nu) I(t).
 \end{aligned}
 \tag{2.2}$$

We set $\Omega = \{x = (S, E, I) \in R^3 | 0 \leq S + E + I \leq 1\}$. It can be easily corrected that the set Ω is positively invariant for the system (2.2). As a result, the system is well presented from a mathematical and epidemiological perspective and we can focus only on the region Ω .

If high contact frequency ($\beta = 0.2$) and low recovery rate ($\gamma = 0.001$) is used in the system (2.1) and the system is solved numerically, the evaluation of the system with initial condition $S(0) = 0.7, E(0) = 0.1, I(0) = 0.2, R(0) = 0$, is shown in the figure below:

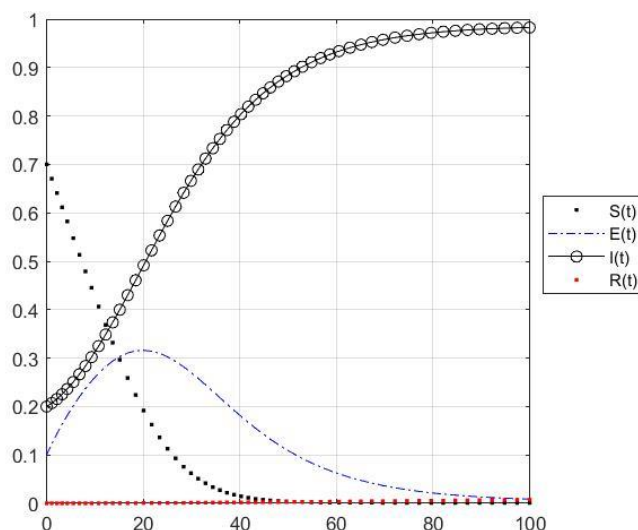


Figure 1. Solution of the system (2.1) with parameters $\beta = 0.2, \gamma = 0.001$ and given initial conditions.

The graphic above demonstrates how quickly the percentage of infected people is growing. In such circumstances some exterior efforts are needed to control the spread of the disease such like isolation, quarantine, raising awareness using the media, vaccination, treatment etc. Since all these have an economic value, it is aimed to get the best results by using the resources in the best way in case the resources are limited. There are various studies in the literature on the control of the spread of epidemic diseases. However, these studies generally appear in the form of optimal control problems [7, 8, 9].

Unlike optimal control problems, in this study, it is aimed to determine the points where the system can be brought at a certain final time by using existing control resources. Let's add two external measures that can be used to prevent the spread of disease:

- $\pi_1(t)$: Vaccination of those who are susceptible at time t,
- $\pi_2(t)$: Treatment operations for infected people.

By adding this control variables to the system (2.1), we obtain the control system as follows,

$$\begin{aligned}
 \dot{S}(t) &= \nu - \beta \frac{I(t)S(t)}{1+\alpha I(t)} - \nu S(t) - S(t) \pi_1(t), \\
 \dot{E}(t) &= \beta \frac{I(t)S(t)}{1+\alpha I(t)} - (\epsilon + \nu) E(t), \\
 \dot{I}(t) &= \epsilon E - (\gamma + \nu) I(t) - I(t) \pi_2(t), \\
 \dot{R}(t) &= \gamma I(t) - \nu R(t) + S(t) \pi_1(t) + I(t) \pi_2(t).
 \end{aligned}
 \tag{2.3}$$

It is considered that $\pi(\cdot) = (\pi_1(\cdot), \pi_2(\cdot)): [0,1] \rightarrow \mathbb{R}^2$ satisfies the integral inequality:

$$\int_0^1 \|\pi(t)\|^2 dt = \int_0^1 (\pi_1^2(t) + \pi_2^2(t)) dt \leq \mu^2
 \tag{2.4}$$

which means in applications that the total stock for the controls to effect spreading of the disease is μ and the stock is depleted by using during the time period.

3. APPROXIMATE CALCULATION OF ATTAINABLE SETS

In this section, at first, attainable sets aspect will be denoted for a general control system whose control functions belong the L_p space and whose L_p norms bounded with a positive certain number μ . Then, we will give the main theorem used in the approximate calculation of attainable sets. This method's algorithm and comprehensive information are provided in [12, 13, 14, 15].

Let us consider the control system whose behaviour is investigated by the differential equations system

$$\dot{y}(t) = g(t, y(t), \pi(t)), \quad y(0) = y_0 \in \mathbb{R}^n
 \tag{3.1}$$

Here, $t \in [0,1]$ is time, $y \in \mathbb{R}^n$ and $\pi \in \mathbb{R}^m$ are the phase state vectors and control vectors of the system respectively.

Assume that $\mu > 0$ and $p > 1$. For all $\pi(\cdot) \in L_p([0,1]; \mathbb{R}^m)$ such that

$$\left(\int_0^1 \|\pi(t)\|^p dt \right)^{\frac{1}{p}} \leq \mu
 \tag{3.2}$$

is called an acceptable control function. Here, $L_p([0,1]; \mathbb{R}^m)$ denotes measurable $\pi(\cdot): [0,1] \rightarrow \mathbb{R}^m$ functions space such that $\|\pi(\cdot)\|_p < +\infty$, $\|\pi(\cdot)\|_p = \left(\int_0^1 \|\pi(t)\|^p dt \right)^{\frac{1}{p}}$.

Ω_p , is the symbol to denoting all admissible control functions set i.e.

$$\Omega_p = \{ \pi(\cdot) \in L_p([0,1]; \mathbb{R}^m) : \|\pi(\cdot)\|_p \leq \mu \},$$

which is the closed sphere with the radius μ and centered in the origin in $L_p([0,1]; \mathbb{R}^m)$.

We assume that the following conditions hold for the system (3.1) :

i) $g(\cdot): [0,1] \times \mathbb{R}^n \times \mathbb{R}^m \rightarrow \mathbb{R}^n$ is continuous;

ii) For every finite set $D \subset [0,1] \times \mathbb{R}^n$, there are constants $C_1 = C_1(D) > 0$, $C_2 = C_2(D) > 0$ and $C_3 = C_3(D) > 0$ such that

$$\|g(t, y_1, \pi_1) - f(t, y_2, \pi_2)\| \leq [C_1 + C_2(\|\pi_1\| + \|\pi_2\|)]\|y_1 - y_2\| + C_3\|\pi_1 - \pi_2\|$$

holds for every $(t, y_1) \in D$, $(t, y_2) \in D$, $\pi_1 \in \mathbb{R}^m$ and $\pi_2 \in \mathbb{R}^m$;

iii) There exists a constant $K > 0$ such that $\|f(t, y, \pi)\| \leq K(1 + \|y\|)(1 + \|\pi\|)$

for every $(t, y, \pi) \in [0,1] \times \mathbb{R}^n \times \mathbb{R}^m$.

Let $\pi_*(\cdot) \in \Omega_p$. The trajectory of the system (3.1) produced by the acceptable function $\pi_*(\cdot)$ from the initial point $y_*(0) = y_0 \in \mathbb{R}^n$ is the absolutely continuous function $y_*(\cdot): [0,1] \rightarrow \mathbb{R}^n$ that holds the equation $\dot{y}_*(t) = g(t, y_*(t), \pi_*(t))$ a.a $t \in [0,1]$, is denoted by $y(\cdot; 0, y_0, \pi_*(\cdot))$.

We set $Y_p(t; 0, y_0) = \{y(t; 0, y_0, \pi(\cdot)): \pi(\cdot) \in U_p\}$ for any given $t \in [0,1]$.

The reachable set of system (3.1) constrained by (3.2) at time t is the set $Y_p(t; 0, y_0)$, which trivially consists of all $y \in \mathbb{R}^n$ into which system (3.1) can be brought to the moment of time $t \in [0,1]$.

Hausdorff distance of sets $U \subset \mathbb{R}^n$ and $V \subset \mathbb{R}^n$ is symbolized by $h(U, V)$ and is defined as

$$h(U, V) = \max \left\{ \sup_{u \in U} d(u, V), \sup_{v \in V} d(v, U) \right\},$$

where $d(u, V) = \inf\{\|u - v\|: v \in V\}$.

For given $\psi > 0$, let $N_\psi = \{n_0, n_1, n_2, \dots, n_K\}$ be a finite ψ -net of unit sphere $S = \{v \in \mathbb{R}^m: \|v\| = 1\}$.

Assume that $\xi = \{0 = t_0 < t_1 < \dots < t_N = 1\}$ and $\xi^* = \{0 = x_0 < x_1 < \dots < x_a = H\}$ are a uniform partition on the intervals $[0,1]$ and $[0, H]$ with diameters $\Delta = t_{i+1} - t_i$, $i = 0, 1, \dots, N - 1$, and $\Delta_* = x_{j+1} - x_j$, $j = 0, 1, \dots, a - 1$ respectively.

By setting

$$\Omega_{p, \Delta, \Delta_*, \psi}^H = \left\{ \pi(\cdot) \in L_p([0,1]; \mathbb{R}^m): \pi(t) = x_{j_i} n_{l_i}, \quad t \in [t_i, t_{i+1}), \right. \\ \left. x_{j_i} \in \xi^*, n_{l_i} \in N_\psi, i = 0, 1, \dots, N - 1 \text{ and } \Delta \cdot \sum_{i=0}^{N-1} x_{j_i}^p \leq \mu^p \right\}$$

we develop a new set of control functions. It is obvious that $\Omega_{p, \Delta, \Delta_*, \psi}^H \subset \Omega_p$.

Since the real numbers $x_{j_i} \in \xi^*$ can be written as

$$x_{j_i} = j_i \Delta_*, \tag{3.3}$$

on the segment $[0, H]$ where $0 \leq j_i \leq a$ is an integer, considering the definition control functions set $\Omega_{p,\Delta,\Delta^*,\psi}^H$, the inequality

$$\sum_{i=0}^{N-1} (j_i)^p \leq \frac{\mu^p}{\Delta(\Delta^*)^p} \quad (3.4)$$

holds. Taking into account (3.3) and (3.4), for $i = 0, 1, \dots, N - 1$, $t \in [t_i, t_{i+1})$, we can rewrite the set $\Omega_{p,\Delta,\Delta^*,\psi}^H$ as

$$\Omega_{p,\Delta,\Delta^*,\psi}^H = \left\{ \pi(\cdot) \in L_p([0,1]; \mathbb{R}^m) : \pi(t) = \Delta_* j_i n_{l_i}, 0 \leq j_i \leq a, n_{l_i} \in N_\psi, \sum_{i=0}^{N-1} j_i^p \leq \frac{\mu^p}{\Delta(\Delta^*)^p} \right\}.$$

By $W_{p,\Delta,\Delta^*,\psi}^H(1; 0, y_0)$, denoting the collection of all points $w(1) = w(t_N)$ calculated by using the recurrence formula

$$w(t_{i+1}) = w(t_i) + (t_{i+1} - t_i)g(t_i, w(t_i), \Delta_* j_i n_{l_i}), \quad w(t_0) = y_0, \quad i = 0, 1, \dots, N - 1, \quad (3.5)$$

where $n_{l_i} \in N_\psi$ and the integers $0 \leq j_i \leq a$, satisfy the inequality (3.4).

The following theorem describes the Hausdorff distance between the sets $W_{p,\Delta,\Delta^*,\psi}^H(1; 0, y_0)$ and $Y_p(1; 0, y_0)$. Here, $W_{p,\Delta,\Delta^*,\psi}^H(1; 0, y_0)$ is the set of points containing finite elements and calculated with the recurrent formula (3.5), while $Y_p(1; 0, y_0)$ is the reachable set that satisfies the constraint of (3.2) of the system (3.1).

Theorem 3.1 [14-15] For given any $\varepsilon > 0$, there exists $\psi(\varepsilon) > 0$, $H(\varepsilon) > 0$, $\Delta^*(\varepsilon) > 0$, $\Delta_*(\varepsilon) > 0$ such that the inequality

$$h\left(Y_p(1; 0, y_0), W_{p,\Delta,\Delta^*(\varepsilon),\psi(\varepsilon)}^H(1; 0, y_0)\right) < \varepsilon \quad (3.6)$$

holds for every $\Delta \leq \Delta^*(\varepsilon)$.

Remark 3.1 Theorem 3.1 allows for the creation of an approximate algorithm for computing the reachable set of the system with the restriction (3.2). For arbitrary $\varepsilon > 0$, the parameters in the theorem 3.1 can be predicted beforehand (see [14-15]). After the numbers $\Delta_*(\varepsilon), \Delta^*(\varepsilon), H(\varepsilon), \psi(\varepsilon) > 0$ have been determined, approximately calculation of attainable set $Y_p(1; 0, y_0)$ can be condensed to the computation of the set $W_{p,\Delta,\Delta^*,\psi}^H(1; 0, y_0)$ containing a finite number of points $w(1) = w(t_N)$ determined by the recursive formula (3.5).

Below, the steps of the algorithm to be used to approximate the set $W_{p,\Delta,\Delta^*,\psi}^H(1; 0, y_0)$ are summarized:

1. For given number $\psi > 0$, finite ψ -net $N_\psi = \{n_0, n_1, n_2, \dots, n_K\}$ of the unit sphere $S = \{v \in \mathbb{R}^m : \|v\| = 1\}$ is constructed (a method for this can be found in [15]).
2. Integers j_0, j_1, \dots, j_{N-1} satisfy the inequality (3.4) are selected.

3. The set $W_{p,\Delta,\Delta,\psi}^H(1; 0, y_0)$ is calculated using the formula (3.5) for all elements $\{n_{l_0}, n_{l_1}, \dots, n_{l_N}\}$ belonging to the set N_ψ , and for all integers $0 \leq j_i \leq a$ selected according to inequality (3.4).

4. APPROXIMATE CALCULATION OF THE ATTAINABLE SETS OF SEIR SYSTEM

Take into consideration the SEIR model, whose behavior is given by the system of equations (2.3). The r.h.s of the function's Lipschitz continuity makes it simple to confirm that the system complies with requirements 3.A, 3.B, and 3.C.

As we mentioned before that $R = R(t)$ does not appear in the first three equations of (2.3) and $S + E + R + I = 1$, we can consider the control system given by

$$\begin{aligned} \dot{S}(t) &= \nu - \beta \frac{I(t)S(t)}{1+\alpha I(t)} - \nu S(t) - S(t) \pi_1(t) , \\ \dot{E}(t) &= \beta \frac{I(t)S(t)}{1+\alpha I(t)} - (\varepsilon + \nu) E(t) , \\ \dot{I}(t) &= \varepsilon E(t) - (\gamma + \nu) I(t) - I(t) \pi_2(t) . \end{aligned} \tag{4.1}$$

Denote

$$\tilde{\Omega}_2 = \{\pi(\cdot) \in L_2([0,1]; \mathbb{R}^2) : \|\pi(\cdot)\|_2 \leq \mu\}$$

Lebesgue-measurable functions $\pi(\cdot) : [0,1] \rightarrow \mathbb{R}^2$ included in the set of control functions $\tilde{\Omega}_2$ that are satisfying inequality (2.4). The symbol $(S(\cdot; 0, S_0, \pi_*(\cdot)), E(\cdot; 0, E_0, \pi_*(\cdot)), I(\cdot; 0, I_0, \pi_*(\cdot)))$ designates the collection of system trajectories (4.1) which are generated by control functions $\pi_*(\cdot) \in \tilde{\Omega}_2$ and satisfy initial condition $(S(0), E(0), I(0)) = (S_0, E_0, I_0)$.

Let

$$\tilde{Y}_2(t; 0, (S_0, E_0, I_0)) = \{(S(t; 0, S_0, \pi(\cdot)), E(t; 0, E_0, \pi(\cdot)), I(t; 0, I_0, \pi(\cdot))) : \pi(\cdot) \in \tilde{\Omega}_2\}.$$

Thus, the set $\tilde{Y}_2(t; 0, (S_0, E_0, I_0))$ is attainable set of the system (4.1) where control functions fulfill (2.4).

For given positive number ψ , a ψ -net in 2-dimensional euclidean space can be defined as

$$N_\psi = \{(\sin k\theta, \cos k\theta) : k = 0, 1, \dots, r\} \tag{4.2}$$

where

$$\theta \leq \frac{\psi^2}{2}, \quad r = \left\lceil \frac{2\pi}{\theta} \right\rceil. \tag{4.3}$$

Since $\theta > 0$, from (4.3) we have

$$\begin{aligned} & \|(\sin(k+1)\theta, \cos(k+1)\theta) - (\sin k\theta, \cos k\theta)\| \\ &= \sqrt{(\cos(k+1)\theta - \cos k\theta)^2 + (\sin(k+1)\theta - \sin k\theta)^2} = \sqrt{2(1 - \cos\theta)} \leq \sqrt{2}\theta \\ &\leq \psi. \end{aligned}$$

Thus, N_ψ defined by (4.2) is really a ψ -net in $S = \{v = (v_1, v_2) \in \mathbb{R}^2: \|v\| = 1\}$.

By $\tilde{W}_{p,\Delta,\Delta^*,\sigma}^H(1; 0, (S_0, E_0, I_0))$, we denote the set of all points $(S(1), E(1), I(1)) = (S(t_N), E(t_N), I(t_N))$ evaluated using the recursive formula

$$\begin{cases} S(t_{i+1}) &= S(t_i) + \Delta \left[\nu - \beta \frac{I(t_i)S(t_i)}{1+al(t_i)} - \nu S(t_i) - \Delta_* j_i |\sin l_i \theta| S(t_i) \right], & S(0) = S_0, \\ E(t_{i+1}) &= E(t_i) + \Delta \left[\beta \frac{I(t_i)S(t_i)}{1+al(t_i)} - (\varepsilon + \nu) E(t_i) \right], & E(0) = E_0, \\ I(t_{i+1}) &= I(t_i) + \Delta [\varepsilon E(t_i) - (\gamma + \nu) I(t_i) - \Delta_* j_i |\cos l_i \theta| I(t_i)], & I(0) = I_0, \end{cases}$$

where for every $i = 0, 1, \dots, N-1$, the integers $0 \leq l_i \leq r$, $0 \leq j_i \leq a$. Here the integers j_i satisfy the inequality (3.4) and r is defined by (4.3).

The following theorem is true in accordance with Theorem 3.1.

Theorem 4.1 For arbitrarily given $\varepsilon > 0$ there exist numbers $H(\varepsilon) > 0$, $\Delta^*(\varepsilon) > 0$, $\Delta_*(\varepsilon) > 0$ and $\psi(\varepsilon) > 0$ such that the inequality

$$h\left(\tilde{Y}_p(1; 0, (S_0, E_0, I_0)), \tilde{W}_{p,\Delta,\Delta_*(\varepsilon),\psi(\varepsilon)}^H(1; 0, (S_0, E_0, I_0))\right) < \varepsilon$$

holds for every $\Delta \leq \Delta^*(\varepsilon)$.

5. NUMERICAL SIMULATIONS

In this section, the possible impact of the use of available resources (vaccination and treatment) on the epidemic in a scenario where the epidemic spreads rapidly will be simulated. Vaccination and treatment resources are limited and also depleted as they are spent.

The model presented here is suitable for any disease model, such as Covid-19, H1N1 (influenza), measles etc. Using the algorithm outlined in [15], we determine the set $\tilde{W}_{2,\Delta,\Delta^*,\sigma}^H(1; 0, (S_0, E_0, I_0))$, which approximates the set $\tilde{Y}_2(1; 0, (S_0, E_0, I_0))$ that is reachable for the system (2.3) at time $t = 1$.

It is assumed that the acceptable control functions are belong to the space $L_2([0,1]; \mathbb{R}^2)$ and their L_2 -norms limited by the positive number μ_0 . For various values of the control stock parameter μ_0 , the set $\tilde{W}_{2,\Delta,\Delta^*,\sigma}^H(1; 0, (S_0, E_0, I_0))$ is approximatively calculated. The full resource for vaccination and treatment in this case is μ_0 , which can be used either continuously or intermittently.

As mentioned in the previous sections, $R(t) = 1 - S(t) - E(t) - I(t)$ can be used to calculate the percentage of recovered people at any point in time t .

In the model examined in the second section (Model 2.1) , an epidemic scenario was created in societies with high contact rate and low natural recovery immunity. As seen in the figure 2.1, in a short period of time, the proportion of individuals exposed to the virus and subsequently infected individuals increased rapidly in the population. The parameters and initial conditions used in the calculations here are as follows:

Table1. Parameters and initial conditions for the system.

S_0	E_0	I_0	β	ϵ	γ	ν	α
0.7	0.1	0,2	0.2	0.06	0.0001	0.0002	0.004

Therefore, in the designed scenario, it is clearly seen that there must be an external influence in order to control the epidemic, since almost the entire society becomes infected in a short time.

The figures below (Figure1, Figure 2, Figure 3) show the sections of approximated attainable sets of system (2.3) for various values of the control stocks μ_0 . Let us interpret how the system is affected under the influence of control.

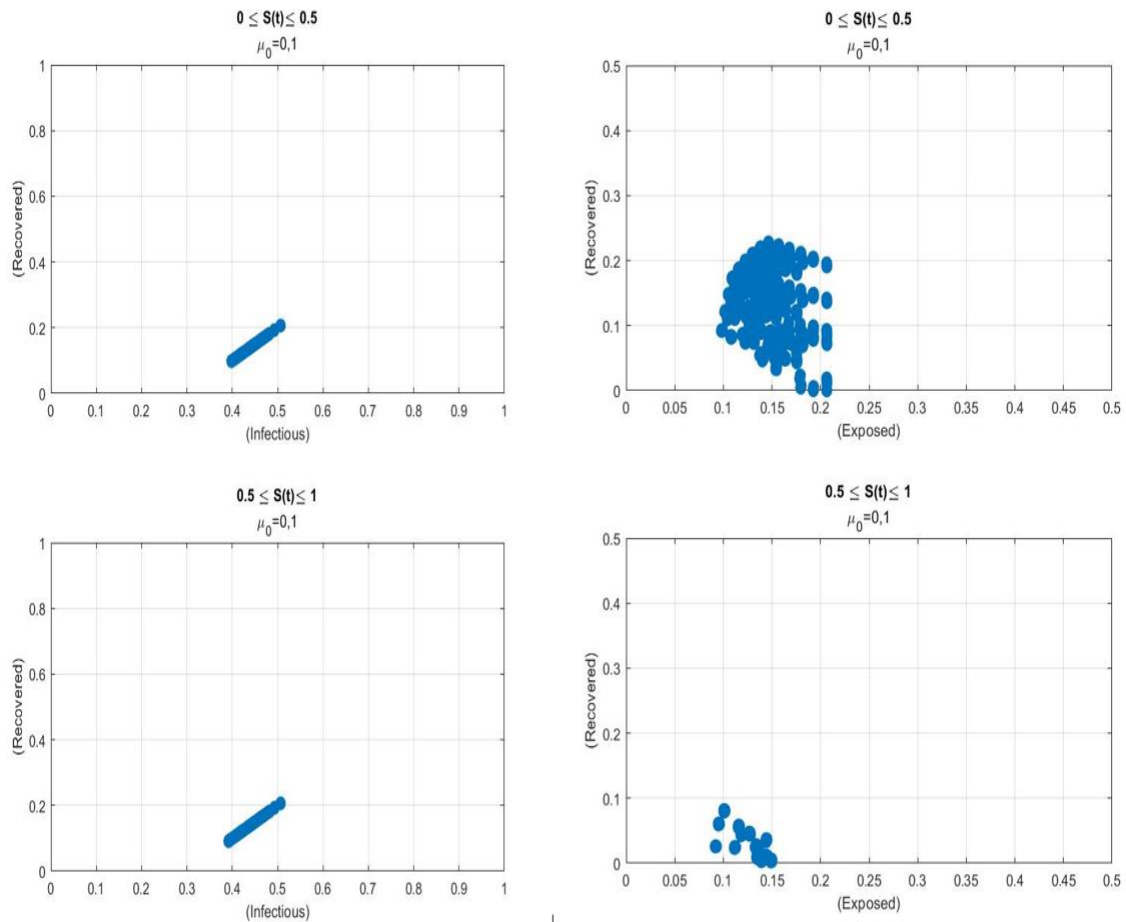


Figure 2. Sections of Infectious-Recovered and Exposed-Recovered Individuals with respect to Susceptible fractions and control stock $\mu_0 = 0.1$.

If $\mu_0 = 0.1$ and $(S_0, E_0, I_0) = (0.7, 0.1, 0.2)$, then according to the Figure 2, we get the conclusion that with this control stock, the proportion of infected individuals remains between 40 and 50 percent, while the proportion of those exposed to the virus varies little from the baseline value. So, this control stock is insufficient to produce a positive outcome. The number of persons who develop a permanent immunity to infection is insufficient, and infection rates are still high.

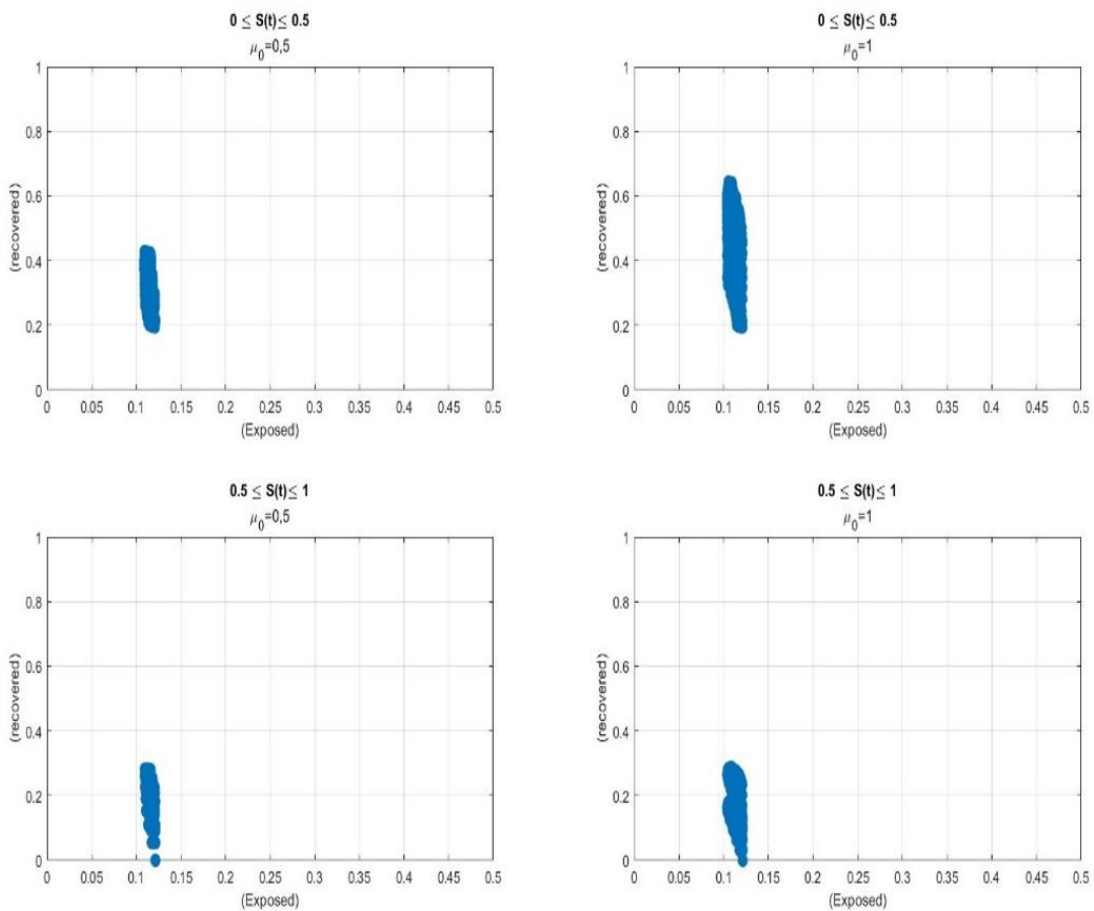


Figure 3. Sections of Exposed-Recovered Individuals with respect to Susceptible fractions and control stocks $\mu_0 = 0.5$, $\mu_0 = 1$.

For $\mu_0 = 0.5$ and $\mu_0 = 1$, in Figure 3, the proportions of individuals exposed to the virus and individuals immunized as treatment are shown in the population. As seen in the graphics, while the rate of individuals exposed to the virus has decreased by half, the rate of individuals who have

acquired permanent immunity exceeds 60 percent. This shows that the controls implemented were successful in bringing the epidemic to the desired level.

Finally, in Figure 4 below, graphs are given for $\mu_0 = 0.5$ and $\mu_0 = 1$, at which points the fraction of infected individuals and individuals who have acquired permanent immunity as treatment in the population can reach under vaccination and treatment controls.

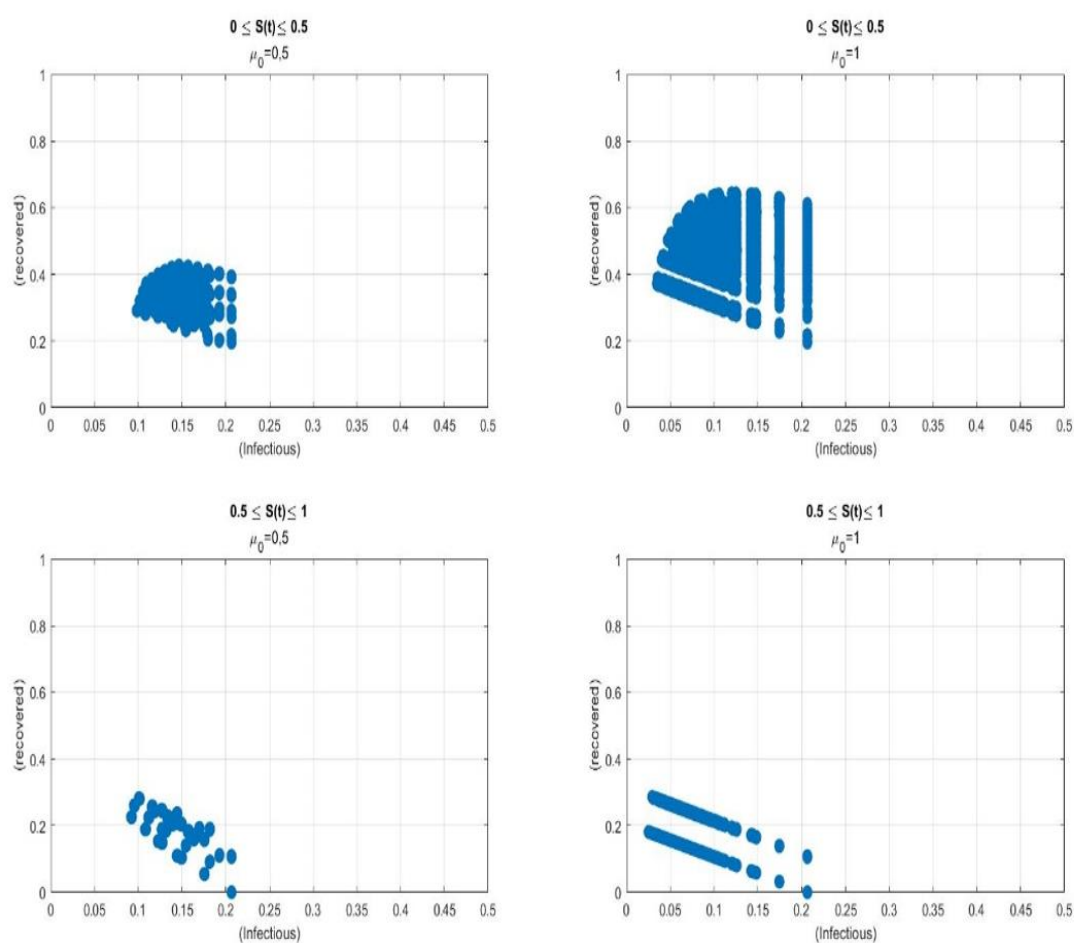


Figure 4. Sections of Infectious-Recovered Individuals with respect to Susceptible fractions and control stocks $\mu_0 = 0.5$, $\mu_0 = 1$.

6. CONCLUSION

In this study, the spread of a disease suitable for the SEIR model in a population with certain demographic conditions was simulated. It has been seen in the approximate calculations that the resources to be used for the control of the spread of the epidemic can stop the spread of the epidemic and bring it to the desired levels. Of course, the use of resources will have an economic cost for a society. However, the study carried out here only aims to determine where the system can reach with the use of existing resources, in other words, how the capacity of the system will be. In this way, resource allocation planning for the measures to be taken can be made in advance.

ACKNOWLEDGEMENT

No particular grants were provided for this research by any funding organizations in the public, private or nonprofit sectors.

REFERENCES

- [1] Kermack W.O., Mckendric A.G. (1927). Contributions to the mathematical theory of epidemics, part i, Proceedings of the Royal Society of Edinburgh. Section A Mathematics, 115 (772), 700-721.
- [2] Hethcote H.W. (2000). The mathematics of infectious diseases, SIAM Review, 42(4), 599–653.
- [3] Hoppensteadt F.C. (1982). Mathematical methods in population biology, Cambridge University Press, Cambridge.
- [4] Anderson R.M. (1982). Population dynamics of infectious diseases: Theory and applications, Chapman and Hall, London.
- [5] Grassly N.C., Fraser C. (2008). Mathematical models of infectious disease transmission, Nature Reviews Microbiology 6, 477-487. doi:10.1038/nrmicro1845.
- [6] Keeling M.J., Danon L. (2009). Mathematical modelling of infectious diseases, Br Med Bull, 92(1), 33-42. doi: 10.1093/bmb/ldp038.
- [7] Biswas M.H.A., Paiva L.T., Pinho M. (2014). A SEIR model for control of infectious diseases with constraints, Mathematical Biosciences and Engineering, 11(4), 761-784. doi:10.3934/mbe.2014.11.761.
- [8] Neilan R.M., Lenhart S. (2010). An Introduction to Optimal Control with an Application in Disease Modeling, Modeling Paradigms and Analysis of Disease Trasmision Models, 49, 67-82.

- [9] Gaff H., Schaffer E. (2009). Optimal control applied to vaccination and treatment strategies for various epidemiological models, *Math. Bio. Sci. Eng. (MBE)*, 6, 469-492.
- [10] Guseinov Kh. G., Ozer O., Akyar E. (2004). On the continuity properties of the attainable sets of control systems with integral constraints on control, *Nonl. Anal.: Theo., Meth. App.* 56, 433–449.
- [11] Guseinov Kh. G., Ozer O., Akyar E., Ushakov V.N. (2007). The approximation of reachable sets of control systems with integral constraint on controls, *Non. Diff. Equat. Appl.* 14, 57–73.
- [12] Guseinov Kh.G., Nazlipinar A.S. (2007). On the continuity property of L_p balls and an application, *J.Math. Anal. Appl.*, 335, 1347-1359.
- [13] Guseinov Kh.G., Nazlipinar A.S. (2008). On the continuity properties of attainable sets of nonlinear control systems with integral constraint on controls, *Abstr. Appl. Anal.*, p.14.
- [14] Guseinov KH.G. (2009). Approximation of the attainable sets of the nonlinear control systems with integral constraints on control, *Nonlinear Analysis, TMA*, 71, 622-645.
- [15] Guseinov Kh.G., Nazlipinar A.S. (2011). An algorithm for approximate calculation of the attainable sets of the nonlinear control systems with integral constraint on controls, *Comp. Math. Appl.*, 62(4), 1887-1895.
- [16] Krasovskii N.N., Subbotin A.I. (1988). *Game-theoretical control problems*, Springer, NewYork.
- [17] Krasovskii N.N. (1968). *Theory of control of motion: Linear systems*, Nauka, Moscow.
- [18] Nazlipinar A.S., Basturk B. (2020). Attainable set of a SIR epidemiological model with constraints on vaccination and treatment stocks, *Tbilisi Mathematical Journal* 13(1), pp. 11-22.
- [19] Hethcote H.W. (1989). Three Basic Epidemiological Models, In Levin SA, Hallam TG, Gross LJ (eds.). *Applied Mathematical Ecology. Biomathematics. Vol. 18*. Berlin: Springer. pp. 119–144. doi:10.1007/978-3-642-61317-3_5. ISBN 3-540-19465-7.
- [20] Padua RN, Tulang A.B. (2010). A Density–Dependent Epidemiological Model for the Spread of Infectious Diseases, *Liceo Journal of Higher Education Research*. 6 (2). doi:10.7828/ljher.v6i2.62.



RESEARCH ARTICLE

**IN VITRO EVALUATION OF ANTIOXIDANT AND CYTOTOXIC ACTIVITIES ON
HUMAN CERVICAL CANCER CELLS IN THREE DIFFERENT PLANT EXTRACTS
FROM TURKEY**

Funda ULUSU*

*Karamanoglu Mehmetbey University, Vocational School of Technical Sciences, Department of Crop and Animal Production,
Karaman, Türkiye, fulusu@kmu.edu.tr, ORCID: 0000-0002-0321-2602

Receive Date: 09.03.2023

Accepted Date: 15.09.2023

ABSTRACT

The objective of this investigation was to assess the total phenolic and flavonoid content within acetone and water extracts derived from *Erica manipuliiflora*, *Ferula communis*, and *Stevia rebaudiana* plants. Additionally, the *in vitro* antioxidant and cytotoxic effects of these extracts were evaluated using the human cervical cancer (HeLa) cell line as a model. Among the three plant species examined, the highest concentrations of total phenols and flavonoids were found in the acetone extract of *E. manipuliiflora*, measuring 365.29 mg GAE/g DW and 105.42 mg QE/g DW, respectively. Acetone and water extracts of *E. manipuliiflora* showed higher DPPH scavenging activities (IC₅₀: 37.57 and 33.27 µg/mL, respectively) compared to other plants. Furthermore, *E. manipuliiflora* acetone extract (IC₅₀: 97.35 µg/mL) exhibited the highest inhibition in the HeLa cell line treated with the extracts, thus being the most effective extract on this cell line. As a result of the analyzes, it has been shown that *F. communis* and *S. rebaudiana* and especially *E. manipuliiflora* are important natural antioxidant sources with their strong radical scavenging effects, as well as the anticancer potential of these plants.

Keywords: *Erica manipuliiflora*, *Ferula communis*, *Stevia rebaudiana*, Antioxidant, Cytotoxic Activities, Phenolic Content.

1. INTRODUCTION

Medicinal plants, employed both in traditional and contemporary medical practices, harbor an array of phytochemicals within their tissues and organs, showcasing diverse potential benefits such as antimicrobial, antioxidant, anticancer, and antifungal properties [1]. Due to the natural and synthetic therapeutic properties used today, interest in medicinal and aromatic plants is increasing both in different industrial areas such as medicine, cosmetics, agriculture and in academic research. In recent times, there has been a growing emphasis on conducting *in vitro* and *in vivo* research involving plant extracts, driven by the recognition of their multifaceted health benefits. Phytochemicals, found

abundantly in these extracts, exhibit a spectrum of therapeutic properties, including but not limited to antioxidants, anticancer agents, and anti-inflammatory agents [2].

Reactive oxygen species (ROS) that occur in plant tissues under biotic and abiotic environmental stress conditions and cause DNA and cell damage are scavenged by many enzymatic [PPO (Polyphenol oxidase), CAT (catalase), APX (ascorbate peroxidase), POD (peroxidase)] and non-enzymatic (ascorbic acid, phenolic compounds, carotenoid, glutathione etc.) antioxidants [3]. Antioxidants are acknowledged for their capacity to promote well-being and mitigate the likelihood of numerous conditions, including various forms of cancer, hypertension, diabetes, asthma, and heart disease [4, 5]. Numerous investigations have demonstrated the utility of plant polyphenols, which encompass essential biological properties such as antioxidant activity, in combatting a variety of oxidative stress-related ailments [6, 7]. Although synthetic antioxidants increase the shelf life of foods, some studies have mentioned their disadvantages for human health. For this reason, many researchers have focused on the development of easily accessible naturally sourced antioxidants [8].

Erica manipuliflora Salisb. (Ericaceae) is a plant species in the form of an upright bush that can reach a height of about 4 m and is known as "broom grass" or "puren" in Turkey. *E. manipuliflora* is commonly found in parts of the Eastern Mediterranean (Turkey, Cyprus, Lebanon, Syria, Greece), Albania, Bosnia and Herzegovina, Croatia, Italy, North Macedonia, Serbia, Montenegro, and Slovenia. The aerial parts (leaf and flower) of *E. manipuliflora* have been used in the treatment of many diseases for ages due to their many medicinal benefits (antioxidant, anticholinesterase, diuretic, astringent) [9]. The main compound of monoterpenoids, which are abundant in the aerial parts of the plant, is germacrene D (13.58%-15.55%) [10]. Although it has been used for therapeutic purposes in traditional medicine in Turkey for many years, there is not enough data on both its phytochemicals and biological activities in the literature. In this context, *E. manipuliflora*, which is accepted as a medicinal plant with various pharmacological effects, is a species worth examining in terms of its biological activities.

Ferula communis L. (Apiaceae) is a tall (1.5-3 m), herbaceous and perennial plant species known as "Caksır otu" or "Atkasnagi" in Turkey. *F. communis* is distributed in the forests and bushes of the Mediterranean, East Africa and Central Asia. In the phytochemical analysis of *F. communis* fruit flower root parts, bioactive compounds such as tannic acid, ferulic acid, catechin, syringic acid, gallic acid, coumarin were determined in varying proportions of each part [11]. Although the mainly roots (β -farnesene, β -cubene, caryophyllene) of this plant, which is rich in especially sesquiterpenes, are used for therapeutic purposes, it has been stated in previous studies that leaf (β -eudesmol, α -eudesmol, hedyariol), flower (α -pinene, γ -terpinene, hedyariol), and fruit (α -pinene, β -pinene, myrcene) extracts also contain different bioactive compounds [12]. *F. communis*, a plant historically employed in traditional pharmacopoeia for treating diverse conditions like fever, skin infections and dysentery, has been the subject of research revealing its multifaceted properties, including anti-inflammatory, antineoplastic, anticoagulant, antiproliferative, cytotoxic, antimicrobial and herbicidal activities [13-15]. In another study, it was reported that this plant has toxic effects for humans and animals [16].

Stevia rebaudiana Bert. (Asteraceae) is a perennial herbaceous plant species that reaches 30-60 cm in length, known as "sugar grass" in Turkey and its natural habitat is subtropical regions (such as

Paraguay and Brazil). The stevioside found in the leaves of *S. rebaudiana* adds sweetness to this plant and is known to be 100-300 times sweeter than table sugar. Therefore, it is a natural sweet source worldwide, especially as an alternative to sucrose and synthetic sweeteners [17]. As a result of GC-MS analysis of leaves, major phytochemicals (1-heptatriacotanol-antihypercholesterolemia; dihydroxanthin-antitumor; β -amyrin and lupenone-anti-inflammatory; phytol-antidiabetic) responsible for different and multiple biological activities were obtained [18]. This plant not only serves as a rich source of numerous antioxidant compounds but is also harnessed for its therapeutic potential in managing neurodegenerative diseases such as Parkinson's and Alzheimer's disease [19]. These therapeutic attributes have propelled it into the spotlight of numerous scientific investigations, including in vitro studies involving cell cultures, callus cultures, as well as tissue and organ cultures [20,21].

The common features of these three species used in the current study are that they belong to the class of medicinal and aromatic plants that contain extremely important compounds in the pharmacopeia and are suitable for the geography of Turkey. In this context, some biochemical contents of *E. manipuliflora*, *F. communis*, *S. rebaudiana* plants were investigated, and antioxidant potentials and cytotoxic activities of these plant extracts were determined and compared with each other.

2. MATERIALS and METHOD

2.1. Plant Material and Preparation of the Extracts

The plant specimens used in this study were sourced from the Zeytinburnu Medicinal Plant Botanic Gardens located in Istanbul, Turkey. Plant samples [*E. manipuliflora*-aerial (leaf and flower), *F. communis*-root, *S. rebaudiana*-leaf] were dried at room conditions and ground into powder in a grinder. To obtain the extracts, 20 g of finely ground plant samples were subjected to extraction in 250 mL of both acetone and water separately using a Soxhlet apparatus for a duration of 12 h. Following extraction, the resulting extracts were subsequently filtered through Whatman No.1 filter paper. The acetone extract was evaporated under vacuum at 40°C with a rotary evaporator, the water extract was lyophilized. All samples were stored in a closed container at -20°C until analysis. The data presented in Table 1 showcases the yield rates of extracts derived from plant samples, specifically those obtained through the use of acetone and water.

Table 1. Yield (%) of obtained the plant extracts.

Samples	Abbreviation of the extracts	Yield (%)
Acetone extract obtained from <i>E. manipuliflora</i>	EE _A	6.14 ± 0.47
Water extract obtained from <i>E. manipuliflora</i>	EE _W	18.21 ± 1.31
Acetone extract obtained from <i>F. communis</i>	FE _A	8.6 ± 0.54
Water extract obtained from <i>F. communis</i>	FE _W	22.34 ± 1.14

Acetone extract obtained from <i>S. rebaudiana</i>	SE _A	3.47 ± 0.67
Water extract obtained from <i>S. rebaudiana</i>	SE _W	26.52 ± 1.23

2.2. Quantitative Determination of Secondary Metabolites in Plant Extracts

2.2.1. Determination of total phenolic content (TPC)

The quantification of total phenolic contents (TPC) in the extracts followed the method outlined by Uluslu and Şahin [22], employing the Folin-Ciocalteu colorimetric assay. A standard calibration curve using gallic acid was used as a reference. 100 µl of extracts (10 mg/mL), 9 mL dH₂O, 200 µl of Folin-Ciocalteu reagent and 600 µl of Na₂CO₃ (2%, w/v) were added, after mixing, the total volume was adjusted to 10 mL with dH₂O. After the samples were incubated for 2 h under dark room conditions, the absorbances of the samples were measured at 750 nm in the Shimadzu UV-1800 spectrophotometer. The total phenolic content was calculated as the mean ± standard error from the calibration curve obtained as gallic acid equivalent (GAE). All experiments were performed in triplicate.

2.2.2. Determination of total flavonoid content (TFC)

The quantification of total flavonoid contents (TFC) in the extracts followed a slightly modified protocol based on the method originally described by Bouasla [23], utilizing quercetin as the standard. In this procedure, 250 µl of extracts at a concentration of 10 mg/mL were combined with 1.25 mL of dH₂O, 75 µl of NaNO₃ (5%, w/v), 150 µl of AlNO₃ (10%, w/v), and 0.5 mL of NaOH (1M). The total volume was adjusted to 2.5 mL using dH₂O to complete the assay. Following thorough mixing, the solution was allowed to incubate at ambient room temperature for a duration of 40 min. Subsequently, the absorbance values were recorded at a wavelength of 415 nm using a spectrophotometer. The quantification in quercetin equivalent (QE) was carried out by applying the standard calibration curve established with quercetin.

2.3. DPPH (1-1-diphenyl 2-picryl hydrazyl) Radical Scavenging Assay

In measuring the DPPH scavenging activity of plant extracts, each extract and DPPH were dissolved in methanol. 0.2 mL of each extract at different concentrations (10, 25, 50, 100, 200, 400 µg/mL) and 1.8 mL of DPPH (0.06 mM) solution was added to it. The solutions were kept in dark room conditions for 30 min (incubation time). Absorbance values were determined at 517 nm following incubation. In this experimental setup, ascorbic acid served as the designated positive control. In addition, all experiments were performed in triplicate. The following equation was used to compute the extracts' percent inhibition of DPPH radical scavenging:

$$DPPH \text{ radical scavenging activity (\%)} = \left[\frac{A_0 - A_s}{A_0} \right] \times 100$$

A₀ = The absorbance of the control

A_s = The absorbance of the extract

2.4. Cell Culture

In this study, the human cervical cancer (HeLa) cell line was cultured in a medium comprising DMEM (Dulbecco's Modified Eagle Medium) supplemented with 10% fetal bovine serum (FBS), 1% penicillin-streptomycin, and 0.01% gentamicin. The culture plates were maintained in a sterile microculture environment within an incubator set at 37°C, with a controlled humidified atmosphere containing 5% CO₂. Subsequent to the incubation period, confluent cells were dislodged from the culture surface employing the standard trypsinization procedure. The cytotoxicity assays were conducted in triplicate for each sample during *in vitro* testing.

2.4.1. Cell viability assay

The evaluation of cytotoxicity on the HeLa cell line was conducted using the Alamar Blue® assay. To facilitate testing, all plant extracts were initially dissolved in a 1 mg/mL DMSO (dimethyl sulfoxide) stock solution. Importantly, the DMSO concentration in the culture medium did not exceed 0.1%. Subsequently, we prepared a series of dilutions to achieve various sample concentrations, including 10, 25, 50, 100, 200, and 400 µg/mL. Cells were introduced to 96-well microculture plates, with each well receiving a seeding of 2×10^4 cells. They were then incubated for 24 h at 37°C to facilitate proper adhesion to the plate surface. After incubation, fresh medium containing different concentrations of plant extracts (10, 25, 50, 100, 200, 400 µg/mL) was added. The negative control group was culture medium containing 0.1% DMSO. The HeLa cell line was exposed to plant extracts in triplicate for 24 h at 37°C. After incubation, Alamar Blue® reagent (1:10, v/v) was added to each microplate well. Subsequently, the plates underwent a 4 h incubation period at 37°C, during which measurements were taken at wavelengths of 570 nm and 600 nm using a spectrophotometric microplate reader (Multiscan Go, Thermo Fisher Scientific, USA). Cell viability was then determined as a percentage of the initial cell count.

3. RESULTS AND DISCUSSION

3.1. The Yield of Crude Extracts

Phytochemical extraction from plant material is the focus of research. Secondary metabolites with different polarities can be included in the solution depending on the polarity of the solvents used in the extraction [24]. In this study, extractions of *E. manipuliiflora*, *F. communis* and *S. rebaudiana* were carried out using polar (water) and apolar (acetone) solvents. From the plant materials used, the highest yield was obtained from SE_W (26.52%), while the lowest yield was obtained from SE_A (Table 1). The water extract was effective in obtaining the highest yield of all plant extracts. This result shows that increasing solvent polarity significantly increases the plant extraction yield. Zaidan [18] emphasized that water was the best solvent compared to methanol, ethanol and acetone solvents in *S. rebaudiana* extraction and obtained the highest yield from the water extract. Again, among the compounds extracted in water, the inclusion of not only secondary metabolites but also high-soluble primary metabolites (such as protein and carbohydrates) in the extract contributes to increasing the yield [25].

3.2. TPC and TFC of the Plant Extracts

TPC and TFC of acetone and water extracts obtained from *E. manipuliiflora*, *F. communis* and *S. rebaudiana* were investigated. The recovery amount of TPC and TFC from *E. manipuliiflora* and *F.*

communis water extracts is significantly higher than from acetone extracts. Also, according to the data, the highest phenol content belongs to EE_w (365.29 mg GAE/g DW), followed by FE_w (132.82 mg GAE/g DW). Similarly, the highest total flavonoid content was found to be EE_w (105.42 mg QE/g DW), while the lowest SE_w (6.53 mg QE/g DW) (Table 2).

It is stated that polar solvents are generally more suitable for revealing the polyphenols in the plant cell, while alcohol-derived solvents are more effective in the degradation of the cell wall and testa. Again, polar solvents such as water and methanol are more efficient than apolar solvents in terms of extraction of phenolic compounds [26, 27]. The dielectric constant of the organic solvents utilized in the extraction process can influence TPC and TFC found in plant extracts [28]. Therefore, this study proves once again that polarity differences of plant phytochemicals and solvents affect phenolic and flavonoid recovery. Prior research has identified the presence of numerous phenolic and flavonoid compounds within the specific plant species under investigation. In these studies, unlike us, methanol and ethanol extracts were used in *S. rebaudiana* plant, and while the highest TPC was obtained from polar solvents (methanol-6.96 and water-6.65 mg GAE/g), the highest TFC was obtained from ethanol extract (10.91 mg QE/g) [18]. Again, TPC in ethanol extracts of four *S. rebaudiana* lines ranged from 55.64 to 58.35 mg GAE/g DW [29]. *E. manipuliiflora*, this situation varied in extraction by different solvents (water, methanol, chloroform, ethyl acetate, n-butanol) and the highest TFC was determined with ethyl acetate (735.5 mg GAE/g) [30]. In another study, the TPC of *E. manipuliiflora* methanol extract was 260 mg QE/g [31]. TPC and TFC of *F. communis* (stem) methanol extract were obtained as 129.86 mg GAE/g DW and 13.37 mg QE/g DW, respectively [11]. Among the extracts of *F. communis* (aerial part) made by different solvents, the highest TPC (0.031 mg GAE/mg extract) was in the ethanol:water (50:50) mixture [32].

Table 2. Total phenolic content (TPC) and total flavonoid content (TFC) of the plant extracts.

Plant extracts	TPC (mg GAE/g DW) ^a	TFC (mg QE/g DW) ^b
EE _A	103.32 ± 5.71	27.43 ± 0.53
EE _w	365.29 ± 1.52	105.42 ± 1.41
FE _A	114.75 ± 2.23	15.21 ± 0.44
FE _w	132.82 ± 2.81	18.43 ± 0.56
SE _A	63.78 ± 0.86	7.87 ± 0.25
SE _w	55.46 ± 0.72	6.53 ± 0.16

Each value is represented as the mean ± standard deviation, based on a sample size of n = 3.

^amg gallic acid equivalent per gram of dry weight.

^bmg quercetin equivalent per gram of dry weight.

3.3. DPPH Scavenging Activities of the Plant Extracts

One of the oldest and most commonly employed *in vitro* techniques for assessing the antioxidant properties of research materials relies on DPPH radical analysis. A dose-dependent increase in DPPH scavenging activities was observed across various concentrations (10, 25, 50, 100, 200, and 400

µg/mL) of the plant extracts. Among the extracts, the treatment of EE_W and EE_A at concentrations of 200 and 400 µg/mL resulted in the highest antioxidant activity with over 85% inhibition, and the results of these two concentration treatments were statistically different ($p < 0.05$) (Figure 1.). In addition, the lowest IC₅₀ value (33.27 µg/mL) was belonged to EE_W, while the highest IC₅₀ value (101.11 µg/mL) was found in SE_A (Table 3.). While both water and acetone extracts of *E. manipuliiflora* had the highest DPPH scavenging activity, the lowest activity was determined in acetone extracts of *S. rebaudiana*. Antioxidant compounds in water and acetone extracts of the studied plant species showed good rate antioxidant activity. In addition, there are many antioxidant studies conducted in these plant species. In the literature, DPPH activity of *E. manipuliiflora* was determined as IC₅₀: 255.9 mg/mL in methanol extract [31], IC₅₀: 0.021 µg/mL in water extract [30]. The DPPH activity of *S. rebaudiana* (leaf) was found to be IC₅₀: 83.45 µg/mL in aqueous extract [33], IC₅₀: 93.46 µg/mL in ethanol extract [34], IC₅₀: 752.6 and 904.4 mg/mL in water and methanolic extract, respectively [35]. *F. communis* (stem) methanol extract has an IC₅₀ value of 168 µg/mL in the DPPH activity [11], in another study, the best antioxidant activity was determined with a parallel effect to the ethanol:water extract, from which the highest antioxidant compounds were obtained [32]. Our results show that water and acetone extracts of *E. manipuliiflora*, *F. communis* and *S. rebaudiana* are potent antioxidants. Oxidizing enzymes (such as peroxidase) contribute to the reduction of oxidative damage in cells by being inhibited by some plant-derived molecules (phenols). In this study, it was determined that *F. communis* and *S. rebaudiana*, and especially *E. manipuliiflora*, contain high levels of phenolic compounds, and thus, it can be thought that they show high antioxidant capacity due to these phytochemicals.

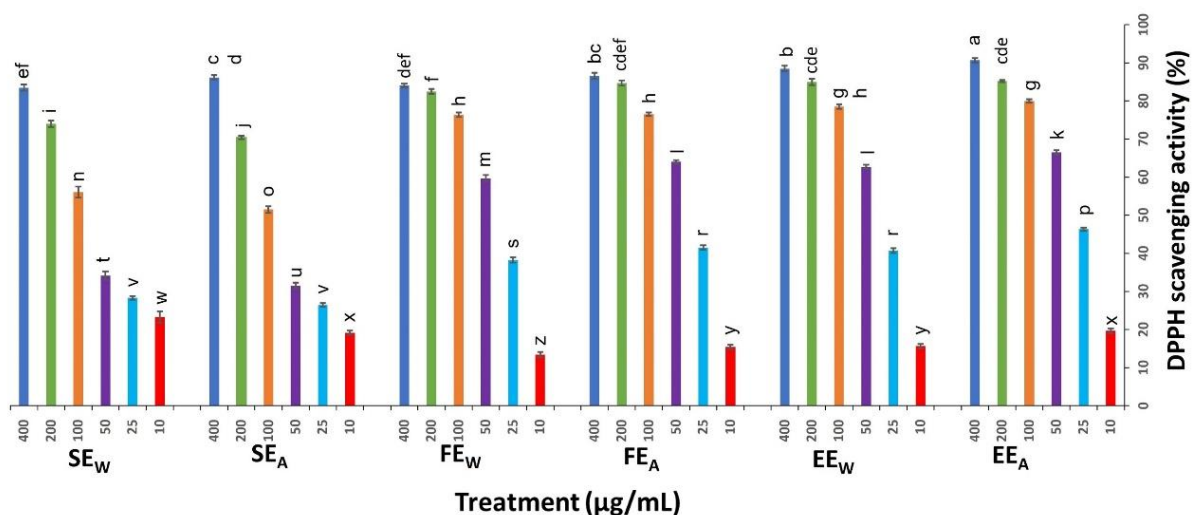


Figure 1. DPPH scavenging activities of different plants extracts.

3.4. Cytotoxicity activities

The Alamar Blue® assay was employed to assess the viability of HeLa cells following exposure to

extracts from *E. manipuliflora*, *F. communis*, and *S. rebaudiana*. Across all tested plant extracts, a concentration-dependent cytotoxic effect on HeLa cells was observed. Particularly noteworthy was the significant reduction in cell viability, which reached 22.26% when exposed to EE_A at a concentration of 400 µg/mL. Furthermore, HeLa cells subjected to the highest concentrations of EE_A, EE_W, FE_A, and FE_W exhibited viabilities below 35%, as illustrated in Figure 2. These percentages were also supported by the IC₅₀ values, and the lowest IC₅₀ value (97.35 µg/mL) belonged to the EE_A. The extract with the lowest effect in this cancer cell line was SE_W (IC₅₀: 341.96 µg/mL) (Table 3). Many different species of *Erica* genus exhibited different biological activities such as cytotoxic [36], antibacterial, antioxidant [37, 38], diuretic [39], anti-inflammatory [40]. These studies indicate *Erica*'s potential for alternative and complementary therapy. In this study, acetone and water extracts of *E. manipuliflora*, which has limited literature, showed cytotoxic activity on HeLa cell line. In the literature, the cytotoxic activities of different species of *Erica* genus on different cell lines (*E. carnea* - MCF-7 [41]; *E. multiflora* - B-16 melanoma [42]) have been investigated and the data obtained support our results. In addition, the fact that *E. manipuliflora* contains more phenolic compounds compared to other species in our study may suggest that these plant extracts support more cytotoxic potential on HeLa cell line.

F. communis and *S. rebaudiana* are important medicinal and aromatic plants grown in the geography of Turkey. The inclusion of both species in the category of medicinal plants has been supported by many biological activity studies. In the researches, besides the antioxidant activities of these plant species, the antimicrobial [43], cytotoxic [15], anti-neuroinflammatory [44] activities of *F. communis*, and the antidiabetic [45], antimicrobial [46], anticancer [47], anti-hyperuricemic [48] activities of *S. rebaudiana* are remarkable. Studies involving various *Ferula* species have consistently reported a range of bioactivities, including cytotoxic, antioxidant, anticholinesterase, and anti-tyrosinase effects, which are often attributed to the presence of phenolic compounds in these plants [49, 50]. On the other hand, the genus *Stevia* has garnered attention due to the substantial inhibitory effects displayed by its metabolites, such as stevioside, steviolbioside, and isosteviol derivatives, on several cancer cell lines, including MDA-MB-231, Hep3B, BxPC-3 [51], HER2+ SKBR-3 [52] and MCF-7 [53]. These findings underscore the potential significance of *Stevia* in alternative and complementary therapies for cancer. Notably, our study aligns with these observations, as we have observed remarkable cytotoxic potential in the HeLa cell line for both *F. communis* and *S. rebaudiana* species. Future investigations into the gene expression and related aspects in other cancer cell lines exposed to *E. manipuliflora*, a plant with limited anticancer information, hold promise for expanding our understanding of its effectiveness in modulating cancer metabolism.

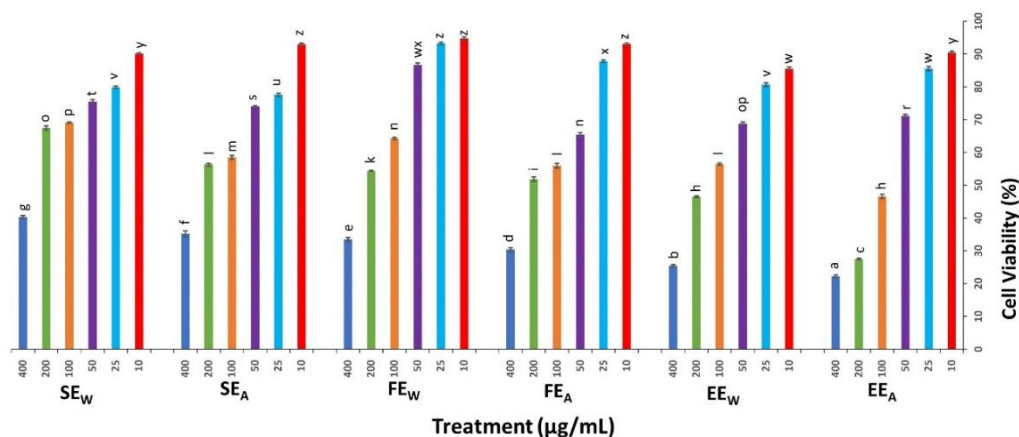


Figure 2. % Cell viability rates on HeLa cells treated with different plant extracts.

Table 3. IC₅₀ values (µg/mL) resulting from DPPH scavenging activities and cytotoxic activities of different plant extracts.

Treatment	DPPH scavenging activities	Cytotoxic activities
	IC ₅₀ (µg/mL)	IC ₅₀ (µg/mL)
EE _A	37.57 ± 0.52	97.35 ± 0.58
EE _w	33.27 ± 0.18	165.44 ± 1.74
FE _A	40.29 ± 0.70	207.13 ± 9.02
FE _w	37.42 ± 0.29	213.35 ± 0.95
SE _A	101.11 ± 1.87	262.31 ± 6.47
SE _w	88.82 ± 1.44	341.96 ± 3.05

4. CONCLUSION

Total phenol and flavonoid contents, antioxidant activities and cytotoxic properties on human cervical cancer (HeLa) cell line of *E. manipuliflora*, *F. communis* and *S. rebaudiana* acetone and water extracts were determined. Among these three species, *E. manipuliflora* species stood out in terms of both phenolic compound content and antioxidant and cytotoxic activity. This study highlights that the plants under investigation serve as readily available natural sources of antioxidants, demonstrating substantial cytotoxic activity. These findings emphasize the potential utility of these plants in pharmacology, owing to their rich reservoir of valuable phytochemicals, for the management and treatment of various diseases.

ACKNOWLEDGEMENT

This research received no specific grants from any funding agency in public, commercial or non-profit sectors.

REFERENCES

- [1] Khan, T., Ali, M., Khan, A., Nisar, P., Jan, S. A., Afridi, S., Shinwari, Z. K., (2019), Anticancer plants: A review of the active phytochemicals, applications in animal models, and regulatory aspects. *Biomolecules*, 10, 47.
- [2] Sen, T., Samanta, S. K., (2015), Medicinal plants, human health and biodiversity: a broad review. *Biotechnological applications of biodiversity*, 59-110.
- [3] Hasanuzzaman, M., Bhuyan, M. B., Zulfiqar, F., Raza, A., Mohsin, S. M., Mahmud, J. A., Fotopoulos, V., (2020), Reactive oxygen species and antioxidant defense in plants under abiotic stress: Revisiting the crucial role of a universal defense regulator. *Antioxidants*, 9, 681.
- [4] Allen, S., Britton, J. R., Leonardi-Bee, J. A., (2009), Association between antioxidant vitamins and asthma outcome measures: systematic review and meta-analysis. *Thorax*, 64, 610-619.
- [5] Myung, S. K., Ju, W., Cho, B., Oh, S. W., Park, S. M., Koo, B. K., Park, B. J., (2013), Efficacy of vitamin and antioxidant supplements in prevention of cardiovascular disease: systematic review and meta-analysis of randomised controlled trials. *Bmj*, 346.
- [6] Saeidnia, S., Abdollahi, M., (2013), Toxicological and pharmacological concerns on oxidative stress and related diseases. *Toxicology and applied pharmacology*, 273, 442-455.
- [7] Salehi, B., Azzini, E., Zucca, P., Maria Varoni, E., V. Anil Kumar, N., Dini, L., Sharifi-Rad, J., (2020), Plant-derived bioactives and oxidative stress-related disorders: a key trend towards healthy aging and longevity promotion. *Applied sciences*, 10, 947.
- [8] Fernandes, R. D. P. P., Trindade, M. A., de Melo, M. P., (2018), Natural antioxidants and food applications: healthy perspectives. In *Alternative and replacement foods* (pp. 31-64). Academic Press.
- [9] Yüksel, A. K., Dikici, E., Yüksel, M., Işık, M., Tozoğlu, F., Köksal, E., (2021), Phytochemicals analysis and some bioactive properties of *Erica manipuliflora* Salisb.(EMS); Antibacterial, Antiradical and Anti-lipid Peroxidation. *Iranian Journal of Pharmaceutical Research: IJPR*, 20, 422.

- [10] Kuş, Ç., Taş, M., Küçükaydin, S., Tel-Cayan, G., Duru, M. E., (2019), Chemical analysis and in vitro antioxidant and anticholinesterase activities of essential oils and extracts from different parts of *Erica manipuliflora*. *J. Res. Pharm*, 23, 1098-1105.
- [11] Rahali, F. Z., Kefi, S., Bettaieb Rebey, I., Hamdaoui, G., Tabart, J., Kevers, C., Hamrouni Sellami, I., (2019), Phytochemical composition and antioxidant activities of different aerial parts extracts of *Ferula communis* L. *Plant Biosystems-An International Journal Dealing with all Aspects of Plant Biology*, 153, 213-221.
- [12] Maggi, F., Papa, F., Dall'Acqua, S., Nicoletti, M., (2016), Chemical analysis of essential oils from different parts of *Ferula communis* L. growing in central Italy. *Natural Product Research*, 30, 806-813.
- [13] Monti, M., Pinotti, M., Appendino, G., Dallochio, F., Bellini, T., Antognoni, F., Bernardi, F., (2007), Characterization of anti-coagulant properties of prenylated coumarin ferulenol. *Biochimica et Biophysica Acta (BBA)-General Subjects*, 1770, 1437-1440.
- [14] Mamoci, E., Cavoski, I., Andres, M. F., Díaz, C. E., Gonzalez-Coloma, A., (2012), Chemical characterization of the aphid antifeedant extracts from *Dittrichia viscosa* and *Ferula communis*. *Biochemical Systematics and Ecology*, 43, 101-107.
- [15] Maiuolo, J., Musolino, V., Guarnieri, L., Macri, R., Coppoletta, A. R., Cardamone, A., Mollace, V., (2022), *Ferula communis* L.(Apiaceae) Root Acetone-Water Extract: Phytochemical Analysis, Cytotoxicity and In Vitro Evaluation of Estrogenic Properties. *Plants*, 11, 1905.
- [16] Marchi, A., Appendino, G., Pirisi, I., Ballero, M., Loi, M. C., (2003), Genetic differentiation of two distinct chemotypes of *Ferula communis* (Apiaceae) in Sardinia (Italy). *Biochemical Systematics and Ecology*, 31, 1397-1408.
- [17] Lemus-Mondaca, R., Vega-Gálvez, A., Zura-Bravo, L., Ah-Hen, K., (2012), *Stevia rebaudiana* Bertoni, source of a high-potency natural sweetener: A comprehensive review on the biochemical, nutritional and functional aspects. *Food chemistry*, 132, 1121-1132.
- [18] Zaidan, U. H., Zen, N. I. M., Amran, N. A., Shamsi, S., Abd Gani, S. S., (2019), Biochemical evaluation of phenolic compounds and steviol glycoside from *Stevia rebaudiana* extracts associated with in vitro antidiabetic potential. *Biocatalysis and Agricultural Biotechnology*, 18, 101049.
- [19] Hajhashemi, S., Geuns, J. M., (2013), Free radical scavenging activity of steviol glycosides, steviol glucuronide, hydroxytyrosol, metformin, aspirin and leaf extract of *Stevia rebaudiana*. *Free Radicals and Antioxidants*, 3, S34-S41.

- [20] Pandey, D. K., Konjengbam, M., Dwivedi, P., Kaur, P., Kumar, V., Ray, D., Dey, A., (2021), Biotechnological interventions of in vitro propagation and production of valuable secondary metabolites in *Stevia rebaudiana*. *Applied Microbiology and Biotechnology*, 1-22.
- [21] Ahmad, M. A., Deng, X., Adeel, M., Rizwan, M., Shakoor, N., Yang, Y., Javed, R., (2022), Influence of calcium and magnesium elimination on plant biomass and secondary metabolites of *Stevia rebaudiana* Bertoni. *Biotechnology and Applied Biochemistry*, 69, 2008-2016.
- [22] Uluslu, F., Şahin, A., (2022), Changes in cytotoxic capacity, phenolic profile, total phenols and flavonoids of *Nigella damascena* L. seed extracts under different liquid fertilization. *South African Journal of Botany*, 150, 500-510.
- [23] Bouasla, I., Bouasla, A., Boumendjel, A., Messarah, M., Abdennour, C., Boulakoud, M. S., El Feki, A., (2014), *Nigella sativa* oil reduces aluminium chloride-induced oxidative injury in liver and erythrocytes of rats. *Biological trace element research*, 162, 252-261.
- [24] Naima, R., Oumam, M., Hannache, H., Sesbou, A., Charrier, B., Pizzi, A., Charrier-El Bouhtoury, F., (2015), Comparison of the impact of different extraction methods on polyphenols yields and tannins extracted from Moroccan *Acacia mollissima* barks. *Industrial Crops and Products*, 70, 245-252.
- [25] Zaidan, U. H., Hamid, S. N. M., Yusof, M. F. M., Ahmad, S., Abd Ghani, S. S., Shamsi, S., (2018), Chemical evaluation and antioxidant properties of extracts and essential oil from *Stevia rebaudiana* leaves. *Malaysian Applied Biology*, 47, 15-23.
- [26] Mahugo Santana, C., Sosa Ferrera, Z., Esther Torres Padrón, M., Juan Santana Rodríguez, J. (2009), Methodologies for the extraction of phenolic compounds from environmental samples: new approaches. *Molecules*, 14, 298-320.
- [27] Mohsen, S. M., Ammar, A. S., (2009), Total phenolic contents and antioxidant activity of corn tassel extracts. *Food chemistry*, 112, 595-598.
- [28] Zhang, Y., Cai, P., Cheng, G., Zhang, Y., (2022), A brief review of phenolic compounds identified from plants: Their extraction, analysis, and biological activity. *Natural Product Communications*, 17, 1934578X211069721.
- [29] Zeng, J., Cai, W., Yang, W., Wu, W., (2013), Antioxidant abilities, phenolics and flavonoids contents in the ethanolic extracts of the stems and leaves of different *Stevia rebaudiana* Bert lines. *Sugar Tech*, 15, 209-213.
- [30] Koroglu, A., Hurkul, M. M., Kendir, G., Kucukboyaci, N., (2019), In vitro antioxidant capacities and phenolic contents of four *Erica* L. (Ericaceae) taxa native to Turkey.

- [31] Turgay, O., Esen, Y., (2015), Antioxidant, total phenolic and antimicrobial characteristics of some species. *Bulgarian Journal of Agricultural Science*, 21, 498-503.
- [32] Aydın, F., Kahraman, Z. A., Türkoğlu, E. A., Müslüm, K. U. Z. U., Severoğlu, Z., (2021), In vitro antioxidant activity and carbonic anhydrase inhibitory features of *Ferula communis* extracts. *International Journal of Agriculture Environment and Food Sciences*, 5, 592-598.
- [33] Shukla, S., Mehta, A., Mehta, P., Bajpai, V. K., (2012), Antioxidant ability and total phenolic content of aqueous leaf extract of *Stevia rebaudiana* Bert. *Experimental and Toxicologic Pathology*, 64, 807-811.
- [34] Shukla, S., Mehta, A., Bajpai, V. K., Shukla, S., (2009), In vitro antioxidant activity and total phenolic content of ethanolic leaf extract of *Stevia rebaudiana* Bert. *Food and Chemical Toxicology*, 47, 2338-2343.
- [35] Tadhani, M. B., Patel, V. H., Subhash, R., (2007), In vitro antioxidant activities of *Stevia rebaudiana* leaves and callus. *Journal of food composition and Analysis*, 20, 323-329.
- [36] Nunes, R., Rodrigues, S., Pasko, P., Tyszka-Czochara, M., Grenha, A., de Carvalho, I. S., (2014), Effect of *Erica australis* extract on Caco-2 cells, fibroblasts and selected pathogenic bacteria responsible for wound infection. *Industrial Crops and Products*, 52, 99-104.
- [37] Guendouze-Bouchefa, N., Madani, K., Chibane, M., Boulekbache-Makhlouf, L., Hauchard, D., Kiendrebeogo, M., Duez, P. (2015). Phenolic compounds, antioxidant and antibacterial activities of three Ericaceae from Algeria. *Industrial crops and products*, 70, 459-466.
- [38] Santos, A., Luís, Â., Ferreira, S., Duarte, A. P., (2019), Antioxidant and antimicrobial activity and potential of heather (*Erica* spp.) extracts in the control of *Listeria monocytogenes*. *International Journal of Food Science & Technology*, 54, 862-870.
- [39] Sadki, C., Hacht, B., Souliman, A., Atmani, F., (2010), Acute diuretic activity of aqueous *Erica multiflora* flowers and *Cynodon dactylon* rhizomes extracts in rats. *Journal of Ethnopharmacology*, 128, 352-356.
- [40] Amroun, D., Hamoudi, M., Khennouf, S., Boutefnouchet, S., Harzallah, D., Amrane, M., Dahamna, S., (2021), In-vivo anti-inflammatory activity and safety assessment of the aqueous extract of Algerian *Erica arborea* L. (Ericaceae) aerial parts. *Journal of Ethnopharmacology*, 271, 113881.
- [41] Ghadimi, F., Mirzaie, A., Arasteh, J., (2019), Antibacterial and cytotoxicity of synthesized silver nanoparticles using *Erica carnea* extract on breast cancer cell line (MCF-7) and analysis of its apoptotic effects. *Razi Journal of Medical Sciences*, 26, 84-94.

- [42] Villareal, M. O., Han, J., Matsuyama, K., Sekii, Y., Smaoui, A., Shigemori, H., Isoda, H., (2013), Lupenone from *Erica multiflora* leaf extract stimulates melanogenesis in B16 murine melanoma cells through the inhibition of ERK1/2 activation. *Planta medica*, 79, 236-243.
- [43] Akaberi, M., Iranshahy, M., Iranshahi, M., (2015), Review of the traditional uses, phytochemistry, pharmacology and toxicology of giant fennel (*Ferula communis* L. subsp. *communis*). *Iranian Journal of Basic Medical Sciences*, 18, 1050.
- [44] Yoshino, Y., Tanaka, N., Tsuji, D., Itoh, K., Kashiwada, Y., (2023), Communiiferulins, farnesylated coumarins from the roots of *Ferula communis* and their anti-neuroinflammatory activity. *Journal of Natural Medicines*, 77, 173-179.
- [45] Shivanna, N., Naika, M., Khanum, F., Kaul, V. K., (2013), Antioxidant, anti-diabetic and renal protective properties of *Stevia rebaudiana*. *Journal of Diabetes and its Complications*, 27, 103-113.
- [46] Ferrazzano, G. F., Cantile, T., Alcidi, B., Coda, M., Ingenito, A., Zarrelli, A., Pollio, A., (2015), Is *Stevia rebaudiana* Bertoni a non cariogenic sweetener? A review. *Molecules*, 21, 38.
- [47] Iatridis, N., Kougioumtzi, A., Vlataki, K., Papadaki, S., Magklara, A., (2022), Anti-cancer properties of *Stevia rebaudiana*; more than a sweetener. *Molecules*, 27, 1362.
- [48] Mehmood, A., Zhao, L., Ishaq, M., Xin, W., Zhao, L., Wang, C., Xu, M., (2020), Anti-hyperuricemic potential of stevia (*Stevia rebaudiana* Bertoni) residue extract in hyperuricemic mice. *Food & Function*, 11, 6387-6406.
- [49] Znati, M., Ben Jannet, H., Cazaux, S., Souchard, J. P., Harzallah Skhiri, F., Bouajila, J., (2014), Antioxidant, 5-lipoxygenase inhibitory and cytotoxic activities of compounds isolated from the *Ferula lutea* flowers. *Molecules*, 19, 16959-16975.
- [50] Deveci, E., Tel-Çayan, G., Duru, M. E., (2018), Phenolic profile, antioxidant, anticholinesterase, and anti-tyrosinase activities of the various extracts of *Ferula elaeochytris* and *Sideritis stricta*. *International journal of food properties*, 21, 771-783.
- [51] Chen, J. M., Ding, L., Sui, X. C., Xia, Y. M., Lu, T., (2016), Production of a bioactive sweetener steviolbioside via specific hydrolyzing ester linkage of stevioside with a β -galactosidase. *Food chemistry*, 196, 155-160.
- [52] Khare, N., Chandra, S., (2019), Stevioside mediated chemosensitization studies and cytotoxicity assay on breast cancer cell lines MDA-MB-231 and SKBR3. *Saudi Journal of Biological Sciences*, 26, 1596-1601.

- [53] Ibrahem, E. S., Ragheb, E. M., Yousef, F. M., Abdel-Azizand, M. F., Alghamdi, B. A., (2020), Nutritional value, cytotoxic and antimicrobial activities of Stevia rebaudiana leaf extracts. J. Biochem. Technol, 11, 108-115.



RESEARCH ARTICLE

EFFECT OF TEMPERATURE ON THE PROTEIN PROFILE OF *MACROVIPERA LEBETINUS* (BLUNT-NOSED VIPER) VENOM: A PRELIMINARY STUDY

Naşit İĞCİ^{1,*}

¹ Nevşehir Hacı Bektaş Veli University, Faculty of Science and Arts, Department of Molecular Biology and Genetics, Nevşehir, Türkiye, igcinasit@yahoo.com.tr, ORCID: 0000-0001-6151-808X

Receive Date: 06.07.2023

Accepted Date: 26.09.2023

ABSTRACT

Snake venom is a complex biological fluid consisting mainly of proteins and peptides possessing diverse biological activities. Snake venoms draw attention due to their bioactive proteins/peptides with therapeutic and diagnostic potential. Testing the stability of snake venom proteins under different conditions including temperature provides useful data for venom research. *Macrovipera lebetinus*, blunt-nosed viper, is the biggest viper species of Türkiye distributed mainly in eastern and southeastern Anatolia. Although its venom components were investigated before, there is limited data regarding the effect of temperature on its venom proteins. The present study aimed to investigate the effect of temperature on the venom proteins of *M. lebetinus*. For this purpose, venom samples were incubated at 25, 37, and 50°C. Thereafter, venom proteins were separated by two-dimensional gel electrophoresis (2D-PAGE) method. Some qualitative and quantitative differences in the protein profile indicating structural changes and degradation were observed especially after 50°C treatment. It has been found that the protein spots most affected by temperature will most likely contain metalloproteinase, phospholipase A₂ and L-amino acid oxidase enzymes, by comparing the experimental molecular weight and pI values with those in the literature. Detailed studies including enzyme activities and toxicity assays will provide more data on the stability of *M. lebetinus* venom under different conditions.

Keywords: 2D-PAGE, *Macrovipera lebetinus obtusa*, Phospholipase A₂, Protease, Snake venom.

1. INTRODUCTION

Snake venom is a proteinaceous secretion of the cells in the venom gland. Viperid venoms, rich in proteases, interfere with the hemostatic system and cause tissue damage [1]. Snakebite is one of the important health problems especially in Africa and Asia [2]. But snake venom is also a source for the discovery of new bioactive proteins and peptides that can be used for therapeutic and diagnostic purposes [3]. Proteins and peptides found in snake venoms can be grouped into major protein families, however, the composition of snake venom shows intra- and inter-specific variation at different degrees [4].

Macrovipera lebetinus (Linnaeus, 1758) (= *Macrovipera lebetina*, *Vipera lebetina*), blunt-nosed viper, is the biggest viper species distributed in Türkiye and Cyprus. The range of this medicinally important viper reaches to Kashmir region towards the east and Kazakhstan and Dagestan (southwest of Russia) to the north [5]. Its bite affects blood coagulation, and causes symptoms like hemorrhage, tissue damage, and swelling [6]. The following protein families have been identified in the venom of *M. lebetinus* up to date: snake venom metalloproteinase (SVMP), snake venom serine proteinase (SVSP), phospholipase A₂ (PLA₂), L-amino acid oxidase (LAAO), hyaluronidase, 5'-nucleotidase, phosphodiesterase (PDE), C-type lectin-like protein (CLP), cysteine-rich secretory protein (CRISP), vascular endothelial growth factor (VEGF), nerve growth factor (NGF), disintegrin, Kunitz-type serine protease inhibitor, bradykinin-potentiating peptide (BPP), and natriuretic peptide [7,8]. These proteins are responsible for the biological activities of *M. lebetinus* venom such as cytotoxic, antimicrobial, antiaggregant, anticancer, anti/procoagulant, necrotic and hemorrhagic activities [9-12].

Effects of the temperature on the biological activities and proteomic profiles of some snake venoms were investigated before. Some of these studies reported the presence of the heat-resistant toxins (even after incubation at 100°C). However, activity losses were also reported in some venoms after heat treatment. These studies have indicated that changes in the activities and structures of snake venom proteins may vary between different protein classes and should be studied for each venom separately [13].

Snake venom is an important natural source for the discovery of peptides and proteins with therapeutic and diagnostic value [3]. Many proteins and peptides were purified and characterized from snake venoms up to date, including *M. lebetinus* venom [7]. Investigating the stability and activity of the venom proteins under different conditions (eg. temperature, pH) is important for venom research, biotechnological product development, antiserum production processes, and treatment of snakebite. In the present study, it was aimed to investigate the effect of temperature on the venom proteins of *M. lebetinus*, a medicinally important viper that causes snakebite cases resulting in hospital care [6,14], by using two-dimensional polyacrylamide gel electrophoresis (2D-PAGE).

2. MATERIAL AND METHODS

2.1. Venom and Reagents

Pooled venom extracted from two adult *M. lebetinus obtusa* (Figure 1) collected from Diyarbakır and Şanlıurfa provinces (southeastern Türkiye) was lyophilized as described before [8,9]. Ethical permission was obtained from Ege University Animal Ethics Committee when the study was conducted (permission no. 2010-43). All the reagents were molecular biology grade and deionized water was obtained from the Milli-Q system (Millipore, Billerica, USA). Agarose was purchased from Sigma-Aldrich (St. Louis, USA), ampholyte and dithiothreitol (DTT) from Fluka (St. Gallen, Switzerland); 3-[(3-cholamidopropyl)dimethylammonio]-1-propane sulfonate (CHAPS) and bovine serum albumin (BSA) were from Amresco (OH, USA), protein ladder was from Fermentas (Vilnius, Lithuania). All the other reagents (e.g., acrylamide/bis 30% solution, bromophenol blue, iodoacetamide, Bradford reagent, urea, tris, sodium dodecyl sulfate) were purchased from Bio-Rad (CA, USA).



Figure 1. In situ photograph of *Macrovipera lebetinus 355btuse* from Şanlıurfa province.

2.2. Treatments

After reconstitution of the venom sample by deionized water, the sample was then aliquoted into three tubes (100 μ L) and incubated at 25, 37, and 50°C for one hour (one tube for each temperature). After the treatment, the samples were immediately mixed with 2D-PAGE rehydration buffer (7 M urea, 2 M thiourea, 4% CHAPS, 1% ampholytes) and prepared for isoelectric focusing.

2.3. Determination of the Protein Concentration

The protein amount of the reconstituted venom was determined using Bradford's method modified for a 96-well microplate as described before [8,9]. BSA was used as a calibration standard. All the measurements were carried out in triplicate and the mean values were used for calculations.

2.4. 2-Dimensional Polyacrylamide Gel Electrophoresis (2D-PAGE)

After treatments, venom samples were immediately mixed with 2D-PAGE rehydration buffer to a total volume of 300 μ L and pipetted into isoelectric focusing wells for active rehydration at 50 V constant voltage overnight. The 2D-PAGE protocol was applied as described in detail before [8]. Protein amount was determined using the reconstituted venom sample and the same volume (175 μ g protein) of each treatment was loaded.

3. RESULTS

Venom proteins of *M. lebetinus* were separated between pH 4-8 isoelectric points and approximately 10-150 kDa molecular weights (Figure 2). Chains of spots were observed, possibly due to the presence of protein isoforms. The profiles of 25 and 37°C samples were similar in general. But some qualitative and quantitative differences were observed after incubation at 50°C (Figure 2). Intense protein spots at around 100-120 kDa and pI 5,8 pH disappeared, or the intensity decreased significantly in the 50°C sample, whereas four spots became visible at \sim 40 kDa and 6.3 pI. Spots at

around 13-14 kDa and 4,4 pI were significantly changed in the 50°C sample with a decrease in the intensities of two spots while the intensities of two lower spots were increased (Figure 2C). The intensity of one spot below the 15 kDa marker and at pH 7 was also altered between samples.

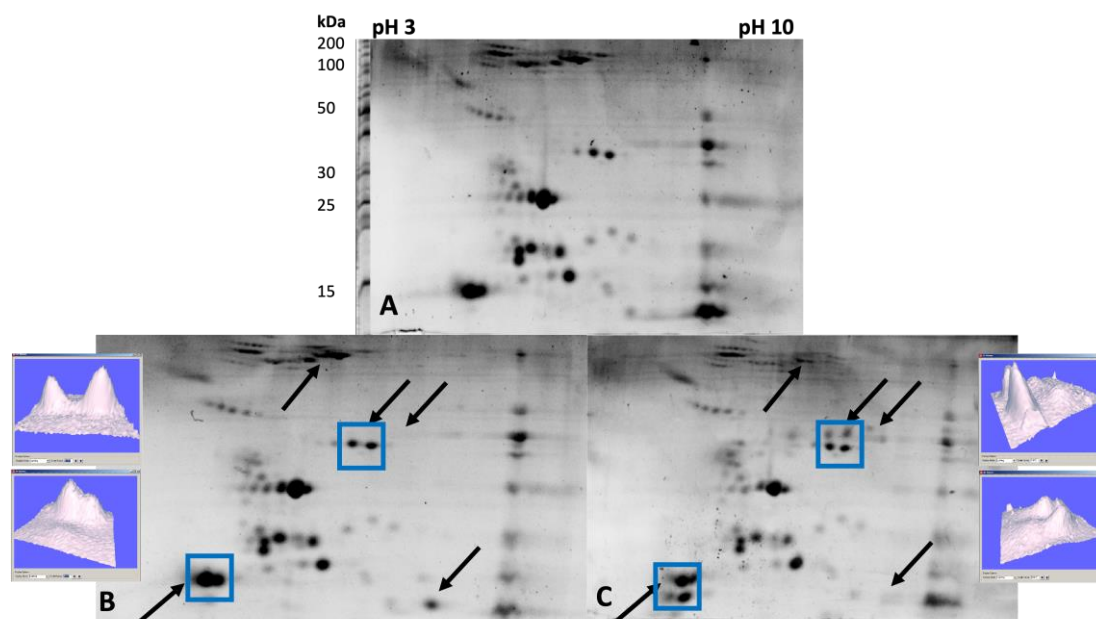


Figure 2. Protein profiles of *Macrovipera lebetinus* venom obtained by 2D-PAGE after incubation at 25 (A), 37 (B), and 50°C (C). Arrows indicate the prominent differences in protein spot patterns. Representative density graphics obtained from the gel analysis software PDQuest were demonstrated for two regions indicated with blue boxes.

4. DISCUSSION

The results of the present study showed that treating venom at 50°C temperature causes some changes in the protein structure, while 25 and 37°C temperatures did not differ significantly. As the main prey of blunt-nosed vipers are mammals and birds, a 25-37°C temperature can be considered within the optimal activity range of the venom [15]. Hence, bioactivity studies using snake venoms are generally carried out at these degrees. But of course, maximum activity temperatures of purified enzymes may change. For example, optimum working temperature can be high up to 75°C for PLA₂s in *Daboia russelli* [16], whereas it can be around 25°C for PLA₂s from *Vipera ammodytes* [17]. A dimeric metalloproteinase in the venom of *Cerastes vipera* was reported to have optimum of 60°C [18].

The effect of temperature on the overall activity and protein profiles of different snake venoms was also investigated by various researchers. The stability of hemorrhagic toxins in different viper species belonging to the genera *Agkistrodon*, *Bothrops*, *Crotalus*, and *Sistrurus* was investigated under

different temperature conditions [19]. Even with incubation at 100°C for 5 min, *in vitro* proteolytic activity and *in vivo* hemorrhagic activity of some species were retained. However, activity loss was observed for some of the species tested. Heat treatment resulted in the denaturation of some proteins but most of the bands remained similar in many species, as assessed by SDS-PAGE. The effect of temperature and different storage conditions on the protein profile, enzyme activity and toxicity of *Crotalus molossus molossus* (a rattlesnake) crude venom was investigated and it was found that incubating the venom sample at 37°C even for a week had little effect on the protein profile and activities while LAAO activity showed greater variation [13]. In another study, effect of the temperature on a new LAAO purified from *Crotalus durissus collilineatus* venom was investigated and significant activity loss was observed after treatment at 37 and 100°C temperatures [20]. Changes in PLA₂ and protease activities were reported in historical venom samples of *Bothrops asper* and *B. atrox* that had been stored by desiccation at room temperature, indicating the effects of the storage conditions on the venom bioactivity [21]. These previous reports show that some proteins are more prone to show variation in their activities dependent to the storage conditions such as temperature change while some of them are more stable.

Effect of the temperature on *Macrovipera lebetinus* venom was assessed by 2D-PAGE method in the present study. Venoms of the two subspecies of *M. lebetinus* (*M. l. obtusa* and *M. l. lebetina*) were compared by 2D-PAGE and protein identification from *M. l. obtusa* venom was achieved using MALDI-TOF mass spectrometry-based bottom-up proteomic analysis in a previous study [8]. Additionally, some other proteomic investigations were carried out on *M. lebetinus* venom from different subspecies using the venomomics approach [22-24] and many of its major venom proteins were purified [7]. The aim of the present study was to investigate the effect of temperature on the venom proteome of *M. lebetinus*. Therefore, mass spectrometry-based protein identification was not performed again in this study, rather the previous studies were referenced to have a clue on the protein classes. SDS-PAGE was used commonly to compare protein profiles in studies investigating the effect of temperature on snake venoms [19,13]. But 2D-PAGE is a more powerful technique that separates more proteoforms allowing to make more detailed comparisons [25,26]. The protein profile of *M. lebetinus* venom as obtained by 2D-PAGE in the present study is consistent with a previous study by İgci and Demiralp [8]. Earlier studies have shown that the most abundant proteins classes found in *M. lebetinus* venom are SVMP, SVSP, PLA₂, CLP, LAAO, and disintegrin [8,22-24], which are responsible for its pathogenesis and biological activities [9-12].

According to the results, one of the altered protein spot regions is around 100-120 kDa and 5.8 pI, in which the intensity of two spots was decreased significantly. Based on the previous studies, it can be concluded that SVMP, LAAO, PDE, and 5'-nucleotidase can be found between this molecular weight in *M. lebetinus* venom and SVMP is more abundant than the others [7,15]. SVMP and LAAO can be found at the same molecular weight and pI in *M. lebetinus* venom [27]. Therefore, it is difficult to separate these proteins by 2D-PAGE. Although reducing conditions were used for 2D-PAGE, subunits, monomeric forms, and/or native multimeric proteins that remained unreduced may present in these spots. Earlier studies have shown that high-molecular-weight snake venom proteins are more affected by heat than low-MW proteins and peptides [28-30]. LAAO isolated from *Macrovipera lebetinus* venom was also found to be stable from 4 to 25°C while heating at 70°C inactivated the enzyme in 15 min [27]. Hence, heat-resistant low-mw toxins/proteins, rather than high-mw ones were

detected and identified in various viperid and elapid venoms [19,26-28]. This conclusion in the literature is also valid for *M. lebetinus* venom, as the results revealed that structural changes/degradation occurred especially in high-MW proteins.

Another group of altered spots was observed at ~ 13 kDa and 4.4 pI. Acidic PLA₂ type II enzymes with aggregation inhibiting and anti-cancer activities were purified from *M. lebetinus* venom, having molecular weights between 13-14 kDa and pI between 4,0-4,6 pH [31,32]. *M. lebetinus* venom also contains heterodimeric disintegrins with a similar molecular weight as PLA₂ enzymes have [7]. Although experimentally determined pI is not available in the literature, theoretical pI calculation (performed through UniProt) of a disintegrin lebein-2-alpha (UniProt: Q3BK13) gives the result as 7,5, which is not consistent with the experimentally observed pI value of the spot of interest. There is another spot that matches these values (~ 12 kDa, 7,8 pI) on 2D-PAGE gels. Moreover, PLA₂ was identified from the same 2D-PAGE spot in a previous study [8]. Although exact identification can be achieved using mass spectrometry or N-terminal sequencing, results of the earlier studies indicate that these protein spots in 2D-PAGE gel possibly contain PLA₂ enzymes. Decreasing PLA₂ activity was also reported for *Crotalus durissus terrificus* venom after heat treatment at 56°C [29]. In the aforementioned study, it was found that heating *Crotalus durissus terrificus* rattlesnake venom at 56, 70, and 100°C gradually decreased the toxic activity (LD₅₀) and PLA₂ activity, which indicated possible changes in protein structures. The results of the present study also indicated a structural change in PLA₂ of *M. lebetinus* venom. Four spots appeared after 50°C heat treatment may originate from the degradation of proteins with higher molecular weight, which was visible on 2D-PAGE images. Altered protein spots below 15 kDa and at pI 7 may contain other types of PLA₂ enzymes or disintegrin.

In conclusion, the present preliminary study showed that 50°C heat treatment led to the structural changes and degradation of some proteins in *M. lebetinus* venom, while most of the protein spots were not affected. Although similar studies were carried out with the venoms of different studies, there is limited data available in the literature about *M. lebetinus* crude venom in this regard. Venom proteins of *M. lebetinus* affected by heat are among the most abundant proteins based on the spot intensities on 2D-PAGE gel. These proteins are possibly PLA₂, SVMP, and LAAO, which play important roles in the pathology of *M. lebetinus* venom [7,9]. Moreover, these proteins have the potential for therapeutic and diagnostic use. For example, metalloproteinases purified from *M. lebetinus* venom interfere with the coagulation cascade by having factor X activating and fibrin(ogen)olytic activities [7]. Snake venom samples are routinely stored in the freezer (preferably -80°C) and freeze-dried. However, investigations on the thermal stability and storage conditions of venom proteins could provide useful data for venom research, antivenom production, and the evaluation of possible treatment methods for snakebites. The study should be extended to include higher temperatures, enzyme activities, *in vivo* and *in vitro* toxicity assays, and protein identification.

ACKNOWLEDGMENTS

I thank Prof. Dr. Bayram GÖÇMEN who passed away on 22 March 2019 and Prof. Dr. Mehmet Zülfü YILDIZ, for their help in obtaining the venom samples. I am grateful to Ankara University Biotechnology Institute for providing laboratory infrastructure.

REFERENCES

- [1] Chippaux, J-P., (2006), Snake Venoms and Envenomations (1st ed.). Florida (USA): Krieger Publishing Company.
- [2] Kasturiratne, A., Wickremasinghe, A. R., de Silva, N., Gunawardena, N. K., Pathmeswaran, A., Premaratna, R., Savioli, R., Lalloo, D. G., and de Silva, H. J., (2008), The Global Burden of Snakebite: A Literature Analysis and Modelling Based on Regional Estimates of Envenoming and Deaths, *PloS Medicine*, 5, 11, e218.
- [3] von Reumont, B. M., Anderluh, G., Antunes, A., Ayvazyan, N., Beis, D., Caliskan, F., Crnković, A., Damm, M., Dutertre, S., Ellgaard, L., Gajski, G., German, H., Halassy, B., Hempel, B.-F., Hucho, T., Iğci, N., Ikonopoulou, M. P., Karbat, I., Klapa, M. I., Koludarov, I., Kool, J., Lüddecke, T., Mansour, R. B., Modica, M. V., Moran, Y., Nalbantsoy, A., Ibáñez, M. E. P., Panagiotopoulos, A., Reuveny, E., Céspedes, J. S., Sombke, A., Surm, J. M., E. A. B. Undheim, Verdes, A., Zancolli, G., (2022), Modern venomics—Current insights, novel methods, and future perspectives in biological and applied animal venom research, *GigaScience*, 11, 1-27.
- [4] Chippaux, J. P., Williams, V., and White, J., (1991), Snake venom variability: Methods of study, results and interpretation, *Toxicon*, 29, 11, 1279-1303.
- [5] Mallow, D., Ludwig, D., and Nilson, G., (2003), True vipers: Natural history and toxinology of old world vipers (1st ed), Florida: Krieger Publishing Company.
- [6] Göçmen, B., Arıkan, H., Özbel, Y., Mermer, A., and Çiçek, K., (2006), Clinical, Physiological and Serological Observations of a Human Following a Venomous Bite by *Macrovipera lebetina lebetina* (Reptilia: Serpentes), *Acta Parasitologica Turcica*, 30, 2, 158-162.
- [7] Siigur, J., Aaspõllu, A., and Siigur, E., (2019), Biochemistry and pharmacology of proteins and peptides purified from the venoms of the snakes *Macrovipera lebetina* subspecies, *Toxicon*, 158, 16-32.
- [8] Iğci, N., and Ozel Demiralp, D., (2012), A preliminary investigation into the venom proteome of *Macrovipera lebetina obtusa* (Dwigubsky, 1832) from Southeastern Anatolia by MALDI-TOF mass spectrometry and comparison of venom protein profiles with *Macrovipera lebetina lebetina* (Linnaeus, 1758) from Cyprus by 2D-PAGE. *Archives of Toxicology*, 86, 3, 441-451.
- [9] İğci, N., Özel Demiralp, F. D., and Yıldız, M. Z., (2019), Cytotoxic Activities of the Crude Venoms of *Macrovipera lebetina lebetina* from Cyprus and *M. l. obtusa* from Turkey (Serpentes: Viperidae) on Human Umbilical Vein Endothelial Cells, *Commagene Journal of Biology*, 3, 2, 110-113.
- [10] Süzergöz, F., İğci, N., Çavus, C., Yıldız, M.Z., Coşkun, M.B., and Göçmen, B. (2016), In vitro cytotoxic and proapoptotic activities of Anatolian *Macrovipera lebetina obtusa* (Dwigubski,

- 1832) crude venom on cultured K562 human chronic myelogenous leukemia cells, *UHOD International Journal of Hematology and Oncology*, 26, 1, 37-46.
- [11] Ozen, M.O., İğci, N., Yalçın, H. T., Goçmen, B., and Nalbantsoy, A., (2015), Screening of cytotoxic and antimicrobial activity potential of Anatolian *Macrovipera lebetina obtusa* (Ophidia: Viperidae) crude venom, *Frontiers in Life Science*, 8, 4, 363-370.
- [12] Yücel Ağan, A. F., and Hayretdağ, S., (2019), The effects of *Macrovipera lebetina* venom on mice, *Toxin Reviews*, 38, 2, 87-92.
- [13] Munekiyo, S. M., and Mackessy, S. P., (1998), Effects of Temperature and Storage Conditions on the Electrophoretic, Toxic and Enzymatic Stability of Venom Components, *Toxicon*, 119B, 1, 119-127.
- [14] Cengiz, M., Sarban, S., and Ganidağlı, S., (2005), Koca Engerek (kör yılan) ısırılması sonrası gelişen ciddi trombositopeni ve ödemin yılan antiserumu ile tedavisi, *Türk Anestezi ve Reanimasyon Dergisi*, 33, 5, 424-428.
- [15] Prinzing, R., Pressmar, A., and Schleucher, E., (1991), Body temperature in birds. *Comparative Biochemistry and Physiology Part A: Physiology*, 99, 4, 499-506.
- [16] Vishwanath, B. S., Kini, R. M., and Gowda, T. V., (1988), Purification and partial biochemical characterization of an edema inducing phospholipase A₂ from *Vipera russelli* (Russell's viper) snake venom, *Toxicon*, 26, 8, 713-720.
- [17] Aleksiev, B., and Tchorbantov, B., (1976), Action on phosphatidylcholine of the toxic phospholipase A₂ from the venom of Bulgarian viper (*Vipera ammodytes ammodytes*), *Toxicon*, 14, 6, 477-485.
- [18] Abdel-Aty, A. M., Salama, W. H., Ali, A. A., and Mohamed, S. A., (2019), A hemorrhagic metalloprotease of Egyptian *Cerastes vipera* venom: Biochemical and immunological properties, *International Journal of Biological Macromolecules*, 130, 695-704.
- [19] Ownby, C. L., Colberg, T. R., and Li, Q., (1994), Presence of heat-stable hemorrhagic toxins in snake venoms, *Toxicon*, 32, 8, 945-954.
- [20] de Freitas, V., Costa, T. R., Nogueira, A. R., Polloni, L., de Melo Fernandes T. A., Correia, L. I. V., Borges, B. C., Teixeira, S. C., Silva, M. J. B., Amorim, F. G., Quinton, L., Saraiva, A. L., Espindola, F. S., Iwai, L. K., Rodrigues, R. S., Yoneyama, K. A. G., de Melo Rodrigues Ávila, V., (2023), Biochemical characterization and assessment of leishmanicidal effects of a new L-amino acid oxidase from *Crotalus durissus collilineatus* snake venom (CollinLA AO-I), *Toxicon*, 230, 107156.

- [21] Almeida J. R., Mendes, B., Patiño, R. S. P., Pico, J., Laines, J., Terán, M., Mogollón, N. G. S., Zaruma-Torres, F., Caldeira, C. A. D. S., da Silva, S. L., (2020), Assessing the stability of historical and desiccated snake venoms from a medically important Ecuadorian collection, *Comparative Biochemistry and Physiology Part C: Toxicology & Pharmacology*, 230, 108702.
- [22] Sanz, L., Ayvazyan, N., and Calvete, J. J., (2008), Snake venomomics of the Armenian mountain vipers *Macrovipera lebetina obtusa* and *Vipera raddei*, *Journal of Proteomics*, 71, 198-209.
- [23] Bazaa, A., Marrakchi, N., El Ayeb, M., Sanz, L., and Calvete, J. J., (2005), Snake venomomics: comparative analysis of the venom proteomes of the Tunisian snakes *Cerastes cerastes*, *Cerastes vipera* and *Macrovipera lebetina*, *Proteomics*, 5, 4223-4235.
- [24] Ghezellou, P., Dillenberger, M., Kazemi, S. M., Jestrzemeski, D., Hellmann, B., and Spengler, B., (2022), Comparative Venom Proteomics of Iranian, *Macrovipera lebetina cernovi*, and Cypriot, *Macrovipera lebetina lebetina*, *Giant Vipers, Toxins*, 14, 10, 716.
- [25] Serrano, S. M. T., Shannon, J. D., Wang, D., Camargo, A. C. M., and Fox, J. W., (2005), A multifaceted analysis of viperid snake venoms by two-dimensional gel electrophoresis: An approach to understanding venom proteomics, *Proteomics*, 5, 2, 501-510.
- [26] Georgieva, D., Risch, M., Kardas, A., Buck, F., von Bergen, M., and Betzel, C., (2008), Comparative Analysis of the Venom Proteomes of *Vipera ammodytes ammodytes* and *Vipera ammodytes meridionalis*, *Journal of Proteome Research*, 7, 3, 866-886.
- [27] Tõnismägi, K., Samel, M., Trummal, K., Rõnnholm, G., Siigur, J., Kalkkinen, N., and Siigur, E., (2006), L-Amino acid oxidase from *Vipera lebetina* venom: Isolation, characterization, effects on platelets and bacteria, *Toxicon*, 48, 2, 227-237.
- [28] Binh, D. V., Thanh, T. T., and Chi, P. V., (2010), Proteomic characterization of the thermostable toxins from *Naja naja* venom, *The Journal of Venomous Animals and Toxins including Tropical Diseases*, 16, 4, 631-638.
- [29] Rangel-Santos, A. C., and Mota, I., (2000), Effect of heating on the toxic, immunogenic and immunosuppressive activities of *Crotalus durissus terrificus* venom, *Toxicon*, 38, 10, 1451-1457.
- [30] Gomes, A., Choudhury, S. R., Saha, A., Mishra, R., Giri, B., Biswas, A. K., Debnath, A., and Gomes A., (2007), A heat stable protein toxin (*drCT-I*) from the Indian Viper (*Daboia russelli russelli*) venom having antiproliferative, cytotoxic and apoptotic activities, *Toxicon*, 49, 46-56.
- [31] Bazaa, A., Luis, J., Srairi-Abid, N., Kallech-Ziri, O., Kessentini-Zouari, R., Defilles, C., Lissitzky, J. C., El Ayeb, M., and Marrakchi, N., (2009), MVL-PLA2, a phospholipase A2 from *Macrovipera lebetina transmediterranea* venom, inhibits tumor cells adhesion and migration, *Matrix Biology*, 28, 4, 188-193.

- [32] Vija, H., Samel, M., Siigur, E., Aaspõllu, A., Trummal, K., Tõnismägi, K., Subbi, J., and Siigur J., (2009), Purification, characterization, and cDNA cloning of acidic platelet aggregation inhibiting phospholipases A₂ from the snake venom of *Vipera lebetina* (Levantine viper), *Toxicon*, 54, 4, 429-439.

APPENDIX

EGE ÜNİVERSİTESİ
HAYVAN DENEYLERİ YEREL ETİK KURULUSAYI: 2010-043
KONU: Onay

25/02/2011

Etik kurulumuza yapmış olduğunuz başvuru doğrultusunda "TÜRKİYE'DE YAYILIŞ GÖSTEREN BAZI ENGEREK ZEHİRLERİNİN MOLEKÜLER İÇERİKLERİ, SİTOKSİSİTELERİ VE KOAGÜLASYON ÜZERİNDEKİ ETKİLERİNİN ARAŞTIRILMASI VE BİYOTEKNOLOJİK KULLANIM POTANSİYELİNİN DEĞERLENDİRİLMESİ" isimli araştırma projeniz değerlendirilmiştir.

Yürütücü: Yrd. Doç. Dr. Fatma Duygu ÖZEL DEMİRALP, Ankara Üniversitesi Biyoteknoloji Enstitüsü
Prof. Dr. Bayram GÖÇMEN, Ege Üniversitesi Fen Fakültesi
Doç. Dr. Ahmet Rüçhan AKAR, Ankara Üniversitesi Tıp Fakültesi
Op. Dr. Serkan DURDU, Ankara Üniversitesi Tıp Fakültesi
Arş. Gör. Mehmet Zülfi YILDIZ, Ege Üniversitesi Fen Fakültesi
Biyo. Naşit İĞCI, Ankara Üniversitesi Biyoteknoloji Enstitüsü

Proje başvuru formunuzda belirtildiği koşullarda deney hayvanı kullanarak araştırmayı gerçekleştirmeniz kurumumuz tarafından uygun bulunmuştur. Saygılarımla bilgilerinizi rica ederim.

Prof. Dr. Rasih YILMAZ
(E.Ü. Hayvan Deneyleri Yerel Etik Kurulu Başkanı)

Prof. Dr. Süleyman AKKAN

Prof. Dr. İsmet DELİLOĞLU GÜRHAN

Prof. Dr. Gülcihan Mehtap KÖKSAL

Doç. Dr. N. Ülkü KARABAY YAVAŞOĞLU

Özcan NALBANTOĞLU

Prof. Dr. Hüseyin TEZEL

Prof. Dr. Lokman ÖZTÜRK

Doç. Dr. Tansel TANRIKUL

Yrd. Doç. Dr. Gülnur SEVİN

Tingiz ÖZCAN



RESEARCH ARTICLE

**CHARACTERIZATION OF MORTALITY PREDICTION: AN ENSEMBLE LEARNING
ANALYSIS USING THE MIMIC-III DATASET**

Anıl Burcu ÖZYURT SERİM^{1,*}

^{1,*} İstanbul Haliç University, Management Information Systems, İstanbul, Türkiye, burcuozyurt@halic.edu.tr,
ORCID: 0000-0001-98682676

Receive Date: 23.08.2023

Accepted Date: 30.09.2023

ABSTRACT

Applications that employ medical data are directly impacted by the classification of imbalanced data. It is vital due to the nature of classification and solutions about medical data. The purpose of this article is to identify a machine learning model that may be successfully applied in the medical field to reduce the number of mortality and optimize the efficiency of hospital resources. For this reason, it is thought that the better the performance of the ML model, the more a different perspective will be gained on the problems in today's medicine. Therefore, in the study, Weighted Random Forest (WRF) and Balanced Random Forest (BRF) which are ensemble machine learning (ML) methods for imbalanced data were implemented to identify the performance of the algorithms for mortality determination from open-source MIMIC-III dataset by using vital signs, comorbidities, and laboratory variables with demographic characteristic information. To evaluate the performance of WRF and BRF, a Random Forest Classifier (RFC) was also implemented to investigate the power of developed models for imbalanced data. In addition, the features used in the ML methods were separated into three groups to explore the impact of the vital signs, comorbidities, and laboratory variables with demographic characteristics separately on mortality identification. In addition to previous applications on UCI datasets, the present study revealed that the BRF method for imbalanced medical data provides high performance in determining the majority and minority classes of the data by using vital signs and laboratory variables with demographic characteristics.

Keywords: *MIMIC-III, Random Forest, Weighted Random Forest, Balanced Random Forest, Ensemble Learning.*

1. INTRODUCTION

Many different data analysis techniques can now be used on massive amounts of data as a result of recent technical advancements. Applying these ideas to the critical care unit is a much more crucial issue because of the intensive care unit's data-rich nature. Decision support systems have made it possible to observe a well-defined set of criteria for rare diseases or unexplained diseases with thorough medical imaging data when they are integrated into ordinary clinical functions [1]. Selection,

analysis, and diagnostic interpretation of radiological imaging have been done using the knowledge acquired in this manner. As a result, healthcare personnel are able to treat more patients securely, operate more productively, and make fewer mistakes than ever before because of data-based decision support systems, recently [1].

Also, artificial intelligence and the integration of automated information systems have greatly enhanced medical practices. The open-source MIMIC-II, MIMIC-III, and MIMIC-IV dataset has recently been the subject of studies examining its performance in forecasting hospital mortality in intensive care patients and comparing its performance with that of different algorithms. It is necessary to estimate mortality among intensive care unit (ICU) inpatients in order to assess the severity of a patient's condition and weigh the advantages of cutting-edge therapies, interventions, and healthcare initiatives [2]. In a number of these research, the ability to forecast hospital mortality in intensive care patients using nonparametric methods based on artificial neural networks was assessed. [3, 4]. These studies came to the conclusion that nonparametric methods may be at least as good at predicting ICU mortality as traditional logistic regression [108]. In a related other study, Karun et al. employed the sandwich regression method to determine the characteristics that increase the risk of pneumonia in patients receiving intensive care. The study found that BMI, kidney disease, hypertension, diabetes, and asthma are some of the major risk factors for pneumonia in the elderly. According to the Poisson regression findings, he also discovered that the middle-aged group had a larger probability of acquiring pneumonia in the elderly [5]. Pirracchio's [6] study examined if an ensemble machine learning technique called Super Learner would improve hospital mortality prediction for critically ill intensive care patients using data from the Medical Information Mart for Intensive Care II (MIMIC-II). The prediction score generated based on Super Learner was demonstrated to provide better results in terms of both discrimination and calibration when compared with mortality scoring outcomes such as SAPS II (Simplified Acute Physiology Score), APACHE II (Acute Physiologic Assessment and Chronic Health Evaluation), and SOFA (Sequential Organ Failure Assessment) [6, 7]. Support Vector Machine (SVM), Logistic Regression (LR), and XGBoost classification algorithms were employed in the study by Ergul Aydn & Kamişli Ozturk, [8] one of the comparable studies in this field, to assess whether the patients' stays in critical care were longer than 3 days. The study found that, similarly to earlier prediction articles, the XGBoost classifier outperformed Support Vector Machine (SVM) and Logistic Regression (LR) [9, 10, 11, 12]. Poucke's study was to compare the predictive performance of Decision Tree, Naïve Bayes, Logistic and Regression methods, and ensemble learning methods (Random Forest, Boosting, and Bagging) when assessing the predictive power of laboratory tests for hospital mortality in patients admitted to the intensive care unit. In this study using ensemble methods, Random Forests provided the best prediction accuracy for mortality risk prediction, consistent with previous research [13, 14]. According to a study by Yang et al., c-med GAN (conditional medical generative adversarial network) offers a strong classification for predicting mortality in critical care patients when compared to the SAPS II score, SVM (support vector machine), and MLP (multilayer perceptron). When the dataset size was reduced, C-med GAN outperformed MLP in terms of death prediction [2]. Xia et al.'s study, which discovered that over 40% of elderly patients were hospitalized to the intensive care unit, observed that longer hospital stays were associated with higher short- and long-term risks of death [15]. In order to predict ICU mortality, Dybowski et al. and Kim et al. [16, 17] show that nonparametric methods may operate better than conventional logistic regression models.

An important alternative for diagnosing and beginning treatments in the healthcare sector is based on supervised machine learning, recently [18]. Ensemble learning, which takes into consideration themes and attributes, is one of the finest supervised machine learning (ML) approaches to categorizing data. The categorization can be difficult by using basic classification algorithms for the complex data structure including many features [18]. At this point, implementation of innovative techniques such as Balanced Random Forest (BRF) [19] and Weighted Random Forest (WRF) [19] can be a solution since these advanced ensemble learning methods has specific strategies for the datasets that are unbalanced ensuring that each class is given the appropriate level of consideration during model training. Unbalanced data, also known as imbalanced data, means the situation in which the number of instances for each class in the dataset is unequal. In other words, a class has significantly more samples than another class or classes.

In this study, BRF and WRF models, which are the improved versions of one of the successful ensemble model Random Forest Classifier (RFC), were implemented to investigate the feature importance for mortality prediction by using MIMIC-III dataset [20] that can be considered a new approach for identification of the mortality by random forest-based algorithms for imbalanced medicine data. With the presented study authorities can plan preparedness, and allocation of financial resources based on how long patients remain in intensive care units with the help of random forest-based machine learning models. Additionally, it offers suggestions for how to allocate resources effectively, enhance the caliber of healthcare services, and prioritize macro policies in the health sectors of nations by using machine learning methods. Since in medical science, the datasets may have imbalanced structure and limited size, the presented work can be an indicator for the usage of an improved version of random forest-based algorithms for unbalanced data by also considering the feature selection effect on model performances. For this purpose, the features in the data were separated into three groups such as comorbidities, laboratory variables with vital signs, and both to understand the impact of the corresponding properties on mortality of the patients with demographic characteristics. To compare the model performances RFC was also applied to the dataset in the similar way.

2. LITERATURE REVIEW

In today's evolving technology, the significance of artificial intelligence-based machine learning (ML) approaches is on the rise across diverse domains, including natural sciences [19,21], anomaly detection [22,23], healthcare [24,25], object recognition [26,27], and business [18] since it has a huge impact by radically changing the way of solving sophisticated problems. As a result of the advancement of machine learning algorithms in the field of health, modeling methodologies have increased in variety [24,25]. Predictive models are useful tools to comprehend the underlying causes of diseases and to expand clinical knowledge, the collection and analysis of massive amounts of critical care data is crucial. Large-scale Critical Care databases are valuable tools for learning about individuals' risk factors, regular critical illness history, and the efficacy of various treatment approaches. Because, patients in the critical care unit are more likely than other patients to experience many problems today, and mortality is also higher [28]. Innovations in disease therapeutics and survival rates are essential in this setting because cancer and comorbidity are more closely associated with aging populations in industrialized countries. Various data sources, including clinical records and

laboratory findings, are used to get this data [29]. Incorrect or missing data during the data collection phase, although unsynchronized time-referenced data, difficulty processing different data formats, and restrictions on digital storage capacity are the difficulties encountered, the MIMIC-III database, which is easily accessible by the researcher, provides the advantage of not having an access fee, unlike other databases [20,30].

All adult patients admitted to Beth Israel Deaconess Medical Center's intensive care units between 2001 and 2007 are included in this database's first version, MIMIC-II. Clinical data and physiological data make up MIMIC-II's two main parts. Physiological data are digital data produced by electronic device signals recorded for vital signs during the patient's stay in intensive care. Clinical data in the database are organized to include data such as the patient's demographic information, intravenous drug administration rates, and laboratory test results [31]. The MIMIC III dataset includes Beth Israel Deaconess Hospital intensive care unit patients from 2001 to 2012 [20]. The extensive MIMIC III database contains details on individuals older than 16 who are admitted to intensive care units. The data comprises vital signs, medications, lab findings, observations and remarks made by medical personnel, fluid balance, procedure and diagnosis codes, imaging reports, length of hospital stay, survival rates, and demographic information. For specialists doing various studies on intensive care research, from the creation of clinical decision support algorithms to a better comprehension of retrospective clinical investigations, the MIMIC-II and MIMIC-III databases are crucial sources of data.

Despite advances in disease identification and treatment, the rate of mechanical ventilation, sepsis infection and mortality in intensive care units have been growing recently [12,29,32,33]. Globally, deaths in intensive care units are seen as a severe health concern. The onset of disease symptoms in intensive care units of patients at high risk of death, diagnosis with methods with low predictive accuracy, and time-consuming access to laboratory data cause the risk of death to reach its highest level. For this reason, various machine learning models have been developed using data obtained from physicians' risk indicators in intensive care patients. Therefore, earlier disease detection and prediction lead to quicker recovery and better results [34].

3. METHOD

Ensemble learning [18] is one of the most effective techniques for a successful ML model. In ensemble learning, multiple learner objects are created and trained to solve the problem. Basic learners can be decision trees from training data. Ensemble learning, which consists of decision trees, can be performed in the form of bagging. In bagging ensemble learning [35], the ML model is trained with a randomly selected subset of the data. In this approach, the classification is made by voting the outputs of the basic learners. RFC, RFC-based WRF and BRF are the bagging ensemble learning-based models that were used in the study.

3.1. Random Forest Classifier (RFC)

One of the decision tree-based bagging models is the RFC model [36]. RFC is made up of decision trees that act as a community, making judgments based on a variety of sub-decisions and defending one another from individual mistakes. Each decision tree has nodes representing the features in the dataset and leaves representing the algorithm's decisions [19]. Nodes are decided by selecting from the

dataset the features to be applied to train the current tree. The model makes sure that the attributes to be used in the nodes for each tree are randomly chosen in order to maintain diversity while minimizing the correlation between trees. The quality of the node separation for each attribute can be evaluated using either the entropy gain or the Gini index, but doing so can entail the risk of misclassification [37].

The RFC method consists of two steps: creating the trees and selecting the decision tree. The initial step is to create decision trees using any randomly chosen model component from the training dataset. After receiving votes from the numerous decision trees in the test set, the final choice is determined in the last phase. The RFC algorithm is shown schematically in Figure 1 [38]. As represented in the figure, the dataset is separated into training and test sets. The RFC model generates the decision trees with the instances in the training set by using the features as random nodes which allows the model to learn the classes with patterns. The algorithm evaluates the test data by the constructed decision trees during training. It categorizes test data according to the most votes from the decision trees. The pseudo code of the algorithm is represented below in which 'X', 'y' and, 'n_estimators' represent the input features, the corresponding target labels, and the number of trees (number of iterations), respectively.

Algorithm 1: Random Forest Classifier

Initialize with a number of trees (n_estimators)

Train the model:

for each tree in n_estimators:

 Create a decision tree using some data (X, y)

 Add the tree to the ensemble

Make predictions:

for each tree in the ensemble:

 Get predictions from the tree

Combine the tree predictions to make a final prediction

The RFC model has many advantages over other ML techniques. One of the main problems in the application of ML models is that the model, which is defined as overfitting, cannot correctly classify data outside the training set. The RFC method is resistant to over-learning because it has a forest of decision trees. Since the importance of each feature in the decision-making process can be calculated, the model can be interpreted and the relationship between the features used and the decisions can be recognized more clearly. The application of the RFC model has the potential to produce successful results for particle identification and event selection [37,38].

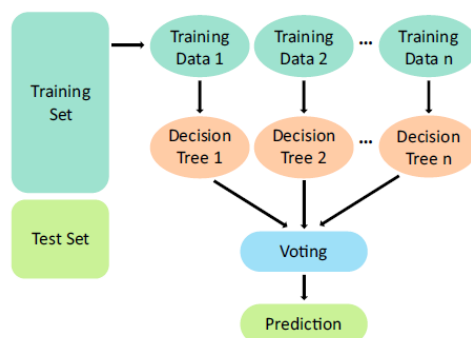


Figure 1. Schematic representation of the RFC classification model [38]. The dataset is divided into training and testing. The algorithm constructs the decision trees with the examples in the training set by using the features in the data as random nodes. It is ensured that the model learns about classes with patterns. Evaluates the completed RFC test dataset according to the created decision trees. It classifies the model test data according to the category with the most votes from the decision trees.

3.2. Weighted Random Forest (WRF)

The WRF model is a class-weighted RFC model adapted to manage groups of different sizes in the dataset. The ARO method was developed to increase the success of the RFC algorithm on skewed datasets [39]. In this model, in order to reduce the effect of majority samples in the dataset on learning and to increase the learning of the minority group, a weight inversely proportional to the size of the classes in the dataset is used in the nodes and predictions of the decision trees in the model [39]. The pseudo code of the WRF is shown in the following where ‘X’, ‘y’ and, ‘n_estimators’ represent the input features, the corresponding target labels, and the number of trees (number of iterations), respectively.

Algorithm 2: Weighted Random Forest

Initialize with a number of trees (n_estimators)

Train the model:

for each tree in n_estimators:

 Create a decision tree using some data (X, y) and consider sample weights

 Add the tree to the ensemble

Make predictions:

for each tree in the ensemble:

 Get predictions from the tree

Combine the tree predictions to make a final prediction

This method has attracted great interest for the classification of data, which often has data imbalances. Unlike the current random forest method, class weights are based on the assignment of separate weights for each class, rather than a single weight. With high accuracy in categorizing majority and minority classes, this recommended approach provides a solution to the problem of classifying between majority and minority classes for unbalanced medical data. It also shows that it improves the overall performance of the classifier.

3.3. Balanced Random Forest (BRF)

The BRF technique is another version of the RFC model developed for skewed datasets. BRF applies a subsampling technique for each decision tree generation process in the RFC algorithm. This is why it is known as the Balanced Random Forest because it combines the sampling technique with the idea of an ensemble where unbalanced data processing becomes an algorithmic process. In the BRF algorithm, the size of the majority group in the dataset is determined randomly and in accordance with the minority group size. The classifier tackles imbalanced data by creating decision trees that are sensitive to both majority and minority classes. For the majority class, it employs balanced sampling, ensuring a representative subset of majority class instances in each tree. For the minority class, it ensures that all minority class instances are included. This approach leads to decision trees that can capture relevant patterns in the minority class while maintaining a fair balance with the majority class, ultimately resulting in a more equitable and accurate classification of both classes when combined in the forest. The pseudo code of the BRF is illustrated below where 'X', 'y' and, 'n_estimators' represent the input features, the corresponding target labels, and the number of trees (number of iterations), respectively.

Algorithm 3: Balanced Random Forest

Initialize with a number of trees (n_estimators)

Train the model:

for each tree in n_estimators:

 Create a balanced training sample from the data (X, y)

 Create a decision tree using the balanced sample

 Add the tree to the ensemble

Make predictions:

for each tree in the ensemble:

 Get predictions from the tree

Combine the tree predictions to make a final prediction

There are studies in the literature comparing the recall or sensitivity of its performance which revealed that BRF performed better than the Random Forest algorithm [40,41]. Although there are studies in which RF's ensemble learning algorithm is applied to unbalanced data for classification [42], it is known that BRF offers a better approach to the classification problem in these unbalanced data with

multiple classification problems [40]. The computational efficiency of BRF over WRF for skewed data was also demonstrated by Chen et al. [39].

4. ANALYSIS

In the analysis, MIMIC-III dataset were studied to investigate the impact of the features on mortality prediction of RFC based ML models. In addition, different groups of features were used in each method application to understand the effect of various categorical properties on decisions of the machine learning algorithms.

4.1. Dataset

MIMIC-III, a substantial and openly accessible database, contains health-related data devoid of personal identification for over 40,000 patients who received care within critical care units at the Beth Israel Deaconess Medical Center from 2001 to 2012 [20]. The following information was included as a feature in the analysis by taking into account prior studies [43,44,45,46], clinical relevance, and available data: comorbidities (hypertension, atrial fibrillation, ischemic heart disease, diabetes mellitus, depression, hypoferric anemia, hyperlipidemia, chronic kidney disease (CKD), and chronic obstructive pulmonary disease [COPD]); and laboratory variables (hematocrit, red blood cells, mean corpuscular hemoglobin [MCH], mean corpuscular hemoglobin concentration [MCHC], mean corpuscular volume [MCV], red blood cell distribution width [RDW], platelet count, white blood cells, neutrophils, basophils, lymphocytes, prothrombin time [PT], international normalized ratio [INR], NT-proBNP, creatine kinase, creatinine, blood urea nitrogen [BUN] glucose, potassium, sodium, calcium, chloride, magnesium, the anion gap, bicarbonate, lactate, hydrogen ion concentration [pH], partial pressure of CO₂ in arterial blood, and LVEF) [47]. The dataset includes demographic information like age, gender, and body mass index (BMI) at admission, as well as vital indicators including heart rate (HR) systolic blood pressure [SBP], diastolic blood pressure [DBP] respiration rate, body temperature, saturation pulse oxygen [SPO₂], and urine output in the first 24 hours [47]. The description of each feature is represented in Table 1 [48].

Table 1. The description of each feature used in the analysis [48].

Name	Description	Unit	Min	Max
age	Patient age	years	0	100
basos	basophils	%	0	50
bicar	bicarbonate	mEq/L	5	50
bmi	body mass index	kg/m ²	18.5	24.9
bun	Blood urea nitrogen	mg/dL	0	200
ca	calcium	mg/dL	4	20
ck	Creatine kinase	IU/L	0	-
cl	chloride	mEq/L	80	130
crea	creatinine	mg/dL	0	15
dbp	Diastolic blood pressure	mmHg	0	200
gender/ sex	patient sex	-	-	-

glu	glucose	mg/dL	0	1000
hct	hematocrit	%	15	60
hgb	hemoglobin	g/dL	4	18
hr	Heart rate	bpm	0	300
inr	international normalized ratio	prothrombin time/international normalized ratio	-	-
k	potassium	mEq/L	0	10
lact	lactate	Mmol/L	0	50
mg	magnesium	mg/dL	0.5	5
lvef	left ventricular ejection fraction	%	52	72
mch	mean corpuscular hemoglobin	pg	0	-
mchc	mean corpuscular hemoglobin concentration	%	20	50
mcv	mean corpuscular volume	fL	50	150
na	sodium	mEq/L	110	165
neut	neutrophils	%	0	100
NT-proBNP	N-terminal pro-B-type natriuretic peptide	pg/mL	0	100
spo2	Oxygen saturation	%	50	100
pco2	partial pressure of CO2 in arterial blood	mmHg	10	150
pH	hydrogen ion concentration	-	6.8	8
plt	platelet count	K/uL	5	1200
pt	prothrombin time	sec	0	-
rbc	red blood cells	m/uL	0	20
rdw	red blood cell distribution width	%	0	100
resp	respiration rate	insp/min	0	120
sbp	systolic blood pressure	mmHG	0	300
temp	temperature	C	32	42
urine	urine output	mL	0	2000
wbc	white blood cells	K/uL	0	-
hp	hypertension	mmHg	90/60	120/80
A-Fib	atrial fibrillation	dk	60	100
ihd	ischemic heart disease	mmol/L	1.20	1.62
iddm	diabetes mellitus	mg/dL	0	100
bdi	Depression (Beck Depression Inventory)	-	-	-
hwa	hypoferric anemia	ng/mL	11	-
hdl	hyperlipidemia	mg/dL	0	200
ckd	chronic kidney disease (CKD)	mL/min	60	-
copd	chronic obstructive pulmonary disease [COPD]	%	88	92

For the analysis, the information of the patients having missing value was removed from the dataset. In the study, 428 records including information of 65 dead (15% of the dataset) and 363 (85% of the dataset) alive patients were analysed with 48 features and outcome information which represents mortality conditions. Table 2 explains the number of instances for each class in total, train and test dataset which indicates that each group has 15% mortality samples.

Table 2. Mortality and alive class sizes for total, train, and test datasets.

Dataset	Total	Train	Test
Alive Class	363	292	71
Mortality Class	65	50	15

4.2. Application of Ensemble Learning

In the analysis, WRF, and BRF algorithms were used to analyze the mortality condition of the patients by using three different feature group. In addition, RFC algorithm was also implemented to compare its performance with its improved versions for imbalanced data. In group 1 all features given in the dataset were utilized by the algorithms as properties to predict the condition of the patient. In group 2 only comorbidities were considered as features by the models. In group 3 laboratory variables with vital signs were used as features by the methods. In all feature groups, demographic characteristics were included. In all models 100 trees (number of iteration) were used [49], and the quality of the node separation was preferred “Gini” for all algorithms. In WRF, the parameter used for setting the class weights was set to ‘balanced’ which modifies the weights inversely proportional to class instances in the input data [50]. Due to the structure of the data 80% of the data was selected for training and the rest for the test.

Figures 2, 3, and 4 represent the significance of features in RFC, WRF, and BRF across three distinct groups. Analyzing the outcomes of models used group 1 features, it is evident that apart from age, vital attributes exert minimal influence on the algorithms. Additionally, the relevance of comorbidity information in group 1 is below 2%. The comparison of feature importance within group 1 leads to the observation that similar attributes wield a shared impact on algorithmic decisions. Plot illustrations concerning group 2 reveal that ‘age’ and ‘bmi’ emerge as dominant features across all algorithms. Interestingly, comorbidity features exerted a modest influence on models, accounting for less than 10%. Analysis of feature importance plots within group 3 suggests that ‘urine output’ is the pivotal feature in BRF and WRF algorithms, while ‘bmi’ and ‘age’ consistently affect decision mechanisms in all models. Notably, gender information held negligible importance in the decision algorithms across all group analyses.

5. RESULTS AND DISCUSSIONS

In the study, sensitivity or recall, precision, and F1 score, performance metrics of the ML, were used for the comparison of model performances by considering the class sizes in which the mortality and alive information were labeled as positive class (signal class) and negative class, respectively. In addition, AUC ROC [51] values were also determined to assess the discrimination power of the algorithms for unbalanced datasets [52,53].

5.1. Performance Metrics

Sensitivity (recall), precision, and F1 score values will be determined using parameters found in the confusion matrix, a table of the real class information in the dataset against the ML model predictions, obtained as a result of the ML model application [54,55]. Recall or sensitivity is used to calculate the percentage of fatalities that may have been accurately predicted, by Equation (1).

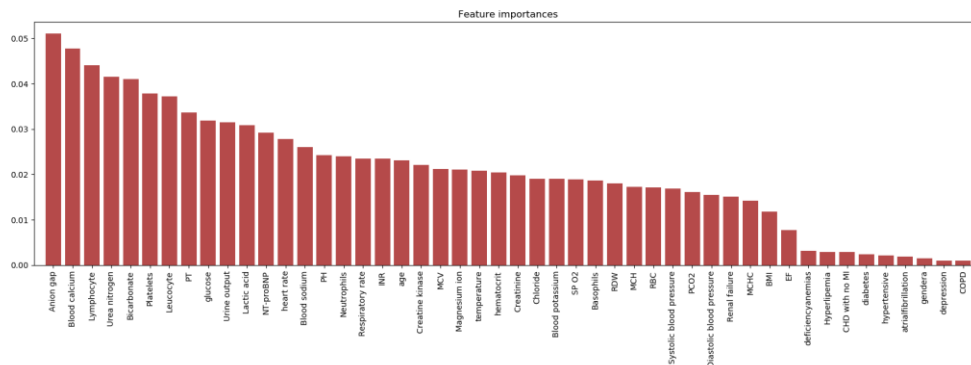
$$\text{Sensitivity} = TP / (TP + FN) \tag{1}$$

In Equation (1), The values for TP and FN correspond to the proportion of information that was mistakenly categorized as alive and correctly classified as mortality, respectively. The expression "precision" is used to describe the accuracy of the predictions made by the model using Equation (2) in which FP represents misclassified mortality samples.

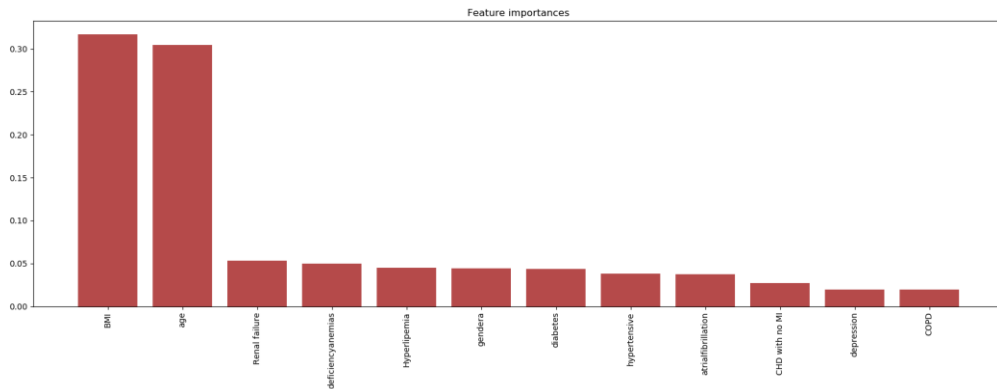
$$\text{Precision} = TP / (TP + FP) \tag{2}$$

The harmonic mean of sensitivity and precision, known as the F1 score, allows for a comprehensive two-sided evaluation of the model represented in Equation (3).

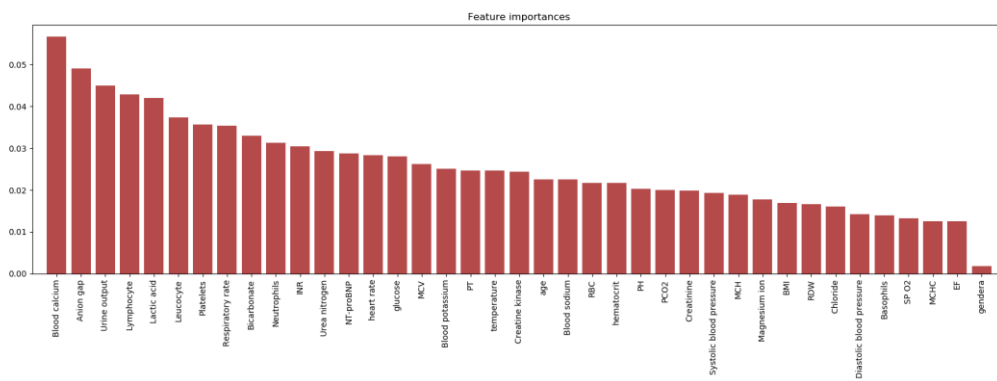
$$\text{F1 score} = (2 * \text{Precision} * \text{Recall}) / (\text{Precision} + \text{Recall}) \tag{3}$$



(a) Feature Group 1

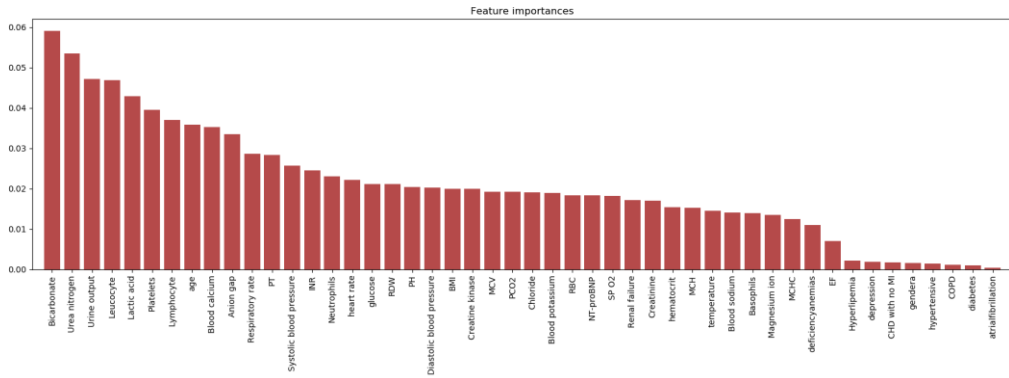


(b) Feature Group 2

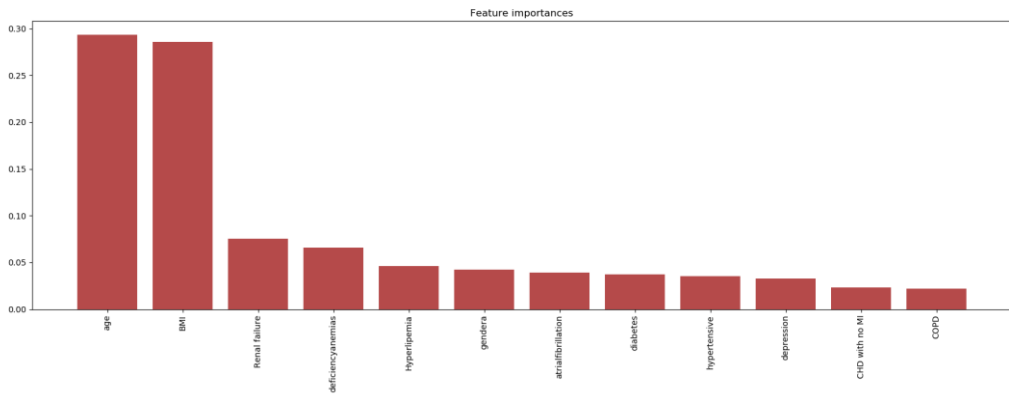


(c) Feature Group 3

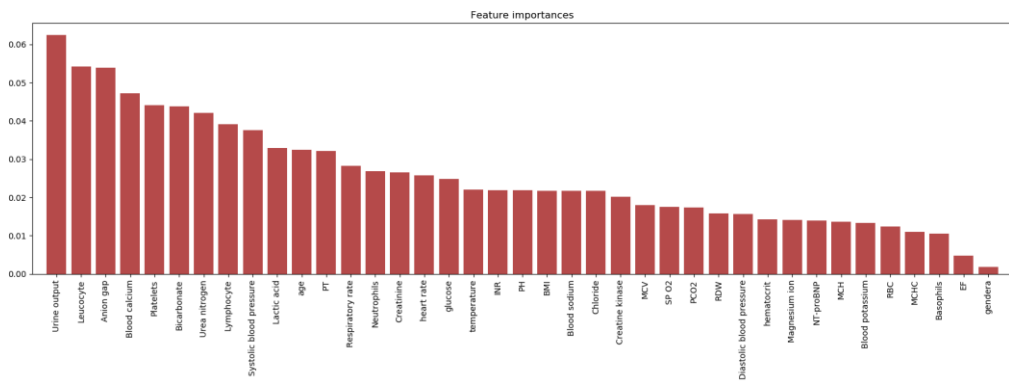
Figure 2. The feature importance in RFC for three feature groups.



(a) Feature Group 1

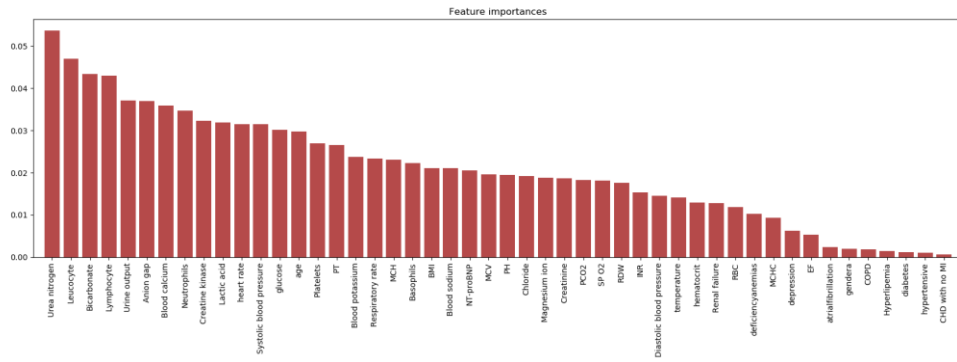


(b) Feature Group 2

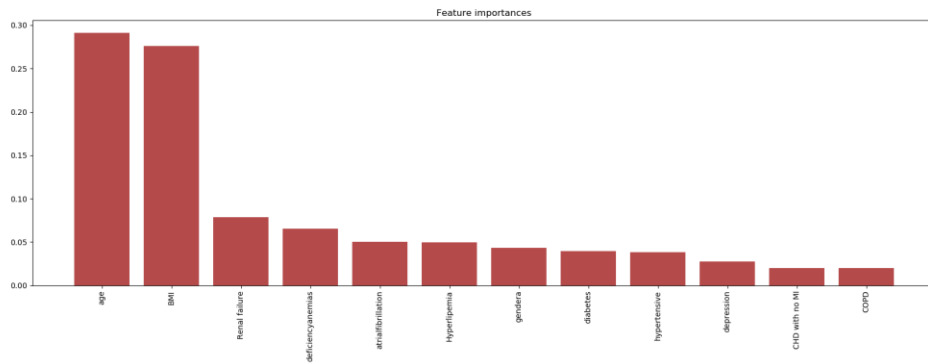


(c) Feature Group 3

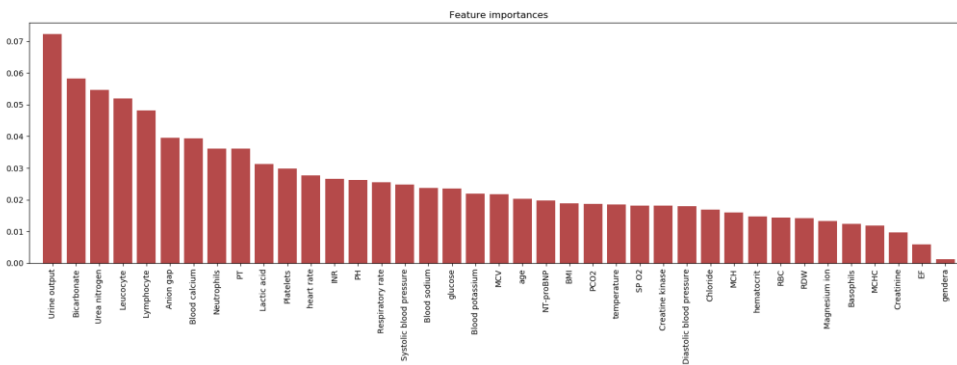
Figure 3. The feature importance in WRF for three feature groups.



(a) Feature Group 1



(b) Feature Group 2



(c) Feature Group 3

Figure 4. The feature importance in BRF for three feature groups.

The Receiver Operating Characteristic Curve (ROC) curve, one of the most important metrics in machine learning, illustrates the relationship between the rate of misclassified positive classes and the rate of mortality instances. The method includes several criteria to identify model performance. The ROC curve is based on determining (iii) two-dimensional graphs of (i) sensitivity or recall and (ii) “false positive rate (FPR=FP/(FP+TN) where TN is correctly categorized alive class.)” criteria and (iv) calculating the area under the curve (AUC ROC). An indicator of how well a metric can discriminate between two diagnostic classes is the area under the ROC curve (AUC ROC). AUC ROC is a measure of how well two classes can be distinguished by the model. A high AUC ROC value signifies an improvement in the model's ability to differentiate between mortality and alive classes [52,53]. If the values of F1 score, and AUC ROC close to 1, that means the model is a perfect classifier [54]. Accuracy, another performance evaluation metric of the ML model, was not used in the analysis since it might not provide sufficient information about the success of models applied to datasets with imbalanced classes [39,40,41].

5.2. Evaluation of Model Performances

Table 2 represents RFC, WRF, and BRF weighted performances by implementing three different features in the algorithms to find the mortality from MIMIC-III dataset with AUC ROC values. The model performances can be comprehended by closeness of each metric to the value 1. For an ideal case, perfect classifier exhibits the maximum performance scores, 1. For performance comparison of machine learning models, the algorithm is outperformed if the scores are higher than the rest. The AUC ROC score implies the success of the algorithm and precision score represents how well the model categorizes the classes. According to the table, 88.095% of BRFs that used group 3 attributes were able to accurately identify mortality at 90.814%. A higher F1 score indicates better model performance which is BRF model using Group 3 features. The table illustrates how all algorithms have low success rates when comorbidities are taken into account as features. The results exhibited that even if RFC is not modified for the dataset its achievement is very close to the improved versions when the discriminative features were used. In general usage of Group 3 features enables all the algorithms to find each class with high precision. The results confirm that BRF handles imbalanced data by training its decision trees in a way that gives equal importance to both the majority and minority classes, ensuring a fair and accurate classification for both.

Table 2. Table of RFC, WRF, and BRF model performances. The performance metrics' top scores are shown in bold.

Model	Feature Group	Precision	Recall	F-1 score	AUC ROC
RFC	Group 1	0.86773	0.87209	0.84850	0.65962
	Group 2	0.80349	0.83721	0.80894	0.58631
	Group 3	0.88064	0.86047	0.81939	0.60000
WRF	Group 1	0.78904	0.83721	0.78242	0.52877
	Group 2	0.77829	0.82558	0.78940	0.55060
	Group 3	0.89756	0.88372	0.84587	0.58333
BRF	Group 1	0.86893	0.73256	0.77716	0.71842
	Group 2	0.77054	0.65116	0.69279	0.59028

Group 3	0.90814	0.84884	0.86390	0.88095
---------	----------------	---------	----------------	----------------

6. CONCLUSIONS

In recent years, digital health record system data has become a valuable research area for data analysis with ML approach. It is thought that machine learning (ML) approaches will provide solutions to the issues brought on by a lack of evidence in their application domains by improving the accessibility of large-scale medical datasets. In addition, potential patients who can be treated are given the opportunity to better predict events such as heart attacks and death in intensive care using machine learning methods. Thanks to mortality estimates, hospitals can now more accurately anticipate resource needs, properly identify illnesses, and decide whether a patient needs additional care before it's too late. [55,56].

In the present study, compared to RFC and WRF models, the results of BRF algorithm in which the laboratory variables with vital signs were used showed the highest performance for the morality determination. RFC approach in general provides the best prediction performance in previous studies, however, due to the data structure BRF, the improved version of RFC for imbalanced data, demonstrated higher success than it. WRF model, another version of RFC in which the class weights were arranged, did not show better discrimination power compared to the other models. From the results of models using different features, it can be concluded that comorbidities and gender information did not affect the morality determination. Class imbalance in the classification of medical data is a problem that is currently being studied and has to be solved. In the study, an algorithm (BRF) is proposed to be used in handling imbalanced and limited medical data. BRF, an improved version of one of the successful ensemble learning algorithms RFC, addresses class imbalance by constructing decision trees in a way that ensures balanced representation of minority and majority classes in each tree's training subset. Considering the values of BRF assessment metrics such as AUC ROC and F-1 score, the model is promising to be used in unbalanced medical data analysis.

ACKNOWLEDGEMENTS

The author is grateful to the MIMIC-III Clinical Database for making the data platform free to use for researchers and other academics in educational institutions.

REFERENCES

- [1] Hanson III, C. W., & Marshall, B. E. (2001). Artificial intelligence applications in the intensive care unit. *Critical care medicine*, 29(2), 427-435.
- [2] Yang, W., Zou, H., Wang, M., Zhang, Q., Li, S., & Liang, H. (2023). Mortality prediction among ICU inpatients based on MIMIC-III database results from the conditional medical generative adversarial network. *Heliyon*, 9(2).

- [3] Dybowski, R., Gant, V., Weller, P., & Chang, R. (1996). Prediction of outcome in critically ill patients using artificial neural network synthesised by genetic algorithm. *The Lancet*, 347(9009), 1146-1150.
- [4] Gortzis, L. G., Sakellaropoulos, F., Ilias, I., Stamoulis, K., & Dimopoulou, I. (2008). Predicting ICU survival: a meta-level approach. *BMC health services research*, 8, 1-8.
- [5] Karun, K. M., Puranik, A., Lintu, M. K., & Deepthy, M. S. (2023). Risk factors of pneumonia among elderly with robust Poisson regression-A study on mimic III data. *Biomedicine*, 43(02), 696-700.
- [6] Data, M. C., & Pirracchio, R. (2016). Mortality prediction in the icu based on mimic-ii results from the super icu learner algorithm (sicala) project. *Secondary Analysis of Electronic Health Records*, 295-313.
- [7] Eya, J., Ejikem, M., Ogamba, C., & Ogamba, C. M. (2022). Admission and Mortality Patterns in Intensive Care Delivery at Enugu State University of Science and Technology Teaching Hospital: A Three-Year Retrospective Study. *Cureus*, 14(7).
- [8] Aydin, Z. E., & Ozturk, Z. K. (2021). Prediction Length of Stay in Intensive Care Unit in the Presence of Missing Data. *Artificial Intelligence Theory and Applications*, 1(2), 48-53.
- [9] Liu, J., Wu, J., Liu, S., Li, M., Hu, K. & Li, K. (2021) Predicting mortality of patients with acute kidney injury in the ICU using XGBoost model. *PLoS One*, 16(2). doi: 10.1371/journal.pone.0246306
- [10] Leung, W. K., Cheung, K. S., Li, B., et al. (2021) Applications of machine learning models in the prediction of gastric cancer risk in patients after *Helicobacter pylori* eradication. *Aliment Pharmacol Ther*, 53 (8), 864– 872.
- [11] Pang, X., Forrest, C. B., Lê-Scherban, F., Masino, A. J. (2021) Prediction of early childhood obesity with machine learning and electronic health record data. *International Journal of Medical Informatics*. 150, 104454. <https://doi.org/10.1016/j.ijmedinf.2021.104454>.
- [12] Silahatoglu, G., & Canbolat, Z. N. (2020). An early prediction and diagnosis of sepsis in intensive care units: An unsupervised machine learning model. *Mugla Journal of Science and Technology*, 6(1), 32-40.
- [13] Poucke, S. V., Zhang, Z., Schmitz, M., Vukicevic, M., Laenen, M. V., Celi, L. A., & Deyne, C. D. (2016). Scalable predictive analysis in critically ill patients using a visual open data analysis platform. *PloS one*, 11(1), e0145791

- [14] Churpek, M. M., Yuen, T. C., Winslow, C., Meltzer, D. O., Kattan, M. W., & Edelson, D. P. (2016). Multicenter comparison of machine learning methods and conventional regression for predicting clinical deterioration on the wards. *Critical care medicine*, 44(2), 368.
- [15] Xia, F., Zhang, J., Meng, S., Qiu, H., & Guo, F. (2021). Association of frailty with the risk of mortality and resource utilization in elderly patients in intensive care units: a meta-analysis. *Frontiers in Medicine*, 8, 637446.
- [16] Dybowski, R., Gant, V., Weller, P., & Chang, R. (1996). Prediction of outcome in critically ill patients using artificial neural network synthesised by genetic algorithm. *The Lancet*, 347(9009), 1146-1150.
- [17] Kim, S., Kim, W., & Park, R. W. (2011). A comparison of intensive care unit mortality prediction models through the use of data mining techniques. *Healthcare informatics research*, 17(4), 232-243.
- [18] Lin, W., Wu, Z., Lin, L., Wen, A., & Li, J. (2017). An ensemble random forest algorithm for insurance big data analysis. *Ieee access*, 5, 16568-16575.
- [19] Yalcin Kuzu, S. (2023). Random Forest Based Multiclass Classification Approach for Highly Skewed Particle Data. *Journal of Scientific Computing*, 95(1), 21.
- [20] Johnson, A., Pollard, T., & Mark, R. (2019). MIMIC-III Clinical Database Demo (version 1.4). PhysioNet. <https://doi.org/10.13026/C2HM2Q>.
- [21] Scheunert, G., Heinonen, O., Hardeman, R., Lapicki, A., Gubbins, M., & Bowman, R. M. (2016). A review of high magnetic moment thin films for microscale and nanotechnology applications. *Applied Physics Reviews*, 3(1).
- [22] Chandola, V., Banerjee, A., & Kumar, V. (2009). Anomaly detection: A survey. *ACM computing surveys (CSUR)*, 41(3), 1-58.
- [23] Salo, F., Injadat, M., Nassif, A. B., Shami, A., & Essex, A. (2018). Data mining techniques in intrusion detection systems: A systematic literature review. *IEEE Access*, 6, 56046-56058.
- [24] Krawczyk, B., Galar, M., Jeleń, Ł., & Herrera, F. (2016). Evolutionary undersampling boosting for imbalanced classification of breast cancer malignancy. *Applied Soft Computing*, 38, 714-726.
- [25] Vuttipittayamongkol, P., & Elyan, E. (2020). Improved overlap-based undersampling for imbalanced dataset classification with application to epilepsy and parkinson's disease. *International journal of neural systems*, 30(08), 2050043.

- [26] Elyan, E., Jamieson, L., & Ali-Gombe, A. (2020). Deep learning for symbols detection and classification in engineering drawings. *Neural networks*, 129, 91-102.
- [27] Zhang, X., Zhuang, Y., Wang, W., & Pedrycz, W. (2016). Transfer boosting with synthetic instances for class imbalanced object recognition. *IEEE transactions on cybernetics*, 48(1), 357-370.
- [28] Tabakoglu, N., & Volkan, I. N. A. L. (2021). Evaluation of Basic Parameters for Prediction of ICU Mortality. *Journal of Critical and Intensive Care*, 12(2), 47.
- [29] Altun, G. T., Arslantas, M. K., Dincer, P. C., Arslantas, R., & Kararmazf, A. (2022). Prognostic value of the lactate–albumin difference for predicting in-hospital mortality in critically ill patients with sepsis. *Marmara Medical Journal*, 35(1), 61-66.
- [30] Harutyunyan, H., Khachatryan, H.D., Kale, C., Ver Steeg, G., Galstyan, A., (2019). “Multitask learning and benchmarking with clinical time series data,” *Sci. Data*, vol. 6, no. 1, p. 96.
- [31] Saeed, M., Villarroel, M., Reisner, A. T., Clifford, G., Lehman, L. W., Moody, G., ... & Mark, R. G. (2011). Multiparameter Intelligent Monitoring in Intensive Care II (MIMIC-II): a public-access intensive care unit database. *Critical care medicine*, 39(5), 952.
- [32] Vincent, J. L., Moreno, R., Takala, J., Willatts, S., De Mendonça, A., Bruining, H., ... & Thijs, L. G. (1996). The SOFA (Sepsis-related Organ Failure Assessment) score to describe organ dysfunction/failure: On behalf of the Working Group on Sepsis-Related Problems of the European Society of Intensive Care Medicine (see contributors to the project in the appendix).
- [33] LaFaro, R. J., Pothula, S., Kubal, K. P., Inchiosa, M. E., Pothula, V. M., Yuan, S. C., ... & Inchiosa Jr, M. A. (2015). Neural network prediction of ICU length of stay following cardiac surgery based on pre-incision variables. *PLoS One*, 10(12), e0145395.
- [34] Ahmad, R. (2021). The role of digital technology and artificial intelligence in diagnosing medical images: a systematic review. *Open Journal of Radiology*, 11(01), 19.
- [35] Aduszkiewicz, A., Ali, Y., Andronov, E., Antičić, T., Antoniou, N., Baatar, B., ... & Wojtaszek-Szwarc, A. (2017). Two-particle correlations in azimuthal angle and pseudorapidity in inelastic p+ p interactions at the CERN Super Proton Synchrotron. *The European Physical Journal C*, 77, 1-15.
- [36] Breiman, L. (2001). Random forests. *Machine learning*, 45, 5-32.

- [37] Trzciński, T., Graczykowski, Ł., Glinka, M., & ALICE Collaboration. (2020). Using random forest classifier for particle identification in the ALICE experiment. In *Information Technology, Systems Research, and Computational Physics 3* (pp. 3-17). Springer International Publishing.
- [38] Yalcin Kuzu, S. (2022). J/ψ production with machine learning at the LHC. *The European Physical Journal Plus*, 137(3), 392.
- [39] Chen, C., Liaw, A., & Breiman, L. (2004). Using random forest to learn imbalanced data. University of California, Berkeley, 110(1-12), 24.
- [40] Agusta, Z. P. (2019). Modified balanced random forest for improving imbalanced data prediction. *International Journal of Advances in Intelligent Informatics*, 5(1), 58-65.
- [41] Khalilia, M., Chakraborty, S., & Popescu, M. (2011). Predicting disease risks from highly imbalanced data using random forest. *BMC medical informatics and decision making*, 11, 1-13.
- [42] Amin, M., & Ali, A. (2018). Performance evaluation of supervised machine learning classifiers for predicting healthcare operational decisions. Wavy AI Research Foundation: Lahore, Pakistan, 90.
- [43] Fonarow, G. C., Adams, K. F., Abraham, W. T., Yancy, C. W., Boscardin, W. J., & ADHERE Scientific Advisory Committee. (2005). Risk stratification for in-hospital mortality in acutely decompensated heart failure: classification and regression tree analysis. *Jama*, 293(5), 572-580.
- [44] Peterson PN, Rumsfeld JS, Liang L, et al. A validated risk score for in-hospital mortality in patients with heart failure from the American heart association get with the guidelines program. *Circ Cardiovasc Qual Outcomes* 2010;3:25–32.
- [45] Kipnis, E., Ramsingh, D., Bhargava, M., Dincer, E., Cannesson, M., Broccard, A., ... & Thibault, R. (2012). Monitoring in the intensive care. *Critical care research and practice*, 2012.
- [46] Wang, N., Gallagher, R., Sze, D., Hales, S., & Tofler, G. (2019). Predictors of frequent readmissions in patients with heart failure. *Heart, Lung and Circulation*, 28(2), 277-283.
- [47] Web ref: Zhou, Jingmin et al. (2021), Prediction model of in-hospital mortality in intensive care unit patients with heart failure: machine learning-based, retrospective analysis of the MIMIC-III database, Dryad, Dataset, <https://doi.org/10.5061/dryad.0p2ngf1zd>
- [48] Bennett, N. (2021). Enabling External Validation for Machine Learning Applications Using Intensive Care Data (Doctoral dissertation, ETH Zurich).

- [49] Probst, P., & Boulesteix, A. L. (2017). To tune or not to tune the number of trees in random forest. *The Journal of Machine Learning Research*, 18(1), 6673-6690.
- [50] Pedregosa, F., Varoquaux, G., Gramfort, A., Michel, V., Thirion, B., Grisel, O., ... & Duchesnay, É. (2011). Scikit-learn: Machine learning in Python. *the Journal of machine Learning research*, 12, 2825-2830.
- [51] Narsky, I., Porter, F.C., (2014). *Statistical Analysis Techniques in Particle Physics*, Almanyay:Wiley–VCH.
- [52] Jeni, L. A., Cohn, J. F., & De La Torre, F. (2013, September). Facing imbalanced data--recommendations for the use of performance metrics. In *2013 Humaine association conference on affective computing and intelligent interaction* (pp. 245-251). IEEE.
- [53] Bauder, R., & Khoshgoftaar, T. (2018, July). Medicare fraud detection using random forest with class imbalanced big data. In *2018 IEEE international conference on information reuse and integration (IRI)* (pp. 80-87). IEEE.
- [54] Müller A. C., Guido, S., (2016). *Introduction to Machine Learning with Python*, O'Reilly Media Inc., Amerika: Sebastopol Kaliforniya.
- [55] Ilhan Taskin, Z., Yildirak, K., & Aladag, C. H. (2023). An enhanced random forest approach using CoClust clustering: MIMIC-III and SMS spam collection application. *Journal of Big Data*, 10(1), 38.
- [56] Zhu, M., Xia, J., Jin, X., Yan, M., Cai, G., Yan, J., & Ning, G. (2018). Class weights random forest algorithm for processing class imbalanced medical data. *IEEE Access*, 6, 4641-4652.